University of Alberta
Department of Civil &
Environmental Engineering

Structural Engineering Report No. 237

CRITICAL BUCKLING STRAINS FOR ENERGY PIPELINES

by
A.B. Dorey
J.J.R. Cheng
and
D.W. Murray

April 2001

CRITICAL BUCKLING STRAINS IN ENERGY PIPELINES

Alfred B. Dorey

J. J. Roger Cheng

and

David W. Murray

Structural Engineering Report No. 237

Department of Civil and Environmental Engineering
University of Alberta
Edmonton, Alberta

April 2001

ABSTRACT

The research reported herein investigates the critical buckling strain of segments of energy pipeline subjected to combined loads. Critical buckling strain equations from literary sources, including the current Canadian Standard, were evaluated using previously collected U of A test results. All of the equations investigated did a poor job of modeling the U of A experimental data. This indicates that there is a need to develop new equations with better predictive abilities.

This research is divided into three parts. The first part involves expanding the current experimental database for segments of energy pipeline at the University of Alberta by testing specimens with a diameter-to-thickness (D/t) ratio of 92 under combined axial load, internal pressure and increasing monotonic curvature. The influence of a circumferential girth weld was also investigated. Initial imperfections present in the segments of line pipe were investigated, including the development of a technique for quantify them.

The second part of this research was the development and validation of a finite element analysis (FEA) model to predict the observed global and local experimental behaviour. The FEA model was explicitly developed to predict the behaviour of the experimental specimens with the D/t ratio of 92 tested in part 1 and was capable of incorporating initial imperfection patterns. Further validation of the FEA model was done using previously collected experimental data from the U of A for specimens with D/t ratios of 51 and 64.

The final part of this research was to develop new critical buckling strain equations. Once the FEA model was validated, critical parameters that influence the critical buckling strain for energy pipelines were identified and a typical range for each parameter was selected based on the limits of the experimental database. A parametric study examining the effects of each of these parameters was conducted. The results of the parametric study were used to develop critical buckling strain equations that account for each of the different influencing parameters. The proposed equations were then validated with critical buckling strains from data sources external to the U of A to validate their predictive ability.

ACKNOWLEDGEMENTS

This study was conducted with the financial assistance of the Natural Sciences and Engineering Research Council of Canada (NSERC) under strategic grant STR19802. I would like to acknowledge the valuable financial and technical assistance received on this project from our industrial sponsors Enbridge Pipelines Inc., TransCanada PipeLines Limited, and Westcoast Energy Inc. In particular, I would like to thank Dr. Z. (Joe) Zhou for his expertise, advice and direction on both the technical and practical sides of this study and for supplying the test specimens used in this investigation. I would also like to thank Mr. Rob Lindemann at the TransCanada Fabrication shop in Spruce Grove, Alberta, for fabricating the specimens and providing the numerous welders who installed the specimens in the test set-up.

The guidance on typical line pipe material properties received from Dr. Laurie Collins of IPSCO Saskatchewan Inc., Mr. Dave Horsley of TransCanada PipeLines Limited, and Mr. Frank Sarko of WellandPipe was greatly appreciated.

At the U of A, I would like to thank the I. F. Morrison Laboratory Technicians for their help with the experimental portion of this project. In particular, I would like to acknowledge the inventive genius of Mr. Richard Helfrich, without which I would still be testing. I would also like to thank Dr. Gilbert Grondin and Dr. Alaa Elwi for their insightful and helpful comments, particularly in reference to ABAQUS and finite element modeling. The guidance and suggestions from Dr. H. Freedman of the Department of Mathematical Sciences on equation fitting was also appreciated.

I would like to acknowledge the contributions from previous students who assisted in the testing phase of this project, who developed previous FEA models as guides, and who collected most of the experimental critical strain used for validation of the FEA model developed in this project. Specifically, I would like to thank: Sreekanta Das, Pat Del Col, Christophe Deniaud, Jeff DiBattista, Magdi Mohareb, Brian Myrholm, Tarcisio Souza, Xu Yao, Amy Yip, and Nader Yoosef-Ghodsi.

TABLE OF CONTENTS

TABLE OF CONTENTS (cont.)

2.0 EXPERIMENTAL PROGRAM (cont.)

TABLE OF CONTENTS (cont.)

TABLE OF CONTENTS (cont.)

TABLE OF CONTENTS (cont.)

6.0 PARAMETRIC STUDY (cont.)

TABLE OF CONTENTS (cont.)

LIST OF TABLES

LIST OF TABLES (cont.)

Chapter 6

LIST OF FIGURES

LIST OF FIGURES (cont.)

LIST OF FIGURES (cont.)

LIST OF FIGURES (cont.)

LIST OF FIGURES (cont.)

LIST OF FIGURES (cont.)

LIST OF SYMBOLS AND ABBREVIATIONS

a	x-coordinate of the center of a circle
A	Cross sectional area of the pipeline
amp_{max}	Maximum amplitude of an initial imperfection
API	American Petroleum Institute
ASTM	American Society of Testing and Materials
b	y-coordinate of the center of a circle
CSA	Canadian Standard Association
C	Applied axial force
^{o}C	Degrees Celsius
$coor_{node\#}$	Distance from amp_{max} to the node at which imperfection is being determined
cos	Cosine function
C_y	Axial yield load under zero circumferential stress
d	Distance between end of specimen and pivot point
d'	Distance between near end of end plate and pivot point
D	Outside diameter of the pipeline
DSAW	Double submerged arc weld
e	Eccentricity of jack (1500 mm)
E	Modulus of elasticity of the pipeline material
Err	Error term for least squares fit
E_s	Modulus of elasticity used in CAN/CSA-Z662-96 = 207 000 MPa
FEA	Finite Element Analysis
F_f	CAN/CSA – Z662-96 design factor
F_u	Ultimate strength
F_y	Yield strength
G	Shear modulus (77 000 MPa for steel)
gw	Girth weld
I	Moment of inertia
Imp	Imperfection expressed as a percent of the wall thickness for blister-type initial imperfection pattern
$Imp_{node\#}$	Amplitude of the imperfection at a specified node number
IR_M	Measured inside radius taken from measured imperfection pattern
J_f	CAN/CSA – Z662-96 joint factor
k	Effective length factor
k_{lat}	Slope of the linear elastic region of the lateral stress-strain material curve
k_{long}	Slope of the linear elastic region of the longitudinal stress-strain material curve
kL/r	Slenderness ratio
kN	Units of kilonewtons
L	Length of specimen
L_{collar}	Length of confinement collars at the ends of the specimens
L_{cur}	Current (deformed) length between nodes corresponding to the Demec gauge span
L_e	Effective length
L_f	CAN/CSA – Z662-96 location factor
$L_{I.I.}$	Length of initial imperfection
L_{ini}	Initial length between nodes that correspond to the Demec gauge span

LIST OF SYMBOLS AND ABBREVIATIONS (cont.)

L_{pipe}	Length of pipe specimen
LVDT	Linear variable differential transducer
L_w	Length of weld element
m	Units of meters
$M_{E\text{-}FEA}$	End moment determined using an FEA
mm	Units of millimeters
MOE	Modulus of elasticity
M_p	Plastic moment capacity
M_p^θ	Plastic moment capacity including reduction for internal pressure
M_{pc}^θ	Plastic moment capacity including reduction for internal pressure and a reduction for axial load
MPa	Units of megapascals (N/mm^2)
M_{pivot}	Moment at a pivot point
M_{top}	Global end moment at top of test specimen
n	Number of regression coefficients
N	Units of newtons
N-mm	Units of newtons times millimeters
NPS	Nominal pipe size
p	Internal pressure
p_e	External pressure
p_i	Internal pressure – CAN/CSA Z662-96
p_y	Internal pressure that causes yielding in the hoop direction
P_{cr}	Euler critical buckling load
P_{jack}	Axial load in eccentric jack
P_{MTS}	Axial load applied through the MTS 6000 Universal Testing Machine
P_N	Net axial force in pipe wall
P_p	Axial load due to the internal pressure
P/R	Ratio of yield plateau material property response divided by rounded material property response
P_{ten}	Net tensile wall force in pipe wall
P_α	Axial load due to the thermal differential
P_v	Axial load due to Poisson's effect
r	Radius of gyration
r_i	Inside radius of test specimen
R	Outside radius of test specimen
R^2	Coefficient of multiple determination
rads	Units of radians
R_p	Outside radius of a perfect pipe
R3D3	3 node rigid shell element from ABAQUS library
S4R	4 node doubly curved shell element from ABAQUS library
sin	Sine function
SMYS	Specified minimum yield strength
t	Time
t	Wall thickness of the pipeline

LIST OF SYMBOLS AND ABBREVIATIONS (cont.)

t_p	Wall thickness of the pipeline
t_w	Thickness of the girth weld
T_f	CAN/CSA – Z662-96 temperature derating factor
T/P	Test-to-predicted ratio
U of A	University of Alberta
V_{end}	Shear at end of specimen
x_{1cur}	Current x-coordinate of FEA node 1 over a corresponding Demec span
x_{2cur}	Current x-coordinate of FEA node 2 over a corresponding Demec span
x_{1ini}	Initial x-coordinate of FEA node 1 over a corresponding Demec span
x_{2ini}	Initial x-coordinate of FEA node 2 over a corresponding Demec span
X	Grade of material
y_{1cur}	Current y-coordinate of FEA node 1 over a corresponding Demec span
y_{2cur}	Current y-coordinate of FEA node 2 over a corresponding Demec span
z_{1cur}	Current z-coordinate of FEA node 1 over a corresponding Demec span
z_{2cur}	Current z-coordinate of FEA node 2 over a corresponding Demec span
y_{1ini}	Initial y-coordinate of FEA node 1 over a corresponding Demec span
y_{2ini}	Initial y-coordinate of FEA node 2 over a corresponding Demec span
z_{1ini}	Initial z-coordinate of FEA node 1 over a corresponding Demec span
z_{2ini}	Initial z-coordinate of FEA node 2 over a corresponding Demec span
z_t	Distance in the longitudinal direction from the top end of a specimen
Z	Plastic section modulus
a,b,c,d,e,f	Coefficients of non-linear regression analysis performed in Chapter 6

Greek Symbols

α	Axial load reduction factor
α_{gw}	Girth weld factor – DNV-OS-F101-2000
α_h	Maximum allowed yield to tensile ratio – DNV-OS-F101-2000
α_T	Coefficient of thermal expansion of the pipeline material
β	Internal pressure reduction factor
$\delta_{assumed}$	Assumed horizontal displacement of a given cross section
δ_h	Horizontal displacement of a given cross section
δ_{LVDT}	Horizontal displacement of a given cross section taken from LVDT measurements
Δ	Deflection
Δ_E	Out-of-plane deflection of an end of a test specimen
Δt	Increment of time
ΔT	The temperature differential
$\varepsilon^C{}_a$	Axial component of critical strain
$\varepsilon^C{}_b$	Bending component of critical strain
$\varepsilon^C{}_{cr}$	Total critical strain
ε_C	Compression strain
$\varepsilon_c{}^{crit}$	Critical buckling strain – CAN/CSA-Z662-96
ε_{comp}	Critical buckling strain – Battelle

LIST OF SYMBOLS AND ABBREVIATIONS (cont.)

ε_{cr}	Critical buckling strain
ε_{cur}	Current level of strain
ε_{ln}^{pl}	True log plastic strain
ε_{lat}	Lateral strain
ε_{long}	Longitudinal strain
$\varepsilon_{long.,Max}$	Critical buckling strain in the longitudinal direction – Vitali
$\varepsilon_{M,c}$	Compressive bending strain capacity
ε_{nom}	Nominal strain (a.k.a. engineering strain)
ε_T	Tension strain
ϕ_G	Total global curvature
ϕ_L	Local curvature
$\mu\varepsilon$	Units of microstrain (10^{-6} strain units)
ν	Poisson's ratio
π	Pi (= 3.141592)
π_1	Pi-parameter number 1 (D/t)
π_2	Pi-parameter number 2 (p/p_y)
π_3	Pi-parameter number 3 (F_y/E)
π_4	Pi-parameter number 4 (imp)
σ_1	Stress in the '1' principal direction
σ_2	Stress in the '2' principal direction
σ_c	Circumferential stress
σ_h	Hoop stress
σ_l	Longitudinal stress
$\sigma_{l\text{-actual}}$	Actual longitudinal stress due to thermal and Poisson's ratio effects
$\sigma_{l\text{-capacity}}$	Longitudinal stress remaining capacity after thermal and Poisson's ratio effects
$\sigma_{l\text{-max}}$	Maximum allowable longitudinal stress under von Mises yield criterion
σ_{nom}	Nominal stress (a.k.a. engineering stress)
σ_θ	Circumferential stress
σ_{true}	True stress including geometric deformations
σ_u	Ultimate stress
σ_y	Yield stress
θ_{bot}	End rotation at bottom of specimen
θ_{top}	End rotation at top of specimen

1.0 INTRODUCTION

Economic and environmental demands on the exploitation of oil and natural gas reserves has led to increased activity in remote regions, specifically the Arctic and sub-Arctic regions of the Canadian North. Buried pipelines have proven to be an effective method for transporting these resources to urban regions. However, increased exploitation of these natural resources has lead to a greater number of buried pipelines being exposed to harsh environments, specifically those located in the areas of discontinuous permafrost in the Canadian sub-Arctic region. This exposure results in the pipelines being subjected to new and often more severe load conditions. These load cases frequently impose a combination of different actions, including internal pressure, axial loads and bending moments in different segments of the pipeline.

Axial loads develop in buried pipelines from a variety of sources. One source of these axial loads is from the construction-operation temperature differential. Pipelines in the Canadian north are usually laid during the winter months at a typical temperature of -30°C, when the ground is frozen and can support the heavy equipment required for installation. Since pipeline-operating temperatures are typically +15°C, this corresponds to a typical temperature differential of approximately 45°C. The thermal differentials, when coupled with geotechnical restraints, such as soil friction, or structural restraints within the system, such as compressor stations, result in the development of compressive forces in the pipeline.

Geotechnical perturbations also give rise to axial forces in pipelines. Pipelines that traverse sloping ground develop axial loads, as do pipelines that cross over a large distance and are subjected to a variety of soil types (Kim and Kim, 1998). These axial forces may be either compressive, such as those at the base of a slope, or tensile, such as those at the crest of a slope. Axial forces can also occur where there is local subsidence that produces catenary action on the pipeline due to local ground movements.

In addition to internal pressure and axial loads, buried pipelines are often subjected to stresses that arise from the bending of the pipeline. When ground subsidence causes settlement of a pipeline, bending moments develop in the pipeline as it maintains its continuity. These bending moments can lead to large stresses and strains, which can result in pipeline buckling. A more detailed discussion of these environmental loads and their laboratory simulation is discussed in Chapter 2.

Despite the significant amount of research conducted on buried pipelines in the past 20 years, there are still a large number of pipeline loading and failure parameters that require additional investigation. Appendix 'C' of the current Canadian Standard - CAN/CSA Z662-96 – (1996) allows for the use of limit states design for buried pipelines, addressing both ultimate limit states (clause C3.4.2) and serviceability limit states (clause C3.4.3). However, there are still limit states that have not been properly identified or quantified.

One such limit state is the strain at the onset of buckling of a pipeline. The local buckling or wrinkling of a pipeline is often classified as a failure due to the magnitude of the deformations that can occur. Excessive deformations may cause flow problems inside the line, an inability to operate inspection tools inside the pipeline, and may act as the initiation point for more catastrophic failures. The magnitude of the longitudinal strain in the wall of a pipeline at the onset of buckling is often referred to as the 'critical buckling strain' or 'critical strain' and has often been identified and used as an important serviceability limit state. However, there is limited experimental based critical buckling strain data for the large diameter, large diameter-to-thickness (D/t) ratio segments of pipeline currently being installed in the field.

The intent of this research project is two fold. First, there is a need for improved understanding of the behaviour of buried pipelines under combined loads. Secondly, there is a need to identify limits that are measurable in the field, which may be used to assess the condition of the pipeline. This research focuses on an expansion of the current experimental database through a rigorous test program and an investigation into the

current critical buckling strain criteria. The critical buckling strain deformational Limit State is a primary focus of this research.

A pipe is a shell structure. If it is subjected to monotonically increasing bending curvatures, then, sooner or later it will buckle, assuming it does not fracture first. This may occur before or after it develops a fully plastic local cross section. If controlled bending is continued beyond the buckling point, the pipe enters into a post-buckling regime of deformation. In this regime the moment that the pipe can sustain reduces, while the curvature continues to increase. If stresses become sufficiently large, plastic deformations concentrate at a critical location and the strains localize in this location while the structure develops a local buckle of large amplitude. This is known as a wrinkle. Souza and Murray (1996) defined a wrinkle as follows:

> "a wrinkle is a local buckle of large amplitude that is clearly visible to the naked eye and possesses the following attributes:
>
> i) its wave form is localized and restricted to approximately a single half-wave, or similar primitive shape,
>
> ii) ii) it is formed from plastic deformations, and
>
> iii) (iii) the amplification (and growth) of the single primitive wave-form occurs coincidentally with softening."

This definition was adopted in this research project.

Typical Load-deformation relationships for shell buckling processes are illustrated in Figure 1.1 (Bushnell, 1980). Generally, a buckling point may be identified as either a bifurcation point, point B in Figure 1.1, or a limit point, points A and/or E in Figure 1.1. All deformations beyond these points are in post-buckling regions.

If the applied loads are gravity loads acting on a free-standing shell structure, that is if they continue to act without reduction regardless of the displacement of the structure, the buckling points become points of catastrophic collapse. This is because the energy

delivered by the load during any incremental displacement in the post-buckling region is greater than the energy that can be absorbed by the structure. Consequently, the structure accelerates and traces a horizontal path to the right of the buckling points shown in Figure 1.1. This process is said to be one of snap-through.

For nonlinear behavior, such as that for the lower equilibrium path of Figure 1.1, snap-through occurs at the point where there is a horizontal tangent, namely, Point E, which is called a limit point. However, if the load is delivered by a controlled displacement of the loading point, such as by a movable loading head on a testing machine, then the structure will not collapse, and snap-through will not occur. This is because the loading head would not deliver any force to the structure if the structure would lose contact with the loading head. Therefore, the rate at which the structure deforms is governed by the displacement control of the loading head and the post-buckling path from E to F that is traced by the structure is stable and can be recorded.

In classical buckling analysis the limit point is the point of instability leading to catastrophic collapse. In terms of local buckling of buried pipe, however, the limit point does not lead to catastrophic collapse because the geotechnical loading imposes a displacement-control deformation. That is, because of the soil movements, deformations are being imposed on the pipe. However, the soil is not only the loading medium but also a restraining medium to prevent the pipe from assuming large global displacements. The limit point of the pipe response becomes the effective initiation point for wrinkle formation. In other words, the point of incipient buckling is the same as the point of wrinkle initiation since the wrinkle forms in the post-buckling branch. This point is also the same as the point of peak moment on the moment-curvature curve (i.e.-the limit point). Consequently, for the purposes of this research project, the point of incipient buckling is defined to be the limit point on the moment-curvature response curve.

It is a fundamental principal of structural engineering that behavior of structures can be determined by testing in the laboratory under conditions that represent those to be expected in-service as closely as possible. This testing is carried out in order to verify

analytical predictions of anticipated behavior. However, if realistic behavior is to be determined for full-sized structures, the testing should be done on specimens that are as close to full-sized as possible. The reason for this is that models are not always able to provide realistic simulation of all structural attributes, such as residual stress distributions or material properties, with realistic post yield behavior. Because of the foregoing considerations, testing of full-sized line pipe is the best way to determine how the pipe will behave under a combined load case of internal pressure, axial load, and imposed curvature.

This chapter presents a review of the current state-of-the-art design criteria and provides the basis and justification for the research program undertaken and included herein. Specifically, this chapter presents a review of previous investigations on line pipe subjected to combined loading, with special focus on the on-going research at the University of Alberta (U of A) in Edmonton, Alberta, Canada. Pipeline research in this area has been on-going at the U of A over the past 12 years and a significant database is being compiled, with deformational limit states being a focus of the research as the limit states design philosophy becomes commonplace in Canadian design standards.

1.1 Previous Investigations on Line Pipe Subjected to Combined Loading

Numerous research projects have been conducted in the past 50 years on the behaviour of line pipe subjected to single load cases or combined loading. A review of some related studies prior to 1994 has been summarized by Yoosef-Ghodsi, *et al.*, 1994. Del Col, *et al.*, 1998, provides a detailed review of the studies conducted between 1994 and 1998. As investigations prior to 1998 have been well documented in the above two research reports, the following literature survey focuses on studies conducted from 1998 to date.

1.1.1 Current Research

Smith, *et al.*, 1998, conducted 20 full-scale wrinkling tests on large diameter corroded pipe. While corrosion is not a variable in this program, the loading scheme used by

Smith was similar to that used in this program. The specimens tested by Smith were subjected to combined loading, including internal pressure, axial loading, and loading designed to simulate longitudinal bending due to settlement. The experimental research by Smith was used to validate a finite element analysis (FEA) model of the test specimens. Smith identified that FEA model results had good correlation with the experimental data, but also identified that the correlation was highly dependent on the ability to accurately predict the material properties for input into the model, specifically in the transition from elastic to plastic behaviour.

Hauch and Bai, 1999, conducted an analytical study on the bending moment capacity of pipes to develop a set of design criteria for pipe wall thickness. Their design equations were based on the fully plastic moment capacity developed by Mohareb, *et al.*, 1994, which is presented in the following section. Hauch and Bai found good agreement between their numerical model and the experimental results. However, they indicate that the geometrical imperfections that are normally allowed in pipeline design do not significantly influence the moment capacity for pure bending. This contradicts the findings of many other research studies, including Del Col, *et al.,* 1998, and Dinovitzer, *et al.,* 1999.

Vitali, *et al.,* 1999, did an extensive numerical study similar to the one undertaken in this project. In their investigation, they conducted no experimental testing, rather they used experimental data generated in previous investigations at the U of A to validate their FEA model. Vitali, *et al.* conducted a total of 120 parametric numerical analyses in which the D/t ratio, internal pressure ratio and the axial load were variables. They used D/t ratios of 20, 30, 40 and 60, however their model was validated using experimental data with D/t ratios of only 50 and 63. It is acknowledged that their model may be more applicable to the higher D/t ratios that they examined. Some concern may exist about how well their model fits for the lower D/t ratios because there was no experimental data to validate their model at the lower D/t ratios.

As previously mentioned, initial imperfections are believed to have a significant effect on the behaviour of line pipe segments subjected to combined load cases. The Vitali *et al.* study makes no attempt to account for any initial imperfection pattern. However, considering the range of the D/t variable in their study, the omission of initial imperfections may not be overly critical. Mohareb, *et al.*, 1994, investigated plain pipe specimens with D/t ratios of 50 and 63. Yoosef-Ghodsi, *et al.*, 1994, and Souza and Murray, 1994, investigated girth welded specimens with D/t ratios of 50 and 63. Initial imperfections were not considered in either of those investigations, yet in both investigations the FEA model was able to provide a reasonably good prediction of the experimental behaviour. It has since been postulated that the observed discrepancies may be due to the fact that initial imperfections were not considered in the numerical model. Del Col, *et al.*, 1998, investigated plain pipe specimens with a D/t ratio of 92 and found that the initial imperfection pattern was of paramount importance in the numerical model. This suggests that initial imperfections have a greater effect on the behaviour of the test specimens with increasing D/t ratio. If this observation is valid, then the omission of initial imperfections in the Vitali study may not be critical given the low D/t ratios that were considered.

The Vitali study provided a significant contribution to understanding the behaviour of line pipe segments with low D/t ratios (<60) and the findings and equations proposed in their study may well be valid for small D/t ratios. However, this project focuses on specimens with D/t ratios ranging from approximately 50 to 90. These D/t ratios lie well above the upper limits investigated in the Vitali study and, therefore, the results of the Vitali study may not be applicable over this range. Nevertheless, the results obtained by Vitali, *et al.* further support the suitability of the FEA modeling technique for this type of application.

1.1.2 Research at the University of Alberta

Several studies in the past and others currently underway at the U of A investigate different facets of line pipe behaviour. A summary of the previous investigations in the area of line pipe buckling conducted at the U of A has been provided by Del Col, *et al.*,

1998. As such, the different research projects will be frequently referenced since this research project is an extension of the previous investigations, but they will not be specifically reviewed in detail in this document. There are two exceptions, namely, the work done by Del Col, *et al.*, 1998, who conducted the preliminary research for this project, and an in-depth review of the development of the Mohareb-Murray fully plastic moment equation.

In the Del Col study, four specimens with a D/t ratio of 92 were tested and an FEA model was developed. Of the four specimens tested, one was unpressurized and the other three had increasing levels of internal pressure. Due to the complexity of measuring the initial imperfections on the outside wall of the test specimens, Del Col developed a simplified technique for measuring initial imperfections around the inside of the test specimens. By assuming that the wall thickness was essentially constant throughout the specimen, the inside initial imperfection measurements were assumed to be a representative measure of the true imperfection pattern. The FEA model developed by Del Col was run with and without the initial imperfections measured on each of the respective test specimens. Inclusion of the initial imperfection pattern in the FEA model resulted in superior agreement between the numerical results and the experimental data. Therefore, it was concluded that initial imperfections played a major role in the behaviour of the D/t = 92 test specimens and should be given due consideration in the numeric model.

During the testing of Del Col's three pressurized specimens, it was observed that a new type of buckle was prevalent. All of Del Col's pressurized specimens failed at their bottom end, immediately adjacent to the end collars in the test set-up. This type of buckle had been previously observed in only one test specimen during the different experimental testing programs conducted at the U of A and it was unclear as to whether or not this phenomenon was random or was influenced by the test set-up. Further to this, it was observed that inadequate local strain data was collected in the buckled region of the test specimen. Therefore, it was decided to expand the original scope of this project to include re-tests of Del Col's three pressurized specimens to verify the results.

One of the most significant contributions to date from the U of A testing program has been the development of a series of equations used to predict the fully plastic moment capacity of a segment of line pipe subjected to combined loads. These equations were developed by Mohareb *et al.* (1994) and are based on an interaction formulation between the axial load and the fully plastic moment capacity. The equations assume an elastic-perfectly plastic, bilinear stress-strain curve and do not contain any provisions to account for buckling failure mode, nor do they account for strain hardening. Nevertheless, the fully plastic capacity determined using these equations is a benchmark condition against which the test values and finite element predictions can be compared. Past research at U of A (Mohareb, *et al.*, 1994 and Del Col, *et al.*, 1998) has established the accuracy of these equations in predicting fully plastic moment capacities of line pipe.

The plastic moment capacity of non-pressurized pipe with no axial load is calculated from

$$M_p = Z\sigma_y \tag{1.1}$$

in which the subscript '$_P$' is used to indicate that this is the plastic moment capacity, Z is the plastic section modulus and σ_y is the yield strength of material, taken as the stress at 0.5% strain.

If a pipe is subjected to an internal pressure, a reduction factor is required because the longitudinal stress at yield is reduced when a circumferential stress, σ_θ, is present. The maximum plastic moment capacity in the presence of σ_θ becomes

$$M_p^\theta = \beta M_p \tag{1.2}$$

in which the superscript '$^\theta$' is used to indicate that the plastic moment capacity has been reduced to account for internal pressure and β is the internal pressure reduction factor. This factor is given as

$$\beta = \sqrt{1 - \frac{3}{4}\left(\frac{\sigma_\theta}{\sigma_y}\right)^2} \tag{1.3}$$

in which σ_θ is the circumferential stress and σ_y is the yield stress. However, the maximum moment in Equation (1.2) cannot be attained without the simultaneous application of the axial load subsequently defined in Equation (1.6).

If, in addition to the internal pressure, a pipe is also subjected to an axial load, a second reduction factor is required and the plastic moment capacity becomes

$$M_{pc}^{\theta} = \alpha M_p^{\theta} = \alpha \beta M_p \tag{1.4}$$

in which the additional subscript '$_C$' is used to indicate that the plastic moment capacity has been reduced to account for an applied axial force, C, and α is the axial force reduction factor. This factor is given as

$$\alpha = \cos\left\{\frac{\pi}{2\beta}\left(\frac{C}{C_y} - \frac{1}{2}\frac{\sigma_\theta}{\sigma_y}\right)\right\} \tag{1.5}$$

in which 'C' is the axial force in the pipe wall ('+' in tension) and 'C_y' is the axial yield load under zero circumferential stress. The maximum moment capacity of Equation (1.4) occurs when α is 1.0. This requires that

$$\frac{C}{C_y} = \frac{\sigma_\theta}{2\sigma_y} \tag{1.6}$$

Equation (1.4) is hereafter referred to as the 'Mohareb-Murray interaction equation' and was used to predict the fully plastic moment capacity of the test specimens, including the influence of the applied internal pressure and axial load.

1.2 Current Critical Strain Criteria

Research into the determination of a critical strain limit state has been conducted for over 50 years and many design equations have been proposed. However, the availability of a large, broad-scale, experimental database has left the experimental validation of a number of these equations in question. While the proposed equations may provide excellent correlation over certain regions of the spectrum of critical strain values, they may not be suitable for all load cases.

The testing of line pipe subjected to combined load effects has been on going at the U of A since the early 1990's. Experimental data collected at the U of A included specimens with a wide range of experimental parameters consistent with those commonly encountered in typical operational pipelines. The experimental test matrix included specimens which have diameter to thickness (D/t) ratios that range from 50 to 92, specimens with an internal pressure that created stresses in the circumferential direction that ranged from 0% to 80% of the specified minimum yield strength (SMYS), specimens with and without circumferential girth welds, and material properties that ranged from grade X50 to X70.

At the time this research project was initiated, more than 20 full-scale specimens have been tested at U of A under combined axial load, internal pressure, and bending moment. The critical strain for the majority of these tests has been determined from the experimental data collected during seven different research projects conducted since 1992. Table 1.1 presents a summary of the plain test specimens with available critical strain results collected at U of A prior to the current study. Table 1.2 presents a summary of the girth welded test specimens with available critical strain results collected at U of A prior to this research.

One of the objectives of this research was to assess a number of current equations used to estimate the value of the critical strain in pipeline buckling problems. This included two code equations currently in practice. A literature review was conducted and a number of

critical strain equations were selected for comparison to the data collected at U of A. The results presented in Tables 1.1 and 1.2 were used to assess these various critical strain equations and to determine if a need existed for additional research in this area. This section reviews these different equations and assesses them, according to current U of A experimental data.

It should be noted that the method for determining the critical buckling strain for use in each of the following equations is often unclear. As such, the method used to determine the critical buckling strains at the U of A may differ from those used in the development of the following equations. This diversity in methodology likely contributed to some of the differences in the following assessments.

1.2.1 Assessment of Critical Strain Equations Selected from Literature

A paucity of critical strain equations exist in the literature. This is due to limited research conducted in this specific area and the fact that the majority of equations are proprietary information. These proprietary equations are often unavailable in the literature because the different line pipe operators use them exclusively as an 'in-house' design tool. Furthermore, equations from different sources are often similar in the input parameters used. As such, it was decided that the following equations would provide adequate representation of those currently available in the literature.

The classical elastic equation for local buckling of tubular shell structures (Column Research Council, 1966) was selected as the first model to be considered. It is recognized that this equation will likely give poor agreement to the test data because its development is based solely on elastic behaviour, whereas the true response includes plastic behaviour. The equation is dependent solely on the D/t ratio of the structure and is given as

$$\varepsilon_{cr} = \left(\frac{1}{\sqrt{3\left(1-\nu^2\right)}} \right) \frac{t}{R} \approx 1.2 \frac{t}{D} \tag{1.7}$$

where ν is Poisson's ratio, R is the radius of the tube, t is the wall thickness of the tube and D is the diameter of the tube. It should be noted that the above approximation is for cases where $\nu \approx 0.3$. For the experimental pipes presented in this paper, the values of ν ranged from 0.26 to 0.31 and therefore the approximation of ν made in equation 1.1 would be applicable.

Equation 1.7 shows that the classically derived elastic critical strain is directly proportional to the inverse of the D/t ratio. In the selection of additional equations for review in this program, it was decided to also examine equations in which the critical strain was a function of the D/t ratio raised to different exponents.

The equation presented by Sherman (1976) was given as

$$\varepsilon_{cr} = 16\left(\frac{t}{D}\right)^2 \tag{1.8}$$

in which the critical strain is an inverse function of the D/t ratio squared. This equation was selected because local wrinkling of line pipe is a buckling phenomenon and can be thought of as analogous to Euler buckling of columns. In the classical Euler equation, the load carrying capacity is a function of the square of the slenderness ratio (kL/r). Since the D/t ratio is used to define the slenderness of a segment of line pipe, it can be rationalized that the critical strain should be a function of the square of the D/t ratio. It is acknowledged that Euler buckling is a global phenomenon and that wrinkling of a segment of line pipe is a local phenomenon. Nevertheless, local buckling criteria often contains the square of a slenderness ratio term.

Stephens *et al.* (1991) developed another equation that was considered. This equation was presented in a reported produced by the Battelle Laboratories of Columbus, Ohio and was derived from test data compiled by a number of researchers. The Battelle equation includes a non-linear function of the D/t ratio and is expressed mathematically as

$$\varepsilon_{comp} = 2.42\left(\frac{t}{D}\right)^{1.59} \tag{1.9}$$

Figure 1.2 presents a graphical representation of Equations 1.1, 1.2 and 1.3 as compared with the experimental data collected for pipes at U of A. As can be seen in this figure, the classical equation (Equation 1.7) often over-predicts the critical strain values. This is because the classical equation is based solely on elastic behaviour and no consideration is given to plastic behaviour in the formulation. The other two equations both provide similar predictions and each appears to act as a lower bound for the test data. This shows that the two equations are conservative.

Tables 1.3 and 1.4 give a numerical evaluation of the three equations investigated. Table 1.3 presents the test-to-predicted ratios between the three equations and the experimental U of A plain pipe specimen critical strains, while Table 1.4 presents the test-to-predicted ratios between the three equations and the experimental U of A girth welded specimen critical strains. As can be seen from the test-to-predicted ratios in both Table 1.3 and Table 1.4 and the respectively coefficients of variation, there is very poor correlation between the predicted critical strain and those measured during testing for all of the equations considered. It is observed that both the Sherman and the Battelle equations are conservative for every load case considered in that all test-to-predicted ratios for both the plain and the welded test specimens were greater than or equal to1.00. While it is good engineering practice to provide a conservative design, the mean test-to-predicted values were much greater than 1.00, indicating that the equations were too conservative. In addition, the range in the test-to-predicted values for each of the equations indicates that there is a large scatter of the predicted data values and that the respective equations have very poor accuracy.

These results are not surprising because all three of the equations are based solely on the D/t ratio and it is instinctively obvious that other parameters, particularly the internal pressure, must affect the complex buckling behaviour of a pipeline. The determination of these other parameters and the development of an appropriate design equation that

incorporates their effects is one of the main objectives of this research. Consideration of these other parameters is presented in Chapter 6, after the analysis of the experimental results has been completed in Chapter 4 and Chapter 5.

Finally, the equation developed by Vitali, *et al.*, 1999, was investigated for the specimens with a D/t ratio less than the upper bound of 60 used in the development of their equation. The Vitali equation for predicting the critical buckling strain in the longitudinal direction, $\varepsilon_{long.,Max}$, includes a D/t ratio term, a term to account for the internal pressure in the specimen, and a term to account for the material properties. Mathematically, the equation can be expressed as

$$\varepsilon_{long.,Max} = \left(\frac{t}{D} - 0.01\right)\left(1 + 5\frac{\sigma_h}{\sigma_y}\right)\left(\frac{\sigma_u}{\sigma_y}\right)^{1.5} \tag{1.10}$$

where σ_h is the stress in the hoop direction, σ_y is the yield stress, and σ_u is the tensile strength. It should be noted that the Vitali equation was developed for plain test specimens. However, it should also be noted that the Vitali equation is limited in its application because it was developed for a single set of material properties. Specifically, it was assumed throughout the development of the equation that σ_y was equal to 450 MPa and that σ_u was equal to 530 MPa. Nevertheless, since the Vitali equation was developed from the U of A data, it should do a reasonable job of predicting this experimental data.

Table 1.5 presents a comparison of the Vitali equation with the U of A experimental data for plain specimens with a D/t ratio less than 60. The data gave a mean test-to-predicted ratio of 0.58 with a coefficient of variation of 0.27 and a range of 0.43 to 0.75. These results show that the equation is unconservative.

This is surprisingly poor agreement considering the model used to develop the equation was validated with most of the data presented in Table 1.5. An explanation for the poor agreement could lie in the sensitivity of the equation to the material property input. As

previously mentioned, the equation is calibrated for that specific set of material properties given above. However, none of the experimental U of A data used in this comparison had the same value for the material properties that was used in the development of equation 1.10. This suggests that the material properties are a significant parameter in the determination of local critical buckling strain for line pipe.

1.2.2 Assessment of Critical Strain Equations In Current Design Codes

While the poor agreement between experimental data and some of the available proposed equations is disconcerting, a more important critique is the comparison of current code-specified design equations with the experimental data. For the purposes of this preliminary assessment, two code design equations were selected for evaluation.

1.2.2.1 Comparison with Current CSA Critical Strain Equation

Of primary interest to the author was the equation used in the Canadian Oil and Gas Pipeline Systems code, CAN/CSA Z662-96. Clause C6.3.3.2 presents the equation for the determination of compressive strain limit, ε_c^{crit} under combined loading as

$$\varepsilon_c^{crit} = 0.5\frac{t}{D} - 0.0025 + 3000\left[\frac{(p_i - p_e)D}{2\,t\,E_s}\right]^2 \qquad (1.11)$$

where p_i is the internal pressure, p_e = external pressure and E_s is the modulus of elasticity for steel, taken as 207 000 MPa.

Examination of Equation 1.11 shows that the equation adopted by CAN/CSA Z662-96 includes a term to account for the effect of a pressure differential across the wall of the line pipe segment, given as $(p_i - p_e)$. These parameters were included as experimental variables in the testing program and will be discussed in detail in Chapters 4 and 5.

The literature survey showed that the equation in clause C6.3.3.2 is based on research done by Gresnigt (1986), with the only difference between the Gresnigt equation and the Z662-96 equation being the value used for the modulus of elasticity of the steel, E_s. It

should be noted that the Canadian code equation is based on the "ultimate compressive strain capacity of the pipe wall" and the values calculated using the Canadian standard should be representative of the total critical strain value, ε_{cr}^{C}. One obvious omission from the Canadian code is a factor to account for the presence of a girth weld, which is known to affect the buckling behaviour of pipelines (Yoosef-Ghodsi, *et al*, 1994).

1.2.2.2 Comparison with draft DNV Critical Strain Equation

A second design standard was also selected for comparison purposes. The most recent standard available was the draft version of the Det Norske Veritas Offshore Standard for Submarine Pipeline Systems, DNV-OS-F101, which was released in January 2000. Clause 507 of the draft DNV-OS-F101 provides the equation for the 'characteristic compressive bending strain capacity, $\varepsilon_{M,c}$,' as

$$\varepsilon_{M,c}=0.78\left(\frac{t_1}{D}-0.01\right)\left(1+5\frac{\sigma_h}{f_y}\right)\alpha_h^{-1.5}\,\alpha_{gw} \tag{1.12}$$

where t_1 is the wall thickness for pressure containment resistance, σ_h is the 'characteristic hoop stress', f_y is yield strength of the pipe material, α_h is the maximum allowed yield to tensile ratio, and α_{gw} is a girth weld factor (=1.0 for specimens with no weld present)

It should be noted that the draft DNV-OS-F101-2000 critical strain equation is based only on the bending strain capacity and will be compared with the bending component of the U of A experimental data, ε_b^C, given in Tables 1.1 and 1.2. It should also be noted that the draft DNV-OS-F101-2000 specification is intended for use in the design of submarine pipelines, however, the critical strain limit equation should be valid for use in all types of loading.

Examination of clause D507 of the draft DNV-OS-F101 shows that there are terms to account for both the pressure effects (σ_h / f_y) and the material properties (α_h), although the yield strain is not directly accounted for. Another observation is that the draft DNV-OS-F101 code has a factor to account for the presence of a girth-weld (α_{gw}).

1.2.2.3 Results of Current Code Equation Comparisons

Table 1.6 presents a test-to-predicted comparison between the CAN/CSA-Z662-96 and the draft DNV-OS-F101 code equations and the U of A experimentally determined values for the plain test specimens. Table 1.7 presents the test-to-predicted comparison between the two codes and the girth welded test specimens. Due to the large number of variables in both equations, it is difficult to present these results graphically. Consequently, only the test-to-predicted ratios were used to assess the suitability of the individual equations.

Examination of Table 1.6 and Table 1.7 shows that there is poor agreement between both the plain and the girth welded specimens and the two code equations under review. For the plain specimens, CAN/CSA Z662-96 gave a mean test-to-predicted ratio of 1.49 with a coefficient of variation of 0.41 and a range of 0.36 to 2.21. The draft DNV-OS-F101-2000 gave a mean test-to-predicted ratio of 1.42 with a coefficient of variation of 0.76 and a range of 0.54 to 3.74.

For the girth-welded specimens, CAN/CSA Z662-96 gave a good mean test-to-predicted ratio of 1.05, however, the data had a coefficient of variation of 0.36 and a range of 0.30 to 1.50. The draft DNV-OS-F101-2000 gave a mean test-to-predicted ratio of 1.37 with a coefficient of variation of 0.96 and a range of 0.43 to 4.94.

1.2.3 Summary of Current Literature and Design Equations

From the test-to-predicted ratio for the two code critical strain equations and the three other critical strain equations considered, it is obvious that further investigation into the development of an accurate critical strain equation is required. As would be anticipated, an equation that contains only the D/t ratio is clearly inadequate for predicting the complex buckling behaviour of pipeline.

The Sherman and Battelle equations were the only ones found to be conservative in every case; however, they are based solely on the D/t ratio of the test specimen, which has

already been identified as being inadequate. Furthermore, the range and scatter of the test-to-predicted ratios indicates that these equations have very poor accuracy.

While both CAN/CSA-Z662-96 and the draft DNV-OS-F101-2000 attempt to include pressure and material property parameters either directly or indirectly, both code equations have been shown to provide very poor correlation between their predictive values and those determined experimentally. It should be noted that both code equations attempt to use a linear D/t ratio term, whereas comparison with the equations plotted in Figure 1.2 show that the critical strain is inversely proportional to the D/t ratio raised to a power greater than 1. That is, there is a non-linear relationship between the critical strain and the D/t ratio. It should be further noted that the draft DNV-OS-F101-2000 is the only equation that attempts to differentiate between plain and welded specimens.

During the assessment of current critical strain criteria, it was observed that none of the equations reviewed made any provisions for an initial imperfection. Initial imperfections have been identified as a critical parameter in line pipe from both a strength and a stability standpoint (Dinovitzer and Smith, 1998). Initial imperfections can trigger premature buckling of line pipe at significantly lower loads and/or strains. Therefore, it was decided to make initial imperfections one of the focus points of this study.

Dinovitzer, *et al.*, 1999 proposed a pipeline dent assessment model in accordance with the 6% of the pipeline's outside diameter allowed by the current Canadian Pipeline Design Standard (CAN/CSA Z662-96). The model primarily focused on the effects of dents that develop due to mechanical damage to a pipeline. The inclusion of the dent model in an analytical model showed that good agreement was achieved between the analytical and experimental results. It is acknowledged that post fabrication dents due to mechanical damage are inherently different from initial imperfections that result from the fabrication process. Nevertheless, the results obtained by Dinovitzer emphasize the importance of considering any irregularities or defects in the load carrying capacity of line pipe.

1.3 Problem Statement

While numerous advancements in the understanding of the behaviour of line pipe have been made in the past 20 years, there is still a large void in the experimental database. The literature survey showed that there are numerous experimental results for small scale test specimens and test specimens under single load effects. However, the database of experimental results for large scale test specimens subjected to combined loading is limited. Expansion of this type of database would substantially enhance the understanding of the behaviour of such structures and reduce the incidence of field failure.

Current typical databases include specimens with D/t ratios covering an approximate range of 20 to 60. With increased demands on supply, the pipeline industry is expanding to include line pipe with diameters of 1.22 meters (48") and D/t ratios in the order of 120. There has been very limited experimental research on line pipe with these dimensions, which introduces a number of safety concerns with current field installation practices. Clearly, additional experimental research into specimens with these dimensions is required.

Another physical characteristic that requires investigation is the presence of initial imperfections. Initial imperfections are known to cause premature buckling of structural elements that are subjected to compressive forces. However, there is little experimental data that includes the effects of an initial imperfection pattern on the behaviour of segments of line pipe. The investigation and development of initial imperfection criteria can be viewed as a crucial component in the understanding of the behaviour of segments of line pipe.

Current state-of-the-art modeling of line pipe segments has been significantly improved with the adoption of finite element modeling techniques (DiBattista, *et al.*, 2000, Smith, *et al.*, 1998, and Souza, *et al.*, 1994, to name a few). One of the key reasons for this is

that the FEA modeling technique can account for any non-linear behaviour in the test specimen. The literature survey has shown that FEA modeling is now becoming the norm for numerical modeling of the behaviour of segments of line pipe. However, the proper application of FEA modeling to segments of line pipe subjected to combined loading has not been fully validated and, as such, is in a state of on-going development with further work required.

The brief comparison between experimental data and the current critical strain design criteria presented in this chapter has shown these equations to be inadequate for many of the load cases considered. Therefore, further investigation and equation development appears to be warranted.

1.4 Scope and Objectives of this Research Program

This research project was designed to address the concerns identified in the above problem statement. Specifically, this project was designed to expand the current database on the behaviour of segments of line pipe tested under combined loading, as would be experienced under field operating conditions. A total of 12 different line pipe segments were tested under a variety of load cases, which were calculated from known operating conditions. For economic and practical reasons, pipeline operators are commonly using large D/t ratio line pipe, despite the limited experimental test data under combined loads in this range. The line pipe segments investigated in this project had a D/t ratio of approximately 92 so that the current experimental database may be expanded in this range.

Using the experimental data for validation, a FEA model was developed to accurately predict the experimental behaviour. The FEA model accounted for all the characteristic features of the experimental segments of line pipe, including initial imperfections, experimental load conditions, and experimentally determined material properties to reflect the actual test specimens as accurately as possible.

Once the FEA model was validated, it was used to numerically expand the current database for segments of line pipe subjected to combined loading. This was done by carefully selecting the pipe geometry and loading conditions to be representative of current field installations. The completed database, the compiled data will be used to develop a set of critical strain criteria. The experimental data were then used to test the accuracy of the new design recommendations.

Therefore, the specific objectives of this research project can be summarized as the need to:

1. expand the current experimental database of large diameter, large D/t ratio segments of line pipe subjected to combined loading;
2. investigate the effects of initial imperfections on the behaviour of line pipe;
3. develop a finite element model that accurately predicts the behaviour of the experimental test specimens investigated in this project;
4. validate the FEA model for use with other size specimens subjected to combined loading;
5. perform a comprehensive parametric study using the validated FEA model to provide data for load cases and test specimens not investigated experimentally;
6. compile all available experimental critical strain data on both plain and girth welded test specimens and develop a critical buckling strain equation that provides greater accuracy than those in current practice; and,
7. propose acceptable performance limits for line pipe under combined loading.

1.5 Layout of this Report

The remainder of this report consists of six chapters. Chapter 2 describes all the components of the testing program conducted to expand the experimental database. This includes details of the experimental parameters considered, the preparation of the test

specimens, the test set-up, and the experimental testing procedure used in testing the segments of line pipe as well as a complete description of the ancillary tests.

A total of 15 tests were conducted, resulting in 12 sets of experimental results, which were later incorporated into the U of A database. During the testing of the other three specimens, failure of the test set-up resulted in no meaningful data being collected. The specimens were re-tested after adjustments had been completed. A summary of the nominal target experimental loads for each of the test specimens is included in Chapter 2.

Chapter 3 outlines the details of the finite element analysis (FEA) model developed for the experimental test specimens. A brief introduction and review of the concepts of FEA is presented, followed by a detailed discussion of the specific features employed in this research project. The details of the development of the mesh size used for the analysis of both the experimental test specimens and the load cases considered in the parametric study are included in this chapter. Finally, the philosophy and details of the development of the FEA model of the circumferential girth weld are presented in Chapter 3.

Chapter 4 presents the results of both the experimental testing program and the FEA numerical modeling. A comparison of the experimental and FEA model results, including the moment-curvature response, the magnitude of the critical strain, and the buckling mode, for each of the 12 test specimens is presented. Validation of the FEA model developed in Chapter 3, using experimental results for D/t=92 specimens from other testing projects, is also included. Finally, a qualitative assessment of the effect of some of the different experimental parameters and a quantitative assessment of the experimental, FEA model, and theoretical results is presented and summarized.

Chapter 5 outlines the details of the further validation of the FEA model developed in the project using the experimental data for different D/t ratio specimens. Once this validation was completed a full parametric study was conducted to examine the effects of different D/t ratios, different internal pressures, different material properties, and the presence of a circumferential girth weld on the critical buckling strain.

Chapter 6 presents the parametric study. A total of 135 different load cases were examined using the validated FEA model and peak moments and critical strain results for each load case were determined. These results were then be used in the development of a new predictive critical strain equation. The Buckingham-Pi Theorem was used to develop a set of non-dimensional parameters to define the critical buckling strain for the different load cases. Using these non-dimensional parameters, a non-linear regression analysis was conducted on the data collected in the parametric study and a design strategy proposed for predicting critical buckling strain.

Chapter 7 provides an overall summary of this research, a summary of the recommended design criteria and equations, and a list of recommendations to further define the critical buckling strain behaviour of segments of line pipe subjected to combined loading.

Table 1.1 – Experimental Test Matrix for Plain Specimens

Specimen ID	Dia. (mm)	Thick (mm)	Yield Strength (MPa)	Ultimate Strength (MPa)	Modulus of Elasticity (MPa)	Exp. Internal Pressure (MPa)	Total Exp. Critical Strain ε_{cr}^{C} (%)	Exp. Bending Critical Strain ε_{b}^{C} (%)
UGA12	318	6.35	378	454	199754	0.00	0.99	0.94
HGA12	318	6.35	378	454	199754	5.67	1.58	1.55
DGA12	318	6.35	378	454	199754	11.34	2.90	2.89
DGA508	500	7.90	391	469	203704	10.20	2.81	2.80
CP0N	762	8.40	472	578	201378	0.00	0.23	0.18
CP20N-1	762	8.40	472	578	201378	2.14	0.31	0.27
KD/t=48	610	12.83	483	580	200000	16.79	3.42	3.35
KD/t=92-1	610	6.76	483	580	200000	0.53	0.47	0.35
KD/t=92-2	610	6.76	483	580	200000	0.00	0.46	0.41
L178P80BP-4	508	8.37	448	550	200000	12.01	3.10	n/a
L178P80BP-8	508	6.07	448	550	200000	8.78	0.46	n/a

Table 1.2 – Experimental Test Matrix for Girth Welded Specimens

Specimen ID	Dia. (mm)	Thick (mm)	Yield Strength (MPa)	Ultimate Strength (MPa)	Modulus of Elasticity (MPa)	Exp. Internal Pressure (MPa)	Total Exp. Critical Strain ε_{cr}^{C} (%)	Exp. Bending Critical Strain ε_{b}^{C} (%)
UGA12W	318	6.35	378	454	199754	0.000	0.64	0.59
HGA12W	318	6.35	378	454	199754	5.67	1.11	1.08
DGA12W	318	6.35	378	454	199754	11.34	1.90	1.89
UGA20W-2	508	7.90	391	469	203704	0.00	0.81	0.76
HGA20W	508	7.90	391	469	203704	5.10	1.04	1.01
DGA20W	508	7.90	391	469	203704	10.20	1.87	1.79
Sp=0	333	6.84	358	429	201530	0.00	0.75	0.70
Sp=40	333	6.84	358	429	201530	6.31	1.20	1.13
Sp=80	333	6.84	358	429	201530	12.62	1.70	1.62
L178P80BW-1	508	8.37	448	550	200000	12.01	1.20	n/a
L178P40BW-2	508	8.37	448	550	200000	6.01	0.97	n/a
L178P00BW-3	508	8.40	448	550	200000	0.00	0.80	n/a
L178P80BW-5	508	6.11	448	550	200000	8.83	0.58	n/a
L178P40BW-6	508	6.09	448	550	200000	4.40	0.35	n/a
L178P00BW-7	508	6.09	448	550	200000	0.00	0.32	n/a

Table 1.3 – Comparison of Plain Specimen Critical Strains with Classical Elastic, Sherman and Battelle Equations

Specimen ID	Experimental		Classical Elastic		Sherman (1976)		Battelle (1991)	
	Total Strain (%)	Bending Strain (%)	ε^{crit}_c (%)	Test-to-Predicted Ratio	ε^{crit}_c (%)	Test-to-Predicted Ratio	ε^{crit}_c (%)	Test-to-Predicted Ratio
UGA12	0.99	0.94	2.40	0.41	0.64	1.55	0.48	2.06
HGA12	1.58	1.55	2.40	0.66	0.64	2.47	0.48	3.28
DGA12	2.90	2.89	2.40	1.21	0.64	4.53	0.48	6.03
DGA508	2.81	2.80	1.90	1.48	0.40	7.04	0.33	8.50
CP0N	0.23	0.18	1.32	0.17	0.19	1.18	0.19	1.23
CP20N-1	0.31	0.27	1.32	0.23	0.19	1.59	0.19	1.66
KD/t=48	3.42	3.35	2.52	1.36	0.71	4.84	0.52	6.57
KD/t=92-1	0.47	0.35	1.33	0.35	0.20	2.40	0.19	2.50
KD/t=92-2	0.46	0.41	1.33	0.35	0.20	2.34	0.19	2.45
L178P80BP-4	3.10	n/a	1.98	1.57	0.43	7.14	0.35	8.76
L178P80BP-8	0.46	n/a	1.43	0.32	0.23	2.01	0.21	2.17
Mean T/P ratio				0.74		3.37		4.11
Coeff. of Variation				0.74		0.64		0.68

Table 1.4 – Comparison of Girth Welded Specimen Critical Strains with Classical Elastic, Sherman and Battelle Equations

Specimen ID	Experimental		Classical Elastic		Sherman (1976)		Battelle (1991)	
	Total Strain (%)	Bending Strain (%)	ε^{crit}_c (%)	Test-to-Predicted Ratio	ε^{crit}_c (%)	Test-to-Predicted Ratio	ε^{crit}_c (%)	Test-to-Predicted Ratio
UGA12W	0.64	0.59	2.40	0.27	0.64	1.00	0.48	1.33
HGA12W	1.11	1.08	2.40	0.46	0.64	1.74	0.48	2.31
DGA12W	1.90	1.89	2.40	0.79	0.64	2.97	0.48	3.95
UGA20W-2	0.81	0.76	1.90	0.43	0.40	2.03	0.33	2.45
HGA20W	1.04	1.01	1.90	0.55	0.40	2.60	0.33	3.14
DGA20W	1.87	1.79	1.90	0.99	0.40	4.68	0.33	5.65
Sp=0	0.75	0.70	2.47	0.30	0.68	1.11	0.50	1.49
Sp=40	1.20	1.13	2.47	0.49	0.68	1.77	0.50	2.38
Sp=80	1.70	1.62	2.47	0.69	0.68	2.51	0.50	3.37
L178P80BW-1	0.44	n/a	1.98	0.61	0.43	2.76	0.35	3.39
L178P40BW-2	1.08	n/a	1.98	0.49	0.43	2.23	0.35	2.74
L178P00BW-3	0.85	n/a	1.98	0.40	0.44	1.83	0.36	2.25
L178P80BW-5	1.13	n/a	1.44	0.40	0.23	2.51	0.21	2.70
L178P40BW-6	0.24	n/a	1.44	0.24	0.23	1.52	0.21	1.64
L178P00BW-7	0.34	n/a	1.44	0.22	0.23	1.39	0.21	1.50
Mean T/P ratio				0.46		2.11		2.57
Coeff. of Variation				0.47		0.42		0.43

Table 1.5 – Comparison of D/t < 60 Specimen Critical Strains with Vitali, *et al.*,1999

Specimen ID	Experimental	Vitali, *et al.*, 1999	
	Total Strain (%)	ε^{crit}_c (%)	Test-to-Predicted Ratio
UGA12	0.99	1.31	0.75
HGA12	1.58	3.68	0.43
DGA12	2.90	6.04	0.48
DGA508	2.81	3.81	0.74
KD/t=48	3.42	7.19	0.48
Mean T/P ratio			0.58
Coeff. of Variation			0.27

Table 1.6 - Comparison of Plain Specimen Critical Strains with CAN/CSA-Z662-96 and DNV-OS-F101-2000

Specimen ID	Experimental		CAN/CSA-Z662-96		DNV-OS-F101-2000	
	Total Strain (%)	Bending Strain (%)	ε^{crit}_c (%)	Test-to-Predicted Ratio	ε^{crit}_c (%)	Test-to-Predicted Ratio
UGA12	0.99	0.94	0.75	1.32	1.02	0.92
HGA12	1.58	1.55	0.89	1.77	2.87	0.54
DGA12	2.90	2.89	1.31	2.21	4.71	0.61
DGA508	2.81	2.80	1.27	2.21	2.97	0.94
CP0N	0.23	0.18	0.30	0.76	0.11	1.64
CP20N-1	0.31	0.27	0.37	0.84	0.22	1.25
KD/t=48	3.42	3.35	1.92	1.78	5.61	0.60
KD/t=92-1	0.47	0.35	0.31	1.53	0.14	2.57
KD/t=92-2	0.46	0.41	0.30	1.51	0.11	3.74
L178P80BP-4	3.10	n/a	1.50	2.06	3.39	n/a
L178P80BP-8	0.46	n/a	1.29	0.36	1.03	n/a
Mean T/P ratio				1.49		1.42
Coeff. of Variation				0.41		0.76

Table 1.7 – Comparison of Girth Welded Specimen Critical Strains with CAN/CSA-Z662-96 and DNV-OS-F101-2000

Specimen ID	Experimental		CAN/CSA-Z662-96		DNV-OS-F101-2000	
	Total Strain (%)	Bending Strain (%)	ε^{crit}_c (%)	Test-to-Predicted Ratio	ε^{crit}_c (%)	Test-to-Predicted Ratio
UGA12W	0.64	0.59	0.75	0.85	0.68	0.86
HGA12W	1.11	1.08	0.89	1.25	1.91	0.56
DGA12W	1.90	1.89	1.31	1.45	3.14	0.60
UGA20W-2	0.81	0.76	0.54	1.50	0.34	2.21
HGA20W	1.04	1.01	0.72	1.44	1.03	0.98
DGA20W	1.87	1.79	1.27	1.47	1.72	1.04
Sp=0	0.75	0.70	0.78	0.96	0.73	0.95
Sp=40	1.20	1.13	0.94	1.27	2.24	0.51
Sp=80	1.70	1.62	1.44	1.18	3.75	0.43
L178P80BW-1	1.20	n/a	1.50	0.80	2.02	n/a
L178P40BW-2	0.97	n/a	0.81	1.20	1.21	n/a
L178P00BW-3	0.80	n/a	0.58	1.39	0.41	n/a
L178P80BW-5	0.58	n/a	1.30	0.45	0.48	n/a
L178P40BW-6	0.35	n/a	0.59	0.60	0.28	n/a
L178P00BW-7	0.32	n/a	0.35	0.92	0.09	n/a
Mean T/P ratio				1.05		1.37
Coeff. of Variation				0.36		0.96

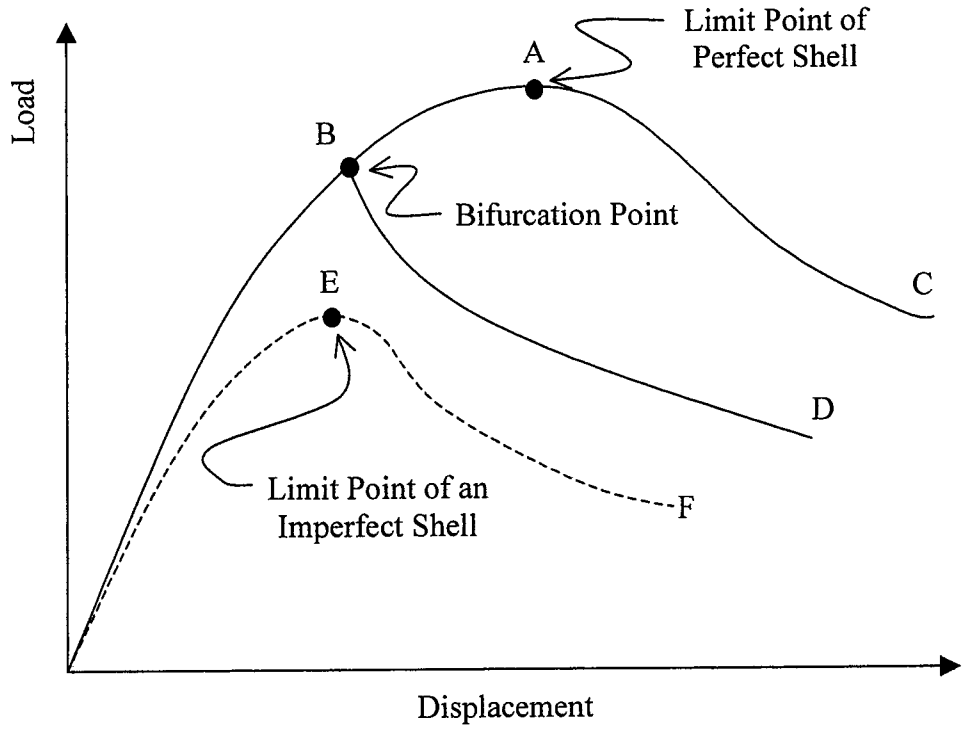

Figure 1.1 – Typical Load-Displacement Response of Shell Structures

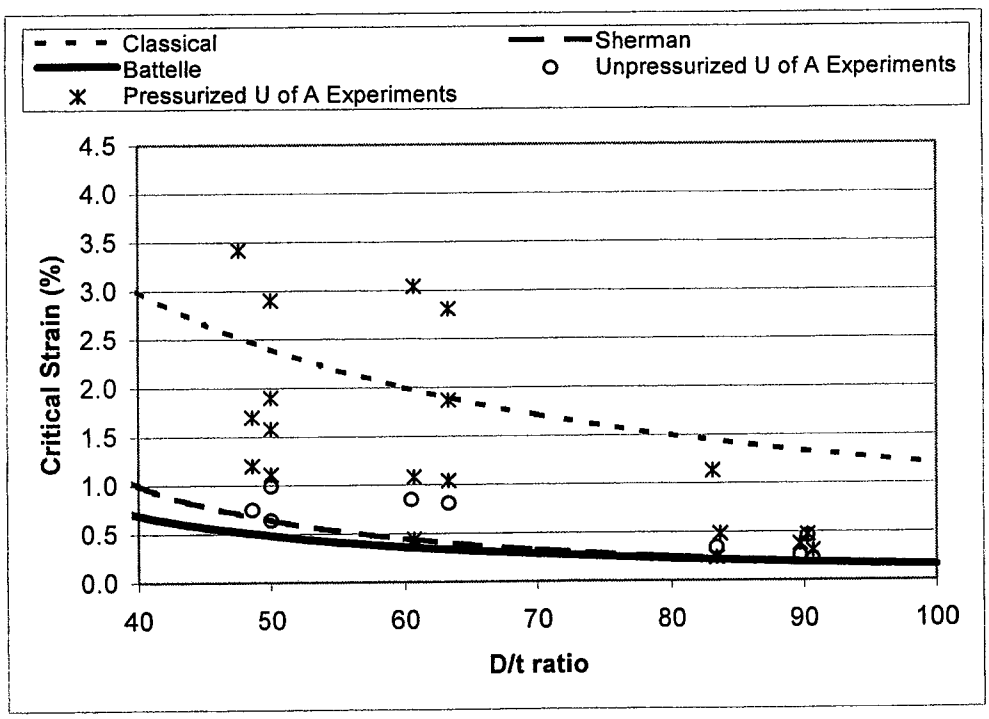

Figure 1.2 – Comparison of the Classical, Sherman and Battelle Equations with U of A Experimental Data

2.0 EXPERIMENTAL PROGRAM

The experimental portion of this research program was designed and implemented to investigate the behaviour of large diameter-to-thickness (D/t) ratio specimens. As outlined in the previous chapter, much research has been done at the U of A on the deformation response of line pipe, both plain and girth-welded, under combined loading. The experimental portion of this program was designed to expand the U of A database by examining the deformation behaviour of test specimens with a D/t ratio of 92 under different combined load cases. Specifically, the experimental program was set up to collect data on the moment-curvature response and critical buckling strains of D/t = 92 line pipe and to provide laboratory observations for comparison with analytical results. This chapter outlines the details of the experimental program.

2.1 Experimental Parameters

One of the main objectives of this project was to investigate the deformation of pipelines subjected to combined loading, as may be experienced by buried pipelines under field conditions. Therefore, it was important to simulate the field conditions as accurately as possible.

For this investigation, it was decided to examine the effects of three basic loads to which a buried pipeline may be subjected. Specifically, the response of the pipeline to monotonically increasing curvature with a constant internal pressure and a constant axial load was examined.

2.1.1 Monotonically Increasing Curvature

A buried pipeline is often subjected to monotonically increasing curvature due to differential ground movements. These differential movements include settlement, frost heave and slope instability considerations. Figure 2.1 shows a schematic of differential

settlement between two adjacent segments of pipeline. From this figure, it can be seen that curvatures develop at both the top and the bottom of the transition zone between the segments. Furthermore, it can be observed that as the differential settlement increases, so does the magnitude of the curvature in the pipeline at these points.

A schematic of the test set-up is shown in Figure 2.3. In order to simulate the effect of increasing curvature in the laboratory, two hydraulic jacks, aligned parallel to the longitudinal axis of the test specimen, were placed in the test set-up at a distance of 1.5 m perpendicular to the longitudinal axis of the test specimen. When load was applied to the end of the moment arms through the eccentrically located jacks, the force in the jacks, acting over the distance of the moment arms, generated a global moment on the end plates. This global end moment was transferred to the end of the test specimens through the welds between the end plates and the ends of the test specimens. During a test the force in the jack was progressively increased, thereby resulting in a monotonically increasing curvature.

2.1.2 Internal Pressure

Internal pressure is developed in a pipeline by the pressure head applied to maintain the flow of the fluid or gas within the line. The presence of internal pressure causes stresses to develop in the pipeline wall in both the longitudinal and hoop directions. Using simple statics it can be shown that the internal pressure that causes the yield stress to develop in the hoop direction (p_y) is

$$p_y = \frac{2 F_y t}{(D - 2t)} \tag{2.1}$$

where F_y is the yield stress (MPa) in the hoop direction, D is the outside diameter (mm) of the pipeline, and t is the wall thickness (mm).

Clause 4.3.3.1.1 of CAN/CSA-Z662-96 states that the allowable design pressure (p) in kPa for a segment of straight pipe using the notation adopted in this research may be determined as

$$p = \frac{2 F_y t}{D} \times 10^3 \times F_f \times L_f \times J_f \times T_f \qquad (2.2)$$

where

F_f = design factor
L_f = location factor
J_f = joint factor
T_f = temperature derating factor.

Considering the most typical type of pipe segment, which would be a section of straight pipe in a remote location, and applying the appropriate values specified in CAN/CSA Z662-96 for F_f, L_f, J_f and T_f, this equation reduces to

$$p = \frac{1.6 F_y t}{D} \quad \text{(MPa)} \qquad (2.3)$$

The maximum experimental design pressure as a percentage of the yield pressure can be calculated by assuming that $(D - 2t) \approx D$, which is a reasonable assumption for large D/t ratio specimens, and then dividing Equation (2.3) into Equation (2.1) as follows:

$$\frac{p}{p_y} = \frac{\frac{1.6 F_y t}{D}}{\frac{2 F_y t}{D}} = 0.80 \qquad (2.4)$$

Internal pressures of 0, 20, 40 and 80% p_y were selected for investigation in this project. The 0% p_y load case is considered a minimum internal pressure that a pipeline may experience under field conditions. This condition exists when there is a complete loss of pressure in the system, which may occur for a variety of reasons.

The 80% p_y load case is the maximum permitted by CAN/CSA-Z662-96, as shown in Equation (2.4) above, and would occur at a point immediately downstream from a pumping or compressor station. The intermediate value of 40% p_y was selected to

provide a data point halfway between the two extreme values. In the study by Mohareb *et al.* (1994), a difference was found in buckling mode between the 0% p_y and 40% p_y load cases. This led to the introduction of the 20% p_y load case under the current investigation in an attempt to determine the transition point between the two different modes.

2.1.3 Axial Load

2.1.3.1 Simulation of Field Applied Loads

The development of axial forces in pipelines can be attributed to a variety of factors. The four primary factors are: the effect of a temperature differential between the tie-in temperature and the operating temperature; Poisson's effect due to the internal pressure in the pipeline; caternary action between adjacent pipeline segments due to settlement or frost heave action; and imposed axial forces that develop when ground movements have a component parallel to the longitudinal axis of the pipe, such as may occur in sloping ground or when geotechnical movements occur.

Due to ground conditions, pipelines are often placed during winter months when the required equipment is able to forge swamplands and other wet terrain because it is frozen. Consequently, pipelines are often installed when the ambient temperature is in the order –30°C. Since pipeline operating temperatures can be as high as +15°C, this would correspond to a temperature differential of approximately 45°C. It is recognized that temperature differentials can vary significantly from the 45°C value, however, this differential was selected as a representative value.

Since the differential temperature is positive, the pipeline will attempt to expand longitudinally. However, the friction forces between the outer wall of the pipeline and the adjacent soil restrain this longitudinal movement. In addition, compressor or pumping stations and bends in the pipe can also offer longitudinal restraint. Consequently, compressive forces due to the thermal differential (P_α) develop. Quantitatively, these forces may be evaluated as

$$P_\alpha = - A E \alpha \Delta T \tag{2.5}$$

where

A = cross sectional area of the pipeline (mm^2)
E = Modulus of Elasticity of the pipeline material (MPa)
α = the coefficient of thermal expansion of the pipeline material (/°C)
ΔT = the temperature differential (°C)

All of the compression test specimens were subjected to a load corresponding to constant thermal differential of +45°C. Since all of the specimens had the same nominal cross section and the same nominal material properties, P_α was a constant for all of the test specimens. Using Equation 2.5 P_α was evaluated as

$$P_\alpha = -\frac{\pi}{4}\left(762^2 - 745.4^2\right)(200000)\left(11.7 \times 10^{-6}\right)(+45) \times 10^{-3}\ \text{kN/N} = -2069\ \text{kN} \tag{2.6}$$

The second factor that influenced the magnitude of the axial force to be applied during testing was Poisson's effect. The applied internal pressure described in Section 2.1.2 causes the specimens to expand in the radial direction. Due to this radial expansion, the test specimens attempt to shorten in the longitudinal direction. However, a buried pipeline in the field may be considered in a condition of plane strain and restrained against this shortening. This results in an axial tension developing in the test specimen due to Poisson's effect. The magnitude of the axial load due to Poisson's effect (P_ν) in the test specimen may be calculated as

$$P_\nu = + A \nu \sigma_h = + A \nu \frac{p}{p_y} F_y \tag{2.7}$$

where ν is Poisson's ratio and σ_h is the stress in the circumferential direction (hoop stress).

Combining these two axial load effects, the net axial force (P_N) in the wall of the compression test specimens can be calculated as

$$P_N = P_\alpha + P_\nu \tag{2.8}$$

where P_α is the axial force due to temperature from Equation 2.5 and P_ν is the axial force due to Poisson's effect from Equation 2.7

The third axial load effect considered in the experimental program was a net tensile force in the wall of the test specimen. When there is differential movement in the vertical direction of two adjacent regions of a pipeline, the elongation of the centerline of the pipeline due to ground movement caternary action causes tensile forces to develop in the pipeline. This is evident in Figure 2.1. It should be noted that tensile forces often develop in a pipeline that has been installed on a sloped surface. At the crest of the slope the pipeline may be subjected to a tensile axial load that may develop due to slope instability, whereas at the base of the slope compressive axial loads would develop.

The tensile forces that may develop in a segment of line pipe are generally not well defined and would be difficult to evaluate. For the purposes of this research a net tensile wall force (P_T) of 20% the yield wall force was selected. This was based on the practical consideration that tensile forces of this magnitude could be readily introduced into the test specimens without significant modifications to the test set-up used for the specimens subjected to the compressive axial forces. Quantitatively, P_T was calculated as

$$P_T = 0.20\ F_y\ A \tag{2.9}$$

Since the 20% SMYS axial was selected to be a constant, P_T was calculated as

$$P_T = 0.20\ (483)\ (\pi/4)\ (762^2 - 745.4^2)\ \times 10^{-3}\ \text{kN/N} = 1898\ \text{kN} \tag{2.10}$$

This tensile axial load was considered as the net total force for the tensile specimens, including temperature, Poisson's ratio, and the caternary action load effects.

2.1.3.2 Compensating Axial Loads Imposed Due to Test Set-Up

Under the laboratory test set-up additional axial loads were imposed on the test specimens. These loads were applied to counteract the internal pressure acting on the closed end of the test specimen (P_p) and to counteract the effects of the jack force (P_{jack}), which was required to induce the monotonically increasing curvatures described in section 2.1.1. These forces are identified on the free body diagram given in Figure 2.2

The axial load due to the pressure acting on the closed ends of the test specimens does not exist for an open-ended pipe installed in the field. In order to maintain the desired level of axial force in the pipe wall, a compensating force must be applied to the test specimens by the MTS machine to account for this. The axial load due to the internal pressure, P_p, may be calculated as

$$P_p = \pi r_i^2 p \tag{2.11}$$

where r_i is the inside radius of the test specimen.

Since the force in the eccentric jack was an experimental variable, the axial load due to the jack force, P_{jack}, also had to be compensated for during testing. The methods used to compensate for P_p and P_{jack} are described in sections 2.4.1.2 and 2.4.1.3, respectively.

2.2 Test Specimen Preparation

2.2.1 Test Specimens

The test specimens used in this experimental program were NPS30 pipe sections with an outside diameter of 762 mm with a thickness of 8.3 mm. This resulted in an experimental D/t ratio of 91.8. The steel used in preparing the test specimens was Grade X70 with a specified minimum yield strength (SMYS) of 483 MPa.

All of the specimens had a single longitudinal seam weld, fabricated using the double submerged arc welding process (DSAW), running the length of the specimen. In this process, flat steel plates are passed through a series of rollers and/or presses until they have been cold-formed into an almost closed circle (Stelco, 1993). The seam is then tacked in place so that the two open edges are perfectly aligned. The pipe segment is then seam welded using the DSAW process. The welding process is accomplished by passing two coincident weld beads along the seam, one from the exterior of the pipe and the other from the interior. The weld beads are laid by striking an electric arc between a consumable electrode and the almost closed edges of the rolled plate. Each of the bead passes is done with the weld in the "down-hand" position. Once the welding procedure is complete, the pipe segment is subjected to hydrostatic testing and/or mechanical expansion. The purpose of these two procedures is to ensure the pipe's ability to withstand a specific internal pressure and to meet roundness and diameter tolerances accurately. It is important to note that the mechanical expansion process imposes a plastic deformation on the segment of pipe, which, theoretically eliminates the yield plateau and results in a pipe yield strength increase. This will be further discussed in section 4.1.1.

For the girth-welded specimens, the longitudinal seam welds were not aligned on either side of the girth weld during fabrication. This is typical of industry field practice. The distance around the circumference of the specimen between the longitudinal seam weld in the two segments varied from specimen to specimen, but never exceeded one-fifth of the circumference of the pipe (~70°). When aligned in the test set-up, special attention was taken to ensure that the longitudinal seam weld was aligned in the tensile region of test specimen so that the seam weld would not affect the buckling characteristics on the compression face of the specimen.

An infrared thickness-measuring device was used to assess the variation in thickness of the pipe wall for the first two test specimens. Reduction of the pipe wall variation data from these two specimens revealed that the variations reported by the device were less than the error limits of the device and, therefore, could not be considered reliable. As a

result, infrared measurements were not carried out on the remaining specimens. Instead, thickness measurements were taken from the coupon specimens used in the material tests described in section 2.4.3.

2.2.2 Specimen Preparation

Prior to delivery to the I.F. Morrison Structural Engineering Laboratory at the U of A, test specimens were cut to a length of 2700 mm and the ends beveled to an angle of 60^{o} to facilitate the welding of the specimens to the testing frame. The exterior surface of the pipe was sandblasted to make the installation of instrumentation easier and for aesthetic enhancement of the post-buckled specimens. A length of 2700 mm was selected to provide an L/D ratio of 3.5 in the specimens. This was considered adequate enough to ensure that the stress distribution over the middle third portion of the specimen would not be significantly affected by the boundary conditions.

Once the specimens were received each specimen was given an identification designation. This designation was selected based on the load case to which the test specimen would be subjected. The number had the following format:

$$F\ \#_1\ P\ \#_2\ Q$$

where,

- 'F' was used to identify the specimens as having either a net compressive wall force (C) or a net tensile wall force (T)
- '$\#_1$' was used to identify the magnitude of the net tensile wall force as a percentage of the force required to cause yield in the longitudinal direction. Since all of the compression specimens were subjected to the same axial load, '$\#_1$' was neglected for all of the compression specimens
- 'P $\#_2$' was used to identify the magnitude of the internal pressure as a percentage of the internal pressure required to cause yielding in the hoop direction (p_y)
- 'Q' was used to identify the specimen as a either a specimen having no circumferential welding (N) or a specimen with a circumferential girth weld at the half-height of the specimen (W).

For example, the specimen with the ID code 'CP20W' was subjected to a compressive load corresponding to the +45°C temperature differential, had an internal pressure of 20% p_y, and had a circumferential girth weld located at the half-height of the specimen. The specimen with the ID code 'T20P80N' was subjected to a net tensile load corresponding to 20% of the longitudinal yield force, had an internal pressure of 80% p_y, and had no circumferential welds.

Once the specimens were identified a grid was drawn on the compression face of the specimen, symmetrical to the half-height circumference. This grid was used to assist in properly locating instrumentation and to enhance the appearance of the buckled configuration. Electronic strain gauges were then installed on the grid. Figure 2.4 provides a frontal view of a test specimen, showing the grid and the installed electronic strain gauges. The strain gauges were positioned to provide measurements around four different cross-sections evenly spaced along the length of the specimen. Additional strain gauges were placed along both the extreme tension and extreme compression fibres, such that the electronic strain gauges were placed at intervals of 254 mm, symmetric to the half-height of the specimen.

2.2.3 Imperfection Measurements

Many researchers have shown that imperfections can cause an order of magnitude error in the buckling load of shells (for example, Galambos, 1988). Therefore, imperfection measurements were taken across the inside surface of the test specimens. A new measuring apparatus, similar to one used previously, was constructed for this investigation. A new apparatus was deemed necessary because the previous makeshift apparatus was believed to lack the required sensitivity to make an accurate assessment of the actual imperfections in the pipe wall. The new apparatus was fabricated using a high-precision machined rail, a tailor fitted carriage, and new end supports that allowed free rotation of the rail about the central vertical axis. Figure 2.5 shows the upper end of a test specimen with the device fabricated to measure the imperfections positioned near the top on the inside of the pipe.

The experimental initial imperfection pattern was measured as follows. The carriage was mounted on the rail and the measuring assembly was positioned vertical on the floor of the testing lab. The specimens were then positioned vertically on their end with the measuring apparatus located inside the wall of the test specimen. Once the specimen was in place, the rail was carefully positioned at the center of each end of the test specimen and then bolted in place, as shown in Figure 2.5.

Imperfections were measured using a linear variable differential transducer (LVDT) mounted on the carriage. The LVDT was installed on an arm bolted to the carriage. A spring-loaded mechanism was installed to ensure that the tip of the LVDT was always in contact with the inside wall of the pipe. Since the end support conditions allowed the rail to rotate around the full inside circumference of the test specimen and the carriage was able to move along the full length of the rail, any point on the inside circumference of the pipe wall could be measured. Initial imperfection measurements were taken on a mesh across in the interior face of each test specimen. The imperfection mesh measured approximately 150 mm around the inner circumference and 180 mm along the length of the specimens.

A total of 16 imperfection measurements were taken at each elevation (every 22.5^{o} around the inside circumference). A total of 14 elevations were taken on the plain pipe specimens. A total of 16 elevations were taken on the specimens with a circumferential girth weld, the extra 2 elevations being directly above and directly below the girth weld so that the offset of the two cans could be assessed and later modeled. Once the imperfection measurements were complete, the specimens were ready for installation into the testing frame.

It should be noted that there are a number of limitations to the set of imperfection data collected. First, the measurements were made prior to the welding of the specimens to the end plates. It is understood that the welding process may affect the magnitude and location of initial imperfections. However, once the end plates were welded on to the test specimens, there was no way to measure the imperfections. Secondly, it is also

understood that the imperfection grid selected may miss some of the more localized initial imperfections such as local dents. Nevertheless, the method employed was felt to provide the most accurate representation measurable and was therefore accepted as the initial imperfection profile of the respective specimens. Finally, the rail used for the imperfection measurements was a high-precision machined rail. However, because the length of the rail was approximately 3.0 m, there was concern that the rail may not be straight. To account for any non-linearity of the measuring device, a set of imperfection measurements were also taken on the rail itself, which were later accounted for in the recorded imperfection measurements, as outlined in section 3.3.7.

2.3 Test Set-up

A substantial amount of research into the behavioral response of buried pipeline to combined load conditions has been conducted at the U of A (Mohareb, *et al.* (1994); Yoosef-Ghodsi *et al.* (1994); and Del Col *et al.* (1998)). The test set-up used in this project was similar to those used in these previous pipeline research programs at the U of A.

Figure 2.6 shows the frontal view of an NPS30 test specimen in the test set-up. An appreciation for the scale of the test specimens can be achieved by comparing the set-up to the two men in the photo. Figure 2.7 shows a side view of a specimen in which both the top and bottom moment arms and the jacks, located above and below the W-section spacer behind the chains, are clearly evident.

2.3.1 Installation of Specimens in the Test Set-up

After the test specimen was prepared, the preliminary instrumentation installed and the imperfection measurements taken, it was ready for installation into the testing assembly. The steps followed during the installation of the specimens in the test set-up were considered critical to ensure proper response. The steps used are outlined below.

1. The upper moment arm was placed in the inverted position on the lab floor and then shimmed such that the upper end plate to which the test specimen was to be welded was level. This made both the alignment of the specimen on the upper end plate and the welding process easier.

2. The test specimen was then centered on the upper end plate to ensure that the load applied through the MTS loading head would be concentric to the test specimen.

3. The test specimen was aligned vertically using shims and plumbs to ensure that the specimen would be perpendicular to the end plate. The alignment of the specimen was checked in both the in-plane and out-of-plane bending directions.

4. The top end of the specimen was then welded to the end plate. Figure 2.8 shows a schematic of the welding passes placed into the joint at the inverted top end plate.

   It should be noted that on the first three specimens, all passes in the weld joint were made with E8018-C3 electrodes (low-hydrogen rods) with increasing diameter as the passes moved out of the root. During the testing of the third specimen, which was a tension specimen, lamellar tearing of the bottom end plate occurred. New 516-Grade70 end plates were ordered and used for all of the remaining tension tests. At that time, the decision was made to use E7018-1 electrodes for greater compatibility with the base metal in the pipe and the end plates.

5. The bottom end moment arm assembly was positioned in the MTS testing machine such that the end plate was leveled. Figure 2.9 shows a view of the bottom moment arm assembly in the MTS testing machine.

6. Once the welding of the top end of the specimen was complete the top moment arm and test specimen assembly was lifted and rotated to the up-right position. The assembly was then transferred to the MTS testing machine using a crane and aligned in the machine between the bottom end plate and the MTS loading head. Figure 2.10

shows a view of the upper end plate, the top moment arm assembly, and the MTS loading head.

7. The bottom end of the test specimen was then welded to the bottom end plate using the same welding process described in step #4 above. Assembling the test specimen in this fashion permitted down-hand welding at both ends of the specimen.

8. Once the test specimen was positioned and aligned in the loading frame the remaining components of the test frame were installed. This included the bracing system, eccentrically located jack assembly, and the pressure hoses.

2.3.2 Additional Instrumentation

After the specimen was mounted in the test set-up additional instrumentation was then installed. This additional instrumentation included:

- a series of nine linear variable differential transformers (LVDT's) spaced at intervals of 254 mm along the extreme compression fibre. These LVDT's were used to record the horizontal displacement of the compression face as the specimen deformed. The LVDT's were mounted in a support frame to a column located a distance of 3.0 meters away from the test specimen to minimize the effect of the vertical displacement in the loaded specimen. Figure 2.11 shows three of the compression face LVDT's in the support frame and Figure 2.12 shows the connection between the LVDT's and a typical pipe specimen.

- a series of three LVDT's centered at the ½ height of the test specimen and spaced at intervals of 254 mm along the extreme tension fibre. These LVDT's were used to measure the horizontal displacement of the tension face and, ultimately, coupled with the compression face LVDT's, allowed the change in in-plane diameter to be determined.

- two rotational meters mounted on the sides of the end plates in line with the centroid of the test specimen. These rotation meters were positioned to measure the absolute rotation of the end plates, which was later used to determine the global curvature of the test specimen.

- a series of six cable transducers mounted on the bottom end plate. Three of the cable transducers were positioned between the rigid strongfloor and the underside of the bottom end plate and the other three were positioned between the top and bottom end plates along the length of the test specimen. From the positioning of the cable transducers the rotation of each of the two end plates could be determined relative to the strongfloor of the lab, thereby allowing for the relative rotation of the ends of a specimen to be determined. It should be noted that the purpose of using the cable transducers was to confirm the global rotations measured by the rotation meters and the rotation data recorded using the cable transducers was not used in any subsequent calculations.

- a series of ten Demec points (allowing for a total of nine measurements) were bonded along both the extreme compression and the extreme tension fibre. A gauge length of 254.0 mm was used for the Demecs. The position of the Demecs alternated with the electronic strain gauges, with the middle Demec spanning the half height elevation of the specimen. Figure 2.12 showed the compression face of one of the test specimens. There is a circumferential girth weld located at the half height of the specimen highlighted by the white line immediately above the label 'DC-5', in Figure 2.12. There are Demec points, which look like small buttons, located at the gridline intersections immediately above and below the girth weld and at every second gridline from the half-height to each end of the specimen. The electronic strain gauges are located under the pieces of black electrical tape, evident in Figure 2.12.

  The purpose of the Demec points was to allow for a set of strain measurements after the specimen buckled. Prior to buckling of the test specimen, the electronic strain gauges provided a set of accurate strain measurements. Once the specimen buckled

the electronic strain gauges in the buckled region gave readings that were not representative of the true local strain because of the disturbance due to the buckle. Therefore, the Demec gauge was used to measure strains in the buckled region. It should be noted that as the magnitude of the buckle grew the Demec gauge also ran out of stroke. Once the Demecs were out of stroke a pair of dividers and a tape measure were used to measure the deformation of the buckled region. These measurements were later converted to units of strain. Figure 2.13 shows a divider reading being taken on a spiral-welded specimen.

This completes the description of the experimental test set-up.

2.4 Experimental Testing Procedure

2.4.1 Application of Experimental Loads

2.4.1.1 Internal Pressure

The internal pressure was applied hydrostatically to the test specimens. Inlet and outlet holes were drilled in the rigid end plates, then tapped and valves were fitted into the holes. This provided access to fill and drain the specimens with water. A manually controlled, pneumatically driven pump was connected to the municipal water supply and then to the inlet valve. A pressure transducer was placed in the line between the pump and the inlet valve. The pressure transducer was then connected to the data acquisition system to allow "instantaneous" pressure readings to be taken. The desired magnitude of internal pressure for each of the test specimens is given in Table 2.1.

2.4.1.2 Axial Load

The MTS 6000 Universal Testing Machine in the I. F. Morrison Structural Engineering Laboratory at the U of A was used to apply the concentric axial load to the test specimens. The MTS machine was put in 'manual stroke control' mode during testing of the specimens. The use of stroke control ensured that the MTS did not cause sudden collapse when the test specimen had a loss of capacity due to buckling. Manual control

was selected such that the MTS load could be readily adjusted to the desired load level in order to achieve the prescribed net axial wall force.

As previously discussed, with the exception of the Poisson's ratio effect, the axial load due to the internal pressure does not exist in a pipeline under field conditions. However, such a load was generated in the laboratory because of the test set-up used and the finite length of the specimens tested. To cancel out the laboratory generated axial load due to the internal pressure applied to the test specimen, the load in the MTS Testing Machine was increased to counteract it.

For the compression specimens the required initial MTS load, prior to application of any moment loads, was calculated as

$$\text{MTS load} = P_N + P_p = P_\alpha + P_\nu + P_p \tag{2.12}$$

Table 2.1 gives the magnitude of the design values for the initial MTS load, P_N, P_p, P_T, and P_ν for the eleven compression specimens tested, based on the nominal dimensions and material properties of the test specimens.

For the tension specimens the required initial MTS load, prior to application of any moment loads, was calculated as

$$\text{MTS load} = P_T + P_p \tag{2.13}$$

Table 2.2 gives the magnitudes of the design values for the MTS load, P_T, and P_p for the four tension specimens tested, based on the nominal dimensions and strength of the test specimens.

2.4.1.3 Monotonically Increasing Curvature

The monotonically increasing curvature was developed through a pair of eccentrically located 1800-kN jacks, as shown in Figure 2.3. Figure 2.14 shows a side view of the jacks and the W-section spacer between the jacks.

It should be noted that the jack force required to apply the end moments also contributed to the tensile force to be developed in the pipe wall in the test specimen, as shown in Figure 2.2. To account for this additional axial load, the respective MTS load calculated using equations (2.12) and (2.13) was adjusted accordingly by increasing the applied MTS load P_{jack} for any given load increment. This ensured that P_N of any test specimen, as presented in Table 2.1 and Table 2.2, was maintained as a constant throughout the duration of a particular test.

2.4.2 Test Procedure

1. Once a test specimen was instrumented and aligned in the load frame, it was then pressurized to the prescribed internal pressure given in Table 2.1 or Table 2.2 using the pneumatic pump.

2. After the correct internal pressure was achieved the MTS load was increased until the desired net axial force in the pipe wall was achieved, as given in Table 2.1 or Table 2.2.

   It should be noted that steps 1 and 2 were often an iterative process because the two loads affected the magnitude of each other. More often than not the two load steps were done concurrently so that neither the specimen's internal pressure nor its net axial wall force exceeded the prescribed levels.

   At this stage, the end collars were tightened into place. The purpose of the end collars was to provide a form of transition zone between the ends of the test specimens, which were rigidly welded to the end plates, and the loaded region. The collars were constructed of a 150-mm segment cut from the original joint of pipe used

to fabricate the test specimens. The collar segment was then cut in half and the diameter increased slightly by applying a prying force to each half segment. Bolt anchors made of angle iron were welded to the exterior of each end of each half. The two half collars were placed around the pipe at each end of the specimen and then bolted in place with two 19-mm bolts at each joint in the collar. Figure 2.15 shows the end collar at the top of the test specimen.

It is imperative to note the time at which the collars were tightened. Del Col *et al.* (1998) tightened the collars on some of their test specimens prior to the application of any loads (i.e., before step #1 outlined in this procedure). After re-evaluation, it was decided that premature tightening of the collars may have influenced the location at which the buckle occurred in the specimens. The desired response was to have the buckle occur in the region that most accurately represents a segment in a continuous pipeline, without any influences from the laboratory set-up. Therefore, it was believed that the specimen should be allowed to deform freely under the internal pressure and the desired net axial wall force. Once this deformation had occurred, the ends could then be constrained by the tightening the collars in preparation for the bending of the test specimen.

3. The force in the eccentric jack was then increased, thereby applying global end moments to the test specimens and increasing the pipe curvature. Initially, the jack force was increased in increments of approximately 100 kN, which corresponded to increase in the global end moment of approximately 150 kN-m.

4. After a prescribed increment in moment was achieved, both the internal pressure and the MTS loads were adjusted in order to re-establish the desired levels. Once the desired load levels had been reached and the loads had stabilized, a set of electronic data was recorded.

5. At intervals in moment of approximately 450 kN-m manual Demec readings were recorded. This was done over the pre-buckling range in order to verify the

consistency between the electronic strain gauge measurements and the manually recorded measurements, which in turn would provide confidence to the post-buckling manual readings for which there was no confirming electronic strain gauge data.

6. A few of the test specimens were depressurized as the peak load was approached to simulate the effect of a loss of pressure in the field. During the depressurization, both the net axial force in the pipe wall and the imposed curvature were maintained as constants, as would occur in the field. The purpose of this depressurization was to examine if a buckling failure could be induced through depressurization, which may occur under operating conditions.

   It should be noted that the depressurization procedure was only performed on a few of the specimens. This was because none of the depressurizations attempted in this phase of the project, nor those attempted by Del Col *et al.* (1998), managed to produce a 'depressurization buckle'. Consequently, it was decided not to continue with the attempts to cause buckling through depressurization. For those specimens for which the depressurization was attempted, the correct internal pressure was restored prior to continuing the testing.

7. When the peak load was approached, as was evidenced by a loss of stiffness or 'flattening' of the jack-load versus rotation curve recorded electronically during testing, the moment interval between readings was reduced to increments of approximately 30 to 50 kN-m. Additional Demec and additional electronic data readings were also taken. This was done in an attempt to capture as much data as possible around the peak of the moment-curvature response. Particular care was given to the unpressurized test specimens ($p/p_y = 0\%$) because of the possibility of 'snap-back' behaviour, which is characterized by a sudden loss of capacity immediately after buckling as evidenced by the $p/p_y = 0\%$ specimen tested by Del Col *et al.* (1998). As a result, the load increments were made even smaller for the $p/p_y = 0\%$ specimens.

8. After the peak moment was achieved incremental loading continued. Since the jack force and, thus, the global end moment reduced after buckling, these were no longer suitable parameters by which the level of the increment could be determined. Instead, increments of imposed curvature or deformation were used. These increments corresponded to varying decrements in the amount of global end moment depending on the location on the post-buckling curve.

   At each increment it was necessary to adjust the level of both the internal pressure and the axial load. This is because the test specimens were undergoing large deformations in the post-buckled region, which had a direct impact on the magnitude of the internal pressure and the axial load. Again, it should be noted that for the entire duration of the test, both the internal pressure and the axial load were maintained at constant values.

   Demec readings were taken in the post buckled region to provide strain measurements across the buckle on the specimen. In the experimental analysis, the electronic strain gauge data in the area around the buckle was not used because the strain at any gauge location becomes dependent on the precise position of the gauge relative to the deformed shape of the buckle. Once the Demec gauges ran out of stroke, a simple pair of dividers and a tape measure were adequate to measure the strain because of the large magnitude of the deformations that had occurred. Figure 2.16 shows what would be considered a large deformation buckle, which will hereafter be called a wrinkle. Observe the strain gauge near the crest of the wrinkle and the Demec points on the gridline at the top and the bottom of the photo, respectively. Due to the amplitude of the buckle the Demec gauge could no longer be placed between these two Demec points, thereby necessitating the use of the dividers and measuring tape.

   It is also interesting to note the location of the strain gauge relative to the buckle. Although this strain gauge was located on the extreme compression fibre of the test specimen, it was nevertheless reporting a tensile strain increment (+4031 $\mu\varepsilon$) after buckling had occurred. This is because the gauge was located in the tension region of

the buckle, despite being on the compression face of the specimen. Clearly, the local effects of the buckle recorded by the strain gauge are not consistent with the overall behaviour exhibited by the test specimen. This provided the basis for ignoring the post-buckling electronic strain gauge data in the region of the buckle.

9. Testing continued over the post-buckled region of the moment-curvature response curve until the negative slope of the jack-load versus curvature curve exhibited signs of 'flattening' and there was sufficient data collected to adequately define the post-buckled region.

This completes the description of the test procedure.

2.4.3 Determination of Material Properties

In order to assess the material properties of the test specimens an additional segment was cut from each joint of pipe that test specimens were taken from. In total, five different joints of pipe were used to produce the 16 coupon test specimens, including those tested by Del Col, *et al.* (1998). Accordingly, five different sets of material properties were determined.

Three longitudinal tension coupons were cut from each of the additional segments. It is realized that the circumferential and longitudinal material properties will differ for a segment of line pipe. However, it was believed that the circumferential material properties would not accurately represent the actual material properties of the specimen because the coupons would have to be straightened in order to be tested. This straightening would introduce a residual stress pattern that was not present in the actual test specimens.

DiBattista (2000) has shown that, in general, there is a significant difference in the proportional limit between the longitudinal and circumferential coupons from line pipe, but that there is little difference in the yield point. It is believed that this is a result of a difference in the residual stress pattern for the different directions. Testing of the

circumferential coupons required straightening of the coupon, which introduces an unknown, unquantifiable residual stress pattern. Since the residual stress pattern is believed to be the main difference between the circumferential and longitudinal coupons, but it could not be accurately assessed, it was decided to only test the longitudinal coupons. This decision is supported by the high level of correlation that DiBattista had between his experimental results and the results of his finite element analysis (FEA), where only the material properties from the longitudinal coupon tests were used in the analysis.

The decision to use only the longitudinal material properties is further supported by the specific objectives of this test program. The test program was designed to assess the buckling response of the pipeline in the longitudinal direction when subjected to the combined load cases. The test specimens were not loaded to develop large circumferential strains and therefore the longitudinal direction was deemed to have the governing material properties.

The longitudinal coupons were prepared at a local machine shop and then tested in the MTS1000 Universal Testing machine at the U of A's I. F. Morrison Structural Engineering Laboratory. The testing procedure was conducted in accordance with ASTM Standard A370-94 (1994). Figure A2.3 of ASTM A370-94 provides dimensions and tolerances for strip tension test specimens for large diameter tubing. Coupons from category 4 of Figure A2.3 with a gauge length of 101.6 ± 0.381 mm (4 ± 0.015 in.) were selected.

Prior to testing, cross section dimensions were measured using an electronic caliper. Strain gauges were mounted in both the longitudinal and lateral directions on both faces of the coupon. The coupons were then placed in the hydraulic grips of the MTS1000. Coupon strains were measured using the electronic strain gauges and an externally mounted exstensometer. The load applied to the coupon was recorded using the MTS1000 output. Figure 2.17 shows a view of a typical tension coupon during testing.

Static data points were used in the determination of the material properties because they provide material properties independent of the rate of loading. The static points was recorded by taking data after the coupon had been held at a constant displacement for a period of approximately two minutes and the corresponding load had stabilized.

Data was recorded using a Fluke Data Acquisition System and electronically stored until the data was reduced at a later date. The reduction of the experimental material property data is discussed in section 4.1.1.

Table 2.1 Nominal Target Axial Loads for Compression Specimens

Specimen ID[1]	p/p_y[2] (%)	p[3] (MPa)	P_T[4] (kN)	P_v[5] (kN)	P_N[6] (kN)	P_p[7] (kN)	MTS Load[8] (kN)
CP0W-1	0	0.00	-2069[9]	0	-2069	0	-2069
CP0W-2	0	0.00	-2069	0	-2069	0	-2069
CP20W	20	2.15	-2069	570	-1499	-938	-2437
CP40W	40	4.30	-2069	1139	-930	-1876	-2806
CP80W	80	8.61	-2069	2278	+209	-3757	-3548
CP20N-2	20	2.15	-2069	570	-1499	-938	-2437
CP40N-2	40	4.30	-2069	1139	-930	-1876	-2806
CP80N-2	80	8.61	-2069	2278	+209	-3757	-3548

Notes:

1. As described in section 2.2.2.
2. As described in section 2.1.2.
3. A specimens internal pressure was calculated as: $p = (p / p_y) (SMYS) (t / r_i)$
4. Calculated using equation 2.5, as shown in equation 2.6.
5. Calculated using equation 2.7
6. Calculated using equation 2.8
7. Calculated using equation 2.11
8. Calculated using equation 2.12
9. A positive load value indicates tension and a negative load value indicates compression.

Table 2.2 Nominal Target Axial Loads for Tension Specimens

Specimen ID	p/p_y (%)	p (MPa)	P_{ten}[1] (kN)	P_p[2] (kN)	MTS Load[3] (kN)
T20P40W	40	4.30	1898	-1876	22[4]
T20P40N	40	4.30	1898	-1876	22
T20P80W	80	8.61	1898	-3757	-1859
T20P80N	80	8.61	1898	-3757	-1859

Notes:

1. Calculated using equation 2.9, as shown in equation 2.10.
2. Calculated using equation 2.11
3. Calculated using equation 2.13
4. The test set-up was not designed for the MTS to apply tensile loads. However, since the magnitude of this load (22 kN) was negligible when compared to the other applied loads and considering the error in the MTS readings due to dynamic effects (~ 20 kN), this load was considered 0 kN during testing.

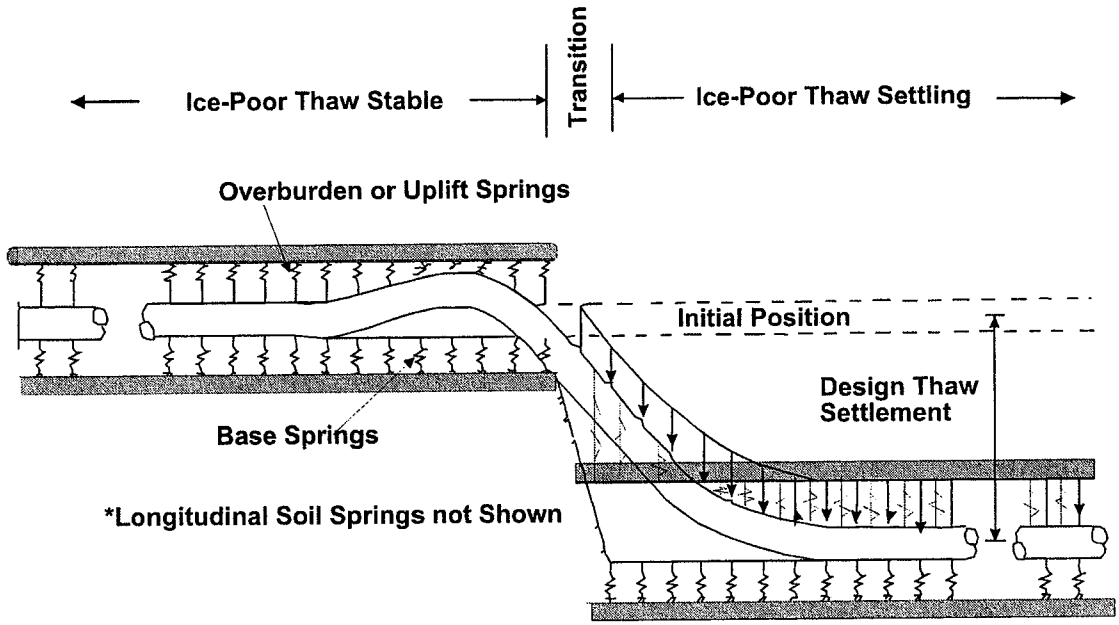

Figure 2.1 – Schematic of Pipeline Response to Differential Settlement

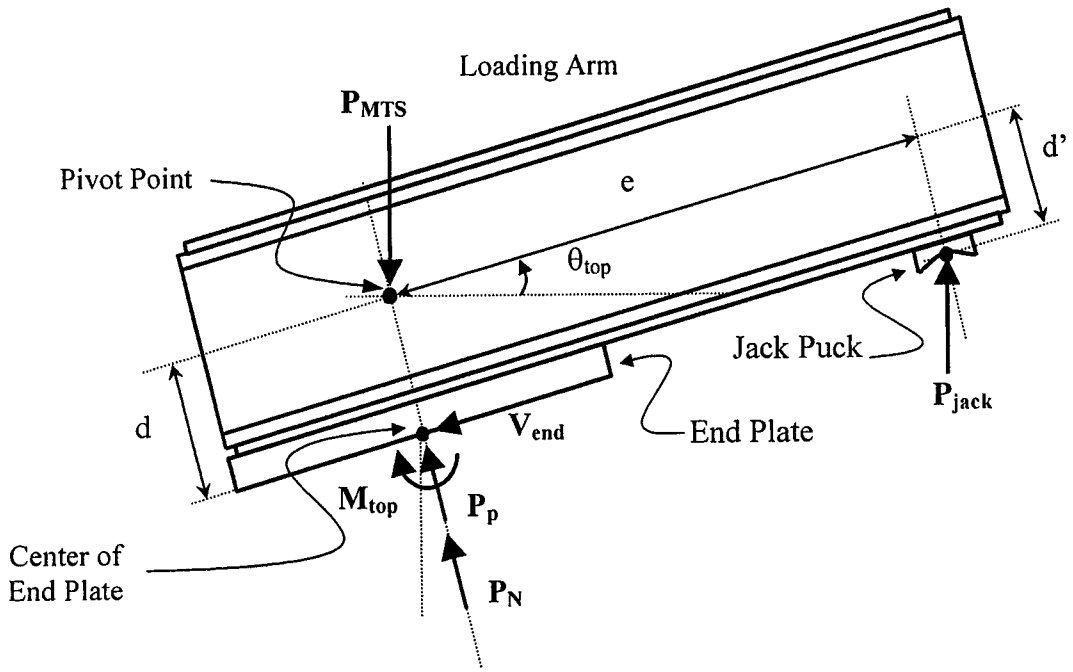

Figure 2.2 – Free Body Diagram of Upper Moment Arm

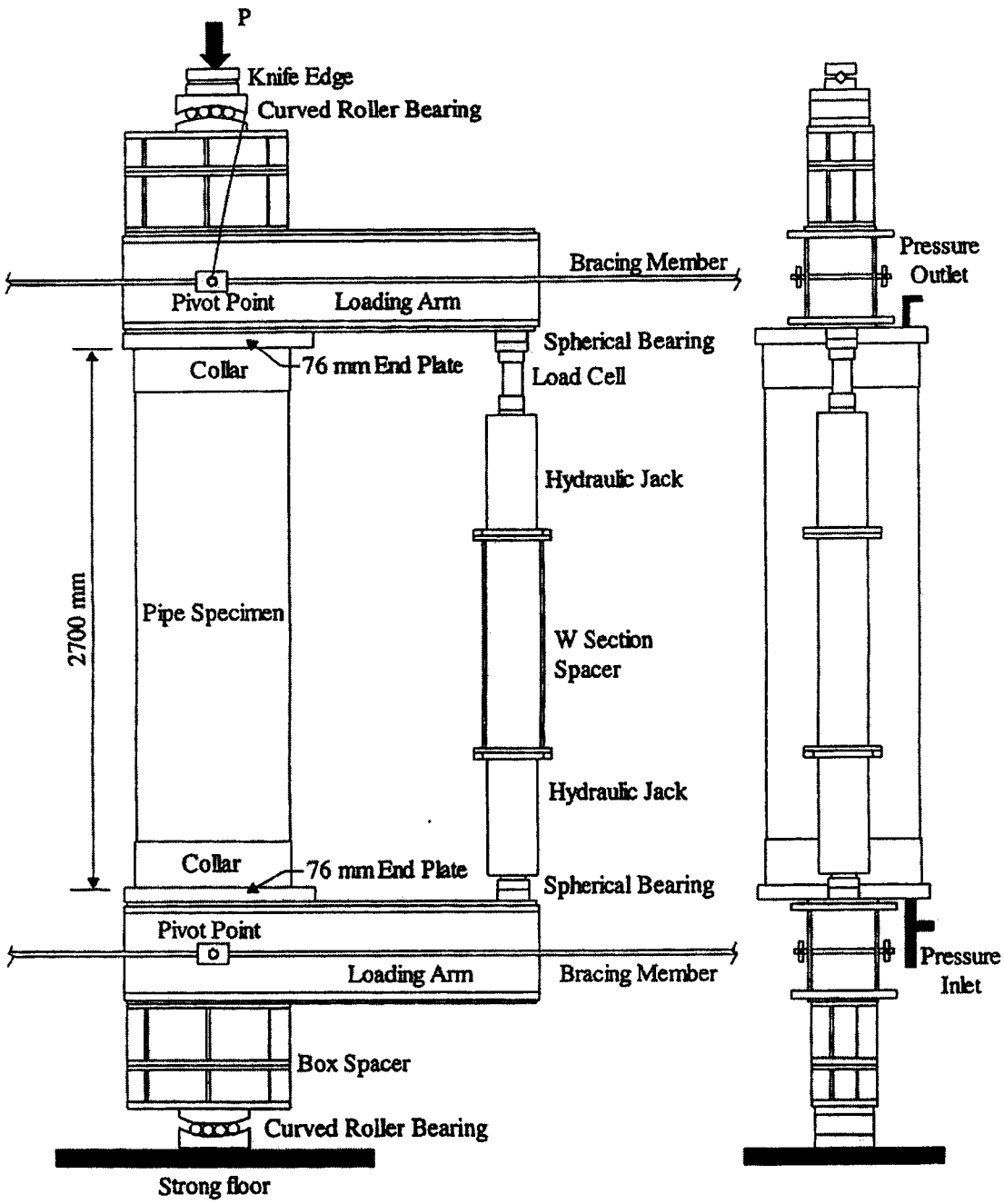

Figure 2.3 – Schematic of Test Set-Up

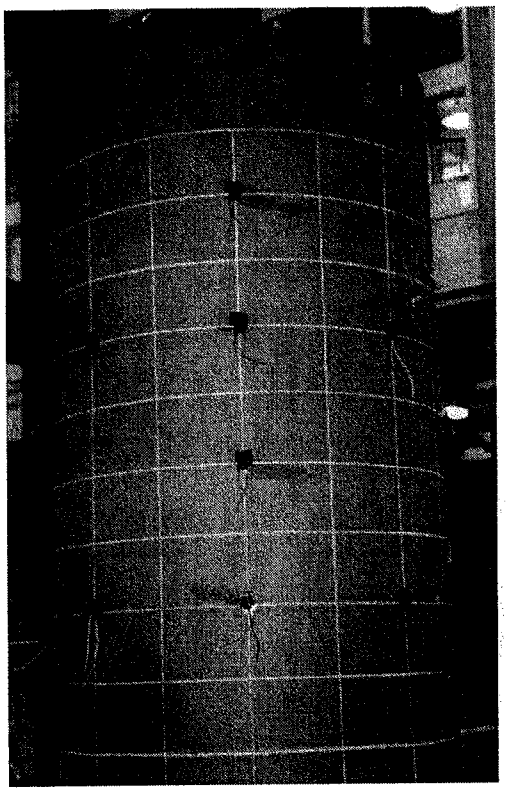

Figure 2.4 – View of Grid and Electronic Strain Gauges

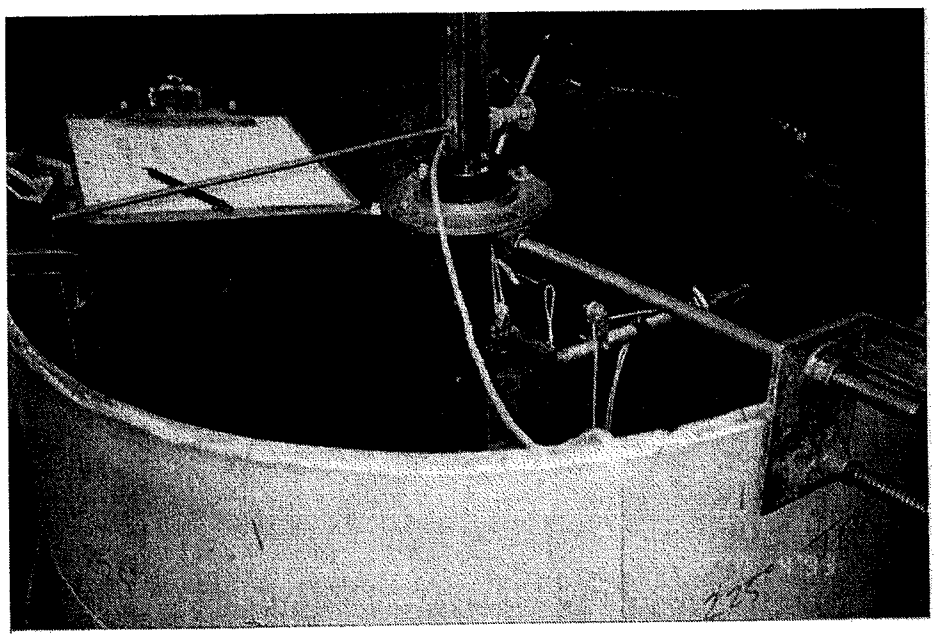

Figure 2.5 – View of the Imperfection Device at the top of a Test Specimen

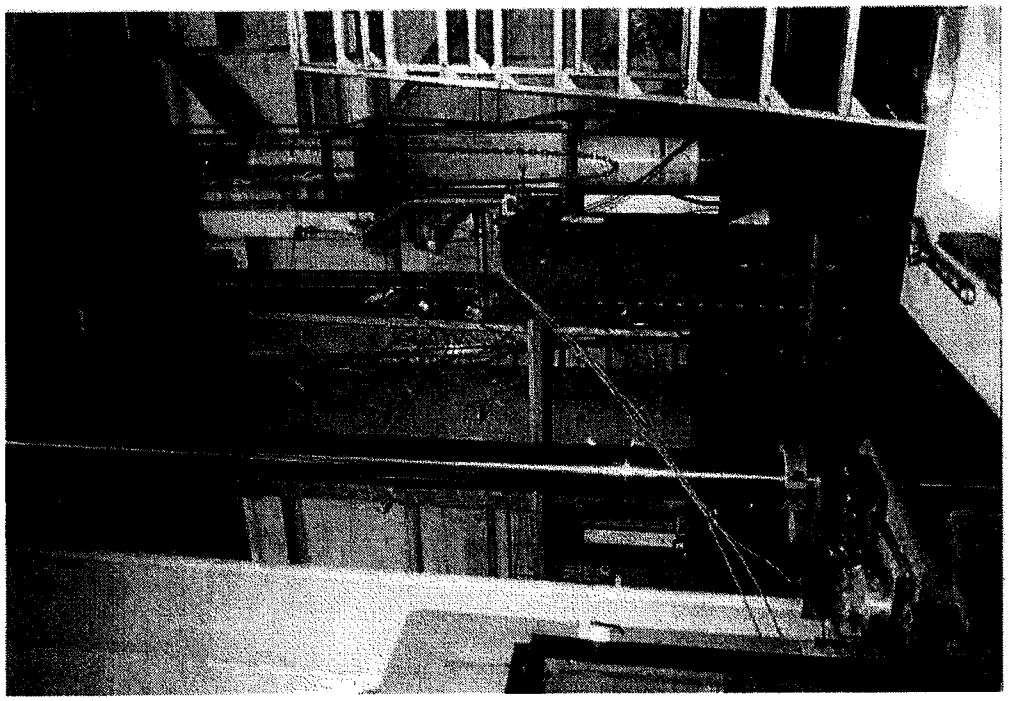

Figure 2.7 – Side View of Test Set-Up

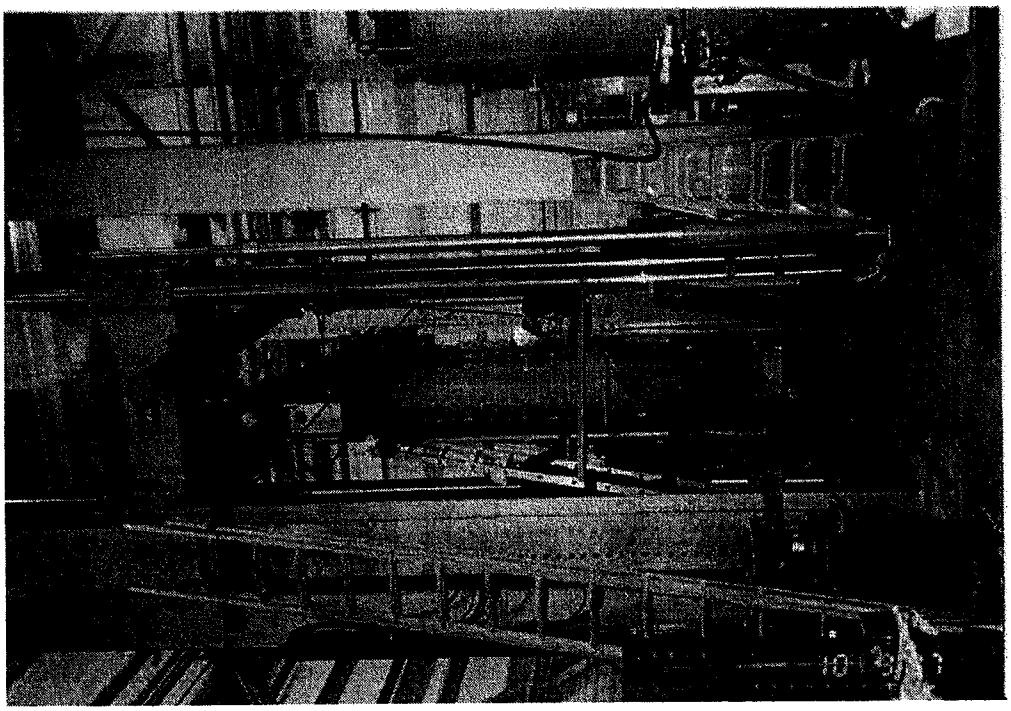

Figure 2.6 – Front View of Overall Test Set-Up

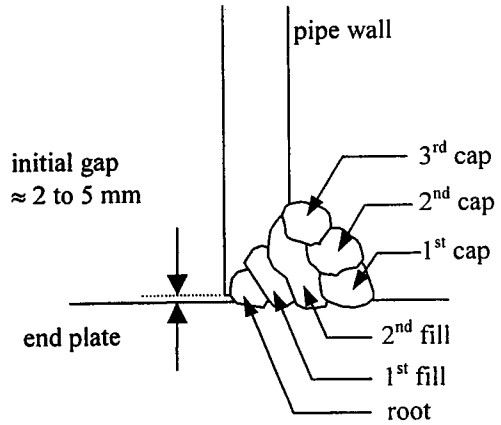

Figure 2.8 – Weld Pass Placement

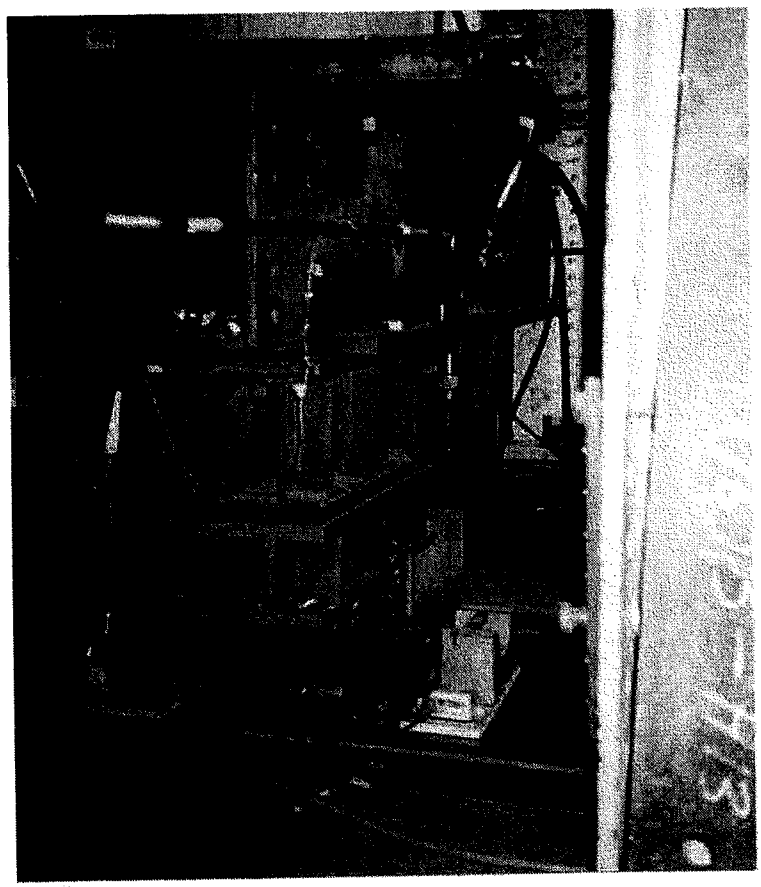

Figure 2.9 – View of Bottom Moment Arm

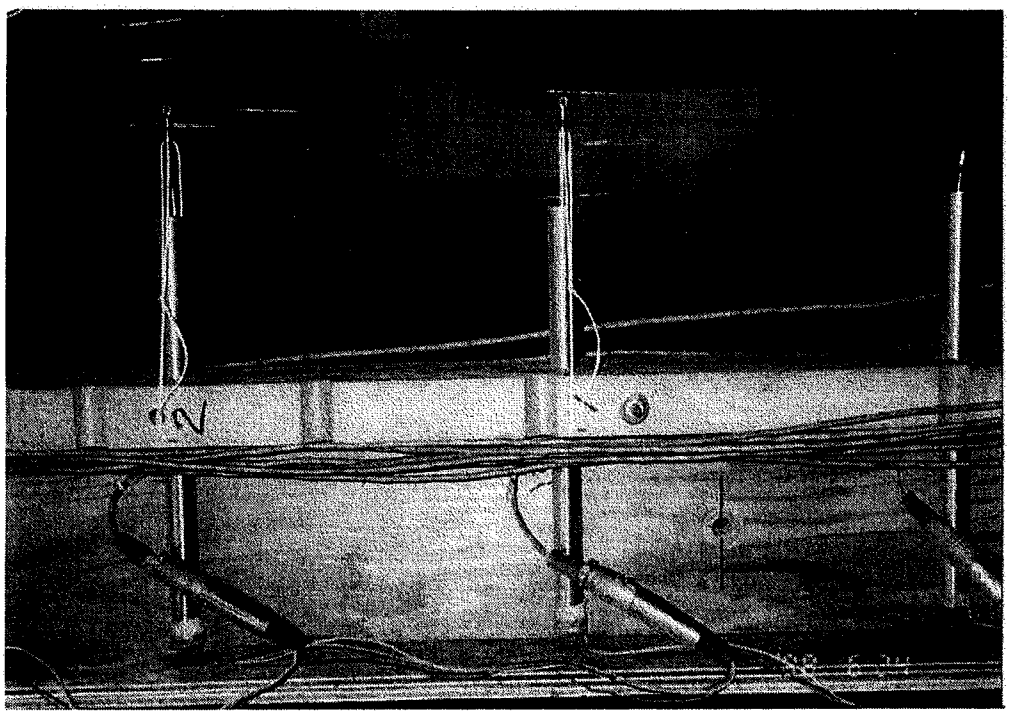

Figure 2.11 – View of LVDT for Compression Face

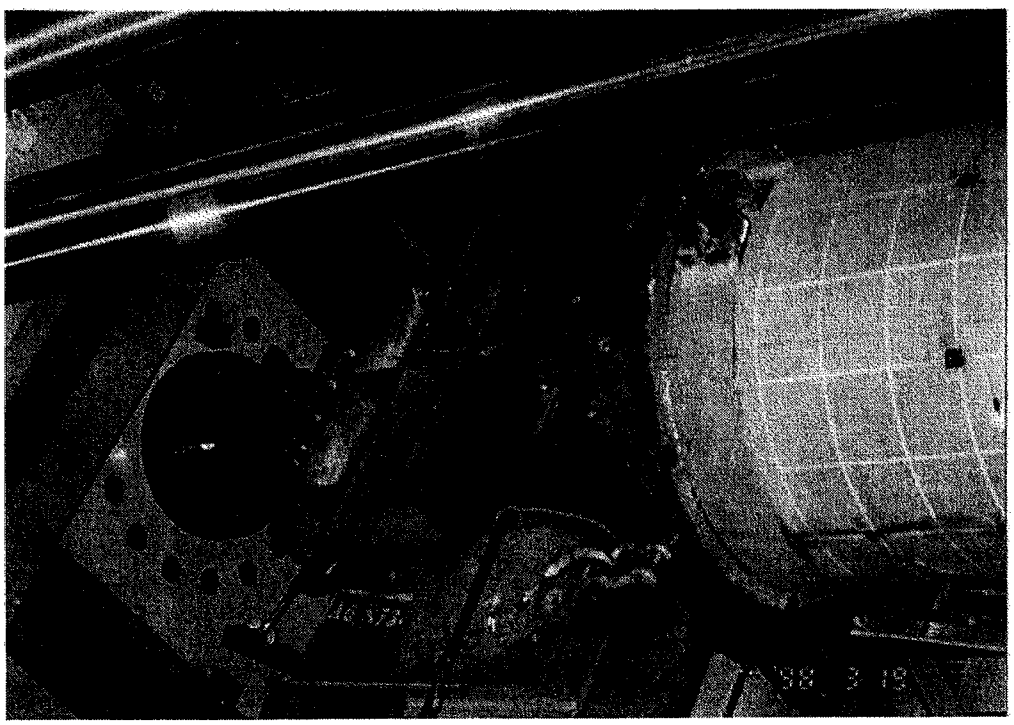

Figure 2.10 – View of MTS Head and Top Moment Arm

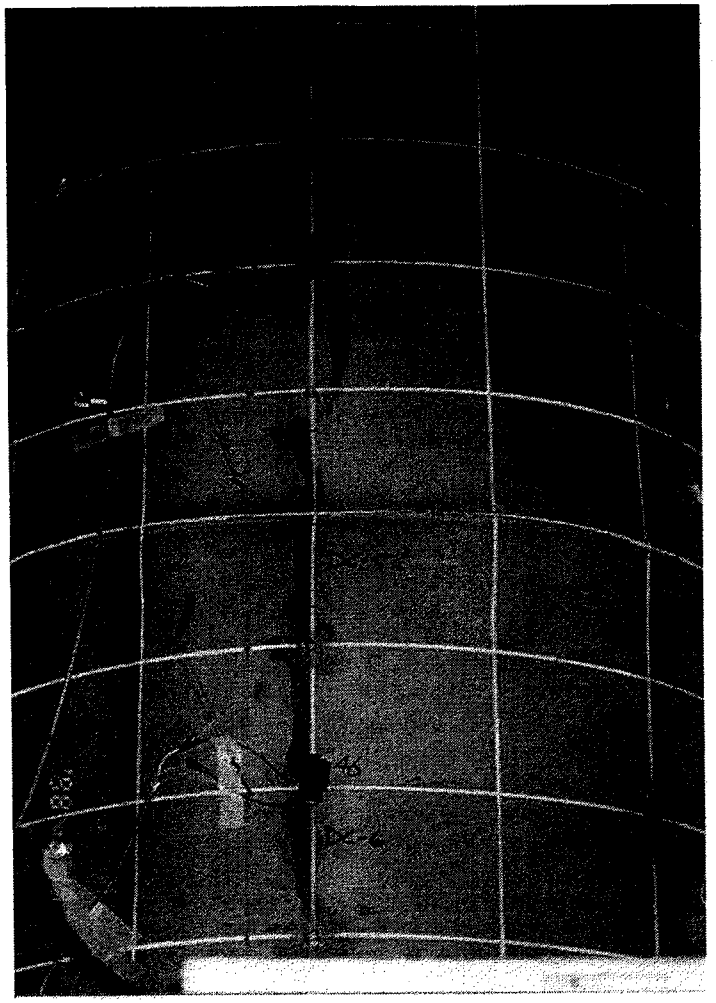

Figure 2.12 – Demecs along Compression Face

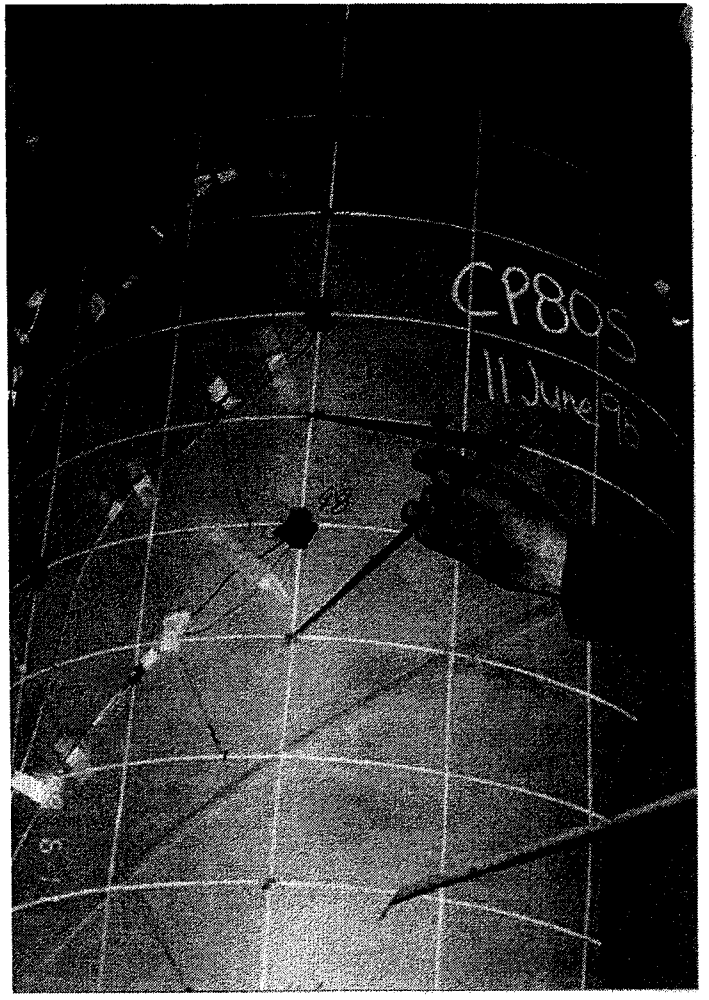

Figure 2.13 – Divider Reading across Demec point

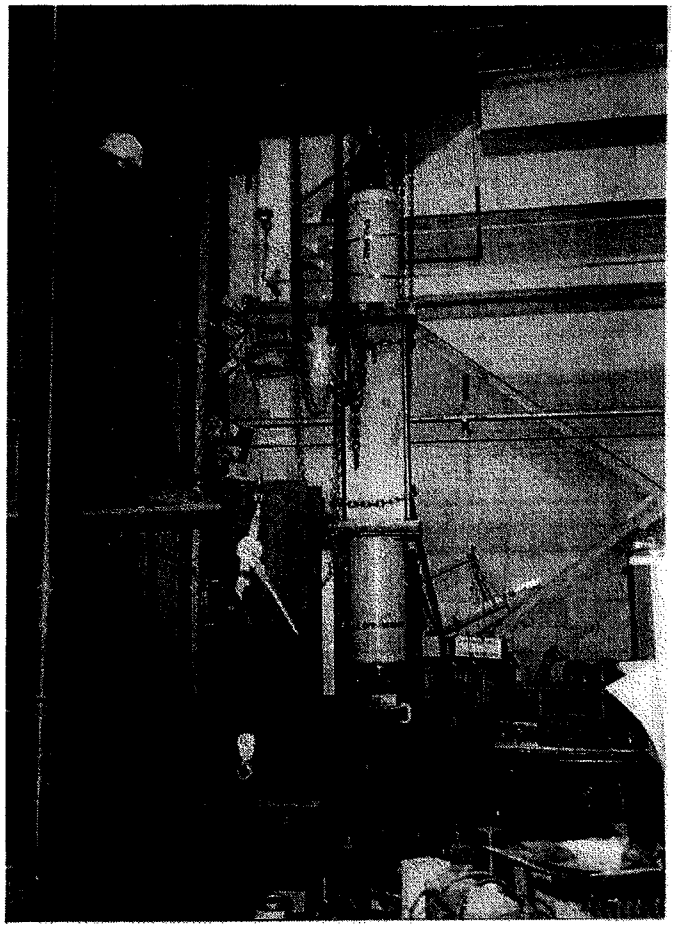

Figure 2.14 - Jack Assembly at End of Moment Arms

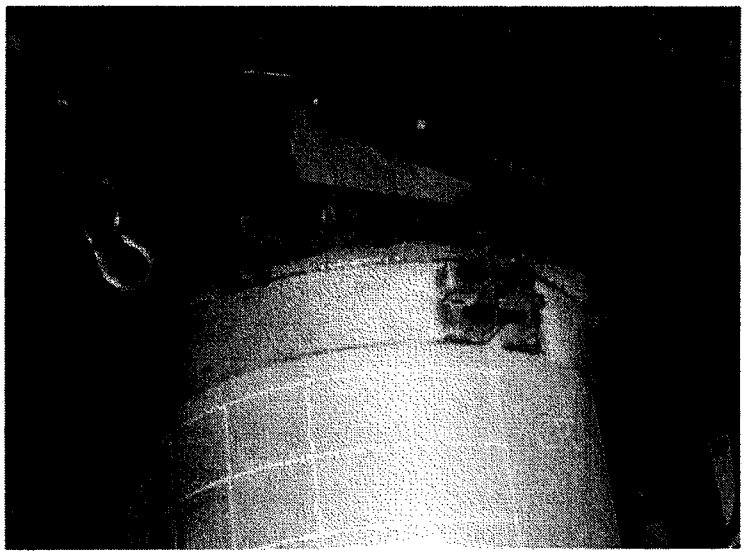

Figure 2.15 – Collar at Top End of Test Specimen

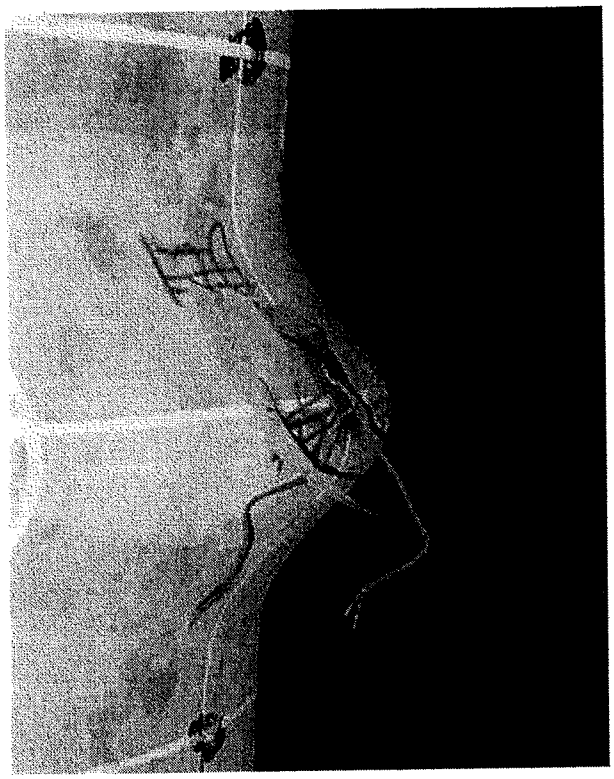

Figure 2.16 – Large Deformation Buckle

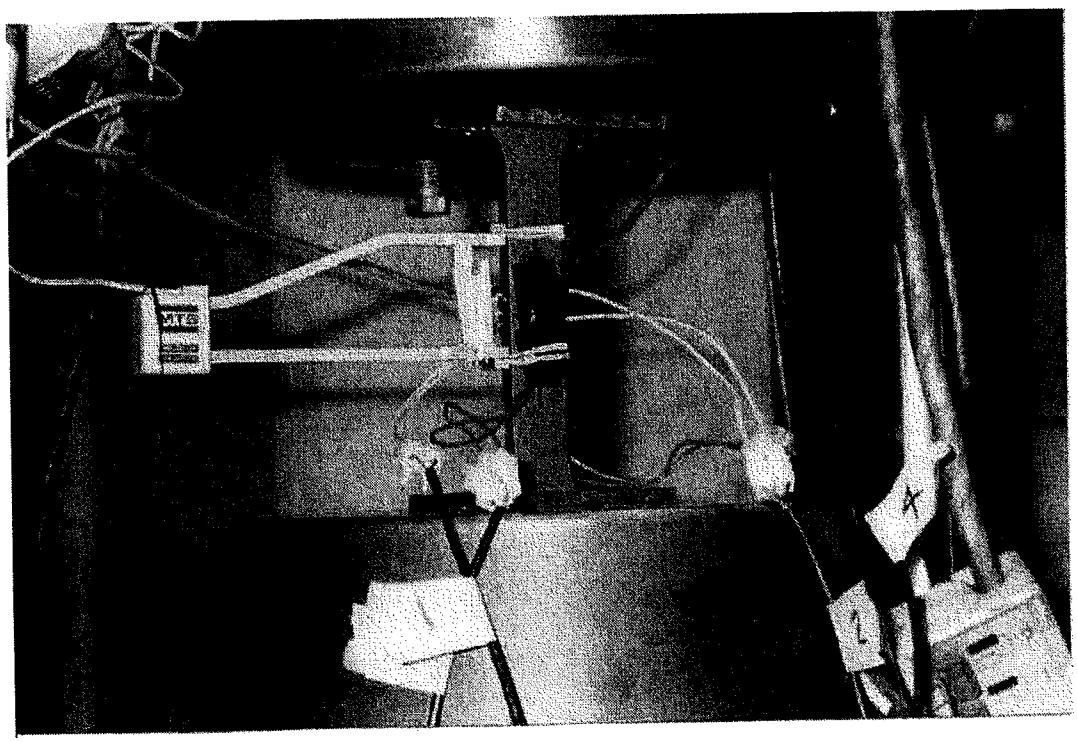

Figure 2.17 – Tension Coupon in MTS1000 Testing Machine

3.0 DEVELOPMENT OF THE FINITE ELEMENT MODEL

3.1 Purpose of Finite Element Model

Experimental testing is undoubtedly the most effective method for determining and understanding the behaviour of line pipe. The 16 laboratory tests conducted in this phase of the research project provide a good addition to the pipe behaviour and critical buckling strain databases being compiled at the University of Alberta. However, it is impractical to consider testing every conceivable load case to which segments of NPS30 line pipe, or segments of any other size pipe segment, may be subjected. Consequently, the development of a reliable numerical model is a more practical approach to the expansion of the above mentioned databases. A non-linear, finite element analysis (FEA), numerical modeling technique was employed to simulate the behaviour of the test specimens. Once the numerical model was developed, comparison of the numerical results with the experimental results obtained in the testing portion of the project was done to validate the model.

The validation of the numerical model was comprised of two main components, the load-carrying response and the deformation response. While the load-carrying response has been the traditional measure of model accuracy, this project is primarily focused on the deformation response. As previously discussed in Chapter 1, exceeding a specified deformation has been recognized as a valid limit state. Critical buckling strain limits, which is the focus of this research project, is one such deformation limit state. Therefore, while significant consideration will be given to the ability of the numerical model to predict critical loads, the main objective of the numerical model is validation of its ability to predict the deformation response of the test specimens.

Once the FEA model has been developed and validated, additional numerically generated load cases will be examined to expand the respective databases. The purpose of this

chapter is to describe the details in the development of the finite element numerical model for the plain and girth-welded test specimens.

3.2 Finite Element Formulation

3.2.1 The Concept of Finite Element Analysis

Finite element modeling is an analysis technique currently used in a wide scope of applications, ranging from structural analysis, through hydrological flow problems to computer simulations in animated movies. Finite element analysis, as considered in structural applications, is based on the application of the principle of virtual work through the structural stiffness method. The structural stiffness method requires the subdivision of a structure into a series of discrete finite elements with their corners being identified as a set of points in space known as nodes. Once the force-displacement properties of each element are determined, they are related to each other through matrix mathematics using the force equilibrium equations written at the nodes. These relationships are then grouped together into the global structural stiffness matrix for the entire structure. After the global structural stiffness matrix has been compiled, the unknown displacements of the nodes can then be determined for any given loading on the structure. Once the nodal displacements are known, the external and internal forces in the structure can be calculated using the force-displacement relations for each of the members. The determination of these external and internal forces is usually done on an incremental loading basis in non-linear analysis.

A complete description of finite element analysis process is beyond the scope of this report, but can be readily reviewed in numerous references (for example, Bathe, 1996). However, more details on the different solution strategies used in this project are discussed throughout the remainder of this Chapter.

3.2.2 Finite Element Analysis Package

The finite element analysis carried out in this research project was conducted using the commercially available finite element analysis package ABAQUS/Standard

Version 5.7-1 (Hibbitt, Karlsson & Sorenson, Inc., 1997a), hereafter referred to as "ABAQUS". This software package was selected for several reasons. The main feature that makes ABAQUS attractive to this particular problem is its capability to deal with large non-linear deformations. Large non-linear deformations can be difficult to model and usually require special formulation techniques (Horrigmoe and Bergan, 1976). Under each of the various load cases, the test specimens in this project underwent large plastic deformations, which the finite element package selected would have to be able to accommodate. The solution technique used in ABAQUS is based on the Newton-Raphson approach using an updated Lagrangian incremental formulation, in which the stress and strain measured at time $t + \Delta t$ are referred back to time t at the end of the previous step. That is, "each step has its own step time, which begins at zero in each step" (Hibbitt, Karlsson & Sorenson, Inc., 1997b). The updated Lagrangian formulation is particularly suited to this project because it is capable of accommodating all kinematic nonlinear effects due to large displacements, large rotations, and large strains. The Lagrangian formulations also has a greater level of numerical efficiency than other similar techniques (Bathe, 1996).

In addition to this, ABAQUS has an automated increment size control feature. ABAQUS automatically updates the size of the increment to allow for optimization of the solution time. If convergence is achieved quickly, then ABAQUS will automatically increase the increment size for the next step. If convergence is not achieved, then ABAQUS will automatically reduce the increment size and make another attempt to achieve convergence. All of this assists in achieving convergence of the finite element solution when a local maximum is encountered in the behaviour.

Consider the load-displacement response given in Figure 3.1. At smaller loads, the load increments can be large because convergence is achieved very quickly due to the 'linearity' of the response curve. However, as the load increases, the structural response becomes increasingly nonlinear until buckling occurs at or near the peak. As such, special solution strategies are required in order to achieve convergence of the solution as the solver passes over the peak (Ramm, 1980). In order to capture the true response

across the peak, smaller load increments are required. To solve for the response shown in Figure 3.1, a load-displacement-constraint method can be used (Riks, 1979). ABAQUS contains a Riks solution strategy feature, which will be employed in the solution of the finite element model in this project. This feature is particularly important for the analysis of the test specimens in this project due to the importance of obtaining post-buckling information.

It should be noted that there was initial concern regarding the suitability of the automatic increment selection by ABAQUS. Analytical tests conducted by DiBattista (2000) showed that there was essentially no difference between user-specified increments and increments generated automatically by ABAQUS. Subsequently, the decision was made to allow ABAQUS to generate the increments automatically, thus permitting the selection of the optimum increment size for each step and reducing the amount of user-specification required.

ABAQUS was also deemed to be advantageous to this project because it has an elastic-plastic material model that allows the constitutive law to be input as a multi-linear curve with isotropic or kinematic hardening. This allows the user to essentially model the monotonic material properties and behaviour from coupon tests, thereby reducing the number of material property assumptions. In addition to this, ABAQUS also has the capability of modeling internal pipeline pressure as a follower force. As a pressurized pipe is deformed, the orientation of the normal to the surface of the individual elements will change. The follower force feature allows the pressure to remain normal to the surface of the shell element, as would be the case in experimental tests or under actual field operating conditions.

Another feature of ABAQUS is that it allows for both load and displacement control. This was a key feature because of the load scheme used in the experimental portion of the project. During the experimental program, target load limits were prescribed based on theoretical calculations outlined in Section 2.1 and previous testing experience. Prior to buckling, the test specimens were loaded to these prescribed loads, as detailed in Section

2.4.2, and the deformational response recorded. That is, the pre-buckling procedure was consistent with a load control scheme.

Post buckling, it was no longer possible to load the test specimens to a prescribed level of loading due to the loss of load carrying capacity. Instead, the test specimens were loaded in increments of curvature and the corresponding load level recorded. As such, the post-buckling procedure used was consistent with a displacement control scheme. Consequently, it was imperative that the finite element package selected for the analysis of the test specimens be capable of addressing both the load and the displacement control schemes. ABAQUS has this capability.

Finally, the necessary software is currently available on the University of Alberta's Sun UltraSparc 1 workstations. All of these features combined to make ABAQUS an ideal choice for the finite element modeling of the test specimens.

3.3 Features of the Finite Element Model

3.3.1 Shell Elements

The test specimens in this project were divided into a series of discrete elements for the finite element modeling. The S4R shell element was selected from the ABAQUS element library to represent these discrete elements in the test specimen. This element is a four-node, double curved element with hourglass control intended for both thick and thin shell applications (Hibbitt, Karlsson & Sorenson, Inc., 1997c), that accounts for finite membrane strains and allows for transverse shear stress. It allows for large deformations and for non-linear material properties and has been shown to be particularly effective in modeling segments of line pipe under the load conditions employed in this project (Del Col, *et al.*, 1998).

The S4R element accounts for finite membrane strains. Membrane strains are those strains that exist in thin shells, but are not due to bending. The membrane strains on the

surface are determined from the derivatives of the position vector of a point on the deformed reference surface with respect to the same point on the undeformed reference surface. Since these position vectors can be determined at any level of deformation, the membrane strains can be evaluated in the element at any load level, thereby being able to account for large deformations. This allows for a variation in the thickness of the shell element at different load increments, as occurs in an actual line pipe test specimen.

The S4R element has an iso-parametric formulation, meaning that the same interpolation functions are used for the displacement field as for the nodal position vectors. Bathe (1996) states that "the basic requirements for monotonic convergence, namely compatibility and completeness, are satisfied by the iso-parametric elements when these elements are of general geometric shape". This is because the iso-parametric element has the ability to represent rigid body motions and constant strain states, thereby guaranteeing convergence.

The interpolation functions used in the S4R element have C_0 continuity, meaning that the primary variable is continuous between elements. This requirement is sufficient for plane strain-plain stress problems. Therefore, the finite membrane strain assumptions used in the S4R element essentially leads to a state of C_0 continuity.

The S4R element uses reduced integration, meaning that approximations have been made that result in the integration formula having an order of integration less than that required for exact integration (Pugh, *et al.*, 1978). This substantially reduces the computational effort required to achieve convergence and may actually improve the level of precision. The numerical integration through the thickness is done using Simpson's Rule. Five integration points are used through the thickness of the element, which allows the non-linear behaviour of the material to be followed through the load history.

There are six independent degrees of freedom, three rotational and three translational, at each node in the S4R element. The two out-of-plane rotational degrees of freedom with respect to the vector normal of the reference surface are directly associated with the

stiffness of the element. The third rotational degree of freedom, which is the rotational degree of freedom about the vector normal, is rarely activated in thin shell applications. Therefore, hourglass control is required in the element formulation to prevent spurious energy modes. The hourglass control is achieved by assigning a small artificial stiffness to the third rotational degree of freedom, either as a user-input or using the default value in ABAQUS, to prevent a singular global stiffness matrix. It should be noted that the default artificial stiffness was used in this project.

Finally, the S4R element is constructed to be shear flexible, thereby allowing shear deformations. Transverse shear strains are measured as the change in the direction of the vector originally normal to the reference surface. A constraint is imposed on this element that forces the material line originally normal to the shell reference surface to remain approximately normal to the surface throughout the deformation. This results in behavior that is consistent with the Kirchhoff assumption in classical thin shell and plate theory. The capability of the S4R shell element to accommodate shear deformations makes it practical for both thick and thin shell analysis (Hibbitt, Karlsson & Sorenson, Inc., 1997c). If the shell is thin, as is the case with the specimens examined in this project, the shear deformation in the through thickness direction will be negligible.

A second set of shell elements was used to model the boundary conditions, as described in Section 3.3.3.

3.3.2 Symmetry

Symmetry has often been used to model test specimens in previous finite element analysis of line pipe test specimens (Zhou and Murray, 1993 & Vitali, *et al.*, 1999). By passing a plane of symmetry though the circumferential direction at the half length of the specimen and a second plane of symmetry along the length of the specimen though a radial axis, it is possible to model only one-quarter of a line pipe specimen and still obtain response behaviour that is representative of the entire test specimen. The advantage of an approach such as this is that the number of degrees of freedom is

significantly reduced, thereby reducing the computational time required to obtain a numerical solution for the model.

During the development of the finite element model for this project, symmetry of the test specimens was not used. As outlined in Section 2.2.3, a set of initial imperfection measurements were taken on each specimen. As would be expected, the imperfections were not symmetric within any given pipe. Therefore, it was necessary to model the entire test specimen, both around its full circumference and along its full length.

3.3.3 Boundary Conditions

The two main components considered in modeling the boundary conditions for the test specimens were the physical arrangements of the end conditions and the kinematic constraints placed on the test specimens due to the test set-up. The physical features required at the ends of the test specimen in order to obtain the desired behaviour created the need for special modeling techniques. This section describes the modeling of these physical features and the corresponding kinematic boundary conditions.

3.3.3.1 Modeling of Physical Components at Boundary Conditions

A schematic of the test set-up was presented in Figure 2.3. Examination of this figure shows that there are three main features that need to be considered in modeling the experimental boundary conditions used in this project. These are (i) the moment arms for the jacks, (ii) the end plates and the effects of the internal pressure acting on them, and (iii) the confining collars used at the end of the test specimens, as described in Section 2.4.2.

Figure 3.2 provides a schematic of the curved end roller bearings and pivot point at the top moment arm assembly. The physical geometry of the moment arms and the roller supports used in the test set-up resulted in the rotation or pivot point for the ends of the test specimens being located a distance of 339 mm beyond the center of the end of the specimen. The distance between the pivot point and the end of the pipe was spanned by the 76 mm thick end plate, to which the test specimen was welded, and the loading arm,

to which the end plate was bolted, as shown in Figure 3.2. Due to the robust nature of the end plates and the components that comprised the loading arms, it was assumed that they were essentially rigid for modeling purposes. Based on this assumption, the ends of the test specimens were connected to the pivot point using the 3-node, rigid element R3D3 from the ABAQUS element library (Hibbitt, Karlsson & Sorenson, Inc., 1997c). The R3D3 rigid element contains only slave kinematic variables so that they may be assigned loads and be connected to other elements, but they do not have their own set of kinematic constraints. That is, the kinematics of the R3D3 elements are dependent on the elements and nodes to which they are attached.

Each rigid element must have an associated rigid body reference node at which the kinematic constraints affecting the overall motion of the rigid body must be specified. The pivot points at the top and bottom of the test specimens were used as the reference nodes in this model. By connecting a series of triangular shape R3D3 elements between the nodes at the end of the test specimen and the pivot points, a closed rigid cone was created on each end of the test specimens. The rigid R3D3 elements prevent the end of the test specimens in the FEA model from deforming, as the weld to the 76 mm thick end plates did in the experimental program. Figure 3.3 shows an example of one of the rigid cones at the top end of one of the FEA models.

The decision to use the closed cone model at the ends of the test specimens was also influenced by the effect of the internal pressure acting within the pipe. In ABAQUS, the internal pressure is applied normal to the reference surface of the R3D3 rigid elements and acts as a 'follower-force' throughout the analysis, as previously described. This means that the normal of the resultant force due to internal pressure on any given element will remain normal to the reference surface of the deformed element. It should be noted that, for the rigid end cones, there was no deformation within a given element. However, there was deformation in the form of rigid body motion of which the most significant was the global rotation of the end caps.

Each reference surface of the elements that make up the cone has components of its position vector in each of the three global directions, given as 1, 2 and 3 in Figure 3.3. However, the 2- and 3-direction components cancel each other on opposite sides of the cone, thereby resulting in only the 1-direction having a non-zero resultant over the entire volume of the cone. This resultant was directed perpendicular to the end of the specimen. The cumulative effect of this approach to modeling is that the pressure defined follower force acts as though there were flat plate perpendicular to the ends of the test specimens, as was the case for the actual test specimens.

In the experimental portion of this project, the test specimens were welded to 76 mm thick plates and restraining collars were placed around the outside of the test specimens adjacent to these welds, as shown in Figure 2.3. The purpose of these collars was to help make a smooth transition in the region that was disturbed by the rigid weld at the ends of the specimens. This technique has been shown to be successful is reducing the incidence of end buckles in the analytical model (Mohareb, *et al.*, 1994). The collars used in the actual test specimens were fabricated from 150 mm of the same section as the test specimens. Therefore, it was decided to model the collars by simply increasing the wall thickness at the ends of the test specimens.

Figure 3.4 shows a schematic of the experimental test set-up at the end collars. Since there was a smooth surface along the entire inside surface of the test specimens, a radial adjustment of one-half the thickness of the test specimens was made to each of the last five sets of nodes before the ends of the pipe segment of the model. This effectively shifted the reference surface for the last four rows of elements outward, resulting in a finite element mesh that was more consistent with the appearance of the test specimens. While this does not truly describe the actual physical arrangement that exists between the collars and the test specimens, it is nevertheless considered a good approximation. It was assumed therefore that the collars simply act to effectively thicken the pipe wall at the end of the test specimens.

This procedure was not followed in the original analysis of the four plain compression test specimens, namely CP0N, CP20N-1, CP40N-1, and CP80N-1, which were reported by Del Col, *et al.*, 1998. However, the re-analysis of these test specimens, which is included in this report, does include the shifted collar elements and partially accounts for the differences between the analysis reported by Del Col and the analysis reported in Chapter 4 of this document.

Initially there was some concern regarding the orientation of the first pipe element above the collar elements, which is shown as the slanted pipe element in the Dorey Model of Figure 3.4. However, a short parametric study examining the effects of the different wall thickness for this element, different orientation, and different connectivity patterns showed that using the slanted pipe element had no effect on the behavioural response when applied to two different pipes. Since the slanted element required the minimum amount of pre-processing prior to input into ABAQUS, it was decided to use the configuration shown in the Dorey Model of Figure 3.4.

3.3.3.2 Kinematic Boundary Conditions

In addition to the components that make up the physical features at the end of the test specimens, the global boundary constraints also had to be input into the FEA model. As previously discussed, the pivot points were selected as the effective points of load application. As such, the boundary conditions developed and discussed in this section were applied at the pivot points.

Figure 2.3 provides a schematic of a typical test specimen installed in the test set-up. As can be seen in this figure, the top end and the bottom end of the test specimen had different physical restraints. At the bottom end, bearing on the strongfloor of the lab, coupled with the corresponding frictional forces, prohibited any type of translational motion of the end loading arm assemblies from occurring. Torsional rotation about the vertical axis of the test specimen was restrained through the two bracing members applied at the pivot point. Figure 2.3 shows only one bracing member. There is a second brace parallel to the one shown in Figure 2.3 on the opposite side of the loading arm. The

force couple generated between the two braces resisted any torsional moment that may have developed during loading. The out-of-plane rotation of the test specimen was restrained because of the geometry of the curved roller bearing at the bottom of the test set-up. It should be noted that there were no applied loads that generated out-of-plane moments or rotation. Out-of-plane rotations may have occurred due to unsymmetric buckling of the test specimens. However, these rotations were considered small enough that any moment that developed could be resisted by the curved roller bearing.

The purpose of the testing program was to develop a moment-curvature response for line pipe. The test set-up was arranged to allow for the specimens to bend in the plane shown in Figure 2.3. The curved roller bearings allowed free in-plane rotation about the bottom pivot point, located by the intersection of the normals at the curved end bearing surface, as shown in Figure 3.2. As such, all of the degrees of freedom at the pivot points were constrained with the exception of the in-plane rotational degree of freedom. This rotational degree of freedom was free at the bottom end of the test set-up because of the roller assembly and was therefore not constrained in the FEA model. It is acknowledged that there is some frictional energy lost at the curved roller bearings. However, the amount of energy lost compared to the amount of energy put into the system was considered negligible and therefore neglected from the FEA model.

At the top end of the test set-up, a different set of restraints existed. The top end of the test set-up was connected to the loading head of the MTS machine. Since axial load was one of the applied loads during testing, the test specimens had to be allowed to deform in the axial direction, allowing for the effects of this load to be included. As such, the vertical translational degree of freedom was not constrained in the FEA model at the upper pivot point. In addition to this, a knife-edge assembly was included at the top of the test set-up. The purpose of this knife-edge was to allow out-of-plane rotation of the test specimen, which may develop due to unsymmetric buckling. To account for the effects of the knife-edge assembly in the test set-up, which allowed out of plane rotations, the out-of-plane rotational degree of freedom was also not constrained in the FEA model.

The remaining degrees of freedom were considered the same as for the bottom end of the test set-up.

3.3.4 Residual Stresses in Plain Pipe Specimens

Segments of line pipe often have residual stresses in them that arise from the cold forming of the circular cross section and from the welding process (Stelco Inc., 1993). All specimens had a longitudinal DSAW seam weld. The residual stresses at the seam weld were deemed to have an essentially negligible effect on the behaviour of the test specimens for a number of reasons. Karamanos and Tassoulas (1996) have shown that the effect of residual stresses in line pipe is not significant for combinations of bending and low levels of axial load, such as those to which the specimens in this project were subjected.

DiBattista (2000) conducted a series of ring expansion tests on segments of the NPS30 line pipe. A ring expansion test is analogous to a stub column test on a typical structural steel member and would include the effects of any residual stresses present in the ring. DiBattista found little difference between the results of the ring expansion and the results obtained from the longitudinal coupon tests. This also suggests that the residual stress pattern has a negligible effect on the behaviour of the test specimens.

A third reason why the residual stress pattern along the seam weld was neglected was because of the difficulty in obtaining data for the pattern. The measurement of a residual stress pattern is usually destructive to the integrity of the test specimen. The pipe is usually cut into segments to determine residual stress patterns. Obviously this can not be done prior to testing the specimen. Once testing was completed, it was felt that any attempts to measure the residual stress pattern would be misleading due to the large stresses induced during testing.

The final, and probably most significant factor in justifying the omission of the residual stress pattern at the seam weld was the orientation of the test specimen during testing. As outlined in Section 2.2.1, the seam weld was positioned in the tension region of the test

specimen. This was done to minimize the effect of the seam weld on the experimental compressive buckling behaviour. Therefore, primarily due to the orientation of the test specimens, it is believed that it is safe to assume that the residual stress pattern at the seam weld would have essentially no effect on the behaviour of interest and, therefore, could be neglected from the FEA model.

3.3.5 Material Properties

As discussed in Section 2.4.3, longitudinal coupons were used to determine the experimental material properties of the different test specimens. As will be presented and discussed in Section 4.1, each of the five sets of longitudinal material properties exhibited typical ductile steel stress-strain behaviour. Each material tested had an initial linear-elastic region with an ensuing strain hardening region.

The material properties determined from the coupon tests are expressed in terms of engineering stress and engineering strain. That is, the stress and strain are a function of the undeformed cross sectional dimensions. This form of input is not satisfactory for use in ABAQUS because ABAQUS is based on a true stress-strain formulation. Furthermore, for input into ABAQUS, a yield criterion and a hardening rule had to be specified.

The yield criterion selected was the Von Mises yield surface. This criterion is based on the determination of the distortion energy in a given material. The Von Mises yield surface is developed from the assumptions that the yield stress associated with the three orthogonal principal stresses are equal. As a result, the yield surface has a cylindrical shape, centered on the hydrostatic stress line. In addition to the selection of the Von Mises yield surface, it was also assumed that the steel used in the test specimens was isotropic. An isotropic material means that the material properties are independent of the direction considered (Beer and Johnston, 1992). From this assumption, it can be deduced that the material properties are the same in both compression and tension, which has long been an accepted assumption of most ductile steels.

Isotropic hardening was selected as the hardening rule for plastic behaviour for this analysis. Isotropic hardening means the Von Mises yield cylinder has a uniform post yielding expansion about the hydrostatic stress line. While it is acknowledged that a kinematic or mixed hardening model may best describe the true behaviour of steel, the fact that monotonic loading was used in this project lends itself to using the isotropic hardening rule. Monotonic loading eliminates the need to consider any Bauschinger effect that would be present in steel test specimens that were cyclically loaded beyond yield such that plastic deformations occurred. Since there is no Bauschinger effect, the more complex kinematic hardening rule can be omitted in favor of the simpler isotropic hardening rule.

Once the yield criterion and the hardening rule had been established, the material properties determined from the coupon tests were converted from the recorded engineering stress-strain formulation to a true stress-strain formulation. ABAQUS uses a log plastic strain formulation in the isotropic hardening rule. The conversions for true stress, σ_{true}, and true log plastic strain, ε_{ln}^{pl}, are provided in volume II of the ABAQUS User's Manual (Hibbitt, Karlsson, & Sorenson, 1997c) and are expressed as

$$\sigma_{true} = \sigma_{nom}\left(1+\varepsilon_{nom}\right) \tag{3.1}$$

$$\varepsilon_{ln}^{pl} = \ln\left(1+\varepsilon_{nom}\right) - \frac{\sigma_{true}}{E} \tag{3.2}$$

where σ_{nom} is the nominal or engineering stress recorded from material property tests, ε_{nom} is the nominal or engineering strain recorded from material property tests and E is the modulus of elasticity.

It should be noted that the engineering stress and strain recorded during material coupon tests usually include loading rate effects. These effects need to be eliminated when

determining the true stress-strain relationship for input into ABAQUS. The details of the elimination of the rate effects from the coupon test results are presented in Section 4.2.

3.3.6 Mesh Study

3.3.6.1 Selection of Mesh Sizes for Consideration

As with any finite element modeling, the selection of an appropriate sized mesh is an integral part to the success of the analysis. A mesh with elements that are too large (coarse) may have difficulty in predicting the actual behaviour of the test specimen. A mesh with elements that are too small (fine) usually provides a better prediction of the experimental behaviour, however there is a significant increase in processing time and costs.

Previous work on line pipe specimens with a D/t ratio of 92 has been done at the University of Alberta (Del Col, *et al.*, 1998) and a finite element mesh study was done at that time. However, due to some uncertainties observed in the finite element predictions of that project, the decision was made to run a full mesh study in this project.

Three criteria assisted in the selection of the size of the different meshes selected for this mesh refinement study. The first criterion was based on the size selected by Del Col in which elements that had a circumferential arc length of 60 mm and a longitudinal length of 34.615 mm were used. Del Col presents no rationale for these size selections. However, reasonable agreement was achieved using elements with these dimensions, so the decision was made to use a mesh size approximately equal to this as a starting point.

A second criterion used in determining the element sizes was the element aspect ratio. The element aspect ratio is the ratio of the greater dimension to the smaller dimension of the element. For two-dimensional quadrilateral elements, Bathe (1996) recommends that the aspect ratio be limited to "a reasonable positive number." Previous experience by pipeline researchers at the University of Alberta indicated that a "reasonable positive

number" for elements used in line pipe analysis is 2. Therefore, the meshes selected in this refinement study had aspect ratios ranging from 1.0 to 2.0.

The third criterion, and probably the most significant, was the physical geometry of the failed test specimens. The experimental portion of the testing project was conducted prior to the development of the FEA model. Because of this, an appreciation for the physical size of the buckles was available prior to the mesh refinement study being undertaken. A typical buckle has already been shown in Figure 2.16. Visualization of a smooth transition of elements across the buckled region of the failed specimens, coupled with the measured dimensions of the buckles, assisted greatly in determining the different mesh sizes considered in the mesh refinement study.

A total of six different mesh sizes were selected for examination in this mesh refinement study. The mesh sizes are expressed as a function of the size of an individual element used in the mesh. The first number refers to the number of elements in the circumferential direction and the second number refers to the number of elements in the longitudinal direction. The six sizes selected were 24x27, 40x45, 40x60, 40x75, 40x90 and 80x90. For the plain pipes, each of these meshes was selected to be uniform across the entire surface of the test specimen. For the pipe with the girth-weld, a discussion of the mesh refinement is presented in Section 3.4.1.

The initial phase of the mesh refinement was conducted using a perfect pipe. The term "perfect pipe" refers to a segment of line pipe free of any defects, including imperfections. In reality, no such segment of line pipe exists. As such, the results of the analyses yielded behaviour that was not realized in any of the test specimens. However, the results of the perfect pipe analysis did serve two purposes. First of all, it provided an upper bound solution under each of the different load cases. As previously discussed in Section 2.2.3, it is widely accepted that initial imperfections not only affect the buckling location, but also the buckling capacity of line pipe. Therefore, since real test specimens contain initial imperfections, the perfect pipe idealization becomes an upper bound solution. This was important when trying to assess the validity of the solution from the

finite element analysis during the initial phase of the analyses. The second advantage realized using the perfect pipe mesh was that the preprocessing was greatly simplified. This substantially reduced the total analysis time for any given configuration during the initial analysis phase.

Despite the suitability of a perfect pipe for conducting some of the parametric studies, it was believed that the effects of the initial imperfections should also be considered as part of the mesh refinement study. As such, the effects of an initial imperfection were also considered in the mesh refinement study. An initial imperfection pattern was assumed and applied to the different size meshes to determine if there were any effects on the mesh refinement from the initial imperfections.

Figure 3.5 provides a view of the cross section of the pipe at the location of the assumed imperfection pattern. The assumed initial imperfection pattern was modeled by creating a uniform bulge around the entire circumference at the half-height of the pipe. In the longitudinal direction, this bulge took on a smooth curve, which was the typical length of an experimentally determined bulge buckle, as shown in Figure 2.16 of the previous chapter, but at a much smaller amplitude. This smooth curve was modeled using a cosine function over a length of 250 mm with varying maximum amplitudes, amp_{max}, where amp_{max} was located at the middle of the 250 mm span of the uniform bulge. The magnitude of the imperfection at a given node number, $Imp_{node\#}$, was calculated as

$$Imp_{node\#} = (amp_{max}) \cos\left(\frac{coor_{node\#}}{125}\pi\right) \qquad (3.3)$$

$$-125 \text{ mm} \le coor_{node\#} \le +125 \text{ mm}$$

where $coor_{node\#}$ is the distance between a node on the selected mesh and the point of maximum imperfection amplitude, as shown in Figure 3.5. A total of nine different maximum amplitudes were selected for examination in this project. The values of the different maximum amplitudes ranged from 0 mm to 8.3 mm, the nominal wall thickness of the test specimens.

For the purpose of the mesh refinement, a fictitious, although not unrealistic, load case was assumed. This load case was an approximation of the loads applied during the test of CP80N-1 and had an internal pressure of 8.00 MPa and an applied axial load of –3500 kN. These applied loads remained constant for the various meshes considered. The meshes were also studied under a load case with no internal pressure. This was done because of the different buckling modes observed between the pressurized and unpressurized test specimens. The applied loads for the unpressurized load case were taken as 0.00 MPa internal pressure and –2070 kN of axial load.

3.3.6.2 Results of Mesh Study

The variation in internal pressure was found to have no effect on the mesh refinement study for either the perfect pipe or the pipe with an assumed imperfection pattern. Consequently, results will not be presented for both load cases. Figure 3.6 presents the results from the pressurized mesh refinement study on the perfect pipe. From this figure, it is observed that all of the meshes give the same moment-curvature response prior to buckling and that all of the responses are smooth curves. However, the peak moment and post buckling response curves are significantly different, depending on the mesh size. Examination of Figure 3.6 shows that convergence is essentially reached with the 40x75 mesh. Although the 80x90 mesh does provide a lower bound solution, the additional refinement is not deemed beneficial because the significant increase in processor time when using the 80x90 mesh instead of the 40x75 mesh. As can be seen in Figure 3.6, the 40x75 mesh and the 40x90 mesh are essentially coincidental with only minor deviations from each other. Since the 40x75 mesh required less processor time, it was selected as the optimal mesh for the perfect pipes.

As discussed in the previous section, the initial phase of the mesh refinement study was conducted on a perfect pipe. Due to symmetry of the mesh and the applied load case, the perfect pipe exhibited an unrealistic buckling mode in which symmetric buckles developed at both ends of the model. Figure 3.7 shows two such buckles, one using the 40x45 mesh and one using the 80x90 mesh. It should be emphasized that such a failure

was never experienced in any of the test specimens investigated. The initiation of multiple buckles was realized in many of the highly pressurized test specimens and will be discussed in Section 4.5.3. Nevertheless, these results provide sufficient information for the purposes of the mesh refinement study.

Figure 3.8 presents a plot showing the effects of the mesh refinement on a pipe with an assumed imperfection pattern that had maximum amplitude of 0.5 mm. Examination of Figure 3.8 shows that convergence is again essentially reached with the 40x75 mesh. Figure 3.9 shows two buckles on the imperfect pipe, one using the 40x45 mesh and one using the 89x90 mesh. Since the imperfection was introduced at the half-height of the mesh, it is not surprising to see that this corresponds with the location of the buckle. The results obtained for the imposed 0.5 mm initial imperfection were the same as those obtained for the different size initial imperfections with respect to identifying the optimal mesh selection. That is, convergence was essentially reached using the 40x75 mesh, regardless of the magnitude of the imposed initial imperfection.

Although the magnitude of the imposed initial imperfection did not make a difference in the optimum mesh size, there were some differences in the results from the analyses with the different magnitude initial imperfections. These differences were exhibited in the peak moment obtained, in the magnitude of the buckle, and in the overall shape of the moment-curvature plots. Comparison of Figure 3.6 for the perfect pipe with Figure 3.8 for the pipe with a 0.5 mm imposed initial imperfection shows that the moment-curvature response has a different shape, because the buckling mode was different.

A variety of different amplitude initial imperfections were examined. From the results of the nine different amplitude initial imperfections, it was observed that the greater the imperfection, the more abruptly the specimen buckled, the lower the peak moment, the lower the curvature at buckling, and the more rapidly the specimen unloaded. This is consistent with previous investigations on the buckling of shells (Kollar and Dulacska, 1984).

A parametric study was conducted on the effect of the size of the initial imperfection. This parametric study was conducted using the 40x75 mesh and a bulge initial imperfection as described in Section 3.3.6.1. This bulge initial imperfection was input into the FEA model as a ring around the entire circumference at the half height of the mesh. The maximum amplitude of the ring imperfection was taken as a percentage of the nominal wall thickness of the pipe and included initial imperfections that had maximum amplitudes of 0%, 1.2%, 2.4%, 6.0%, 12%, 25%, 50%, 75% and 100% of the nominal wall thickness.

Table 3.2 provides the numerical results of the parametric study on the effect of the amplitude of the initial ring imperfection and Figure 3.10 provides a graphical representation of the relationship between peak moment and magnitude of the initial imperfection. It should be noted that the buckling mode for the perfect pipe (0% imposed initial imperfection) was different than the pipes which had a non-zero initial imperfection. Figure 3.7 shows that the buckling mode for the perfect pipe was a doubly symmetric end buckle. Pipes with a non-zero initial imperfection had a buckling mode in which a single symmetric buckle developed at the location of the initial imperfection. A typical example of this type of buckle can be seen in Figure 3.9. Due to the different buckling modes, it was felt that the results of the perfect pipe analysis were not comparable to the data from the imperfect pipes. Therefore, the peak moment of the pipe with an initial imperfection of 1.2% the wall thickness was selected as the reference moment for determining the reduction in moment capacity presented in Table 3.2.

As expected, Figure 3.10 shows that there is a reduction in peak moment with an increase in initial imperfection. It is cautioned that the moment reduction values presented in Table 3.2 are based on there being a very small initial imperfection in the specimen and not a perfect pipe. It is postulated that the actual moment reduction may be greater than the values given in Table 3.2 when compared with a perfect pipe. It should also be noted that the results obtained in this parametric study are based on a D/t ratio of 92 and may not be applicable to a segment of line pipe with a different D/t ratio. The effects of the magnitude of the initial imperfections on the moment capacity of different D/t ratio pipes

is discussed in Section 5.2.2 for plain D/t = 51 specimens and Section 5.2.4 for girth welded D/t = 51 specimens.

Nevertheless, the results of this parametric study show that initial imperfections play an important role in the load carrying capacity of line pipe. It is not unreasonable to assume that most segments of line pipe have an initial defect or imperfection of at least 1.0 mm as a result of the fabrication procedure. Examination of Table 3.2 and Figure 3.10 shows that an imperfection as small as 1.0 mm in amplitude can cause a reduction of 9.6% in the moment capacity. This is a significant reduction and supports the findings of Del Col, *et al.*, 1998 and Dinovitzer, *et al.*, 1999.

However, it should be cautioned that the results presented in Table 3.2 and Figure 3.10 are greatly influenced by the physical aspects of the test specimen, specifically the D/t ratio and the material properties, used in the FEA model. Mohareb, *et al.*, 1994 and Yoosef-Ghodsi, *et al.*, 1994, both conducted investigations on a series of pipes in which each specimen developed its fully plastic moment capacity prior to the initiation of local buckling. As will be shown in Chapter 5, small initial imperfections do not have the same appreciable effect on the moment capacity of the FEA model specimens as was observed in this brief parametric study. Instead, they only significantly influence the curvature, and thus the critical strain, at which local buckling initiates. Therefore, it is concluded that the results presented in Table 3.2 and Figure 3.10 are only applicable to grade X70 specimens with a nominal diameter of 30" and a D/t ratio of 92. As will also be presented in Chapter 5, the assumed initial imperfection pattern also has an effect on the reduction in moment capacity. This will be discussed in detail in Chapter 5.

Based on the results of this mesh study, the 40x75 mesh was selected as optimal for modeling the plain pipe test specimens. The level of agreement obtained between the finite element analysis results and the laboratory test results, which is presented and discussed in Chapter 4, further support this selection. It is also concluded that the initial imperfections play a significant role in the load carrying capacity of line pipe and, therefore, will be included in all subsequent numerical analysis.

3.3.7 Reduction of Measured Initial Imperfections

As detailed in Section 2.2.3, the imperfections of each test specimen were measured prior to installation of the pipe into the testing frame. The imperfections was measured on a grid that was 150 mm in the circumferential direction and 180 mm in the longitudinal direction, resulting in a recorded mesh size of 16x15. Clearly the mesh on which the imperfections were measured was not consistent with the 40x75 mesh selected as optimal in Section 3.3.6. As a result, the measured imperfection pattern had to be mapped to the selected optimum mesh before use in the finite element model. The following procedure details how that mapping was done.

1. The imperfection of the machined rail was determined by plotting the LVDT reading as a function of distance along the length of the rail. The difficulty in determining the imperfection of the machined rail was to find a reference from which to measure the imperfections. The guide rails of the MTS machine were used as the reference. The MTS guide rails are precision-machined columns that are used to guide the MTS load head. They were considered to be the straightest element of adequate length available in the I.F. Morrison Structural Engineering Lab.

   Figure 3.11 provides a graphical representation of the imperfection readings for the rail, as compared to the MTS guide rails. By passing a straight line through the two data points corresponding to the ends of the rail, as shown in Figure 3.11, a linear correction for each radial measurement at each elevation was determined.

2. The imperfection data recorded for each test specimen was adjusted using the linear rail correction factor determined in step 1, applied at the appropriate elevation in each set of measurements.

3. Although special attention was paid to ensure that the rail was aligned vertically prior to each set of measurements being recorded, it was found that the rail was never aligned exactly vertical inside any of the test specimens. Since the specimens were

aligned vertically in the test set-up and in the FEA model, a second correction factor was needed to account for any vertical misalignment of the device inside each test specimen during recording of the imperfection measurements. These correction factors were calculated as follows:

- Each end cross section was assumed to follow the equation of a circle. It is acknowledged that this is not the exact case because of the imperfections. However the equation of a circle was deemed to most accurately represent the shape of a typical cross section.

- The center of each end cross section was determined using a least squares polynomial fit of the 16 data points collected at each end of the respective test specimens. This was done by converting the measured inside radius, IR_M, which included the measured imperfection, at a given angle, θ, into x and y coordinates. These conversions were calculated as

$$x = IR_M(\cos\theta) \tag{3.4}$$

$$y = IR_M(\sin\theta) \tag{3.5}$$

- Once the x-y coordinates of each node were known, the data for the top end cross section were input into an equation of a circle, which was defined as

$$(x-a)^2 + (y-b)^2 = (R_p)^2 \tag{3.6}$$

where 'a' and 'b' are the coordinates of the center of the top end cross section and R_p is the radius of a perfect circle passing through the x-y coordinates. Rearranging Equation 3.6 and introducing an error term, 'Err', results in

$$(x-a)^2 + (y-b)^2 - (R_p)^2 = Err \tag{3.7}$$

where 'Err' was considered the error between a given pair of x-y coordinates and R_p. By repeating this procedure for each of the 16 measurements at the end cross section in which the values of a, b and R_p were kept constant for each of the 16 measurements, the value of Err for each data point could be determined.

The 16 resulting simultaneous equations were then solved for values of a, b and R_p that minimized the total error, E_{TOT} in the system of equations, which resulted in the best fit coefficients for the system of equations. It was assumed that the resulting values of 'a' and 'b' gave the best least squares fit for the coordinates of the center of the top end cross section and provided the x and y cross sectional adjustments required to align the rail in the center of the top end cross section.

- The same procedure was repeated for the 16 radial imperfection measurements that were taken at the bottom end cross section, thereby providing the x and y cross section adjustments required to align the rail in the center of the bottom end cross section.

- Knowing the cross sectional adjustment required at both the top and bottom ends of the pipe to align the rail vertically inside the pipe, a correction factor, as a function of elevation, could be linearly interpolated between the two adjusted center points. This resulted in the center of each elevation at which imperfections were measured now being located on a vertical line passing through the ideal center at each end of the pipe. In other words, the corrected imperfection measurements were now referenced to a vertical line passing through the center cross section at each end of the test specimen. This vertical line corresponded to the line of action of the loading head of the MTS machine when the specimen was aligned in the test set-up, as described in Section 2.3.1. The resulting vertical line of action allowed for the imperfection mesh to be oriented in the FEA model the same as it was in the actual test specimens.

4. The resulting corrected imperfection mesh was then input into MacGRIDZO (Rockware, Inc. 1988a) and mapped from the recorded 16x15 mesh onto the 40x75 finite element mesh for use in the FEA model. Figure 3.12 shows a typical recorded imperfection mesh (a) and the corresponding mapped finite element mesh (b). It should be noted that the meshes shown in Figure 3.12 were plotted on a flat plane instead of the cylindrical tube on which they were measured for clarity.

   The data used to generate the two meshes presented in Figure 3.12 came from specimen CP20W, which has a girth weld at the half height of the specimen. The girth weld is indicated by the transverse line in the 2-direction at the half height of the two meshes.

   It may also be noted that there is a distinct depression parallel to the 1-direction in both meshes of Figure 3.12. This corresponds to the longitudinal DSAW seam weld. Figure 3.12 (a) shows that the longitudinal DSAW seam weld on either side of the girth weld is offset by a small circumferential distance. Finally, it should be noted that the FEA model mesh in Figure 3.12 (b) includes the end collar offsets discussed in Section 3.3.3.1, whereas the measured initial imperfection mesh shown in Figure 3.12 (a) does not.

While this procedure is similar to that used by Del Col *et al.* (1998), one fundamental difference exists. The MacGRIDZO input mesh used by Del Col was one full circumference of the test specimen wide. As a result, there was no continuity of deformation across the edge boundaries. This resulted in inconsistent deformations at the edges of the mesh. To rectify this problem, the input mesh for MacGRIDZO was extended one-quarter the diameter of the test specimen beyond the edge of the mesh. This was done by imposing the same imperfection measurement at a radial measurement of $\theta \pm 360^{\circ}$, thereby creating continuity beyond the edge boundary of the input mesh. As a result, the mapped imperfection measurements at 0° and 360^{0} around the test specimens were essentially identical. As can be seen in Figure 3.12, the mapped finite element mesh

closely contours the recorded experimental mesh and there appears to be continuity at the edges of the mesh, that is, the two longitudinal edges of the mesh have essentially the same imperfections.

3.3.8 Loading scheme

The loading scheme was divided into a series of load steps as prescribed in the ABAQUS User's Manual (Hibbitt, Karlsson & Sorenson, Inc., 1997c). The first step in the load scheme was a pressurization of the test specimens to zero internal pressure. The default initial pressure in ABAQUS is 0.0 MPa, however this step was still included so that the initial geometry of the test specimens, which was required for later post-processing, would be included in the results file. The remaining steps followed the same procedure as was used in the experimental program. The next load step was specified to increase the internal pressure in the specimen to the level recorded during testing. This load step was achieved in ABAQUS using a single increment of loading.

Once the pipe was loaded to the correct internal pressure, the axial load was then applied. The axial load was applied at the top pivot point, as was done during the experimental testing, to the level recorded during testing. The load step to increase the axial load was also done with a single increment of loading.

The final step was to monotonically increase the moment applied to the top pivot point. It should be noted that during the experiment, the moment was applied equally to the top and bottom moment arms. In the FEA model, the same procedure was followed. Equal increments of moments were applied at the top and bottom pivot points to simulate the laboratory conditions. The load step for the application of the external moment was not as straight forward as it was for the internal pressure and the external axial load. Preliminary analysis in this project using Newton's approach, which is the default strategy in ABAQUS, resulted in frequent crashes of the analysis package. This was because the solution was unable to converge as it passed over the peak on the curve. However, the capacity for varying solution strategies was one of the features that made ABAQUS the finite element package of choice for this analysis. The load-displacement constraint

method, also known as the Riks method or the constant arc-length method (CALM), is particularly effective at passing over limit points (Bathe, 1996). Riks method is one of the solution strategies contained in the ABAQUS software (Hibbitt, Karlsson & Sorenson, Inc., 1997b). Using Riks method, ABAQUS was able to converge over the limit points and continue the analysis through the post-buckling region. However, while the Riks method ensured convergence over the limit point, it was found to be very inefficient because it requires a substantial amount of computational capacity. Therefore, it was decided to investigate using Newton's approach, which required less computational capacity, until the peak was approached. ABAQUS would be programmed to then change strategies and adopt the Riks method in order to achieve convergence over the peak. It was felt that this would substantially reduce the analytical computational time.

Three different strategies were investigated. The first strategy involved using Riks method from the beginning of the analysis until it was completed. As previously mentioned, this required substantial computational capacity and may not be the most efficient solution strategy. The second and third strategies involved using Newton's approach until moments of 1000 kN-m and 1700 kN-m, respectively, were reached. Once the appropriate level of moment was achieved a new load step using Riks method was initiated and continued until completion of the analysis. The purpose of this was to see if the different strategies would result in different softening regions of the moment-curvature responses.

Figure 3.13 provides the moment-curvature responses from these three strategies. As can be clearly seen in this figure, the solution strategy makes no difference in the moment-curvature response. As a result, the second strategy was selected for this project. This was because the lowest experimental peak moment from any of the test specimens was 1211 kN-m and using a moment value of 1000 kN-m for the transition from Newton's to Rik's method would ensure that the peak moment would not be exceeded prior to initiation of the Rik's method.

3.4 Special Features in the Development of the Weld Model

Of particular interest in this research was the effect of circumferential girth welds on the moment-curvature response of line pipe. Work previously conducted at the University of Alberta by Yoosef-Ghodsi *et al.* (1994) and Souza and Murray (1994) has shown that girth welds substantially reduce the buckling strain, with little or no effect on the moment capacity of a segment of line pipe under combined loads. The effect of the presence of a girth weld has been considered to be significant enough that it is receiving special consideration in design codes and specifications (DNV OS-F101, 2000).

Seven of the test specimens in this project had circumferential girth welds. Since the effect of a girth weld has been shown to significantly affect the behavioural response of line pipe, special attention to the girth weld was taken in development of the FEA model. A number of factors can affect the analytical response of a segment of line pipe with a girth weld. These factors include, but are not limited to, the mesh selected, the thickness of the weld elements, the length of the weld elements, and the presence of residual stresses located at the girth weld. This section discusses these specific issues and how they were addressed in the FEA model developed for this research project.

3.4.1 Different Meshes

A variety of meshes were initially proposed during the development of the FEA model. As previously discussed in Section 3.3.6, the geometry and characteristics of the mesh selected for an FEA model can influence the analytical results (Sussman and Bathe, 1986). Initially, two basic meshes were considered in this project. The first mesh was an exact replica of the 40x75 mesh used in the analysis of the plain pipe specimens with a refined ring of two longitudinal elements at the half height of the mesh. The purpose of this refined ring of elements was to simulate the weld elements located at the half height of the test specimens.

The second mesh used the 40x75 mesh over the first and last third of the model with a refined mesh over the middle third. The elements in the refined middle portion had the

same circumferential dimension as the rest of the mesh, but the elements were half as long in the longitudinal direction. The ring of elements located at the half height of the model was grouped separately from the other refined elements to simulate the weld. Figure 3.14 shows a typical view of the one-third coarse, one-third fine, one-third coarse mesh layout after the specimen has buckled. As can be seen in this figure, the specimen buckled at the interface between the coarse and fine regions of the mesh. This is a common occurrence in graded meshes.

Initially special care was taken to ensure that the transition between the coarse and fine regions was sufficiently removed from the half height of the specimen where the maximum second order moment effects act. However, due to the effects of the unsymmetric imperfection pattern, the combination of mesh size transition and local imperfection frequently resulted in the buckle occurring at the interface between the two mesh sizes, as shown in Figure 3.14.

Figure 3.15 provides a plot showing a preliminary comparison between the experimental data and the two different meshes initially developed for use in the modeling of the girth welded specimens. As can be seen in this figure, the mesh with the refined middle third had very poor agreement with the experimental data prior to buckling. This is because of the discontinuity between the meshes in the transition zone. As a result, this mesh pattern was abandoned.

Failure of the mesh with the refined middle third lead to the consideration of a third mesh. This third mesh had a gradation that provided a smooth transition between the 40x75 mesh at the ends of the specimen and the more refined mesh over the middle third of the model. Such a mesh pattern had proved to be very effective in predicting the behaviour of girth welded specimens (Souza and Murray, 1994). A number of attempts were made during this research project to develop the graded mesh. However, since there was no commercially available software that could map the uniform measured imperfection pattern to the desired graded mesh and the measured initial imperfections were considered to be of greater importance to the FEA model than the graded mesh, the

graded mesh was abandoned. This left only the regular uniform mesh used for the plain test specimens available for use on the girth welded specimens.

As will be shown in Chapter 4, further refinement of some of the other features in the girth weld FEA model resulted in more than adequate agreement using the uniform mesh. As such, the decision was made to abandon any further mesh refinement for the girth welded specimens and to use a uniform 40x75 mesh with special welds elements, which are discussed in Section 3.4.2.

3.4.2 Weld Element Length and Thickness

The physical dimensions of the mesh weld elements were also a consideration that was unique to the model for the welded test specimens. It was postulated that the model would respond differently to variations in the length and thickness of the weld elements. Figure 3.16 provides a schematic showing how the length and thickness of the weld are defined. To investigate the effects of varying the thickness and length of the weld elements on the response of the model, a short parametric study was conducted on each variable.

For purposes of the parametric study, weld lengths of 6 mm, 10 mm and 16 mm were chosen. Physical measurements of the test specimens showed that the length of the weld at the inside surface varied from approximately 2 mm to 5 mm and the length of the weld on the outside surface varied from approximately 10 to 15 mm. A mean weld length of approximately 10 mm was assumed from these measurements.

Figure 3.17 presents the results of the weld element length parametric study. From this figure, it can be seen that the weld elements with a length of only 6 mm were found to reduce the capacity of the model. This is not consistent with the observed weld effects on actual test specimens (Yoosef-Ghodsi, *et al.*, 1994) in which there was no significant reduction in moment capacity due to the presence of the weld. Figure 3.17 shows that there is no effective difference between the 10 mm long weld element and the 16 mm long weld element in terms of the moment-curvature response. However, the different

weld lengths did result in a different location for the buckle in the model. The analysis conducted with the 10 mm long weld element was 'soft' enough at the location of the weld to allow the specimen to buckle at this point, as was seen in the actual test specimens. The use of the 16 mm long weld element resulted in an overall stiffer weld around the pipe and inhibited the formation of the buckle at this location. These observations, coupled with the physical measurements on a typical weld, resulted in the selection of a 10 mm long weld element for use in the modeling of the test specimens.

A similar parametric study was conducted by varying the thickness of the weld element. Physical measurements on the test specimens showed that the weld thickness ranged from approximately the thickness of the pipe wall up to approximately 50% thicker than the pipe wall. Typically, the welds were found to be approximately 25% thicker than the pipe wall. For the purposes of the parametric study, weld thicknesses ranging from 100% to 200% the thickness of the pipe wall were selected.

Figure 3.18 shows the results of the weld thickness parametric study. From this figure it can be seen that using a weld thickness equal to the thickness of the pipe wall had a significantly lower moment capacity than for any of the other weld thickness and moved the solution away from the experimental results. As such, a weld element thickness of 100% the pipe wall thickness was rejected.

The use of a weld element with a thickness that was 200% the thickness of the pipe wall resulted in a different buckling location which was not consistent with that observed during the experimental portion of the project. Therefore, this option was also rejected from the model.

The parametric weld elements that were 125% and 150% the thickness of the pipe wall produced essentially identical moment curvature responses and both had buckling locations that were consistent with the results of the experimental project. As such, both would have been suitable to use in the finite element modeling of the test specimens. The decision was made to select a weld element with a thickness of 125% the wall thickness

of the pipe because it was found to be most consistent with the physical measurements taken on the girth welds in the laboratory.

3.4.3 Residual Stresses at Girth Weld

Residual stresses are commonly associated with welding procedures due to the differential cooling rates within a weld (Dieter, 1987). Seven test specimens had a girth-weld located at the half-height of the specimen. As such, it was deemed necessary to consider residual stresses for the girth welded specimens.

In past research, it was believed that one of the key aspects of the girth welded test specimen behaviour was the presence of the residual stress pattern generated during the welding process (Hu, 1991). A residual stress pattern at the girth welds was considered to play a significant role in the buckling behaviour of the test specimens because of both the longitudinal and circumferential stress components. As a result, many different methods have been developed to model residual stresses in finite element analysis, including direct input of a measured or assumed residual stress pattern. One of the more simplified methods for developing a residual stress pattern in tubular steel members is through the thermal generation of the stresses (Obaia, *et al*, 1991).

However, the use of this approach may not be valid for this research project. Examination of the experimental results obtained for line pipe test specimens with D/t ratio's ranging from 50 to over 90 presented in Chapter 1 reveals that the strain at buckling was in excess of the yield strain for every test specimen, indicating that the specimens yielded prior to buckling. Therefore, while the residual stresses usually affect the proportional limit, the yield strength of the material will nevertheless be reached and there is little effect on the post yield behaviour of a specimen.

This appears to be in contrast to the results obtained by others (Hu, 1991; and, Souza and Murray, 1994), which have achieved extremely good correlation between experimental results and finite element results using the thermally generated residual stress patterns. Close review of the procedure used to generate the residual stresses revealed an

interesting observation. While a residual stress pattern was developed, it was observed that the procedure used also introduced an imperfection into the test specimens. This imperfection was directly proportional to the applied thermal gradient, therefore, by varying the magnitude of the thermal gradient, the magnitude of the introduced imperfection also varied. As previously discussed in Section 2.2.3, imperfections are one of the most important factors in the buckling of thin-shelled members. As was shown in Table 3.2 and Figure 3.10, an imperfection of 12% the wall thickness (1.0 mm in amplitude) can result in a moment capacity reduction of over 9.6%. Therefore, it is postulated that the level of agreement achieved in previous projects that used a thermal gradient to generate residual stresses could also have been attributed to the initial imperfections introduced through the thermal loading cycle, and not the imposed residual stress pattern. It is acknowledged that the resulting residual stress pattern does contribute to the correlation around the proportional limit, but the residual stress pattern has minimal effect the buckling moment capacity since the specimens are well into the plastic region prior to buckling.

To support this hypothesis, a small parametric study was conducted to determine the effect of the initial residual stress pattern on the overall moment-curvature response of a representative test specimen. A FEA model was developed in which thermally generated residual stresses were incorporated. These stresses were generated by heating the weld elements in the model to a prescribed temperature and then cooling the elements back to the initial temperature, such that there was no net thermal change in any of the elements prior to the application of any loading. By applying a large enough thermal change, the weld elements went beyond yield so that once they were cooled back to the initial temperature, a permanent deformation existed, resulting in a non-zero residual stress pattern. The FEA generated specimens were then loaded using the same loading scheme so the effects of the initial residual stress pattern could be assessed.

Both Hu and Souza found that a thermal change of 300°C gave the best agreement between the FEA prediction and the experimental data. As such, the model was run using thermal changes of 200°C, 300°C and 500°C. Table 3.1 presents the numerical

results of the different thermal effects. For purposes of this parametric study, the yield strength of the weld was assumed to be the same as the yield strength for the pipe material, since the electrodes used in fabricating the girth weld were matched to the strength of the pipe material. The yield strength for the pipe material was found to be 523 MPa, as will be discussed in Section 4.2. Therefore, a yield strength of 523 MPa was also assumed for the weld elements. As can be seen from this table, the temperature change of 200°C was insufficient to cause the weld to yield. Correspondingly, once the specimen was cooled there were no resulting residual stresses, as shown in Table 3.1. It should be noted that both Souza and Hu used temperature dependent material properties. Temperature dependent material properties were not used during the preliminary phase of this investigation, nor at any other time. The following results of the preliminary phase will show that temperature dependent material properties do not have a significant effect on the results, if an initial imperfection pattern is considered. The level of agreement achieved between the experimental results and the FEA model results presented in Chapter 4 and Chapter 5 further supports this.

When a temperature of 300°C was used, the weld elements yielded at the completion of the heating phase. As a result, when the elements were cooled there were net residual stresses in the weld elements with the maximum value equal to 427 MPa, as shown in Table 3.1. The same behaviour was observed using the greater 500°C temperature change, with the resulting maximum residual stress equal to 437 MPa.

The effect of the different initial residual stress patterns was assessed by comparing the global moment-curvature response of the three specimens subjected to these different thermal changes. Figure 3.19 shows a plot of the moment-curvature response for the three analyses containing the residual stresses of Table 3.1. As indicated in this figure, there appears to be no significant difference between the three analyses. This is because the mesh used in the analyses included a measured initial imperfection pattern. The effect of the initial imperfection pattern was to increase the total imperfection in the pipe, evaluated as the sum of the measured imperfection plus the imperfections developed during the thermal generation of the residual stress pattern. The maximum measured

imperfection in a typical welded mesh was found to be approximately 25% of the wall thickness of the pipe and was exclusively located at the girth weld. While is it referred to as an imperfection in this discussion, it could be more accurately described as an offset at the weld between the two adjacent segments of the test specimen. Examination of Figure 3.10 shows that if there is an initial imperfection with a magnitude of approximately 25%, the additional imperfection due to the thermal change, which was typically four to five percent, will have little to no effect on the global moment capacity. That is, there is very little difference in the moment capacity of a test specimen when the initial imperfection varies between 21% to 29% because this magnitude of imperfection corresponds to the flattening of the curve as shown in Figure 3.10.

Figure 3.20 shows an enlargement of the peak moment region from Figure 3.19. This figure shows that there is in reality a slight reduction of moment carrying capacity with an increase in the temperature used to generate the thermal stresses. However, this reduction in moment carrying capacity is very small, which is consistent with the results presented in Figure 3.10.

Hu and Souza did not include a measured initial imperfection pattern in their analyses. However, they did consider two different types of initial deformation: a lateral offset of the segments of the specimen on either side of the weld; an initial ovalization of the pipe; or a combination of the two. These localized deformations were based on judgement and not experimental measurements. Souza used lateral offset values of 1.0 mm and 2.0 mm. Measured lateral offsets recorded in this investigation sometimes exceeded 2.0 mm, indicating that Souza may have underestimated the actual magnitude of the offset. Examination of Figure 3.10 shows that an underestimate of the initial imperfections may correspond to the initial steep region of the graph. If this was the case, then the additional imperfection of four to five percent of the wall thickness due to the residual stress thermal cycle would have a significant effect on the moment capacity, resulting in the misinterpretation that the varying residual stress pattern was having a significant effect. This provides a rational explanation as to why Hu and Souza were both able to obtain a reduction in moment capacity by applying the thermal loading, but this reduction

was not realized in this project. Furthermore, it should be noted that by using temperature dependent material properties, Hu and Souza both generated initial imperfection patterns greater than those generated in this investigation, which would result in a greater loss of moment capacity when plotted on Figure 3.10.

There is no way to support or refute either the method used by both Hu and Souza or the method used in this program without a detailed investigation. It is acknowledged that the technique used by both Hu and Souza did provide good correlation between the experimental data and the FEA data. However, it will be shown in Chapter 4 and Chapter 5 that by simply making a reasonably accurate estimate of the initial imperfections, including the lateral offset at the weld, good correlation can be achieved between the experimental data and the FEA model proposed in this work.

Therefore, based on the results of this limited parametric study and supported by the results for the plain pipe specimens, it was concluded that the initial imperfections continue to be one of the most significant factors in accurately predicting the experimental response of a test specimen using an FEA model. However, for the purposes of this investigation, the decision was made to include both the measured imperfection pattern and the thermally generated residual stresses from a 300°C temperature change applied to the weld elements. This decision was based on the observation that the thermal loading cycle only marginally increased computational time, the residual stress pattern should be included for completeness and to help achieve correlation of the model in the region around the proportional limit.

Table 3.1 – Residual Stresses from Thermal Parametric Study

Temperature Change	Maximum Stress at Weld After Heating	Maximum Stress at Weld After Cooling
$\Delta T = 200°C$	396 MPa	0.2 MPa
$\Delta T = 300°C$	552 MPa	427 MPa
$\Delta T = 500°C$	554 MPa	437 MPa

Table 3.2 – Numeric Results of Parametric Study On the Magnitude of the Initial Imperfections

Analysis ID[1]	amp_{max} (mm)	% of Nominal Wall Thickness[2]	Peak Moment (kN-m)[3]	% Moment Reduction[4]
40x75-p	0.0	0.0	1474	n/a
40x75-01	0.1	1.2	1502	0
40x75-02	0.2	2.4	1495	0.5
40x75-05	0.5	6.0	1439	4.2
40x75-10	1.0	12.0	1358	9.6
40x75-21	2.1	25.0	1219	18.9
40x75-42	4.2	50.0	1198	20.2
40x75-63	6.3	75.0	1098	26.9
40x75-83	8.3	100.0	1051	30.0

Notes:

1. The ID characterizes the size of the mesh used (all the results reported in this table used a 40x75 mesh) and the maximum amplitude of the initial imperfection as indicated by the last two digits. For example, the last two digits in the last specimen listed in the above table (-83) indicate an initial imperfection with a maximum amplitude of 8.3 mm. The '-p' on the first specimen indicates a 'perfect' specimen, or one with no initial imperfection.
2. The nominal wall thickness was selected as 8.3 mm in this study.
3. The peak moment was the maximum value for the moment taken from the ABAQUS output file.
4. The % Moment Reduction was calculated as:

   % Moment Reduction = 100 * (1 – (Peak Moment/1502)

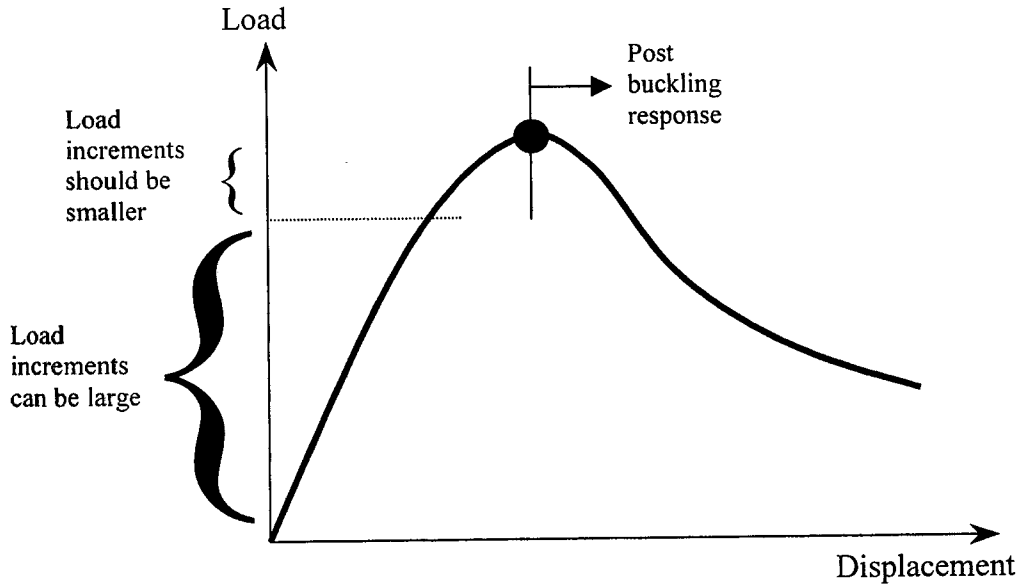

Figure 3.1 – Collapse or Buckling Response

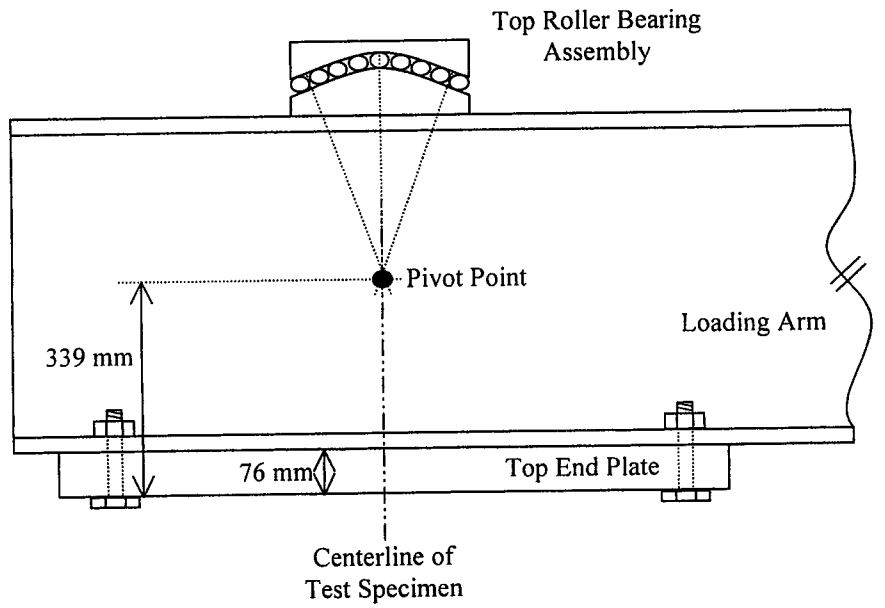

Figure 3.2 – Schematic of Curved End Roller Bearings and Pivot Point On Top Moment Arm

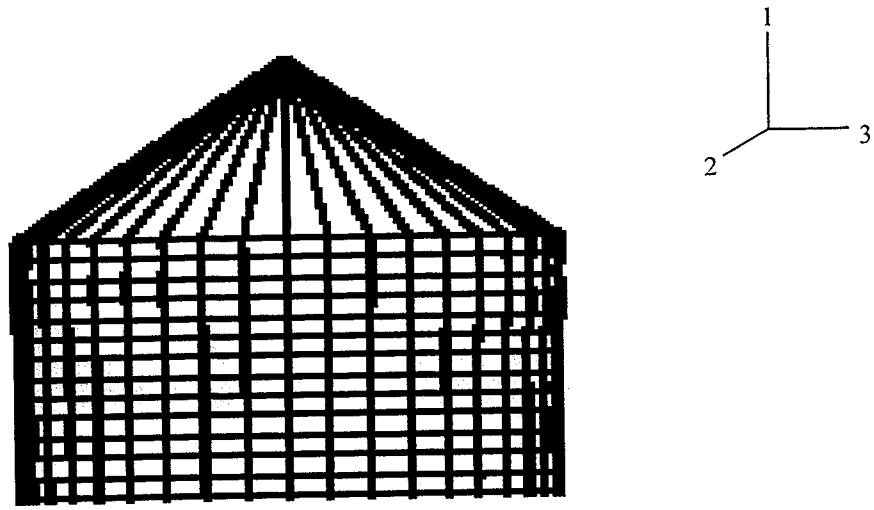

Figure 3.3 – Rigid Cone at End of Test Specimen Comprised of R3D3 Elements

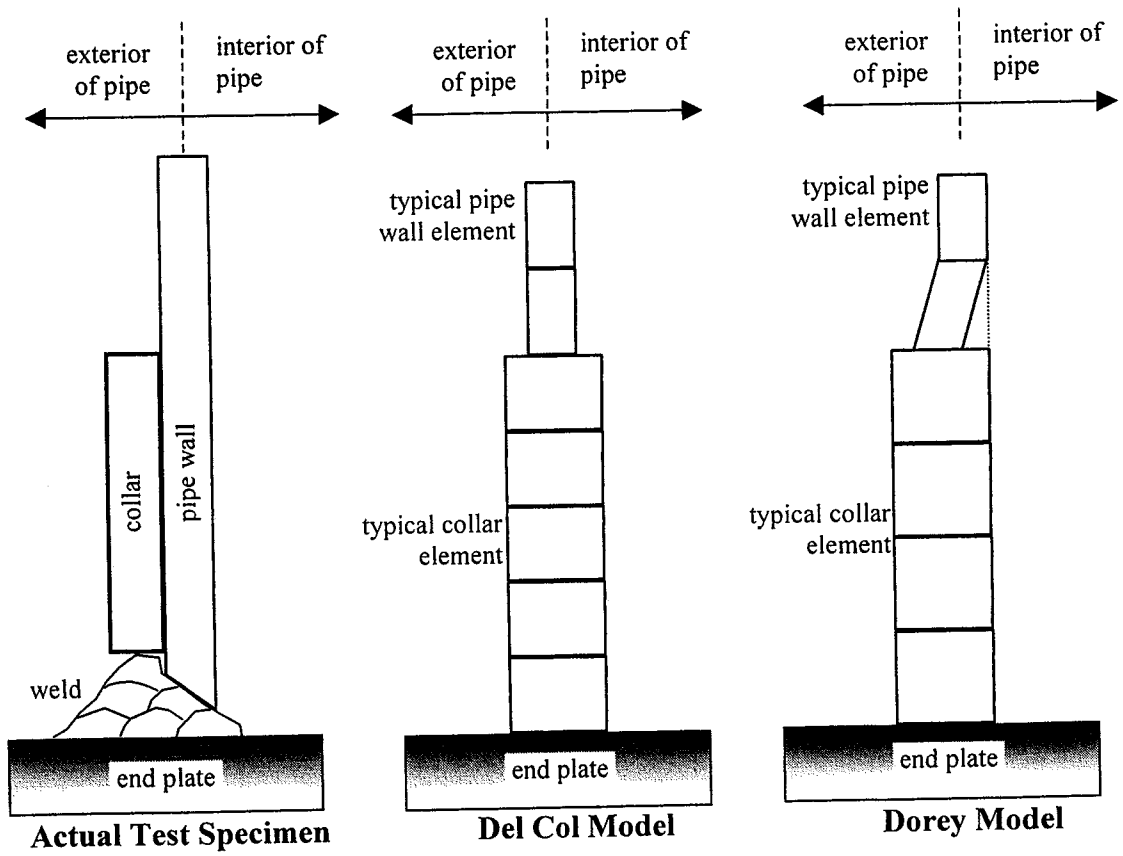

Figure 3.4 – Comparison of Different Collar Models

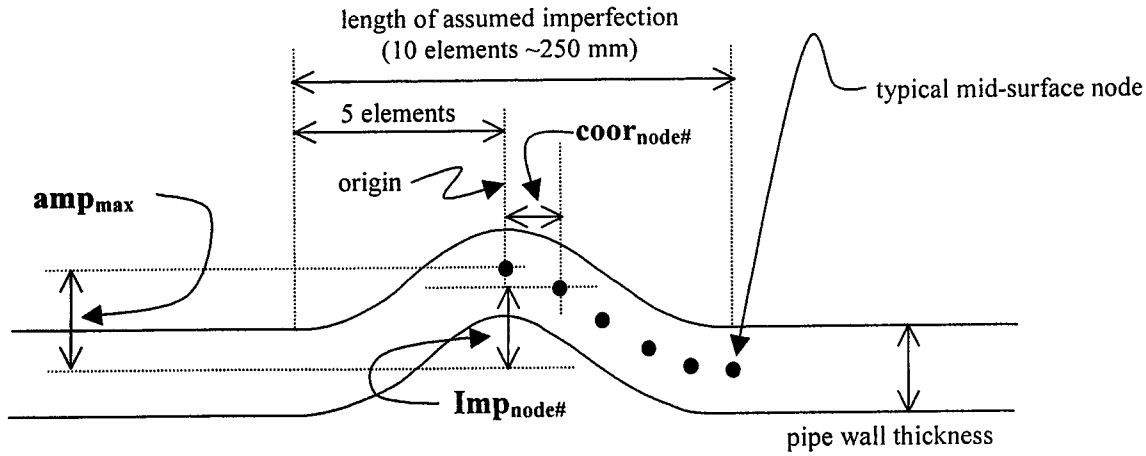

Figure 3.5 – Wall Variation for the Assumed Imperfection Pattern

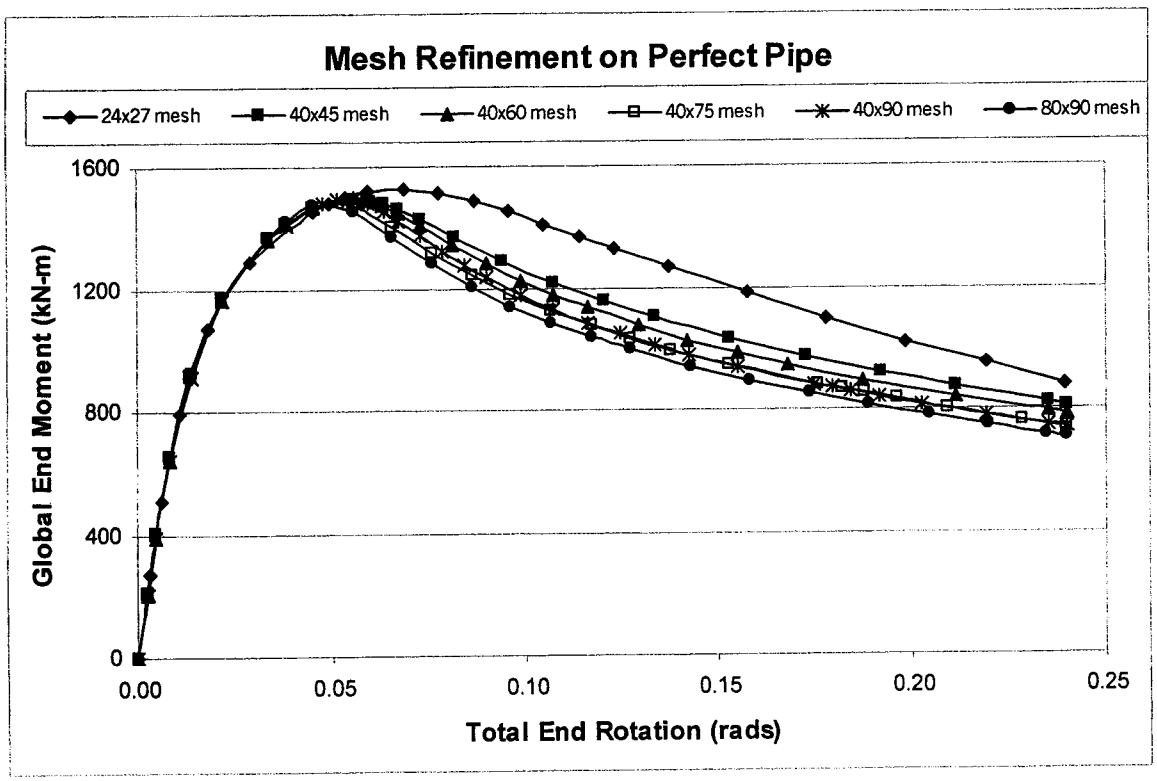

Figure 3.6 – Results of the Mesh Refinement Study Using the Perfect Pipe Formulation

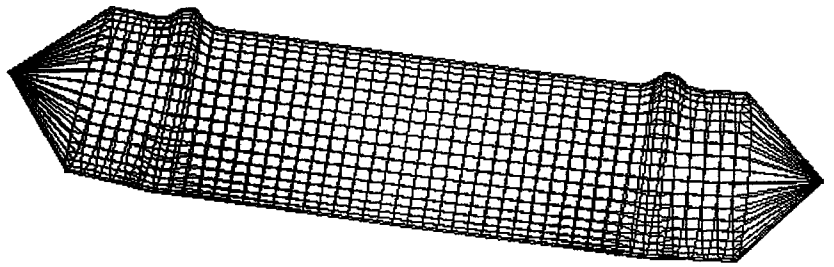

40x45 Mesh

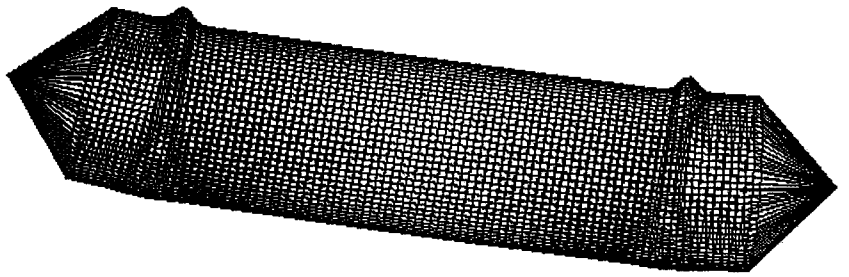

80x90 Mesh

Figure 3.7 – Perfect Pipe Buckling Mode

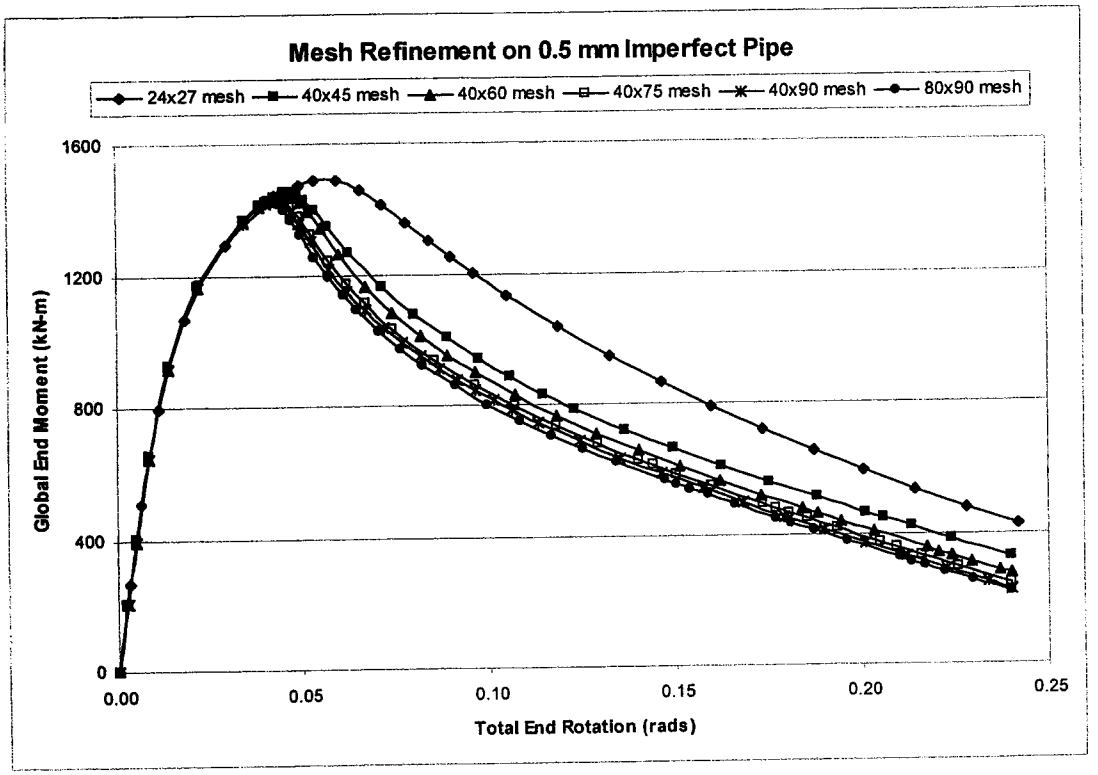

Figure 3.8 – Results of the Mesh Refinement Study Using
An Initial Imperfection of 0.5 mm

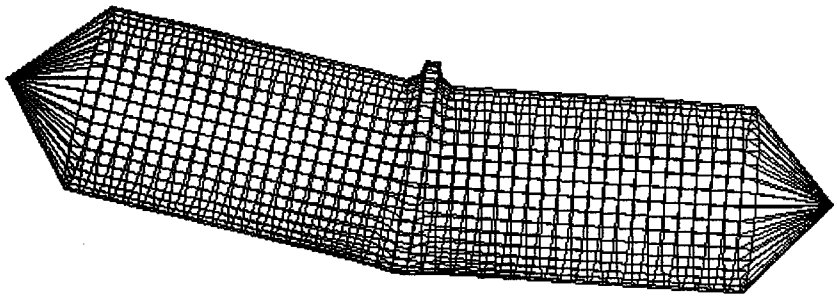

40x45 Mesh

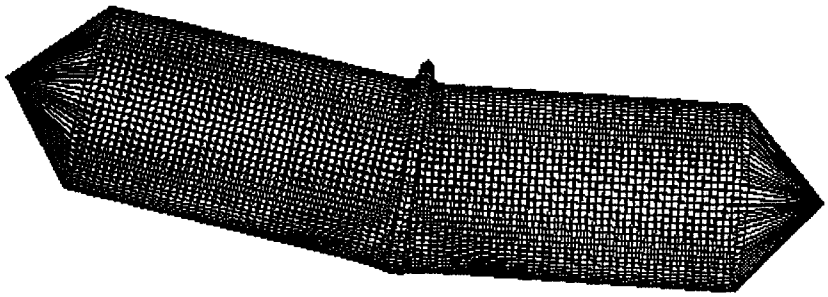

80x90 Mesh

Figure 3.9 – 0.5 mm Imperfect Pipe BucklingMode

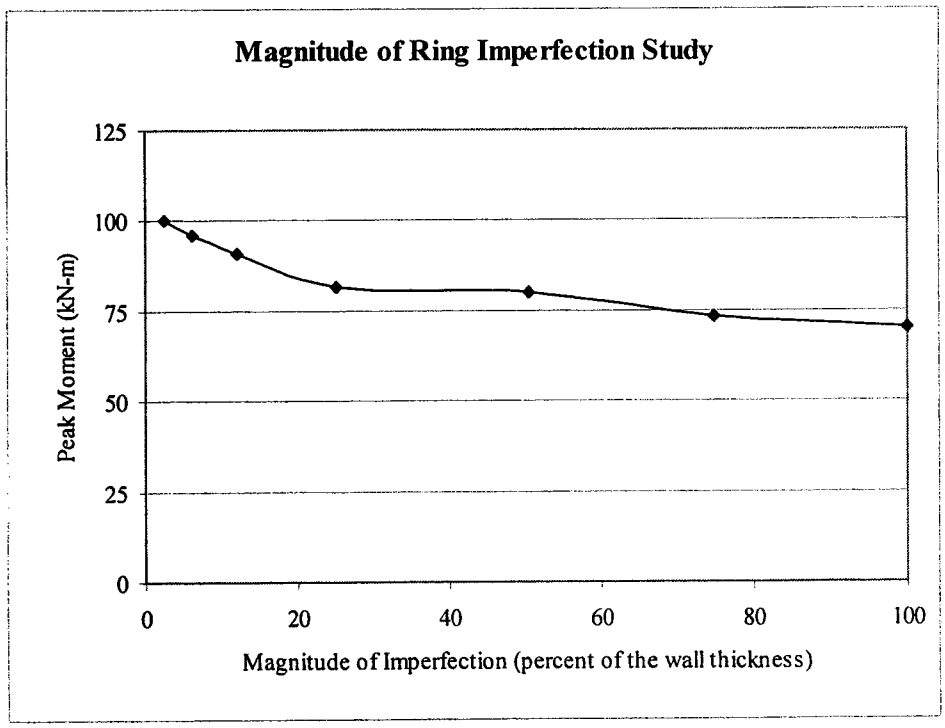

Figure 3.10 – Results of Parametric Study on the Magnitude of the Initial Imperfection on Moment Capacity of D/t = 92 Plain Specimens Using A 'Ring' Initial Imperfection Pattern

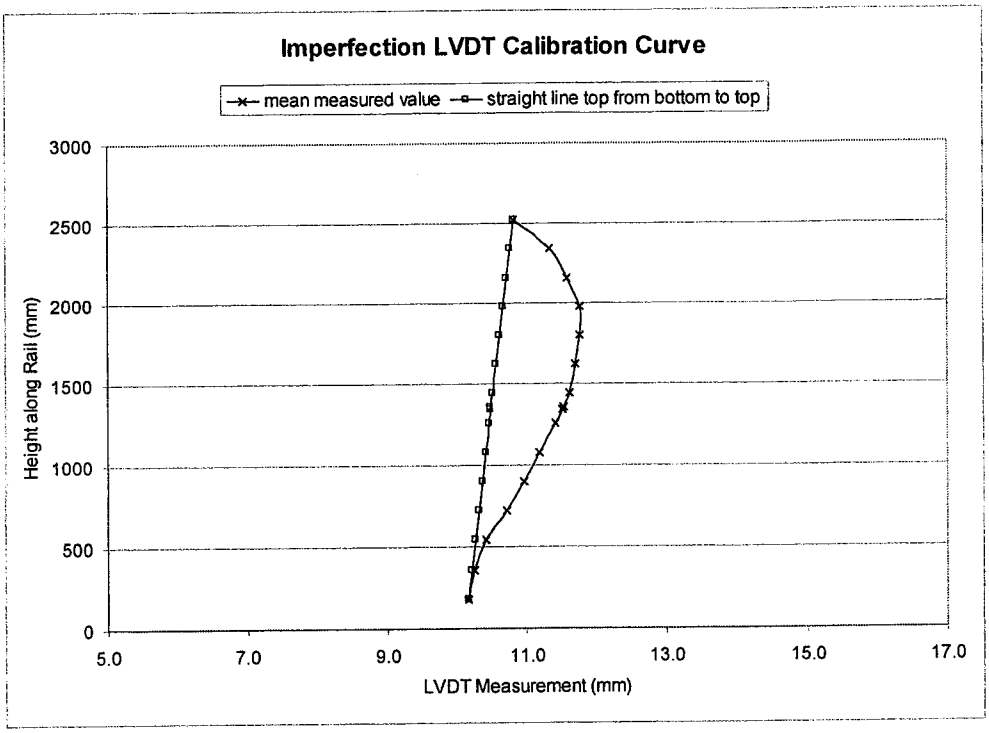

Figure 3.11 – Imperfection Measurements Recorded for the Imperfection Device Rail

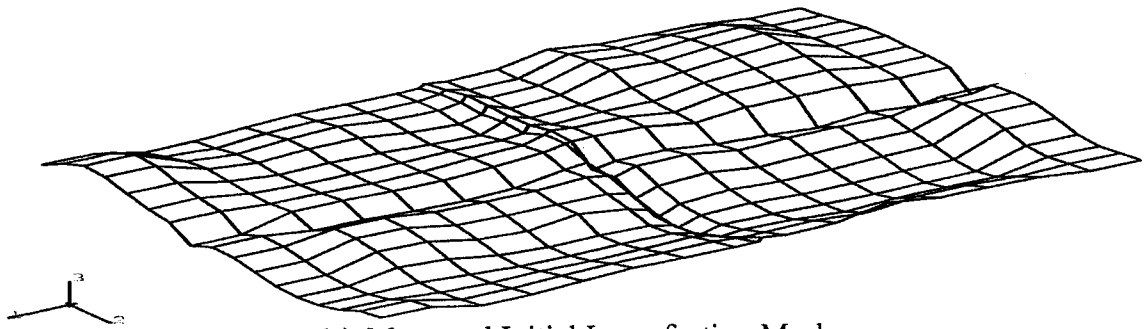

(a) Measured Initial Imperfection Mesh

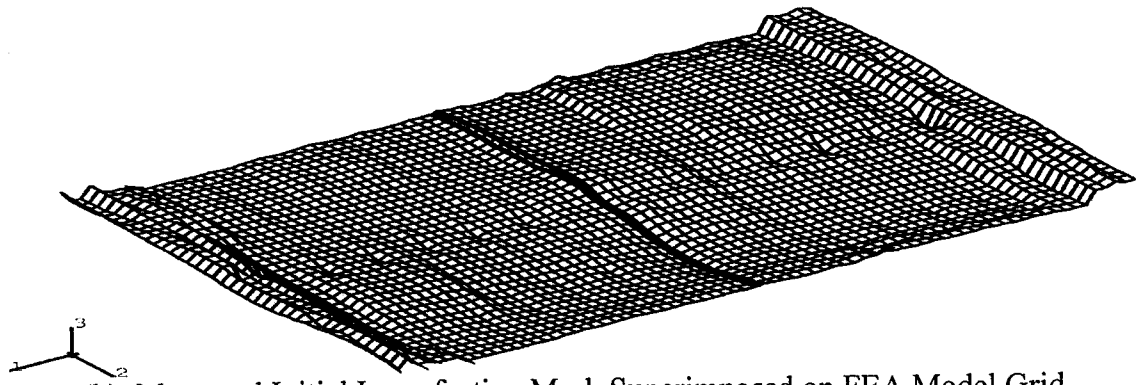

(b) Measured Initial Imperfection Mesh Superimposed on FEA Model Grid

Figure 3.12 – Comparison of Imperfection Meshes

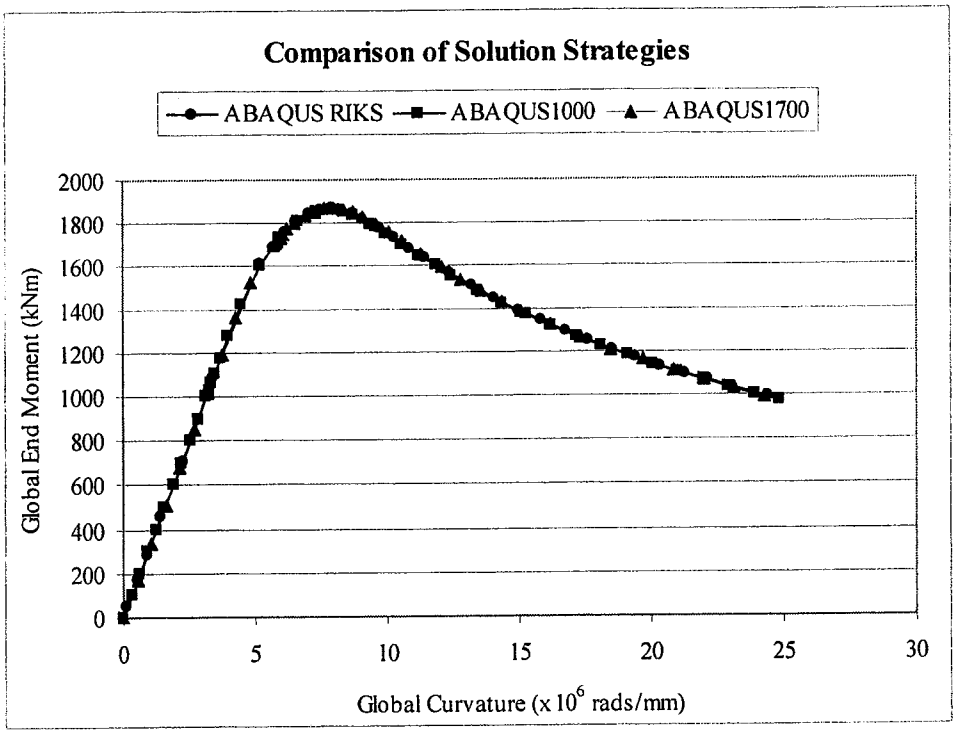

Figure 3.13 – Moment-Curvature Responses for the Different Loading Strategies Considered

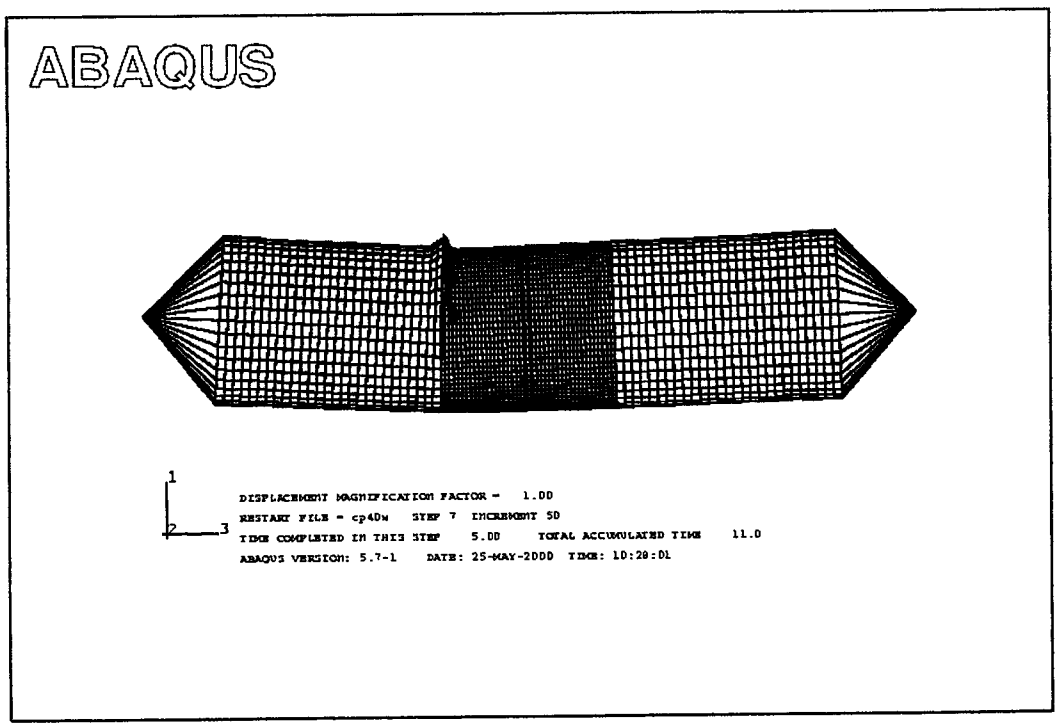

Figure 3.14 – Coarse/Fine Mesh for Welded Specimens

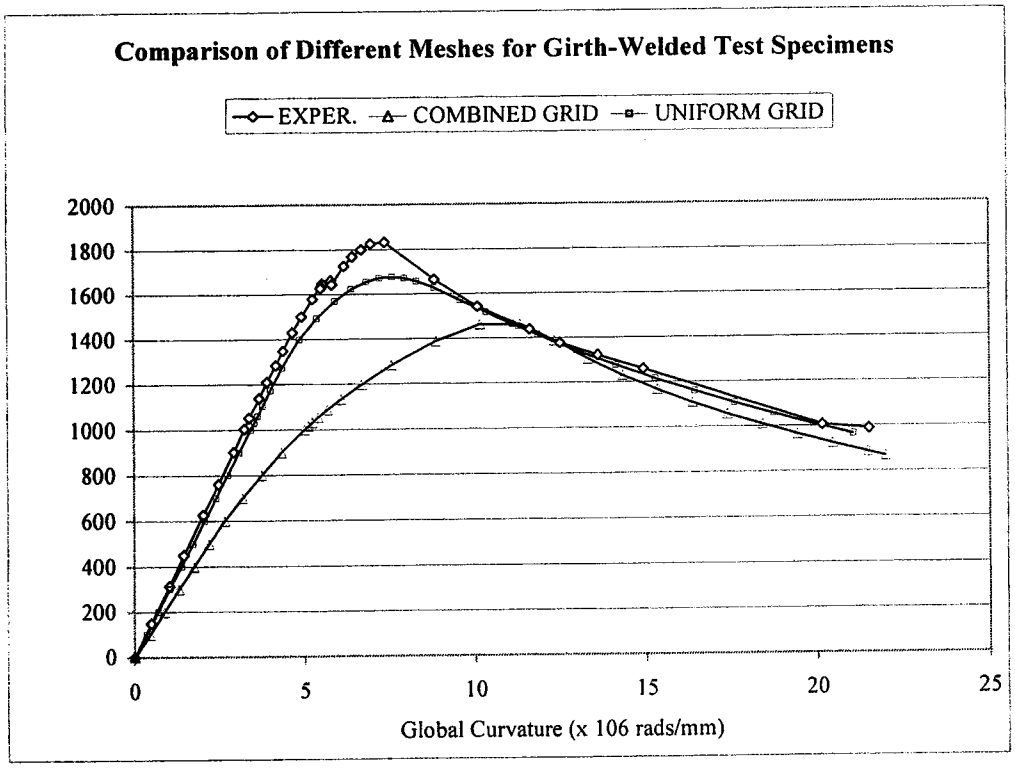

Figure 3.15 – Comparison of Refined Meshes for Girth Welded Test Specimens

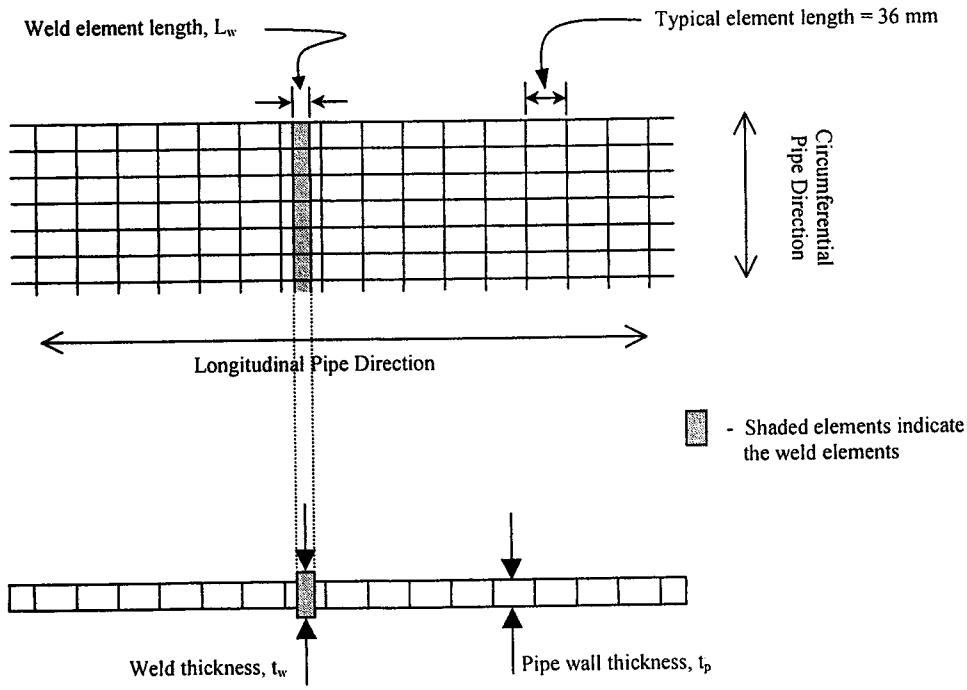

Figure 3.16 – Definition of Weld Element Length and Thickness

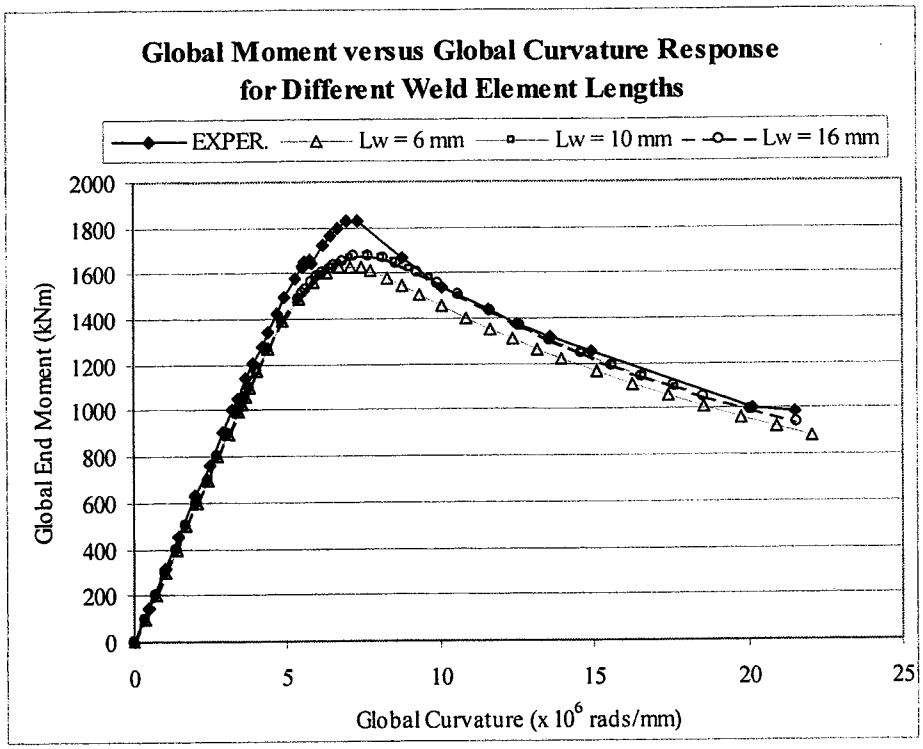

Figure 3.17 – Results of the Parametric Study for Different Weld Element Length

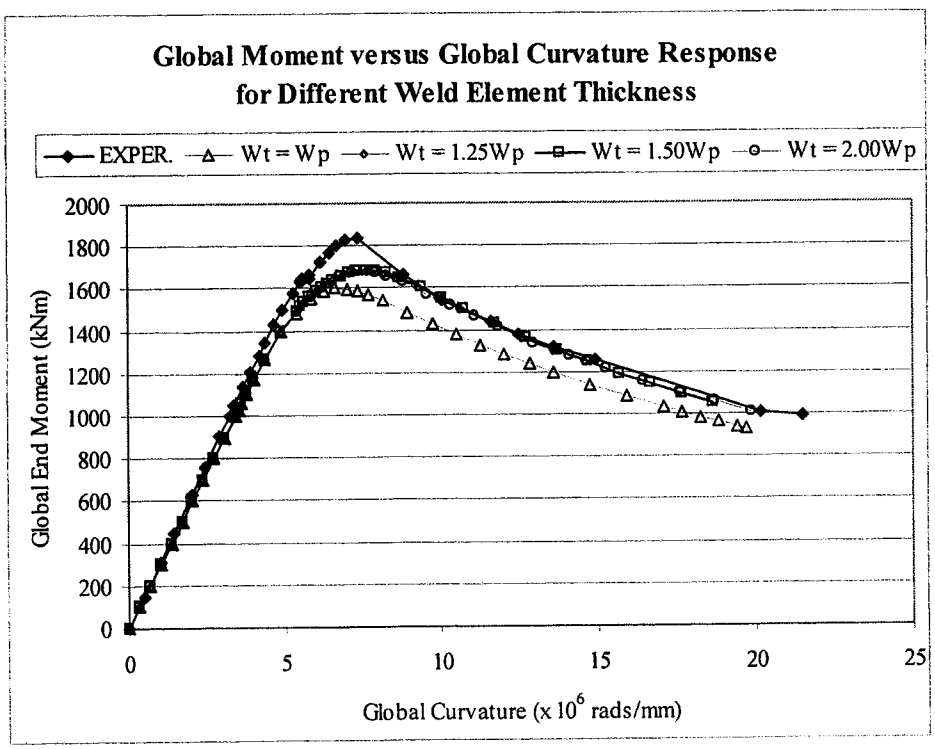

Figure 3.18 – Results of the Parametric Study for Different Weld Element Thickness

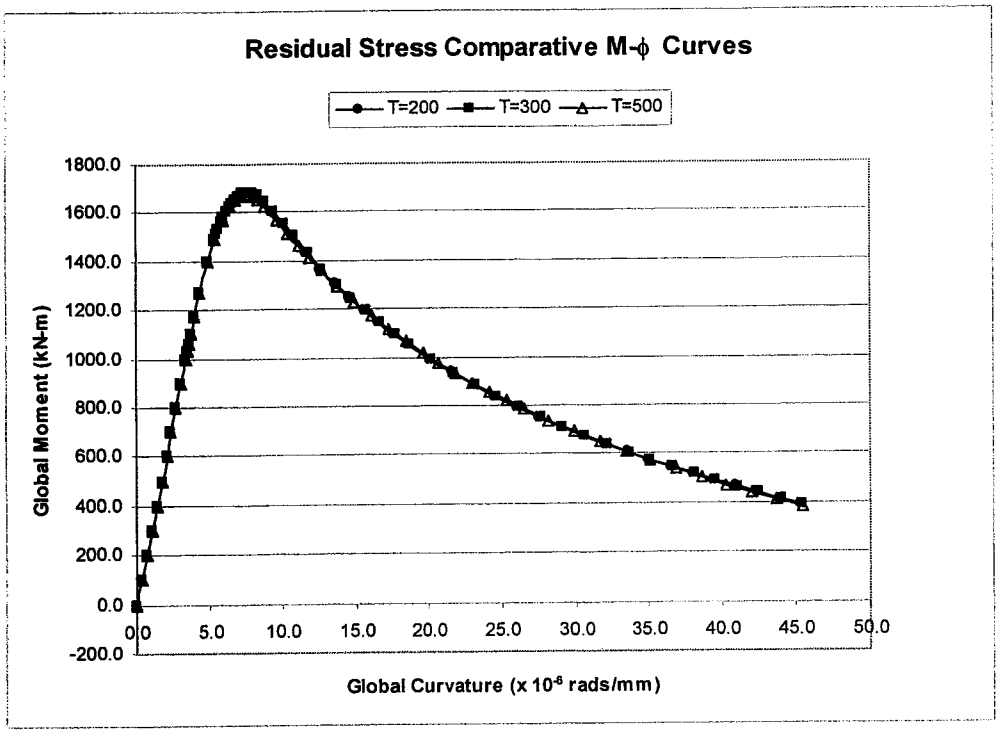

Figure 3.19 – Results of Parametric Study on Different Residual Stress Patterns

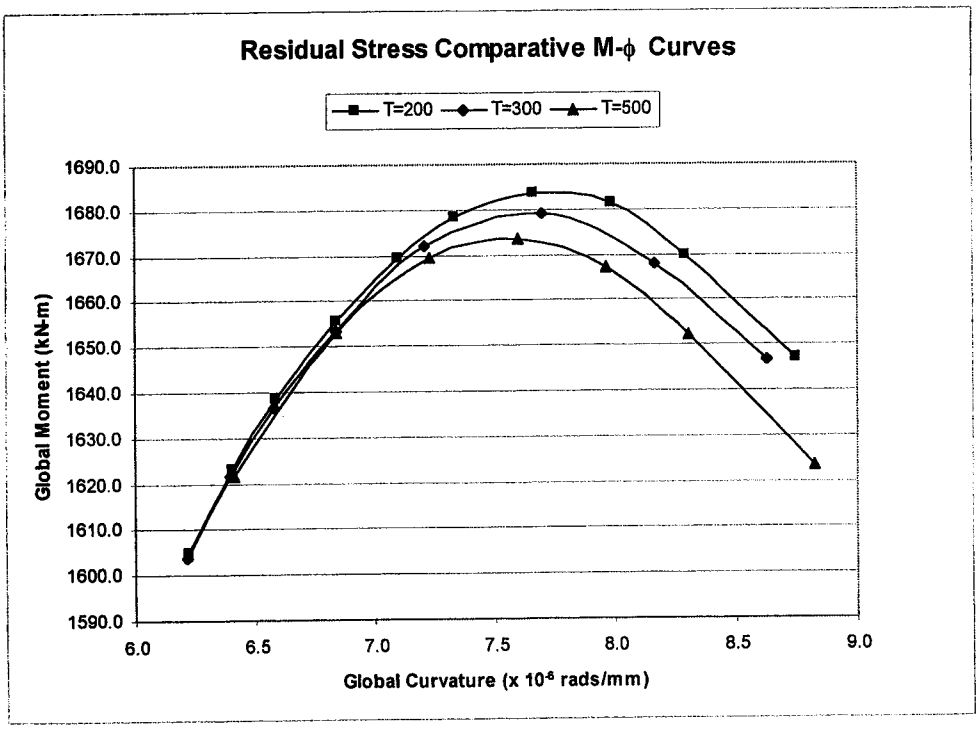

Figure 3.20 – Enlargement of Peak Moment Region for Residual Stress Study

4.0 EXPERIMENTAL AND FINITE ELEMENT RESULTS

One of the major goals of this project was to expand the database for the deformational response of line pipe, specifically the moment-curvature response and critical strain limits. The instrumentation described in Chapter 2 was selected and positioned to allow for the determination of the applied global end moments, global curvatures, local curvatures over a variety of gauge lengths, and the second order local moments due to the deformed configuration of the test specimen during loading. Once the experimental data was reduced for each of the test specimens the experimental critical buckling strains were determined. The experimental results were then used to calibrate the FEA model developed in Chapter 3.

This chapter presents the results of the experimental testing program, including a description of the reduction of the experimental data collected and the results for the FEA validation. Experimental results and FEA generated data are presented and compared both graphically and numerically.

4.1 Results of Material Property Tests

The test specimens used in this study were fabricated using a longitudinal seam DSAW pipe, as described in Section 2.2.1. The DSAW process significantly alters the material properties of the finished pipe from the original steel plate. Consequently, material properties were determined for each of the respective pipe specimens and then used in all subsequent analysis.

Two different sets of material properties were required for each set of test specimens. The first set was determined from the experimental coupon data and was used in all calculations based on the experimental data. The experimental coupon data was based on an engineering stress-strain formulation where the stress and strain at any point on the

coupon curve are referred back to the original undeformed geometry of the coupon. As discussed in Section 3.3.5, this form of material property is unsuitable for input into ABAQUS for carrying out finite strain analysis. As such, a second set of material properties were developed from the coupon test results. ABAQUS requires a true strain-strain formulation where the stress and strain at any point on the material property curve is reflective of the exact current state of stress and incorporates the deformed geometry of the coupon.

This section outlines the determination of the experimental material properties based on the engineering stress-strain formulation and the conversion of the experimental material properties to the true stress-strain formulation required for input into the FEA model.

4.1.1 Experimental Material Properties

A total of five different joints of pipe were used to fabricate the 15 test specimens that were used in the experimental portion of this project. Once the data had been collected, as outlined in Section 2.4.3, a longitudinal stress-strain curve and a longitudinal stress versus lateral strain curve were plotted for the coupons from each test specimen. Figure 4.1 provides a typical longitudinal stress-strain curve, showing both the mean strain measured from the two longitudinal foil strain gauges mounted on the coupon and the strain measured using the externally mounted extensometer. It should be noted that the foil strain gauges usually de-bonded when the strain reached a value of approximately 75,000 $\mu\varepsilon$, whereas the extensometer was usually left in place on the coupon until failure. Figure 4.2 provides a typical longitudinal stress versus lateral strain curve showing the mean strain measured using the two lateral foil strain gauges mounted on the test specimen. The lateral strain data was used to determine Poisson's ratio for the different material specimens.

From the experimental coupon data material properties were determined as follows. The modulus of elasticity was determined for each coupon by determining the slope from a linear regression of the straight-line portion of the elastic region of the stress-strain plot. The regression analysis routine, found in the commercially available Microsoft Excel

program (Microsoft, 1998), was used to perform this analysis. The yield stress was determined using the static point data. Due to loading rate effects there is a loading rate load component to the recorded stress-strain data, which varies as a function of the loading rate. For consistency, this loading rate effect should not be considered when reporting material properties. Material properties independent of the loading rate effect are known as static point data and correspond to the material properties when the strain rate is zero (Lay, 1982). This is done by temporarily halting a non-zero strain-rate test without reversal of strain and waiting for the load to reach a static value. Typical static points are evident in Figure 4.1 as small cusps in the stress-strain curves.

Interpolating between static points, the yield stress is defined as the stress that corresponds to 0.5% strain. This is in accordance with the method described in the API Specification 5L, Specification for Line Pipe (American Petroleum Institute, 1995). The ultimate stress was determined by calculating the peak static stress.

Poisson's ratio, ν, is defined as the ratio of the lateral strain, ε_{lat}, to the longitudinal strain, ε_{long}. Both ε_{long} and ε_{lat} can be expressed as a function of a given value of longitudinal stress, σ_l,

$$\varepsilon_{long} = \sigma_l / k_{long} \tag{4.1}$$

$$\varepsilon_{lat} = \sigma_l / k_{lat} \tag{4.2}$$

where k_{long} is the slope of the linear elastic region of the longitudinal stress-strain curve or the modulus of elasticity and k_{lat} is the slope of the linear elastic region of the lateral stress-strain curve. Substituting Equations 4.1 and 4.2 into the definition of ν, ν can be calculated as

$$\nu = \frac{\varepsilon_{lat}}{\varepsilon_{long}} = \frac{\sigma_l / k_{lat}}{\sigma_l / k_{long}} = \frac{k_{long}}{k_{lat}} \tag{4.3}$$

All of these experimental material properties were determined using interpolated data from the static points recorded during testing.

A total of five different sets of material coupons were tested, with each being given a different letter for identification. Each letter was selected to correspond to the characteristics of the different test specimens they came from. For example, 'W-type' material properties are typically associated with the girth *(W)*elded test specimens. Of the five sets of material coupons, the materials designated 'N-type', 'W-type', and 'E-type' had their experimental material properties determined as described in Section 2.4.3 and require no further explanation. The conversion of the experimental material properties to the form required by the finite element package will be discussed in Section 4.1.2. Table 4.1 presents the results from the individual coupons for these three material property tests and the mean material properties for each of the three different respective materials. It should be noted that the thickness, t, of the coupon presented in Table 4.1 was used as the thickness of the entire test specimen. As previously discussed in Section 2.4.3, it was decided that the mean longitudinal material properties would be used in all subsequent numerical analysis.

Determination of the two remaining sets of material properties, P1-type and P2-type, requires additional clarification. During the precursory work done on this project, a total of seven test specimens were delivered to the I. F. Morrison Structural Engineering Lab. At that time, only one set of material test specimens was delivered, indicating that the original seven specimens were fabricated from the same joint of pipe. During the preliminary experimental analysis, there appeared to be two different materials used to fabricate the original seven test specimens. Discussions with the specimen supplier confirmed this observation. In an attempt to identify the material properties of the two different joints of pipe, additional longitudinal tension coupons were fabricated and tested from available segments of the original seven test specimens. Table 4.2 presents the results of ten coupons tested from the original seven test specimens. As shown in Table 4.2, the results can be divided into two different groups of properties. While it is

impossible to say with complete certainty which material was used in the respective test specimens, different material properties fit more accurately with respective specimens as evidenced by the test-to-predicted calculations presented in Section 4.5.4 and with the finite element analysis comparisons. It was therefore decided to use the material properties for these specimens that fit most consistently with the results of the analyses.

With the exception of the P1-type and P2-type materials, the remaining three material tests revealed some peculiarities. Of particular interest was the fact that the N-type, W-type and E-type materials all exhibited distinct yield plateaus, as shown in Figure 4.3 for one of the E-type coupons. This is not consistent with the fabrication procedures for DSAW line pipe that have been hydrotested and/or mechanically expanded. The effect of the hydrotesting and/or mechanical expansion should result in material specimens that exhibit no yield plateau, as discussed in Section 2.2.1.

There are three possible explanations for the observed material test results. The first explanation may be that the material tests were carried out incorrectly. However, considering that there is such excellent agreement between coupons of the same material, that different coupons were tested at different times, and that different people were in control of different tests, it seems unlikely that the same errors in testing would have occurred. The second explanation may be that the material was not properly hydrotested nor mechanically expanded when fabricated. There is no way to confirm or refute this explanation. The third explanation may be that the material is exhibiting some degree of strain aging. Dieter (1987) describes strain aging as "the reappearance of the yield point due to the diffusion of carbon and nitrogen atoms to the dislocations during the aging period to form new atmospheres of interstitials, anchoring the dislocations". Once a material has yielded, atomic level dislocations occur. If the material is then unloaded and allowed to remain undisturbed, these atomic level dislocations are filled with carbon and nitrogen atoms, which re-bond to the adjacent atoms. This results in the re-establishment of a yield plateau.

Figure 4.4 gives a graphical representation of this phenomenon. Consider a steel material coupon that is loaded beyond the yield point at (A) to a point on the strain hardening curve at (B). If the load is then relieved, the material unloads parallel to the initial stiffness of the coupon to point (C). If a short period of time elapses and the same material is re-loaded, the load path will initiate at point (C) and remain linear to point (B) at which point it will continue along its original load path toward point (D). Now consider the exact same material, which is loaded to point (D) on the stress-strain curve. If the material is unloaded at point (D) it will unload parallel to the initial stiffness of the coupon to point (E). If the coupon is then allowed to strain-age over a period of time, which may be accelerated by an increase in temperature, then the re-loading response will be different. Upon re-loading, the load path will initiate at point (E) and remain linear to point (D) at which time a new yield point and/or plateau will emerge. The material will then load parallel to the original load path as it approaches point (F). Lay (1982) suggests that the strain aging effect "virtually creates a new material with a significantly different response than the original material."

With respect to the experimental material results obtained in this investigation, it is difficult to ascertain whether or not the observed effects are due to a strain aging effect. This is because there is no well established time period over which strain-aging occurs and there is no record as to the age of the test specimens. As such, while the material properties recorded from the coupon tests are not consistent with typical line pipe material, they were nevertheless used in all subsequent analysis of the test specimens since they are the best representation available for these test specimens.

4.1.2 Determination of FEA Model Material Properties

The engineering stress-strain curve generated directly from the experimental coupon data is not adequate for use as input in ABAQUS. The data needed to be converted to a true stress-strain formulation. In addition, the material property curve for input into ABAQUS needed to be based on the static points recorded during testing. Figure 4.5 shows a typical static curve approximation. There are no known conversion equations available that relate static stress-strain data to data that was recorded under experimental

loading conditions because of the dependence of the experimental response on loading rate, test set-up, and coupon size. As such, approximate static material property curves were generated as follows. The recorded material property curves from the two coupons of each type were plotted graphically. Using the recorded static points as control points on the new curve, a smooth curve coincidental with the recorded data in the linear elastic region and then passing through the static points was generated by approximating the graphical data such that it provided a visual approximation of a 'best-fit' curve.

As can be seen in Figure 4.5, the method used provides a good representation of the static data. DiBattista (2000) has previously used this method with very good correlation between the experimental and analytical results. Use of this method is further supported by the agreement achieved between the experimental and analytical results for this project presented in Section 4.4.

Once the static coupon curve was generated for each set of material properties, a reduced set of data points was selected to adequately define the curve. This was necessary because of the large amount of data used in the generation of the original stress-strain curve. The reduced stress-strain data set was generated by selecting data points from the full stress-strain data set, plotting them, and visually ensuring that all regions of the curve were adequately represented. The data was then converted to the true stress-strain formulation required for input into the FEA model. This conversion was done using equations 3.1 and 3.2 presented in Section 3.3.5. Table 4.3 presents the engineering stress-strain and the corresponding true stress-strain data for a typical coupon. The results for each set of the material specimens are provided in Appendix A.

4.2 Reduction of Experimental Data

Sections 2.3.2, 2.4.1 and 2.4.2 describe the testing procedure and the instrumentation applied to the test specimens in the experimental portion of this testing project. With the exception of the Demec data, the data was collected in electronic form using the Fluke

data acquisition system and stored on computer disk for data reduction at a later time. The experimental instrumentation was selected and positioned to determine a number of experimental parameters that influence the behaviour of line pipe under combined loading. However, the raw experimental data collected during the testing project was not in a form that was readily comparable to data from other sources, namely the results of the FEA model. As such, the data had to be reduced to a comparable form. This section discusses the reduction of the experimental data and the determination of the various experimental parameters.

An experimental data reference volume (Dorey, 1998) was compiled for this project, which contains the analytical spreadsheets used in the reduction of the experimental data for each of the test specimens. Due to the enormous amount of data that was generated for each test specimen, it is impossible to present the analysis of each individual test specimen in this document. As such, the following discussion includes the details of the equations and procedures used to reduce the experimental data from the raw data collected in the laboratory for one representative test specimen. Test specimen CP80N-2 was randomly selected as the representative specimen. The following discussion is supported by numerous reference figures taken from the experimental data reference volume for specimen CP80N-2. Since the remaining test specimens were analyzed using the same procedure, only the final reduced data for the rest of the specimens will be presented.

It should be noted that all the analyses performed on the experimental data was done using the initial set of readings as a reference. As discussed in Chapter 2, once the test specimen was aligned in the test set-up and ready for testing, an initial set of readings for all the electronic and manual data was taken. This initial reading was then subtracted from the recorded data at all subsequent load steps. The resulting data is referred to as the 'zeroed data' throughout the remainder of this document and can be considered the actual value of the recorded variable relative to the initial readings.

4.2.1 Generation of Experimental Global Moment-Curvature Plots

Global behaviour is the most common method used for assessing the overall strength and stability of a segment of line pipe. Global end moments can be considered the total end moment applied to the test specimens, including any deformation of the test set-up without considering the local deformation of the test specimen itself. This is the most common value used for determining moments in a segment of line pipe because it can be determined from simple statics without knowing the magnitude or location of any local deformations. Global curvature can be considered the overall rotation across a segment of line pipe divided by its length, including any localized buckles or wrinkles. This section describes the reduction of the experimental global moment-curvature responses. Appendix B provides the spreadsheet used to reduce the experimental data for the global moment-curvature response for specimen CP80N-2 and will be referenced throughout the following discussion.

4.2.1.1 Global End Moments

For the purpose of this project, the global moment is defined as the average of the end moments applied to the pipe by the end plates in the test set-up during testing. The free body diagram of the upper moment arm presented in Figure 2.2 was used to determine the global end moment for each test specimen. As the eccentric force applied through the jacks increased, the line of action of the different forces acting on the top moment arm assembly changed because the moment arm rotated. By summing the moments about the center of the end of the test specimens in the assumed deformed configuration shown in Figure 2.2, the global end moment at the top of the test specimen, M_{top}, can be calculated as

$$M_{top} = P_{jack}\left(e \cdot \cos\theta_{top} + (d'-d) \cdot \sin\theta_{top}\right) + P_{MTS} \cdot d \cdot \sin\theta_{top} \qquad (4.4)$$

where the variables are defined in Figure 2.2. Referring to the spreadsheet in Appendix B, column M provides the zeroed experimental top rotational meter data using the rotational meters, column S provides the zeroed jack force data, and column U provides the global end moment as calculated using Equation 4.4. A discussion on the

determination of the top rotation and the instrumentation used is presented in Section 4.2.1.2.

Since the end assemblies at the top and bottom of the test set-up shown in Figure 2.2 provide identical out-of-plane moments, the applied global moment at the bottom of the test specimen was determined using the same equation and should be equal to the moment at the top. It should be noted that the experimental data for the top and bottom rotations were not exactly equal. However, the differences between the top and bottom moments (and the top and bottom rotations) were found to be negligible and were attributed to experimental error. It should also be noted that, as described in Section 3.3.3, the loading arms were assumed to be rigid and the deformation of these arms was not considered in subsequent calculations.

4.2.1.2 Global End Curvatures

The global end curvature was defined as the overall rotation between the ends of the test specimen divided by the length of the specimen. In past research, the average global curvature at the end of the test specimens, ϕ_G, has typically been calculated as

$$\phi_G = \frac{|\theta_{top}| + |\theta_{bot}|}{L_{pipe}} \tag{4.5}$$

where θ_{top} is the rotation of the top end plate, θ_{bot} is the rotation of the bottom end plate, and L_{pipe} is the overall length of the test specimens between the two end plates.

However, each test specimen had a collar placed at each end of the pipe, as described in Section 2.4.2. The purpose of these collars was to stiffen the region of the pipe adjacent to the end welds to decrease the probability of producing a wrinkle at the end of the specimen. Considering this, it can be seen that using the full length between the end plates in the denominator of Equation 4.5 underestimates the value of ϕ_G because it overestimates the length of the flexible portion of the specimen. Therefore, using Equation 4.5 results in the test specimen having an apparent stiffness greater than it

actually is because the rotation over the length of the two end collars is significantly reduced due to the increased stiffness provided by the collars over this region. If it is assumed that the collars offer perfect rigidity to that region of the pipe, then it can be argued that Equation 4.5 should be modified to

$$\phi_G = \frac{|\theta_{top}| + |\theta_{bot}|}{(L_{pipe} - 2L_{collar})} \tag{4.6}$$

where L_{collar} is the length of one end collar. Since the collars are not infinitely stiff, using Equation 4.6 provides an overestimate of ϕ_G. In reality, the correct value for ϕ_G lies somewhere between the values determined by Equations 4.5 and 4.6.

Del Col, *et al.* (1998), tested similar specimens to those tested in this project and used equation 4.5 to determine the experimental ϕ_G. Examination of the comparison between experimental and FEA results presented by Del Col showed that in every load case the experimental data had a greater stiffness than the FEA model predicted. This is consistent with his using equation 4.5 to determine ϕ_G.

Preliminary analysis in this project also showed that using equation 4.5 to determine ϕ_G led to a stiffer set of experimental data than FEA model data for every load case examined. However, when the experimental ϕ_G was determined using equation 4.6, the experimental and FEA model global moment-curvature plots were essentially coincidental over the initial linear elastic region, indicating that they had essentially the same initial stiffness. As such, it was decided to use equation 4.6 in the determination of ϕ_G.

The values of θ_{top} and θ_{bot} were evaluated using two different sets of instrumentation. Figure 4.6 presents a graphical comparison of the experimental data using the two different techniques for determining global curvature. The first set of instrumentation was the rotational meters mounted on the side of the top and bottom end plates. These

rotational meters recorded the rotation of the end plates in degrees. Referring to the spreadsheet in Appendix B, column I provides the zeroed data for the rotational meter mounted on the bottom end plate and column L provides the zeroed data for the rotational meter mounted on the top end plate. These values were converted to radians for plotting the moment-curvature response. The radian measures are provided in columns J and M.

The second set of instrumentation consisted of the six cable transducers mounted on the bottom end plate, as described in Section 2.3.2. Knowing the original position and the displacements recorded by the six transducers at each load increment, the total rotation between the two end plates was determined relative to the strongfloor of the laboratory. Referring to the spreadsheet in Appendix B, columns B through G provide the zeroed data for the six cable transducers, which are identified by their position in the test set-up. For example, the data in column B is for cable transducer NWB. The 'NWB' identifies this cable transducer as being located at the ***(N)***orth***(W)***est corner of the ***(B)***ottom end plate. Columns H and K provide the rotation of the bottom and top end plates, respectively, based on the displacements measured by the cable transducers.

Once the rotations of the two end plates were known, they were converted to curvatures using Equation 4.6. Columns Q and R of Appendix B provide the total curvature of the test specimen using the cable transducer and the rotational meter data, respectively. The data in columns Q, R and U were used to generate the global moment-curvature plot presented in Figure 4.6.

Examination of Figure 4.6 shows reasonably good agreement between the two methods. However, it is also observed that the data plotted from the reduction of the cable transducer appears to lack the linearity of the data reduced from the rotational meters. The reason for this difference is two-fold. Since the cable transducer data was reduced from a series of six different instruments, there exists the probability of cumulative systematic errors. In addition, the calibration of the cable transducers was checked after the completion of the testing program. Instrument errors in the LVDT's were discovered at that time. The calibration curves were no longer linear for two of the transducers. The

calibration of the rotational meters was also checked and revealed no loss of linearity post-testing. It was therefore decided that the reduced data from the cable transducers would be used merely to check the rotational meter data and that the curvature data reduced from the rotational meters would be used in all subsequent calculations and analysis.

4.2.2 Generation of Experimental Local Moment-Curvature Plots

While global behaviour is the more common and convenient method for presenting load-deformation (P-Δ) characteristics of line pipe, local behaviour triggers the initiation of the pipe failure. Local behaviour can be classified as the response of a test specimen over a very localized region or length and is usually characterized by local deformations, which are often manifested as significant disturbances in the geometry. This results in a local geometry that is significantly different in the deformed state from that in the original state. These significant deformations result in changes in geometric properties and, correspondingly, in changes in resultant stresses. For the specimens tested in this project, once peak moments were achieved, the specimens buckled in a localized region, resulting in a loss of load carrying capacity.

As would be expected, the local moment-curvature response of the test was essentially identical to the global moment-curvature response prior to buckling. This is because the second order P-Δ effect due to localized deformations is minimal and the curvatures are more or less uniformly distributed along the length of the specimen. However, in the post-buckling region, the local moment-curvature response differs greatly from the global moment-curvature response. This section describes the details for the determination of the local moments and local curvatures.

4.2.2.1 Local Moments

Figure 4.7 presents a free body diagram of the top segment of a typical specimen with its bottom at a distance of z_t below the pivot point prior to buckling. Summing the moments about the centroid of the cross section at the bottom of this free body diagram in Figure 4.7, the local moment, M_z, may be calculated as

$$M_z = P_{jack}(e \cdot \cos\theta_{top} + d' \cdot \sin\theta_{top} - \delta_h) + P_{MTS} \cdot \delta_h \qquad (4.7)$$

where the variables are defined in Figure 4.7.

Figure 4.7 is based on the cross section of the test specimen prior to buckling. Since post-buckling information is one of the objectives of this project, local moments and curvatures had to be determined on a deformed cross section. Figure 4.8 shows a typical cross section with a bulge buckle located a distance of z_t below the pivot point on the compression face of the cross section.

As described in Section 2.3.2, a series of LVDT's were placed along both the compression and tension faces of the specimens during testing. These LVDT's measured the horizontal displacement of the test specimen, δ_{LVDT}, at each load step and were able to capture the deflected profile of any given test specimen. Figure 4.9 provides the deflected profile along a typical compression face where each curve in the figure corresponds to a different increment of loading. This figure shows that a local disturbance in the wall of the pipe occurred at a distance of approximately 1610 mm above the bottom of the test specimen. This is shown in Figure 4.9 by the reduced compression face deflection at that distance from the bottom of the pipe. The measured location of the peak of the buckle in specimen CP80N-2 was 1625 mm above the bottom of the specimen. This shows that the compression face LVDT's provided a good indication as to the location of the buckle. However, the values of δ_{LVDT} in the buckled region are no longer indicative of the lateral displacement of the cross section because of the distortion created by the buckle. The distortion results in an underestimate of the local moment in that region because of the apparent reduction of δ_h due to the buckle as shown in Figure 4.9. Therefore, the lateral deflection of the cross section had to be estimated in the buckled region.

Classical beam theory arises from the Bernoulli assumptions, which require, among other things, that the beam cross-section does not warp nor distort in its own plane, that is,

plane sections remain plane. However, at a wrinkle location the deformations violate both of these conditions. Consequently, the centroidal axis of the deformed cross-section no longer has the properties that would uncouple the axial and flexural effects throughout the length of the wrinkle. Furthermore, significant plastic strains occur in a mature wrinkle, which further disrupt the simple elastic theories related to the geometric centroid. The wrinkle is also limited in length, and usually has a length less than or equal to one-third the diameter of the specimen. Therefore, the geometric centroid shifts from the centroid of the circular cross-section to that at the crest of the wrinkle and then back again over the length of the wrinkle. It is unreasonable to expect a transverse movement of the resultant force on the cross-section consistent with this variation.

Because of the these complexities, the second order moment produced by the P-Δ effect, which gives rise to the last term in Equation 4.7 ($P_{MTS} \bullet \delta_h$), are computed in a different fashion across the wrinkle than in other regions of the pipe. It was assumed that the resultant force follows a smooth curve formed in the longitudinal direction by interpolating between the centroidal axis positions of the original circular cross sections above and below the wrinkle and the second order moment is computed with respect to this axis.

The procedure to determine the second order moment at the wrinkle location was done as follows. Ignoring the values of δ_{LVDT} in the immediate vicinity of the buckle and fitting a smooth equation through the remaining data points, a deflected profile along the compression face of the specimen could be determined assuming no buckle existed. Figure 4.10 presents the assumed deflected profile of an unbuckled test specimen along with the accompanying equation for the load step recorded in scan #38. It should be noted that for the convenience of the equation fitting, the axes for this plot were reversed from those shown in Figure 4.9. This procedure was repeated for each load step where local strain Demec data were collected and a new equation generated at each load step. This was required because of the continually varying cross section in the post-buckled configuration.

The experimentally recorded value of δ_{LVDT} was then replaced by the assumed value of the deflection, $\delta_{assumed}$, in the buckled region. This procedure for determining $\delta_{assumed}$ was repeated at each increment of load that local data was recorded. The calculated values of $\delta_{assumed}$ was then used as δ_h in Equation 4.7 across the buckled region in the determination the local moment, M_z, for the buckled configuration shown in Figure 4.8.

Appendix C provides an example of the spreadsheet used to determine the local moments for one increment of loading, scan #38 in specimen CP80N-2. This increment of load was recorded after the buckle had formed in the specimen. The procedure outlining how the local curvature was determined along the length of the pipe, ϕ_L, is presented in the following section. Row 5 of the spreadsheet in Appendix C provides the values of P_{jack}, P_{MTS}, and θ_{top} for the specific increment of loading. Row 8 provides the different elevations, z_t, measured from the top end plate where the local moments were determined. These values of z_t coincide with the midspan of each set of Demec gauge points, identified in row 7 of columns C through K, that were used to measure local strains. Row 12 provides the values of δ_{LVDT}. As previously discussed, δ_{LVDT} was used as the value of δ_h in Equation 4.7 prior to buckling. Once the specimen buckled, the LVDT measurements were still used as the value of δ_h in the regions not disturbed by the buckle.

Examination of the spreadsheet in Appendix C shows that since scan #38 was taken post buckling, the values of δ_h in row 14 are a combination of δ_{LVDT} from row 12 and the values of $\delta_{assumed}$ given in row 13. It should be noted that the buckle in this specimen was approximately centered on Demec position D4 and appeared to influence Demec positions D3 and D5 as well. Because of the influence of the buckle, the values of $\delta_{assumed}$ were used as the δ_h values for Demec positions D3, D4, and D5, as shown by the non-zero values of $\delta_{assumed}$ in row 13. Row 15 provides the value of the local moment determined using Equation 4.7 for the different values of z_t for scan #38 of specimen CP80N-2.

4.2.2.2 Local Curvatures

Local curvatures were measured using a manually operated Demec gauge and then a pair of dividers and a measuring tape once the magnitude of the deformation exceeded the range of the Demec gauge. The Demec and measuring tape data was manually entered into a spreadsheet and converted to units of strain. For the data collected in the pre-buckling region, the Demec data were compared with the data recorded electronically from the foil strain gauges. This was done to ensure that no errors were made in the calibration of the Demec data or in the recorded initial Demec readings. Figure 4.11 provides a comparison of the electronic foil gauge strain data with that recorded using the manual Demec gauge.

Once the local strains were determined they were converted to local curvatures. Local curvatures were calculated based on three different gauge lengths: the diameter of the pipe divided by 3 (D/3), the diameter of the pipe (D), and the entire length of the pipe (L). The D/3 gauge length was selected because that was the gauge length of the Demec gauge. The D gauge length was selected because of the industry practice of using diameter as a universally accepted pipe characteristic. The L gauge length was selected so that the local curvature data could be compared with the global curvature data. This comparison has been shown to give a reliable method for determining the magnitude of the critical strain (Yoosef-Ghodsi, *et al.*, 1994).

As shown in Figure 4.12, the local curvature, ϕ_L, which is the angle change per unit length along the middle axis of the cross section, may be calculated as

$$\phi_L = \frac{|\varepsilon_C| + |\varepsilon_T|}{D} \tag{4.8}$$

where ε_C is the strain on the compression face over the specified gauge length and ε_T is the strain on the tension face over the specified gauge length. It is acknowledged that this is an approximation, but considering that the discrete gauge lengths used are small and that the recorded curvatures are also relatively small, the common small deformation

assumption of $\sin\theta \approx \tan\theta \approx \theta$ should be valid and is expected to have negligible effect on the results.

A plot of the variation in local curvature along the length of a test specimen under increasing levels of applied moment would be expected to show that the local curvature in the region immediate adjacent to the location of the buckle was substantially larger than the local curvatures away from this region. Figure 4.13 provides a local curvature versus length plot for a typical test specimen showing the distribution of local curvature along the length of the specimen at all of the increments of loading recorded using the Demec gauge. Figure 4.14 shows an enlargement of the local curvatures prior to buckling, as indicated by the scale on the vertical axis. From the recorded experimental data, it was determined that this particular test specimen reached its peak moment capacity at load scan number 34. This agrees very well with the initiation of a buckle at load scan number 32, shown in Figure 4.14.

Figure 4.15 shows a typical set of three local moment-curvature plots, each plotted over a different gauge length, for which the local moments are computed, as described in Section 4.2.2.1. For the gauge length of D/3, the values of ε_C and ε_T were taken directly from the Demec gauge strain measurements. For the gauge length of D, the values of ε_C and ε_T were taken as the average of the three Demec strains centered on the buckle. For the gauge length of L, the values of ε_C and ε_T were taken as the average of all the Demec strains, which were at the same elevation on both the tension and compression faces, along the entire length of the pipe. The global moment-curvature plot was included in this figure for comparison purposes.

From Figure 4.15 it can be seen that the initial portion of all four curves (up to a moment of approximately 1400 kN-m) are essentially co-linear, indicating that the pre-buckling behaviour is independent of gauge length over which the local curvature is measured. It can also be seen that with increasing gauge length the local moment-curvature plots more closely resemble the global moment-curvature plot.

As discussed in Chapter 1, one of the main purposes of this investigation was to determine a critical strain limit state criterion. The influence of the gauge length on post-buckling behaviour was found not to have a significant affect on this point of initiation. Therefore, it was decided to use the gauge length of D to accentuate the change in slope between the pre- and post- buckling regions as much as possible while providing a relative gauge length that can be compared for different sizes of line pipe. This will be discussed further in the following section.

Finally, it may be observed in Figure 4.15 that the local moment-curvature plot using the gauge length of L is not coincidental with the global moment curvature plot. The reason for this it that the Demec points on the wall of the pipe specimen did not extend fully to the end plates where the rotational meters used to determine the global curvatures were placed. The first and last Demec points on the test specimens were located approximately 50 mm above and below the end collars, respectively. This difference in distance, coupled with the additional stiffness across the collared regions, results in the global moment-curvature plot appearing stiffer than the local moment-curvature plot across the entire length of the test specimen, as observed in Figure 4.15.

4.2.3 Determination of Experimental Critical Buckling Strains

Once the local curvatures were calculated the critical buckling strain was determined. As has been reported in previous investigations (Yoosef-Ghodsi, *et al.*, 1994), a global versus local curvature plot shows an essentially bilinear shape. A typical plot is presented in Figure 4.16. As can be seen in the figure, there are essentially two linear relationships between local and global strains, one in each the pre-buckling and post-buckling regions. The point where the slope changes is the point at which the strains began to localize, which indicates that the specimen has buckled and a wrinkle is beginning to form. The local strain at the intersection point corresponds to the incipient critical buckling strain, hereafter referred to as the critical strain.

It should be noted that had a different gauge length been used for the local curvatures, the only difference in the plot would have been a different slope over the post-buckling

region. Further examination of Figure 4.16 shows that the pre-buckling region of the curve does not have a slope of unity, as would have been expected. While the slope is close to unity, it should be recognized that the global curvature was measured at the end plates in the test set-up and included the effects of a stiffened region near the ends of the pipes in the test set-up. The local curvature measurements did not account for the effects of the stiffened region, resulting in the observed non-unity slope. As a result, the "local strain value" at the point of intersection is more representative of the true critical strain and is used, herein, to define the experimental critical strain value.

To determine the value of the critical strain two linear regression analyses were performed, one using the data in the pre-buckling region (the first straight-line segment of Figure 4.16) and the second using the data in the post-buckling region (the second straight-line segment of Figure 4.16). Once the results of the two regression analyses were obtained, the critical strain was determined by equating the two equations and solving for the local strain at the point of intersection.

Appendix D provides a typical analysis of the critical buckling strain. The local and global moments, curvatures, and strains were calculated as described in the previous two sections of this report. The pre-buckling and post-buckling regression equations were determined using the regression analysis routine included in the spreadsheet data analysis package. Equating the two regression equations, the value of the local strain at the point of intersection was determined, as shown in Appendix D.

It should be noted that the above procedure describes the process for determining the total critical strain on the compression face of the test specimen because the recorded strains were based on the total strain measured during the experimental program. Since each test specimen was subjected to a constant axial force in addition to the global end moments, this total strain formulation was comprised of an axial strain component, ε_a^C, in addition to a bending strain component, ε_b^C. Mathematically, the total critical strain on the compression face of the test specimens, ε_{cr}^C, can be expressed as

$$\varepsilon_{cr}^{C} = \varepsilon_{b}^{C} + \varepsilon_{a}^{C} \tag{4.9}$$

The axial strain component of the total strain, ε_a^C, was determined as

$$\varepsilon_{a}^{C} = \frac{P_N}{AE} \tag{4.10}$$

where P_N is the net axial force, A is the cross sectional area, and E is the modulus of elasticity for each of the respective test specimens. Once ε_{cr}^C and ε_a^C were determined using the regression technique described above and Equation 4.10 respectively, ε_b^C was determined from Equation 4.9.

To be consistent with the sign convention used in the other design criteria investigated in this document, the critical strain values reported herein are considered to be positive in compression.

4.3 Reduction of FEA Generated Data

As with the experimental data, the data generated using ABAQUS was not in a form suitable for comparison with other data and required some data reduction. A post-processor data extraction routine was written for each of the test specimens to extract the global moment applied at the pivot point of the model specimen, the global rotation at the pivot point and the local nodal displacements over the entire loading history. This section describes the reduction of the extracted FEA data.

4.3.1 Generation of FEA Global Moment-Curvature Plots

Once the FEA model and the extraction routine had been run for each of the test specimens the data was reduced and the global end moments and the global curvatures

were determined. The output from ABAQUS gave the moment applied at the two pivot points in the model in units of N-mm and the rotation in units of radians. The total curvature for the FEA model was determined using Equation 4.6. Figure 4.17 shows the global moment-curvature plot a typical FEA model. The experimental global moment-curvature plot is included in this figure for reference purposes only. Comparison of the global moment-curvature FEA model results with the experimental results will be discussed in detail in Section 4.4.1.

4.3.2 Determination of FEA Critical Buckling Strains

The determination of the FEA critical buckling strains was approached in a somewhat similar manner to the determination of the experimental strain measurements using the caliper and measuring tape. One of the post-processing features that made ABAQUS attractive for this project was that the nodal co-ordinates at the end of each load step could be written to the output file. If the nodal co-ordinates are known at the initial step and at any intermediary step then the strain at that intermediary step could be readily determined.

The initial nodal co-ordinates, which are the co-ordinates generated during the imperfection mapping described in Section 3.3.7, were written to the output file during the FEA of each specimen. By determining the position of the individual Demec points in terms of the corresponding node on the imperfection mesh, a direct measure of the strain could be evaluated. It should be noted that the Demec points on the test specimens were offset from nodal positions on the imperfection mesh by a distance of 2.0 mm over a Demec gauge length of 254.0 mm. This error was considered to be negligible.

The reduction of the nodal co-ordinate data to strain data was completed as follows. First, the length between the FEA mesh points that corresponded to the experimental Demec points was determined. The Demec gauge measures the straight-line distance between two Demec points. Using the co-ordinates, the initial (subscript 'ini') straight-line distance, L_{ini}, between the two FEA mesh points could be determined as

$$L_{ini} = \sqrt{(x_{1ini} - x_{2ini})^2 + (y_{1ini} - y_{2ini})^2 + (z_{1ini} - z_{2ini})^2} \quad (4.11)$$

where x_{1ini}, y_{1ini}, and z_{1ini} refer to the initial co-ordinates of the mesh node at one end of the Demec span and x_{2ini}, y_{2ini}, and z_{2ini} refer to the initial co-ordinates at the other end.

The straight-line distance between the Demec mesh nodes at the current (subscript 'cur') increment of loading, L_{cur}, may also be determined using Equation 4.11. The current co-ordinates of the mesh nodes, x_{1cur}, y_{1cur}, z_{1cur}, x_{2cur}, y_{2cur}, and z_{2cur}, at the two respective ends of the Demec span for the given load level are substituted into the equation in place of the initial co-ordinates.

Once the two straight-line distances are known, the corresponding current strain,ε_c, at any load level may be determined as

$$\varepsilon_{cur} = \frac{L_{cur} - L_{ini}}{L_{ini}} \quad (4.12)$$

Using this procedure, the strains along both the tension and the compression face of an FEA model specimen were determined. Once the strains were known from the displaced positions of the mesh Demec nodes, the local curvatures were calculated using equation 4.8, as was done for the experimental data. A global curvature versus local strain plot was then created and the procedure for determining the experimental critical strain described in Section 4.2.3 was used to determine the FEA model critical strain for each test specimen. It should be noted that since the objective is to determine local strain criteria, it was decided that it would be more useful to generate a global curvature versus local strain plot instead of global versus local curvature. This was decided because global curvature is linearly proportional to global strain and using global curvature in place of global strain reduced the post processing calculations with no numerical effect on the value of critical strain.

Figure 4.18 gives a typical global curvature versus local strain plot generated from the FEA displaced nodal positions. The experimental global versus local curvature plot is

included in this figure for reference purposes only. Comparison of the critical strains from the FEA model with the experimental results will discussed in detail in Section 4.5.2.

4.4 Classification of Buckling Modes

The emergence of a buckle on the compression face of both the experimental specimens and the FEA model did not occur until after the peak moment capacity had been reached. With increasing applied load these buckles grew in amplitude, either outward or inward, until the termination of the test. No test, either experimental or analytical, was allowed to progress to the point where the pipe walls on either side of the buckle made contact. A series of photographs and corresponding FEA model meshes of the progressive growth of the buckle on the compression face of specimen CP40W are shown in Figure 4.19. Each set of figures corresponding to a different increment of loading in Figure 4.19 are referenced to the corresponding global moment-curvature plot shown in Figure 4.20. It should be noted that test specimen CP80N-2 was not used in this comparison because a series of photographs showing the progressive growth of the buckle was not available for that specimen. The specimen used to show the buckle progression in Figures 4.19 and 4.20 was test specimen CP40W.

Examination of Figures 4.19 and 4.20 indicate no evidence of buckling until the peak moment was approached. By the time the peak moment was reached, the buckle had initiated. Once the peak curvature had been exceeded, the buckle continued to grow in amplitude as the moment-curvature relationship softened.

During the experimental phase of this project, two different types of buckling modes were observed. These were a "bulge" buckle and a "diamond-shape" buckle. The magnitude of the internal pressure appears to be the most significant factor in determining which of these two buckling modes would develop. The diamond-shape buckle was exclusive to the non-pressurized specimens, with the exception of one FEA

model result of a test specimen at a very low level of internal pressure. Figure 4.21 shows a typical diamond-shape buckle on an unpressurized girth-welded test specimen.

In all of the specimens tested with internal pressure, the observed failure was a bulge-type buckle. The local outward bulges in the pipeline that characterize bulge buckles were classified into two categories. The first is the 'mid-height' bulge, which occurs somewhere within the middle third of the height of the test specimen, away from any end effects. Figure 4.22 shows a mid-height bulge buckle in specimen CP40W. The second category of bugle buckles was the end bulge buckle, which occurred immediately above/below the collar at the end of the test specimen. End buckles are commonly referred to as "elephant's foot" buckles because of their location and appearance. It is recognized that a true 'elephant's foot' buckle extends to the end of the specimen, however, because of the confinement provided by the end collars used in this project, the 'elephant's foot' buckles terminated at the edge of the collar. Nevertheless, the buckles that occurred at the edge of the collars will hereafter be referred to as 'elephant's foot' buckles.

Figure 4.23 shows an "elephant's foot" buckle in specimen CP20N-1. It should be noted that because of the presence of the end collars the elephant's foot buckle does not occur at the very end of the specimen, as would be seen in the normal instance of an elephant's foot buckle. In essence, the collar acted to shift the elephant's foot away from the end plate such that it occurred at the edge of the collar instead.

The presence of a circumferential girth weld also affected the location of the local buckle in the test specimens. Experimental results showed that whenever a circumferential girth weld was present, buckling occurred in the immediate vicinity of that weld. This is consistent with previous experimental and FEA model results from U of A, however, a unique phenomenon occurred during the testing of the welded specimens in this project. Previous investigations conducted at U of A were done on specimens with a lower D/t ratio, typically either 50, 60 or 63. For the D/t equal to 53 or 60 specimens, it was observed that the buckle usually occurred either immediately above or immediately

below the girth weld (Yoosef-Ghodsi, *et al.*, 1994). Figure 4.24 shows a photograph of a pressurized test specimen with a D/t ratio of 60 tested by Myrholm, *et al.* (2001). As can be seen in this figure, the buckle is located approximately half of a diameter below the girth weld.

In this investigation, the specimens had a D/t ratio of approximately 92. In all but one of the tests conducted on the welded specimens the buckles, regardless of the shape, intercepted the girth weld. Figure 4.21 showed a photograph of a D/t = 92 unpressurized test specimen and Figure 4.22 showed a photograph of a D/t = 92 pressurized test specimen. As can be seen in these figures, the weld is incorporated through the diamond-shape buckle and the bulge buckle, respectively. This phenomenon of the weld intercepting the buckle will be discussed further in Chapter 5.

4.5 Comparison of Experimental Test Results and FEA Model Results

After completion of the data reduction, the experimental data was used to validate the FEA model. This section presents a comparison of the experimental and FEA model data for each of the test specimens investigated in this project. Three different comparisons are made between the two data sources. Specifically, the global moment-global curvature responses, the buckling modes, and the global curvature versus local strain responses are all compared, both graphically and numerically, in order to assess the accuracy of the FEA model. It should be noted that the figures in this section are not referred to in numerical order. This is because it was decided to keep all of the figures related to one particular test specimen grouped together so that their inter-dependence could be more readily observed without flipping through a large number of pages.

4.5.1 Comparison of Experimental and FEA Model Global Moment-Curvature Plots

Figures 4.25, 4.29, 4.33, 4.37, 4.41, 4.49, 4.53, 4.57, 4.61, and 4.65 present a comparison of the experimental and FEA model global moment-curvature plots for specimens CP20N-2, CP40N-2, CP80N-2, T20P40N, T20P80N, CP20W, CP40W, CP80W,

T20P40W, and T20P80W, respectively. Figure 4.45 presents a comparison of the FEA model global moment-curvature plot with the results from the two experimental CP0W load case specimens, CP0W-1 and CP0W-2.

As can be seen from each of these figures, the FEA Model did an exceptional job of predicting the experimental behaviour for almost all of the test specimens. However, a few peculiarities were observed. Figure 4.37 presents the global moment-curvature plot for test specimen T20P40N. This figure shows three different curves. Examination of the recorded experimental data (represented by the solid black diamond shapes) shows that there was a slip or offset in the rotational meters at the first increment of applied experimental load. This slip caused an initial upward offset of the experimental curve, resulting in the experimental and FEA Model data not being coincidental over the initial linear elastic region. To account for this slip, a numerical correction was applied to the experimental data to shift it along the horizontal global curvature axis so that the experimental data and the FEA Model results started off coincidental as all of the other test specimens did. Once this correction factor was applied, the corrected experimental data was also plotted on the curve in Figure 4.37 using an 'x' to represent the experimental data points. As can be seen in Figure 4.37, the corrected experimental data and the FEA Model show similar agreement as is seen in the remaining test specimens. It was therefore decided to use the corrected experimental data for all subsequent analysis.

Figure 4.45 presents the global moment-curvature plot for the test specimen CP0W-1 and CP0W-2. The CP0W load case was actually tested twice. The first time the load was applied to a test specimen, CP0W-1, data near the peak moment capacity was not properly recorded. This is shown in Figure 4.45 by the solid black triangles. As can be seen in the figure, there is no data collected immediately around the peak moment capacity of the test. This led to another test specimen being subjected to the CP0W load case. The experimental data from the second CP0W load case (CP0W-2) is shown in the figure using solid black diamond shapes. During the second test, the specimen buckled very abruptly and the stability of the test could not be re-established until substantial end rotations had occurred. This is evident in Figure 4.45 by the lack of data immediately

after the peak moment was reached. It should be noted that despite the problems encountered during both CP0W tests, the two experimental moment-curvature responses are coincidental in the regions where data was collected during both tests. This shows that the test results from a given load case are reproducible between different test specimens.

A second observation in Figure 4.45 is that the FEA Model and the experimental test results do not have the exceptional agreement observed in other test specimens in the post buckling region. This phenomenon was observed in all of the unpressurized specimens tested in this project, as well as those tested in other programs at the University of Alberta (Del Col, *et al.,* 1998, Mohareb, *et al.,* 1994, and Yoosef-Ghodsi, *et al.,* 1994). It is uncertain as to why this discrepancy only occurs in the unpressurized specimens, but it may be related to the numerical solution capabilities of the FEA package used. However, this was not investigated further at this time due to the excellent agreement between the experimental and FEA results for peak moment and critical buckling strain, which were the primary focus of this project.

Figure 4.57 shows the experimental versus FEA model moment-curvature plot for test specimen CP80W. Examination of this figure shows that the predicted moment capacity from the FEA model is substantially lower than that obtained during the experimental project and shows the greatest discrepancy in the peak moment capacities for the eleven specimens presented in Table 4.4. There is no conclusive explanation for this. During the development of the FEA model, it was found that failure of a model to achieve the experimental moment was usually the result of using incorrect material properties as input in the FEA model. As an aside, it should be noted that it was observed that failure of the model to achieve the experimental curvature was usually the result of using an incorrect initial imperfection pattern. This will be discussed in detail in Chapter 5. Given the confusion over which material property coupon was representative of which individual specimen, it is possible that the incorrect material properties were used as input into the FEA model for specimen CP80W. However, it was impossible to state with certainty that this was the case, therefore, it was decided to use the one that was

recorded at the time of coupon testing, despite the lack of agreement between the FEA model results and the experimental results.

Table 4.4 provides a numerical comparison of the experimental peak moment and the peak moment determined from the FEA model. The mean test-to-predicted ratio for the peak moments was found to be 1.035 with a coefficient of variation of 0.047 and a range of 0.970 to 1.161. If the moment result from specimen CP80W (t/p ratio = 1.161), which was considered suspect, is eliminated from the statistical analysis, the mean test-to-predicted ratio becomes 1.022 with a coefficient of variation of 0.026 and a range of 0.970 to 1.060.

4.5.2 Comparison of Experimental and FEA Model Critical Strains

Figures 4.26, 4.30, 4.34, 4.38, 4.42, 4.46, 4.50, 4.54, 4.58, 4.62, and 4.66 present a comparison of the experimental and FEA model global curvature versus local strain plots for specimens CP20N-2, CP40N-2, CP80N-2, T20P40N, T20P80N, CP0W-2, CP20W, CP40W, CP80W, T20P40W, and T20P80W, respectively.

As can be seen from each of these figures, the FEA model did an exceptional job of predicting the experimental behaviour for most of the test specimens. All of the graphs exhibited essentially a bi-linear response that has previously been discussed in Sections 4.2.3 and 4.3.2. However, a few peculiarities were observed. In general, the first few FEA model data points were not coincidental with the experimental data. This is attributed to the limitations on the FEA model output. The FEA model output reported nodal displacement distances in units of millimeters to the nearest one hundredth of a millimeter. Given that the gauge length used was approximately 250 mm, the accuracy of strains determined from the FEA output was limited to $\pm$ 40 $\mu\varepsilon$. Since the magnitude of the strains at the first few FEA model data points were typically between 0 and 250 $\mu\varepsilon$, this error was considered significant and could easily result in the discrepancies observed.

Figure 4.42 is the plot of global curvature versus local strain for test specimen T20P80N. Examination of this figure shows that there is limited experimental data in the pre-

buckling region and no experimental data in the post-buckling region due to a malfunction of the Demec gauge. Nevertheless, global experimental data for the test specimen agreed very well with the global FEA model data and it was therefore assumed that the local behaviour would show similar agreement. This is further supported by the agreement between the experimental data and the FEA model data over the range for which the Demec gauge was working, as shown in Figure 4.42.

Figure 4.66 presents the experimental and FEA model data for the global curvature versus local strain for specimen T20P80W. The experimental data in the post-buckling range is somewhat limited because shortly after buckling a component of the test set-up failed and the test was terminated prematurely. However, examination of both Figures 4.65 and 4.66 show that the experimental data collected is in excellent agreement with the data generated from the FEA model.

Table 4.5 provides a numerical comparison of the experimental critical strain and critical strain determined from the FEA model. The mean test-to-predicted ratio for these critical strains was found to be 0.967 with a coefficient of variation of 0.066 and a range of 0.819 to 1.028. As mentioned earlier, test specimen T20P80W failed prematurely. Examination of the test-to-predicted ratio shows poor agreement between the experimental and FEA model critical strains for this specimen. This was because insufficient data was available post-buckling to accurately determine the critical strain because the test set-up failed shortly after the specimen buckled and the test was terminated. At the time of testing it was believed that sufficient post buckling data had been collected. Examination of Figure 4.66 shows that there is insufficient data in the post-buckling region on which to perform the linear regression. Therefore, it is concluded that the experimental critical strain for specimen T20P80W can not be properly determined and should not be included in any subsequent analysis. If the critical strain data for specimen T20P80W is eliminated from the database in Table 4.5, the mean test-to-predicted ratio becomes 0.984 with a coefficient of variation of 0.040 and a range of 0.910 to 1.028.

4.5.3 Comparison of Experimental and FEA Model Buckling Modes

Figures 4.27, 4.31, 4.35, 4.39, 4.43, 4.47, 4.51, 4.55, 4.59, 4.63, and 4.67 present a front view and a profile view of the buckled region for the experimental test specimens CP20N-2, CP40N-2, CP80N-2, T20P40N, T20P80N, CP0W-2, CP20W, CP40W, CP80W, T20P40W, and T20P80W, respectively.

Figures 4.28, 4.32, 4.36, 4.40, 4.44, 4.48, 4.52, 4.56, 4.60, 4.64, and 4.68 present a front view and a profile of the FEA model generated buckles for specimens CP20N-2, CP40N-2, CP80N-2, T20P40N, T20P80N, CP0W-2, CP20W, CP40W, CP80W, T20P40W, and T20P80W, respectively.

As can be seen from these figures, the FEA model does a very good job of predicting the buckling mode for each of the test specimens with the exception of the specimens with an internal pressure producing a stress of 20% SMYS in the hoop direction. Comparison of Figure 4.27 with Figure 4.28 shows that the buckle on the experimental test specimen subjected to load case CP20N-2 is clearly a bulge type buckle, whereas the buckle generated by the FEA model is a combination of the bulge buckle and the diamond buckle. A similar comparison of Figure 4.51 with Figure 4.52 shows the same observation for specimen CP20W. It is unclear as to why this combination of buckling modes occurs in the FEA model specimens with an internal pressure causing a stress of 20% SMYS in the hoop direction.

DiBattista *et al.* (2000) conducted studies on segments of line pipe in bearing on sleeper supports. In that program, it was shown that there was a change in buckling mode from one with an inward folding component, which is analogous to the diamond buckle observed in this project, to one with no inward component, which is analogous to the bulge buckle, occurred at an approximate internal pressure of 20% SMYS in the hoop direction. It should be emphasized that the loading conditions and structural response of the line pipe segment in the DiBattista study were substantially different than this project. However, the effect of the internal pressure on the buckling mode appear to be somewhat similar. From the results of the DiBattista study and this project it could be inferred that

internal pressures that cause stresses less than 20% SMYS in the hoop direction are not large enough to stabilize the pipe wall against an inward buckling component, whereas internal pressures that cause stresses greater than 20% SMYS in the hoop direction create a large enough force on the inside wall surface to prevent an inward component to the buckle.

It should be further noted that the diamond buckle did not fully develop until well into the post-buckling region for the CP20 load cases. Initially, the FEA model appeared to be developing a typical bulge buckle, as shown in the FEA model for CP20N-2 (Figure 4.28). The diamond buckle did not begin to be observed until the amplitude of the buckle was quite large, as shown in the FEA model figures for CP20W (Figure 4.52).

Since the loading of neither CP20 load case test specimens extended as far as the FEA model loading, it is possible that the observed experimental bulge buckle might have eventually evolved into the diamond shape had substantially greater rotations been applied prior to the termination of the testing. Souza, *et al.* (1996) has also documented this type of shift in buckling mode for unpressurized pipe. In his analysis, Souza showed that the diamond pattern wrinkle appeared very late in the wrinkle development. Therefore, it may be that the diamond pattern would have emerged in the experimental tests on the CP20 load cases if the test had continued further than they did and the wrinkle had been subjected to a greater change in angle.

The final observation from the comparison of the buckling modes was that the buckle generated by the FEA model did not always occur at the same location as the buckle in the experimental test specimen. Examination of the experimental local curvature along the length of the test specimen, as previously shown in Figure 4.14, shows that as the peak moment was approached (scan 32 in Figure 4.14) there were actually buckles initiating at a variety of locations. Figure 4.14 shows that there was a buckle developing at the bottom of the pipe as well as one approximately 1600 mm above the bottom of the pipe. This phenomenon of multiple buckle initiation points was typical for all of the experimental test specimens, but was particularly prominent in the specimens with large

internal pressure ratios, namely the CP80 and T20P80 load cases. This suggests that wrinkles may have formed in these specimens in any one of a number of locations. Any one of these buckles may have triggered the wrinkle to occur at that location. It is unclear, and unimportant, as to why one location may have been favored over another.

4.5.4 Further Validation of the FEA Model Using Additional U of A D/t=92 Specimens

As previously discussed, the specimens tested by Del Col *et al.* (1998) were considered precursory work to the investigation conducted in this program. The FEA model developed in this phase of the program had a number of enhancements over the model developed and used by Del Col. The experimental test specimens considered in the precursory research were considered part of the specimen group considered in this study. As such, the experimental data collected by Del Col was used to further validate the new FEA model and the experimental data is included in subsequent analytical comparisons.

This section outlines the comparison of the Del Col experimental data with the FEA results from the model developed in this project. The comparison of the different buckling mode shapes will not be presented pictorially for these specimens; however, a verbal description of the buckling shapes will be included.

4.5.4.1 Comparison of Experimental and FEA Model Global Moment-Curvature Plots

Figures 4.69, 4.71, 4.73, and 4.75 present a comparison of the experimental and FEA model global moment-curvature plots for the four specimens CP0N, CP20N-1, CP40N-1, and CP80N-1 tested by Del Col, *et al.*

For the unpressurized specimen CP0N shown in Figure 4.69, the discrepancy between the experimental data and the FEA model around the peak moment is evident, and is consistent with that observed in the unpressurized specimens tested in this project and presented in Figure 4.45. The difference is similar to that discussed in Section 4.5.1. Further along in the post-buckling region shown in Figure 4.69, a sudden drop in the global moment can be observed. This was due to an error during the recording of the experimental data and a correction was applied at this point (Del Col, *et al.*, 1998).

For the three pressurized specimens shown in Figures 4.71, 4.73, and 4.75 the experimental and FEA model developed in this project show a poorer level of agreement than was observed for the comparisons made in Section 4.5.1. Nevertheless, the FEA model developed in this project provided a better fit with the experimental data than did the model developed by Del Col. *While* the agreement is not as good as for the specimens tested in this project, the agreement is nevertheless reasonable. This suggests that the FEA model developed in this phase of the project can be extended to other plain pipe test specimens with a D/t ratio of 92.

4.5.4.2 Comparison of Experimental and FEA Model Critical Strains

Figures 4.70, 4.72, 4.74, and 4.76 present a comparison of the experimental and FEA model critical strain plots for the four specimens CP0N, CP20N-1, CP40N-1, and CP80N-1 tested by Del Col.

Examination of Figure 4.70 shows that the FEA model does a very good job of predicting the experimental critical strain data for test specimen CP0N. However, examination of the other three figures shows that there are some significant differences between the experimental data and the FEA model data. In each of these three cases, it can be observed that the FEA model appeared to have greater local strains than the experimental data for any given curvature in the post-buckling region. All three of these test specimens buckled in an elephant's foot mode, which was located immediately adjacent to the top of the collar at the bottom end of the test specimen.

Figure 4.77 shows a typical view of one of these end bulge buckles. As can be seen in this figure, the bottom gridline intercepts the buckle at its approximate mid-height. Since the Demec points that were used to measure the local strain were mounted on the gridline they clearly did not span the entire buckle. This resulted in an under-estimate of the experimental local strain in the buckled region and accounts for the discrepancies in the critical strains observed in Figures 4.72, 4.74, and 4.76 for Del Col's three pressurized specimens, CP20N-1, CP40N-1, and CP80N-1, respectively. Consequently, it may be

assumed that the discrepancies can be attributed to incorrectly placed instrumentation during the testing of Del Col's specimens. It was therefore decided to eliminate the experimentally determined critical strains for these three test specimens from all subsequent analysis.

4.5.4.3 Comparison of Experimental and FEA Model Buckling Modes

Specimen CP0N failed in the diamond-shape buckling mode. The buckle intercepted the half height of the specimen and was symmetrical about the extreme compression fibre. This failure is similar to the typical diamond-shape buckles observed in other unpressurized test specimens.

All of the remaining specimens tested by Del Col buckled with an elephant's foot bulge at the bottom end of the test specimens. As discussed in Section 2.4.2, it is believed that the test procedure used by Del Col influenced the location of these buckles. By tightening the end collars prior to the beginning of the test, it is believed that the subsequently applied internal pressure introduced second-order imperfections at the edges of the collars. It is believed that this resulted in the buckle occurring at these locations. As a result, Del Col's three pressurized specimens were re-tested under this program as CP20N-2, CP40N-2, and CP80N-2, which have already been presented and discussed.

As would be expected, the FEA model did not capture the same behaviour in the re-tested specimens as was observed in the original three tests conducted by Del Col. Del Col reported that, despite the prevalence of end bulge buckles, there was a distribution of possible initiation points for a dominant buckle in each of his specimens. His analysis showed that there appeared to be no preference for a buckle initiated at one location over a buckle initiated at another location. This is consistent with the findings in this project. However, the additional imperfections induced at the edges of the collars through his testing procedure did influence the buckle to occur at the edge of one of the two end collars. It is unclear why the buckle always occurred at the bottom collar.

Despite poor local behaviour results, the FEA model developed in this project was able to represent Del Col's global behaviour accurately. It was therefore concluded that the model appears to work well for all available specimens with a diameter of 762 mm and a D/t ratio of 92. Further validation of the FEA model is presented in Chapter 5 using experimental data from test specimens with varying diameters and D/t ratios.

4.6 Comparison of Experimental Data with Mohareb-Murray Equation

Table 4.6 provides a comparison of the experimental moment capacity with the fully plastic capacity predicted by the Mohareb-Murray equation given in Equation 1.4. It should be noted that Del Col's specimen CP0N was included in this comparison for completeness of the load cases because no plain pipe specimens under a net compressive axial load were tested in the present project. Furthermore, since the buckle in specimen CP0N was located at the approximate half height of the specimen, the local strain behaviour was accurately captured, as shown in Figure 4.70. All of Del Col's pressurized specimen load cases were re-tested in this project and, therefore, it was decided to use the data collected in this project and not that collected by Del Col. This was further supported by the incomplete local data collected for Del Col's pressurized specimens as discussed in Section 4.5.4. Examination of the test-to-predicted ratios given in Table 4.6 shows that they range from 0.75 to 1.10. This variation is not unexpected because the equation offers no consideration of initial imperfections, nor local buckling, which are known to reduce the moment capacity. As expected, the specimens typically have test-to-predicted ratios less than 1.0.

From the data presented in Table 4.6, it is also observed that the internal pressure appeared to have an effect on the test-to-fully plastic ratios. For test specimens with a low level of internal pressure, the test-to-fully plastic ratios were typically around 0.80 with this ratio increasing to approximately 1.0 with the highly pressurized specimens. It is believed that this is due to stabilizing effect of the internal pressure previously observed in the comparison of post buckling regions of the moment-curvature responses.

It is believed that the high internal pressure stabilizes the test specimen wall against buckling thereby reducing the effect of the initial imperfections on the moment capacity. This will be further investigated in Section 4.7.1.1.

This observation was not evident in the test specimens tested by Mohareb (1994) and Yoosef-Ghodsi (1994), where the test-to-predicted ratios from the Mohareb-Murray equation were all essentially equal to 1.0. However, consideration of the differences in the specimen D/t ratios and in the experimental moment-curvature responses may account for the failure of the D/t = 92 specimens to attain this value. The experimental specimens with the smaller D/t ratio developed a fully plastic plateau on the moment-curvature response prior to buckling. While it is anticipated, and will be further investigated in Chapter 5, that the D/t ratio and the magnitude of the initial imperfections affect the location along this plastic plateau where buckling occurs, the fully plastic moment was nevertheless obtained prior to buckling in the previous test series presented by Mohareb and Yoosef-Ghodsi. Therefore, the experimental-to-fully-plastic-moment ratio for each of the smaller D/t specimens was very close to unity and any effects due to the initial imperfections were not reflected in the ratio. This suggests that the D/t ratio may be appropriate to classify line pipe segments.

Table 1 of CAN/CSA S16.1-94 (Canadian Standards Association, 1994) provides a classification for segments of line pipe as a function of their D/t ratio. In Table 1 of CAN/CSA S16.1-94, a small D/t ratio results in a member being given a Class 1 qualification, meaning that the section develops its fully plastic moment capacity with substantial ductility prior to local buckling. With an increase in the D/t ratio the specimen may become a Class 2 section, in which the fully plastic moment is developed, but there is little ductility in the member prior to local buckling. A further increase in D/t ratio will result in the section becoming Class 3, which develops the initial yield moment, but local buckling occurs prior to the fully plastic moment being developed or a Class 4 section in which local buckling occurs prior to any yielding. The class limits provided in Table 1 of CAN/CSA S16.1-94 are expressed mathematically as

Class 1 - Plastic Design: $$\frac{D}{t} \leq \frac{13000}{F_y} \quad (4.13a)$$

Class 2 – Compact: $$\frac{D}{t} \leq \frac{18000}{F_y} \quad (4.13b)$$

Class 3 – Non-compact: $$\frac{D}{t} \leq \frac{66000}{F_y} \quad (4.13c)$$

Applying the experimental values of D/t and F_y for each of the respective specimens, all of the specimens listed in Table 1.1 and Table 1.2, as well as the specimens tested in this project, were classified as 'Class 3 – Non-compact' sections using the limits given in CAN/CSA S16.1-94 given in equation 4.13. Table 4.7 provides the classification results of this analysis.

The line pipe segments with a D/t ratio of 92 tested by Del Col and in this project developed a moment that exceeded the yield moment, as shown in the experimental moment-curvature plots, but did not generally attain their fully plastic moment capacity prior to local buckling. This resulted in a test-to-prediction ratio with the Mohareb-Murray equation less than 1.0. This suggests that the line pipe segments with a D/t ratio of 92 were analogous to a 'Class 3 – Non-compact' section specified in CAN/CSA S16.1-94, which is consistent with the results presented in Table 4.7.

However, for the D/t = 51 and D/t = 64 ratio specimens, a class 3 classification is not consistent with the experimental observations. From the experimental test results, the line pipe segments with a D/t ratio of 51 obtained their fully plastic moment capacity, resulting in a test-to-prediction ratio with the Mohareb-Murray equation of approximately 1.0. They also had substantial ductility, evidenced by a long plastic plateau, prior to buckling (Mohareb, *et al.*, 1994). This suggests that the line pipe segments with a D/t ratio of 51 meet the criteria of a 'Class 1 – Plastic Design' section specified in CAN/CSA S16.1-94.

The line pipe segments with a D/t ratio of 64 attained their fully plastic moment capacity, resulting in a test-to-prediction ratio with the Mohareb-Murray equation of approximately 1.0, but had little ductility, evidenced by a short plastic plateau, prior to buckling. This suggests that the line pipe segments with a D/t ratio of 63 satisfy the criteria of a 'Class 2 – Compact' section specified in CAN/CSA S16.1-94.

These results are not surprising because the limits proposed in Table 1 of CAN/CSA S16.1-94 were primarily developed for hollow structural steel tubes with no internal pressure. As such, application of these criteria to segments of pressurized line pipe may not be consistent with the intent of local buckling criteria presented in Table 1 of CAN/CSA S16.1-94. Furthermore, as has been discussed in Chapter 1, it is essentially impossible to establish criteria for the complex phenomenon of local buckling of line pipe based solely on a single geometric property such as the D/t ratio. Experimental results have shown that the phenomenon is also dependent on many parameters, including the level of internal pressure and the initial imperfection pattern. These results suggest that the class limits provided in CAN/CSA S16.1-94 do not extend to pressurized segments of line pipe and that further research is required in order to develop a set of criteria for the classification of line pipe.

In summary, the Mohareb-Murray equation appears to offer an upper bound to the moment capacity of segments of line pipe. The equation predicts the fully plastic moment capacity assuming an elastic-perfectly-plastic material model, which is the peak moment that may be developed by a line pipe specimen prior to buckling. It should be noted that the equation does not include any strain hardening behaviour nor does the equation account for any initial imperfections, which affect the moment capacity of specimens with a large D/t ratio by inducing local buckling prior to the development of the fully plastic moment capacity. Nevertheless, the Mohareb-Murray equation will be used to predict the peak moment capacity for the segments of line pipe under combined load investigated in this project.

4.7 Effects of Different Experimental Parameters

Now that the comparison of the experimental and analytical results for the individual test specimens is complete, an examination of the different experimental parameters can be undertaken. Specifically, the effects of the variation of internal pressure, the material strength, and the presence of the circumferential girth weld are examined at a global level. A more detailed examination of the effects of these different parameters on the local response is presented in Chapter 6. This section presents the results of the global comparisons, including the results from the D/t = 92 specimens tested by Del Col *et al.* (1998) that were presented in the previous section. In order to clarify the summary plots presented in this section only the experimental data is presented. It should be noted that due to the excellent agreement between the experimental data and the FEA model data, either data series could have been used in the following comparison with the same observations and conclusions being drawn. However, at this stage of the FEA model development it was decided to use only the experimental data until further validation of the FEA model is carried out in Chapter 5.

4.7.1. Effects of Varying Pressure on a Family of Test Specimens

4.7.1.1. Plain Compression Specimens

A total of seven plain compression specimens were tested. Six of these were made from pairs of specimens tested under the same load case. Only the CP0N load case was not re-tested. The final digit in the specimen name indicates whether they were tested by Del Col (-1) or by Dorey (-2). For clarity, Del Col's CP0N load case and the plain pressurized specimens tested in this project will be used to examine the effects of varying pressure on the plain compression specimens. This gives one test result for each load case. The experimental global moment-curvature plots for the four different levels of internal pressure investigated in the plain compression specimens is presented in Figure 4.78. It should be noted that the CP0N specimen was fabricated from a different grade material, which has an effect on the behaviour of the specimen. This effect will be discussed in section 4.7.2. Therefore, while the discussion in this section includes specimen CP0N in order to complete the set of plain compression specimens, it should be

noted that the discussion will focus on the pressurized specimens, all of which had very similar material properties.

Examination of Figure 4.78 shows that, for the pressurized specimens, there is a decrease in peak moment capacity and a corresponding increase in global curvature at the peak moment for increasing levels of internal pressure. The phenomenon of decreasing moment with increasing levels of internal pressure is readily explained through examination of the Mohareb-Murray Interaction Equation, given in Equation 1.4. Increasing the level of circumferential stress, σ_θ, by increasing the level of internal pressure results in a lowering of both the axial force reduction factor, α, given in Equation 1.5, and the internal pressure reduction factor, β, given in Equation 1.3. Since the fully plastic moment capacity, M^θ_{pc}, is linearly proportional to both α and β, increasing the level of internal pressure corresponds to a decrease in M^θ_{pc}. This is evident in Figure 4.78, as well as in subsequent comparisons of specimens with varying levels of internal pressure.

The phenomenon of increasing curvature at peak moment with increasing internal pressure can be readily explained by considering the stress in conjunction with a yield criterion. Since the Von Mises yield criterion was used as the yield criterion for the FEA model it will also be used in this discussion. For an isotropic material under plane stress, as would be the state of stress in the wall of the test specimens in this project, the Von Mises yield criterion can be expressed mathematically as

$$\sigma_1^{\,2} - \sigma_1\sigma_2 + \sigma_2^{\,2} = F_y^{\,2} \tag{4.14}$$

where σ_1 is the stress on the '1' principal plane, σ_2 is the stress on the '2' principal plane, and F_y is the yield stress. Equation 4.14 is expressed graphically in Figure 4.79

Examination of Equation 4.14 shows that if the stress is changed in one of the two principal directions then it must change in the other direction in order to satisfy the yield

criterion. If the longitudinal direction in the test specimens is considered the '1' principal axis and the circumferential direction is considered the '2' principal axis, then increasing σ_2 would cause the value of σ_1 to decrease. This indicates that, at increasing levels of internal pressure, the absolute value of the longitudinal bending stress at first yield decreases and results in a lower proportional limit as the internal pressure increases.

Using the horizontal axis to represent the longitudinal stress, σ_L, and the vertical axis to represent the circumferential stress, σ_C , with tensile stresses plotted as positive on both axes, the four plain pipe load cases may be plotted on the Von Mises yield criterion. It should be noted that the total longitudinal stress in the wall of the pipe only includes the effects of the thermal change and Poisson's ratio. The axial loads due to the internal pressure on the end plates and due to the eccentric jack are carried directly by the MTS load head. Table 4.8 presents the circumferential and longitudinal stresses normalized against the yield stress for a series of specimens subjected to increasing internal pressure. These points are plotted on the von Mises yield surface in Figure 4.80.

Examination of Figure 4.80 provides an explanation for the observed differences in proportional limit for the different plain pipe specimens in compression. With increasing levels of internal pressure (increasing values of σ_C along the vertical axis), it can be seen that the distance between the initial state of stress, represented by the solid black square, and the state of stress at yield, represented by the solid black circle, decreases with increasing internal pressure. This indicates that by increasing the internal pressure and, therefore, the circumferential stress, the longitudinal stress capacity prior to yielding and, therefore, the proportional limit, decreases. This can be further interpreted to mean that the higher the internal pressure, the lower the bending moment when the proportional limit is reached. This is also shown in the last column of Table 4.8 where the normalized value of remaining capacity to carry the bending stress at first yield in the longitudinal direction, $\sigma_{1\text{-capacity}}$, decreases with increasing values of internal pressure. Because of the lower proportional limit a specimen develops greater curvatures prior to the buckling moment being reached, thereby accounting for the increase in peak curvature with increasing internal pressure.

Further examination of Figure 4.78 shows that the unpressurized specimen has a lower capacity than one of the pressurized specimens. This is not consistent with the results of the numerical analysis presented in Figure 4.80 and Table 4.8. It is believed that the unpressurized specimen has a reduced capacity due to the different buckling mode, the diamond buckle, which may be a lower energy mode than the bulge buckle. The lower energy mode diamond buckle results in a reduction in the load carrying capacity of the unpressurized specimens. However, for the pressurized specimens the internal pressure acts to stabilize the pipe wall against this failure mode, resulting in the bulge buckle becoming the lower energy mode. Neither the Mohareb-Murray Interaction Equation nor the von Mises Yield Criterion take different buckling modes into account. As such, any differences that arises due to the different modes would not be reflected in the above analysis. This would explain the lack of agreement between the values presented in Figure 4.80 and Table 4.8 and the experimental data.

Finally, it can be observed in Figure 4.78 that the post-buckling region softens more gradually with increasing internal pressure. This may be a result of the stabilizing effect that the internal pressure has on the load carrying characteristics of the test specimen. The greater the internal pressure, the more gradually the post buckling region of the curve softens. Again, this observation will be found to be consistent throughout the remaining families of specimens presented in Section 4.7.1.

4.7.1.2.Plain Tension Specimens

Figure 4.81 shows the effect of internal pressure on the plain tension specimens. The previously observed phenomenon of decreasing capacity with increasing internal pressure is clearly evident in this figure. Using the von Mises Yield Criterion presented in Equation 4.14, a similar argument to that presented in the previous section can be made regarding the effects of the internal pressure on the longitudinal stress capacity. This would account for the significantly lower proportional limit for T20P80N observed in Figure 4.81 and the substantially greater curvature at the peak moment. However, it should be noted that different grade materials were used in each of these two specimens. The effects of this will be discussed in Section 4.7.2.

4.7.1.3. Welded Compression Specimens

Figure 4.82 shows the effect of internal pressure on the welded compression specimens. All of the specimens shown in this figure were fabricated from the same pipe stock and thus had the same material properties. Therefore, the relationships shown in Figure 4.82 are theoretically independent of material properties and based solely on the effects of pressure variation.

Using the Mohareb-Murray Equation and Von Mises yield criterion, identical arguments regarding the relationships shown in Figure 4.82 can be made as for the plain compression specimens. Specifically, it can be readily observed that, with the exception of the unpressurized specimen, there is a decrease in moment capacity and an increase in global curvature at peak moment capacity with increasing internal pressure. The reduction in moment capacity is again a direct result of a reduction in the α and β reduction factors in Equation 1.4 and the increased curvature is a direct result of the reduction in the proportional limit when considering the Von Mises yield criterion of Figure 4.80.

The unpressurized specimen has a lower moment capacity than the 20% internal pressure specimen, as was the case for the plain compression specimens. This is once again attributed to the different buckling modes between the two specimens, as discussed in Section 4.7.1.1. Finally, the previous observation of a more gradual softening of the post-buckling region with increasing internal pressure is also evident in Figure 4.82. This shows that the results of the welded compression specimens mirror the results of the plain compression specimens.

4.7.1.4. Welded Tension Specimens

Figure 4.83 shows the effect of internal pressure on the welded tension specimens. The previously observed phenomenon of decreasing capacity with increasing internal pressure is also clearly evident in this figure. Figure 4.83 shows a similar trend to Figure 4.81. However, both welded tension specimens were made from the same stock pipe. Therefore, the results from the welded tension specimens in Figure 4.83 will not have any

material property effects influencing the observed variations in behaviour that were evident in Figure 4.81 for the plain tension specimens. The difference in material property, as will be discussed in the following section, accounts for the observed differences between Figure 4.81 and Figure 4.83.

Examination of Figure 4.83 shows that the general trend of a decrease in moment capacity and an increase in global curvature at the peak moment for cases of increasing internal pressure is followed. Again, these phenomena can be readily explained using the Mohareb-Murray Interaction Equation and the Von Mises Yield Criterion.

4.7.2. Effects of Different Grade Material

Figure 4.84 shows the two different specimens for CP80N load case. Comparison of the Del Col data (CP80N-1) with the data collected in this project (CP80N-2) shows significant differences. While the peak moment capacities are approximately equal (1486 kN-m versus 1547 kN-m), the global curvatures at the peak moment are substantially different. It is believed that there are two reasons for this difference. The two test specimens were each fabricated from different pipe stock. As such, each had a different set of material properties, as shown in Table 4.2. CP80N-1 had 'P2-type' material properties and CP80N-2 had 'P1-type' material properties. The most significant difference in material properties of the two specimens was the yield strength, with the ultimate strength and the Modulus of Elasticity being approximately equal. As shown in Table 4.2, CP80N-1 had a yield strength of 472 MPa, whereas CP80N-2 had a yield strength of 501 MPa. Because the value of F_y is lower for CP80N-1, the size of the Von Mises ellipse will be smaller than for CP80N-2. As a result, the value of $\sigma_{l\text{-capacity}}$ is less for CP80N-1 because of the lower F_y. Consequently, it would be anticipated that the specimens tested by Del Col would have a lower proportional limit.

This becomes evident when the proportional limits for each of the test specimens in Figure 4.84 are examined. It can be clearly seen that the CP80N-1 specimen tested by Del Col reached its proportional limit at a much lower moment than CP80N-2, which was tested in this project. Furthermore, since CP80N-1 yielded earlier, greater plastic

deformations occurred prior to the buckling moment being achieved. This resulted in the observed greater global curvatures at the peak moment.

In addition to the lower yield strength, a second factor that may have contributed to the significantly greater curvatures at peak moment for the Del Col specimens is the effect of premature tightening of the end collars. The pressure-induced imperfections at the edges of the collars may have led to an apparent early softening of the overall test specimen, which may have contributed to the substantially greater curvatures. There is no way to confirm this observation. Nevertheless, it appears that the lower material yield strength was the major factor contributing to the observed differences and that the global responses of all seven test specimens remain valid. This is supported by the level of agreement between the FEA model and the two different responses for the CP80 load case previously presented in Figures 4.33 and 4.75.

4.7.3. Effects of Girth Weld on Specimens Subjected to the Same Load Case

Pressure is not the only factor that may affect the critical buckling strain of line pipe under combined loading. Tests conducted by Yoosef-Ghodsi, *et al.* (1994) showed that critical buckling strain is greatly influenced by the discontinuity introduced by a circumferential girth weld in the wall of a line pipe segment. In this project, pairs of specimens were subjected to the same load case with the only difference being the presence or absence of a circumferential girth weld. This section provides a comparison of the plain versus girth welded specimens subjected to the same load case.

The load cases studied in this project can be classified into one of three categories: unpressurized pipe with a net compressive wall force; pressurized pipe with a net compressive wall force; and, pressurized pipe with a net tensile wall force. Since all three categories showed similar comparison for the plain and girth welded test specimens only one typical load case from each category will be presented. Therefore, the effects of the girth weld on the CP0, CP80 and T20P40 load cases are presented in Figures 4.85, 4.86, and 4.87, respectively.

The test results for load case CP0 in Figure 4.85 show that if the experimental recording errors previously discussed in Sections 4.5.1 and 4.5.4.1 are neglected then all three specimens have essentially the same global moment curvature response, irrespective of the presence of the girth weld. It should be noted that slight differences are present due to the different material properties and due to the variable nature of experimental testing. However, it is evident that there does not appear to be any systematic effect due to the presence of the girth weld.

A similar observation can be made from Figure 4.86 for the CP80 load case. Examination of this figure shows that specimen CP80N-2 and CP80W, which had similar material properties, have similar global moment curvature responses, despite CP80W having a girth weld at the half height of the specimen. Specimen CP80N-1 had substantially different material properties, previously discussed in Section 4.7.2, than the other two specimens in Figure 4.86 as well as end collar tightening effects, which resulted in the differences between the two CP80N load specimens observed in this figure.

Figure 4.87 shows the effect of the girth weld on the T20P40 load case. Again, the test curves show very close agreement in the moment capacity with the slight differences readily accounted for in the different material properties between the two test specimens. However, there is a significant difference in the global curvature at peak moment. As previously discussed, a difference in material properties will be shown to have a significant effect on the curvature, and hence the critical strain, that develops in a test specimen. The T20P40 and the T20P80 load cases were the only ones that showed this significant a difference in global curvature at peak moment between the plain and girth-welded specimens. It should be noted that they were the pair of plain and girth-welded specimens with the most significant difference in material properties within the pair and that they were the only specimens tested under net tensile wall load for which there is strain data to make a comparison.

There is no apparent reason why only the tensile load cases would be affected by the presence of a circumferential girth weld. Therefore, based on the response of the other pairs of test specimens subjected to the same load case and only differentiated by the presence of the girth weld, it is assumed that the observed differences are due to the differences in material properties and are independent of the tensile load case. This will be examined in greater detail during the parametric study conducted in Chapter 6.

From Figures 4.85, 4.86, and 4.87 and the effects of the material properties as discussed in this section, it is evident that the presence of the circumferential girth weld at the half height of the specimen has little to no effect on the global behaviour response of specimens tested under the same load case.

When comparing specimens with D/t ratios of 51 and 64, Yoosef-Ghodsi, *et al.* (1994) also observed that the girth weld had little to no effect on the global behaviour. However, they also observed that the girth weld had an effect on the local critical buckling strain. Local critical buckling strain reduced with increasing D/t ratio. As reviewed in Chapter 1, DNV (2000) has proposed a girth weld factor for critical buckling strain, which reduces with increasing D/t ratio.

Table 4.9 presents a comparison of the local critical strains of the plain versus girth welded specimens for the given load cases. For every load case, with the exception of T20P40, which was discussed previously, the values for the plain local critical strain and the girth welded local critical strain are within 10% of each other. This difference can be considered systematic, which would indicate that at large D/t ratios the girth weld has no significant effect on the value of the critical buckling strain. This phenomenon will be further investigated in the parametric study in Chapter 6.

4.8 Summary of Experimental Parameters that Influence Line Pipe Wrinkling

From the results and discussion presented in Chapters 3 and 4, a number of experimental parameters have been shown to have significant effects on both the global and local

behaviour of line pipe specimens subject to combined loading. Internal pressure has been shown to be one of the most influential experimental parameters on the behaviour of the test specimens. The results from the experimental portion of this project show that internal pressure affects the load carrying capacity, the global curvature, the local strain and the stiffness of the post-buckling region of the moment-curvature response. With such a broad-scale significance, ***internal pressure*** is one parameter that must be given some attention when considering any type of additional study on the behaviour of line pipe.

From the results of the FEA parametric studies in Chapter 3 and the level of agreement achieved in comparison with the experimental data in Chapter 4, it is clear that another important factor for large D/t ratio specimens is the ***initial imperfection pattern***. The results presented throughout these two chapters clearly show that the initial imperfections have a significant effect on the location of the buckle as well as the maximum load carrying capacity of the specimen prior to buckling. Therefore, all subsequent analysis in this project will include an initial imperfection pattern typical of that existing in all line pipes.

The final experimental factor that had significant influence on the behaviour of the test specimens was the ***material properties*** of the pipe. While the material properties obviously influence the load carrying capacity of the test specimens, they also had a significant influence on the location of the proportional limit, which in turn influences the global and local curvatures at the time of buckling. Therefore, material properties are another factor that plays a significant role in the buckling capacity and critical strain of line pipe and must also be carefully considered in the parametric study presented in Chapter 6.

It must be noted that the D/t ratio is also an important factor in the response of the test specimens and has not been neglected. Previously conducted studies discussed in Chapter 1, and the critical strain equations developed from them, have shown that the ***D/t ratio*** is probably the single *most important factor* affecting the behaviour of line pipe

specimens. Therefore, while the D/t ratio was not an experimental variable in this project, it will nevertheless be included in all subsequent parametric studies included in this research.

Each of these issues will be further addressed during the design and execution of the parametric study and in the development of a new critical buckling strain equation, which is presented in Chapter 6. Prior to starting the parametric study, further validation of the Dorey model using experimental results for different D/t ratios will be conducted. Chapter 5 presents this further validation.

Table 4.1 – Results of Longitudinal Material Property Test Coupons[1]

Material Coupon ID	F_y (MPa)	F_u (MPa)	MOE (MPa)	ν	t (mm)
N-1	521.2	591.4	202626	-0.27	8.507
N-2	527.1	593.5	201044	-0.26	8.490
Mean N	**524.2**	**592.5**	**201835**	**-0.27**	**8.499**
W-1	518.9	569.6	203528	-0.27	8.707
W-2	527.0	568.0	203355	-0.26	8.690
Mean W	**523.0**	**568.8**	**203442**	**-0.27**	**8.699**
E-1	529.3	572.2	202247	-0.26	8.843
E-2	550.8	589.3	209962	-0.27	8.743
E-3	548.6	586.3	207867	-0.27	8.763
Mean E[2]	**549.7**	**587.8**	**208915**	**-0.27**	**8.753**

Notes:
1. All material properties are based on the static point readings taken.
2. In accordance with ASTM A370-94 (1994), a third coupon was tested (E-3) because of the difference in the material properties determined from E-1 and E-2. Since the results from E-3 were more consistent with E-2, the results from E-1 were rejected from further calculations.

Table 4.2 – Results of Additional Longitudinal Material Property Test Coupons[1]

Material Coupon ID[2]	F_y (MPa)	F_u (MPa)	MOE (MPa)	ν	t (mm)
1A	498.7	577.6	203995	-0.28	8.517
1B	509.9	581.0	199410	-0.28	8.483
1X	501.2	594.8	200025	-0.27	8.490
1Y	490.5	596.2	204447	-0.28	8.513
2X	501.8	592.1	202003	-0.28	8.400
2Y	501.9	582.3	198548	-0.27	8.413
Mean P1	**500.7**	**587.3**	**201405**	**-0.28**	**8.469**
2A	470.0	581.2	203717	-0.28	8.330
2B	466.1	580.9	202671	-0.28	8.300
Del Col 1	472.0	571.7	193855	-0.27	8.503
Del Col 2	478.7	576.0	205269	-0.28	8.477
Mean P2	**471.7**	**577.5**	**201378**	**-0.28**	**8.403**

Notes:
1. All material properties are based on the static point readings taken.
2. The coupon ID is as follows. There were two additional test specimens left over in the laboratory, each having a circumferential girth weld. This resulted in 4 separate cans, two in each specimen, being available for additional material tests. The number in the coupon ID refers to which one of the pipes the coupon came from. The letter refers to which can, with 'A' and 'B' corresponding to the same can and 'X' and 'Y' referring to the other can. The results show that the two cans in pipe 1 were made from the same material ('1A', '1B', '1Y', and '1Y' have the same properties), but that pipe 2 had two different material properties in the two cans ('2A' and '2B' material properties differ from '2X' and '2Y').

Table 4.3 – Typical Engineering Stress-Strain and Corresponding True Stress-Strain Data

Engineering Stress[1] (MPa)	Engineering Strain[2] (με)	True Stress[3] (MPa)	Natural Log of the Plastic Strain Component[4]
531.3	2562	531.3	0.0000
571.1	3350	573.1	0.0006
570.5	11014	576.8	0.0082
572.5	24547	586.6	0.0214
598.8	37870	621.5	0.0342
612.1	56175	646.5	0.0516
617.7	77425	665.5	0.0714
618.2	103442	682.2	0.0952
617.2	123798	693.6	0.1134
611.6	143209	699.2	0.1305
598.3	165900	697.5	0.1502
586.5	183219	697.4	0.1649
572.9	202732	689.1	0.1813
550.9	221256	672.7	0.1967
484.0	258461	609.2	0.2270

Notes:
1. As determined from the experimental coupon data
2. As determined from the experimental coupon data.
3. As determined from equation 3.1.
4. As determined from equation 3.2.

Table 4.4 – Comparison of Experimental and FEA Model Peak Moments

Specimen	Experimental Peak Moment (kN-m)[1]	FEA Model Peak Moment (kN-m)[2]	Test-to-Predicted Ratio
CP20N-2	1924	1889	1.018
CP40N-2	1805	1861	0.970
CP80N-2	1547	1518	1.019
T20P40N	2350	2253	1.043
T20P80N	1861	1839	1.011
CP0W-2	1684	1690	0.996
CP20W	1910	1819	1.050
CP40W	1833	1729	1.060
CP80W	1626	1400	1.161
T20P40W	2315	2277	1.017
T20P80W	1920	1850	1.038
		mean[3]	**1.035**
		standard deviation	**0.049**
		Coefficient of variation	**0.047**

Notes:
1. The experimental peak moment was the maximum value for moment recorded during the testing program.
2. The FEA model peak moment was the maximum value for moment recorded in the ABAQUS output file.
3. The statistical values for mean, standard deviation and variance were computed using the subroutines available in the commerically available Microsoft Excel spreadsheet.

Table 4.5 – Comparison of Experimental and FEA Model Critical Strains

Specimen	Experimental Critical Strain (%)	FEA Model Critical Strain (%)	Test-to-Predicted Ratio
CP20N-2	0.320	0.326	0.982
CP40N-2	0.288	0.294	0.980
CP80N-2	0.401	0.390	1.028
T20P40N	0.465	0.497	0.936
T20P80N	n.d.	0.462	n.d.
CP0W-2	0.302	0.294	1.027
CP20W	0.299	0.302	0.990
CP40W	0.314	0.314	1.000
CP80W	0.446	0.490	0.910
T20P40W	0.227	0.227	1.000
T20P80W	0.354	0.432	0.819
		mean	**0.967**
		standard deviation	**0.064**
		Coefficient of variation	**0.066**

Table 4.6 – Comparison of Experimental Moment Capacities with Mohareb-Murray Predictions

Specimen	Peak Experimental Moment Capacity (kN-m)	Mohareb- Murray[1] Predicted Peak Moment Capacity (kN-m)	Test-to-Predicted Ratio
CP20N-2	1921	2558	0.75
CP40N-2	1804	2405	0.75
CP80N-2	1548	1627	0.95
T20P40N	2352	2403	0.98
T20P80N	1865	1697	1.10
CP0W-2	1883	2622	0.72
CP20W	1911	2389	0.80
CP40W	1834	2236	0.82
CP80W	1627	1566	1.04
T20P40W	2316	2456	0.94
T20P80W	1921	1936	0.99

Notes:

1. The Murray-Mohareb Equation is given in Equation 1.4. The values used as input in Equation 1.4 were based on the experimentally recorded values. The values not directly recorded experimentally were calculated using equilibrium and the free body diagram shown in Figure 2.2. Specifically, the value of the P_p was calculated using equation 2.11 and the value of P_N was calculated using Equation 2.8.

Table 4.7 –Comparison of Class of Section From CAN/CSA S16.1-94 with Experimental Data

ID	F_y (MPa)	Class 1 Limit	Class 2 Limit	Class 3 Limit	D/t	Class of Section
UGA12	378	34	48	175	51	3
HGA12	378	34	48	175	51	3
DGA12	378	34	48	175	51	3
UGA12W	378	34	48	175	51	3
HGA12W	378	34	48	175	51	3
DGA12W	378	34	48	175	51	3
UGA20	391	33	46	169	64	3
UGA20W	391	33	46	169	64	3
HGA20W	391	33	46	169	64	3
DGA20W	391	33	46	169	64	3
L178P80BP-4	448	29	40	147	61	3
L178P80BP-8	448	29	40	147	84	3
CP0N	472	28	38	140	91	3
CP20N-1	472	28	38	140	91	3
CP20N-2	550	24	33	120	87	3
CP20W	523	25	34	126	88	3
CP40N-2	550	24	33	120	87	3
CP40W	523	25	34	126	88	3
CP80N-2	524	25	34	126	90	3
CP80W	523	25	34	126	88	3
T20P40N	524	25	34	126	90	3
T20P40W	523	25	34	126	88	3
T20P80W	523	25	34	126	88	3
L178P80BW-1	448	29	40	147	61	3
L178P80BW-2	448	29	40	147	61	3
L178P80BW-3	448	29	40	147	61	3
L178P80BW-5	448	29	40	147	61	3
L178P80BW-6	448	29	40	147	61	3
L178P80BW-7	448	29	40	147	61	3

Table 4.8 – Normalized Circumferential and Longitudinal Stress for Increasing Internal Pressure

σ_θ / σ_y	$E \alpha \Delta T / \sigma_y$	$\nu \sigma_\theta / \sigma_y$	$\sigma_{l\text{-actual}}$ [1] $/ \sigma_y$	$\sigma_{l\text{-max}}$ [2] $/ \sigma_y$	$\sigma_{l\text{-capacity}}$ [3] $/ \sigma_y$
0.0	- 0.191	+ 0.00	- 0.191	- 1.000	- 0.809
0.2	- 0.191	+ 0.06	- 0.131	- 0.885	- 0.754
0.4	- 0.191	+ 0.12	- 0.071	- 0.738	- 0.667
0.8	- 0.191	+ 0.24	+ 0.049	- 0.321	- 0.370

Notes:

1. $\sigma_{l\text{-actual}}$ is the actual logitudinal stress in the specimen due to thermal change and Poisson's effect.
2. $\sigma_{l\text{-max}}$ is the maximum longitudinal stress that can develop in the specimen at the given level of σ_θ. This is calculated using the von Mises yield criterion present in Equation 4.14.
3. $\sigma_{l\text{-capacity}}$ is the remaining longitudinal stress capacity once the thermal change and Poisson's effect loads have been considered.

Table 4.9 – Effect of the Presence of a Girth Weld on Critical Buckling Strains[1]

Load Case	Plain Specimen Local Buckling Strain (%)	Girth Welded Specimen Local Buckling Strain (%)	Percent Difference[2] (%)
CP0	0.294	0.302	2.72
CP20	0.320	0.299	6.56
CP40	0.288	0.314	9.03
CP80	0.401	0.446	11.2
T20P40	0.465	0.227	105
T20P80[3]	0.462	0.432	6.49

Notes:

1. The values reported in this table are the critical buckling strains measured from the experimental testing program, unless otherwise noted.
2. The percent difference was caculated as

$$\% = \frac{(\text{plain strain} - \text{welded strain})}{\text{plain strain}} \times 100\%$$

3. There was no experimental critical buckling strain for specimen T20P80N due to premature failure of the set-up during testing. Therefore the critical strain values reported for the T20P80 load case were taken from the FEA model results.

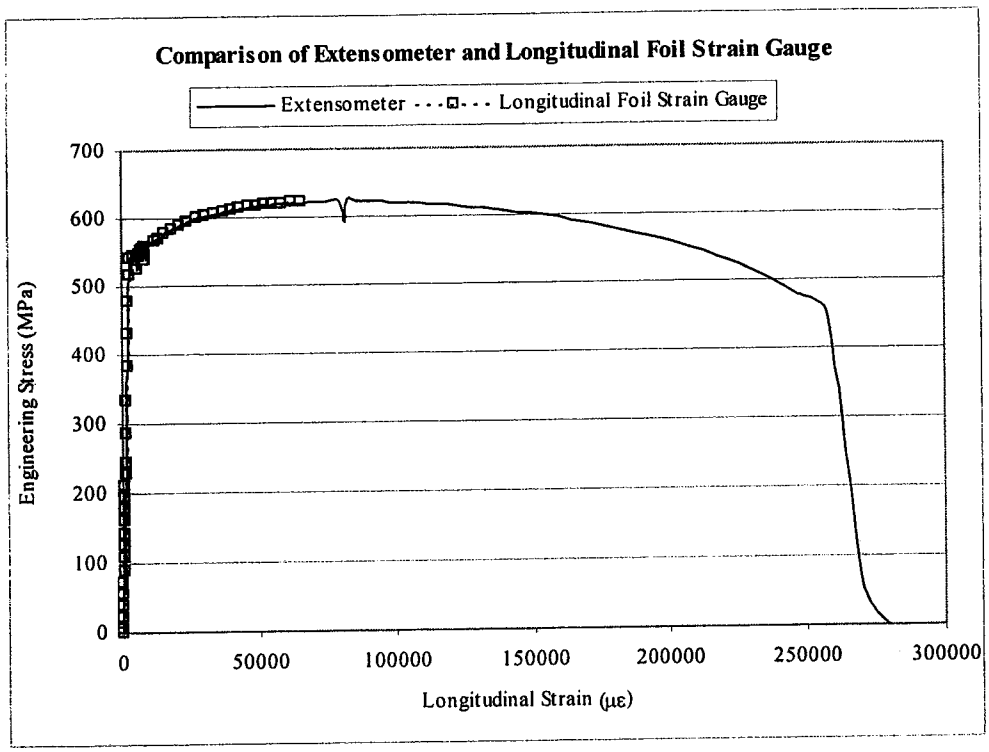

Figure 4.1 – Typical Longitudinal Foil Gauge and Extensometer Material Property Curve

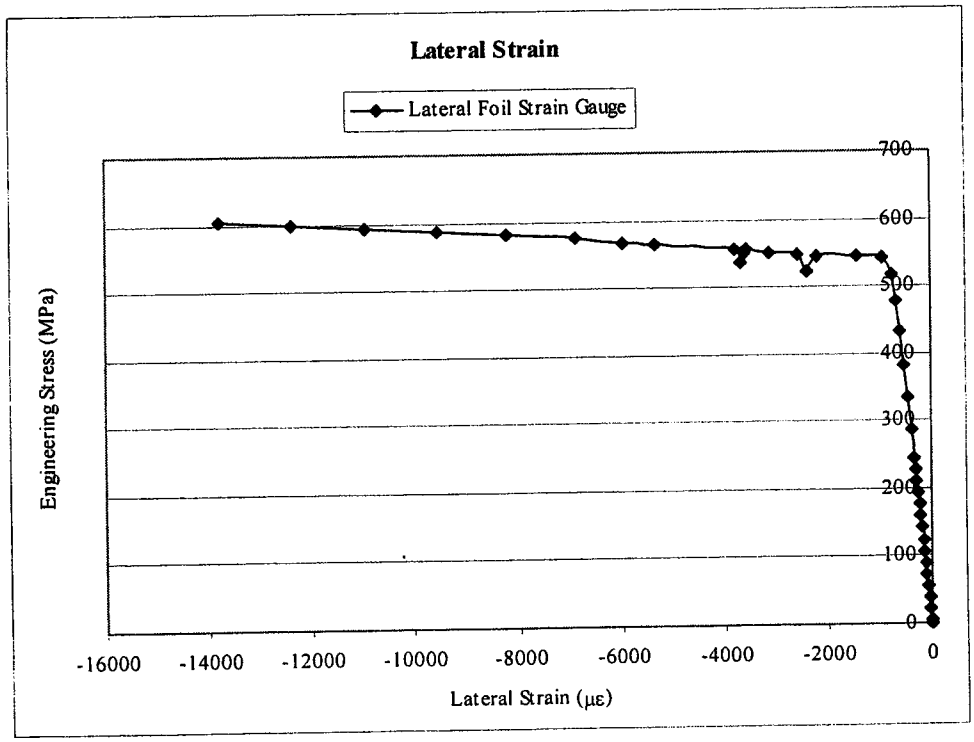

Figure 4.2 – Typical Lateral Foil Gauge Material Property Curve

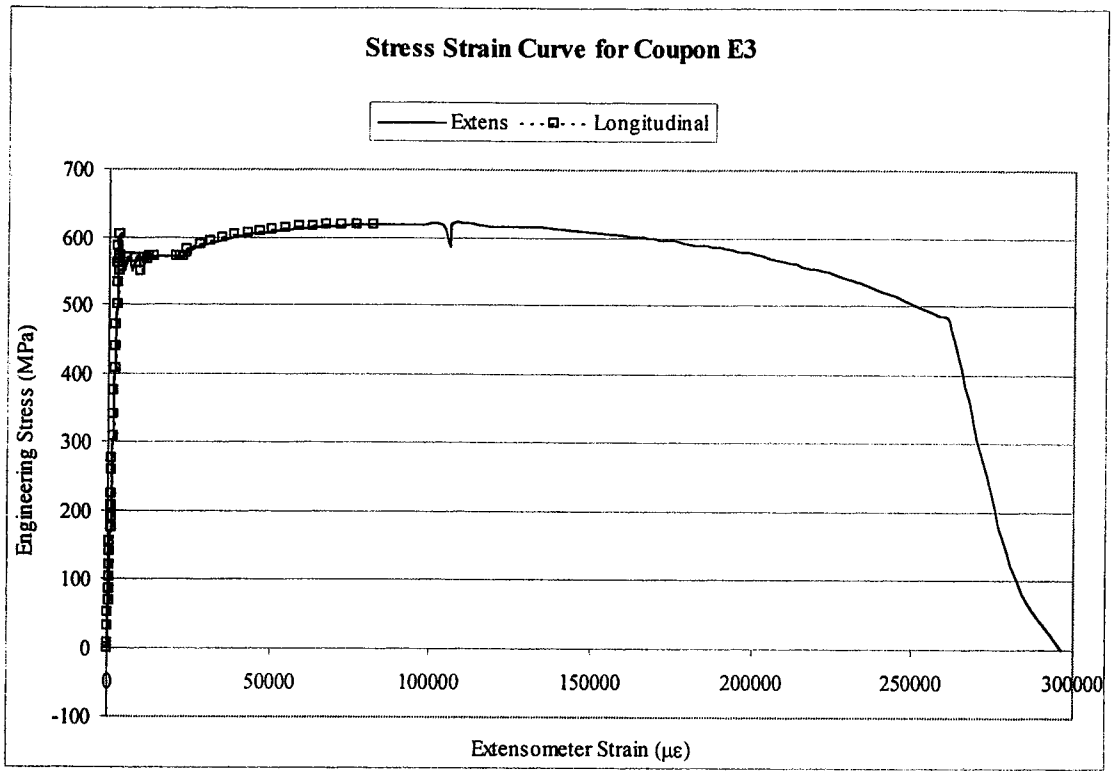

Figure 4.3 –Test Results for an E-type Material Coupon

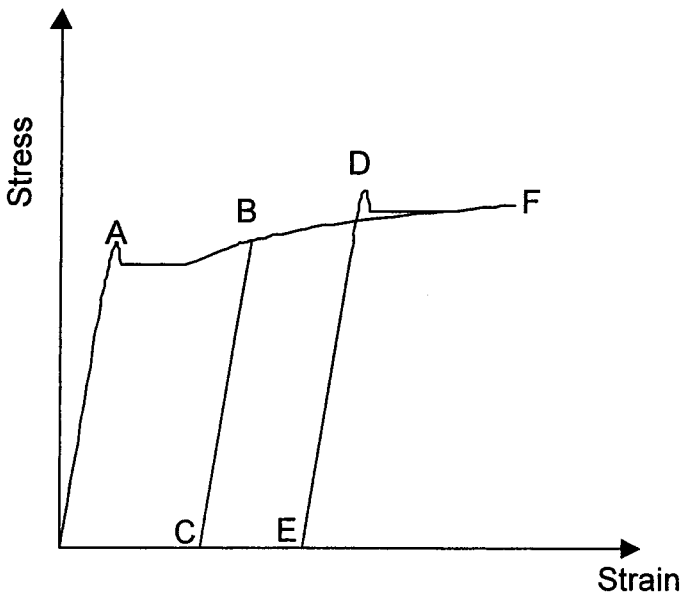

Figure 4.4 – Effects of Strain-Aging

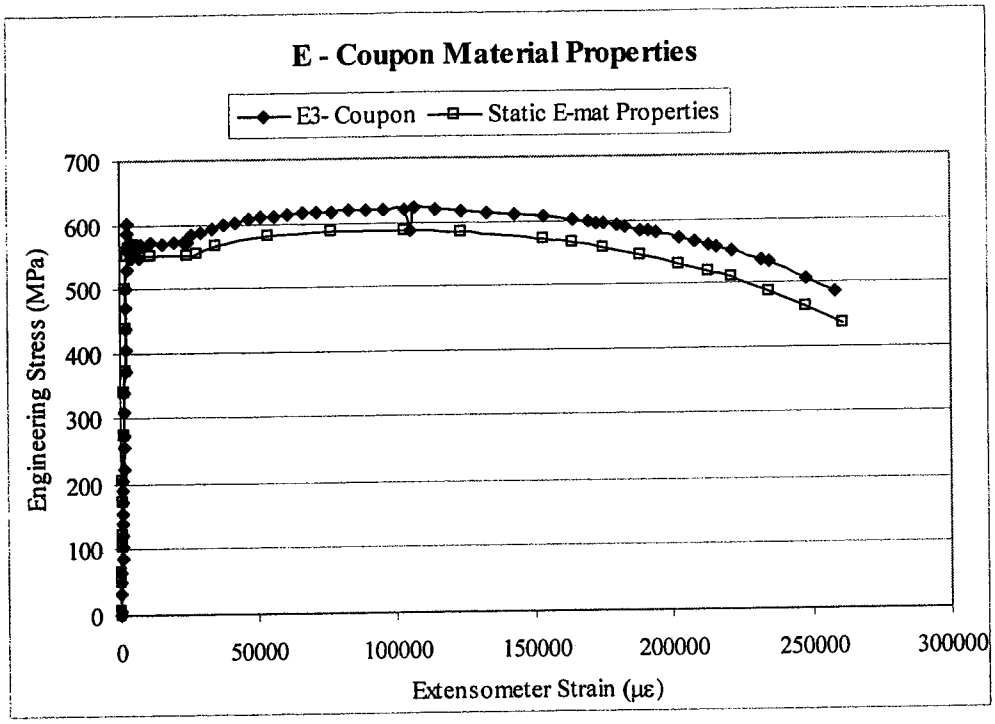

Figure 4.5 – Typical Approximation of Static Material Properties

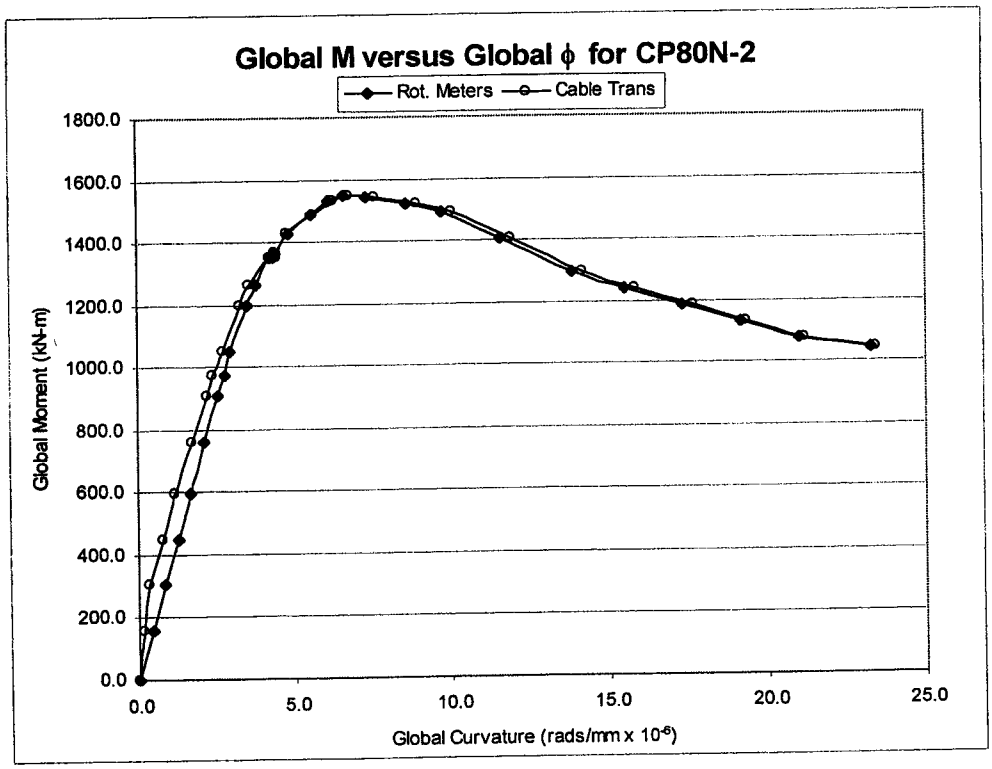

Figure 4.6 – Comparison of Different Methods for Determining Global M-ϕ Curves

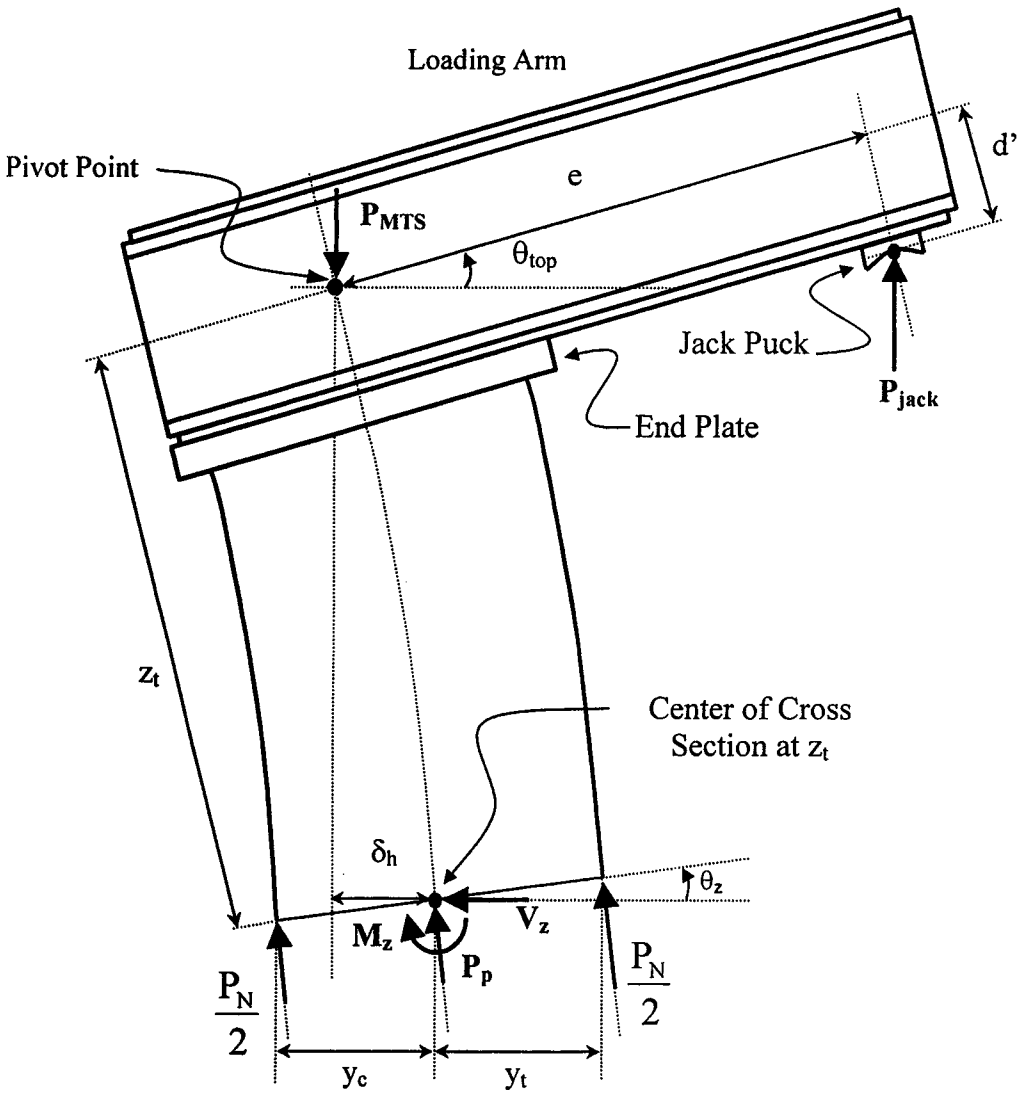

Figure 4.7 – Free Body Diagram at Random Distance (z_t) Along Pipe Segment

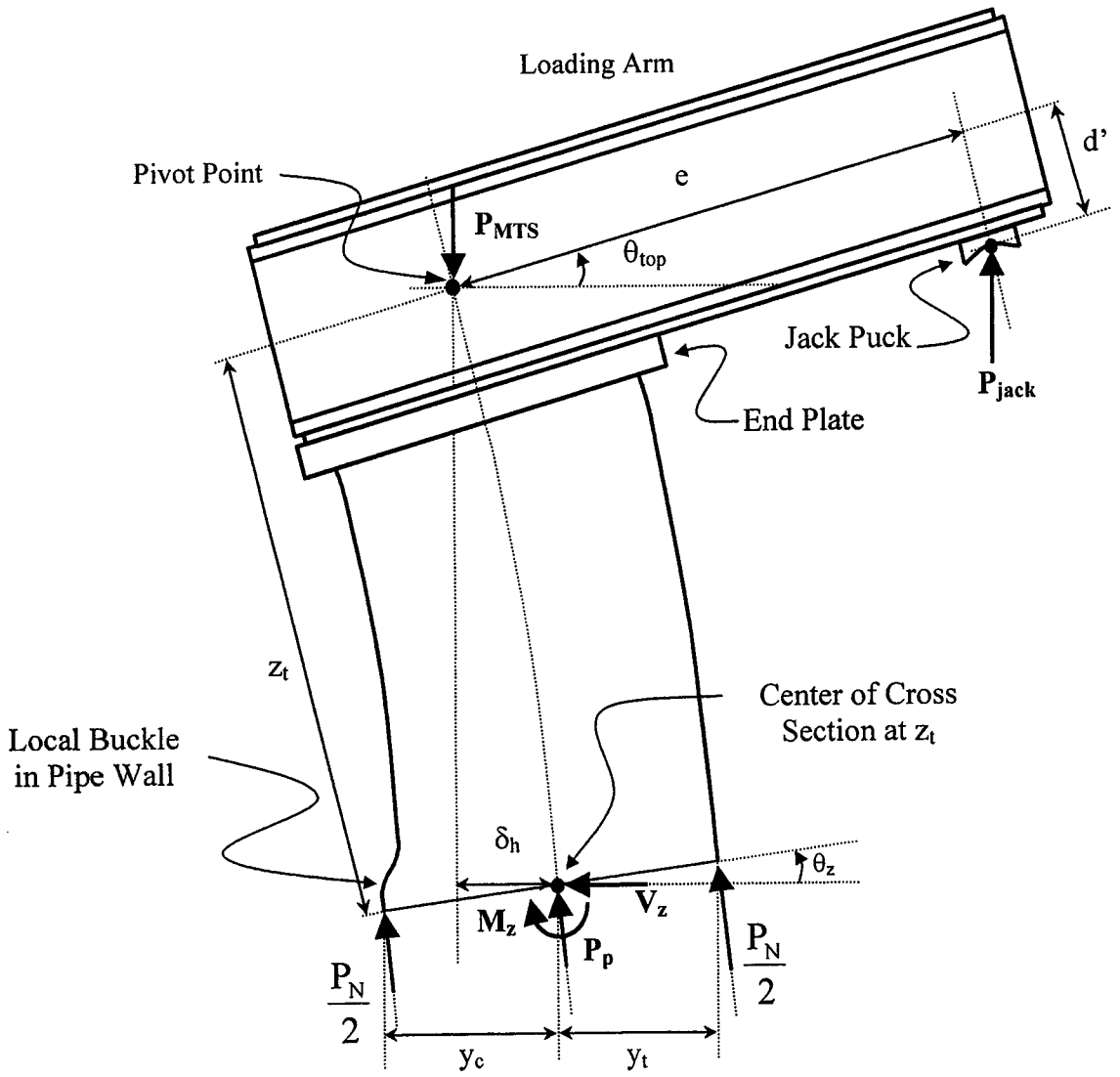

Figure 4.8 – Free Body Diagram Sectioned at a Deformed Cross Section

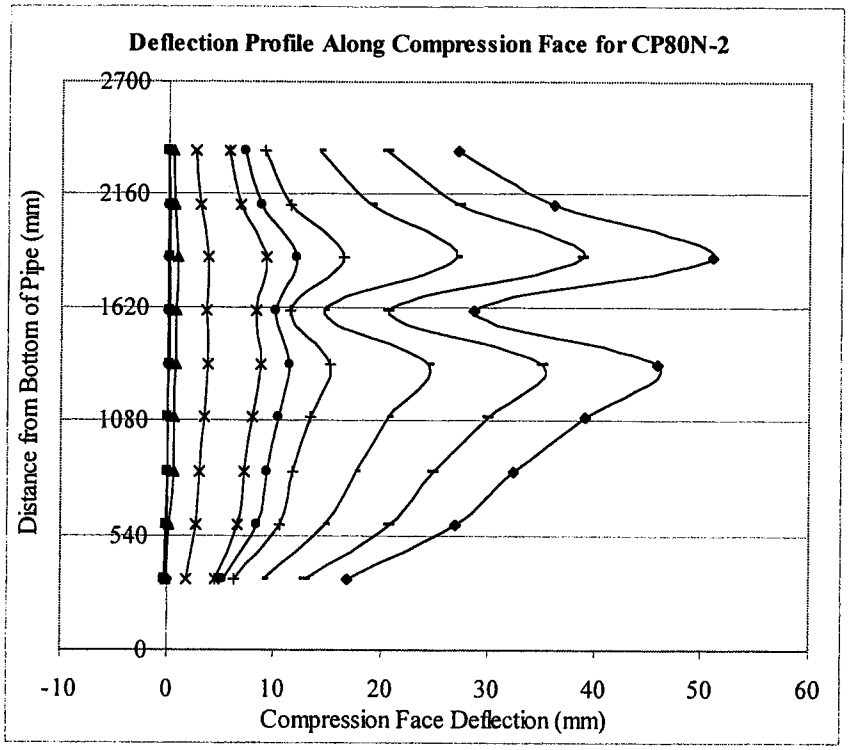

Figure 4.9 – Deflected Profile along Compression Face (δ_{LVDT})

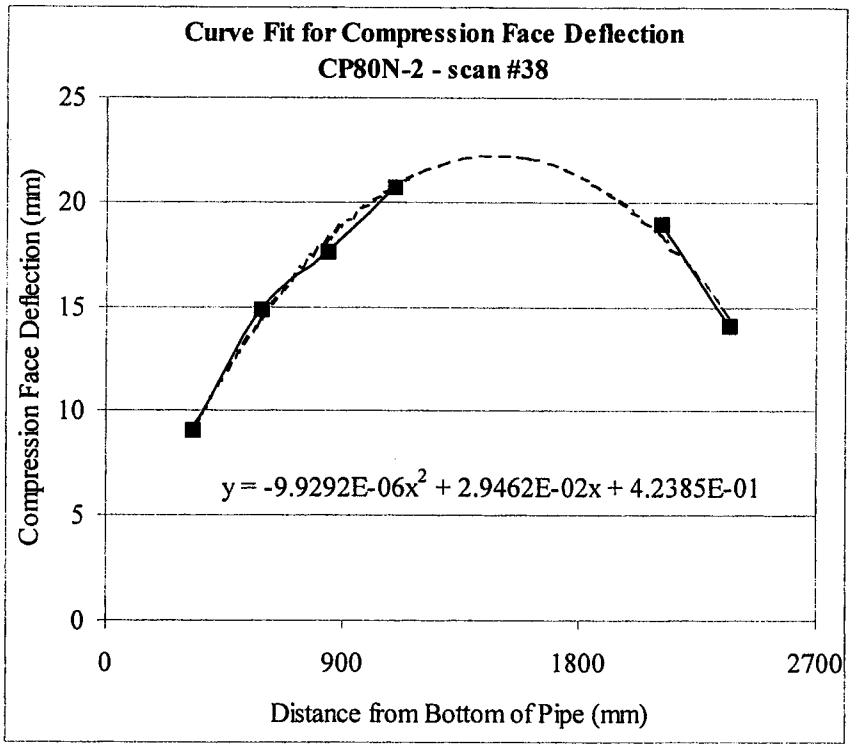

Figure 4.10 – Deflected Profile Equation Fit ($\delta_{assumed}$)

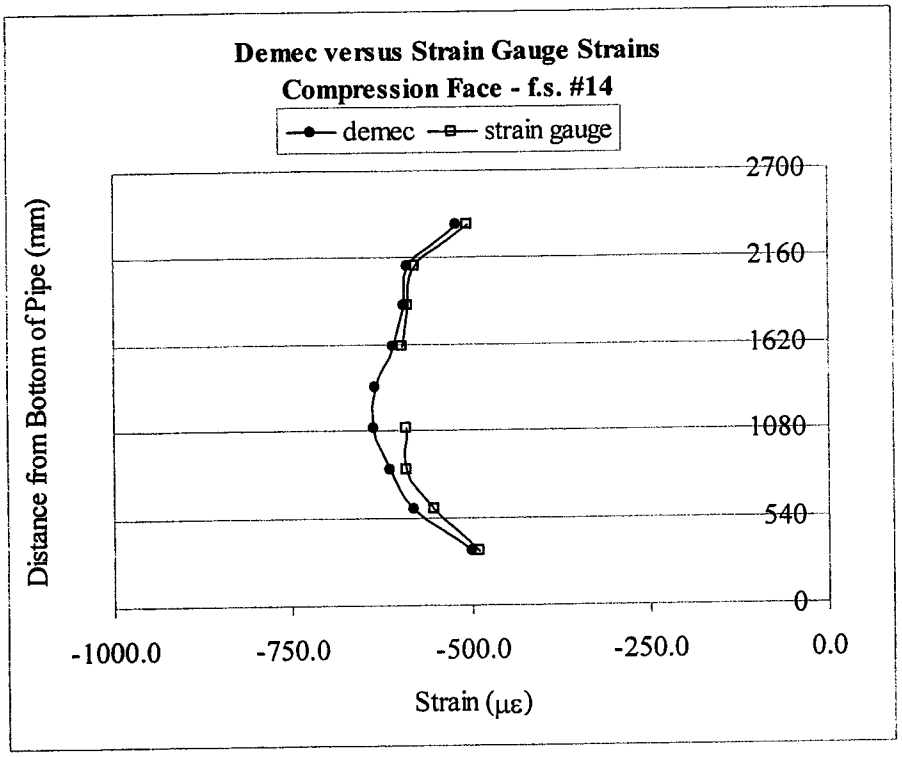

Figure 4.11 –Typical Foil Strain Gauge versus Demec Gauge Data Prior to Buckling

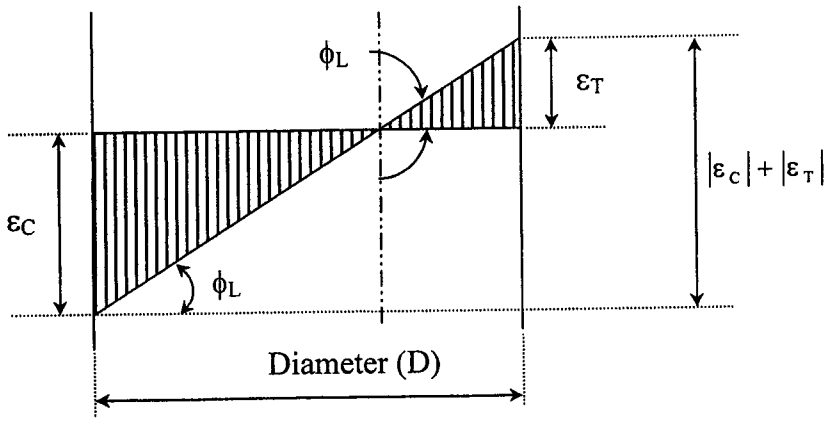

Figure 4.12 – Strain Distribution Used to Determine Local Curvature

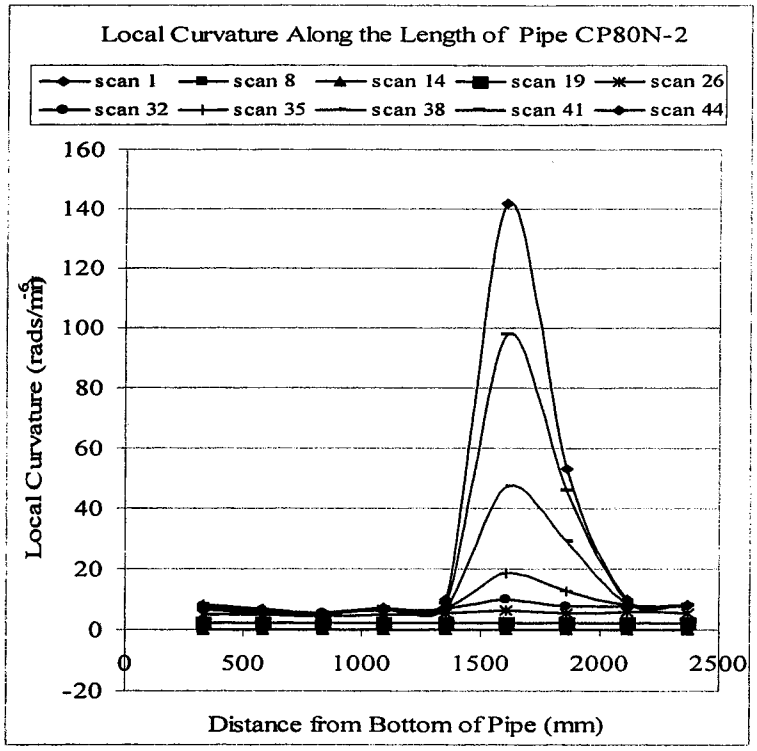

Figure 4.13 – Local Curvature Along Length of Pipe at Increasing Load Levels

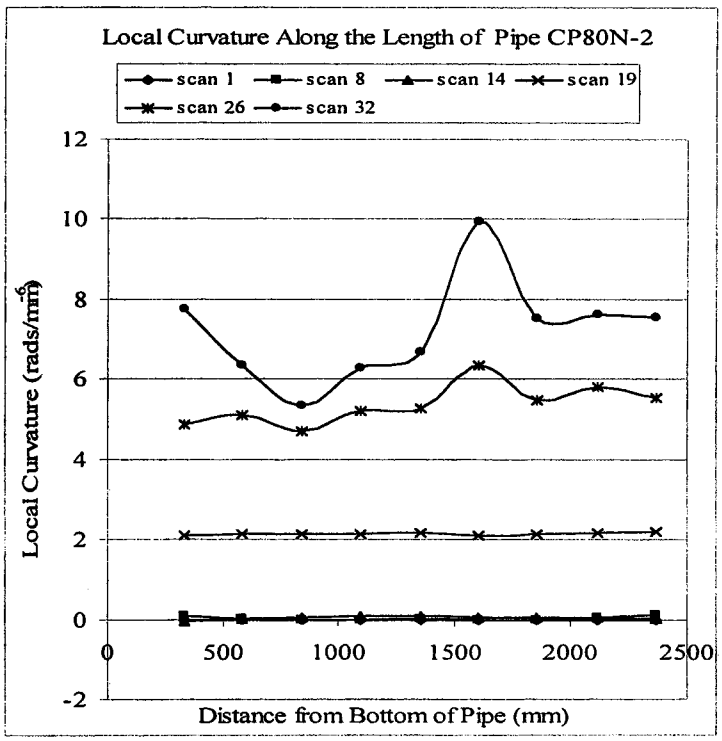

Figure 4.14 – Enlargement of Lower Load Level Region of Figure 4.13

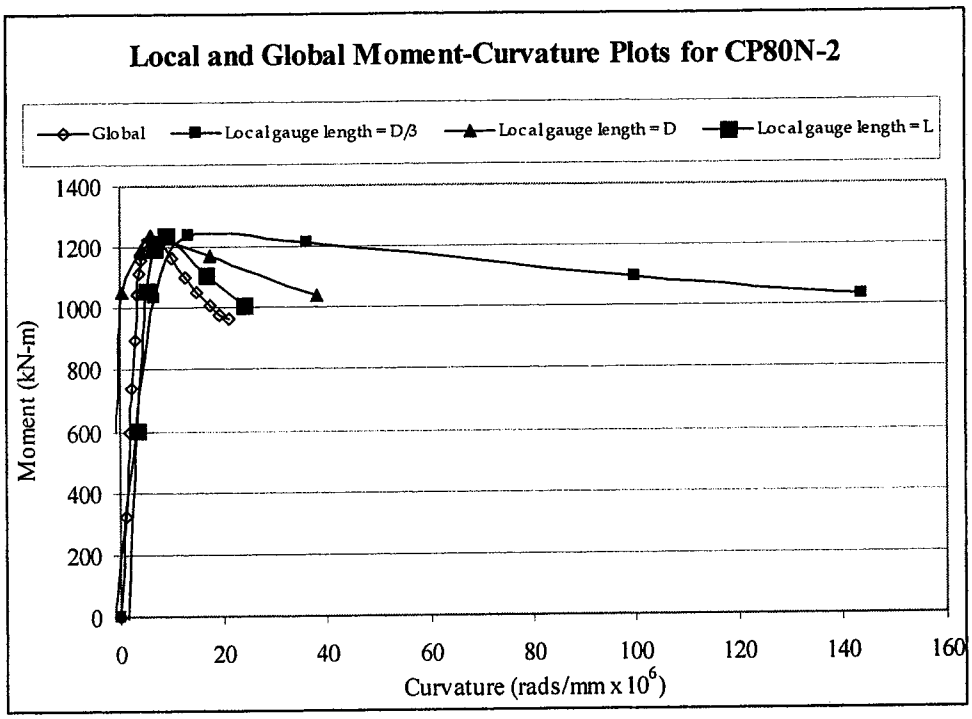

Figure 4.15 – A Set of Typical Local and Global Moment-Curvature Plots

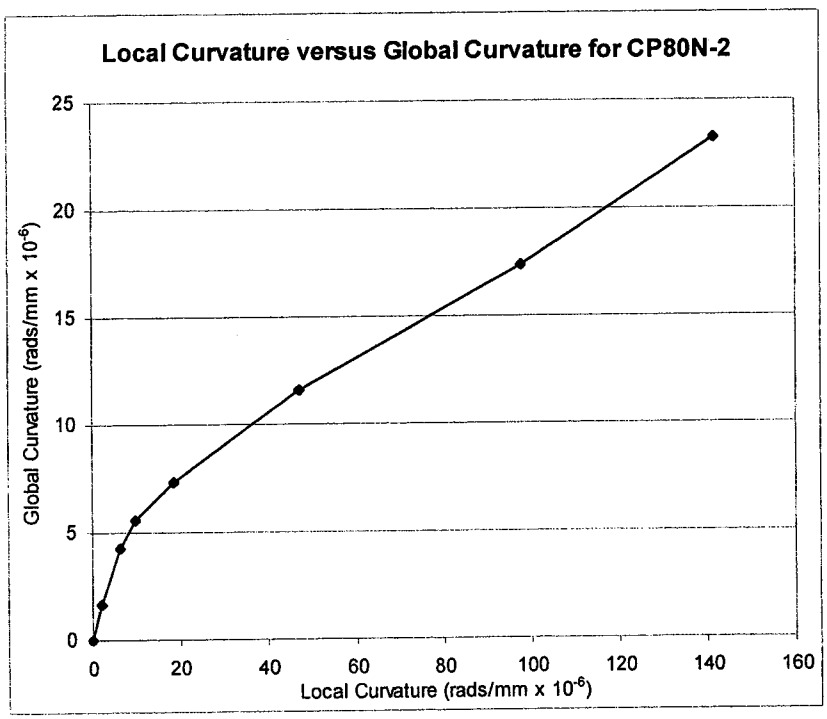

Figure 4.16 – Typical Local versus Global Curvature Plot

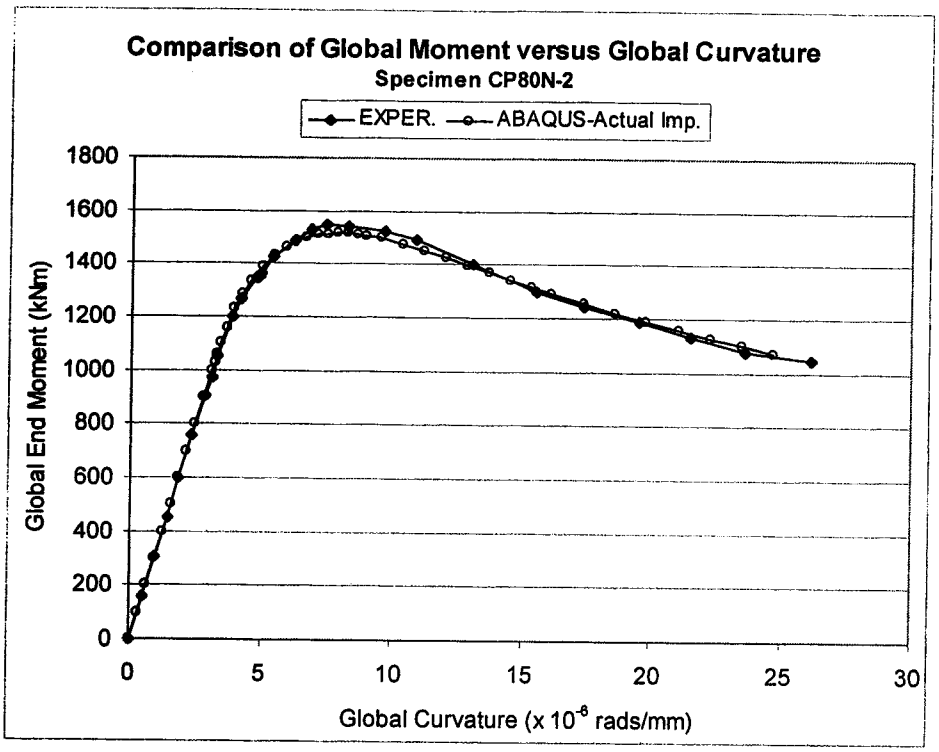

Figure 4.17 – Typical FEA Model Moment-Curvature Plot

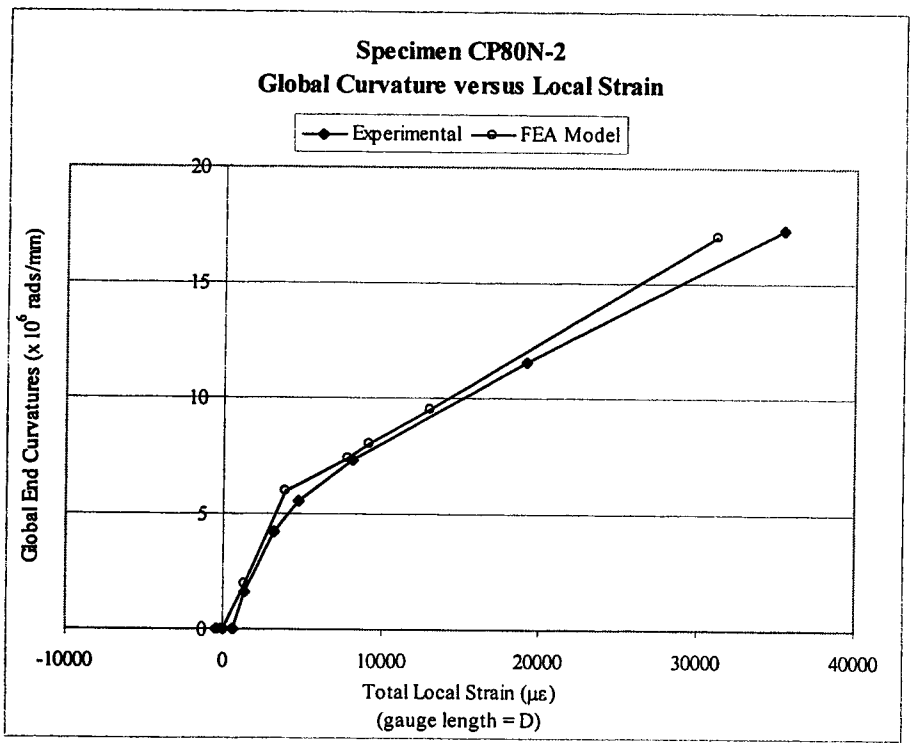

Figure 4.18 – Typical FEA Model Global Curvature versus Local Strain Plot

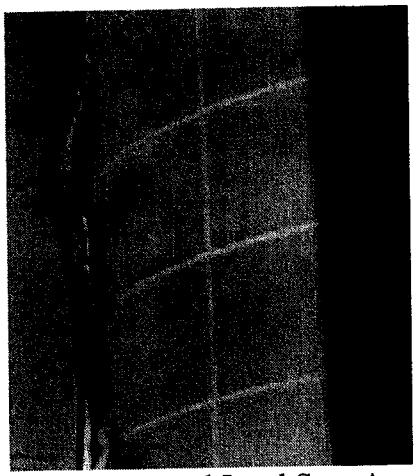

Experimental Load Step A

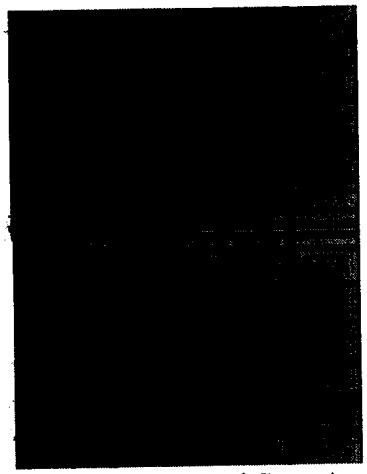

FEA Model Load Step A

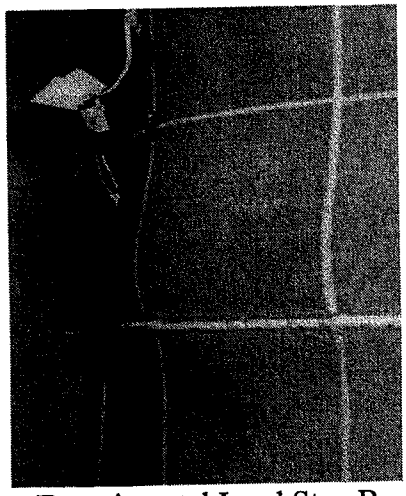

Experimental Load Step B

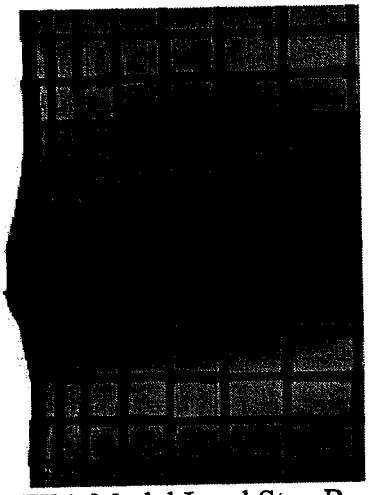

FEA Model Load Step B

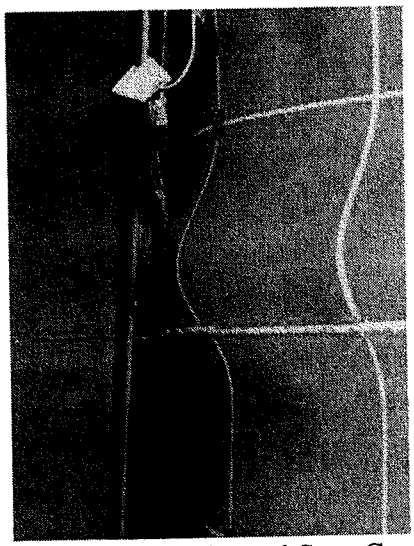

Experimental Load Step C

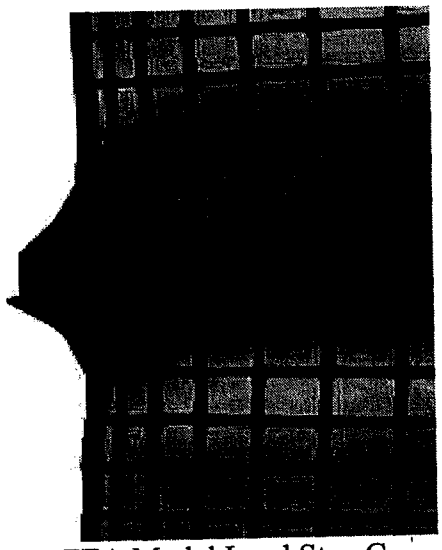

FEA Model Load Step C

Figure 4.19 - Progression of Buckle Growth with Increasing Load Increment (cont.)

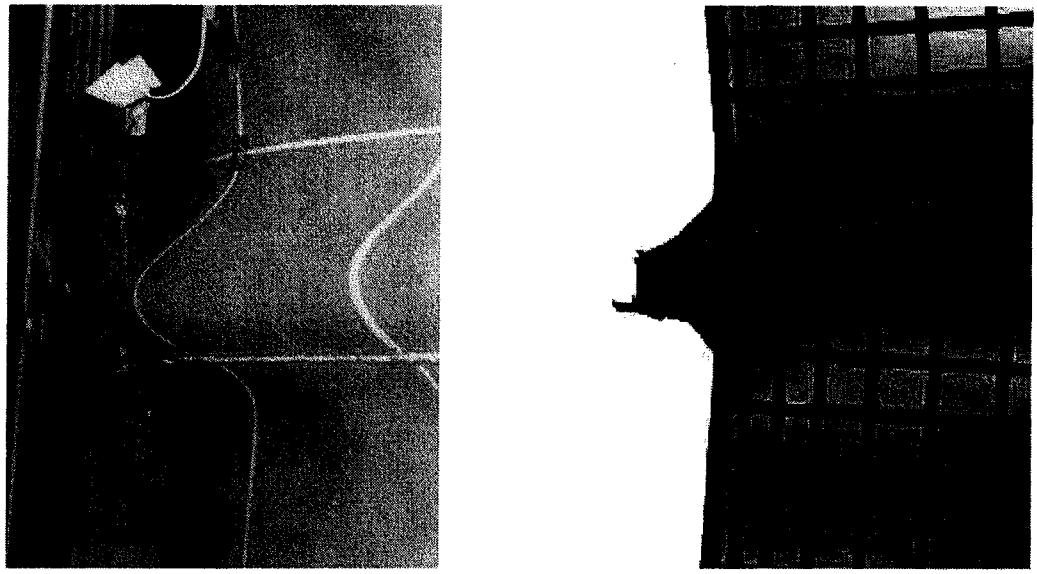

Experimental Load Step D FEA Model Load Step D

Figure 4.19 – Progression of Buckle Growth with Increasing Load Increment

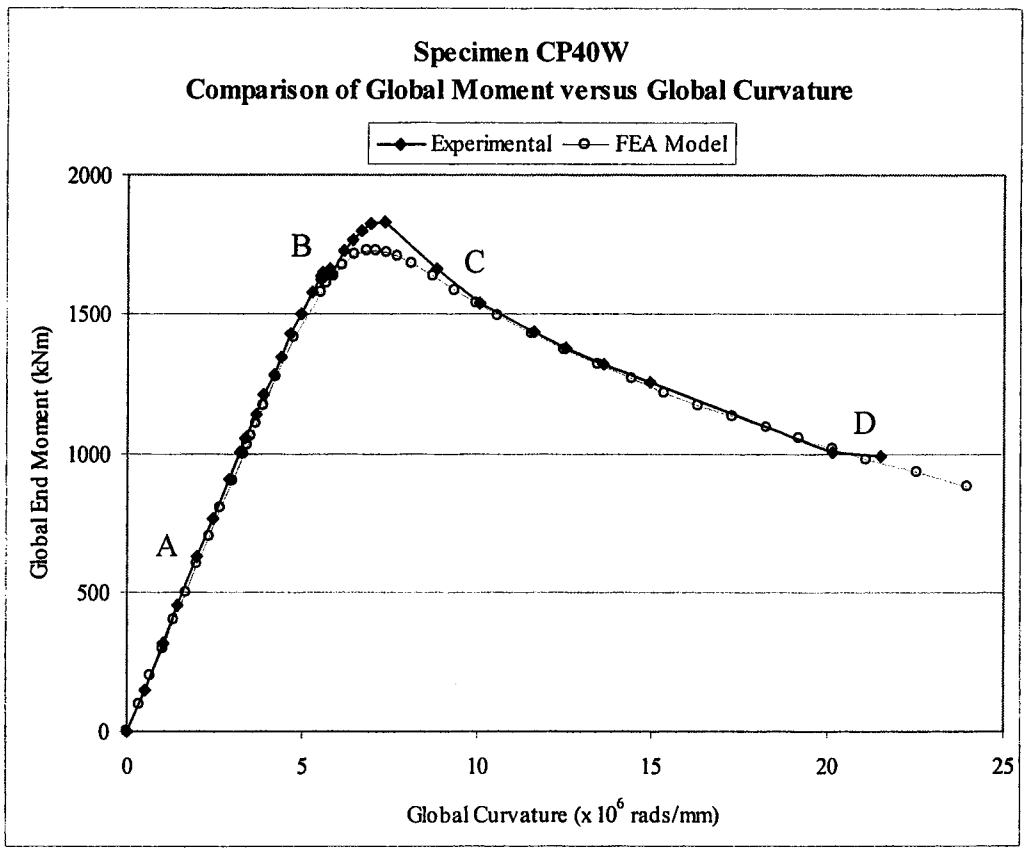

Figure 4.20 – Experimental versus FEA Model Response showing Load Steps for Figure 4.19

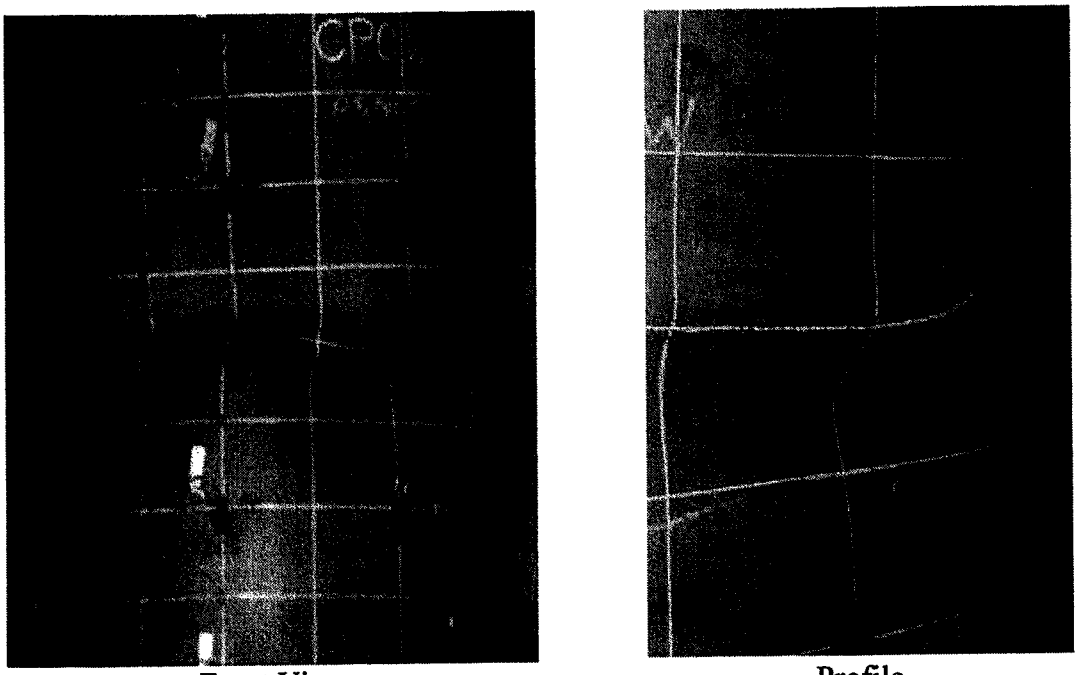

Front View Profile

Figure 4.21 – Typical Diamond-shaped Buckle on an Unpressurized Girth-Welded Specimen

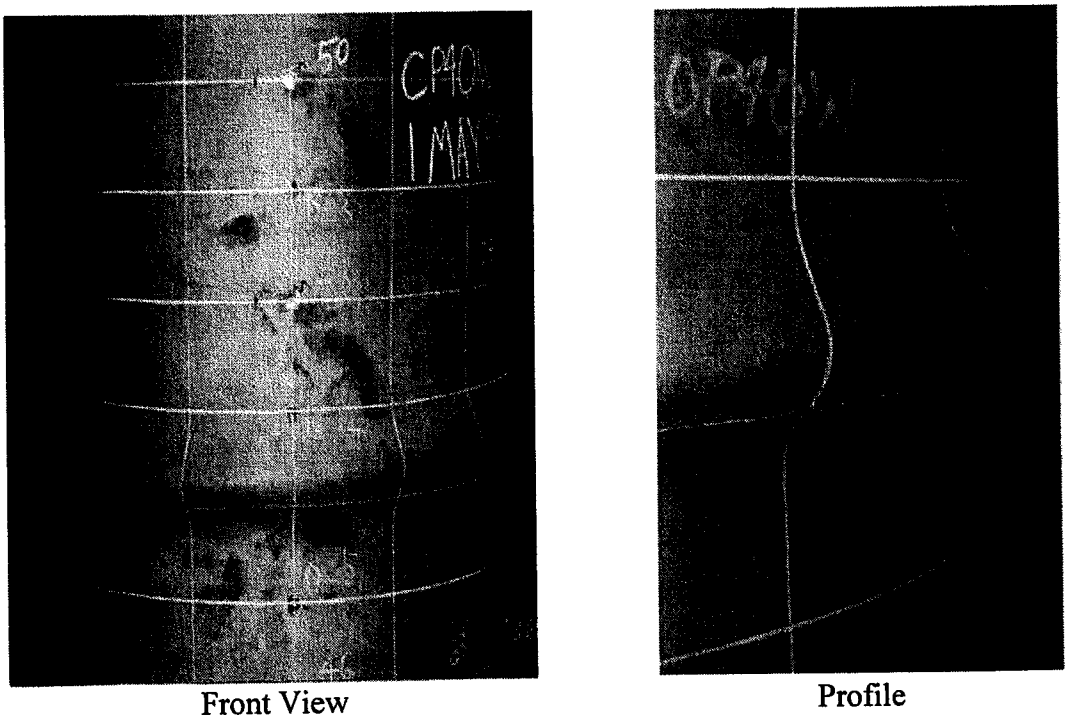

Front View Profile

Figure 4.22 – Typical Mid-Height Bulge Buckle on a Pressurized Girth-Welded Specimen

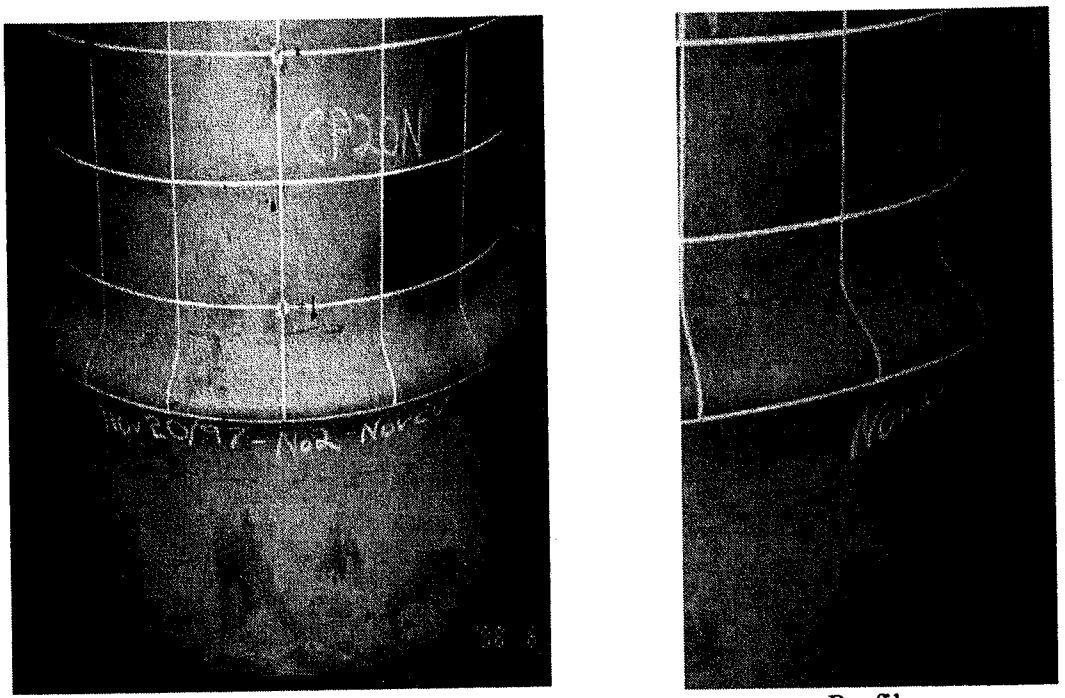

Front View Profile

Figure 4.23 – Typical Elephant-Foot Buckle on a Pressured Plain Specimen

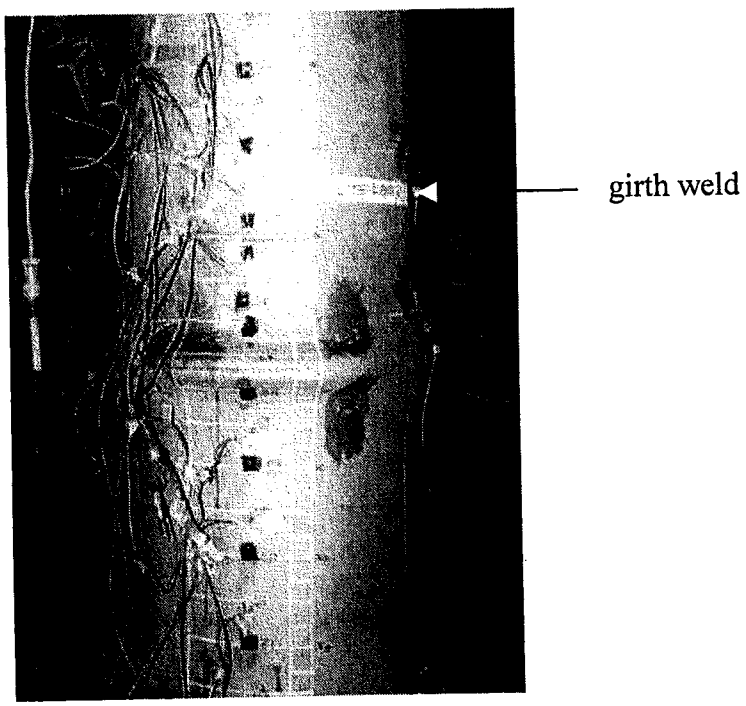

Figure 4.24 – Typical Buckle on Girth-Welded Low D/t Ratio Test Specimen

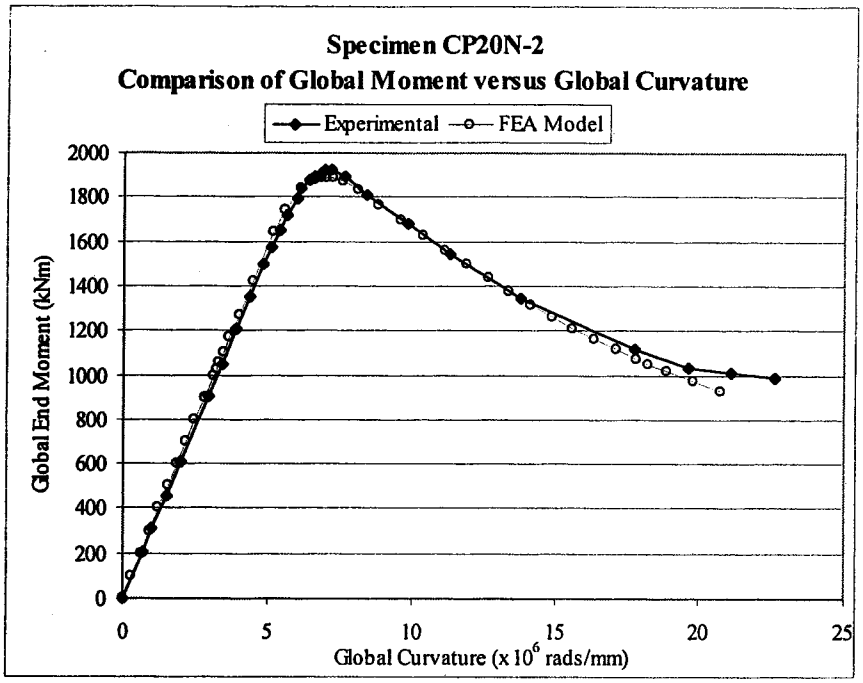

Figure 4.25 – Global Moment versus Global Curvature Comparison for Specimen CP20N-2

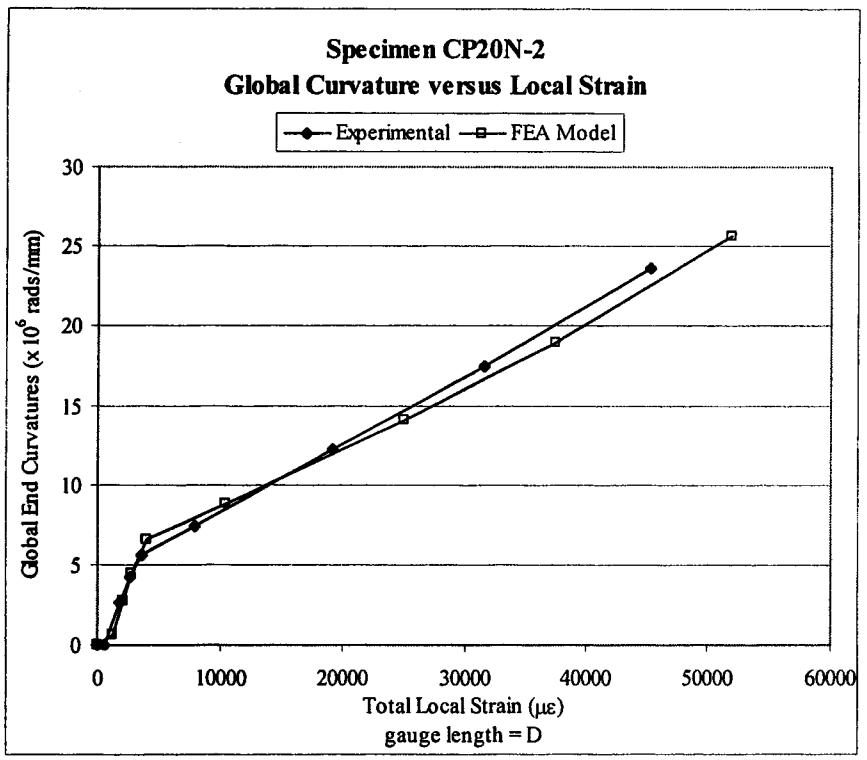

Figure 4.26 – Global Curvature versus Local Strain Comparison for Specimen CP20N-2

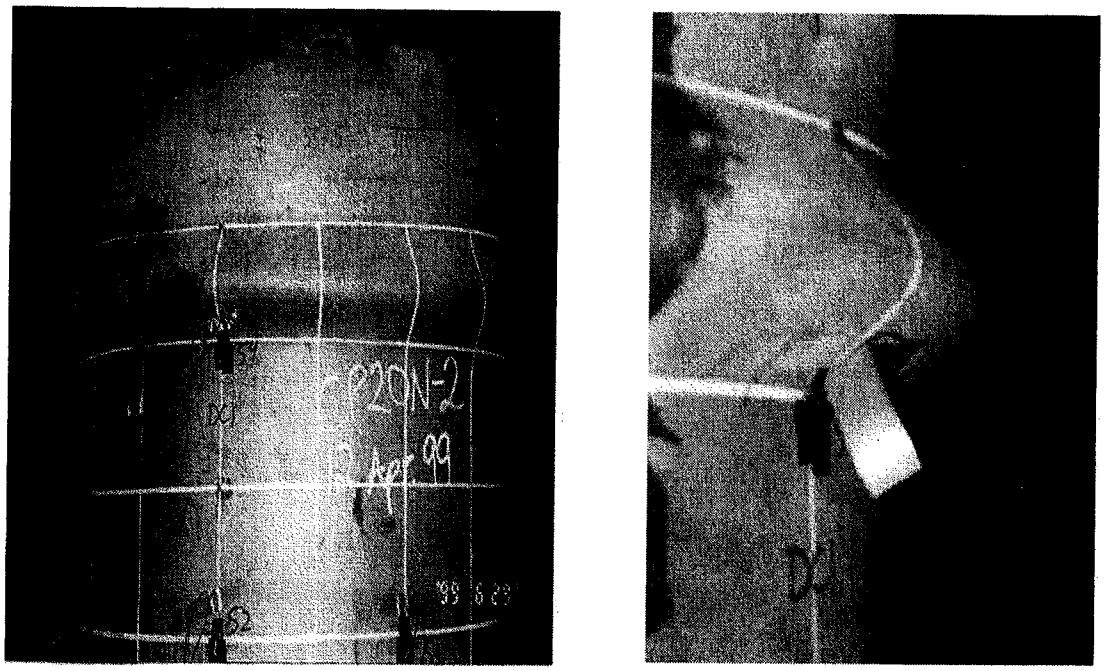

Front View Profile

Figure 4.27 – Photograph of Experimental Buckling Mode for Specimen CP20N-2

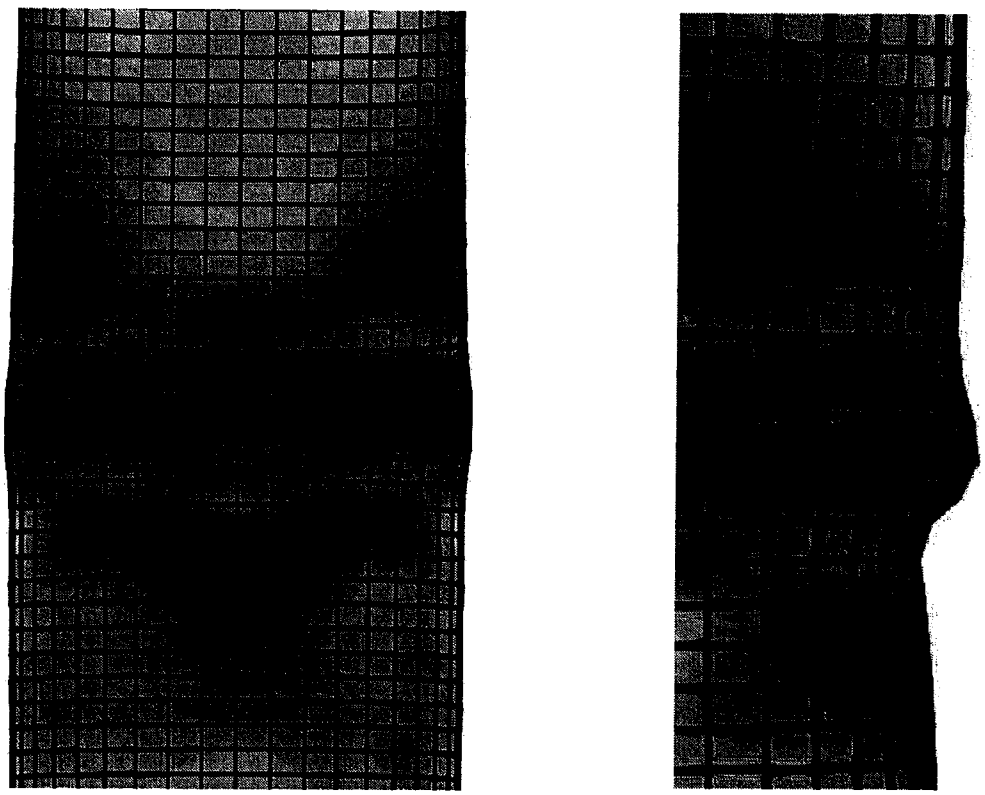

Front View Profile

Figure 4.28 – FEA Model Generated Buckling Mode for Specimen CP20N-2

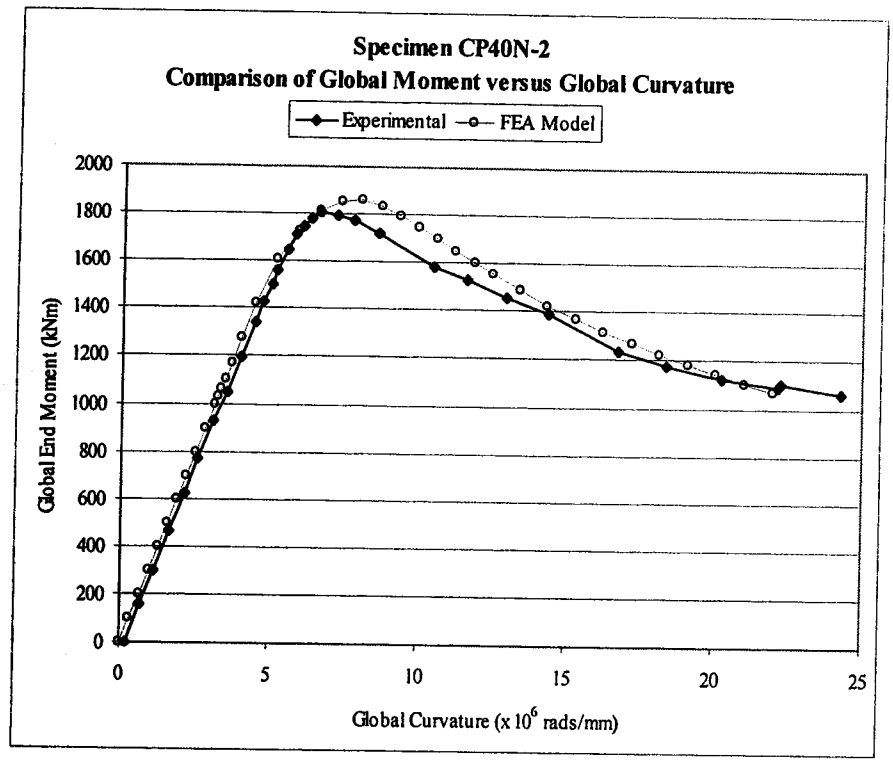

Figure 4.29 – Global Moment versus Global Curvature Comparison for Specimen CP40N-2

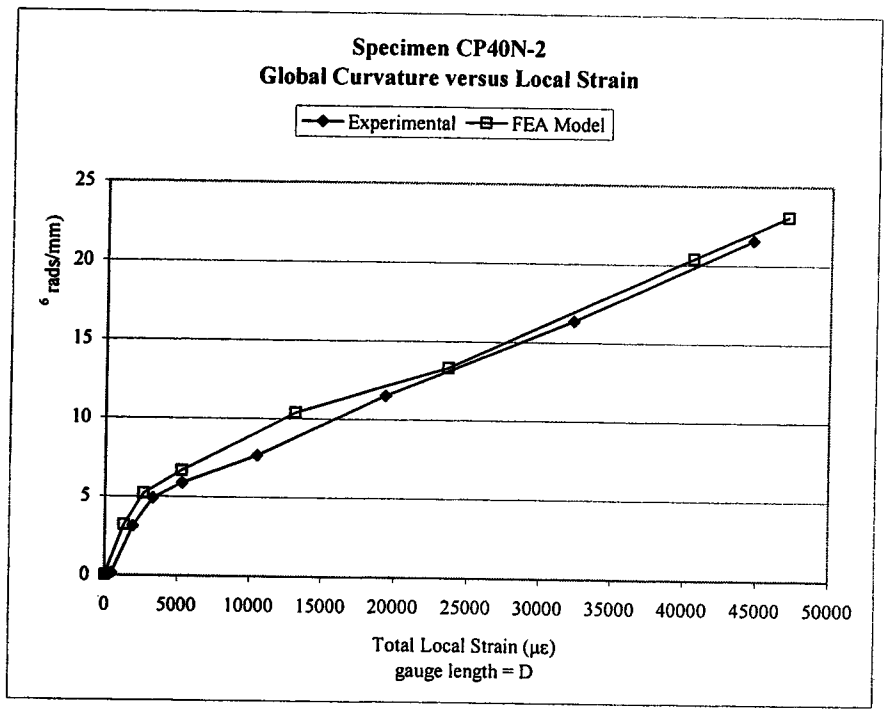

Figure 4.30 – Global Curvature versus Local Strain Comparison for Specimen CP40N-2

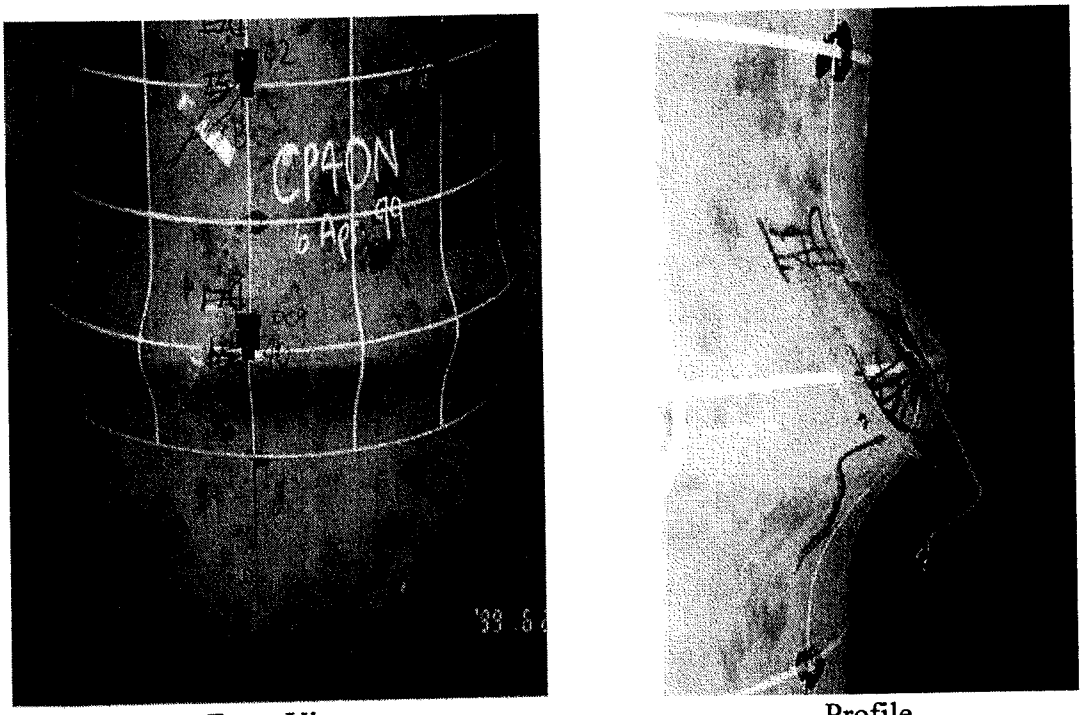

Front View Profile

Figure 4.31 – Photograph of Experimental Buckling Mode for Specimen CP40N-2

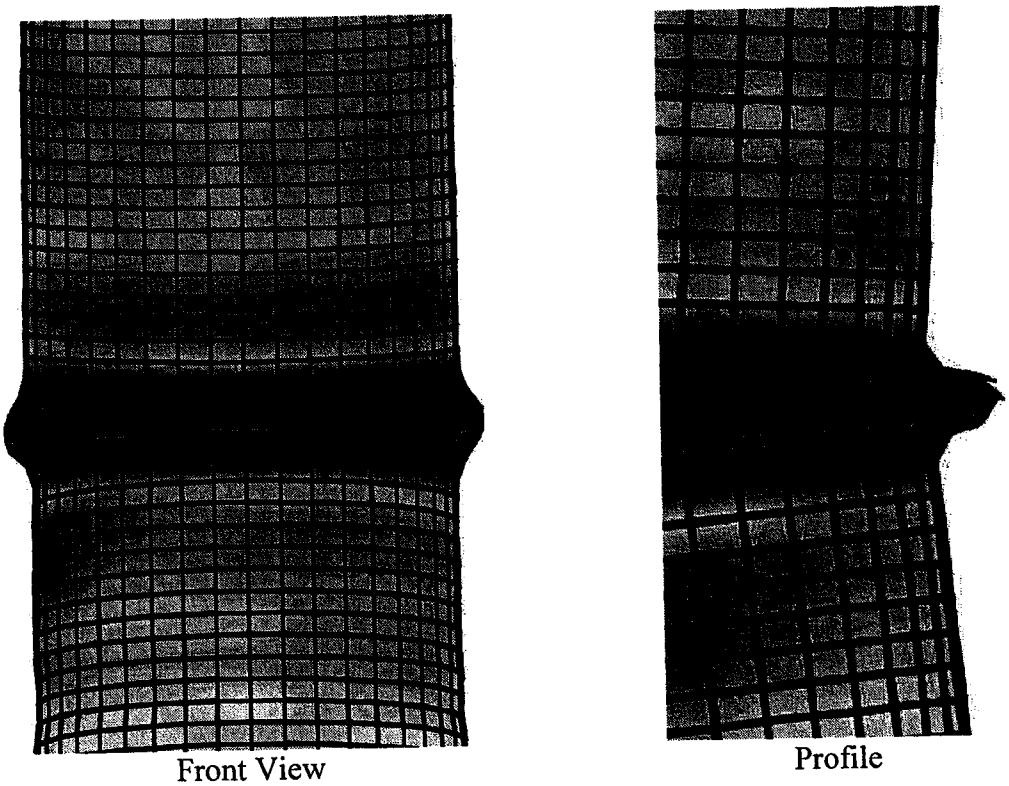

Front View Profile

Figure 4.32 – FEA Model Generated Buckling Mode for Specimen CP40N-2

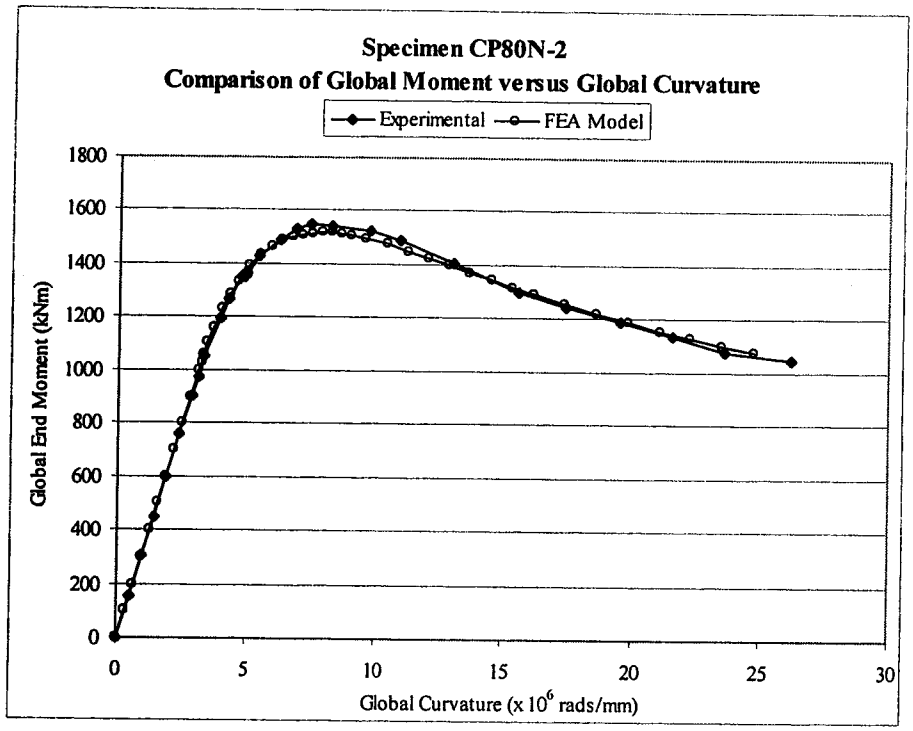

Figure 4.33 – Global Moment versus Global Curvature Comparison for Specimen CP80N-2

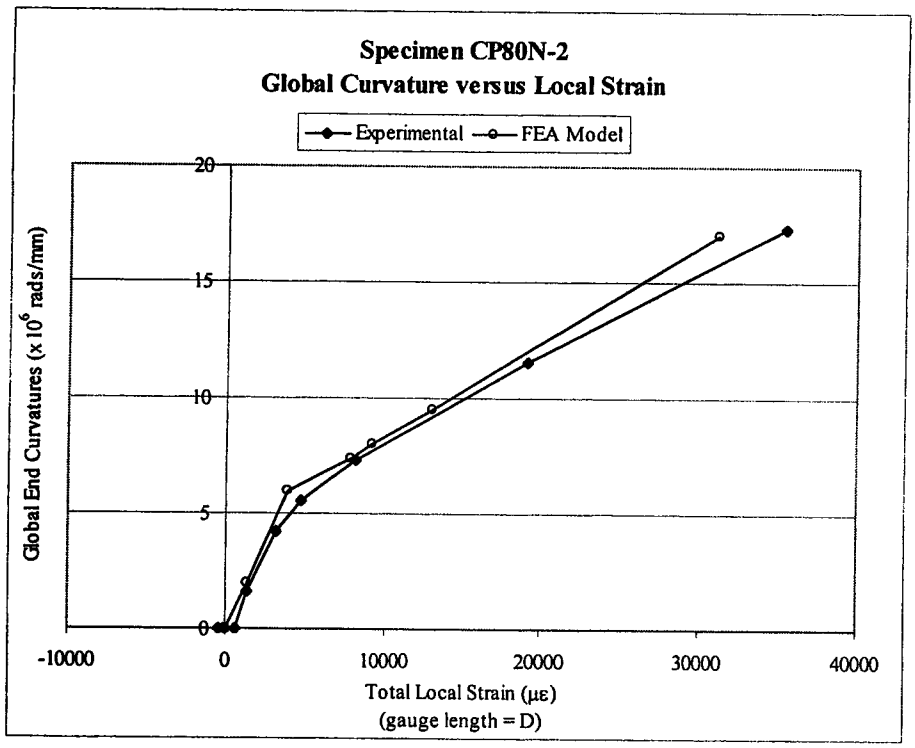

Figure 4.34 – Global Curvature versus Local Strain Comparison for Specimen CP80N-2

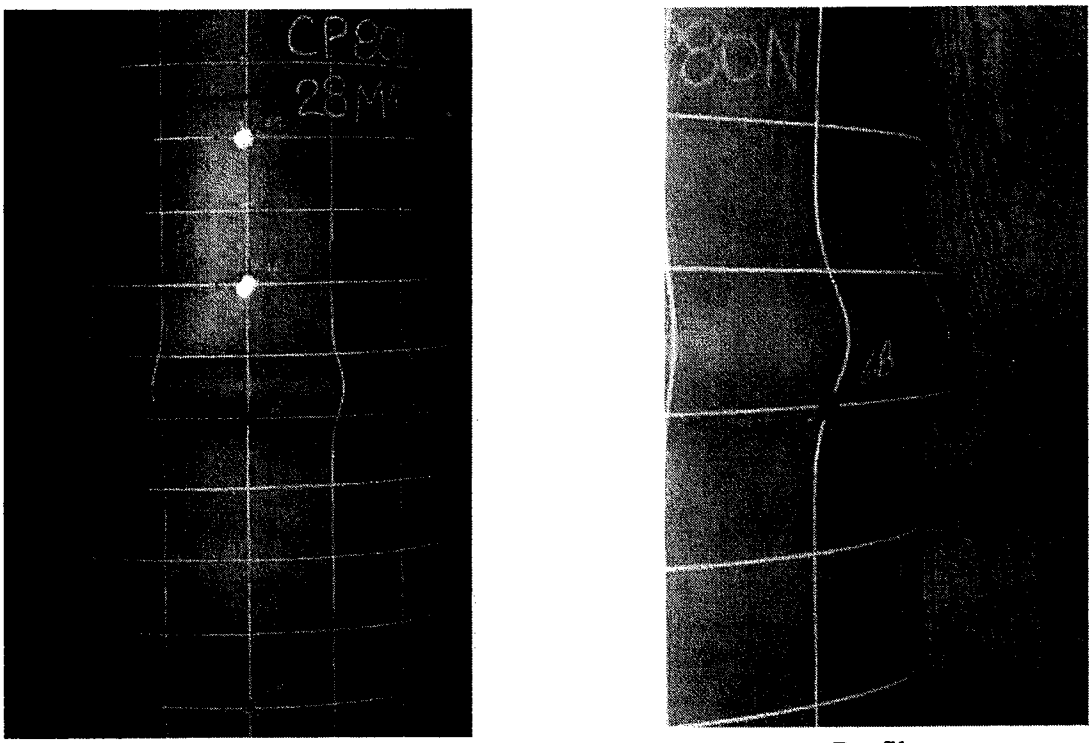

Front View Profile

Figure 4.35 – Photograph of Experimental Buckling Mode for Specimen CP80N-2

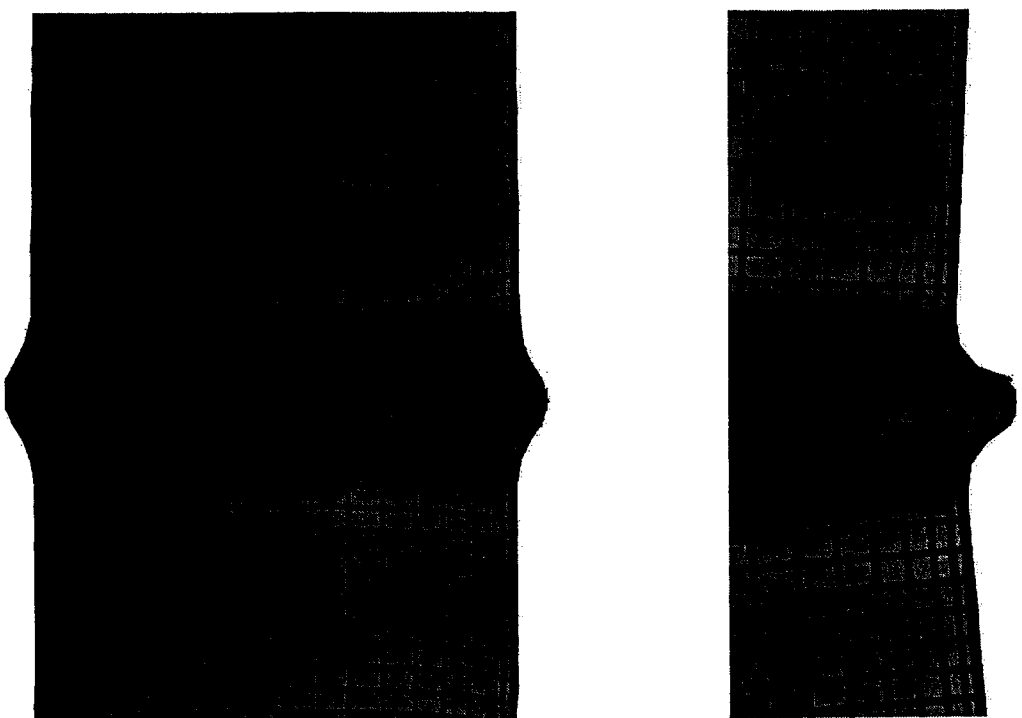

Front View Profile

Figure 4.36 – FEA Model Generated Buckling Mode for Specimen CP80N-2

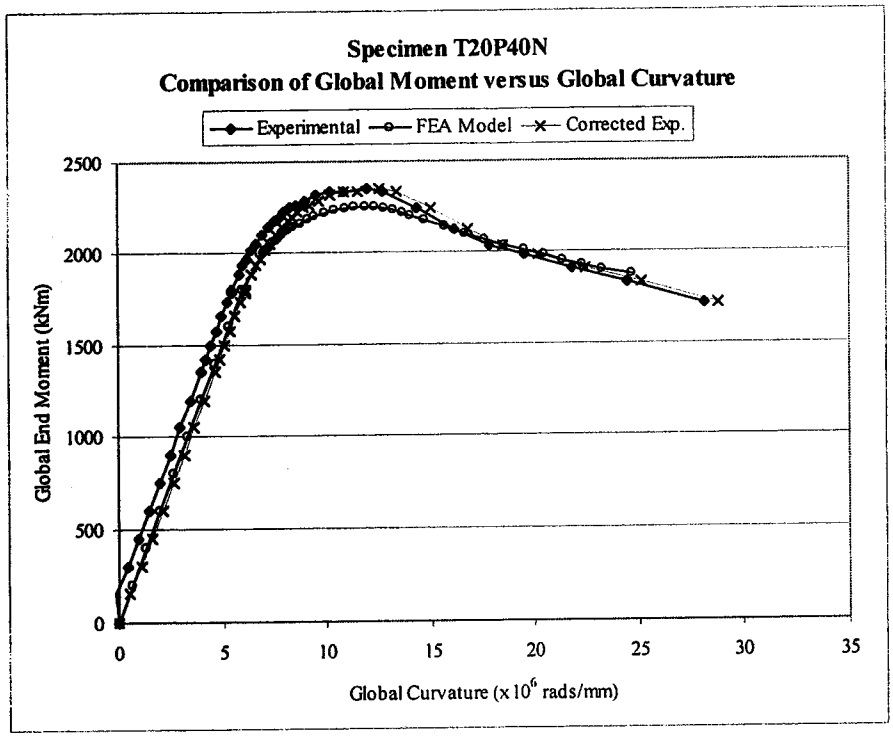

Figure 4.37 – Global Moment versus Global Curvature Comparison for Specimen T20P40N

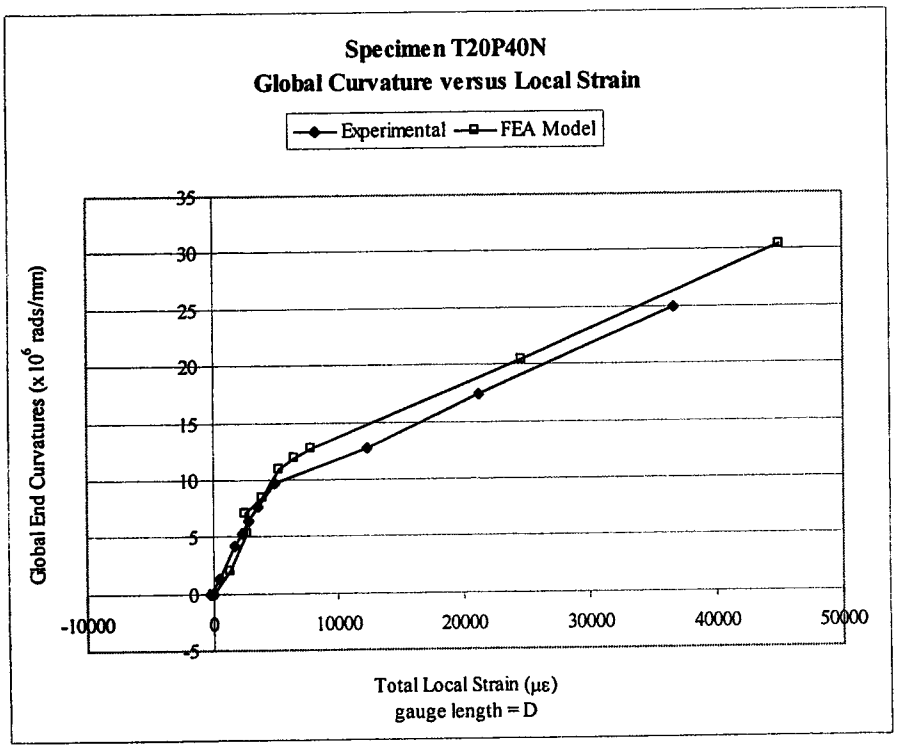

Figure 4.38 – Global Curvature versus Local Strain Comparison for Specimen T20P40N

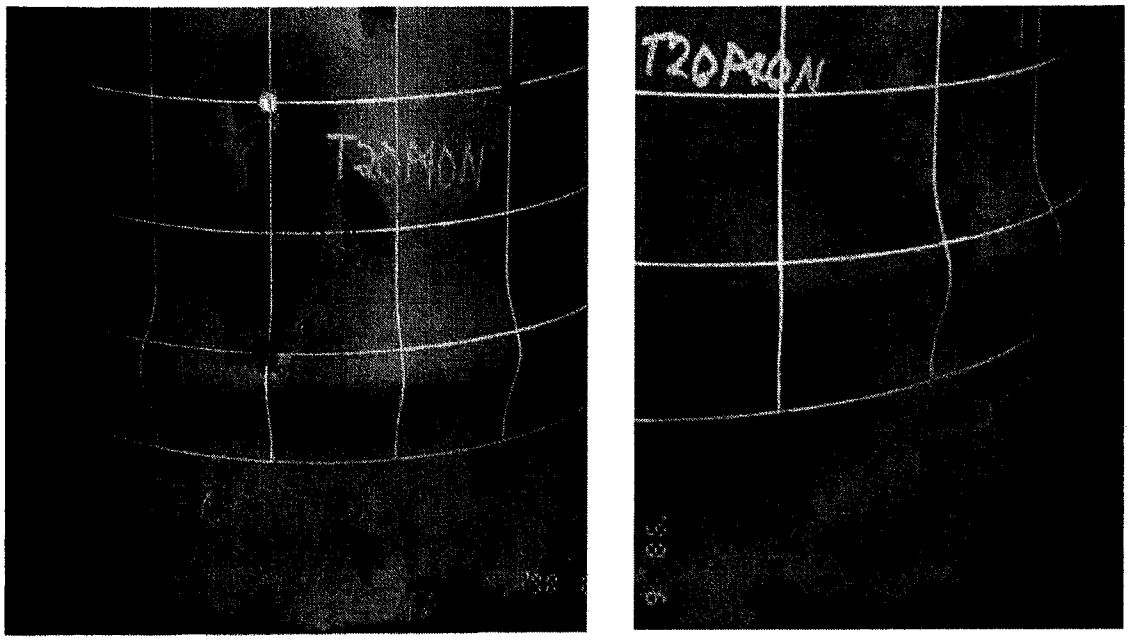

Front View Profile

Figure 4.39 – Photograph of Experimental Buckling Mode for Specimen T20P40N

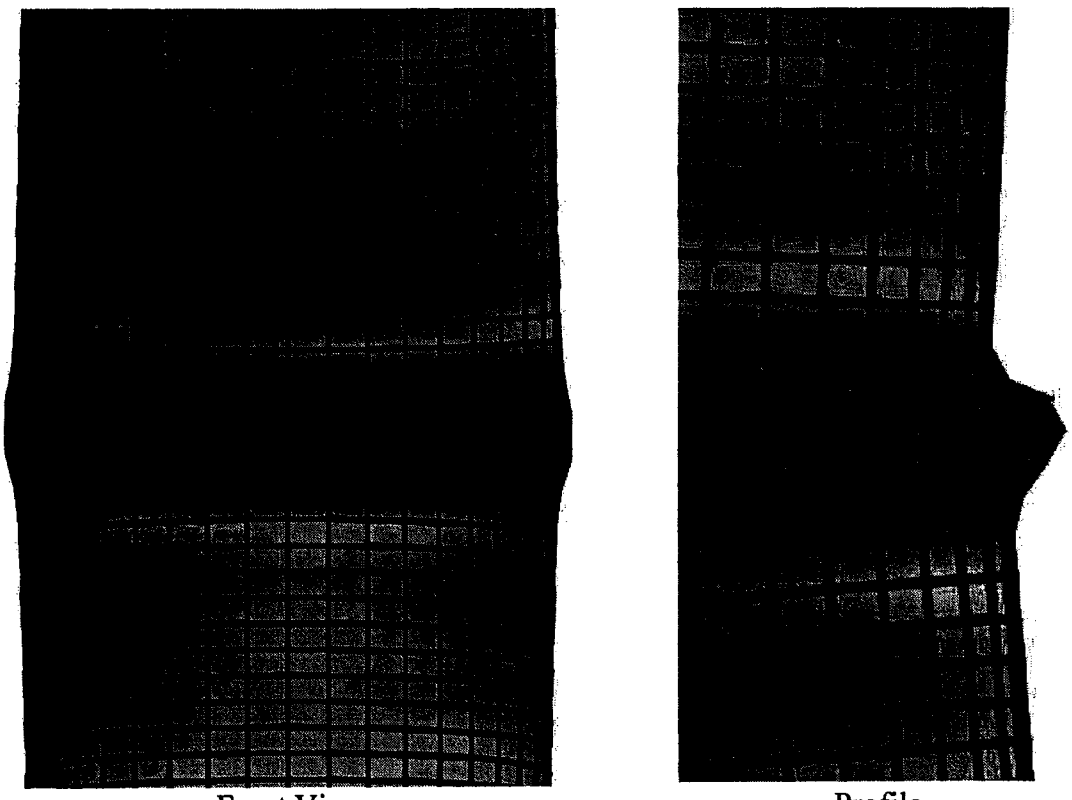

Front View Profile

Figure 4.40 – FEA Model Generated Buckling Mode for Specimen T20P40N

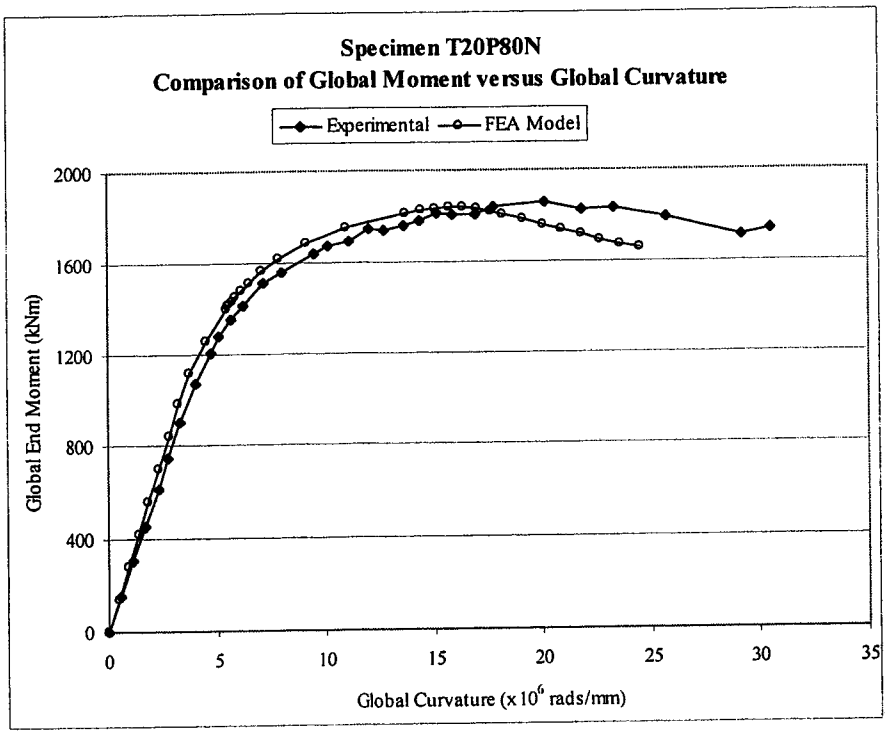

Figure 4.41 – Global Moment versus Global Curvature Comparison for Specimen T20P80N

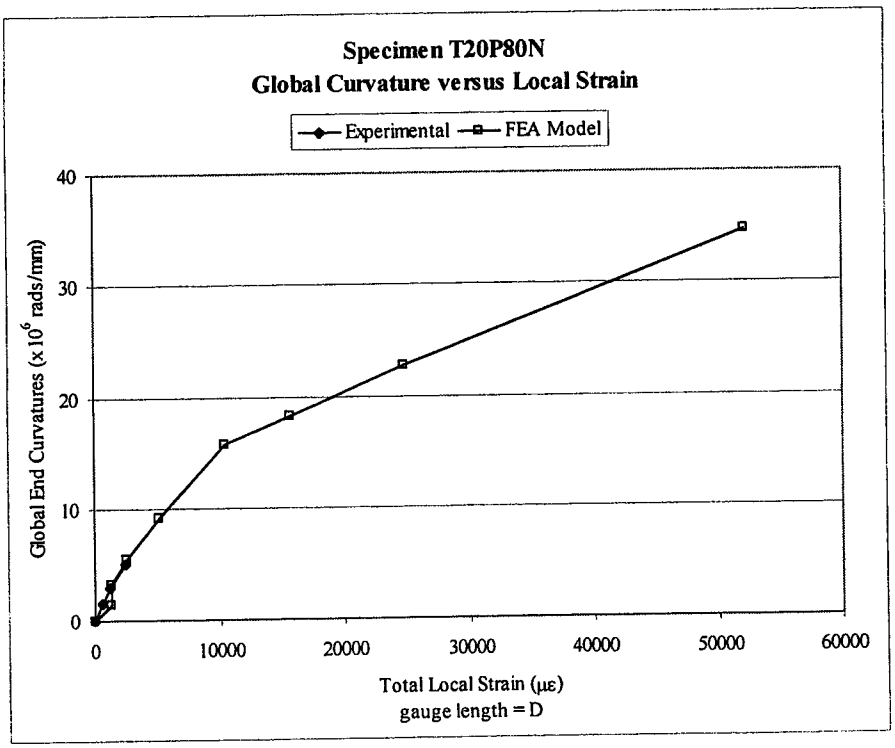

Figure 4.42 – Global Curvature versus Local Strain Comparison for Specimen T20P80N

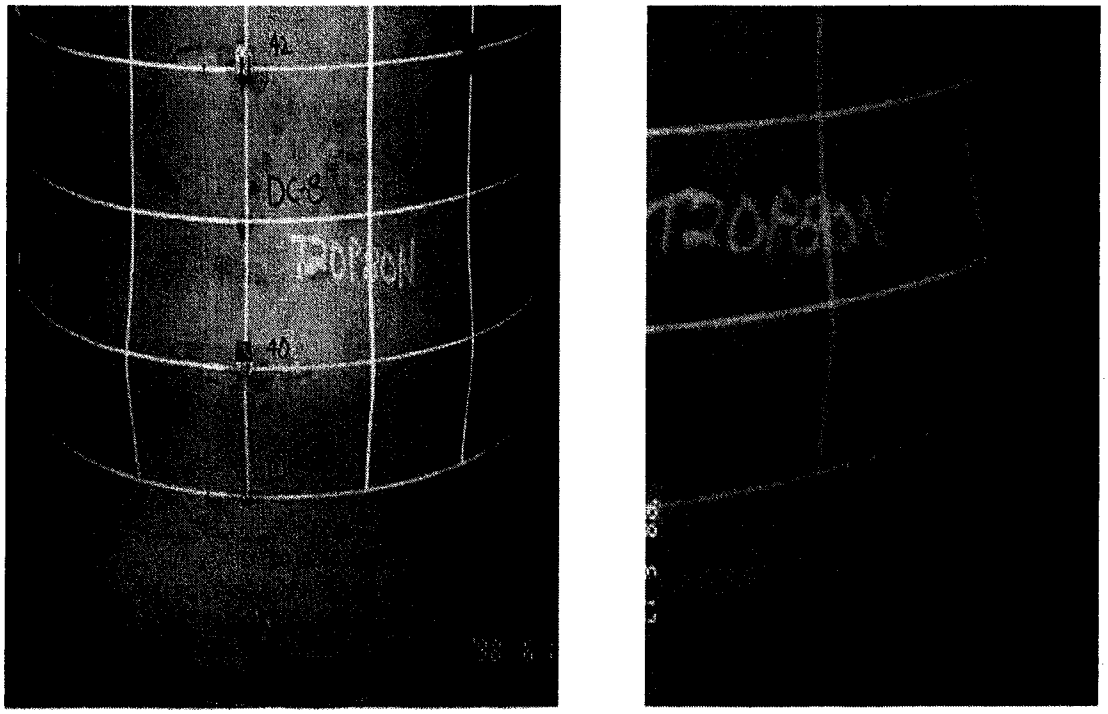

Front View Profile

Figure 4.43 – Photograph of Experimental Buckling Mode for Specimen T20P80N

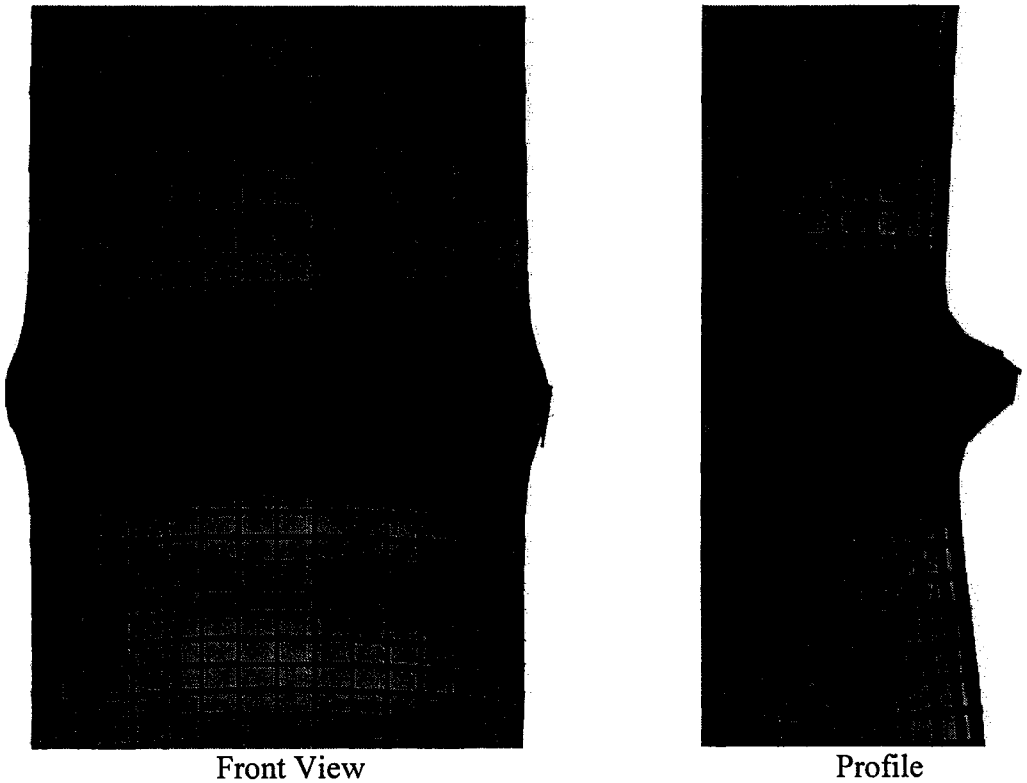

Front View Profile

Figure 4.44 – FEA Model Generated Buckling Mode for Specimen T20P80N

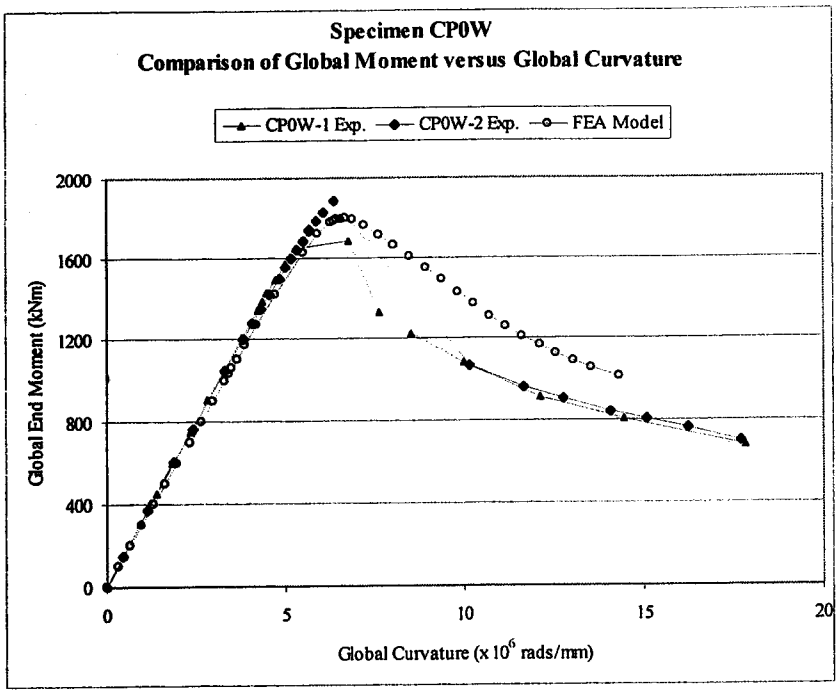

Figure 4.45 – Global Moment versus Global Curvature Comparison for Specimens CP0W-1 & -2

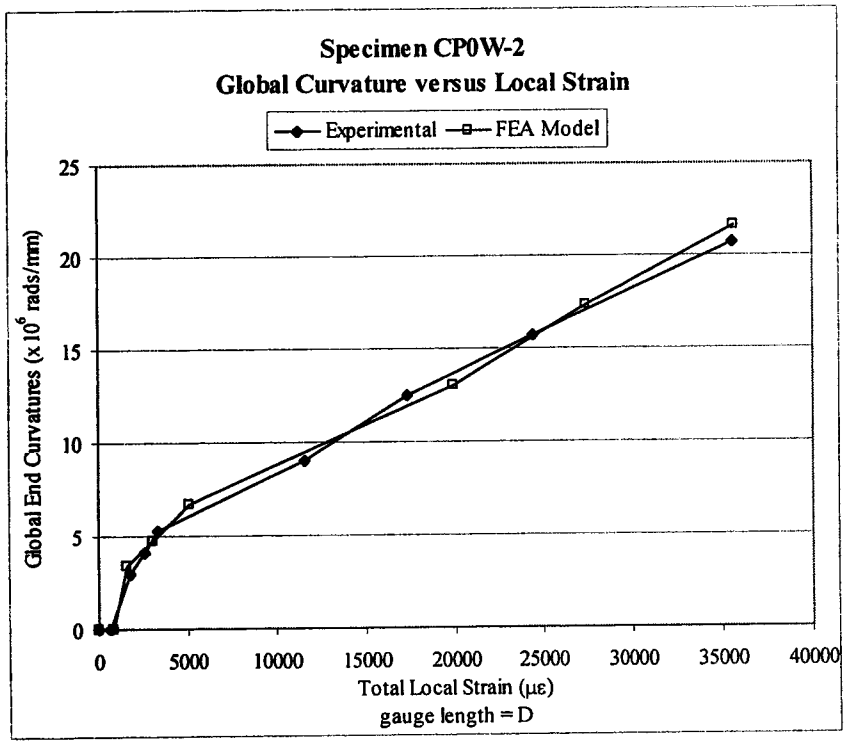

Figure 4.46 – Global Curvature versus Local Strain Comparison for Specimens CP0W-1 & -2

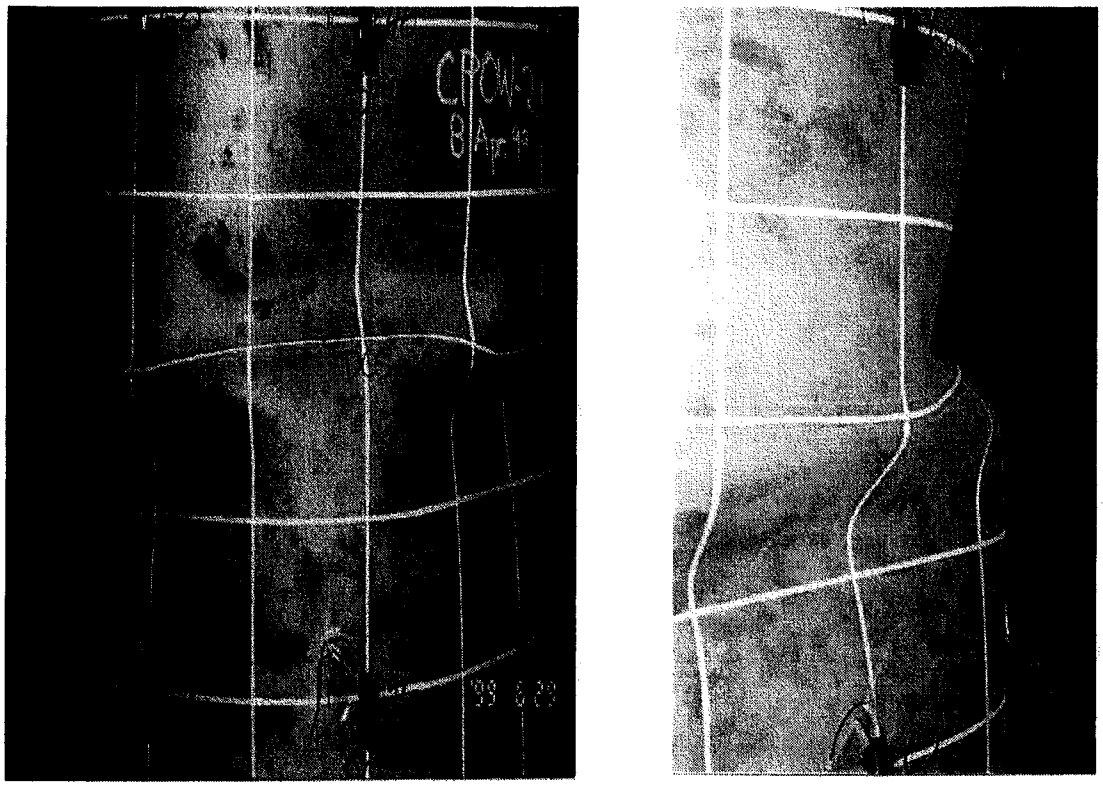

Front View Profile

Figure 4.47 – Photograph of Experimental Buckling Mode for Specimens CP0W-1 & -2

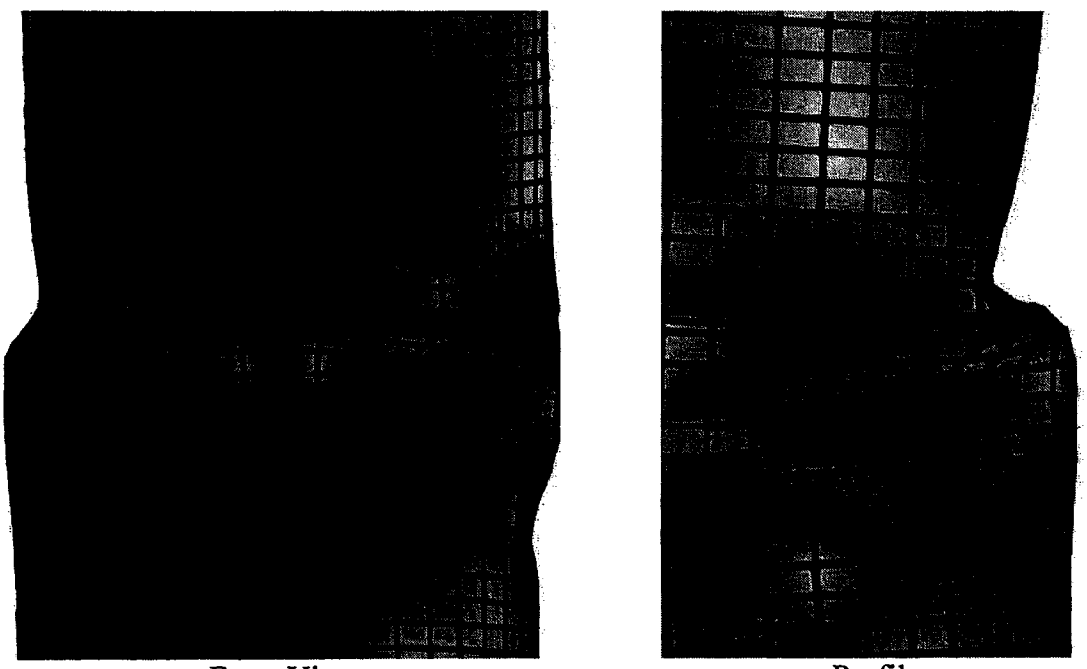

Front View Profile

Figure 4.48 – FEA Model Generated Buckling Mode for Specimens CP0W-1 & -2

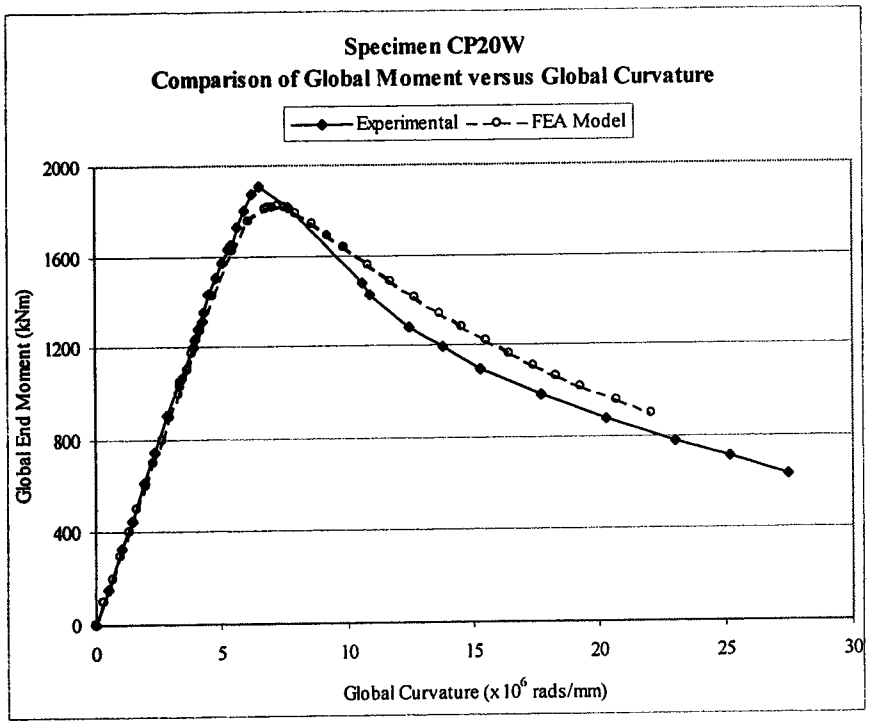

Figure 4.49 – Global Moment versus Global Curvature Comparison for Specimen CP20W

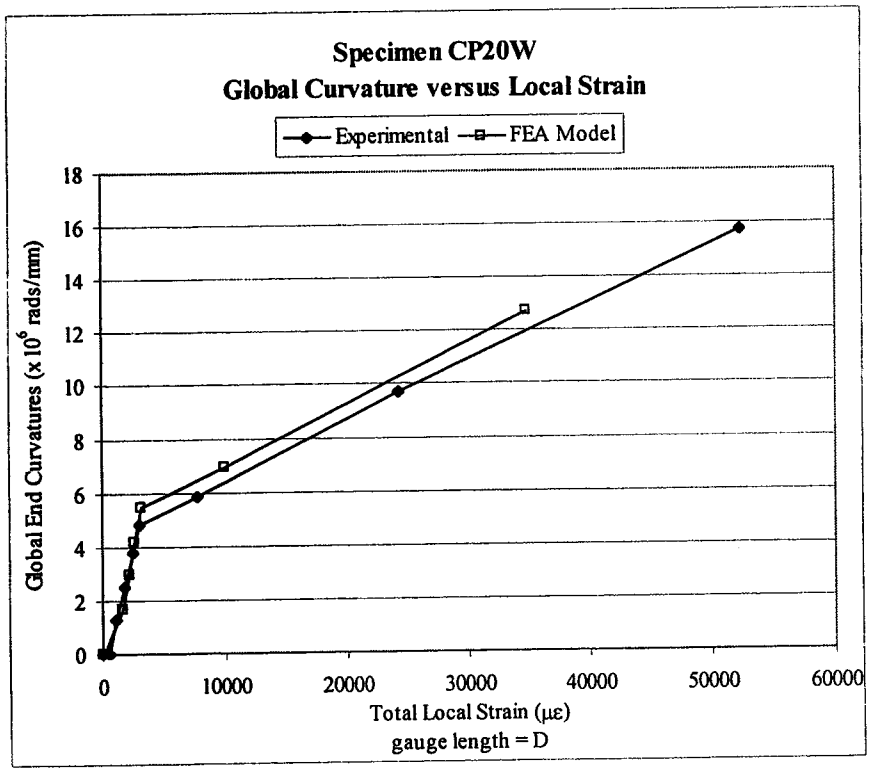

Figure 4.50 – Global Curvature versus Local Strain Comparison for Specimen CP20W

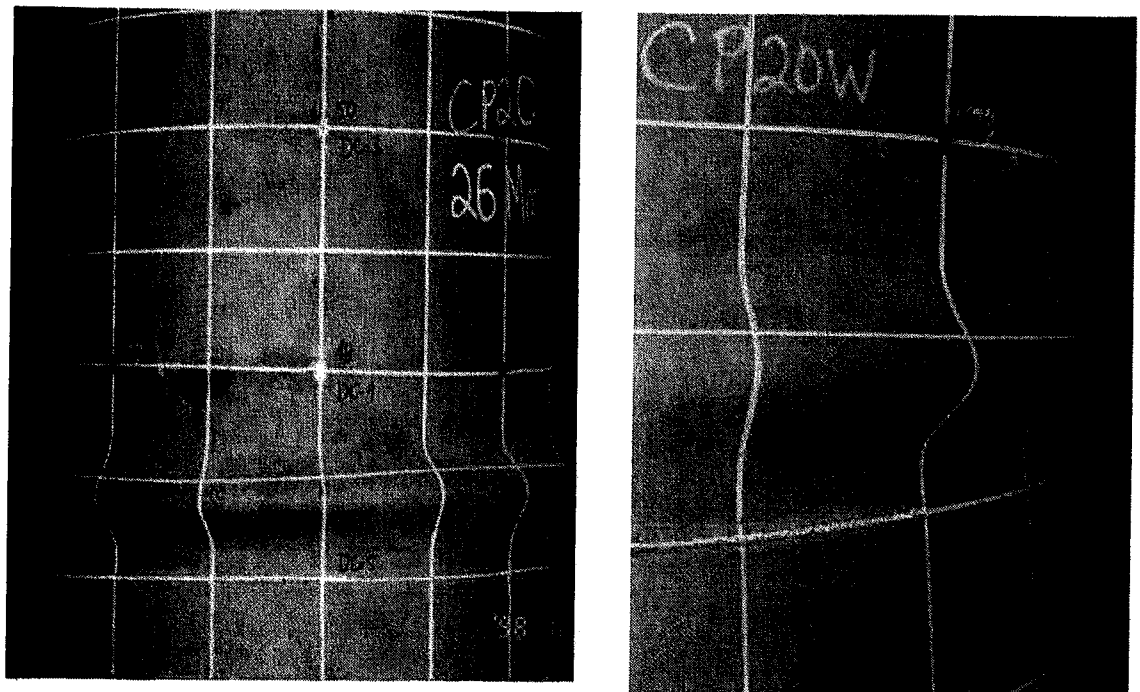

Front View Profile

Figure 4.51 – Photograph of Experimental Buckling Mode for Specimen CP20W

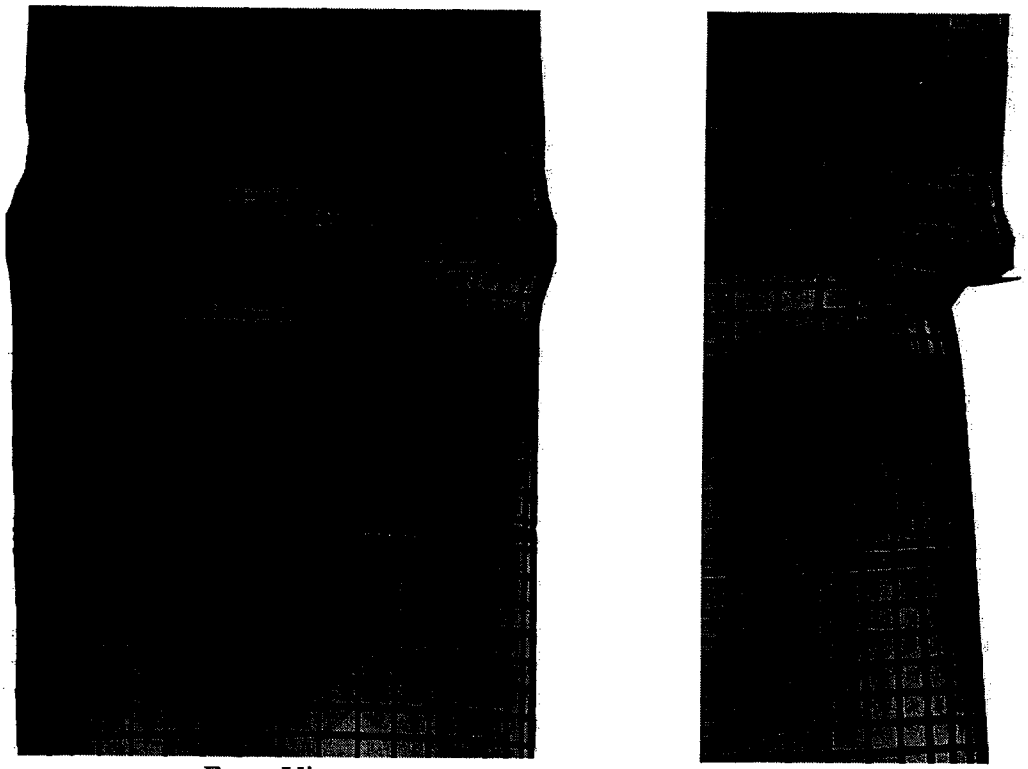

Front View Profile

Figure 4.52 – FEA Model Generated Buckling Mode for Specimen CP20W

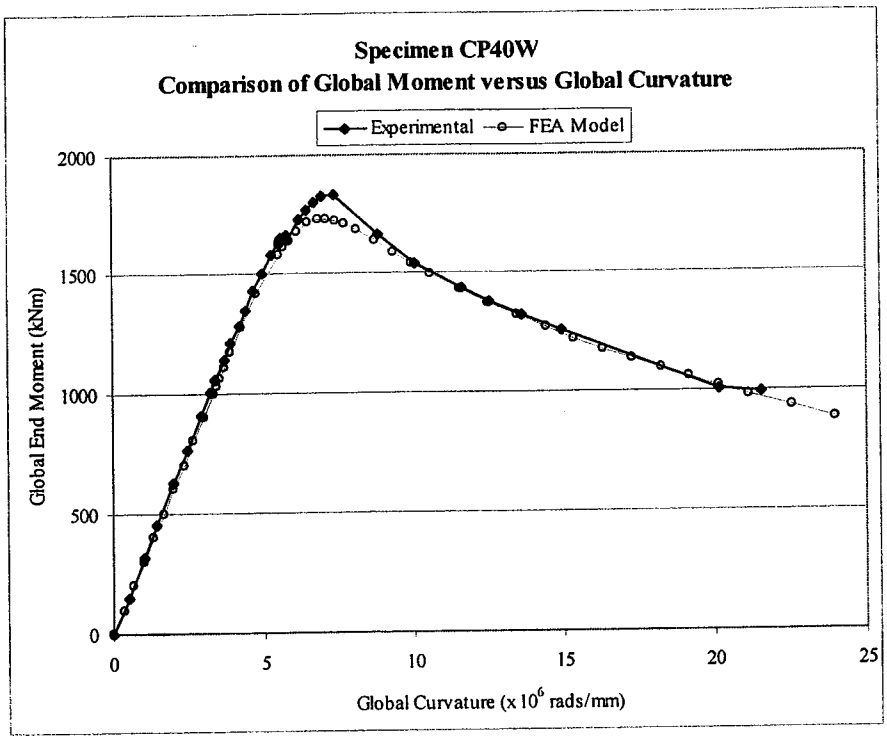

Figure 4.53 – Global Moment versus Global Curvature Comparison for Specimen CP40W

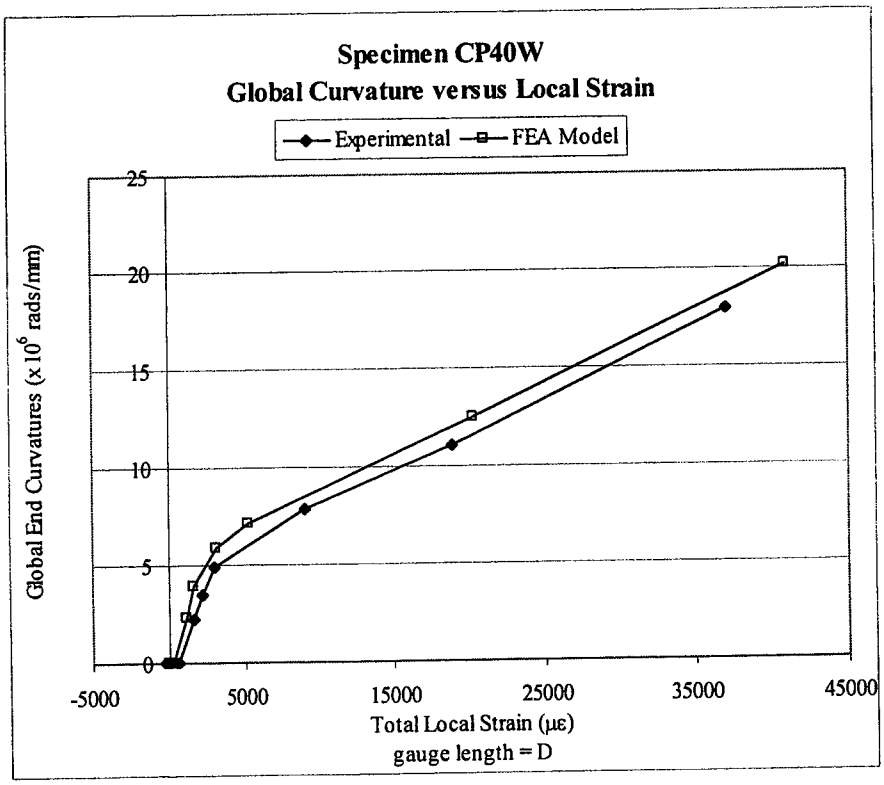

Figure 4.54 – Global Curvature versus Local Strain Comparison for Specimen CP40W

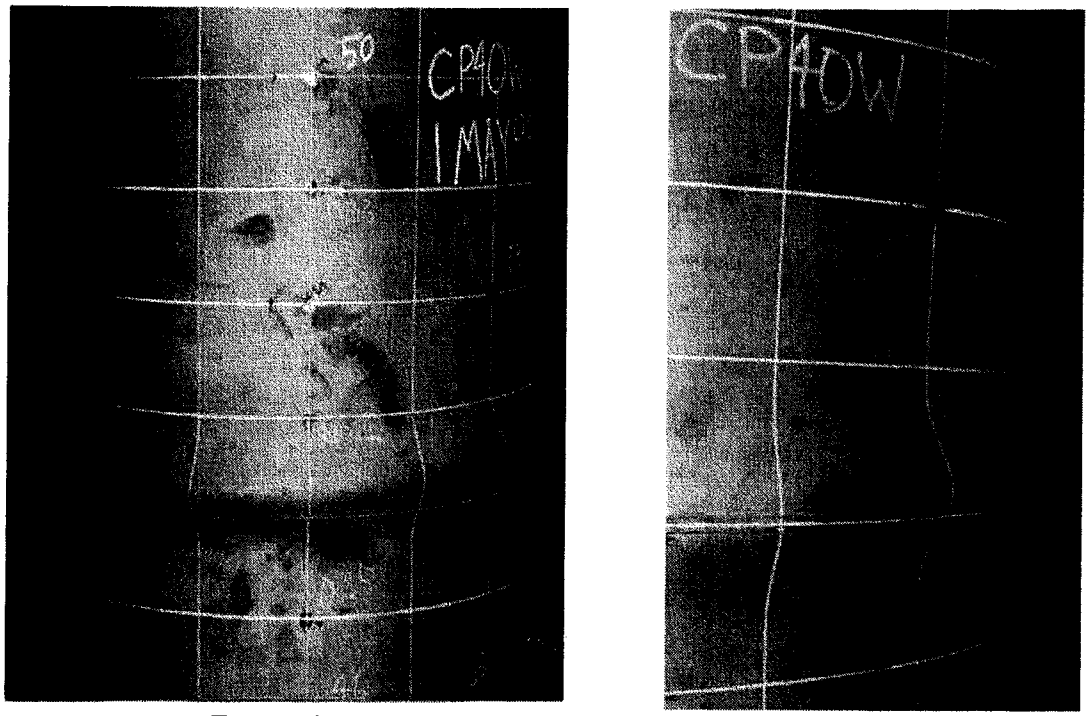

Front View Profile

Figure 4.55 – Photograph of Experimental Buckling Mode for Specimen CP40W

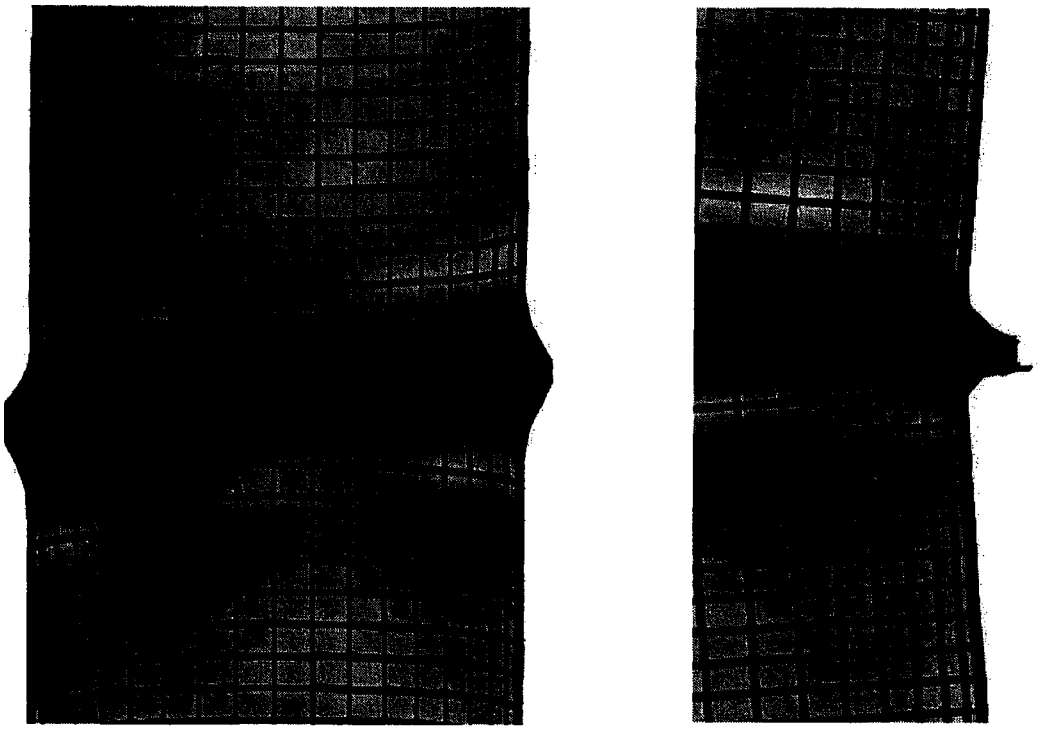

Front View Profile

Figure 4.56 – FEA Model Generated Buckling Mode for Specimen CP40W

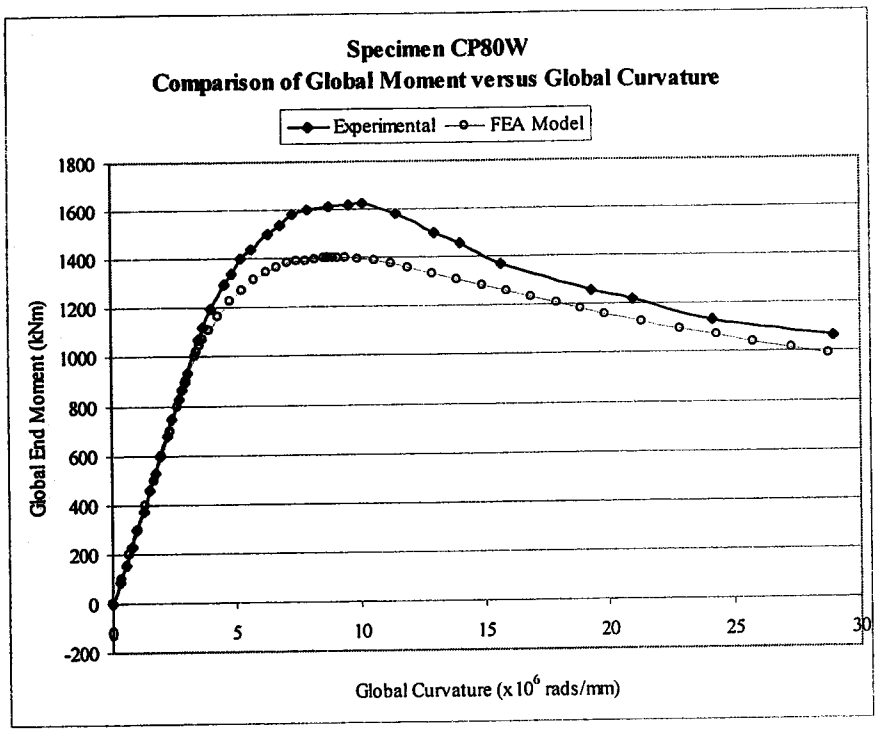

Figure 4.57 – Global Moment versus Global Curvature Comparison for Specimen CP80W

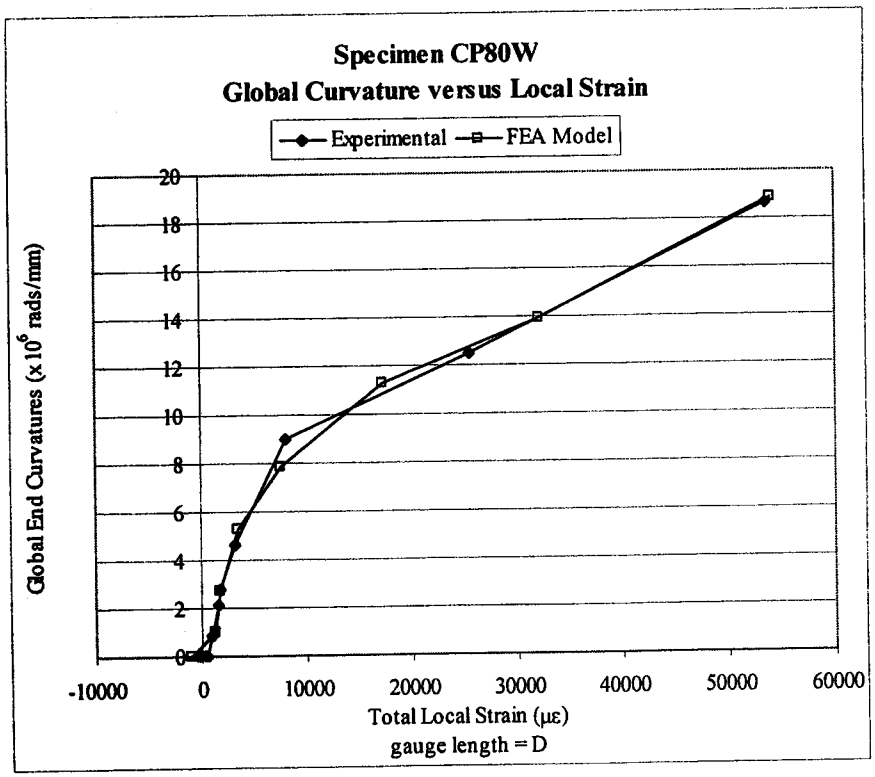

Figure 4.58 – Global Curvature versus Local Strain Comparison for Specimen CP80W

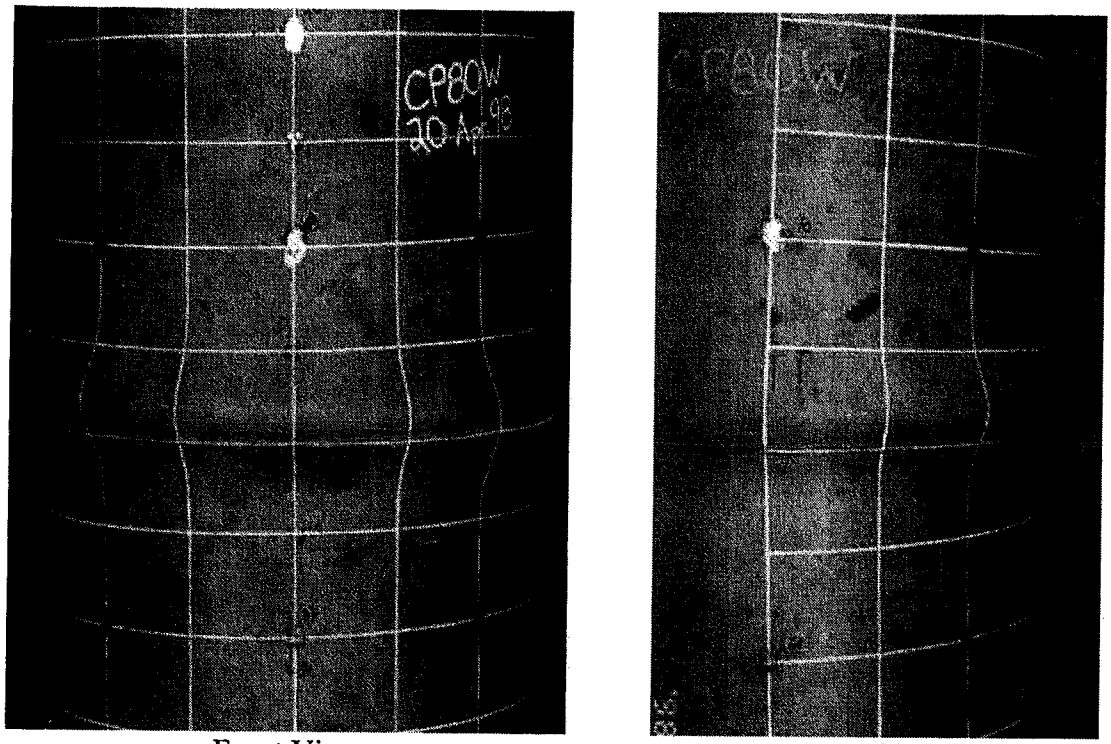

Front View Profile

Figure 4.59 – Photograph of Experimental Buckling Mode for Specimen CP80W

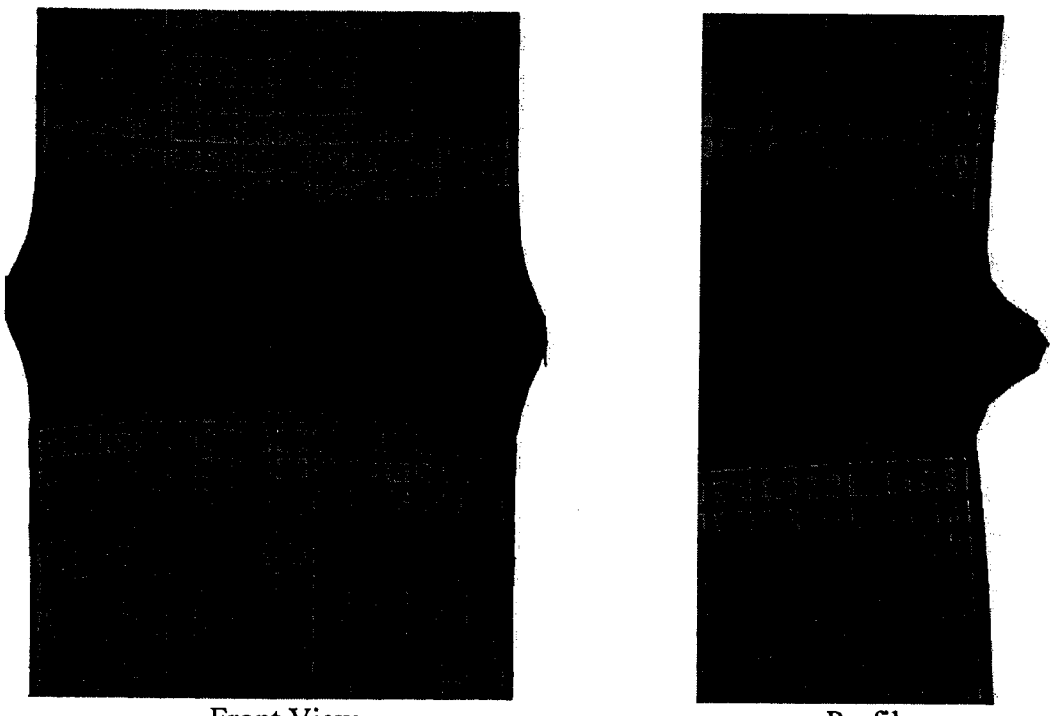

Front View Profile

Figure 4.60 – FEA Model Generated Buckling Mode for Specimen CP80W

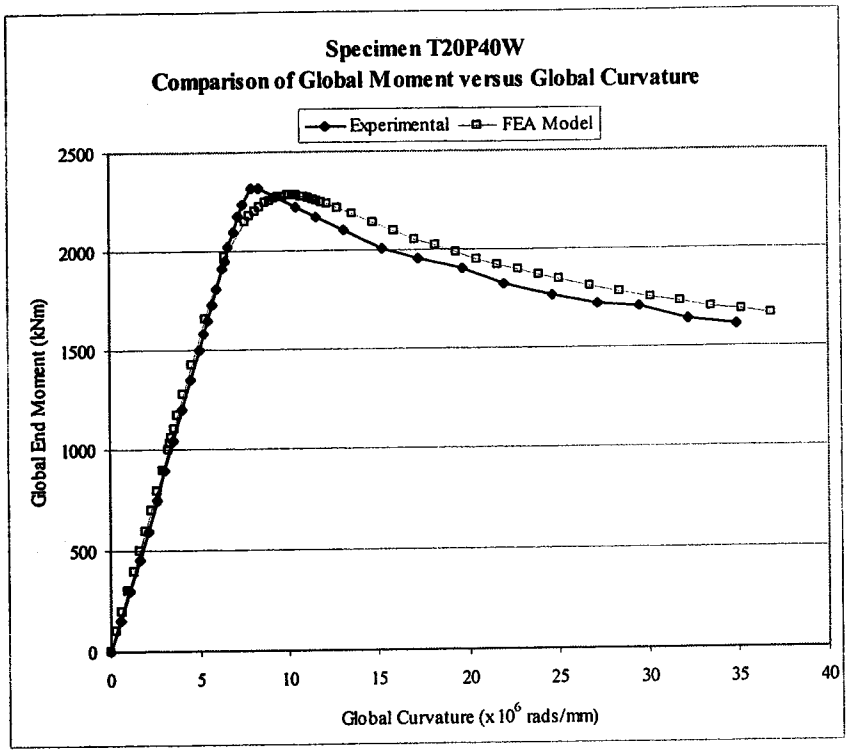

Figure 4.61 – Global Moment versus Global Curvature Comparison for Specimen T20P40W

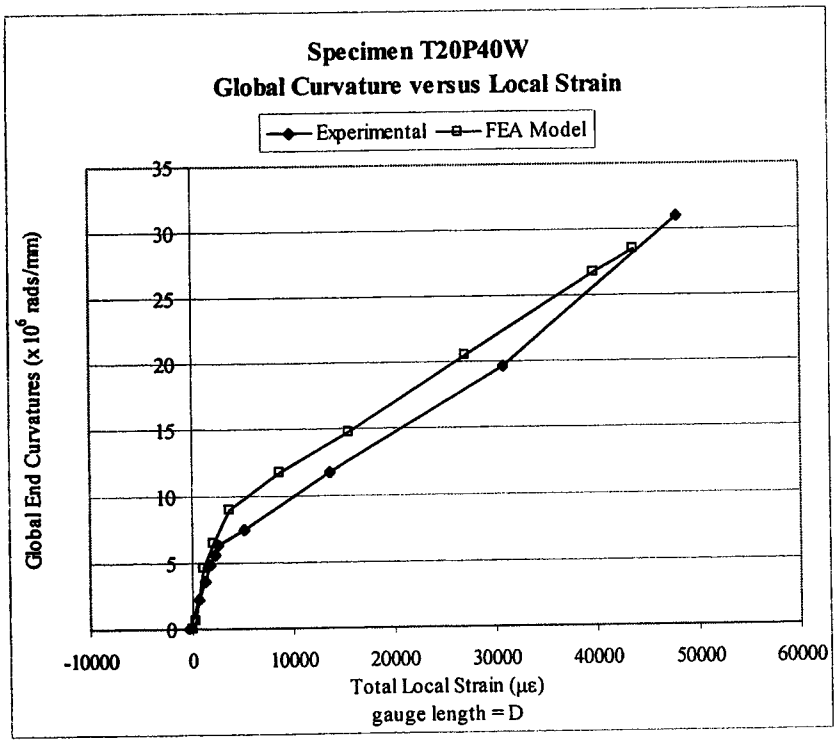

Figure 4.62 – Global Curvature versus Local Strain Comparison for Specimen T20P40W

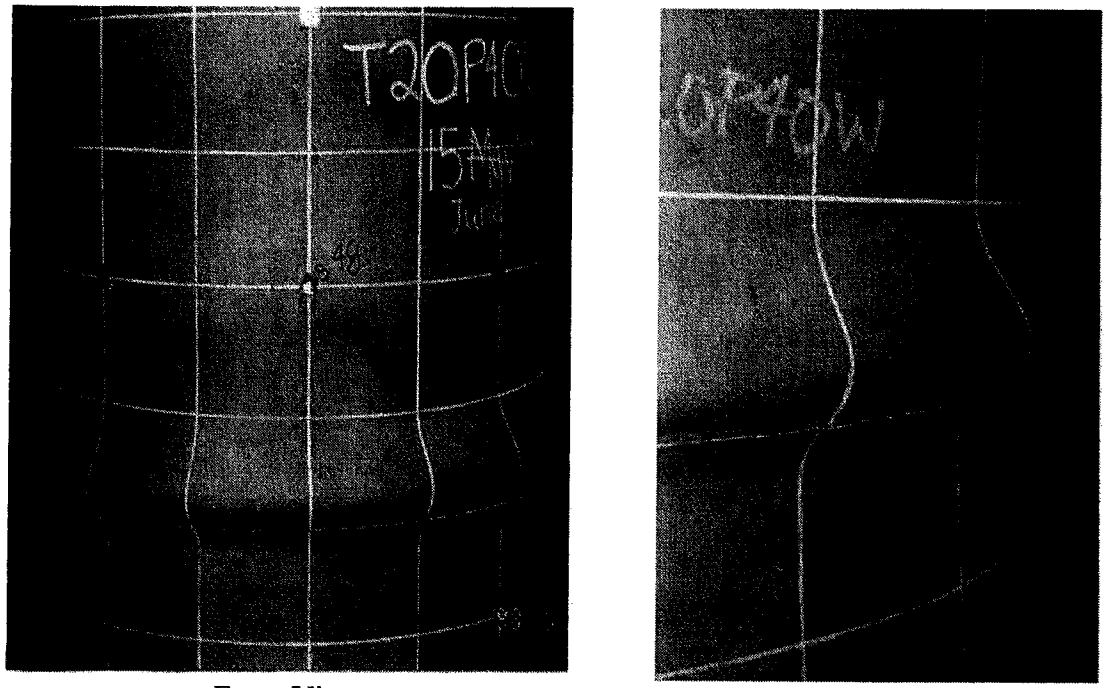

Front View Profile

Figure 4.63 – Photograph of Experimental Buckling Mode for Specimen T20P40W

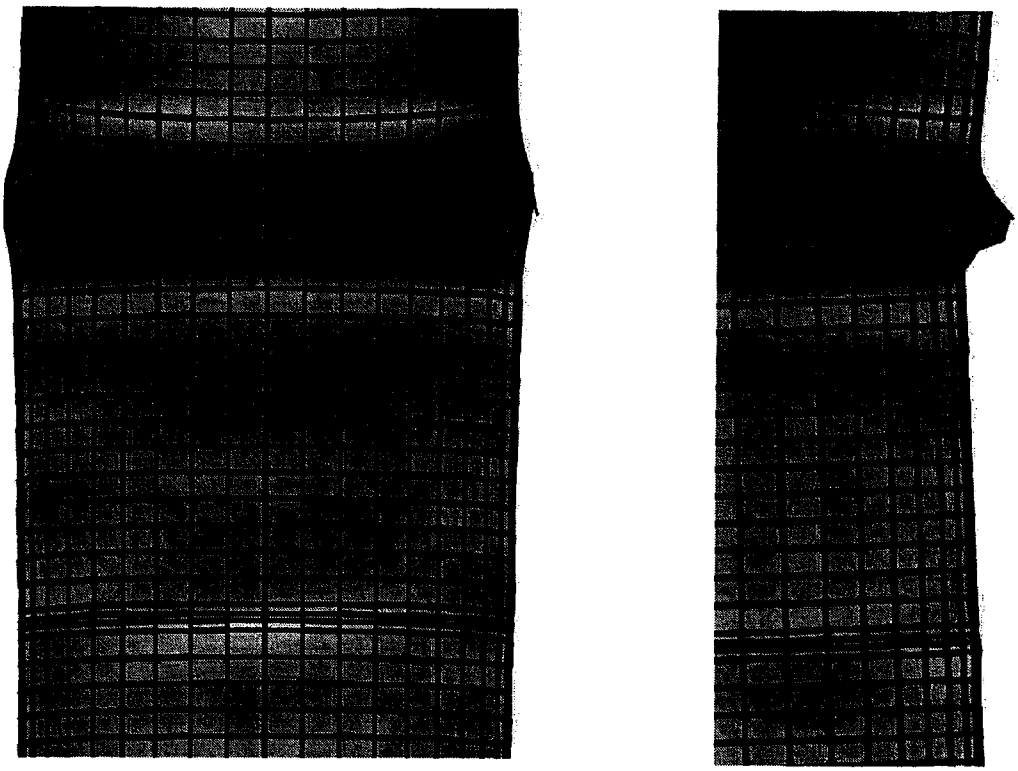

Front View Profile

Figure 4.64 – FEA Model Generated Buckling Mode for Specimen T20P40W

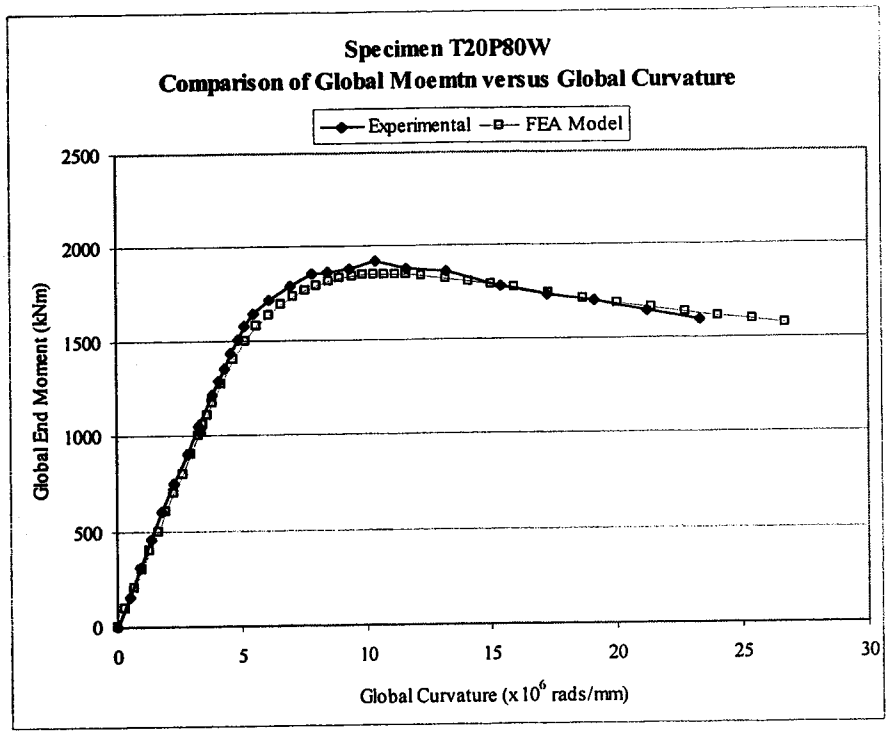

Figure 4.65 – Global Moment versus Global Curvature Comparison for Specimen T20P80W

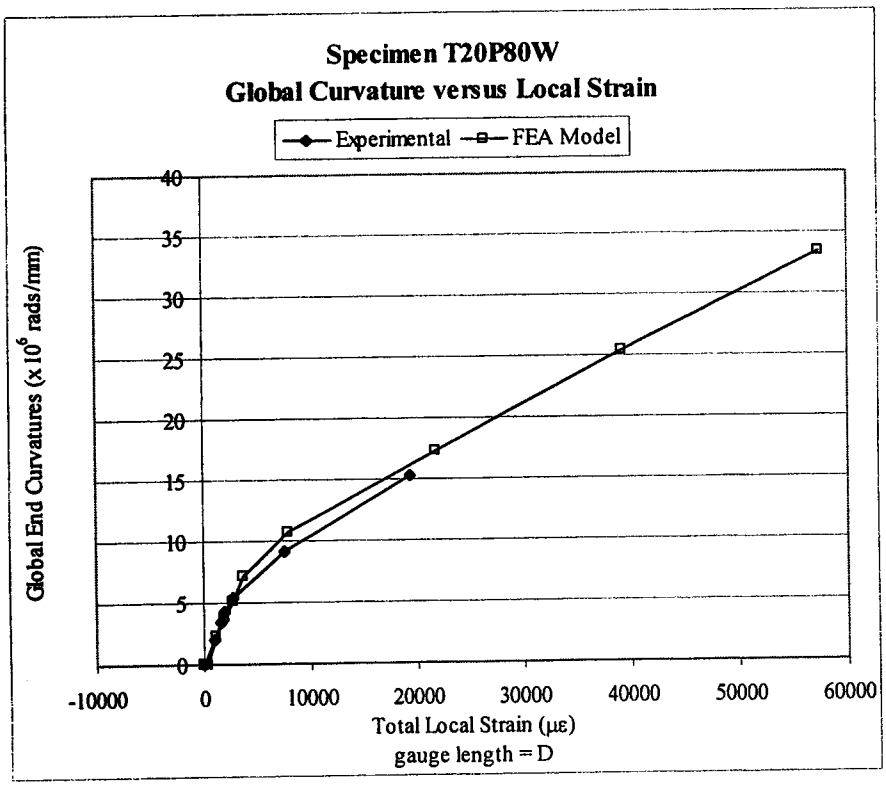

Figure 4.66 – Global Curvature versus Local Strain Comparison for Specimen T20P80W

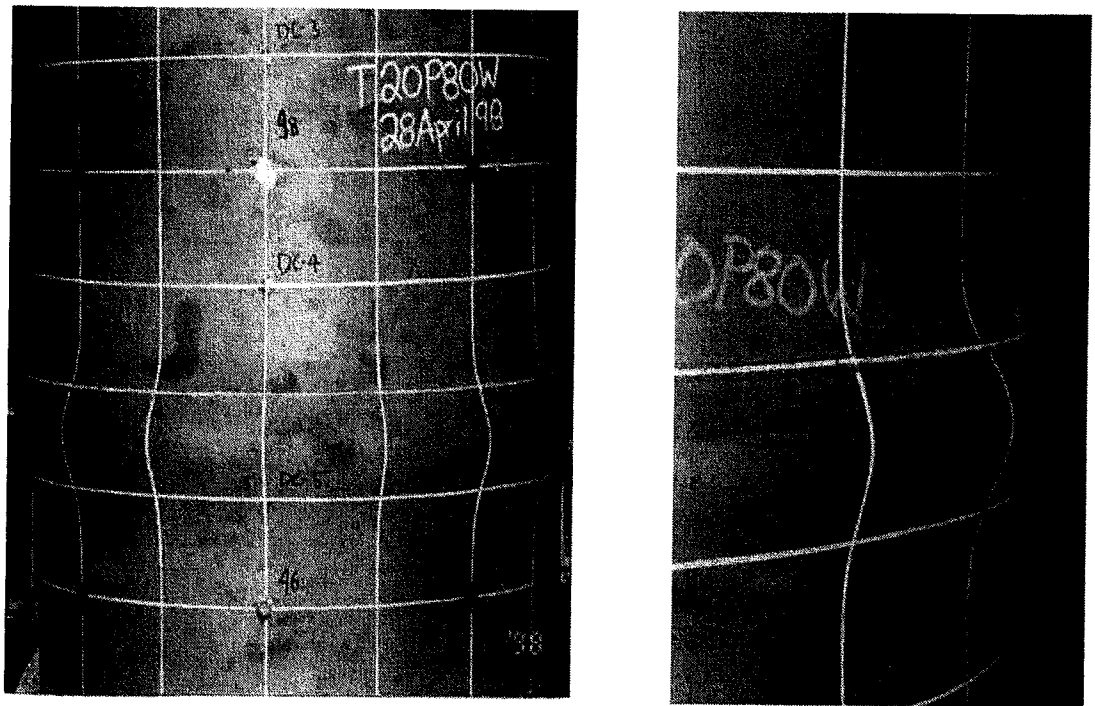

Front View Profile

Figure 4.67 – Photograph of Experimental Buckling Mode for Specimen T20P80W

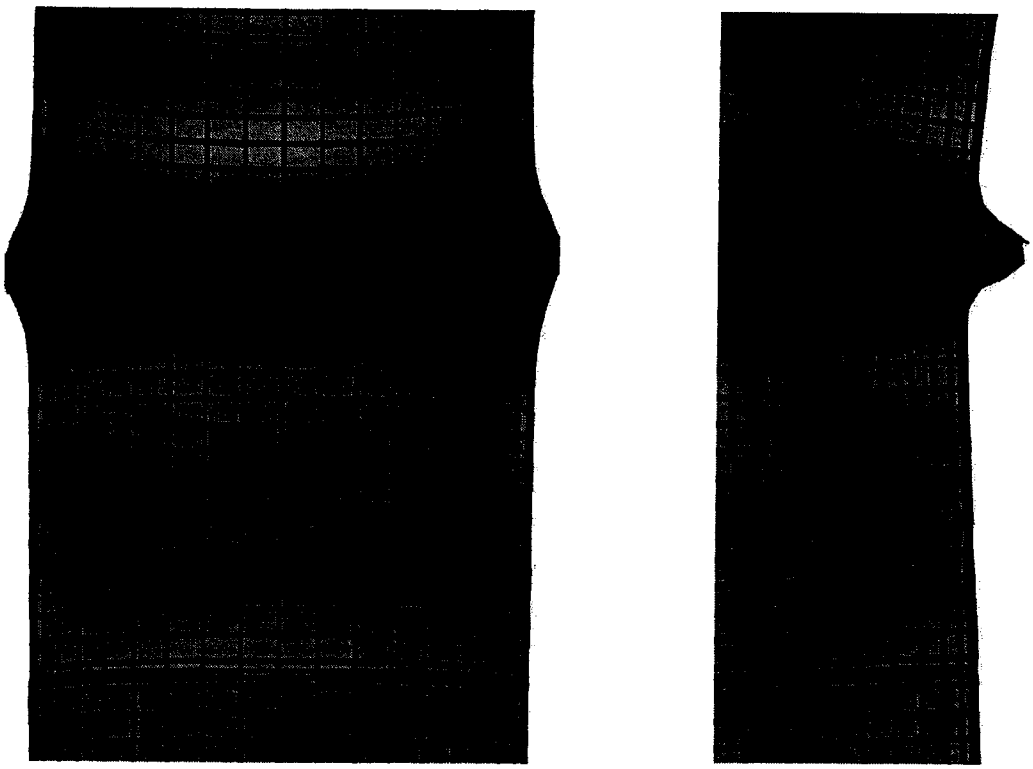

Front View Profile

Figure 4.68 – FEA Model Generated Buckling Mode for Specimen T20P80W

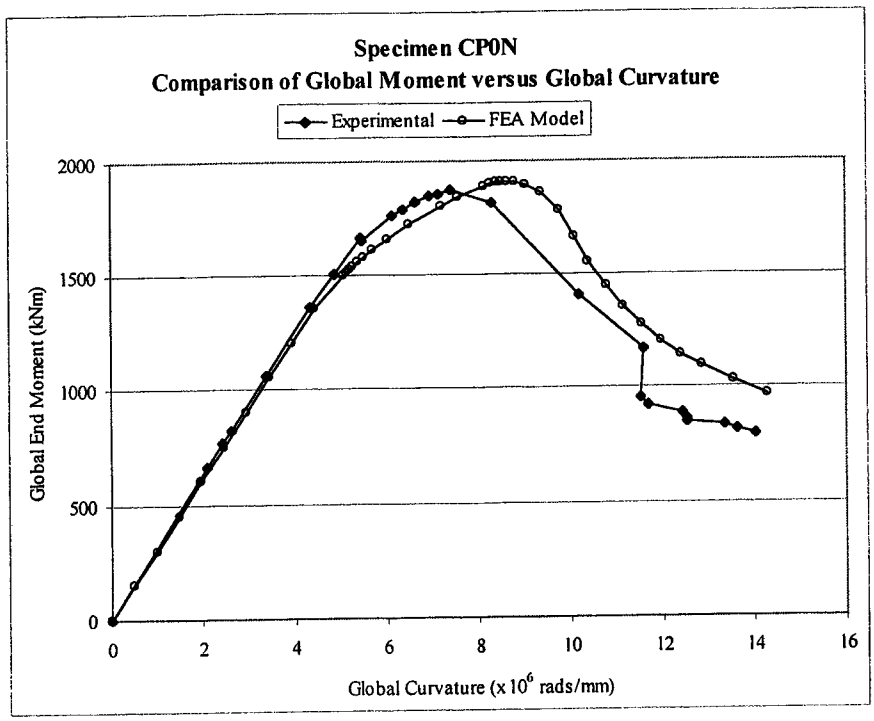

Figure 4.69 - Global Moment versus Global Curvature Comparison for Specimen CP0N

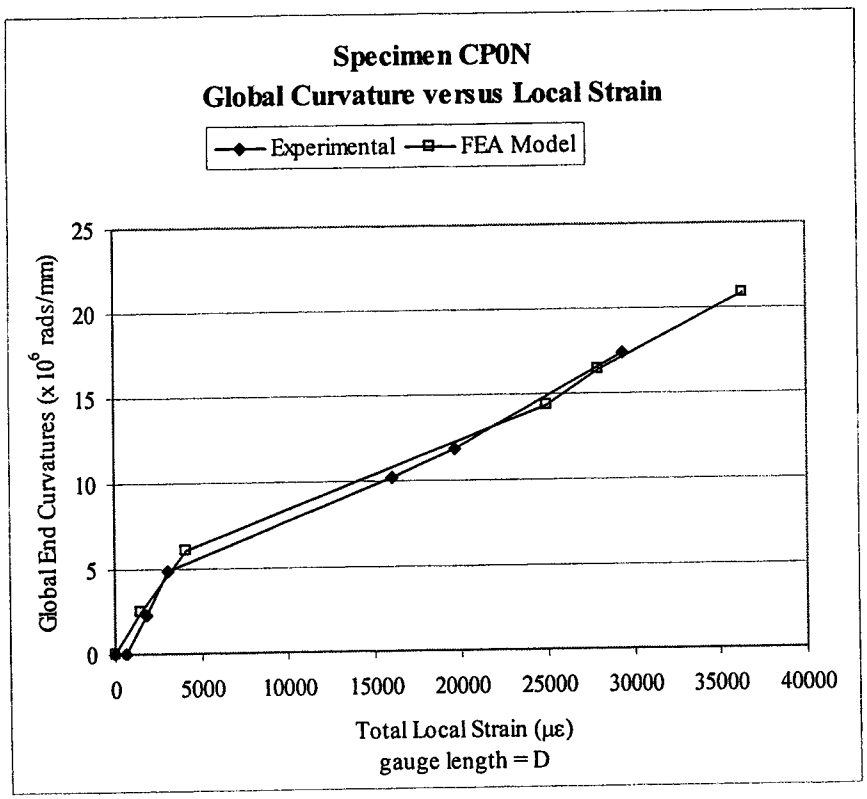

Figure 4.70 – Global Curvature versus Local Strain Comparison for Specimen CP0N

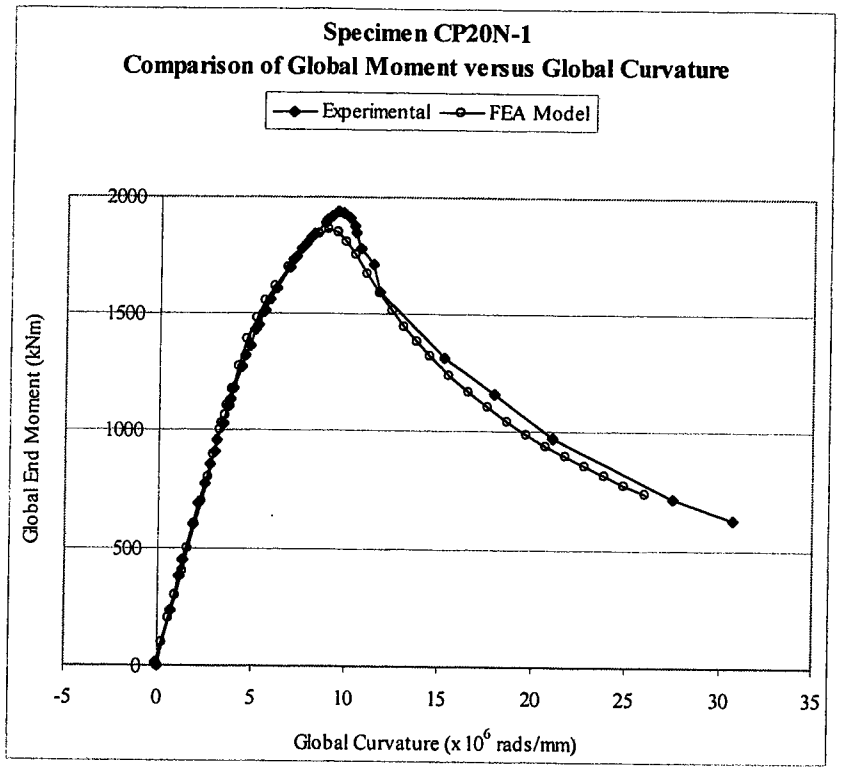

Figure 4.71 - Global Moment versus Global Curvature Comparison for Specimen CP20N-1

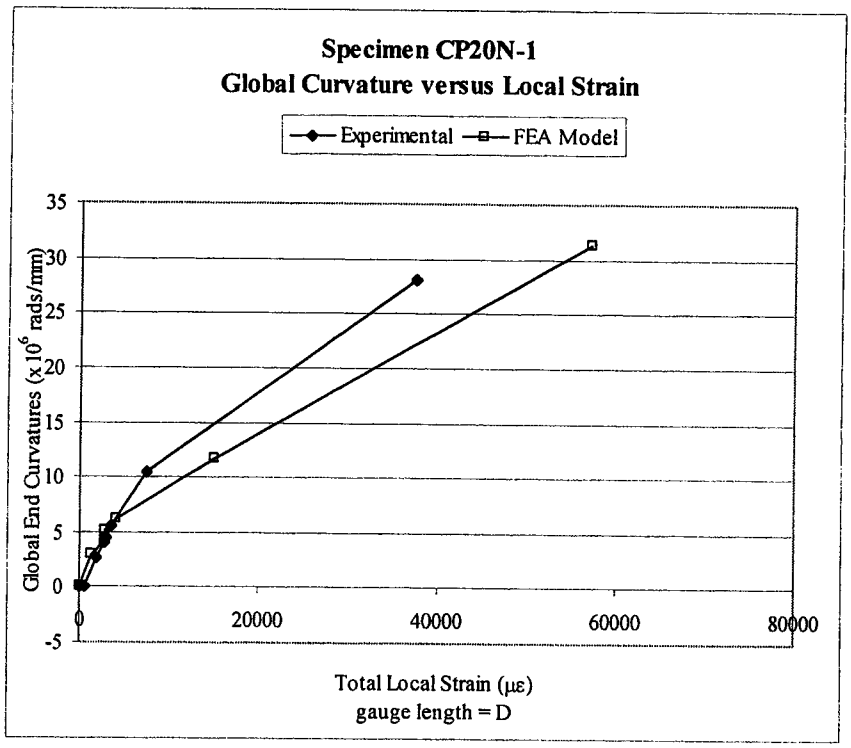

Figure 4.72 – Global Curvature versus Local Strain Comparison for Specimen CP20N-1

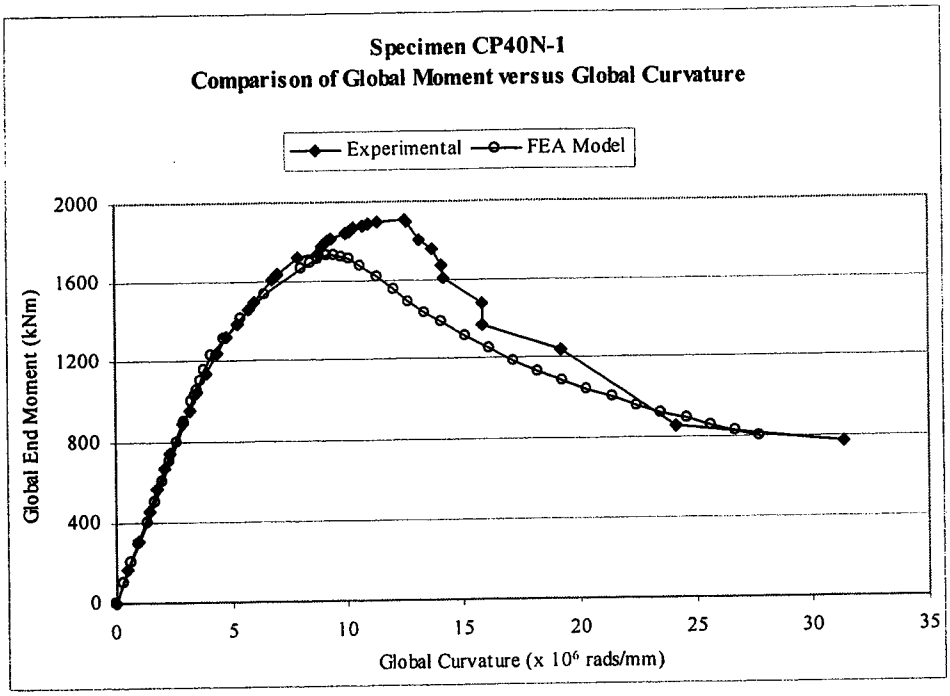

Figure 4.73 - Global Moment versus Global Curvature Comparison for Specimen CP40N-1

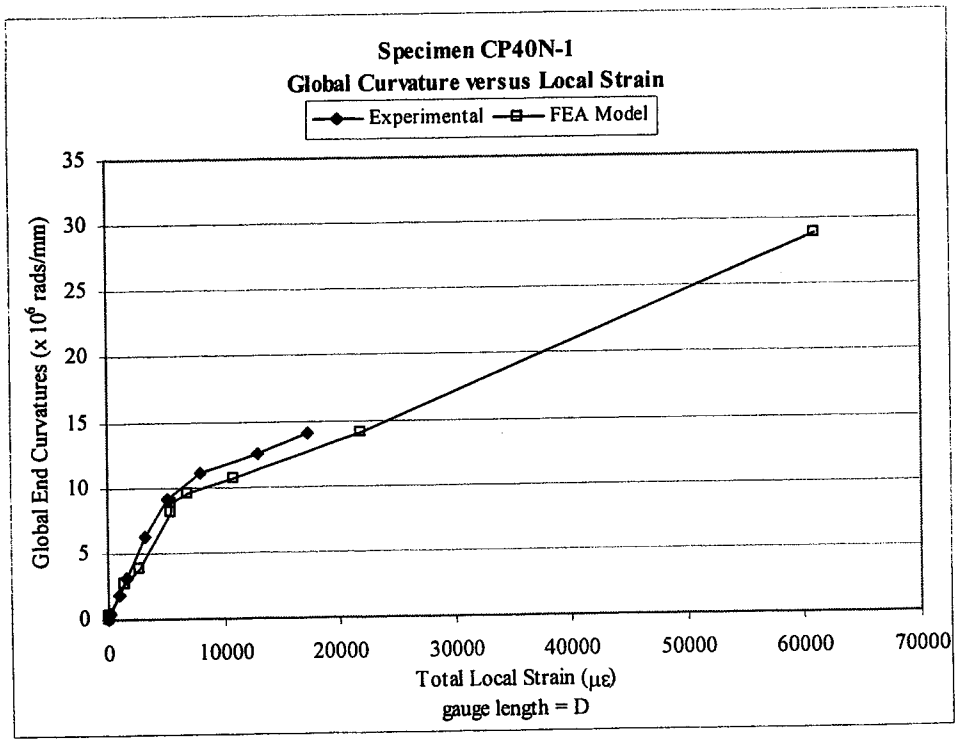

Figure 4.74 – Global Curvature versus Local Strain Comparison for Specimen CP40N-1

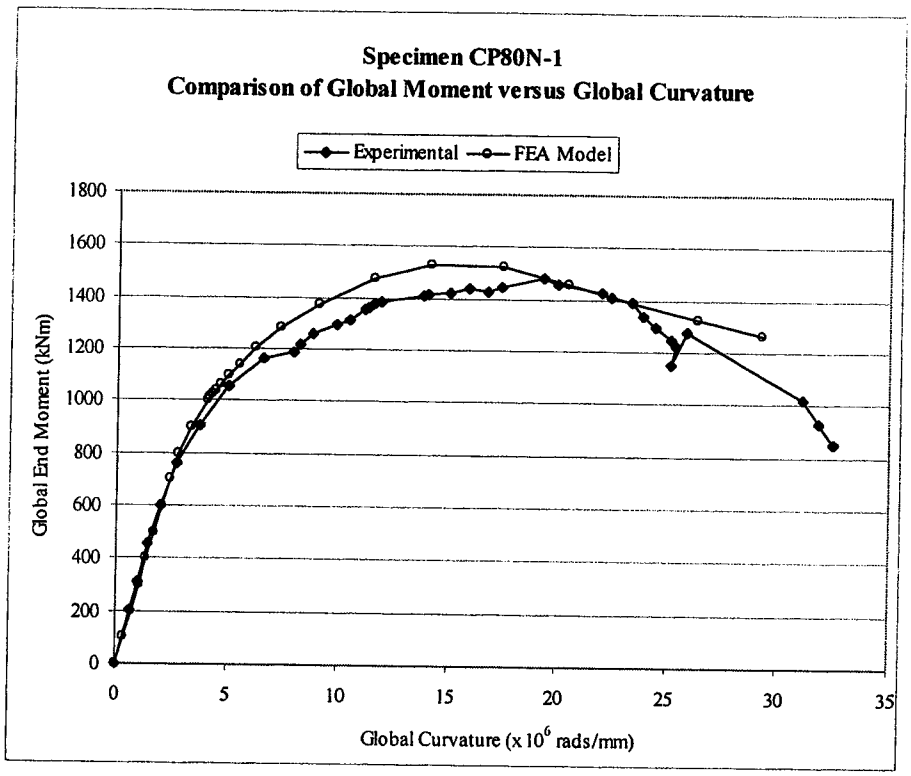

Figure 4.75 - Global Moment versus Global Curvature Comparison for Specimen CP80N-1

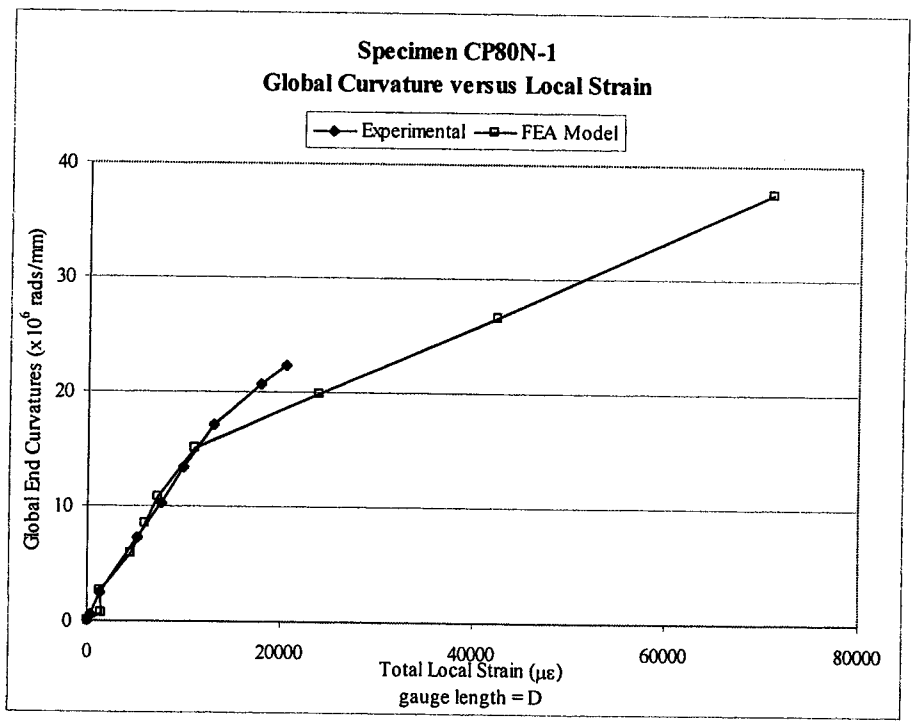

Figure 4.76 – Global Curvature versus Local Strain Comparison for Specimen CP80N-1

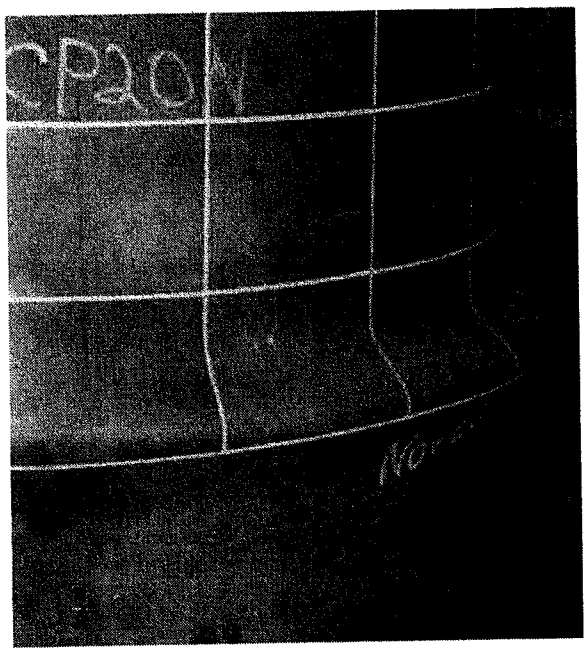

Figure 4.77 – End Bulge Buckle on Specimen CP20N-1

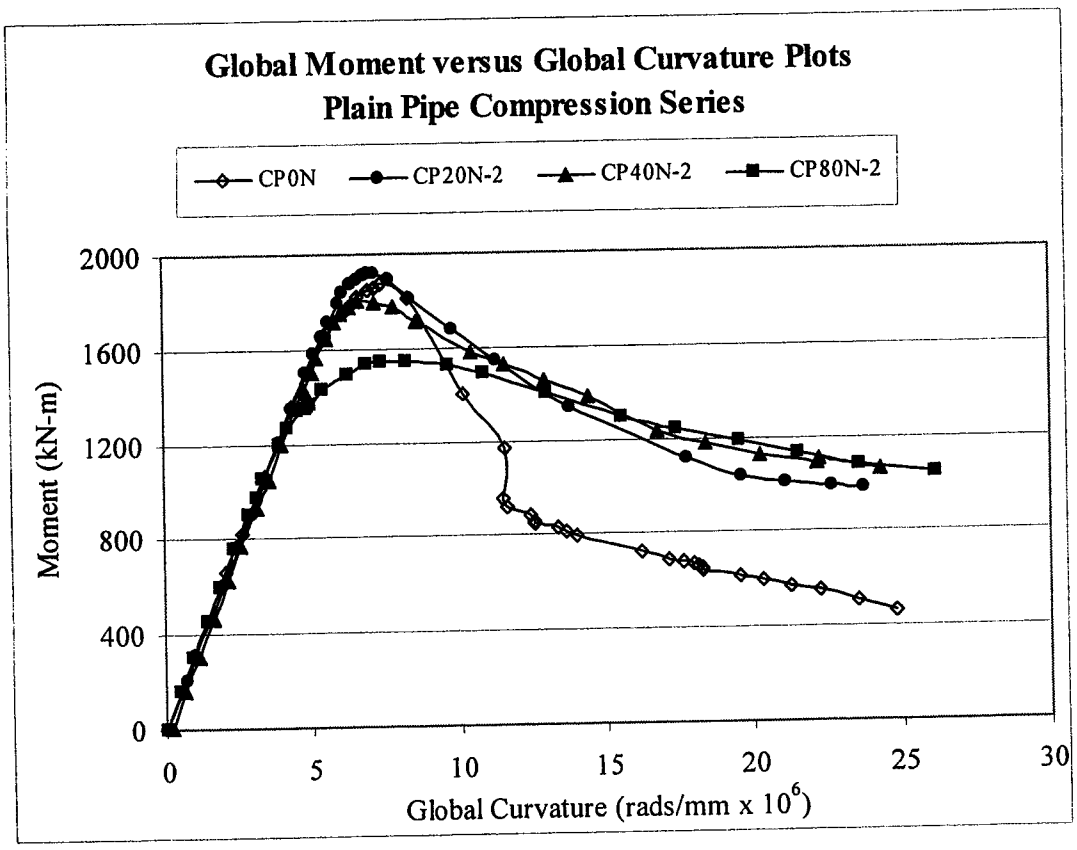

Figure 4.78 – Effects of the Variation in Internal Pressure on Plain Compression Specimens

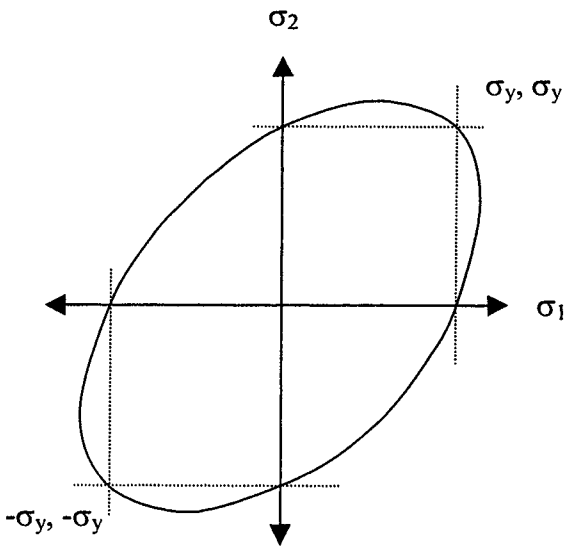

Figure 4.79 – Graphical Representation of the von Mises Yield Criterion

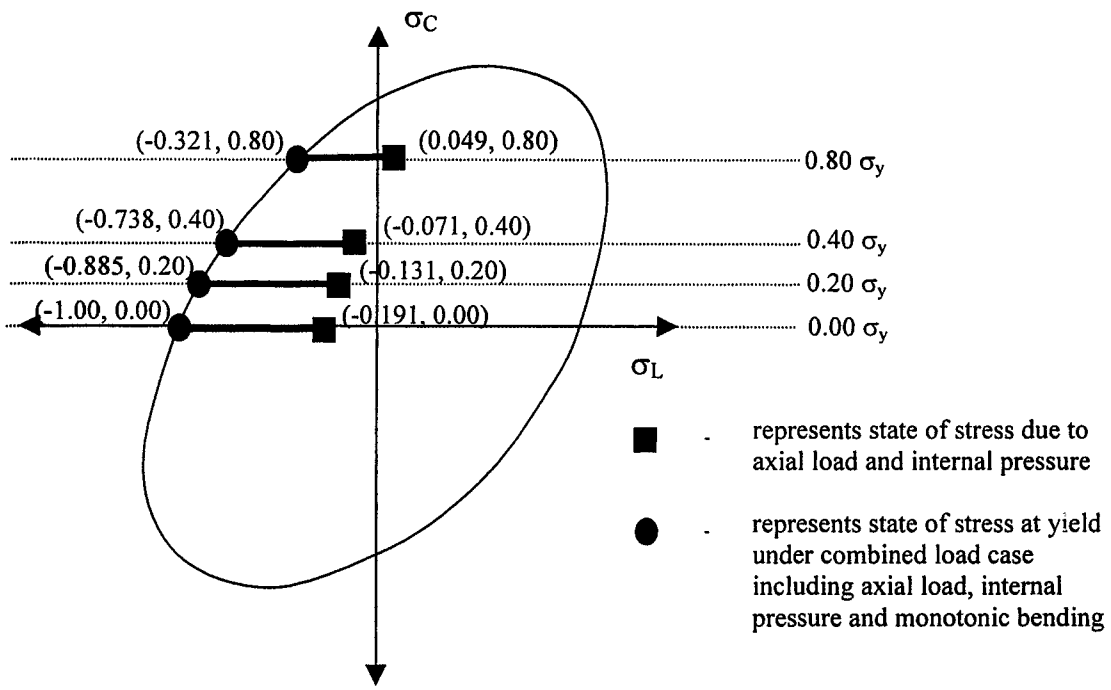

Figure 4.80 – Analysis of Plain Pressurized Compression Specimens Using Von Mises Yield Criterion at First Yield

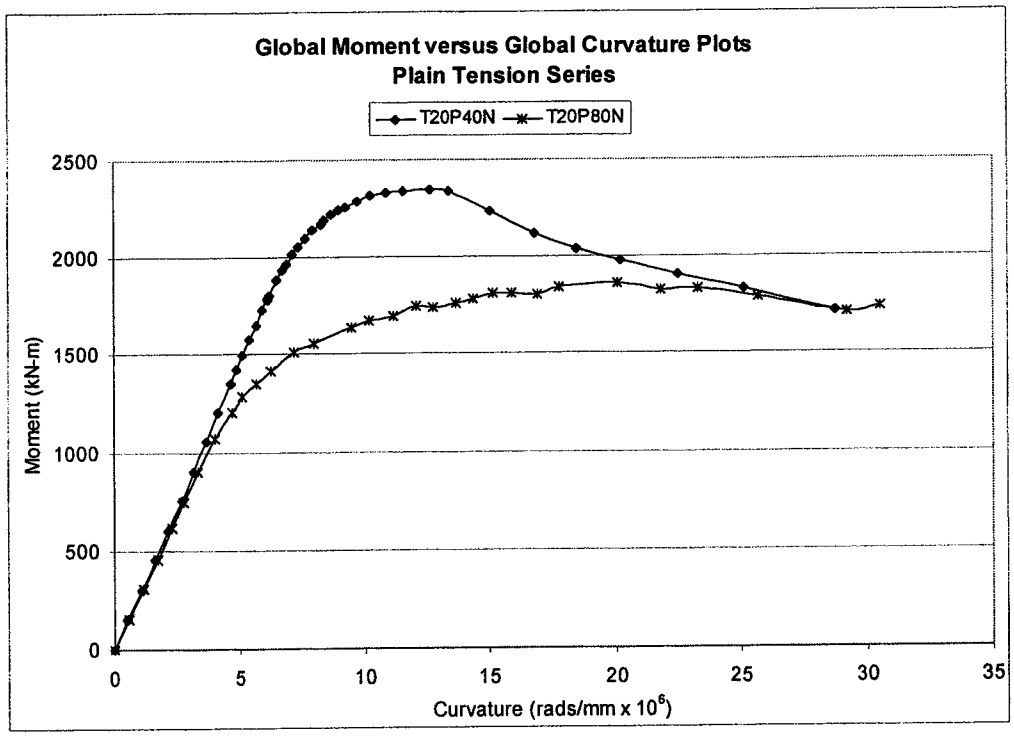

Figure 4.81 – Effects of the Variation in Internal Pressure on Plain Tension Specimens

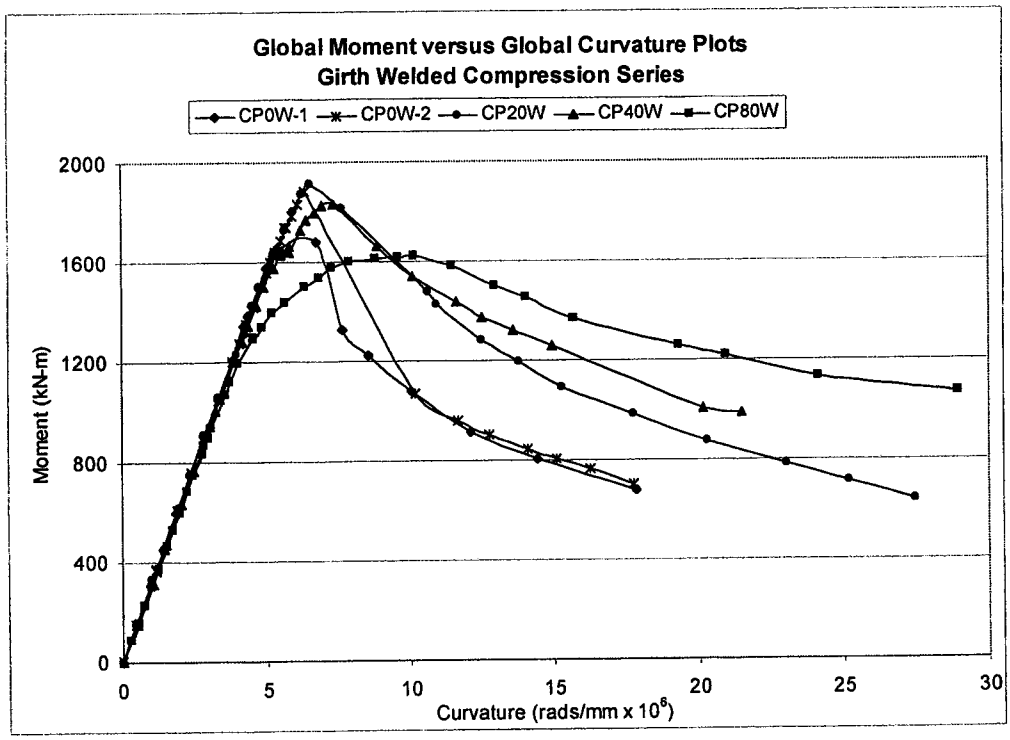

Figure 4.82 – Effects of the Variation in Internal Pressure on Welded Compression Specimens

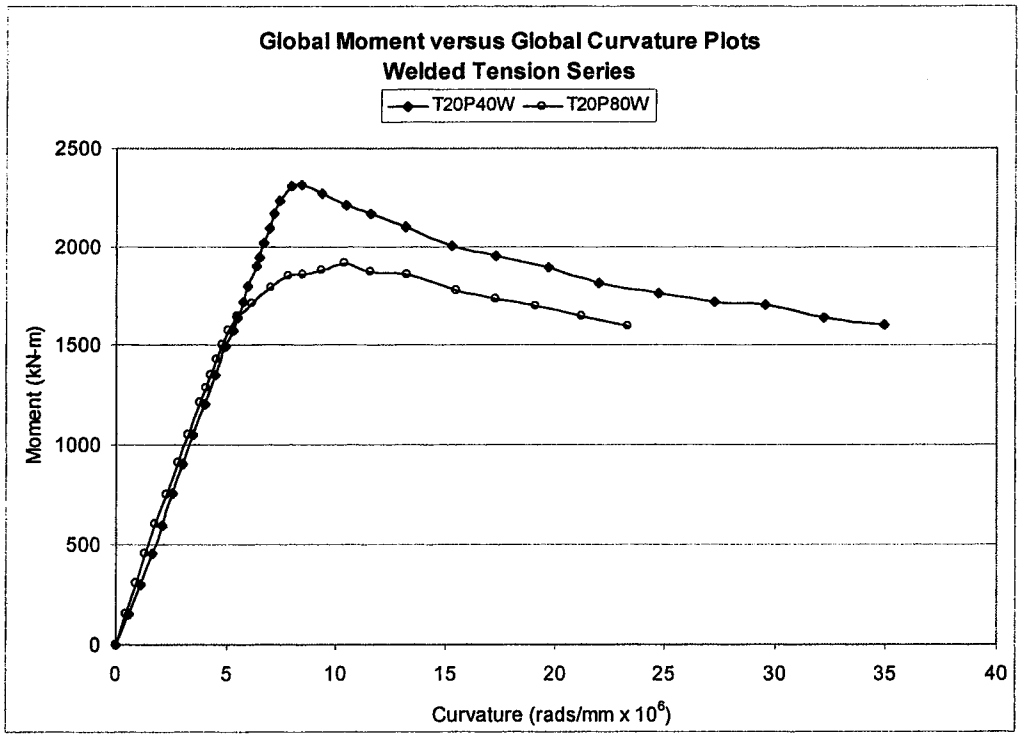

Figure 4.83 – Effects of the Variation in Internal Pressure on Welded Tension Specimens

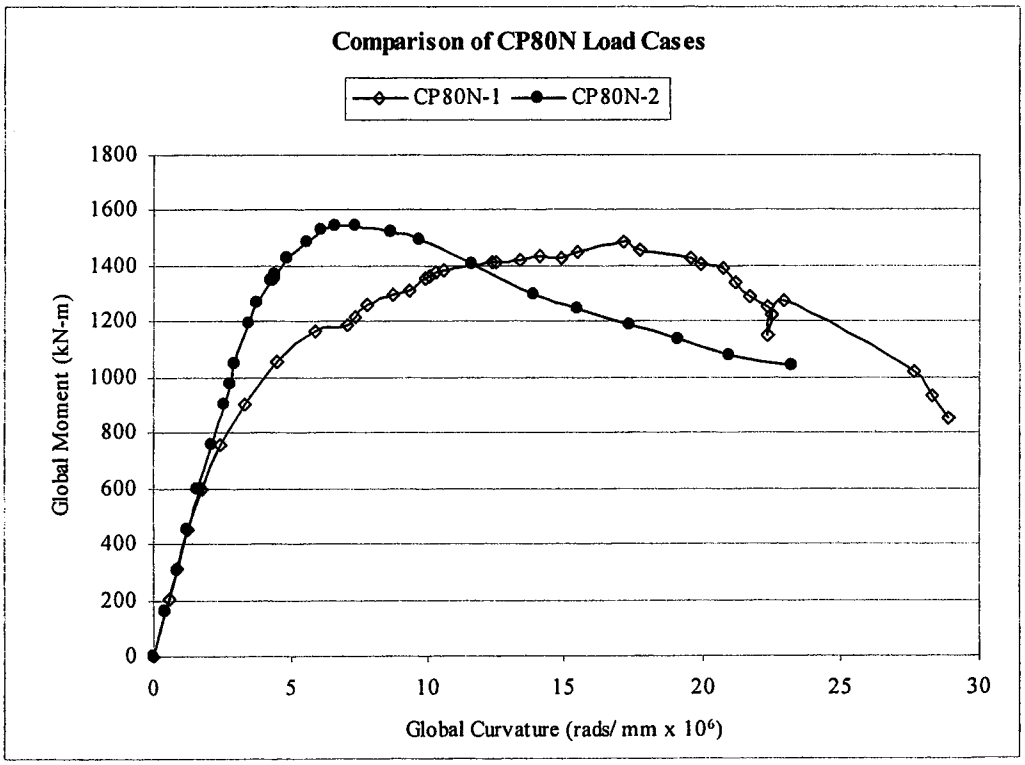

Figure 4.84 – Comparison of CP80N-1 and CP80N-2

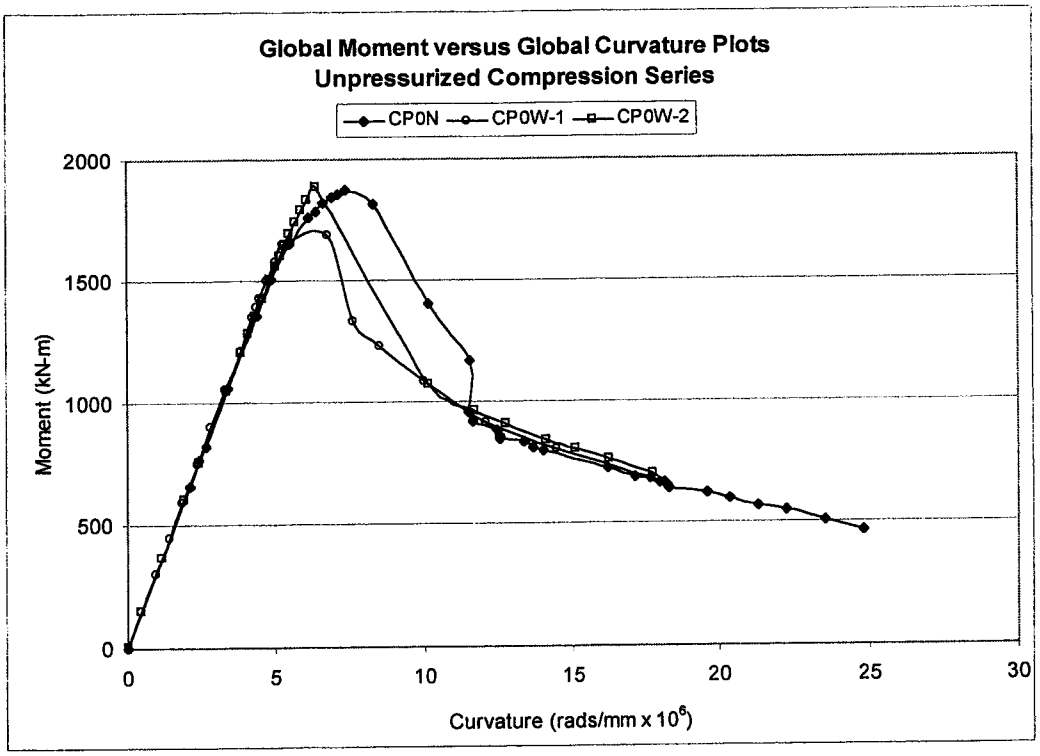

Figure 4.85 – Effects of Circumferential Girth Weld on CP0 Load Case

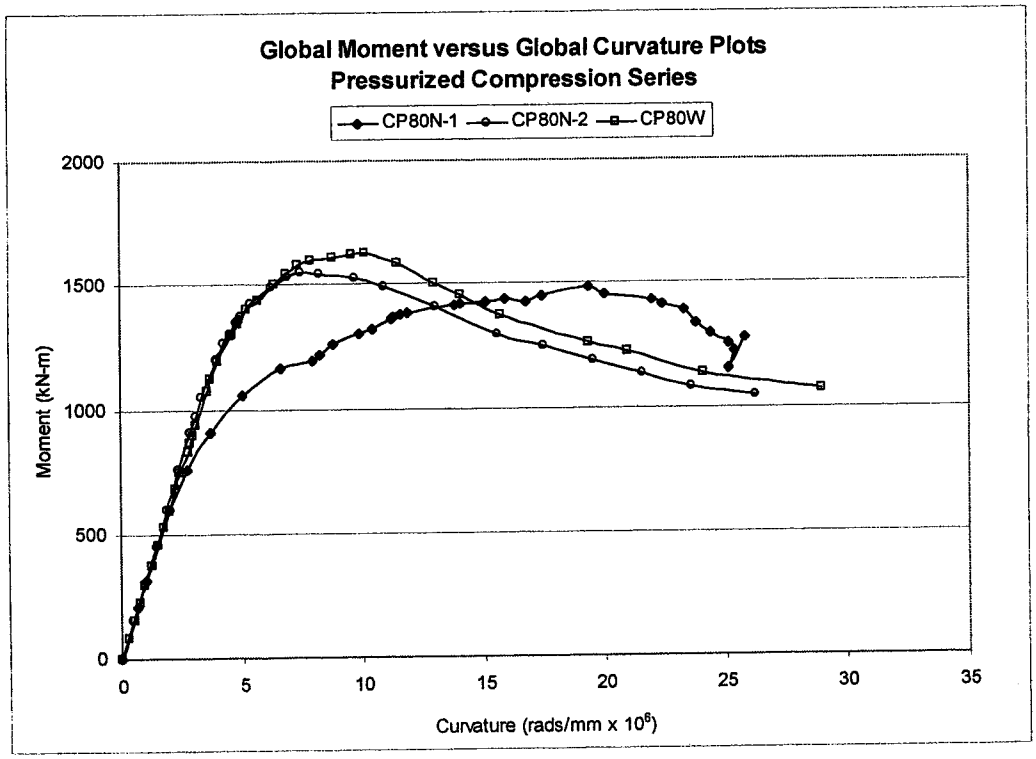

Figure 4.86 – Effects of Circumferential Girth Weld on CP80 Load Case

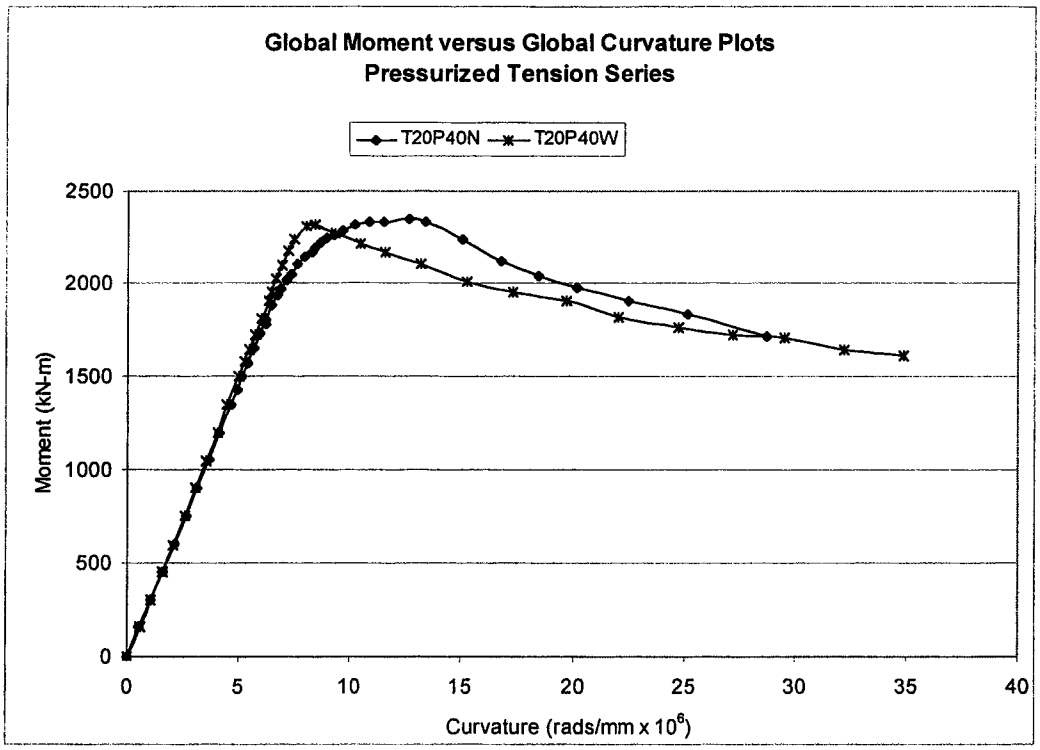

Figure 4.87 – Effects of Circumferential Girth Weld on T20P40 Load Case

5.0 FEA MODEL VALIDATION

The results presented in Chapter 4 show that the FEA model developed in this research project does an excellent job of predicting the behaviour of segments of line pipe subjected to combined loads. The FEA model provides not only accurate peak moment predictions, but also accurate critical strain predictions. However, the validation of the FEA model in Chapter 4 was limited to test specimens with a D/t ratio of approximately 92 for which the FEA model was specifically developed. Since one of the more influential parameters in the behaviour of line pipe is the D/t ratio, the decision was made to validate the FEA model for different D/t ratios prior to proceeding with the parametric study.

The experimental data from previous investigations conducted at the U of A with different D/t ratios will be used to determine if the FEA model developed in this project can accurately predict the behaviour of segments of line pipe with different D/t ratios. Specifically plain pipe specimens with D/t ratios of 50 and 63 (Mohareb, *et al.*, 1994) and girth welded specimens with D/t ratios of 50 and 63 (Yoosef-Ghodsi, *et al.*, 1994) will be used to validate the model.

Results using different FEA models developed at the U of A are presented in this chapter. To avoid any confusion between the models, they will hereafter be referred to by the author's name. For example, the FEA model developed by Mohareb will be referred to as the 'Mohareb model'. The FEA model developed in Chapters 3 and 4 of this document will be referred to as the 'Dorey model'.

Prior to this additional validation of the Dorey model, an assumed initial imperfection pattern has to be selected for the D/t = 51 and D/t =64 specimens because no laboratory initial imperfection data was collected. Section 5.1 discusses the development of these assumed initial imperfection patterns. Section 5.2 presents the comparison of the Dorey model with the experimental test data from specimens with different D/t ratios and

different grade materials. Once the Dorey model was validated, it was used as the basis to conduct a full parametric study on the different parameters that influence the behaviour of line pipe, which will be presented in Chapter 6.

5.1 Development of Assumed Initial Imperfection Meshes

As discussed throughout this document, initial imperfections are one of the more influential factors in the behaviour of line pipe. In the projects conducted by Mohareb and Yoosef-Ghodsi, no attempt was made to measure experimental imperfections, nor were they included in their respective FEA models. Comparison of their experimental data with the results of their FEA shows that the respective FEA models did a reasonably accurate job of predicting the experimental behaviour up to the experimental limit point. However, as will be shown and discussed, significant improvements to the FEA model prediction at or near the limit point and in the post-buckling region can be achieved by incorporating an assumed initial imperfection pattern. This section describes the development of an assumed initial imperfection for both the plain and the girth welded specimens.

5.1.1 Plain Pipe Assumed Initial Imperfection Pattern

Three different assumed initial imperfection patterns were investigated for use in the following parametric study. These three initial imperfection patterns were based primarily on previous experience and observations made in this investigation. Figure 5.1 provides a schematic of the three initial imperfection patterns investigated.

The first initial imperfection pattern assumed a 'ring' initial imperfection around the entire circumference at the half height of the test specimen, as shown in Figure 5.1 (a). It should be noted that this is the assumed initial imperfection pattern previously used in the mesh refinement study described in Section 3.3.6. The second initial imperfection pattern assumed a 'half-ring' across the compression face at the half height of the test specimen, as shown in Figure 5.1 (b). The third initial imperfection pattern assumed a

'blister' located at the half height of the test specimen. A 'blister'-type initial imperfection pattern has an outward bulge shape, as shown in Figure 5.1 (c). Each of these initial imperfection patterns was developed using a cosine function, as previously described in Equation 3.3 of Section 3.3.6.1 and shown in Figure 3.6. The value of amp_{Max} was taken directly from the measured initial imperfection pattern from the laboratory. The length of the initial imperfection, $L_{I.I.}$, as shown in Figure 5.1, was selected as the length of five longitudinal elements used in the model. This approximation was based on measurements from the experimental test specimens included in this project and an approximation from the photographs available for other test specimens.

Each assumed initial imperfection pattern was mapped onto the 40x75 mesh. Specimen CP20N-2 was arbitrarily selected as the reference specimen. A total of five different analyses were run using the Dorey model and CP20N-2 input file, but varying the input mesh. These analyses were comprised of the three assumed initial imperfection patterns described above, the laboratory measured initial imperfection pattern, and the results using a perfect pipe, with no initial imperfections. Figure 5.2 presents the results of the five analyses. The experimental global moment-curvature plot is also included in Figure 5.2.

Examination of Figure 5.2 shows that the experimental results and those generated from the Dorey model using the complete laboratory measured imperfection pattern are essentially coincidental, as previously shown in Figure 4.25. The results using the 'perfect pipe' mesh are substantially greater than the results from any of the other meshes. This behaviour was anticipated since the known effects of initial imperfections are to reduce the moment capacity. Consequently, the 'perfect pipe' results were considered an upper bound solution for the given load case.

Comparison of the results for the three assumed initial imperfection patterns presented in Figure 5.2 show that the 'ring' imperfection and the 'half ring' patterns are essentially coincidental and noticeably less than the experimental results. This was not unexpected.

The 'ring' and 'half ring' initial imperfections cover a large area of the mesh. While they were not any larger than the 'blister' imperfection in terms of peak amplitude, they did make up a significant portion of the surface area of the mesh and therefore are 'large imperfections' in terms of the surface area they cover. Furthermore, as can be seen in the cross sections of each imperfection type given in Figure 5.1, both the 'ring' and the 'half ring' assumed patterns not only introduce a local imperfection, but they also introduce an initial out-of-roundness of the cross section. Significant out-of-roundness can also result in a reduction of the moment capacity (Souza, *et al.*, 1994). Therefore, it was decided that the 'ring' and 'half ring' patterns were probably not realistic representations of the actual initial imperfection pattern that existed in the test specimen.

Examination of the results obtained for the 'blister' pattern show that they are essentially coincidental with the experimental results and the Dorey model results using the measured initial imperfections. To reinforce this observation, a second test specimen, CP80N-2, was subjected to an assumed 'blister' pattern imperfection analysis. It should be noted that the value of amp_{Max} used for specimen CP80N-2 was also taken directly from the laboratory measured initial imperfection pattern and differed from that measured for specimen CP20N-2. The magnitude of amp_{Max} was taken as the maximum initial imperfection measurement at any point in the test specimen and ranged from 0.50 mm to 2.75 mm for the different test specimens. The value of amp_{Max} taken from the measured initial imperfection pattern for CP20N-2 was 2.07 mm, whereas the value of amp_{Max} from the measured initial imperfection pattern for CP80N-2 was 1.60 mm.

Figure 5.3 presents the comparison of the experimental results and the Dorey model results using both the measured initial imperfections and the 'blister' pattern for specimen CP80N-2. Again, it can be observed that there is excellent agreement between the three data sets. This is not surprising considering that typical imperfections would take the form of a dent and would be expected to radiate in a reasonably symmetrical pattern from the point of maximum amplitude. Physically, the 'blister' pattern most closely represented this. It was therefore decided to use the assumed 'blister' pattern as the form of the initial imperfection pattern for all subsequent analysis. A discussion of the

selection of the value of amp_{Max} used for the different size specimens follows in Section 5.2.

A short parametric study on the effect of the amplitude of the blister on the moment capacity was conducted. Figure 5.4 provides the results of that study. It should be noted that to help observe the differences more clearly, only the results up to and including initial imperfections of 25% of the wall thickness are included and are plotted on a magnified vertical scale.

The results of this study show that as the amplitude of the initial imperfection increases, the moment capacity decreases. This is similar to the results of the ring pattern initial imperfection study presented in Section 3.3.6.2 and Figure 3.10, which are included in Figure 5.4 for reference. However, as shown in Figure 5.4, the rate of decrease in moment capacity for the blister imperfection is significantly different than for the ring imperfection pattern used to develop the results previously presented in Figure 3.10.

Examination of Figure 5.4 shows that the ring initial imperfection pattern has a greater effect on the reduction in moment capacity. This was anticipated because, as discussed in this section, the ring initial imperfection used resulted in a larger overall imperfection than did the local blister with the same magnitude. Therefore, it would be expected that the ring initial imperfection would cause a more significant reduction in the moment capacity. This is evidenced in Figure 5.4. From these results it is clear that the shape of the initial imperfection pattern plays a significant role in the magnitude of the moment capacity reduction.

Again, it should be noted that the perfect pipe buckled in a different configuration (symmetric end buckles as shown in Figure 3.7) and, as such, gave a moment capacity that was not consistent with the specimens that had an initial imperfection pattern included in the analysis. Therefore, for the blister initial imperfection pattern, all of the moment capacities were normalized with respect to the 1% blister initial imperfection pattern. However, it requires a 2% ring initial imperfection for the model to develop the

mid-height bulge buckle. Examination of Figure 5.4 shows that the two curves cross each other. This is because of the different reference moment capacity for the two assumed initial imperfection patterns. Examination of Figure 5.4 shows that it is possible that the curve for the ring initial imperfection pattern to lie completely below the curve for the blister initial imperfection pattern. This would be possible assuming the 1% ring initial imperfection had given a usable result and the difference between the 1% and the 2% ring was large enough. However, no attempt was made to address this problem because the purpose of Figure 5.4 was to establish that the reduction in moment capacity was dependent on the shape of the initial imperfection pattern. Figure 5.4 clearly indicates this difference. Additional studies on this phenomenon are presented throughout the remainder of this chapter and the purpose and results hold true for the subsequent initial imperfection pattern comparisons.

5.1.2 Girth Welded Assumed Initial Imperfection Pattern

For the girth welded specimens, examination of the test specimens revealed that, in most cases, there was a physical offset of the two cross sections immediately on either side of the girth weld. Figure 5.5 shows a schematic of a typical offset at a girth weld. Souza and Murray (1994) and Hu (1991) included offsets in their analysis and found good agreement between the experimental and analytical results.

The laboratory measurements on the specimens tested in this project showed that the maximum magnitude of the offset between the top half, or 'top can', of the test specimen and the bottom can was generally greater than the maximum amplitude of the largest local 'blister' in a given test specimen. In addition, the offset imperfection at the girth weld was located at the half height of each test specimen, which is also the point of the largest total moment. As such, it was decided to develop an assumed initial imperfection mesh for use in the Dorey model for the girth welded test specimens that included only an initial offset at the girth weld, as shown in Figure 5.5. Any other initial imperfections that may be present in the specimen were neglected. The magnitude of the offset used in the assumed initial imperfection mesh was taken as the value of the offset between the

top and bottom can at the compression face of the specimen, as measured in the laboratory set of initial imperfections for each respective specimen.

Figure 5.6 provides the comparison of the results between the experimental data, the Dorey model prediction using the exact measured initial imperfection pattern, and the Dorey model prediction using the offset mesh model of Figure 5.5 for specimen CP40W. The measured offset between the top and bottom cans at the girth weld along the extreme compression fibre of specimen CP40W was 0.843 mm as shown in Table 5.1. It should be noted that this was not necessarily the maximum offset at any point around the girth weld, but that it was the magnitude of the offset at the most critical location around the circumference of the weld.

It may be observed that the offset in specimen CP40W has a smaller magnitude than some of the measured blisters reported in the previous section. However, the offset is located at the half height of the specimen whereas the blisters were randomly distributed across the entire surface area of the specimen. Therefore, even though the offset is lower in magnitude, its effect is likely more significant than the local blister with the greater amplitude because of its location at the point of maximum moment. Furthermore, the offset at the girth weld is similar to the 'ring' imperfection examined in Section 5.1.1. As was shown in Figure 5.2, a ring imperfection has a greater effect on lowering the moment capacity than a blister imperfection does. Therefore, it was assumed that the offset imperfection would have a significantly greater impact on the moment-curvature response than a local blister would and any local blister imperfections were neglected from the offset imperfection pattern, despite the potential of having a greater amplitude.

Examination of Figure 5.6 shows that the results using the 'offset method assumed initial imperfection pattern' is essentially identical to the results obtained using the measured initial imperfection pattern. It should be noted that the peak moment using the offset method assumed initial imperfection pattern resulted in a slightly greater peak moment capacity, approximately 2 %, than the measured initial imperfection pattern did. This was expected since the offset method only included the imperfections at the girth weld

and did not account for the other imperfections throughout the pipe. That is, the offset method slightly overestimates the moment capacity by slightly underestimating the overall initial imperfection pattern. However, the level of agreement between the results using the simplified offset method and the results using the actual measured initial imperfection pattern provide more than adequate agreement. Therefore, the offset method described in the section will be used in all subsequent analysis on girth welded specimens. A discussion of the selection of the value of the offset used for the different specimens follows in Section 5.2.

5.2 Model Validation Using U of A Experimental Data from other Test Programs

5.2.1 Specimen Nomenclature

At this juncture, it is imperative to establish a consistent nomenclature because each of the experimental research projects referred to hereafter use a different code to identify their respective test specimens and load cases. For consistency and easy reference, all specimens will hereafter be assigned a nomenclature of the following arrangement:

$$dt\#_1\ d\#_2\ x\#_3\ ip\#_4\ p\#_5$$

where

- 'dt' indicates a D/t ratio of '$\#_1$';
- 'd' indicates a nominal outside diameter of '$\#_2$' in units of millimeters;
- 'x' indicates a grade of material of '$\#_3$' in units of ksi – kips per square inch;
- 'ip' indicates a maximum amplitude of the initial imperfection of '$\#_4$' percent of the wall thickness for the plain specimens; or
- 'ip' indicates an offset of '$\#_4$w' millimeters for the welded specimens, where the 'w' indicates that there is a circumferential girth weld at the half height of the specimen; and,
- 'p' indicates an internal pressure that causes a stress of '$\#_5$' percent of SMYS in the circumferential direction.

For example, the ID code 'dt50d324x52ip1.5wp00' is for a specimen with a D/t ratio of 50 and a nominal outside diameter of 324 mm, made from grade X52 material with an offset of 1.5 mm at the girth weld in the input mesh and an internal pressure that causes a stress of 0% SMYS in the hoop direction. Where applicable, the load case will be followed by the original nomenclature in brackets for the specimen given by the actual researcher.

5.2.2 D/t = 51 Plain Test Specimens

The two different initial imperfection patterns developed in Section 5.1 were based on the specimens tested in the experimental portion of this project. In order to extend the model to other D/t ratios and validate it with current experimental data for specimens with varying D/t ratios, appropriate values for the maximum amplitude of the blister imperfection in the plain pipe specimens and for the magnitude of the offset in the girth welded pipes had to be determined. There was no measured data available for either of these two variables. Therefore, the following method was used to determine appropriate values.

The maximum amplitude of the blister for the plain pipes was developed using the specimens with an outside diameter of 324 mm and a D/t ratio of 51, which were tested by Mohareb, *et al.*, 1994. There are no current standards that place tolerances on this type of initial imperfection for segments of line pipe. Therefore, it was decided to select a trial series of different initial imperfections to determine an appropriate maximum amplitude for the blister for the 324 mm diameter specimens. The trial maximum amplitudes were selected as a function of the wall thickness of the test specimen. The 324 mm diameter specimens had a wall thickness of 6.35 mm. A range of amplitudes from 0% of the wall thickness to 15 % of the wall thickness was selected for study. Figure 5.7 presents the results from the Dorey model using these different amplitude blister initial imperfection patterns.

The load case selected for this study was approximately equal to the dt51d324x52p36 (HGA12-Mohareb) load case used by Mohareb. The experimental data for

dt51d324x52p36 is included in Figure 5.7 for reference to determine an approximate magnitude that should be used in a blister mesh to model this specimen. As previously discussed in Chapter 4, discrepancies in the magnitude of the peak moment usually arise from differences in the material properties, while discrepancies in the magnitude of the curvature at buckling usually arise from differences in the imperfection patterns. Since only approximate material properties were used at the time this imperfection study was done, this accounts for the difference in the peak moment between the experimental and analytical data presented in Figure 5.7. However, this was not significant to the objectives of the study presented in Figure 5.7. The objective of the imperfection study shown in Figure 5.7 was to determine an estimate for the level of initial imperfection to be used in the complete model of dt51d324x52p36. Examination of Figure 5.7 shows that the experimental data buckles at approximately the same global curvature as the assumed blister mesh with a maximum amplitude of approximately 2% the wall thickness of the specimen would. As a result, it was decided to use a blister imperfection with a maximum amplitude of 2% the wall thickness for all of the D/t = 51 plain specimens. It is recognized that none of the pipes will have the same measured initial imperfection pattern. However, the 2% value selected from Figure 5.7 provides a reasonable estimate for this particular size specimen.

Figure 5.4 presented the results of a parametric study on the effects of the magnitude of the initial imperfection on the moment capacity for the D/t = 92 test specimens. As shown in Figure 5.4 and discussed in Section 5.1.1, it was observed that with an increasing magnitude in the initial imperfection, there was a substantial reduction in moment capacity of the D/t =92 test specimens for both the ring and the blister initial imperfection patterns. Figure 5.8 presents a plot of the reduction in moment capacity as a function of the blister type initial imperfection for the D/t = 51 plain specimens. The responses for the D/t = 92 plain specimens previously presented in Figure 5.4 are included for reference. It should be noted that Figure 5.8 only presents the results up to an initial imperfection of approximately 25% the wall thickness because the range of initial imperfections for the D/t = 51 plain pipe specimens only extended to 15%.

Figure 5.8 shows that the moment capacity reduction varies with the different D/t ratios. This can be observed by comparing the D/t = 92 blister initial imperfection pattern response with the D/t = 51 response. This is not unexpected. The D/t = 51 specimens reached the fully plastic moment capacity of the cross section prior to buckling. This is shown by the plateau reached in the global moment-curvature response shown in Figure 5.7 and in subsequent figures for low D/t ratio specimens. Increasing the magnitude of the initial imperfection only served to initiate buckling at a lower global curvature with little or no reduction in moment capacity, as seen in Figure 5.7. This explains the essentially constant moment capacity observed in Figure 5.8 for the D/t = 51 specimens.

The D/t = 92 specimens did not attained their fully plastic moment capacity, as discussed in Section 4.6.3. At the point of buckling the moment-curvature curve still had a positive slope, as shown in both Figure 3.6 and Figure 3.8. Therefore, an increase in initial imperfection not only reduced the global curvature, but also the global moment capacity. This explains the response observed in Figures 3.10 and 5.4 for the D/t = 92 plain specimens. Therefore, it was concluded that the moment capacity reduction as a function of the initial imperfection is dependent on the D/t ratio. It can also be seen that the shape of the initial imperfection pattern is an influential parameter in the shape of the response curves given in Figure 5.8. This will be investigated further and commented on again when the assumed initial imperfection pattern for the D/t = 51 welded specimens is developed in Section 5.2.4. Nevertheless, the purpose of the initial imperfection study presented in this section was to establish an approximate size for use as input into the Dorey model for validation of the model and the 2% wall thickness blister initial imperfection pattern was selected for the D/t = 51 specimens.

Once the assumed initial imperfection pattern was selected, a mesh was generated. The appropriate mesh, the material properties determined from coupon tests and the measured loads used in the experimental testing done by Mohareb *et al.*, (1994), were input into the Dorey model and analyzed. Figures 5.9, 5.10 and 5.11 present the global moment-curvature responses for specimens dt51d324x52ip2p00 (UGA12-Mohareb), dt51d324x52ip2p36 (HGA12-Mohareb), and dt51d324x52ip2p72 (DGA12-Mohareb),

respectively. The figures include the experimental results, the Mohareb model results, and the Dorey model results.

It should be noted that a different technique was used to determine the global moment at the end cross section for the Dorey model with the smaller D/t ratio specimens than was described in Section 4.2.1.1. Due to the length of the end caps used in the Dorey model to simulate the distance between the pivot points and the ends of the specimen, the line of action of the axial load no longer passed through the centroid of the end cross sections once the pipe had developed some curvature. This resulted in a second-order end moment developing at end cross sections due to the global rotation of the end caps.

Figure 5.12 provides a schematic showing the displacement of the end cross section due to the rotation of the end caps. Examination of Figure 5.12 shows that the end cross section, which is the border between the triangular elements of the end caps and the rectangular elements of the specimen, has moved off of the line of action of the axial load and that the centroid of the end cross section had displaced by the amount Δ_E. It should be cautioned that this is due to a rigid body translation and not a distortion of the cross section. The end cross section in the displaced configuration remains unchanged from the original cross section because of the rigid R3D3 elements that comprise the end caps. Nevertheless, a second-order end moment is generated at the centroid of the end cross section.

This second-order end moment was not considered in the analysis of the test specimens presented in Chapter 4. Determination of these second-order end moments for the specimens presented in Chapter 4 showed that the maximum value developed was approximately 25 kN-m. When compared to the overall moments applied to the end cross section of those specimens, which ranged from 1547 kN-m for specimen CP80N-2 to 2350 kN-m for specimen T20P40N, it can be seen that the resulting error by not considering these second-order end moments is approximately 1.0 to 1.5 %. Considering the results presented in Table 4.4, where it was shown that the mean test-to-predicted ratio was 1.035, increasing the overall moment for the FEA model by 1.5% would only

decrease this error. Since a test-to-predicted ratio of 1.035 was considered more than adequate, it was decided not to re-do the analysis of those specimens.

However, the second-order end moments were found to be significant for the smaller D/t ratio specimens, in some cases accounting for as much as 33% of the total end moment. Therefore, they were included in the determination of the global end moment for each of the smaller D/t ratio specimens. The reason the second-order end moments are significant for the smaller D/t ratio specimens and not the D/t = 92 specimens is primarily due to the relative stiffness of the different D/t ratio specimens. The high D/t ratio specimens have a much higher stiffness, related through a cubic function, meaning that there is significantly less rigid body rotation at the end caps than there is for the smaller D/t ratio specimens. Since there is significantly less rigid body rotation, there is significantly less displacement of the end cross section off of the line of action between the pivot points. This results in a substantially lower second-order end moment relative to the total applied moment at the pivot point. However, it should be noted that all specimens from this point onward include the second-order end moment in the value of the total global moment applied at the ends of the specimens.

As outlined in Section 4.3.1, the FEA model output provided the moment at the pivot point in units of N-mm. The FEA data extract files were then modified to include the coordinates of the node on the extreme compression face at the bottom end of the specimen. Since each node at the end of the specimen was connected through the rigid cap elements, the out-of-plane displacement of any node would be equivalent to the out-of-plane displacement of the centroid of the cross section. The displacement of the node at the end of the specimen on the extreme compression fiber was used to determine the value of Δ_E. For each increment of loading, the axial load, which remained constant through a given analysis, was multiplied by Δ_E to determine the second-order end moment. Mathematically, the total moment applied to the end of a specimen in the FEA model, $M_{E\text{-}FEA}$, may be calculated as

$$M_{E-FEA} = M_{pivot} + P_{MTS} \cdot \Delta_E \quad (5.1)$$

where M_{pivot} is the pivot point moment taken from the output of the FEA model.

Examination of Figures 5.9, 5.10 and 5.11 shows excellent agreement between the Dorey model predictions and the experimental data. In all but one case the Mohareb model, which did not include an initial imperfection pattern, over predicted the curvature at buckling. This is to be expected because of the 'reduction in buckling curvature effect' of the initial imperfections. Table 5.2 presents a numerical comparison of the results presented in Figures 5.9, 5.10 and 5.11. The test to predicted ratios for the peak moments given in Table 5.2 for these three specimens are 0.99, 0.97 and 1.02. This confirms the outstanding agreement observed in the three figures.

The method used by Mohareb to determine the critical buckling strain was modified by Yoosef-Ghodsi, *et al.* (1994) and therefore the strains reported by Mohareb will not be reported herein. Yoosef-Ghodsi used a method similar to the one reported in Section 4.3.2.. However, there are two important differences between the method used by Yoosef-Ghodsi and the one used in this project. Firstly, Yoosef-Ghodsi determined the softening-point by inspection. This introduces a degree of supposition because of the limited amount of Demec gauge data collected during the experimental testing for a given specimen. In this project, the softening point was not used to define the local critical strain because of the amount of human interpretation that would be required to identify it and it would be based on the limited Demec data. Instead, the regression analysis performed to identify the critical strain was based solely on data points that were not influenced by the changing slope in the softening region. This removes some of the human interpretation of the data. Secondly, Yoosef-Ghodsi defined the intersection point as the point where the post-buckling curve intercepted a line starting at the origin of the plot with a slope of unity. As previously discussed in Section 4.2.3, the physical nature of the test set-up prohibited the pre-buckling region of the global curvature versus local strain plot from having a slope of unity, instead the slope was less than unity in all experimental cases tested in this project. This is consistent with the experimental results

of Yoosef-Ghodsi, Mohareb, and Del Col. Therefore, it was decided to re-evaluate all of the local critical buckling strains reported by Yoosef-Ghodsi for the specimens tested by Mohareb and himself so that they were determined using the same technique developed and used throughout is this project.

Table 5.2 presents the experimental and Dorey model local critical strains for specimen dt51d324X52ip2p00 (UGA12 – Mohareb), dt51d324X52ip2p36 (HGA12 – Mohareb) and dt51d324X52ip2p72 (DGA12 – Mohareb), which were determined using the methods described in Section 4.3.2. The test-to-predicted ratios were 1.10, 1.08 and 1.09, respectively. While these test-to-predicted ratios show good agreement, they could have been reduced to a value closer to unity by varying the amplitude of the initial imperfection pattern. In all cases, the Dorey model results under-estimated the experimental results by approximately 9%. It is assumed that a slight reduction in the magnitude of the initial imperfection used would result in a slight increase in the Dorey model critical strain predictions, with little change in the moment predictions, as is evidenced in Figure 5.8, thereby reducing this average 9% error in the test-to-predicted values. However, since the purpose was to prove that the Dorey model, with an appropriate initial imperfection pattern, was capable of predicting the experimental behaviour of the dt51d324X52 test specimens it was decided that these results were adequate and that these results have shown the reliability of the Dorey model for this different D/t ratio.

5.2.3 D/t = 64 Plain Test Specimens

A similar magnitude of initial imperfection study for the plain specimens with a D/t ratio of 64 was conducted. Since the details of the study are identical to those conducted for the D/t = 51 specimens presented in the previous section, only the results will be presented. The D/t = 64 plain specimens tested by Mohareb were fabricated from segments of NPS20 line pipe with a 508 mm nominal outside diameter and a wall thickness of 7.90 mm.

The requirements of Table 11.2 of CAN/CSA Z245.1–95 (1995) allows for a wall thickness tolerance from –10.0% to +17.5% for segments of line pipe with a nominal outside diameter of 457 mm or larger. Therefore, an additional initial imperfection pattern with an initial imperfection of 18% the wall thickness was considered for the D/t = 64 plain specimens. The results of the D/t = 64 plain specimen study indicated that a blister imperfection with a maximum amplitude of 3% the wall thickness should be used.

Only specimen dt64d508x56ip3p00 (UGA20 – Mohareb) was available for comparison purposes. Figure 5.13 provides a graphical comparison between the experimental data, the Mohareb model, and the Dorey model. Examination of this figure shows that the Mohareb model once again over predicts the global curvature at buckling. This is again attributed to the omission of initial imperfections in his model. The Dorey model, which includes the 3% wall-thickness, blister-type initial imperfection, buckles at nearly an identical global curvature to the experimental specimen. The numerical results for specimen dt64d508x56ip3p00 (UGA20 – Mohareb) are also included in Table 5.2, with a moment capacity test-to-predicted ratio of 1.01 using the Dorey model results. The experimental critical strain was not available.

Although there are only limited results for the dt64d508x56 specimen group, those results presented here show that the Dorey model developed in this research project provides very good agreement, thereby further verifying its capabilities to model different D/t ratio specimens.

5.2.4 D/t = 51 Welded Test Specimens

An initial imperfection study similar to that used for the plain D/t = 51 specimens was conducted for the girth welded D/t =51 specimens. The fundamental difference from the plain D/t = 51 specimen initial imperfection study was the method which the initial imperfections were determined. As discussed in Section 5.1.2., an offset of the top and bottom cans was decided upon for the type of initial imperfection to impose on the welded specimens. A series of meshes were constructed using different levels of offset

between the two cans. The levels of offset ranged from 0% to 100% of the wall thickness of the test specimens, which corresponded to offsets ranging from 0.0 mm to 6.0 mm.

Figure 5.14 provides the results of the initial imperfection study for the welded D/t = 51 specimens. The experimental data for specimen dt51d324x52p40 (HGA12W – Yoosef-Ghodsi) is included for reference. From Figure 5.14, it can be seen that an offset of 0.20 mm best matches the experimental data presented. It was therefore decided to use an offset of 0.20 mm as the assumed initial imperfection pattern for input into the Dorey model for the dt51d324x52 test specimens.

In addition to using Figure 5.14 to determine the assumed initial imperfection offset for the dt51d324x52 specimens, the data presented in the figure was also used to support the discussion of the effects of the magnitude of the initial imperfection pattern on the moment capacity of the specimen. Figure 5.15 provides a graphical representation of the effects of the offset initial imperfection on the moment capacity of the specimens. The data was plotted with the previous data used in Figure 5.8 for comparison purposes with other initial imperfection patterns.

As can be seen in Figure 5.15, the response of the offset imperfection for the D/t = 51 welded specimens varies from the responses of the D/t = 51 and the D/t = 92 plain specimens. As previously mentioned, this was not unexpected and, therefore, no universal relationship or set of equations can be developed to cover all D/t ranges for both plain or welded specimens.

Figures 5.16, 5.17 and 5.18 present the experimental and Dorey model results for specimens dt51d324x52ip0.20wp00 (UGA12W – Yoosef-Ghodsi), dt51d324x52ip0.20wp36 (HGA12W – Yoosef-Ghodsi) and dt51d324x52ip0.20wp72 (DGA12W – Yoosef-Ghodsi), respectively. Examination of these three figures shows the same excellent level of agreement as has been achieved using the Dorey model to predict other load cases.

Table 5.2 presents a comparison of the experimental and Dorey model peak moments and the critical strains for these three load cases. The test-to-predicted ratios for the peak moments are 1.05, 1.02 and 1.04 for each of the three respective specimens. The test-to-predicted ratios for the critical strains are 0.98, 1.03 and 0.96 for each of the three respective specimens. All of these test-to-predicted ratios confirm the level of agreement shown in Figure 5.16, 5.17 and 5.18 and show that the Dorey model provides an exceptional level of agreement with the experimental data. This validates the model for use with welded specimens that have a D/t ratio of 51.

5.2.5 D/t = 64 Welded Test Specimens

A similar magnitude of initial imperfection study for the welded specimens with a D/t ratio of 64 was conducted. Since the details of the study are identical to those conducted for the welded D/t = 51 specimens presented in the previous section, only the results will be presented. The results of the welded D/t = 64 specimen study indicated that an initial imperfection with an offset of 0.25 mm should be used for input into the Dorey model for the dt64d508x56 test specimens.

Figures 5.19 and 5.20 present the experimental and Dorey model results for specimens dt64d508x56ip0.25wp00 (UGA20W – Yoosef-Ghodsi) and dt64d508x56ip0.25wp40 (HGA20W – Yoosef-Ghodsi), respectively. Examination of these two figures shows the same exceptional level of agreement that has been used by the Dorey model to predict other load cases.

Table 5.2 presents a comparison of the experimental and Dorey model peak moments and the critical strains for these two load cases. The test-to-predicted ratio for the peak moments was 1.00 for each of the two respective specimens. The test-to-predicted ratios for the critical strains are 1.00 and 1.03 for the two respective specimens. All of these test-to-predicted ratios confirm the level of agreement shown in Figure 5.19 and 5.20 and show that the Dorey model provides an exceptional level of agreement with the experimental data. This validates the model for use with welded specimens that have a D/t ratio of 64.

5.3 FEA Model Validation Summary

The current database at the U of A is not limited to the specimens identified and evaluated in this section. However, it was felt that the results presented herein provide conclusive evidence that the Dorey model is adaptable to a variety of D/t ratio test specimens, with or without a circumferential girth weld, and that any further validation was unnecessary.

From the results discussed through Section 5.2 and presented numerically in Table 5.2, it is evident that the Dorey model is not limited to specimens with a D/t ratio of 92 for which it was developed. All of the peak moment test-to-predicted ratios were well within experimental error for a testing program of this complexity.

The test-to-predicted ratios for the critical strains showed a little more variation than did the peak moment test-to-predicted ratios. However, given that they were developed based on a model with an assumed initial imperfection pattern, the results are extremely good. The critical strain test-to-predicted ratios for the D/t = 51 plain specimens could have been improved by selecting a slightly more conservative initial imperfection. Furthermore, some variation in the test to predicted ratios for the critical strain is expected because the initial imperfection pattern would not be the same for the different pipes. By varying the initial imperfection pattern within one of the groups of specimens presented in Table 5.2, it is probable that all of the critical strain test-to-predicted ratios could have been reduced closer to a value of 1.00. However, that was not done because the study fulfilled its purpose of validating the Dorey model for D/t ratios other than 92.

Table 5.1 – Measured Can Offsets for the Girth Welded Specimens

Specimen	Measured Can Offset at Girth Weld (mm)
CP0W-1	1.868
CP0W-2	0.295
CP20W	0.780
CP40W	0.843
CP80W	0.561
T20P40W	2.243
T20P80W	0.917

Table 5.2 – Comparison of Experimental and Dorey Model Results for D/t =51 and D/t=64 Specimens

Specimen ID	Experimental		Dorey Model		Test-to-Predicted Ratio	
	Peak Moment (kN-m)	Critical Strain (%)	Peak Moment (kN-m)	Critical Strain (%)	Peak Moment (kN-m)	Critical Strain (%)
D/t = 51 Plain Specimens						
dt51d324x52ip2p00	206.0	1.49	208.6	1.357	0.99	1.10
dt51d324x52ip2p36	187.4	1.70	193.7	1.579	0.97	1.08
dt51d324x52ip2p72	148.6	3.90	145.8	3.593	1.02	1.09
D/t = 64 Plain Specimens						
dt64d508x52ip3p00	680.3	n/a	674.0	0.994	1.01	n/a
D/t = 51 Welded Specimens						
dt51d324x56ip0.20wp00	209.4	0.80	199.9	0.813	1.05	0.98
dt51d324x56ip0.20wp36	191.8	1.23	188.8	1.198	1.02	1.03
dt51d324x56ip0.20wp72	143.8	2.37	138.4	2.481	1.04	0.96
D/t = 64 Welded Specimens						
dt64d508x56ip0.20wp00	636.8	0.81	634.6	0.811	1.00	1.00
dt64d508x56ip0.20wp40	590.4	1.27	591.7	1.075	1.00	1.03

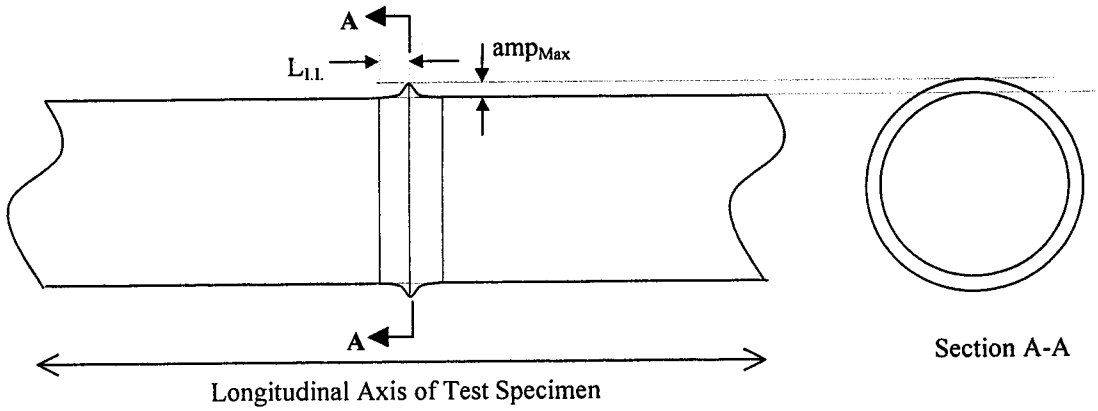

(a) Schematic of "Ring" Assumed Initial Imperfection

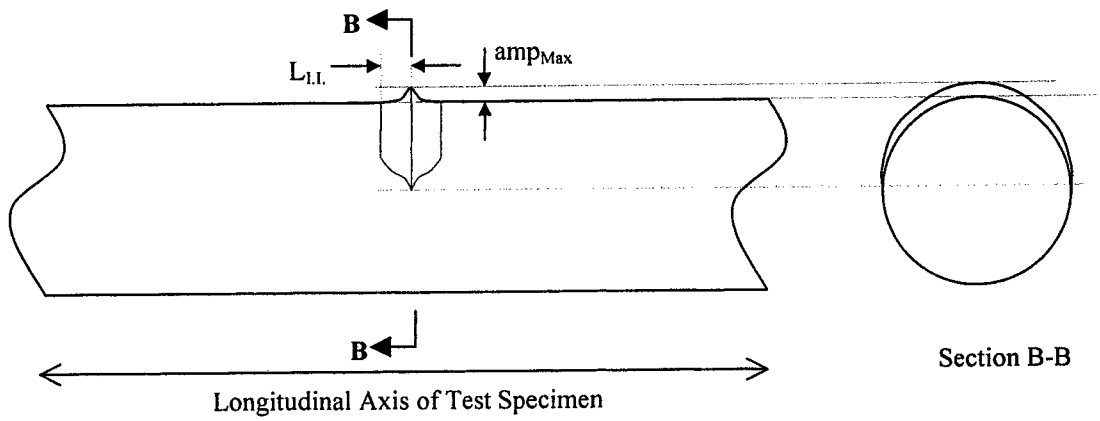

(b) Schematic of "Half-Ring" Assumed Initial Imperfection

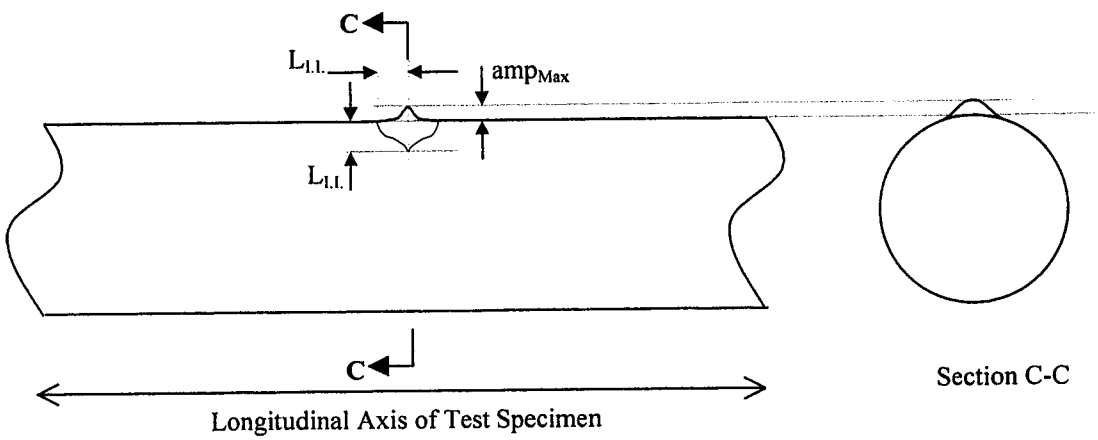

(c) Schematic of "Blister" Assumed Initial Imperfection

Figure 5.1 – Schematics of Different Assumed Initial Imperfection Patterns

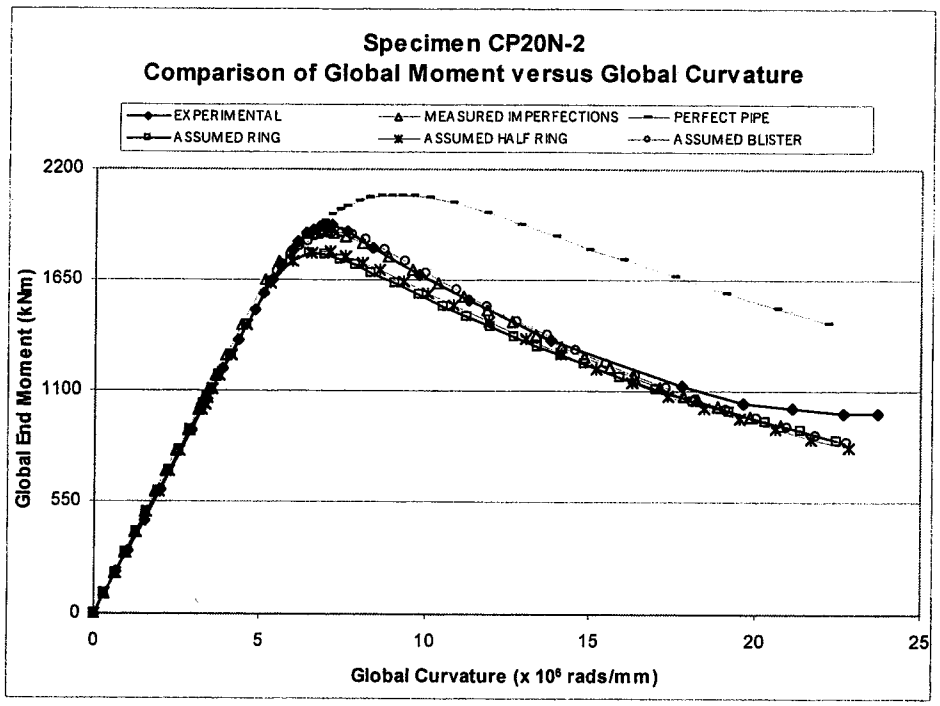

Figure 5.2 – Comparison of Global Response for the Different Initial Imperfection Patterns for Specimen CP20N-2

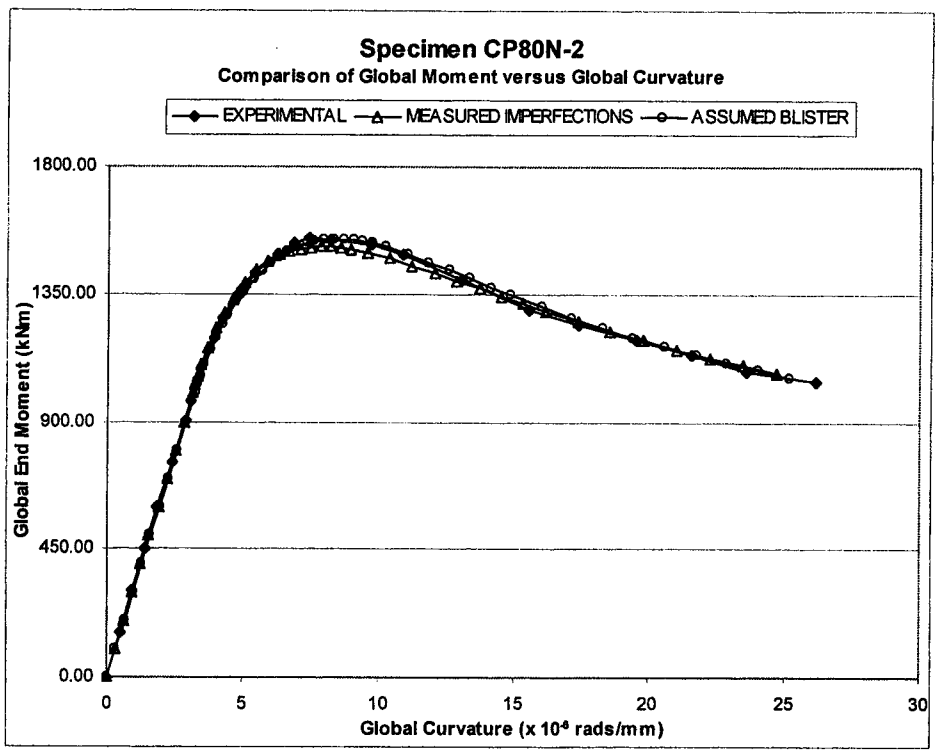

Figure 5.3 – Comparison of Experimental, Measured and 'Blister' Imperfections for Specimen CP80N-2

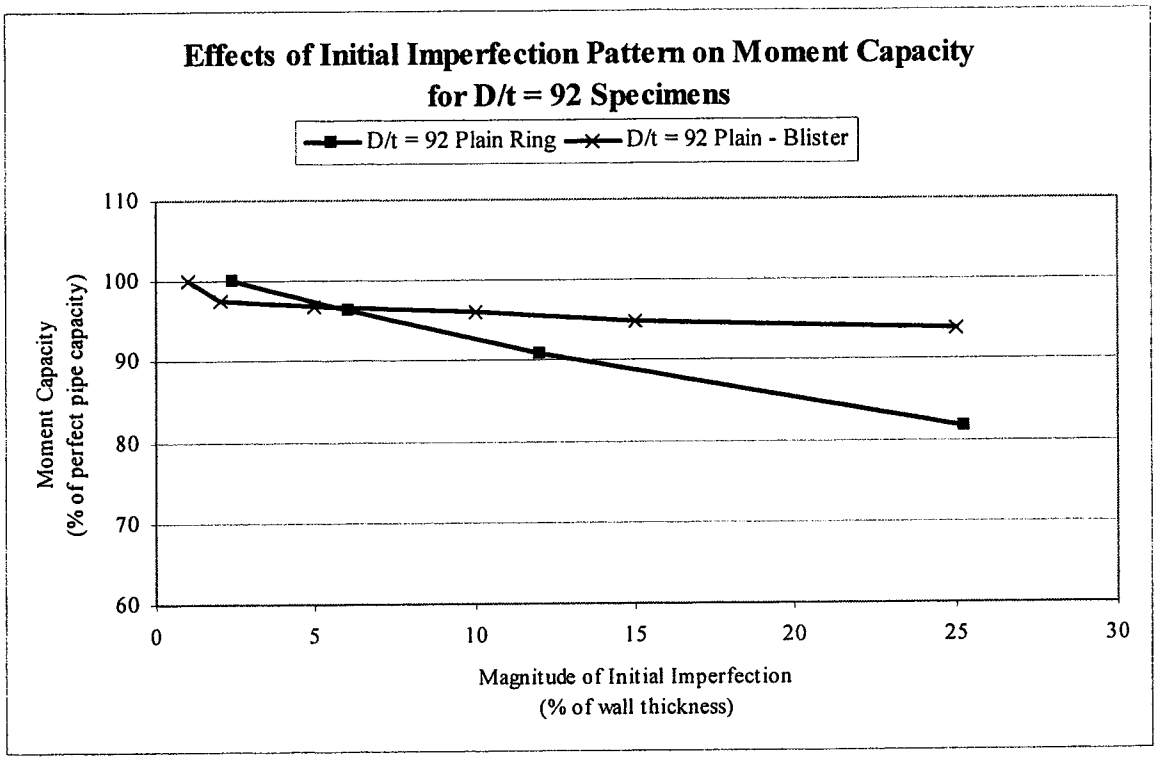

Figure 5.4 – Effects of Initial Imperfection Pattern on the Moment Capacity for Specimens with D/t = 92

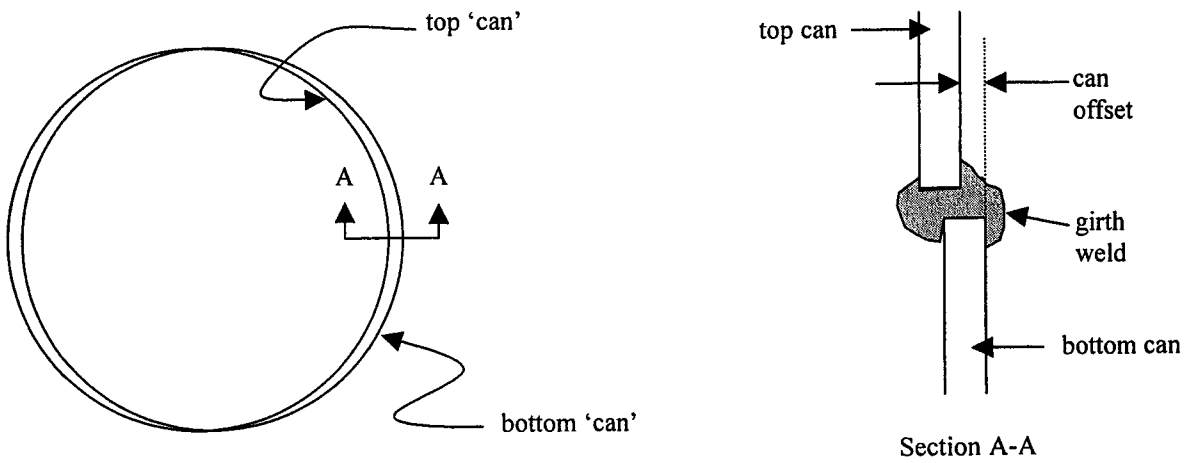

Figure 5.5 – Typical Offset at a Girth Weld Between Top and Bottom Cans

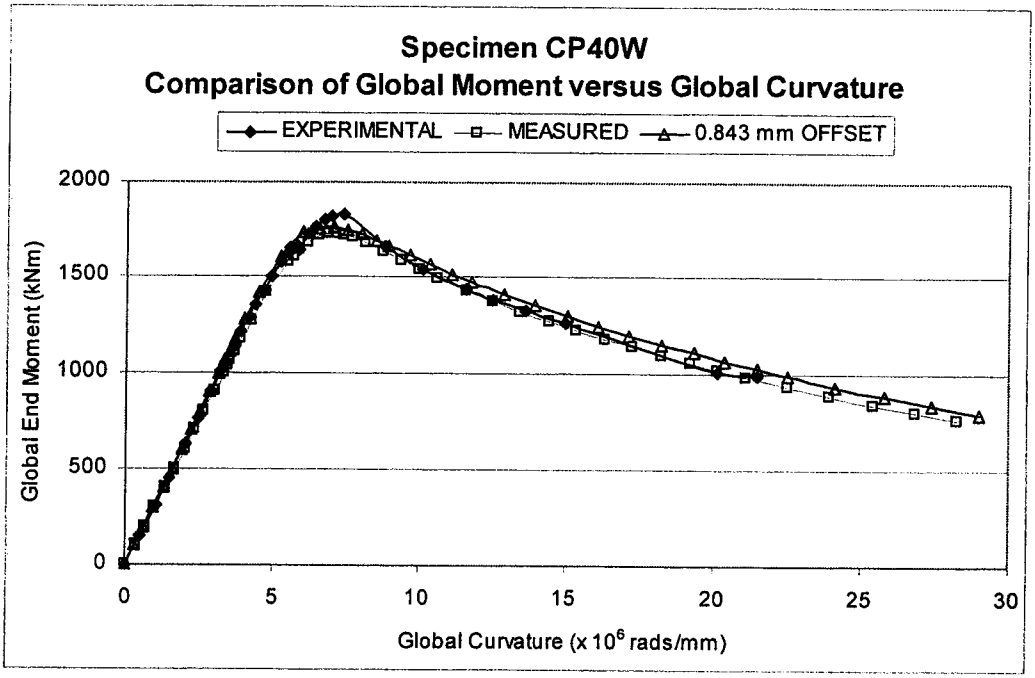

Figure 5.6 – Comparison of Experimental, Measured and 'Offset' Imperfections for Specimen CP40W

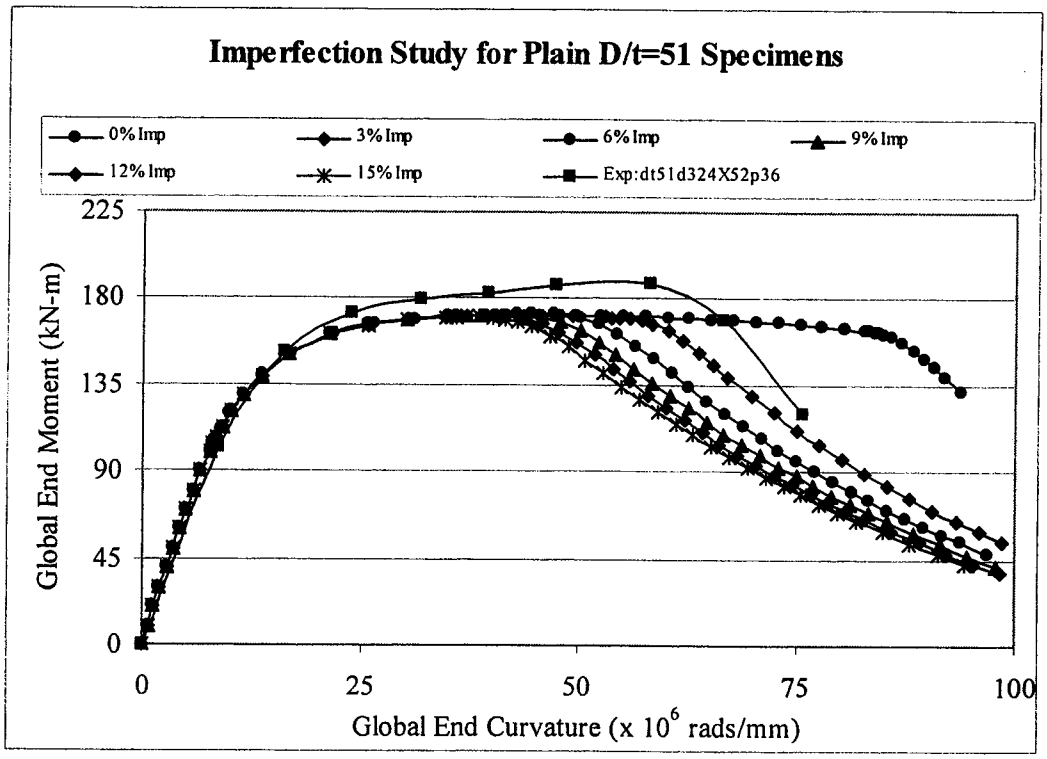

Figure 5.7 – Results of Initial Imperfection Study for Plain D/t = 51 Specimens

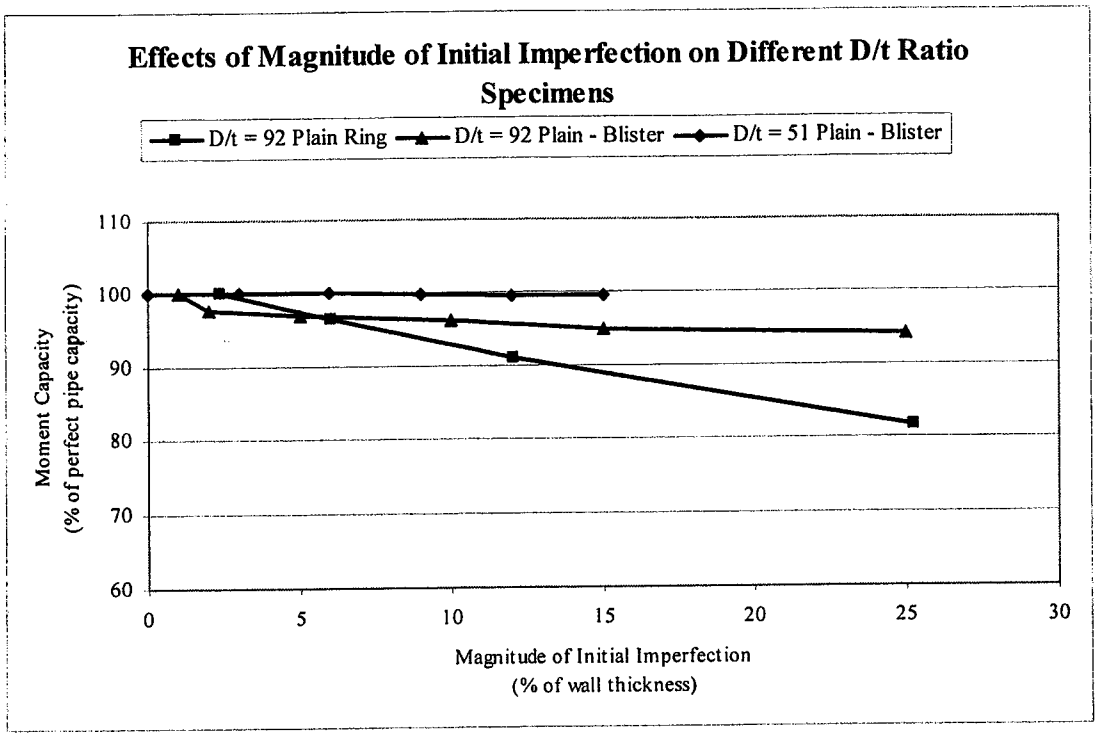

Figure 5.8 – Results of Parametric Study on the Magnitude of the Initial Imperfection on the Moment Capacity of D/t =51 Plain Specimens

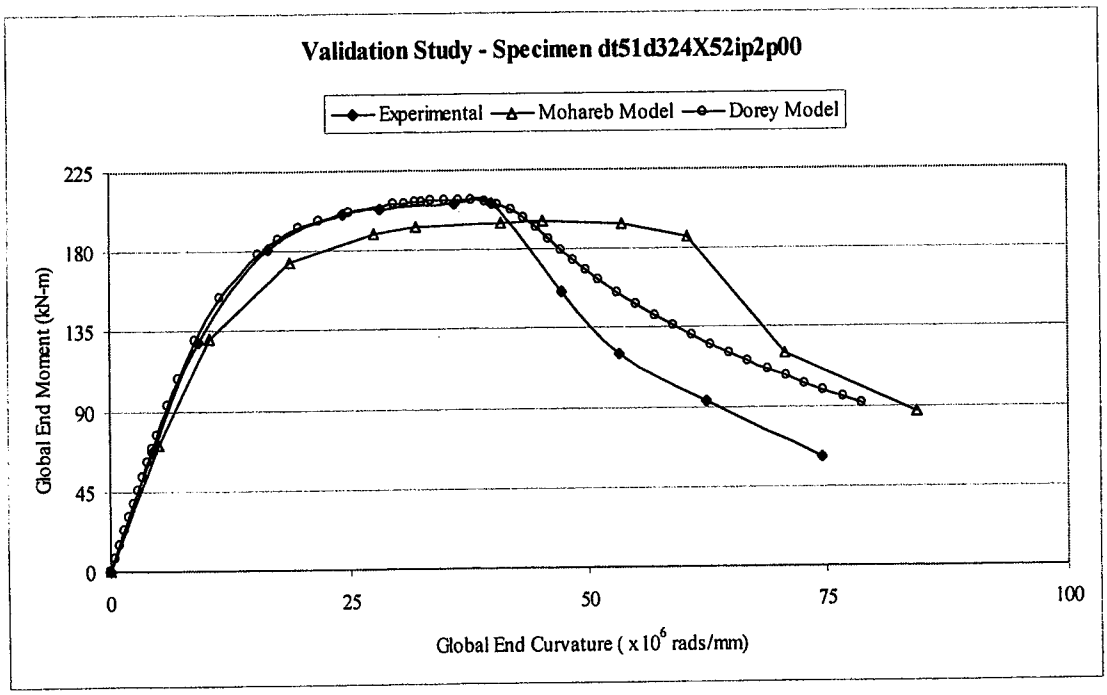

Figure 5.9 – Experimental and FEA Model Comparison for dt51d324X52ip2p00

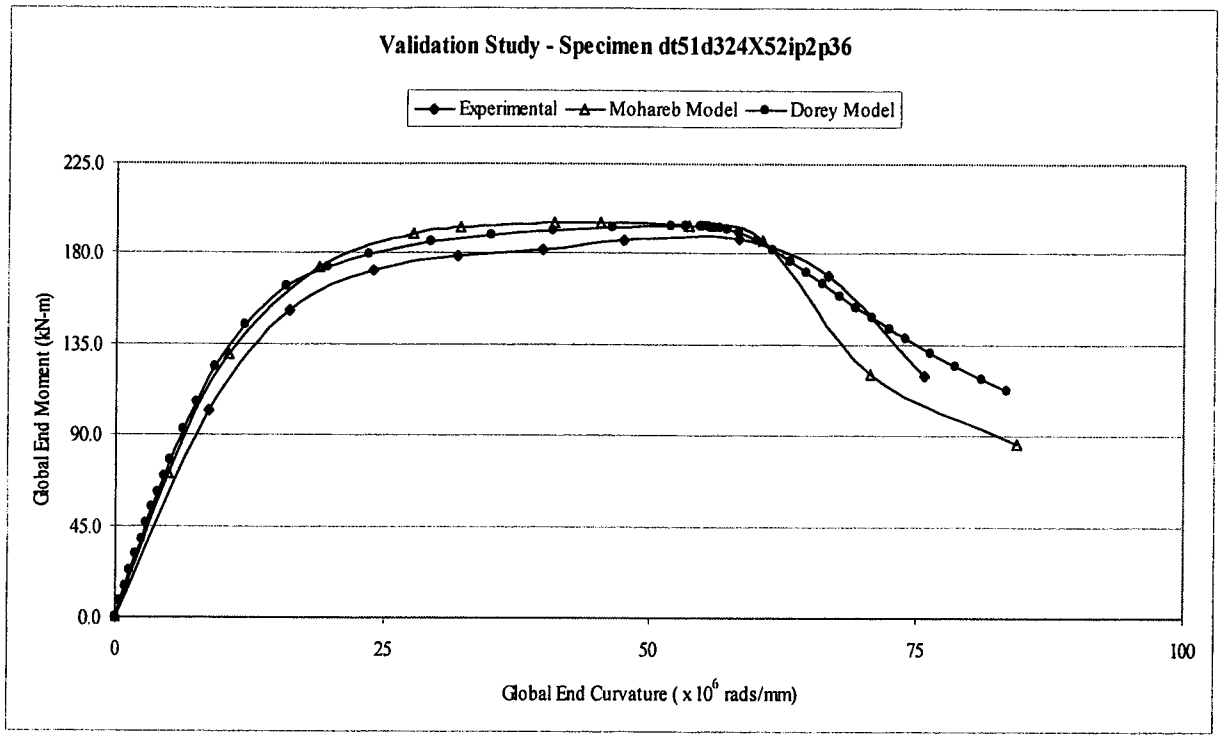

Figure 5.10 – Experimental and FEA Model Comparison for dt51d324X52ip2p36

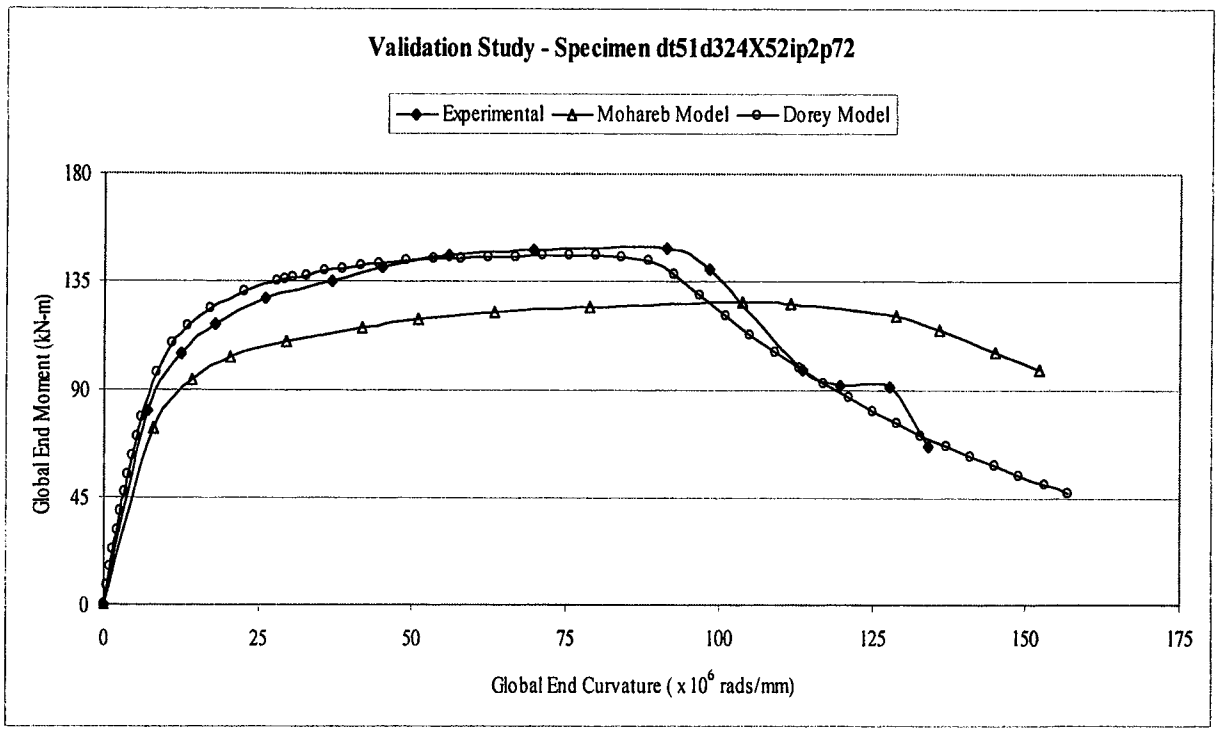

Figure 5.11 – Experimental and FEA Model Comparison for dt51d324X52ip2p72

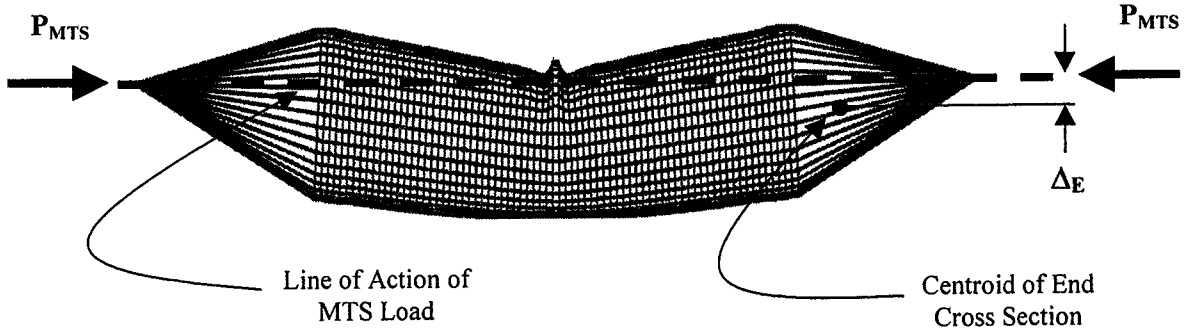

Figure 5.12 – Schematic for Determining Second-order End Moments

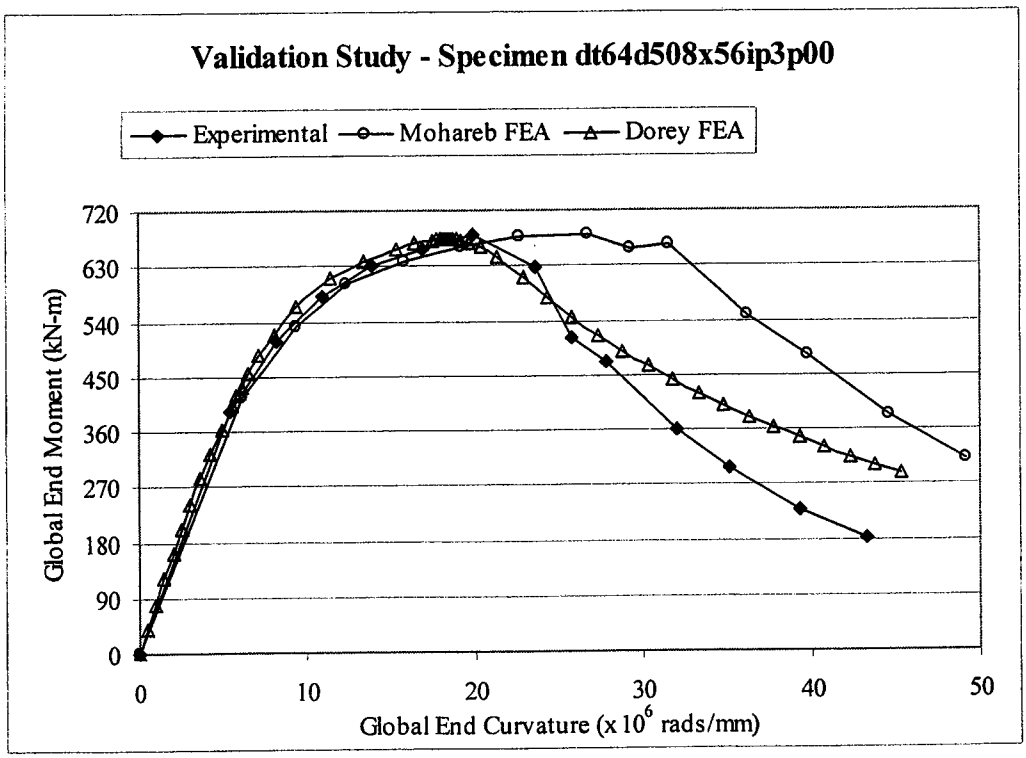

Figure 5.13 – Experimental and FEA Model Comparison for dt64d508x56ip3p00

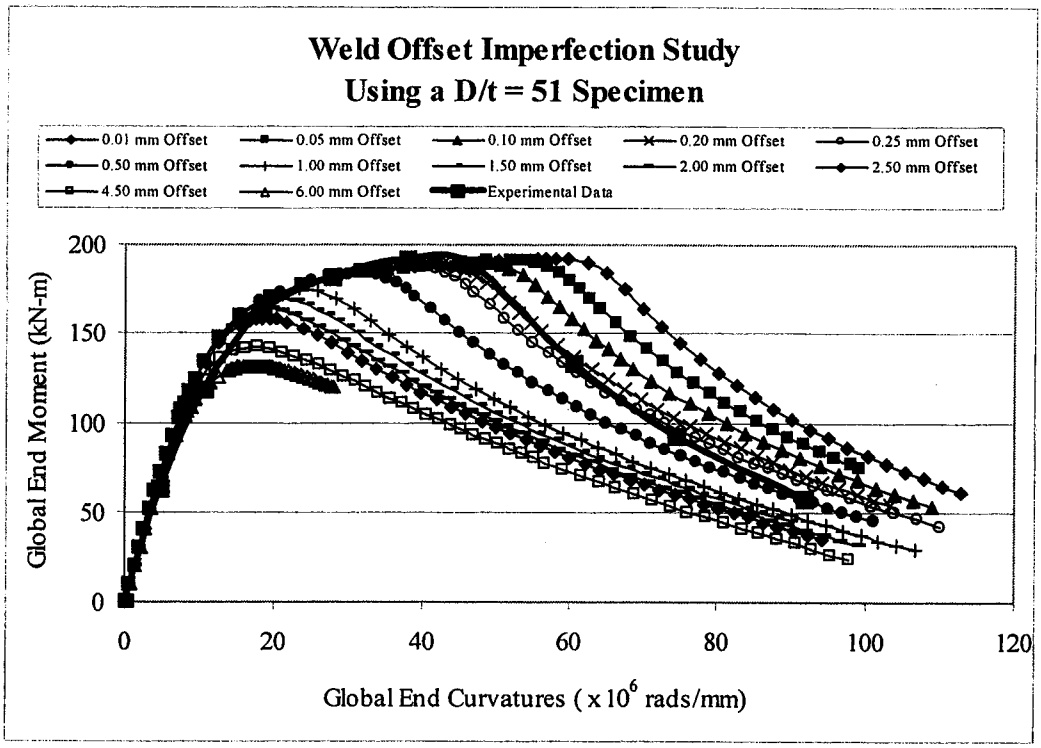

Figure 5.14 – Results of Initial Imperfection Study for Welded D/t=51 Specimens

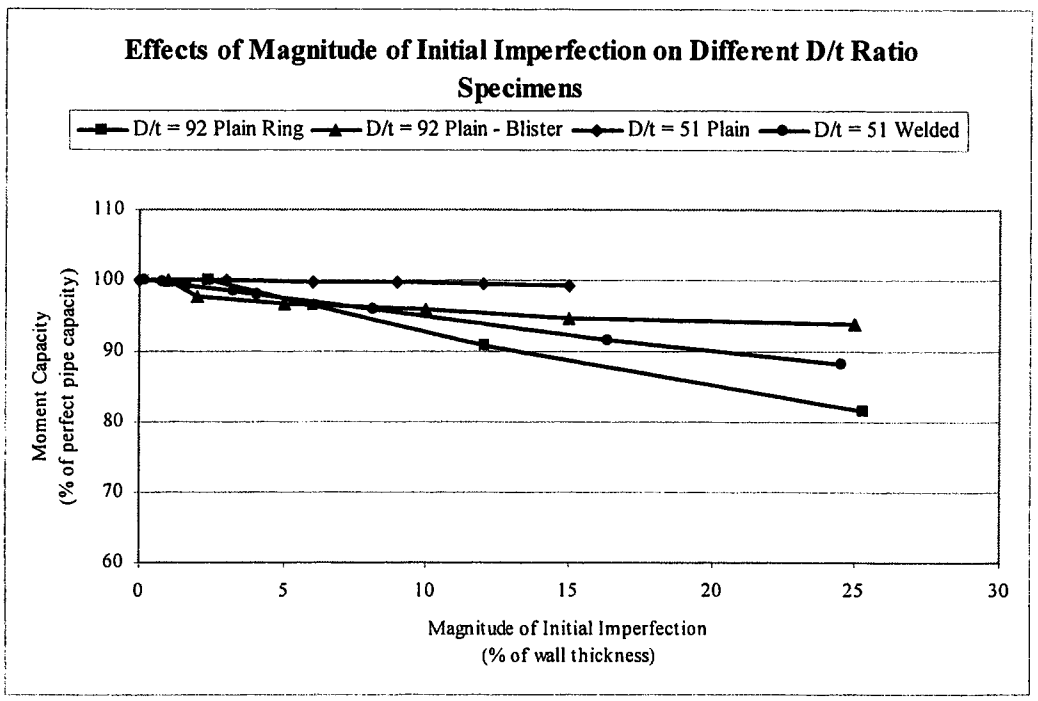

Figure 5.15 – Results of Parametric Study on the Magnitude of the Initial Imperfection on the Moment Capacity of D/t = 51 Welded Specimens

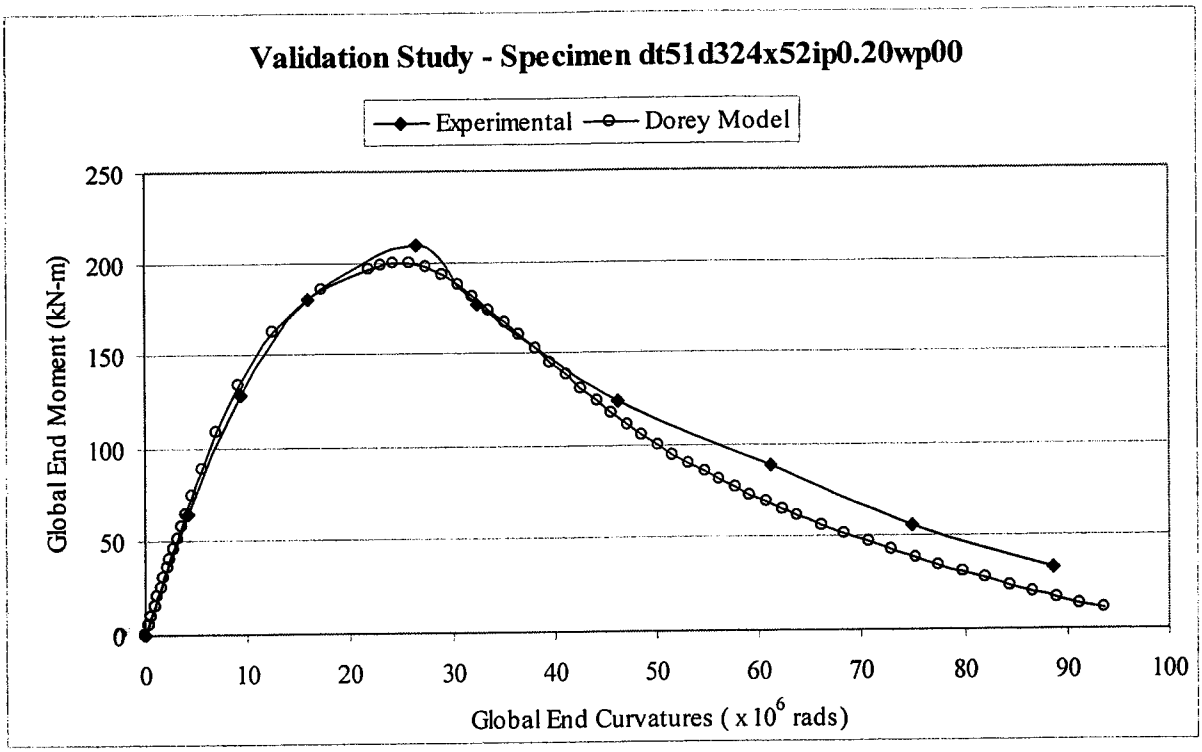

Figure 5.16 – Experimental and FEA Model Comparison for dt51d324x52ip0.20wp00

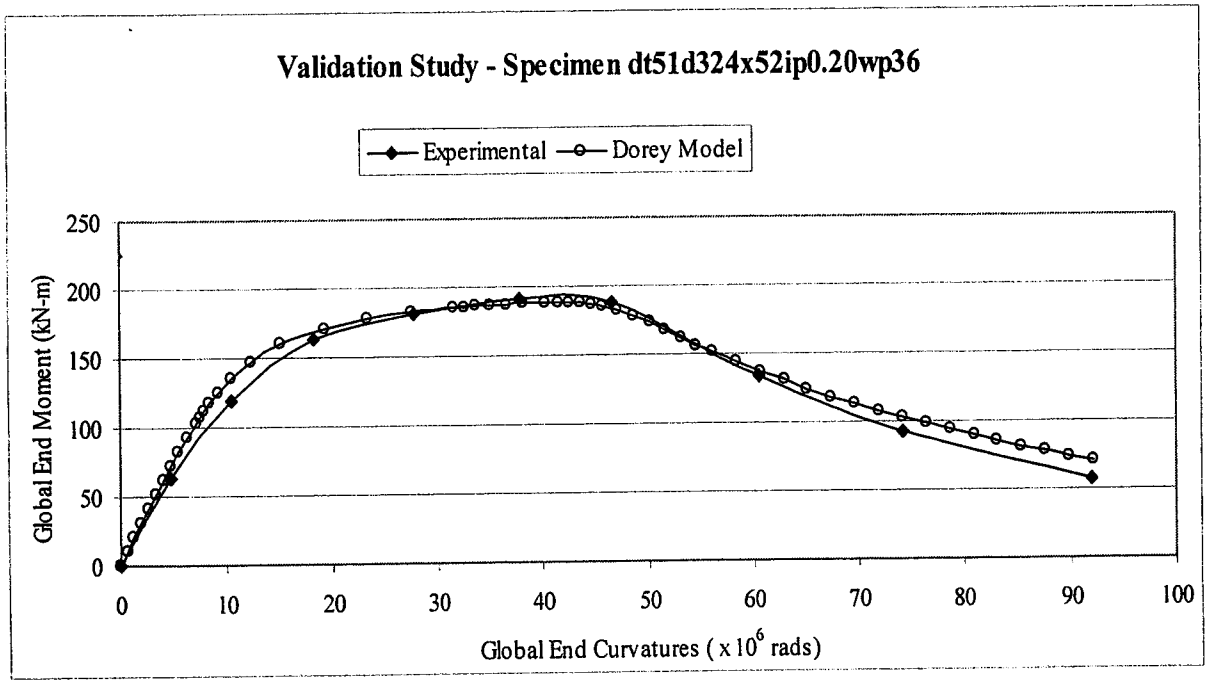

Figure 5.17 – Experimental and FEA Model Comparison for dt51d324x52ip0.20wp36

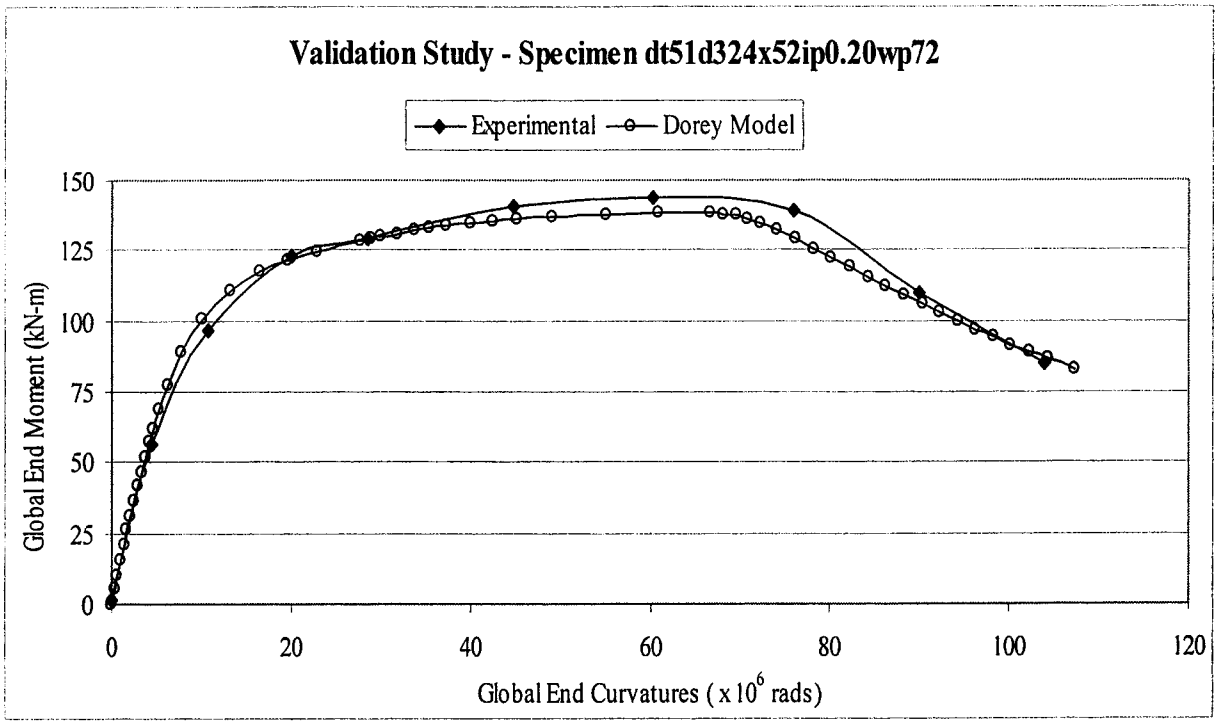

Figure 5.18 – Experimental and FEA Model Comparison for dt51d324x52ip0.20wp72

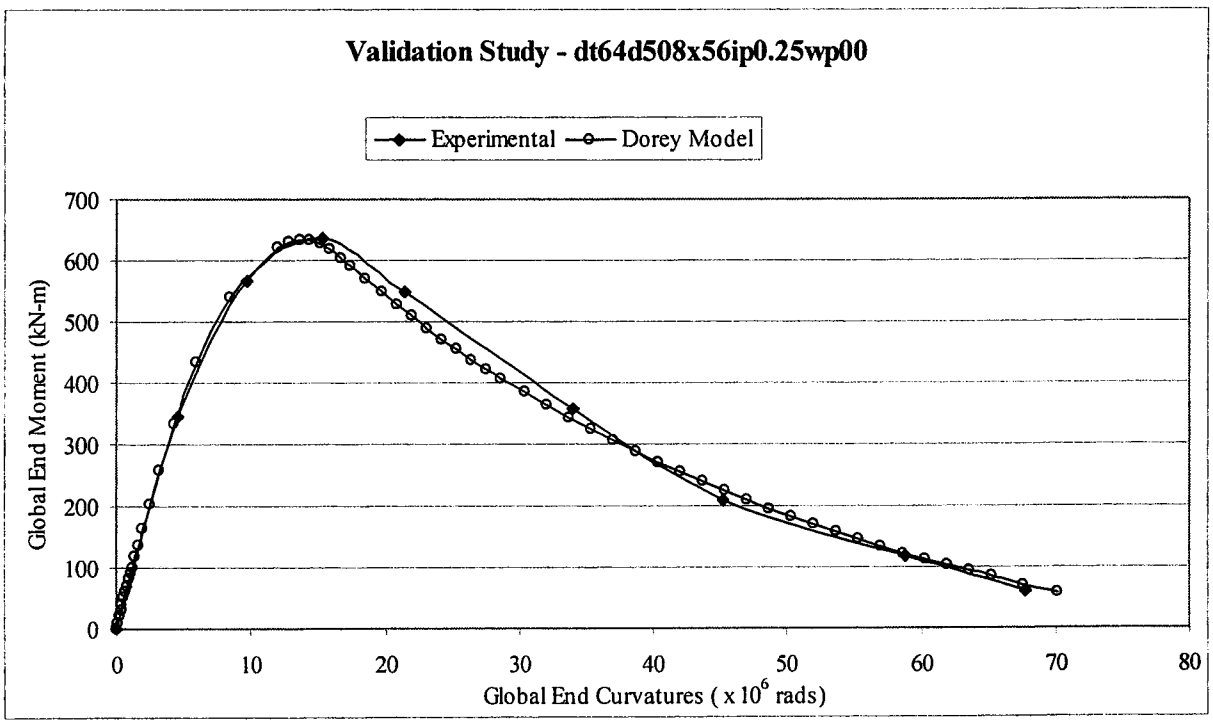

Figure 5.19 – Experimental and FEA Model Comparison for dt64d508x56ip0.25wp00

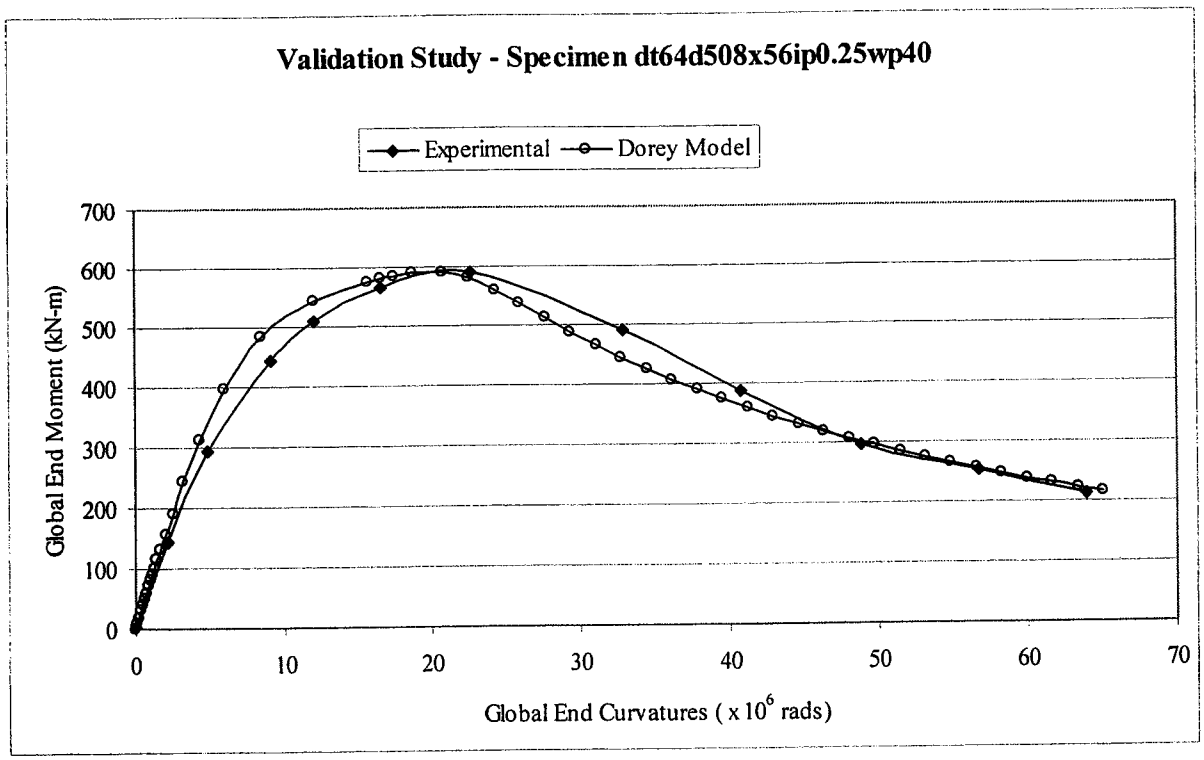

Figure 5.20 – Experimental and FEA Model Comparison for dt64d508x56ip0.25wp40

6.0 PARAMETRIC STUDY

The review of current critical strain criteria presented in Chapter 1 has shown that there is a need to establish a more accurate equation for predicting critical strain criteria. The development of an accurate computer model for predicting the response of segments of line pipe to a variety of different model parameters results in not having to conduct an expensive, time consuming testing program to examine all possible load cases. It also provides pipeline designers with a desktop tool that can analyze any particular load case and provide accurate response for each different load case.

From the comparison of the experimental and FEA results presented in Chapter 4 and Chapter 5, it is clear that the Dorey model is capable of providing accurate predictions of the load response, buckling mode and critical strain for a variety of different load cases. However, due to its complex and time-consuming nature, it is unreasonable to expect a designer to perform an FEA analysis for each segment of line pipe being designed. Therefore, a full spectrum parametric study was performed using the Dorey model to assess a variety of different load cases that are typical to buried pipelines. From the results of the parametric study, simplified design equations was developed that predict the response of selected line pipe to the different loading parameters.

Critical buckling strains are the focus of this research. Therefore, the parametric study was directed to determining the critical buckling strain for the selected pipe when different load cases are considered. Using the data extracted from the parametric study, an equation for determining the critical buckling strain, as a function of the load case parameters, was developed. This chapter presents the details of the parametric study including the characteristic values used to describe the load cases, the results of the parametric study, and the development of a critical buckling strain equation.

6.1 Determination of the Parameters to be Investigated

Through the discussions in Chapter 4 and Chapter 5, a number of variables have been identified as having a major influence on the peak moment and the critical strain developed under a given load case for a particular specimen. These parameters include the diameter, D, the thickness, t, the internal pressure, p, the material properties, including σ_y and E, the magnitude of the maximum initial imperfection and the presence or absence of a circumferential girth weld.

Noticeably absent from this list of parameters, with the exception of internal pressure, are the different load functions. This is because the critical buckling strain is a stability phenomenon and stability problems are usually considered as a function of the geometry. This is supported by examination of the universally accepted buckling criterion for columns, the Euler buckling equation. Mathematically, the Euler equation can be expressed as

$$P_{cr} = \frac{\pi^2 E I}{L_e^2} \tag{6.1}$$

where P_{cr} is the critical buckling load, I is the moment of inertia of the cross section and L_e is the effective length of the column. It should be noted that the Euler equation given above is actually intended to describe a global buckling phenomenon, while the wrinkling strains determined in this project are a local phenomenon. Therefore, the Euler equation is only cited here as an accepted example of the parameters that influence buckling and will not be further applied to the problem investigated in this project. The Euler equation can be re-arranged in terms of the critical strain instead of the critical load, giving

$$\varepsilon_{cr} = \frac{\pi^2}{\left(L_e/r\right)^2} \tag{6.2}$$

where r is the radius of gyration of the cross section . Examination of Equation 6.2 shows that the critical strain is solely a function of geometry and is independent of the applied load. It should be noted that since Equation 6.2 is for global behaviour, length is included as a variable. The length variable is not usually considered in local buckling because it is the characteristics of the local cross section that influence the buckling behaviour and length is a global variable.

In addition to this, it is logical to include a representation of the material characteristics in a strain limit formulation. That is, different materials will be able to withstand different levels of strain before local buckling occurs. This is consistent with the local buckling criteria given in CAN/CSA S16.1-94, which was presented in Equation 4.13. Examination of Equation 4.13 shows that the local buckling criteria are expressed as a function of the geometry (D/t) and the material properties (F_y).

Therefore, it can be argued that as long as the strain that develops in the wall of a pipe segment is from a combination of loads, it should be independent of the relative contribution from the different loads. That is, the critical buckling strain is a function of the level of strain in the wall of the pipe and should be independent of how the strain was developed.

This can be expanded further to consider the load history of the specimen. The load history to which a segment of line pipe has been subjected often has an effect on the strain behaviour of the specimen. As shown in Figure 4.4, the loading and unloading response of a test specimen may be influenced by the level of strain developed during the previous load cycles. However, since critical buckling strain will be assumed to be a specific level of strain, it is consistent to assume that the critical buckling strain is independent of the path by which the critical level of strain was reached. That is, a test specimen will not buckle until the critical strain is reached, regardless of the load history. Current studies in-progress at the U of A will investigate this more thoroughly. Nevertheless, the load history will not be considered to be a dependent variable in the development of a critical buckling strain equation.

While most of the load parameters are absent from the critical buckling strain formulation, this is not true for the internal pressure, which is also considered an applied load. The discussion in Chapter 4 using the von Mises yield criterion showed that the level of internal pressure affects the load carrying capacity of a test specimen and, with increasing internal pressure, the longitudinal stress capacity reduces. This is consistent, in principle, with the other applied loads. However, internal pressure has an additional effect not produced by the other applied loads. Examination of the response of the test specimens to the level of the internal pressure shows that the buckling mode is dependent on the level of internal pressure. As discussed in Chapter 4, the change from the diamond shape buckle at the unpressurized pipes to the bulge buckle for the pressurized pipes may be indicative of a change to a higher energy mode of buckling. This supports the observation that the internal pressure assists in stabilizing a specimen. This is not observed for the other applied loads, which only serve to de-stabilize the cross section. As such, it can be argued that the level of internal pressure should be included in any critical strain formulation because it plays a role in the stability of the pipe wall and stability criteria govern the buckling phenomenon.

From this discussion, it can be concluded that the local buckling strain is a function of the variables identified at the start of this section. Mathematically, they can be expressed as

$$\varepsilon_{crit} = \varepsilon\left(D, t, p, \sigma_y, E, imp, gw\right) \tag{6.3}$$

where 'imp' is the magnitude of the initial imperfection and 'gw' indicates the presence or absence of a circumferential girth weld.

6.2 Dimensional Analysis

In order to develop a critical buckling strain criteria, which is the main objective of this project, the above listed parameters need to be investigated to determine their effect on

the critical buckling strain. To perform a parametric study on the nine variables presented in Equation 6.3, a large number of analyses would be required to study the effects of each one individually. Therefore, it was decided to use dimensional analysis to reduce the magnitude of a parametric study involving each of these different variables. The details of dimensional analysis will not be presented in this report, but can be readily reviewed in a variety of sources, including Taylor (1974). However, simply stated, dimensional analysis involves relating the effect of two or more variables to produce a new non-dimensional parameter, which reflects the effect of the variables combined. By dealing with the combined variables, the number of independent variables can be reduced to a more manageable number of parameters for performing a parametric study. Dimensional analysis seems appropriate for this application. It should also be noted that using dimensional analysis will produce further simplified design criteria that can accommodate the same spectrum of variables.

DiBattista, *et al.*, 2000 conducted a short parametric study to examine the effects of assuming E is not an influential parameter in non-dimensional analysis. It is illogical to think that the critical buckling strain is independent of the bending stiffness of the material, nor independent of the strain at first yield of the material, both of which are influenced by E. From the results of that study, DiBattista concluded that E was not independent of the scaling effects present in non-dimensional analysis and that omitting E as a variable in such analysis "will lead to incorrect predictions of the behaviour."

Finally, there is no way to quantify 'gw', or convert it into a non-dimensional parameter. An individual test specimen either had a girth weld or did not have a girth weld. Due to the influence of the girth weld on the critical strain observed in previous experimental programs (Souza and Murray, 1994) and the difficulty associated with quantifying the presence or absence of the girth weld, it is accepted that separate critical buckling strain equations will be developed for the plain pipe test specimens and the girth welded specimens. This is supported by the findings from the effect of the different initial imperfection patterns presented in Chapter 5. As was observed in Chapter 5, different initial imperfection patterns have different effects on the response of the FEA model to a

particular load case. Different initial imperfection patterns were used to simulate the plain pipes (blister initial imperfection) and the girth welded pipes (can offset at the girth weld). Therefore, it would be virtually impossible to assimilate the two different initial imperfection patterns into a single, comprehensive design equation that provided accurate predicted values for the critical buckling strain. Consequently, two critical strain equations will be proposed, one for the plain pipe specimens and one for the girth welded specimens.

This leaves six variables for consideration in the dimensional analysis. That is,

$$\varepsilon_{crit} = \varepsilon\left(D, t, p, \sigma_y, E, imp\right) \tag{6.4}$$

There are a variety of different methods that can be used to reduced the number of variables to be used in dimensional analysis (Langhaar, 1951). For engineering applications, one of the more popular methods is the Buckingham-Pi Theorem, which will be used in this project. The theorem states that "if an equation is dimensionally homogeneous, it can be reduced to a relationship among a complete set of dimensionless products." The number of dimensionless variables that are required to form a complete set of dimensionless products is 'v-r', where 'v' is the total number of variables used to construct a dimensional matrix of the variable and 'r' is the highest rank of the dimensional matrix. It should be noted that the magnitude of the initial imperfection, 'imp', is already a non-dimensional parameter because it is expressed as the maximum amplitude of the initial imperfection, in units of mm, divided by the wall thickness of the specimen, also in units of mm. As such, the inclusion or omission of 'imp' will not affect the total number of non-dimensional parameters determined using the Buckingham Pi Theorem. For completeness, 'imp' will be included in the analysis.

The dimensional matrix, expressed in the fundamental units of mass (m), length (L) and time (T), used to describe each of the six variables in Equation 6.4 takes the following form:

	D	T	p	σ_y	E	'imp'
m	0	0	1	1	1	0
L	1	1	-1	-1	-1	0
T	0	0	-2	-2	-2	0

The total number of variables is six and the rank of this dimensional matrix is two, therefore, using the Buckingham-Pi Theorem, the variables of equation 6.4 can be reduced to four independent, non-dimensional, π-terms. Considering the first five variables presented in the dimensional matrix, three common pipeline industry terms are evident, namely D/t, σ_h/σ_y (or p/p_y), and σ_y/E. As previously mentioned, 'imp' is a non-dimensional parameter on its own. Therefore, the critical buckling strain, as a function of the four non-dimensional parameters that were derived using the Buckingham-Pi Theorem, can be expressed as

$$\varepsilon_{crit} = \varepsilon\left(\pi_1, \pi_2, \pi_3, \pi_4,\right) \tag{6.5}$$

where

$$\pi_1 = \frac{D}{t}$$

$$\pi_2 = \frac{\sigma_h}{\sigma_y} = \frac{p}{p_y}$$

$$\pi_3 = \frac{\sigma_y}{E}$$

$$\pi_4 = \frac{amp_{Max}}{t} \times 100\%$$

- for plain pipe specimens with 'blister' type initial imperfections

or,

$$\pi_4 = \frac{offset}{t} \times 100\%$$

- for girth welded specimens with 'offset' type initial imperfections

6.3 Range of π-Parameters Investigated

6.3.1 Range for Diameter-to-thickness (D/t) Ratio

Segments of line pipe currently in-service in Canada have D/t ratios that range from as low as D/t = 10 to as high as D/t =120. While it would be advantageous to develop critical strain criteria that cover the entire spectrum of these D/t ratios, this is not practical. Furthermore, the range for which experimental data exists and for which the Dorey FEA model has been validated is limited to approximately $50 \leq D/t \leq 90$. Since one of the mandates of this project is to develop reliable critical buckling strain criteria, it was decided to use D/t ratios of 50, 70, and 90 for the π_1 parameter (D/t ratio) in the subsequent parametric study. By limiting the D/t ratio to these three values, experimental data would be available to compare with the values predicted by the criteria developed from the results of this parametric study.

Current research at the U of A has been proposed to expand the D/t ratio to as high as 120, but this experimental testing program has not been completed as yet. Upon completion of the additional testing program, the Dorey model will be used to predict a comparison value for the experimental data and further expand the current critical strain database.

A short parametric study was conducted to examine the influence of the diameter of the specimen. This was done to determine if there was a size effect on the critical strain due to a variation in the diameter while holding all of the non-dimensional parameters constant. The results of this short parametric study would confirm whether the critical strains from different sized specimens can be included in the same data set for comparison purposes.

The results of this parametric study are presented in Table 6.1. As would be expected, the moment capacity increased with increasing D. This is due to the increased area and stiffness of a larger diameter cross section. However, as can be seen in the results presented in Table 6.1, the critical buckling strain appears to remain essentially constant

for a given load case, regardless of the diameter of the test specimen used. That is, D did not influence the response of the FEA model in terms of the predicted critical buckling strain. Therefore, it was decided to use a specimen with a diameter of 324 mm for the D/t ratio of 50 mesh, a specimen with a diameter of 508 mm for the D/t ratio of 70 mesh and a specimen with a diameter of 762 mm for the D/t ratio of 90 mesh. The different diameters and lengths used in the parametric study are given in Table 6.2. This was done to minimize the number of input meshes required to conduct the entire parametric study. These sizes for the diameters were picked based on common pipe sizes used in the field and on the size of the experimental test specimens for which the critical strain data had been recorded at the U of A.

6.3.2 Range for Internal Pressure (p/p_y) Ratio

As was discussed in Section 2.1.2, under field operating conditions, the level of internal pressure can range from zero to full operating pressure, as defined in the current CAN/CSA Z662-96 standard. The current CAN/CSA Z662-96 standard limits the maximum operating pressure in segments of line pipe to a value that corresponds to a stress of 80% SMYS in the hoop direction, as was shown in Equation 2.4. Therefore, the two extremes of zero internal pressure (hereafter referred to as '0% pressure') and full internal pressure (hereafter referred to as '80% pressure'), as allowed by CAN/CSA Z662-96, will be used as boundaries for the parametric study. It should be noted that for the purposes of this parametric study, the value of σ_y was equated to SMYS. It is acknowledged that this is not true of actual steel line pipe materials, however, there is no industry standard that relates the value of SMYS to σ_y. except that SMYS provides a lower bound on σ_y. Furthermore, it is common practice in industry to use SMYS as σ_y when performing numerical calculations. This issue will be addressed further in Section 6.8.

In order to try to capture the behaviour between these two boundaries, an intermediate value for the internal pressure was included. This intermediate value corresponds to a stress of 40% SMYS in the hoop direction (hereafter referred to as '40% pressure').

These three values for the π_2 parameter were also selected based on their comparability to existing data in the experimental database.

6.3.3 Range for Material Properties

The third π-parameter (σ_y/E) accounts for the variation in material properties between different load cases investigated. Since E is assigned a constant value of 207 000 MPa in CAN/CSA Z662-96, the value of π_3 will be directly proportional to the yield strength of the material, as defined in the following section. The experimental value of the SMYS for the different specimens modeled in Chapter 4 and Chapter 5 ranged from 359 MPa (Grade X52) to 483 MPa (grade X70). However, the actual yield strength of the materials as determined in the coupon tests, ranged from 378 MPa (55 ksi) to 550 MPa (80 ksi). Therefore, it was decided that the experimental data would be adequate to support a parametric study with specimens that had SMYS ranging from 359 MPa (grade X52) to 550 MPa (grade X80). These two values were used as the upper and lower bounds for the π_3-parameter. An intermediate value was also selected for the SMYS of the load cases examined in the parametric study. The value of 448 MPa (grade X65) was chosen because it is approximately halfway between the two bounds and because it corresponds to a common commercial grade of steel used in the pipeline industry.

It should be noted that the mathematical definition of π_3 given in Equation 6.6 was selected as a convenient non-dimensional π-parameter, given the available dimensional analysis variables. The literal engineering definition of π_3 given in Equation 6.6 is commonly referred to as the yield strain. However, this common definition of yield strain is somewhat misleading in the analysis of line pipe. In the pipeline industry, the yield stress is commonly accepted as the stress that corresponds to 0.5 % strain (Zhou, *et al.*, 1996), which has been adopted throughout this document. Adhering to this definition indicates that the yield strain is a constant 0.5 %. Clearly the yield strain and the modulus of elasticity, E, can not both be constant for different grades of material since the stress is the product of strain and E over the linear elastic region. Therefore, while the expression 'yield strain' is inferred in the definition of the π_3-parameter, it is not indicative of the strain that corresponds to the yield stress.

6.3.3.1 Development of a Material Model

Unlike the first two π-parameters, the FEA model input of the material properties for a given load case is not as simple as inputting the value of the π_3-parameter. Material properties can vary significantly within a given grade of material. Specifically, significant variations can exist in the proportional limit, the actual yield stress, the ultimate stress and the corresponding strains for each of these stresses. The effect of these variations on two load cases subjected to the same grade of material, but having different proportional limits and ultimate strengths, can be quite significant. An example of this can be seen in Figure 4.84, which compared the CP80 load case tested under two different material properties, although both were the same grade, X70. Examination of the two different material curves used for specimen CP80N-1 (material type P2) and specimens CP80N-2 (material type N) shows that the P2-type material coupon had a smooth rounded shape whereas the N-type material coupon had a distinct yield plateau. As was discussed in Section 4.1.1, a distinct yield plateau is not a typical characteristic of segments of line pipe (Zhou, *et al.*, 1996), which are usually hydrotested and/or mechanically expanded during fabrication. The effect of the hydrotesting and/or mechanical expansion should result in material specimens that essentially exhibit no yield plateau, as discussed in Section 2.2.1. It is therefore concluded that the presence of a yield plateau is not a normal characteristic of line pipe and the smooth rounded curve will be adopted in the material model for the parametric study.

Selecting the exact shape of the smooth rounded material curves was rather subjective. As discussed in Section 4.7.2, the proportional limit can have a significant effect of the global curvature that develops and the resulting critical buckling strain. In this section it was observed that the higher the proportional limit, the lower the resulting critical buckling strain. Consultation with numerous industry sources indicated that the proportional limit typically ranges from 0.5 to 0.75 σ_y. It was therefore decided to select the proportional limit as 0.75 σ_y to provide a conservative critical strain prediction. It is acknowledged that a material coupon with a proportional limit greater than this, or with a

distinct yield plateau, will result in a reduction in the critical buckling strain. This will be further addressed in Section 6.6.2.1.

The industry accepted standard for the yield point for segments of line pipe is the stress that corresponds to a strain of 0.5%. However, the stress at 0.5% strain can vary significant for a specific grade of pipe. Examination of the coupon data collected in this project and presented in Tables 4.1 and 4.2 shows that the different material coupons for the grade X70 pipe had yield stresses that ranged from 472 MPa to 550 MPa. Furthermore, it should be noted that in all but one case, the actual yield strength was greater than the SMYS of 483 MPa. However, there is no accepted industry standard for determining how much greater the actual yield stress is than the SMYS without actual material coupon data. Therefore, for simplicity and reproducibility of the results, it was decided to equate the value of the yield stress used in the material model for the parametric study to the grade of the material. That is, the yield stress of a grade X65 (448MPa) specimen will be 448 MPa. It is realized that for most cases, this assumption introduces a substantial underestimate of the actual yield strength, nevertheless, it was decided that this assumption provided the most rational approach available. This influence of this decision will be discussed further in Section 6.7.

As with the proportional limit and yield stress, there can also be a large variation in the ultimate strength achieved by line pipe material. Referring again to the five different grade X70 material properties presented in Tables 4.1 and 4.2, the ultimate stress ranged from 569 MPa to 593 MPa. However, Table 8.1 of CAN/CSA Z245.1-95 specifies the tensile property requirements of segments of line pipe after fabrication. It is acknowledged that using the minimum specified tensile strength provided in Table 8.1 of CAN/CSA Z245.1-95 as the ultimate yield strength will result in an unconservative estimate of the critical strain. Again there is no industry standard for the maximum tensile strength of a particular grade material. However, the effect of underestimating the tensile strength was considered negligible since all of the specimens reached their critical buckling strains and lost capacity well before the ultimate stress was reached. Therefore,

the slope of the assumed material curve between the yield stress and the ultimate stress had only a minor influence on the critical buckling strain.

There is no standardized value of the strain at ultimate for different grades of line pipe. To address this issue, different industry sources were again consulted. As would be expected, a range of values was suggested. From the suggested values, a value of 12% strain at ultimate was selected as a typical, representative value.

The coordinates of the point of rupture on the stress strain curve were selected as (ε=22%, σ_y). It is acknowledged that the coordinates of the point of rupture can vary significantly from this value, however, it should be noted that this point was not relevant to the problem under investigation because the maximum critical buckling strain that was observed in any of the parametric study results is only 5.4% strain, which occurs prior to the ultimate stress. Therefore, the assumed material property curve in the post ultimate region did not influence the critical buckling strain. The point of rupture is only included for completeness of the material property curve.

From the foregoing discussion, the following key data points were selected to represent the assumed material properties used in the parametric study:

Proportional limit:	stress: $0.75\sigma_y$	strain: $0.75\sigma_y/E$	(6.7)
Yield :	stress: σ_y	strain: 0.5 %	
Ultimate:	stress: Table 8.1 Z245.1-95	strain: 12 %	
Rupture:	stress: σ_y	strain: 22 %	

where σ_y is assumed to be equal to SMYS or the grade of the material and E is equal to 200 000 MPa. This value of E was selected based on the results from the material coupon tests presented in Tables 4.1 and 4.2. Once these points were selected and calculated for each of the three grades of material selected for used in the parametric study, grades X52, X65 and X80, a material property curve was generated. This curve was generated by plotting the points listed above and then visually selecting data points

in between to provide a smooth rounded curve. Figures 6.1, 6.2, and 6.3 provide a graphical representation of the assumed material curves for grade X52, X65 and X80, respectively, used in the parametric study. Table 6.3 provides the numerical data for the curves presented in Figures 6.1, 6.2, and 6.3, as well as the true stress/strain data, calculated using Equations 3.1 and 3.2, required for input into the FEA model. The experimental grade X52 material properties, as recorded by Mohareb during his testing program, are included in Figure 6.1 for comparison with the assumed material properties used in the parametric study.

The final required value needed to complete the definition of the material properties assumed for the parametric study was the value of Poisson's ratio. The accepted industry value for ν is 0.3, therefore, the value of 0.3 was used throughout the parametric study.

6.3.4 Range for Initial Imperfections

The fourth π-parameter (imp) accounts for the initial imperfection pattern in the pipe. As has been discussed and developed in Section 5.1, a different assumed initial imperfection pattern was developed for the plain specimens than for the welded specimens. In the discussion of Section 6.2, it was concluded that the response of the FEA model is different for different initial imperfection patterns. As such, it was decided to compile a database of critical strain data for the plain specimens separate from the welded specimens.

6.3.4.1 Blister-Type Pattern for Plain Pipe Specimens

For the plain pipe specimens, a total of 4 different amplitude initial imperfections were selected for study. These different amplitude initial imperfections included 2%, 8%, 16% and 30% of the wall thickness of the individual specimens. The 2% wall thickness amplitude was selected because using an amplitude less than this often resulted in doubly symmetric end buckles as was shown in Figure 3.7. This type of buckling mode has never been experienced in any of the specimens tested at the U of A. Furthermore, it would be difficult to properly assess the critical buckling strain for this type of failure. This decision was also based on the fact that it is highly unlikely that a typical segment of

line pipe would have an initial imperfection less than 2% of the wall thickness as was presented in Section 5.1.1

Review of the current CSA and API standards did not directly specify a limit for initial imperfections of this nature. Both codes offered wall thickness and out-of-roundness limits, but neither of these could be translated directly to the 'blister-type' initial imperfection selected for modeling. Therefore, the upper limit selected for study in the parametric study was based on experimental measurements. The maximum amplitude for the blister initial imperfection of 30% the wall thickness was selected by adding approximately 20% to the maximum imperfection measured in the experimental portion of this project. The additional two initial imperfection amplitudes were selected to provide intermediary data between the lower bound of 2% wall thickness and the upper bound of 30%.

It should be noted that the buckled shape of a number of the unpressurized specimens examined in the parametric study had a symmetric, indentation, buckling mode. An example of this buckling mode is shown in Figure 6.4. This buckling mode was not consistent with any of the laboratory observations, nor validation study buckling modes. It is believed that the observed buckle developed as shown due to the symmetry included in the smooth blister used as the initial imperfection pattern.

It is unclear why this mode appears in only some of the load cases. The critical buckling strain corresponding to this buckling mode is difficult to quantify and often results in strains that were not consistent with complimentary experimental data by as much as 500%. It was therefore decided to shift the location of the initial imperfection along the length of the specimen by 5% of the total length. This shift caused less than 1% difference in the peak moment capacity, but created a small amount of asymmetry in the initial imperfection pattern. This asymmetry resulted in the typical diamond buckle developing in every one of the unpressurized specimens examined in the parametric study and provided critical buckling strains that were consistent with the experimental data.

6.3.4.2 Offset-Type Pattern for Girth Welded Specimens

As discussed in Section 5.1, either a blister-type or an offset-type initial imperfection pattern was used on a given test specimen, but not both. Since an initial imperfection pattern of some type exists in all segments of line pipe, it was decided to use the 2% wall thickness amplitude initial imperfection data described in the previous section to represent a perfectly aligned weld. That is, it was felt that the 2% blister initial imperfection pattern was representative of a welded specimen with no offset. Therefore, the data collected in the plain pipe parametric study for the 2% blister initial imperfection was also used as a data series for the welded specimens.

Weld meshes with initial offsets of 1.5 mm and 3.0 mm were also selected for study. The upper bound offset (3.0 mm) was selected based on knowledge of the equipment used to align the two cans under field conditions and on the offsets recorded in this program. These offsets were previously presented in Table 5.1. The maximum experimentally recorded offset was 2.24 mm. Therefore, to ensure that the range of likely offsets was covered, the 3.0 mm upper bound was selected.

It is recognized that this upper bound is excessive for the D/t = 50 specimens, which had a diameter of 324 mm and a wall thickness of 6.48 mm and would be unlikely to occur in field installations. Nevertheless, this ensured a conservative boundary for the parametric study. The initial offset value of 1.5 mm was selected to provide intermediary data between the two extremes that were selected.

6.3.5 Additional Parameters Used in the Parametric FEA Model

Prior to starting the parametric study, two additional parameters need to be clarified. It was decided to make the length of each parametric study specimen a function of the diameter. For the experimental specimens with a D/t ratio of 92, the length of the specimen was approximately 3.5 diameters and the elephant's foot buckle was predominant in the plain specimens. For the experimental specimens with a D/t ratio of 51, the length of the specimen was approximately 5 diameters and the buckles were predominately located away from the end collars. Therefore, it is believed that the

elephant's foot buckles experienced in the large D/t ratio specimens may have been avoided had the specimen length been increased. One of the recommendations of research done by Del Col, *et al.*, 1998 was to use specimens of greater length to avoid the elephant's foot buckle. As such, it was decided that all FEA model specimens would have a length of 5 times the diameter of the test specimen. Table 6.3 provides the lengths used for each different diameter specimen.

The 40x75 mesh selected in the mesh refinement study presented in Section 3.3.6 was used for all of the different meshes in the parametric study. It is acknowledged that this mesh was developed specifically for the D/t = 92 ratio specimens and a mesh refinement study was not conducted for the specimens with the different D/t ratio. However, the mesh refinement study conducted by Mohareb, *et al.*, 1994, for specimens with D/t ratios of 51 and 64 showed that convergence of the solution was achieved with a 36x60 mesh. Since the 40x75 mesh is actually finer than the one optimized by Mohareb, it is obviously acceptable. It should be noted that the 40x75 mesh is finer than required and, therefore, requires additional computational time. However, a 40x75 mesh generator had already been developed for use in this project and developing new mesh generators would have required more time to do than the cumulative additional time to run the smaller D/t ratio specimens with the finer mesh.

Finally, the location for the pivot points in the model had to be selected. Theoretically, the location of the pivot points should not influence the moment-curvature response or the critical buckling strain because the end caps are modeled as rigid bodies and no deformations within these rigid caps is allowed to occur. It should be noted that the distance between the pivot points and the ends of the test specimens would affect the global moment applied at the end cross section, as discussed in Section 5.2.2. However, as mentioned in Section 5.2.2, the moment applied to the end of each specimen will be calculated using Equation 5.1, as represented in Figure 5.12. Therefore, the distance between the pivot points and the ends of the specimens is irrelevant. Nevertheless, a value had to be specified. It was decided to use the value of 339 mm which was the distance measured experimentally for the specimens with a D/t ratio of 92 investigated in

the experimental portion of this project. Table 6.2 provides the longitudinal coordinate of the two pivot points for each different length specimen. Since the centroid of the bottom end of the test specimen was selected as the reference origin, the negative sign for the bottom pivot point indicates that it is located below the bottom of the specimen, as was the case in the experimental test set-up.

6.4 Load Cases Analyzed

From the discussion in Section 6.3 the following test matrix was developed for each level of initial imperfection considered:

D/t Ratio	p/p_y Ratio	Material Grade	Initial Imperfection
			2% blister
			8% blister
50	0.00	X52	16% blister
70	0.40	X65	30% blister
90	0.80	X80	1.5 mm offset
			3.0 mm offset

(6.8)

From the test matrix given in Equation 6.8, a total of 162 (3 x 3 x 3 x 6) input files were generated for the parametric study. Appendix E provides six tables, one for each level of initial imperfection, showing the parameters used for each specimen investigated in the parametric study. All of the load cases presented in each of the six tables in Appendix E are identical, with the exception of the level of initial imperfection.

Examination of the first table in Appendix E, which corresponds to a 2% blister-type initial imperfection, shows each of the 27 load cases run at each level of initial imperfection. The nomenclature used in identifying the different load cases was previously identified in Section 5.2.1. For each D/t ratio, nine load cases were run, providing all possible combinations of grade of material and internal pressure. The

D/t = 50 load cases are shown in the first block of rows for each level of initial imperfection, the D/t = 70 load cases are in the second block and the D/t = 90 load cases are in the third block. The second column of each table provides the D/t ratio for the specific load case and the third column provides the level of internal pressure as a ratio of the pressure required to cause yielding in the circumferential direction. The fourth column gives the diameter of the specimen and the fifth column presents the yield strength.

The sixth column is the thickness required to be input into the FEA model. This thickness was calculated based on the D/t ratio and diameter for each load cases. The seventh and eighth columns provide the inside radius, r_i, and cross sectional area, A, which are required for subsequent calculations in the spreadsheet. The ninth column provides the internal pressure required to cause yielding in the circumferential direction, p_y, for the specified cross section. The equation to calculate p_y is provided in 'Note 1.' at the bottom of the table. The tenth column, 'FEA pres.', presents the internal pressure input into the FEA model for the specified load case. 'Note 2.' provides the equation for determining the value of FEA pres.

The last four columns provide the details of how the required axial load for each load case was calculated. The equation used to calculate each of the different axial load effects experienced by a specimen under each of the respective load cases is indicated at the top of the respective columns, above the variable which was calculated. For example, Equation 2.5 was used to calculate the value of P_α. These equations are the same ones that were used to determine the experimental loads, as described in Chapter 2.

The three shaded columns in each of the tables of Appendix E are the variables required as direct input into the FEA model for the respective load cases. The specimen diameter, level of initial imperfection, and the length of specimen were all incorporated in the generation of the 40x75 mesh used, and were input into the FEA model by importing the respective mesh for each load case. The location of the pivot points, the values of E and

ν, and the generation of the rigid end caps were all specified directly in the FEA model template.

This completes the description of the variables investigated in the parametric study, the corresponding load cases, and how they were input into the FEA model template.

6.5 Results of the Parametric Study

Once all 162 FEA analyses were run for the parametric study, the data was reduced to determine the peak moment capacity and the critical buckling strain for each of the load cases. Tables 6.4 through 6.9 present the results of the parametric study and the different π-parameters for each load case. Each table presents the peak moment and critical buckling strain results for a different level of initial imperfection. The data reduction to determine the peak moments and the critical buckling strains was done using the same approach as was used for the FEA data reduction for the experimental load cases. The generation of the FEA global moment-curvature plots was done using the procedure described in Section 4.3.1 and the FEA critical buckling strains were determined using the procedures described in Section 4.2.3 and Section 4.3.2.

Once the data was collected, the effect of the different π-parameters on the response of the model was examined. This was done for two main reasons. The first reason was to determine the sensitivity of the model to the different π-parameters. It is important to establish the sensitivity of the model to the different π-parameters so that future users of the results will be able to assess the importance of the input they select.

The second reason was to determine the effect of the different π-parameters on the critical buckling strain. The effect of the different π-parameters on the critical buckling strain will be presented primarily in graphical form. From these plots, the general relationship between the π-parameters and the critical buckling strain can be observed and will aid in the development of a predictive equation. It should be noted that since

there are four different π-parameters used to define the critical strain, as shown in Equation 6.6, it is not possible to simply plot the critical strain as a function of all the variables in 3D space. Instead, the effect of each π-parameter will have to be examined on an individual basis. Because of this and due to the vast quantity of data, over 150 plots were generated to examine each of the different π-parameters. Only a representative sample of the plots will be presented in the following sections, which outline the results of the effects of the different π-parameters.

6.5.1 Effects of the D/t Ratio (π_1-parameter)

Only the effects of the D/t ratio on the critical strain data will be presented in this section. This is because of the different diameter specimens used for each of the D/t ratios. It was discussed and concluded in Section 6.2.1 that diameter was an independent variable in the determination of the critical buckling strain. However, the results presented in Table 6.1 clearly indicate that the diameter variable is not independent of the peak moment capacity. Since all of the D/t = 50 load cases were generated using 324 mm diameter specimens, it is obvious that they will have a different moment capacity than the D/t = 70 specimens, which were generated using a 508 mm diameter specimen, or the D/t = 90 specimens, which were generated using a 762 mm diameter specimen. Therefore, no meaningful representations or conclusions can be drawn from the effects of the D/t ratio on the peak moment capacity.

Due to the fact that the D/t ratio is a single specified number, there is no ambiguity in the value used as input for the FEA model. Therefore, the sensitivity of the model to the D/t π-parameter can be observed simply by plotting the critical buckling strain as a function of the D/t ratio.

Figures 6.5, 6.6, and 6.7 present the effect of the D/t ratio at different pressures. All of the specimens plotted in these three figures have a blister-type initial imperfection pattern with a maximum amplitude of 16% the wall thickness. Figure 6.5 presents the effect of the D/t ratio on the critical strain for the unpressurized plain pipe specimens. Figure 6.6 presents the effects of the D/t ratio on the critical strain for the specimens with a 40%

internal pressure. Figure 6.7 presents the effects of the D/t ratio on the critical strain for the specimens with an 80% internal pressure. Three curves are presented on each figure, representing the three different grade materials (π_3-parameter).

A number of observations from Figures 6.5, 6.6, and 6.7 are evident. The first observation from the three figures collectively is that there is a decrease in the magnitude of the critical buckling strain with increasing D/t ratio. This is consistent with the collective findings from the experimental portion of this project, the testing done by Mohareb, *et* al., 1994, the testing done by Yoosef-Ghodsi, *et al.*, 1994, as well as with the results of over twelve research programs presented in the Battelle report (Stephens, *et al.*, 1991). A second observation is that with increasing material grade (π_3-parameter), there is a decrease in the critical strain as a function of the D/t ratio (π_1-parameter). This is evident by examining the three different curves plotted on each figure. The final observation is that there is an increasing concave curvature with increasing internal pressure (π_2-parameter). Again, this observation is consistent with all previous experimental data available in the literature and across all of the different initial imperfection patterns examined in this parametric study. Therefore, it is believed that the relationship between the D/t ratio (π_1-parameter) and the critical strain is a decreasing non-linear function. This will be further addressed in the basic form of the critical strain equation developed in Section 6.6.

6.5.2 Effects of the p/p_y Ratio (π_2-parameter)

Figure 6.8 provides a typical curve showing a 'family of specimens' for the load case dt50x52ip2. Each 'family of specimens' in the parametric study is comprised of a group of three specimens in which the only variable that changes between the three curves presented is the level of internal pressure. Since 162 FEA analyses were completed, 54 different families were generated from the parametric study. The results presented in Figure 6.8 are typical of all 54 families. Examination of Figure 6.8 shows that with increasing internal pressure, there is a decrease in peak moment capacity and an increase in the global curvature at the peak moment. These results are similar to the results obtained from plotting the families for the experimental specimens investigated in this

project, which were presented in Figure 4.78, 4.81, 4.82, and 4.83. Therefore, the explanations provided in Section 4.7.1 for the observed patterns in the experimental data can be extended to, and remains valid for, the results of the parametric study.

Due to the fact that the p/p_y ratio is also a single specified number, there is no ambiguity in its value used as input for the FEA model. Therefore, the sensitivity of the model to the p/p_y π-parameter can also be observed simply by plotting the critical buckling strain as a function of the p/p_y ratio.

Figures 6.9, 6.10, and 6.11 present the effect of the p/p_y ratio for different grades of material. All of the specimens plotted in these three figures have a blister-type initial imperfection pattern with a maximum amplitude of 16% the wall thickness. Figure 6.9 presents the effect of the p/p_y ratio on the critical strain for the grade X52 specimens. Figure 6.10 presents the effects of the p/p_y ratio on the critical strain for the grade X65 specimens. Figure 6.11 presents the effects of the p/p_y ratio on the critical strain for the grade X80 specimens. Three curves are presented on each figure, representing the three different D/t ratios (π_1-parameter).

A number of observations from Figures 6.9, 6.10, and 6.11 are evident. The first observation from the three figures collectively is that there is an increase in the magnitude of the critical buckling strain with increasing p/p_y ratio. This is consistent with the findings from the experimental portion of this research as well as the results from the other research discussed in this project. A second observation is that with increasing material grade (π_3-parameter), there is a decrease in the critical strain as a function of the p/p_y ratio (π_2-parameter). This is evident by examining the three different curves plotted on each figure. These results are consistent with presented by Yoosef-Ghodsi, *et al.*, 1994. However, Yoosef-Ghodsi presented the critical strain as a function the p/p_y ratio as having a bi-linear response where the intersection of the two linear regions was located at an internal pressure of approximately 40%. There is no fundamental reason as to why the intersection should have been located at the data point presented by Yoosef-Ghodsi, other than the arrangement of the available data points.

Since the curves presented by Yoosef-Ghodsi were based on three data points, a bi-linear curve provided an excellent fit of the data, but a parabola or other increasing non-linear function would also provide an excellent fit of the data, given that there were only three data points. Since a bi-linear formulation is difficult to fit into a single critical buckling strain equation, it was therefore decided to attempt to model the data from the parametric study conducted in this project using an increasing non-linear function of the p/p_y ratio (π_2-parameter). This will be further addressed in the basic form of the critical strain equation developed in Section 6.6.

6.5.3 Effects of the F_y/E Ratio (π_3-parameter)

Unlike the two previous π-parameters discussed, there is a high level of subjectivity for the π_3-parameter input. Due to the variable nature of material properties within even a single group of test specimens made from the same stock of line pipe, a representative material model is rarely able to capture the true response of each specimen. This variation is even greater if specimens made to the same specifications, but in different heats are considered. As was presented in Section 6.3.3, 'generalized' material property curves were created based on experimental experience and input from a variety of industry sources. Therefore, it is unlikely that the assumed material property curves described in Section 6.3.3.1 and Figures 6.1, 6.2 and 6.3 will be capable of providing exact predictions of experimental data since these curves are generalizations. Nevertheless, it was decided in Section 6.3.3.1, that the curves defined by the points defined in Equation 6.7 give the best representation of a 'typical' material property curve for line pipe. Similar material property curves that have this general 'rounded' shape are reported by Zhou, *et al*, 1996 and are described as having " the advantage that their shapes are more representative of real material behaviour" for segments of line pipe.

Figures 6.12, 6.13, and 6.14 present the effect of the F_y/E ratio for different grades of material. All of the specimens plotted in these three figures have a blister-type initial imperfection pattern with a maximum amplitude of 16% the wall thickness. Figure 6.12 presents the effect of the F_y/E ratio on the critical strain for the unpressurized specimens. Figure 6.13 presents the effects of the F_y/E ratio on the critical strain for the specimens

with an internal pressure of 40%. Figure 6.14 presents the effects of the F_y/E ratio on the critical strain for the specimens with an internal pressure of 80%. Three curves are presented on each figure, representing the three different D/t ratios (π_1-parameter).

Collectively, Figures 6.12, 6.13, and 6.14 show that there is a decrease in the magnitude of the critical buckling strain with increasing F_y/E ratio. This is consistent with the findings from the experimental portion of this research as well as the results from the other research discussed in this project.

A second observation is that with increasing D/t ratio (π_1-parameter), there is a decrease in the critical strain as a function of the grade of the material (π_3-parameter). This is evident by examining the three different curves plotted on each figure. These observation indicates that as the yield strength of the material in a given specimen increases, the specimen will buckle at a lower level of strain. This is in contrast to what might be expected. However, these observations can be rationalized by plotting the moment-curvature response of a series of load cases in which the only variable is the grade of the material in each of the load cases.

Figure 6.15 provides the moment-curvature response of all of the dt50ip2p80 load cases. Three curves are shown on this Figure, corresponding to grades of material of X52, X65 or X80, respectively. All other parameters are constant between the three curves. Examination of Figure 6.15 shows that with increasing grade of material, there is an increase in peak moment capacity. This is as would be expected. However, Figure 6.15 also shows that there is a decrease in global curvature at the point of peak moment capacity with increasing grade of material. The point which corresponds to the point at which local buckling is initiated resembles a bifurcation point (Bushnell, 1980), where the primary load path intercepts the load path for a higher order mode. If an assumed curve is passed through the bifurcation points for the different load cases it may assume a shape similar to that shown in Figure 6.15 by the heavy dashed line. This heavy dashed line essentially forms a upper bound for the global curvature as a function of global moment and is independent of the grade of material. By limiting the global curvature to

such an upper bound, the effect of increasing the grade of the material would be to increase the moment capacity but with a reduction in the global curvature capacity. Since strain and curvature have a direct relationship, as was presented in Figure 4.12 and Equation 4.8, if there is a reduction in the global curvature, it follows that there will be a corresponding reduction in the strain along the length of the specimen. This would account for the observations of Figures 6.12, 6.13 and 6.14 (as well as the other 54 critical strain plots) that the critical buckling strain decreases as the grade of material increases for curves generated from the parametric study results.

As was discussed in Section 6.1, the critical buckling strain is associated with a stability phenomenon. As such, it generally falls within an upper bound limit, which is a function of the geometry of the specimen and independent of load carrying strength capacity. This type of upper bound limit as a function of geometry is not a new phenomenon. One of the most well known upper bound buckling limits is derived from the Euler equation, which was presented in Equation 6.1. When the critical buckling load determined using the Euler equation is plotted as a function of the slenderness ratio, a geometric parameter, a shape similar to that shown by the heavy dashed line in Figure 6.15 results. Since the behaviour plotted in Figure 6.15 is the global moment-curvature response of the different segments of line pipe, the comparison with the Euler equation, which also assess global behaviour, is interesting. From the observations in Figure 6.15, it is not difficult to conclude that there may be a line pipe inelastic global buckling relationship, which is triggered by the local buckling at the wrinkle, that is analogous to the global Euler relationship. However, since the establishment of global buckling criteria is not one of the objectives of this project, this will not be investigated any further in this project.

6.5.4 Effects of the Magnitude of the Initial Imperfection (π_4-parameter)

The magnitude of the initial imperfection (π_4-parameter) behaves much like the D/t (π-parameter) and the p/py (π-parameter) in that the maximum amplitude of the initial imperfection whether blister-type or offset-type, is a single specified number. However, there is still a level of ambiguity in the measure of the level of the initial imperfection. This is because there is no standard for the assumed imperfection patterns used in the

parametric study. The assumed initial imperfection patterns used were developed using a 'best-fit' technique to match the results of the simplified initial imperfection FEA analyses with the experimental data, as described throughout Chapter 5.

The effect of the initial imperfection pattern on the peak moment capacity of the different specimens has already been discussed in Section 5.2.2 for the blister-type pattern used for the plain specimens and Section 5.2.4 for the offset-type pattern used for the girth welded specimens. Figure 5.8 showed the sensitivity of the FEA model to the different amplitude blister-type imperfections for the plain specimens and Figure 5.15 shows the sensitivity of the FEA model to the different magnitude offset-type imperfections for the welded specimens. As was previously discussed, an increase in the initial imperfection resulted in a reduction of the peak moment capacity of a given specimen under a constant load case.

Figures 6.16, 6.17, and 6.18 present the effect of the different amplitude blister-type initial imperfection on the plain pipe specimens with an internal pressure of 40% for the various grades of material examined in the parametric study. Similar relationships to those observed in these three figures are obtained at different levels of internal pressure and for the offset-type initial imperfection used for the girth welded specimens.

Figure 6.16 presents the effect of the amplitude of the blister initial imperfection (π_4-parameter) on the critical strain for the grade X52 specimens. Figure 6.16 presents the effect of the amplitude of the blister initial imperfection on the critical strain for the grade X65 specimens. Figure 6.16 presents the effect of the amplitude of the blister initial imperfection on the critical strain for the grade X80 specimens. Three curves are presented on each figure, representing the three different D/t ratios (π_1-parameter).

Collectively, Figures 6.16, 6.17, and 6.18 show that there is a decrease in the magnitude of the critical buckling strain with increasing amplitude of the blister initial imperfection. This is consistent with theoretical analysis (Brush and Almroth, 1975). A second observation is that with increasing D/t ratio (π_1-parameter), there is a decrease in the

critical strain as a function of the amplitude of the blister initial imperfection (π_4-parameter). This is evident by examining the three different curves plotted on each figure. This is as would be expected. Further examination of the plots presented in Figures 6.16, 6.17, and 6.18 shows that the critical strain response to the magnitude of the initial imperfection is predominantly linear, although there appears to be some non-linear response as well. This will be further addressed in the basic form of the critical strain equation developed in Section 6.6.

6.5.5 Summary of Effects of Different π-parameters

This section presents the effect of each of the individual π-parameters on the critical buckling strain determined in the parametric study. From the observations of the typical graphical relationships presented in Section 6.5, it is apparent that the critical buckling strain is dependent on the four π-parameters identified using the Buckingham-Pi theorem. The observed relationships presented in this section will be used in Section 6.6 as the fundamental basis for the development of an empirical design equation.

6.6 Development of Simplified Design Equations

With the compilation of 162 parametric study results, sufficient data has now been collected to derive a simplified design equation that can be used to predict the critical buckling strain capacity of a given segment of line pipe subjected to combined loads. Many attempts have been made to develop previous critical buckling strain equations, as was reviewed in Chapter 1. Some of these models, such as the Classical Elastic equation given in Equation 1.7, were based on fundamental mechanics. However, as was presented in the numerical assessment of these various equations in Section 1.2.1, none of these attempts appear to have resulted in an equation that provides accurate predictions over a broad range of variables. It should be noted that many of the equations may work quite well for the ranges over which they were derived, but do not appear to be suitable for the range of parameters covered by the U of A database (Dorey, *et al.*, 2000).

It is not surprising that the attempts to derive equations starting from first principles have not produced suitable, broad-scale design criteria. This is because many of the variables, identified both numerically and experimentally in this project, influence the behaviour of the specimen. Also, the response of the specimen to some of these variables is non-linear. This makes the derivation of a suitable design equation extremely complicated and virtually impossible to perform using a fundamental mechanical model. It was therefore decided to use an empirical approach to the solution of the critical buckling strain problem.

Empirical problem solving for engineering applications often uses an iterative procedure of experimental testing, analysis, design and assessment. With each iteration the behaviour is better understood and more suitable experiments can be design to enhance the knowledge developed in the next iteration. This procedure has been used since the problem of line pipe critical buckling strain was first investigated at the U of A.

As was discussed in Section 6.2, it was decided to develop two different critical buckling strain equations, one for use with plain pipe segments and one for use with segments of line pipe with girth welds in them. In the development of these simplified design equations, over 200 different forms for an equation were identified and analyzed in an attempt to identify an equation of suitable form to account for the critical strain response to each of the different π-parameters reviewed in Section 6.5.

To help simplify the analysis of the two different equations, it was decided to develop a basic form for the critical buckling strain equation that would be used for both the plain and the girth welded specimens. This was decided because the same four π-parameters were identified for both the plain and the girth welded specimens. However, to account for the observed differences in behaviour, once the basic form was developed, two sets of regression coefficients would be developed, one for the plain specimens and the other for the girth welded specimens.

The different equations considered include both polynomial and non-linear expressions. Each form has its advantages and disadvantages. With a sufficient number of terms, a polynomial expression can be used to fit any smooth continuous function, with a high coefficient of multiple determination. A coefficient of multiple determination, R^2, is a measure of how well an equation predicts a set of data (Devore, 1991) and can be expressed mathematically as

$$R^2 = 1 - \frac{\sum_{i=1}^{n}(X_i - P_i)^2}{\sum_{i=1}^{n}(X_i - \overline{X})^2} \tag{6.9}$$

where n is the number of observations, X_i is the value of the i^{th} measured value, P_i is the i^{th} predicted value and $\overline{X}$ is the mean of the measured values. Examination of Equation 6.9 shows that the term in the brackets in the numerator $(X_i - P_i)$ is the residual error between the measured value and the predicted value. The term in the brackets of the denominator numerator $(X_i - \overline{X})$ is the deviation of the observed values about the sample mean. By minimizing the second term, which indicates a minimization of the residual errors, the value of R^2 approaches 1. Therefore, the closer the value of R^2 to unity, the better the prediction equation accounts for the variation in the data set, which results in a more accurate fit of the predicted equation to the data set.

Based on the observed relationships discussed in Section 6.5, it was decided that a second-order polynomial equation would best represent the parametric study results. Khurri and Cornell, 1996 give the number of coefficients required to define a complete second-order equation as

$$n = \frac{(k+1)(k+2)}{2} \tag{6.10}$$

where n is the number of regression coefficients and k is the number of factors that are to be fit using the equation. Using the four π-parameters developed in this project and

applying Equation 6.9 to the critical buckling strain equation to be developed, a total of 15 coefficients are required to fit the parametric study data.

Therein lies the disadvantage of the polynomial expression. The objective of this project is to develop a simplified design equation. While over 125 attempts were made to use a Taylor series expansion polynomial fit, an acceptable value of R^2, which was selected as > 0.95 for this project, could not be achieved without at least thirteen terms in the equation. Clearly, this would not be considered a 'simplified design equation'. Therefore, non-linear expressions were investigated.

The advantage of a non-linear expression is that it allows for a more compact form of the prediction equation. However, the disadvantage of this type of equation fitting is that the system of equations is non-linear and usually requires computer software to perform the iterative analysis. Fortunately, there are many commercially available desktop packages that readily perform non-linear regression analysis. The package used to perform the non-linear regression analysis in this project was SigmaPlot 5.0 (SPSS, 1999).

Over 100 critical buckling strain prediction equations were investigated. This is because in empirical equation fitting, the form of the equation is not known, other than the basic knowledge that an investigator may have based on experimental results. A preliminary equation was adopted with the basic form

$$\varepsilon_{crit} = \varepsilon[f_1(\pi_1), f_2(\pi_2), f_3(\pi_3), f_4(\pi_4)] \tag{6.11}$$

which was derived from the Buckingham-Pi analysis presented in Equation 6.6 of Section 6.2.

Using the observations and discussions included in Section 6.5 of this project, the form of each $f_i(\pi_i)$ term was modified and a new set of regression coefficients determined. With each set of regression coefficients, the value of R^2 was examined to ensure that the current form of the equation provided a greater value of R^2 than the previous iteration.

Modifications to the $f_i(\pi_i)$ terms continued until all terms had a general form that satisfied the observations of Section 6.5.

As with most empirical equation fitting strategies, the final form of the equation is unknown, although, as discussed in Section 6.5, examination of the response of the data to the different parameters can assist in proposing each of the $f_i(\pi_i)$ terms. Nevertheless, statistical measures are the best available tool for assessing the suitability of the proposed equation. Thus, once the general form of the $f_i(\pi_i)$ terms had been determined, additional modifications were made to improve the value of R^2.

Based on this procedure and the value of R^2, the best fit general form of the equation was found to be

$$\varepsilon_{crit} = \left(\frac{a}{\pi_1}\right)^b * \left(\frac{1}{1 - c(\pi_2)}\right) * \left(\frac{1}{\pi_3}\right)^d * \left(e - \left(\frac{\pi_4}{100}\right)^f\right) \qquad (6.12)$$

where a, b, c, d, e, and f are the non-linear regression coefficients determined by SigmaPlot.

Substituting for the π-parameters in terms of the experimental variables, Equation 6.12 becomes

$$\varepsilon_{crit} = \left(\frac{a}{D/t}\right)^b * \left(\frac{1}{1 - c\left(\frac{p}{p_y}\right)}\right) * \left(\frac{1}{F_y/E}\right)^d * \left(e - \left(\frac{imp}{100}\right)^f\right) \qquad (6.13)$$

6.6.1 Regression Analysis Using Plain Pipe Parametric Study Data

The parametric study included 106 results for plain pipe test specimens. These results are included in Tables 6.4 through 6.7, inclusive. These 106 data points were input into

SigmaPlot and the optimal non-linear regression coefficients determined. Inputting these optimal coefficients, Equation 6.13 becomes

$$\varepsilon_{crit} = \left(\frac{2.9398}{D/t}\right)^{1.5921} * \left(\frac{1}{1-0.8679\left(\frac{p}{p_y}\right)}\right) * \left(\frac{1}{F_y/E}\right)^{0.8542} * \left(1.2719 - \left(\frac{imp}{100}\right)^{0.1501}\right) \quad (6.14)$$

The value of R^2 for this set of regression coefficients for the plain pipe specimens is 0.9873, which indicates an excellent degree of predictive ability for the parametric study data. Additional statistical analyses of the fit of the parametric study data to Equation 6.14 were also conducted. The test-to-predicted ratios between the parametric study result, which was considered the 'test data' for the equation fitting, and the value predicted by Equation 6.14 was determined for each of the 106 load cases. The mean test-to-predicted ratio was found to be 1.00 with a coefficient of variation of 0.083 and a range from 0.80 to 1.16. This shows that Equation 6.14 is capable of predicting the critical strains determined from the parametric study to an acceptable engineering accuracy.

The majority of the test-to-predicted ratios that lay outside the range from 0.90 to 1.10 (± 10%) were from specimens with a high D/t ratio (D/t = 90). This is not surprising. As has been shown in the data from both the parametric study and the experimental testing program, the higher the D/t ratio, the lower the critical buckling strain. As was discussed in Section 4.3.2, the FEA model critical strain was determined using a nodal displacement formulation. However, the output from ABAQUS had a limited number of significant figures for the displacement of the nodes, which may have created an error as large as 400 με, or 0.04 %. Since some of the critical buckling strains determined in the project had a magnitude as low as 0.30 %, a systematic error as large as 13 % may have existed in some of the critical strain data for the high D/t specimens. This could account for the observed range in the test-to-predicted ratios. Nevertheless, the statistical results

and the value of R^2 indicate that Equation 6.14 provides superior predictive ability to any of those reviewed in Chapter 1.

6.6.2 Regression Equation Validation Using Plain Pipe Experimental Test Data

The final measure of assurance for predictive ability of Equation 6.14 was to examine the test-to-predicted ratios between the experimental data and the value predicted by Equation 6.14. Table 6.10 presents the π-parameters for a number of the plain pipe specimens, the experimental critical buckling strain, the critical strain prediction using Equation 6.14 and the test-to-predicted ratio. As can be seen from the mean test-to-predicted ratio (0.74) and the coefficient of variation (0.169), Equation 6.14 does not represent the experimental data very well.

Review of the discussion of the different π-parameters presented in Section 6.5 showed that π_3 was the only π-parameter for which there was significant ambiguity in the input for the parametric study. As was discussed in detail in Section 6.3.3.1, the material model used in the parametric study was an assumed pattern based on the characteristics presented in Equation 6.7. In the material model, as shown in Figures 6.1, 6.2, and 6.3, there was no yield plateau. However, the majority of the experimental specimens tested in this project did have material properties with a distinct yield plateau. It was therefore decided to run an additional short parametric study to investigate where the presence of a yield plateau has a significant effect on the moment-curvature response and/or the critical strain.

6.6.2.1 Effect of the Variation in Material Curve For a Specific Grade of Material

Figure 6.19 shows an assumed material model curve that contains a distinct yield plateau. For clarity, the original material curves used in the parametric study and shown in Figures 6.1, 6.2, and 6.3, will be referred to as 'rounded material curves' because they contain no yield point, yield plateau, or other slope discontinuities. The material curves with the yield plateaus, as shown in Figure 6.19 for the grade X65 material, will be referred to as 'yield plateau material curves' for distinction.

The grade X65 material curve in Figure 6.19 was generated in the same manner as the original material curves used in the parametric study, except that the proportional limit was raised to 1.00 σ_y and that the yield plateau ended at 0.5% strain. As such, the following data points were used to reflect the yield plateau material curves

Proportional limit:	stress: $1.00\sigma_y$	strain: σ_y/E	
Yield :	stress: σ_y	strain: 0.5 %	
End of Yield Plateau	stress: σ_y	strain: 0.5 %	(6.15)
Ultimate:	stress: Table 8.1 Z245.1-95	strain: 12 %	
Rupture:	stress: σ_y	strain: 22 %	

The data points in the above matrix were used to generate Figure 6.19, which has a characteristic yield plateau. To emphasize the difference between the rounded and the plateau material curves, an enlargement of the region around the yield plateau and the yield stress for two different curves for grade X65 material curves is presented in Figure 6.20. The solid line shows the rounded material curve used in the parametric study and the heavy dashed line shows the plateau material curve.

It is acknowledged that the plateau material curve is not truly reflective of any of the material properties measured in the laboratory during this project, however, its shape is a close approximation to the stress-strain curves presented in Section 4.1.1, although at a different scale. Nevertheless, the purpose of this new assumed material curve is to determine if the presence of a yield plateau has a significant effect on the moment-curvature response and/or the critical strain. The yield plateau material curve represented in Equation 6.15 will satisfy this purpose.

Eight random load cases were selected to study the effect of varying the shape of the material model curve. These eight load cases include variations in the D/t ratio, the grade of material, the initial imperfection pattern and the internal pressure. Table 6.11 provides the data for the eight load cases examined and the results of the parametric study to examine the effect of the presence of a yield plateau on the peak moment and the critical

strain. Figures 6.21 and 6.22 provide the moment-curvature response for two of the load cases. As can be seen in these two figures, in some cases the moment-curvature curves gave almost identical responses (Figure 6.21) and in other cases, the responses were substantially different (Figure 6.22). There is no evident explanation for these observed discrepancies and further investigation is required.

The data in Table 6.11 shows that the peak moment capacities for the rounded material curve and the plateau material curve are nearly identical, regardless of the presence of the yield plateau. This is evidenced by the mean P/R ratio of 1.018 with a coefficient of variation of 0.035 for peak moment capacity ratios given in Table 6.11. This is not unexpected and can be supported using the previous discussion in Section 6.5.3 and the observed effects of the different grade of material presented in Figure 6.15.

However, the data in Table 6.11 also shows that there is a significant difference in the critical strain developed for the two different shaped material property curves. This is evidenced by the mean P/R ratio of 0.71 with a coefficient of variation of 0.201 for the critical strain ratios given in Table 6.11. Again, the arguments presented in the discussion of the effect of the different grade of material presented in Section 6.5.3, support the observations in the critical strain results presented in Table 6.11. With an increase in the proportional limit such that a yield plateau emerges, the amount of longitudinal strain that develops in the pipe wall is reduced for any given level of moment that corresponds to a stress between the 0.75 σ_y proportional limit and the yield stress. Therefore, by increasing the proportional limit such that a yield plateau emerges, the total strain reduces. This results in the large discrepancies between the results for the plateau material and the rounded material observed in Table 6.11. This effect is particularly evident in the high D/t specimens. Since many of the high D/t ratio specimens have critical buckling strains close to the yield strain of 0.5 %, the effect of the yield plateau becomes much more significant, as evidenced by the T / P ratios presented in Table 6.10.

Examination of some of the specimens in Table 6.10 that had more rounded material property curves, such as UGA12 and L178P80BP-4, shows that the T / P ratios using Equation 6.14 are very close to unity (0.92 and 0.95, respectively). However, the specimens that had material coupon results that exhibited a distinct yield plateau (i.e. CP20N-2 and T20P40N) have very poor T / P ratios (0.65 and 0.69, respectively).

This presents a difficulty in the development a universal critical buckling strain equation. Typical segments of line pipe have material that exhibits no yield plateau because of the hydrostatic or mechanical expansion included as part of the fabrication process. For such specimens, Equation 6.14 provided reasonably accurate critical buckling strain predictions. However, for specimens in which the material property curve includes a proportional limit greater than 0.75 σ_y, Equation 6.14 provides an unconservative estimate of the critical buckling strain. It was therefore decided to develop an additional critical buckling strain equation that would provide a conservative critical buckling strain prediction for material property curves that exhibit a yield plateau. An equation that satisfies material property curves with a distinct yield plateau should provide a conservative estimate for the more rounded material curves.

From the results of this additional parametric study, it is evident that the critical buckling strain of a segment of line pipe is highly dependent on the material properties and that any predictive equation will be sensitive to a term similar to the π_3-parameter developed in this project. This result is consistent with observations made at the Centre for Frontier Engineering Research (C-FER) in Edmonton, Alberta (Zimmerman, *et al., 1994)*. The critical strain equation developed at C-FER is proprietary and may not be published in this document. Nevertheless, the results of the C-FER study indicated that the critical buckling strain is highly sensitive to the 'material property' term used in their equation.

6.6.2.2 Regression Analysis Using Plain Pipe Experimental Test Data

All of the observations and arguments that led to the proposal of Equation 6.13 still remain valid in the development of a critical buckling strain equation that would account for the effects of a material property curve that includes a yield plateau. Therefore,

Equation 6.13 was used as the basis for the development of a new equation and SigmaPlot was used to develop a new set of regression coefficients. Inputting the π-parameters from the experimental data for the plain specimens reported in Table 6.10 into SigmaPlot and using the Equation 6.13 template, the following non-linear regression equation was generated:

$$\varepsilon_{crit} = 40.4 * \left(\frac{t}{D}\right)^2 * \left(\frac{1}{1 - 0.906\left(\frac{p}{p_y}\right)}\right) * \left(\frac{E}{F_y}\right)^{0.80} * \left(1.12 - \left(\frac{imp}{100}\right)^{0.15}\right) \qquad (6.16)$$

The value of R^2 from the regression analysis that generated the coefficients for Equation 6.16 is 0.9742, which is still very good. Table 6.12 provides an evaluation of Equation 6.16 with the experimental critical buckling strain data. The mean test-to-predicted ratio in Table 6.12 is 1.03 with a coefficient of variation of 0.092. Given this excellent level of agreement, it is evident that Equation 6.16 provides an acceptable prediction of the experimental critical buckling strains.

One final step in the validation of Equation 6.16, which is developed for material properties with a distinct yield plateau, is to assess the effect of the new regression coefficients on the parametric results, which were based on rounded material curves. Table 6.13 provides a random selection of parametric load cases and how well they fit with Equation 6.16. Examination of Table 6.13 shows that Equation 6.16 provides a conservative estimate of the critical buckling strain in all cases, with a mean test-to-predicted ratio of 1.35 and a coefficient of variation of 0.164.

6.6.3 Regression Analysis Using Girth Welded Pipe Parametric Study Data

Again, using Equation 6.12 as the basis for the analysis, a set of non-linear regression coefficients were generated by inputting the girth welded pipe parametric study data into SigmaPlot. A total of 78 data points, presented in Tables 6.4, 6.8, and 6.9, were used to generate the following equation

$$\varepsilon_{crit} = \left(\frac{8.9948}{D/t}\right)^{1.7239} * \left(\frac{1}{1-0.8920\left(\frac{p}{p_y}\right)}\right) * \left(\frac{E}{F_y}\right)^{0.7012} * \left(1.0868 - \left(\frac{offset}{t}\right)^{0.0863}\right) \qquad (6.17)$$

The value of R^2 for this set of regression coefficients for the girth welded parametric study specimens is 0.9860, which indicates an excellent degree of predictive ability for the parametric study data. Additional statistical analysis was also performed using the parametric study data. The test-to-predicted ratios between the parametric study result, which was considered the 'test data' for the equation fitting, and the value predicted by Equation 6.17 was determined for each of the 78 load cases. The mean test-to-predicted ratio was found to be 0.986 with a coefficient of variation of 0.093 and a range from 0.79 to 1.17. This shows that Equation 6.17 is capable of accurately predicting the critical strains determined from the parametric study.

6.6.4 Regression Analysis Using Girth Welded Pipe Experimental Test Data

As was done in Section 6.6., the equation generated from the parametric study data for the girth welded specimens was validated using the experimental data. Table 6.14 presents the π-parameters for a number of the girth welded specimens, the experimental critical buckling strain, the critical strain prediction using Equation 6.17 and the test-to-predicted ratio. As can be seen from the mean test-to-predicted ratio (0.66) and the coefficient of variation (0.296), Equation 6.17 does not represent the experimental data very well.

As was the case for the plain pipe specimens, it is believed that the presence of the yield plateau in the material property curves of the actual test specimens was also responsible for the observed discrepancies. This observation is supported by the results of the girth welded load cases presented in Table 6.11 and the test-to-predicted ratios (0.85, 0.87, and 0.88) of the experimental specimens (UGA12W, UGA20W-2 and HGA20W, respectively) that had rounded material property curves. Therefore, a second regression

analysis was performed using the basic form of the critical buckling strain equation presented in Equation 6.12 and the experimental critical strain data from the girth welded specimens in order to assess the effects of the yield plateau. The results that this second regression analysis provided the following design equation

$$\varepsilon_{crit} = 106*\left(\frac{t}{D}\right)^2 * \left(\frac{1}{1-0.50\left(\frac{p}{p_y}\right)}\right) * \left(\frac{E}{F_y}\right)^{0.70} * \left(1.10-\left(\frac{offset}{t}\right)^{0.09}\right) \qquad (6.18)$$

The value of R^2 from the regression analysis that generated the coefficients for Equation 6.18 is 0.9721, which is also very good. Table 6.15 provides an evaluation of Equation 6.18 with the experimental critical buckling strain data for the girth welded specimens. The mean test-to-predicted ratio in Table 6.15 is 1.04 with a coefficient of variation of 0.113. Given this excellent level of agreement, it is evident that Equation 6.18 provides an acceptable prediction of the experimental critical buckling strains for the girth welded specimens.

6.7 Validation of Critical Strain Equations with External Data

The final step in the validation of the equations developed in Section 6.6 was to test the equations using external sources of data. Prior to providing a comparisons, it is important to note that the method used in the determination of the external critical strain data reported in this section may not be consistent with the bi-linear regression analysis technique used in this project. It was unclear what effect of the different methods would have on the results obtained in this section.

Unfortunately, very limited 'useable' external data exists. This is because there is very little data available to start with. For the data that is available, not all of the required parameters needed for input into the equations developed in Section 6.6 is reported. For

the plain pipe specimens, a total of five different sources of data were found that fit the range of π-parameters for use in the equations developed in Section 6.6 and was complete enough to evaluate the critical buckling strain equations in Section 6.6. Other than the data reported in this document, no other sources of data for girth welded specimens were found.

Table 6.16 presents the results from 18 available test results from external sources which had the majority of the required data to fit the parameters of the parametric study equations. Unfortunately, some assumptions still had to be made on the available data, specifically in terms of the level of initial imperfection and in the assumed shape of the material property curve.

The inclusion of a level of initial imperfection in a critical strain formulation was developed in this project. Numerous papers on the buckling of segments of line pipe provide discussions on the effects of initial imperfections on the buckling response (for example, Bushnell, 1980). However, none of the studies referenced in the literature made an attempt to quantify the level of initial imperfection, with the exception to the precursory work to this project done by Del Col, *et al.* (1998). As such, a level of initial imperfection had to be assumed for use in the equations of Section 6.6. Figure 6.23 provides a graphical representation of the average level of initial imperfection as a percentage of the thickness of the wall of the specimen that was used to model the different D/t ratio experimental specimens presented throughout Chapter 5. It is acknowledged that each individual specimen will have its own initial imperfection pattern. However, Figure 6.23 is the best representation of the available data and was used to assess the level of initial imperfection for the various D/t ratio specimens presented in Table 6.16. Therefore, based on the recorded D/t ratio of the individual specimens presented in Table 6.16, Figure 6.23 was used to provide an estimate of the level of initial imperfection.

Most segments of line pipe have material property curves that fit into the 'rounded' category developed in Section 6.6. However, there are some that have material properties

that exhibit a distinct yield plateau, as was the case for many of the D/t = 92 specimens tested in the experimental portion of this project. Since few of the actual material curves were presented in the sources of the external data, it was decided to input the different π-parameters into both Equation 6.14 for the rounded material curve and Equation 6.16 for the material curve with a distinct yield plateau. By doing so, it was assumed that the test-to-predicted ratios derived using Equation 6.14 would typically be less than or equal to 1.0 and the test-to-predicted ratios derived using Equation 6.16 would typically be greater than or equal to 1.0.

Examination of the data in Table 6.16 shows that the mean test-to-predicted ratio using Equation 6.14 is less than 1.0 (mean = 0.788) and that the mean test-to-predicted ratio using Equation 6.16 is greater than 1.0 (mean 1.150). Examination of the last two columns shows that almost every specimen is bounded by the two different equations, which indicates that the actual material property curve has a proportional limit somewhere between 0.75 σ_y and σ_y. All of these results are consistent with experimental observations.

Some concern may be expressed over the coefficients of variation presented in Table 6.16. However, considering the uncertainty in the level of initial imperfection, the shape of the material curves, and the importance of these two factors in predicting the critical strain, a larger coefficient of variation is expected. Nevertheless, the collective agreement between the results from the specimens tested in this project, the results from previous experimental projects at the U of A, and the results from the external experimental sources indicate that the equations developed in Section 6.6 are capable of accurately predicting the critical buckling strain of segments of line pipe.

6.8 Design Considerations – Practical Application

While the results of Sections 6.6 and 6.7 show significantly greater promise than previous published critical strain limits, there a still a number of reservations with the proposed

equations. Equations 6.14 and 6.17 show excellent predictive ability for the parametric plain and girth welded specimens, respectively. However, when compared with the experimental data, poor correlation was observed. The coefficients of regression were thus modified to form Equations 6.16 and 6.18 for the plain and girth welded specimens, respectively. The fundamental difference between the two pairs of equations was the shape of the material property curves. This reinforces the previous observation in this study and in the C-FER study that the critical buckling strain is highly sensitive to the material properties. Nevertheless, a designer is faced with the problem of deciding which set of equations to adopt.

In this study, it was assumed that the test specimens were fabricated from 'typical' segments of line pipe. Therefore, it was assumed that the material property curves would have the usual 'rounded' shape accepted in industry practice and discussed in Section 6.3.3.1. However, this is not always the case as evidenced by the distinct yield plateau observed in the experimental coupon test results. If a designer were to use Equations 6.14 and 6.17 but the actual material property had a distinct yield plateau, then the design would undoubtedly be unconservative and result in a potentially undesirable *in situ* condition. However, if a designer were to use Equations 6.16 and 6.18 and the material had a rounded material property curve, then the resulting design could be uneconomically conservative by as much as 35 to 50%.

The solution to this dilemma is not straightforward and can not be solved conclusively with the current available database. However, it is evident that measured material properties for the field installed line pipe are required to verify the critical strain limits proposed in the design phase. The need for reliable, accurate material property data is further supported by the second difficulty associated with the results of field application of the parametric study discussed below.

In the development of the parametric material properties, the yield stress was made equivalent to the value of SMYS. 'SMYS' indicates the '***s***pecified ***m***inimum ***y***ield ***s***trength'. By definition, the actual yield strength of the material should be equal to or

greater than SMYS. The results of the parametric study revealed that as the yield stress increases, the critical strain decreases. This was presented in the 'typical' critical strain versus grade of material curves presented collectively in Figures 6.12, 6.13, and 6.14. Since the actual yield strength is almost invariably greater than the SMYS for a given material, it can be concluded that by using the value of SMYS in the proposed critical strain equations, the equations will over-estimate the actual value of the critical strain. This will also lead to an unconservative design. This provides further justification for the determination of the actual material properties used for field installations. It is realized that it is unlikely that exact material property results will be available at the design stage. However, assumptions can be made at the design stage and material property specimens can be collected and tested either during or after the installation to verify or update the assumptions made. Knowing the actual material properties will allow a much greater degree of confidence in the anticipated response of the line pipe and the point at which critical buckling may initiate.

Finally, the assessment of initial imperfections from a designer's perspective needs to be addressed. Figure 6.23 provided a rather crude attempt to quantify the level of initial imperfection that can be expected in different D/t ratio specimens. At this point, it is unclear what parameter should actually be plotted on the horizontal axis in Figure 6.23. Arguments can be made for the D/t ratio, thickness of the pipe wall, diameter of the specimen, as well as other variables. Additional studies are required to clarify which would be the most realistic parameter to plot. Furthermore, of all the levels of initial imperfection plotted in Figure 6.23, only the level of initial imperfection for the D/t = 92 specimens tested in this project are based on actual experimental data and that experimental data had a range for the level of initial imperfection from 8% to 23% the wall thickness. The other levels of initial imperfection plotted in Figure 6.23 were based on 'best-fits' of the FEA model data to the experimental data. As presented throughout Chapter 5, even the 'best-fit' assumptions could have had further refinement. It is evident that additional experimental data is required to quantify this variable before definitive relationships can be developed. Nevertheless, given the predictive ability of Equations 6.16 using the level of initial imperfection read from Figure 6.23, it is evident

that Equation 6.16 can provide a designer with a greater level of confidence than previous equations, even without more refined levels of initial imperfection.

There is no conclusive evidence to make the same statements regarding Equations 6.17 and 6.18 for the girth welded specimens because of the lack of external data for which to validate them. However, since these two equations were developed in an identical fashion to Equations 6.14 and 6.16 and because they work so well with the U of A experimental girth welded specimen data, it may be assumed that the girth welded equations will provided that same level of agreement.

6.9 Parametric Study Summary

This chapter presented the details and results of a parametric study conducted to develop equations capable of accurately predicting the critical buckling strain of segments of line pipe subjected to combined loads. Four non-dimensional parameters were identified using the Buckingham-Pi theorem for defining the critical buckling strain. Using these four π-parameters, a total of 162 parametric study load cases were developed and analyzed using the FEA model developed in Chapter 3 and validated in Chapters 4 and 5.

The results of the parametric study provided a number of important observations and equations. The parametric study was not designed to specifically assess the peak moment capacity of the different load cases examined, nor the relationships evident in the global behaviour. However, the results of the parametric study did lead to the observation that there may be a governing critical load equation for the buckling of segments of line pipe that is a function of the geometry of the specimen. The results tended to indicate that such a governing equation is similar in shape to the Euler equation for the global buckling of columns. No further study was done to identify the form of this relationship.

Once the parametric study was completed, non-linear regression analysis was used to develop a 'best-fit' equation for the data. Two analyses were performed, one for the

plain pipe data and one for the girth welded data. The results of the regression analyses provided two critical buckling strain equations for the different type of pipe segments, each with a coefficient of multiple determination (R^2) greater than 0.98. This is excellent agreement. However, comparison of the equations that were developed with the experimental critical strain data resulted in poor test-to-predicted ratios.

Review of the different π-parameters indicated that the FEA model appeared to be very sensitive to the shape of the assumed material property curve. A short extension to the parametric study to examine the effect of the shape of the assumed material property curve revealed that the FEA model is indeed very sensitive to this parameter. Subsequent regression analysis were conducted to more accurately fit the experimental data to the basic form of the critical buckling strain equation which was developed from an examination of the individual π-parameters. The results of this subsequent regression analysis provided two design equations, both with R^2 values greater than 0.97 and mean test-to-predicted ratios of 1.03 for the plain pipe experimental results and 1.04 for the girth welded experimental results.

Further validation of the proposed critical strain equations with experimental data from external sources was restricted by a number of uncertainties and assumed values had to be developed for some of the different π-parameters. Nevertheless, despite these uncertainties and using assumed values, the ability of Equations 6.16 and 6.18 to predict the critical buckling strains for a variety of experimental test specimens is remarkable.

Table 6.1 – Results of the Diameter Parametric Study

Specimen ID	D	D/t	p/py	Material Grade	Initial Imperfection	Peak Moment (kN-m)	Critical Strain (%)
dt50d324p00	324	50	0.00	X65	2% blister	261.8	1.30
dt50d508p00	508	50	0.00	X65	2% blister	936.7	1.19
dt50d762p00	762	50	0.00	X65	2% blister	3366.6	1.26
dt50d324p40	324	50	0.40	X65	2% blister	240.2	2.30
dt50d324p40	508	50	0.40	X65	2% blister	899.2	2.19
dt50d324p40	762	50	0.40	X65	2% blister	3037.6	2.18
dt70d324p00	324	70	0.00	X52	1.5 mm offset	118.8	0.57
dt70d508p00	508	70	0.00	X52	1.5 mm offset	475.5	0.51
dt70d762p00	762	70	0.00	X52	1.5 mm offset	1657.3	0.55
dt70d324p80	324	70	0.80	X52	1.5 mm offset	97.7	1.83
dt70d324p80	508	70	0.80	X52	1.5 mm offset	299.3	1.78
dt70d324p80	762	70	0.80	X52	1.5 mm offset	1094.5	1.69
dt90d324p00	324	90	0.00	X80	16% blister	174.8	0.33
dt90d508p00	508	90	0.00	X80	16% blister	637.0	0.37
dt90d762p00	762	90	0.00	X80	16% blister	2129.6	0.33
dt90d324p40	324	90	0.40	X80	16% blister	174.4	0.66
dt90d324p40	508	90	0.40	X80	16% blister	593.1	0.65
dt90d324p40	762	90	0.40	X80	16% blister	1974.4	0.47

Table 6.2 – Length of Specimens and Coordinates of Pivot Points[1]

D/t	Diameter	Length	Bottom Pivot	Top Pivot
50	324	1620	-339	1959
70	508	2540	-339	2879
90	762	3810	-339	4149

Notes:

1. All dimensions are in mm.

Table 6.3 – Assumed Material Properties for Parametric Study

	Engineering Stress-Strain Data		True Stress-Strain Data	
	Stress (MPa)	Strain (με)	Stress (MPa)	Strain (με)
GRADE X52	0.0	0	0.0	0.00000
X52 Proportional Limit (75% σ_y)	269.3	1346	269.3	0.00000
	290.0	1500	290.4	0.00005
	310.0	1800	310.6	0.00025
	330.0	2500	330.8	0.00084
	345.0	3500	346.2	0.00176
X52 Yield Stress (σ_y)	359.0	5000	360.8	0.00318
	380.0	10000	383.8	0.00803
	410.0	30000	422.3	0.02745
	435.0	60000	461.1	0.05596
	448.0	90000	488.3	0.08374
X52 Ultimate Stress (σ_u)	455.0	120000	509.6	0.11078
	452.0	150000	519.8	0.13716
	430.0	180000	507.4	0.16298
X52 Rupture	359.0	220000	438.0	0.19666
GRADE X65	0.0	0	0.0	0.00000
X65 Proportional Limit (75% σ_y)	336.0	1680	336.0	0.00000
	375.0	1900	375.7	0.00002
	400.0	2500	401.0	0.00049
	420.0	3200	421.3	0.00109
	435.0	3900	436.7	0.00171
X65 Yield Stress (σ_y)	448.0	5000	450.2	0.00274
	465.0	10000	469.7	0.00760
	490.0	30000	504.7	0.02704
	510.0	60000	540.6	0.05557
	525.0	90000	572.3	0.08332
X65 Ultimate Stress (σ_u)	531.0	120000	594.7	0.11036
	525.0	150000	603.8	0.13674
	500.0	180000	590.0	0.16256
X65 Rupture	448.0	220000	546.6	0.19612
GRADE X80	0.0	0	0.0	0.00000
X80 Proportional Limit (75% σ_y)	412.5	2063	412.5	0.00000
	450.0	2350	451.1	0.00009
	480.0	2750	481.3	0.00034
	510.0	3250	511.7	0.00069
	530.0	3800	532.0	0.00113
X80 Yield Stress (σ_y)	550.0	5000	552.8	0.00222
	570.0	10000	575.7	0.00707
	590.0	30000	607.7	0.02652
	605.0	60000	641.3	0.05506
	615.0	90000	670.4	0.08283
X80 Ultimate Stress (σ_u)	620.0	120000	694.4	0.10986
	613.0	150000	705.0	0.13624
	598.0	180000	705.6	0.16199
X80 Rupture	550.0	220000	671.0	0.19550

Table 6.4 - Results of 2% Initial Imperfection Parametric Study

2% WALL THICKNESS INITIAL IMPERFECTION				Initial Imperfection % wall t	Peak Moment (kN-m)	Critical Strain (%)
Specimen ID	D/t	p/py	Fy MPa			
dt50x52ip2p00	50.0	0.0	359	2	206.4	1.699
dt50x52ip2p40	50.0	0.4	359	2	190.9	2.961
dt50x52ip2p80	50.0	0.8	359	2	137.2	5.433
dt50x65ip2p00	50.0	0.0	448	2	261.8	1.299
dt50x65ip2p40	50.0	0.4	448	2	240.2	2.298
dt50x65ip2p80	50.0	0.8	448	2	165.5	4.846
dt50x80ip2p00	50.0	0.0	550	2	325.7	1.021
dt50x80ip2p40	50.0	0.4	550	2	301.1	1.781
dt50x80ip2p80	50.0	0.8	550	2	205.6	4.197
dt70x52ip2p00	70.0	0.0	359	2	556.3	1.055
dt70x52ip2p40	70.0	0.4	359	2	508.4	1.495
dt70x52ip2p80	70.0	0.8	359	2	354.9	3.234
dt70x65ip2p00	70.0	0.0	448	2	698.9	0.842
dt70x65ip2p40	70.0	0.4	448	2	645.7	1.295
dt70x65ip2p80	70.0	0.8	448	2	445.0	3.106
dt70x80ip2p00	70.0	0.0	550	2	864.2	0.706
dt70x80ip2p40	70.0	0.4	550	2	810.1	1.080
dt70x80ip2p80	70.0	0.8	550	2	563.5	n/a
dt90x52ip2p00	90.0	0.0	359	2	1422.3	0.647
dt90x52ip2p40	90.0	0.4	359	2	1298.2	1.055
dt90x52ip2p80	90.0	0.8	359	2	887.6	n/a
dt90x65ip2p00	90.0	0.0	448	2	1771.0	0.521
dt90x65ip2p40	90.0	0.4	448	2	1638.0	0.752
dt90x65ip2p80	90.0	0.8	448	2	1113.9	1.607
dt90x80ip2p00	90.0	0.0	550	2	2172.9	0.475
dt90x80ip2p40	90.0	0.4	550	2	2039.2	0.651
dt90x80ip2p80	90.0	0.8	550	2	1418.4	1.336

Table 6.5 - Results of 8% Initial Imperfection Parametric Study

8% WALL THICKNESS INITIAL IMPERFECTION				Initial Imperfection % wall t	Peak Moment (kN-m)	Critical Strain (%)
Specimen ID	D/t	p/py	Fy MPa			
dt50x52ip8p00	50.0	0.0	359	8	205.0	1.516
dt50x52ip8p40	50.0	0.4	359	8	187.8	2.245
dt50x52ip8p80	50.0	0.8	359	8	134.1	4.401
dt50x65ip8p00	50.0	0.0	448	8	259.7	1.142
dt50x65ip8p40	50.0	0.4	448	8	237.0	1.728
dt50x65ip8p80	50.0	0.8	448	8	163.5	4.092
dt50x80ip8p00	50.0	0.0	550	8	322.8	0.872
dt50x80ip8p40	50.0	0.4	550	8	297.3	1.292
dt50x80ip8p80	50.0	0.8	550	8	204.2	3.169
dt70x52ip8p00	70.0	0.0	359	8	551.8	0.907
dt70x52ip8p40	70.0	0.4	359	8	500.1	1.327
dt70x52ip8p80	70.0	0.8	359	8	349.6	2.818
dt70x65ip8p00	70.0	0.0	448	8	691.5	0.774
dt70x65ip8p40	70.0	0.4	448	8	633.9	1.214
dt70x65ip8p80	70.0	0.8	448	8	436.7	2.608
dt70x80ip8p00	70.0	0.0	550	8	849.8	0.641
dt70x80ip8p40	70.0	0.4	550	8	793.3	0.988
dt70x80ip8p80	70.0	0.8	550	8	549.9	1.768
dt90x52ip8p00	90.0	0.0	359	8	1409.4	0.580
dt90x52ip8p40	90.0	0.4	359	8	1274.8	0.946
dt90x52ip8p80	90.0	0.8	359	8	867.6	1.890
dt90x65ip8p00	90.0	0.0	448	8	1745.1	0.515
dt90x65ip8p40	90.0	0.4	448	8	1608.6	0.651
dt90x65ip8p80	90.0	0.8	448	8	1113.9	1.607
dt90x80ip8p00	90.0	0.0	550	8	2149.0	0.377
dt90x80ip8p40	90.0	0.4	550	8	2003.3	0.549
dt90x80ip8p80	90.0	0.8	550	8	1400.0	1.167

Table 6.6 - Results of 16% Initial Imperfection Parametric Study

16% WALL THICKNESS INITIAL IMPERFECTION				Initial	Peak	Critical
Specimen ID	D/t	p/py	Fy MPa	Imperfection % wall t	Moment (kN-m)	Strain (%)
dt50x52ip16p00	50.0	0.0	359	16	203.2	1.212
dt50x52ip16p40	50.0	0.4	359	16	185.4	2.067
dt50x52ip16p80	50.0	0.8	359	16	132.0	3.937
dt50x65ip16p00	50.0	0.0	448	16	256.6	1.100
dt50x65ip16p40	50.0	0.4	448	16	235.0	1.475
dt50x65ip16p80	50.0	0.8	448	16	161.8	3.518
dt50x80ip16p00	50.0	0.0	550	16	313.9	0.841
dt50x80ip16p40	50.0	0.4	550	16	294.5	1.142
dt50x80ip16p80	50.0	0.8	550	16	202.8	2.775
dt70x52ip16p00	70.0	0.0	359	16	547.0	0.721
dt70x52ip16p40	70.0	0.4	359	16	491.5	1.187
dt70x52ip16p80	70.0	0.8	359	16	336.7	2.376
dt70x65ip16p00	70.0	0.0	448	16	683.3	0.629
dt70x65ip16p40	70.0	0.4	448	16	623.3	1.042
dt70x65ip16p80	70.0	0.8	448	16	428.0	1.926
dt70x80ip16p00	70.0	0.0	550	16	838.8	0.564
dt70x80ip16p40	70.0	0.4	550	16	780.8	0.854
dt70x80ip16p80	70.0	0.8	550	16	543.3	1.617
dt90x52ip16p00	90.0	0.0	359	16	1387.3	0.526
dt90x52ip16p40	90.0	0.4	359	16	1260.5	0.869
dt90x52ip16p80	90.0	0.8	359	16	854.8	1.749
dt90x65ip16p00	90.0	0.0	448	16	1737.3	0.445
dt90x65ip16p40	90.0	0.4	448	16	1578.9	0.618
dt90x65ip16p80	90.0	0.8	448	16	1078.8	1.227
dt90x80ip16p00	90.0	0.0	550	16	2129.6	0.329
dt90x80ip16p40	90.0	0.4	550	16	1974.4	0.470
dt90x80ip16p80	90.0	0.8	550	16	1383.8	0.977

Table 6.7 - Results of 30% Initial Imperfection Parametric Study

30% WALL THICKNESS INITIAL IMPERFECTION				Initial	Peak	Critical
Specimen ID	D/t	p/py	Fy MPa	Imperfection % wall t	Moment (kN-m)	Strain (%)
dt50x52ip30p00	50.0	0.0	359	30	200.8	1.024
dt50x52ip30p40	50.0	0.4	359	30	181.6	1.483
dt50x52ip30p80	50.0	0.8	359	30	129.2	3.498
dt50x65ip30p00	50.0	0.0	448	30	253.2	0.888
dt50x65ip30p40	50.0	0.4	448	30	231.4	1.247
dt50x65ip30p80	50.0	0.8	448	30	159.3	3.248
dt50x80ip30p00	50.0	0.0	550	30	313.1	0.668
dt50x80ip30p40	50.0	0.4	550	30	287.7	1.046
dt50x80ip30p80	50.0	0.8	550	30	200.4	2.348
dt70x52ip30p00	70.0	0.0	359	30	538.7	0.720
dt70x52ip30p40	70.0	0.4	359	30	484.6	0.993
dt70x52ip30p80	70.0	0.8	359	30	334.2	1.981
dt70x65ip30p00	70.0	0.0	448	30	676.5	0.572
dt70x65ip30p40	70.0	0.4	448	30	615.2	0.738
dt70x65ip30p80	70.0	0.8	448	30	423.0	1.771
dt70x80ip30p00	70.0	0.0	550	30	830.9	0.500
dt70x80ip30p40	70.0	0.4	550	30	766.9	0.710
dt70x80ip30p80	70.0	0.8	550	30	539.7	1.293
dt90x52ip30p00	90.0	0.0	359	30	1372.9	0.484
dt90x52ip30p40	90.0	0.4	359	30	1236.8	0.637
dt90x52ip30p80	90.0	0.8	359	30	834.5	1.380
dt90x65ip30p00	90.0	0.0	448	30	1717.7	0.337
dt90x65ip30p40	90.0	0.4	448	30	1556.4	0.546
dt90x65ip30p80	90.0	0.8	448	30	1053.2	0.975
dt90x80ip30p00	90.0	0.0	550	30	2084.7	0.302
dt90x80ip30p40	90.0	0.4	550	30	1928.7	0.431
dt90x80ip30p80	90.0	0.8	550	30	1363.3	0.761

Table 6.8 - Results of 1.5 mm Offset Initial Imperfection Parametric Study

1.5 mm WELD OFFSET INITIAL IMPERFECTION				Initial	Peak	Critical
Specimen ID	D/t	p/py	Fy MPa	Imperfection mm offset	Moment (kN-m)	Strain (%)
dt50x52ip15wp00	50.0	0.0	359	1.5	182.1	n/a
dt50x52ip15wp40	50.0	0.4	359	1.5	166.5	1.123
dt50x52ip15wp80	50.0	0.8	359	1.5	104.0	3.140
dt50x65ip15wp00	50.0	0.0	448	1.5	226.8	0.717
dt50x65ip15wp40	50.0	0.4	448	1.5	212.7	1.024
dt50x65ip15wp80	50.0	0.8	448	1.5	134.8	3.094
dt50x80ip15wp00	50.0	0.0	550	1.5	278.5	0.528
dt50x80ip15wp40	50.0	0.4	550	1.5	266.5	0.831
dt50x80ip15wp80	50.0	0.8	550	1.5	177.1	2.558
dt70x52ip15wp00	70.0	0.0	359	1.5	475.5	0.514
dt70x52ip15wp40	70.0	0.4	359	1.5	446.6	0.769
dt70x52ip15wp80	70.0	0.8	359	1.5	299.3	1.784
dt70x65ip15wp00	70.0	0.0	448	1.5	594.0	0.443
dt70x65ip15wp40	70.0	0.4	448	1.5	556.8	0.672
dt70x65ip15wp80	70.0	0.8	448	1.5	387.1	1.457
dt70x80ip15wp00	70.0	0.0	550	1.5	711.0	0.430
dt70x80ip15wp40	70.0	0.4	550	1.5	701.8	0.519
dt70x80ip15wp80	70.0	0.8	550	1.5	506.0	1.295
dt90x52ip15wp00	90.0	0.0	359	1.5	1187.2	0.308
dt90x52ip15wp40	90.0	0.4	359	1.5	1134.2	0.550
dt90x52ip15wp80	90.0	0.8	359	1.5	779.7	1.256
dt90x65ip15wp00	90.0	0.0	448	1.5	1492.6	0.280
dt90x65ip15wp40	90.0	0.4	448	1.5	1425.8	0.390
dt90x65ip15wp80	90.0	0.8	448	1.5	1008.1	1.015
dt90x80ip15wp00	90.0	0.0	550	1.5	1816.2	0.260
dt90x80ip15wp40	90.0	0.4	550	1.5	1715.7	0.358
dt90x80ip15wp80	90.0	0.8	550	1.5	1286.5	0.904

Table 6.9 - Results of 3.0 mm Offset Initial Imperfection Parametric Study

3.0 mm WELD OFFSET INITIAL IMPERFECTION				Initial Imperfection mm offset	Peak Moment (kN-m)	Critical Strain (%)
Specimen ID	D/t	p/py	Fy MPa			
dt50x52ip30wp00	50.0	0.0	359	3.0	165.0	0.601
dt50x52ip30wp40	50.0	0.4	359	3.0	156.0	1.041
dt50x52ip30wp80	50.0	0.8	359	3.0	101.0	2.378
dt50x65ip30wp00	50.0	0.0	448	3.0	206.0	0.537
dt50x65ip30wp40	50.0	0.4	448	3.0	198.1	0.763
dt50x65ip30wp80	50.0	0.8	448	3.0	131.8	1.759
dt50x80ip30wp00	50.0	0.0	550	3.0	251.8	n/a
dt50x80ip30wp40	50.0	0.4	550	3.0	247.3	0.665
dt50x80ip30wp80	50.0	0.8	550	3.0	173.6	1.919
dt70x52ip30wp00	70.0	0.0	359	3.0	410.9	0.428
dt70x52ip30wp40	70.0	0.4	359	3.0	409.9	0.559
dt70x52ip30wp80	70.0	0.8	359	3.0	284.8	1.339
dt70x65ip30wp00	70.0	0.0	448	3.0	510.5	0.367
dt70x65ip30wp40	70.0	0.4	448	3.0	519.3	0.541
dt70x65ip30wp80	70.0	0.8	448	3.0	397.4	1.204
dt70x80ip30wp00	70.0	0.0	550	3.0	629.5	0.304
dt70x80ip30wp40	70.0	0.4	550	3.0	647.7	0.462
dt70x80ip30wp80	70.0	0.8	550	3.0	489.0	1.162
dt90x52ip30wp00	90.0	0.0	359	3.0	1027.6	0.285
dt90x52ip30wp40	90.0	0.4	359	3.0	1036.2	0.394
dt90x52ip30wp80	90.0	0.8	359	3.0	742.3	0.966
dt90x65ip30wp00	90.0	0.0	448	3.0	1279.3	0.259
dt90x65ip30wp40	90.0	0.4	448	3.0	1320.5	0.398
dt90x65ip30wp80	90.0	0.8	448	3.0	964.7	0.784
dt90x80ip30wp00	90.0	0.0	550	3.0	1588.8	0.212
dt90x80ip30wp40	90.0	0.4	550	3.0	1630.5	0.296
dt90x80ip30wp80	90.0	0.8	550	3.0	1242.3	0.654

Table 6.10 – Evaluation of Equation 6.14 with Experimental Critical Strain Data

Specimen	D/t	p/py	Fy/E	%Imp	Experimental ε_{crit}	Equation 6.14 ε_{crit}	T / P Ratio
UGA12	51.0	0.00	0.001892	2	1.49	1.613	0.92
HGA12	51.0	0.36	0.001892	2	1.70	2.346	0.72
DGA12	51.0	0.72	0.001892	2	3.90	4.299	0.91
L178P80BP-4	60.7	0.80	0.002270	3	3.10	3.259	0.95
UGA20	64.3	0.00	0.001919	3	0.80	1.049	0.76
HGA20	64.3	0.40	0.001919	3	1.23	1.606	0.77
DGA20	64.3	0.80	0.001919	3	2.37	3.431	0.69
CP0N	90.7	0.00	0.002342	18.6	0.23	0.372	0.62
CP20N-2	87.1	0.14	0.002631	23.6	0.25	0.384	0.65
CP40N-2	87.1	0.33	0.002631	22.1	0.29	0.482	0.60
CP80N-2	89.7	0.68	0.002597	18.9	0.51	0.839	0.61
T20P40N	89.7	0.36	0.002597	9.8	0.40	0.577	0.69
						mean	**0.74**
						coeff. of var.	**0.169**

Table 6.11 – Effect of Yield Plateau on the Peak Moment and Critical Strain

Load Case	Rounded Material Curve		Plateau Material Curve		P/R[1]	P/R
	Peak Moment	Critical Strain	Peak Moment	Critical Strain	Peak Moments	Critical Strains
dt50x52ip2p80	137.2	5.433	138.0	4.809	1.01	0.89
dt50x65ip15wp40	212.7	1.024	223.9	0.617	1.05	0.60
dt50x80ip16p00s	313.9	0.841	320.3	0.393	1.02	0.47
dt70x52ip16p80	336.7	2.376	351.2	1.832	1.04	0.77
dt70x80ip15wp00	711.0	0.430	690.7	0.397	0.97	0.92
dt90x52ip15wp80	779.7	1.256	843.0	0.775	1.08	0.62
dt90x65ip16p40	1578.9	0.618	1557.0	0.477	0.99	0.77
dt90x80ip2p40	2039.2	0.651	2004.8	0.433	0.98	0.67
				mean	**1.018**	**0.71**
				coef. of var.	**0.035**	**0.201**

Notes:

1. 'P/R' indicates the plateau material property value divided rounded material property value.

Table 6.12– Evaluation of Equation 6.16 with Experimental Critical Strain Data

Specimen	D/t	p/py	Fy/E	%Imp	Experimental ε_{crit}	Equation 6.16 ε_{crit}	T / P Ratio
UGA12	51.0	0.00	0.001892	2	1.49	1.320	1.13
HGA12	51.0	0.36	0.001892	2	1.70	1.958	0.87
DGA12	51.0	0.72	0.001892	2	3.90	3.795	1.03
L178P80BP-4	60.7	0.80	0.002270	3	3.10	0.771	1.04
UGA20	64.3	0.00	0.001919	3	0.80	1.209	1.02
HGA20	64.3	0.40	0.001919	3	1.23	2.800	0.85
DGA20	64.3	0.80	0.001919	3	2.37	2.748	1.13
CP0N	90.7	0.00	0.002342	18.6	0.23	0.214	1.07
CP20N-2	87.1	0.14	0.002631	23.6	0.25	0.222	1.13
CP40N-2	87.1	0.33	0.002631	22.1	0.29	0.284	1.02
CP80N-2	89.7	0.68	0.002597	18.9	0.51	0.520	0.98
T20P40N	89.7	0.36	0.002597	9.8	0.40	0.362	1.11
						mean	**1.03**
						coeff of var	**0.092**

Table 6.13– Evaluation of Equation 6.16 with Parametric Critical Strain Data

Specimen	D/t	p/py	Fy/E	%Imp	Parametric ε_{crit}	Equation 6.16 ε_{crit}	T / P Ratio
dt50x52ip2p00	50	0.00	0.001795	2	1.699	1.433	1.19
dt70x65ip2p00	70	0.40	0.002240	2	1.295	0.962	1.35
dt90x80ip2p00	90	0.80	0.002750	2	1.336	1.144	1.17
dt50x65ip8p40	50	0.40	0.002240	8	1.728	1.454	1.19
dt70x80ip8p80	70	0.80	0.002750	8	1.768	1.460	1.21
dt90x52ip8p00	90	0.00	0.001795	8	0.580	0.342	1.70
dt50x80ip16p80	50	0.80	0.002750	16	2.775	2.366	1.17
dt70x52ip16p00	70	0.00	0.001795	16	0.721	0.468	1.54
dt90x65ip16p40	90	0.40	0.002240	16	0.618	0.372	1.66
						mean	**1.35**
						coeff of var	**0.164**

Table 6.14 – Evaluation of Equation 6.17 with Experimental Critical Strain Data

Specimen	D/t	p/py	Fy/E	offset/t	Experimental ε_{crit}	Equation 6.17 ε_{crit}	T / P Ratio
UGA12W	51.0	0.00	0.001892	0.031	1.20	1.404	0.85
L178P80BW-1	60.7	0.75	0.002270	0.036	1.20	2.702	0.44
L178P80BW-2	60.7	0.37	0.002270	0.036	0.97	1.335	0.73
L178P80BW-5	83.1	0.78	0.002270	0.049	0.58	1.600	0.36
UGA20W-2	64.3	0.00	0.001919	0.032	0.81	0.932	0.87
HGA20W	64.3	0.40	0.001919	0.032	1.27	1.450	0.88
CP0W-2	87.1	0.00	0.002631	0.034	0.30	0.438	0.69
CP20W	87.6	0.18	0.002571	0.090	0.30	0.424	0.71
CP40W	87.6	0.35	0.002571	0.097	0.31	0.504	0.62
CP80W	87.6	0.73	0.002571	0.064	0.45	1.104	0.40
						mean	**0.66**
						coeff. of var.	**0.296**

Table 6.15 – Evaluation of Equation 6.18 with Experimental Critical Strain Data

Specimen	D/t	p/py	Fy/E	offset/t	Experimental ε_{crit}	Equation 6.18 ε_{crit}	T / P Ratio
UGA12W	51.0	0.00	0.001892	0.031	1.20	1.205	1.00
L178P80BW-1	60.7	0.75	0.002270	0.036	1.20	1.172	1.02
L178P80BW-2	60.7	0.37	0.002270	0.036	0.97	0.899	1.08
L178P80BW-5	83.1	0.78	0.002270	0.049	0.58	0.601	0.97
UGA20W-2	64.3	0.00	0.001919	0.032	0.81	0.751	1.08
HGA20W	64.3	0.40	0.001919	0.032	1.27	0.938	1.35
CP0W-2	87.1	0.00	0.002631	0.034	0.30	0.325	0.93
CP20W	87.6	0.18	0.002571	0.090	0.30	0.291	1.03
CP40W	87.6	0.35	0.002571	0.097	0.31	0.314	1.00
CP80W	87.6	0.73	0.002571	0.064	0.45	0.451	0.99
						mean	**1.04**
						coeff. of var.	**0.113**

Table 6.16 – Evaluation of the Critical Buckling Strain Equations for Plain Pipes Using External Sources of Data

Source[1]	D/t	p/py	Fy/E	% Imp	Test[2] ε_{crit}	Eq. 6.14[3]	Eq. 6.16[4]	T/P Eq. 6.14[5]	T/P Eq. 6.16[6]
A	80.9	0.00	0.002141	11	0.42	0.539	0.339	0.779	1.239
A	71.9	0.00	0.001841	7	0.49	0.803	0.541	0.610	0.905
A	62.0	0.00	0.001803	3	1.36	1.173	0.872	1.160	1.560
A	55.3	0.00	0.001993	3	1.01	1.293	1.012	0.781	0.998
A	51.4	0.00	0.002337	2	1.24	1.330	1.097	0.932	1.130
A	48.6	0.00	0.001682	2	1.38	1.927	1.599	0.716	0.863
A	39.8	0.00	0.001986	2	2.06	2.294	2.082	0.898	0.990
B	97.0	0.70	0.002189	20	0.45	0.896	0.533	0.502	0.844
B	98.6	0.72	0.002189	20	0.56	0.909	0.540	0.616	1.037
B	98.6	0.11	0.002189	20	0.29	0.376	0.208	0.770	1.393
B	82.1	0.08	0.002517	11	0.48	0.494	0.313	0.971	1.535
B	102.8	0.11	0.002344	20	0.28	0.331	0.181	0.845	1.549
C	80.0	0.00	0.001875	11	0.27	0.614	0.385	0.439	0.701
C	80.0	0.00	0.001803	11	0.68	0.635	0.398	1.070	1.710
D	27.7	0.00	0.001689	1	4.36	5.053	5.370	0.869	0.817
D	89.9	0.00	0.001865	18	0.30	0.462	0.265	0.650	1.134
D	67.6	0.00	0.002168	4	0.84	0.839	0.601	1.001	1.397
E	78.4	0.00	0.001893	10	0.37	0.641	0.408	0.577	0.907
							mean	**0.788**	**1.150**
							Coeff. of Var.	**0.252**	**0.266**

Notes:

1. All critical strain values for these different research programs were compiled in Battelle Report: NG-18 No. 188 (Stephens *et al.*, 1991). The respective sources of data are:
   'A' = Sorenson, *et al.*, 1970.
   'B' = Bouwkamp and Stephen, 1974.
   'C' = Korol, 1979.
   'D' = Sherman, 1983/84.
   'E' = Wilhoit, *et al.*, 1972
2. The test critical strain as reported by the respective source.
3. The critical strain predicted using Equation 6.14.
4. The critical strain predicted using Equation 6.16.
5. The test-to-predicted ratio when the test critical strain is divided by the prediction from Equation 6.14.
6. The test-to-predicted ratio when the test critical strain is divided by the prediction from Equation 6.16.

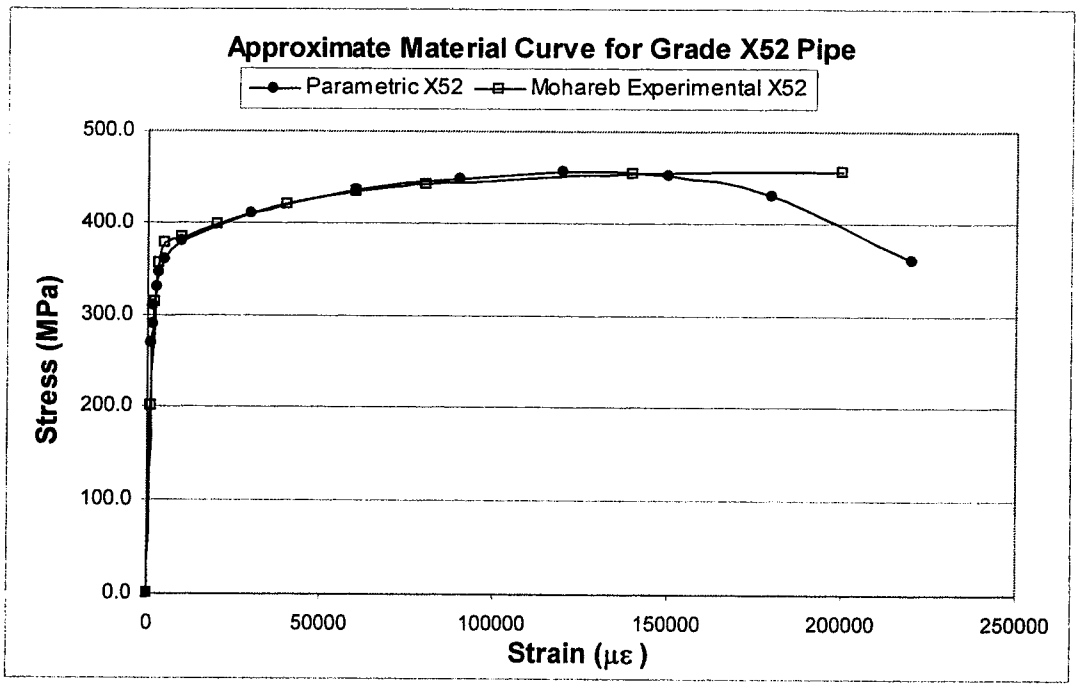

Figure 6.1 – Material Curve for Assumed X52 Grade Material

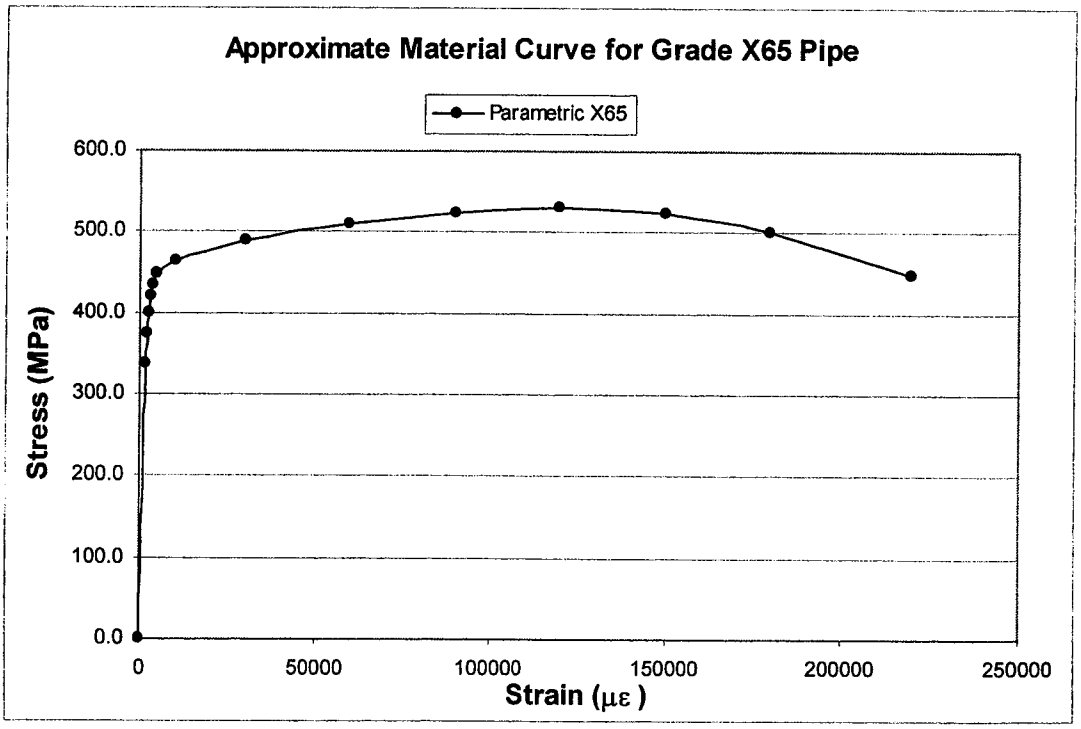

Figure 6.2 – Material Curve for Assumed X65 Grade Material

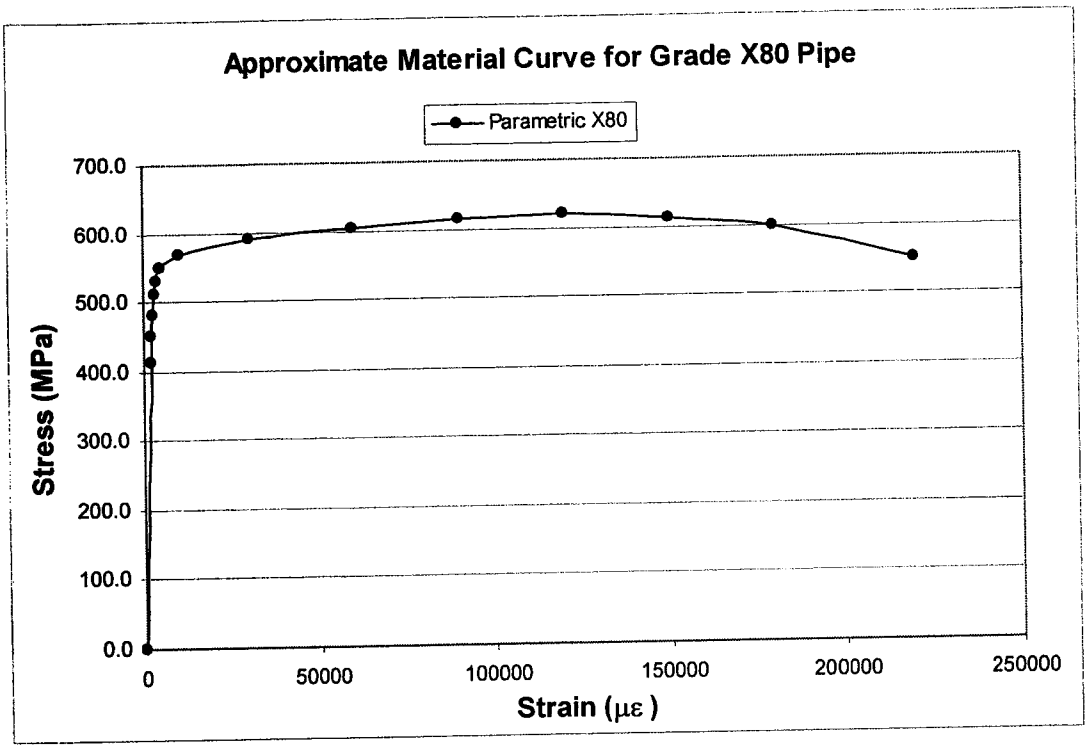

Figure 6.3 – Material Curve for Assumed X80 Grade Material

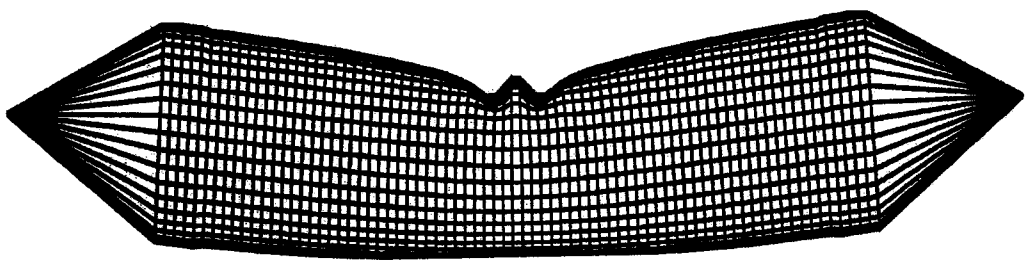

Figure 6.4 – Symmetric Indentation Buckle

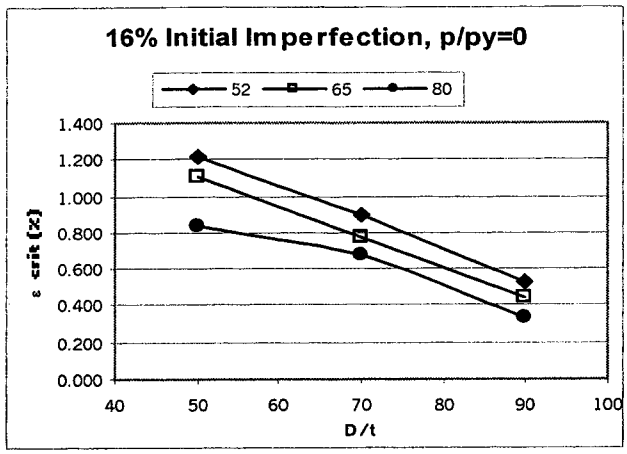

Figure 6.5 – Effect of D/t Ratio on Critical Strain for Unpressurized Plain Pipes with a Blister-type Initial Imperfection of 16% the Wall Thickness

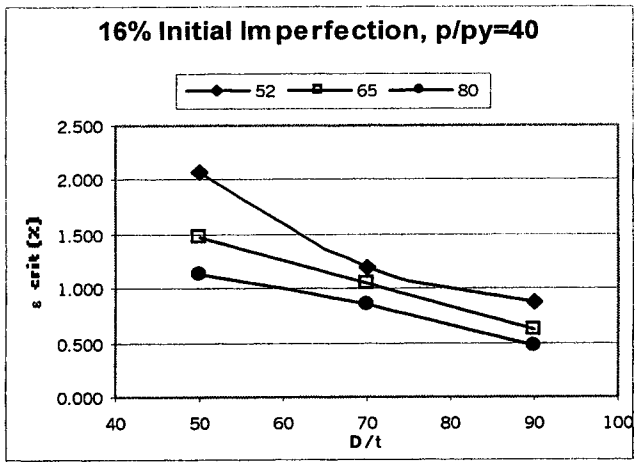

Figure 6.6 – Effect of D/t Ratio on Critical Strain for Plain Pipes with and Internal Pressure of 40% and a Blister-type Initial Imperfection of 16% the Wall Thickness

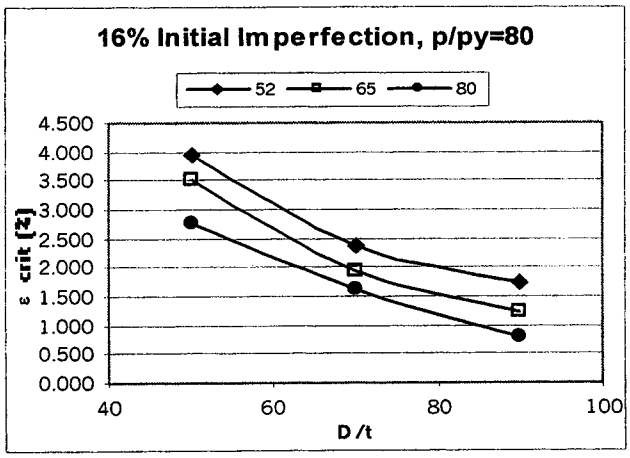

Figure 6.7 – Effect of D/t Ratio on Critical Strain for Plain Pipes with and Internal Pressure of 80% and a Blister-type Initial Imperfection of 16% the Wall Thickness

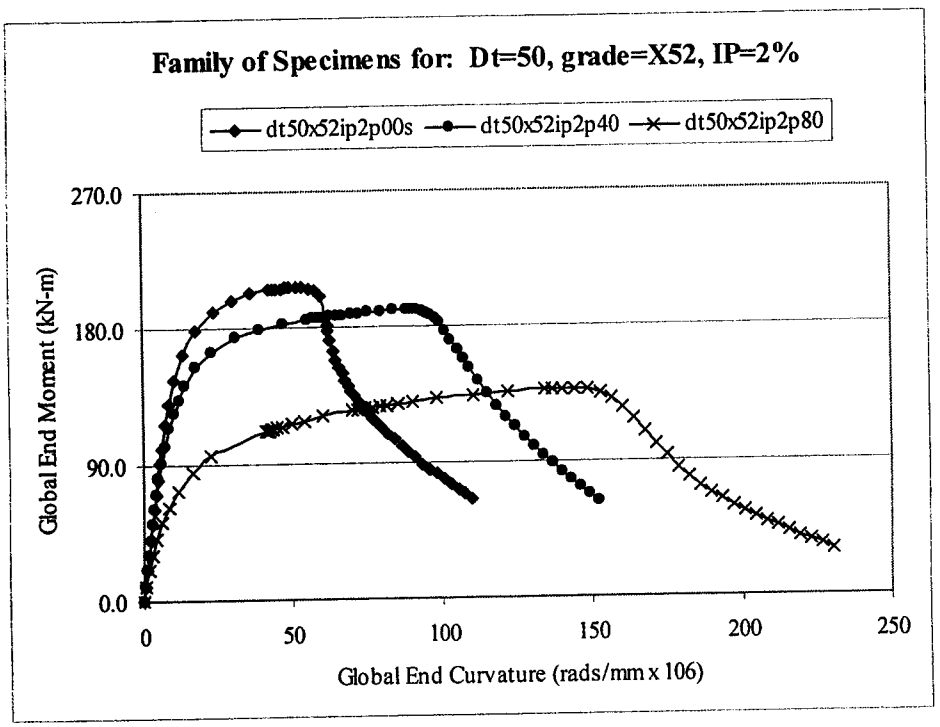

Figure 6.8 – Family of Specimen Plot for dt50x52ip2 Load Case

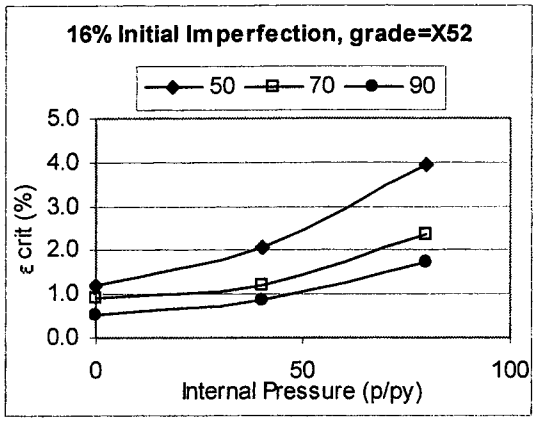

Figure 6.9 – Effect of p/p_y Ratio on Critical Strain for Specimens Made from Grade X52 Material with a Blister-type Initial Imperfection of 16% the Wall Thickness

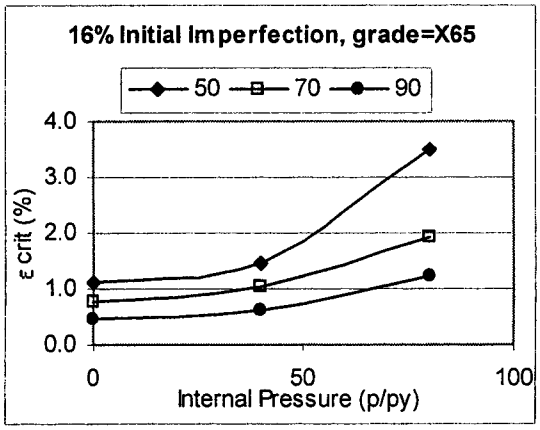

Figure 6.10 – Effect of p/p_y Ratio on Critical Strain for Specimens Made from Grade X65 Material with a Blister-type Initial Imperfection of 16% the Wall Thickness

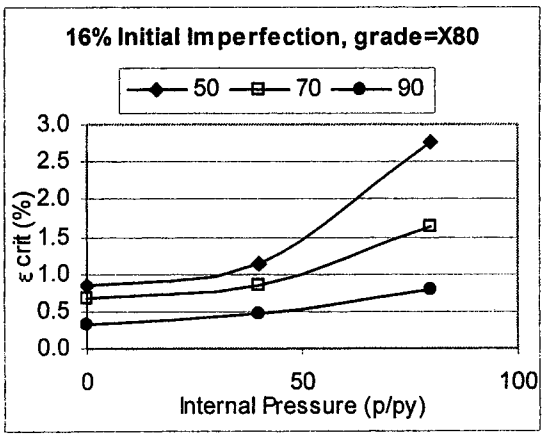

Figure 6.11 – Effect of p/p_y Ratio on Critical Strain for Specimens Made from Grade X80 Material with a Blister-type Initial Imperfection of 16% the Wall Thickness

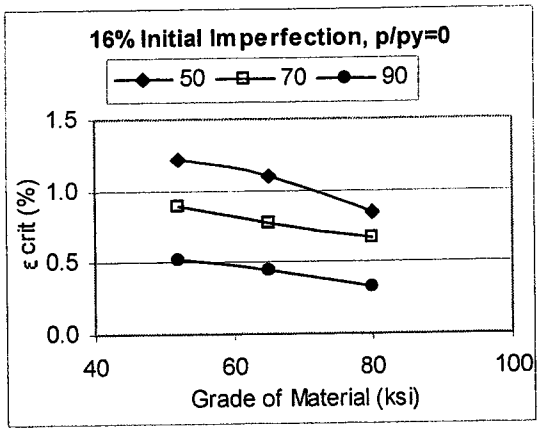

Figure 6.12 – Effect of F_y/E Ratio on Critical Strain for Unpressurized Specimens with a Blister-type Initial Imperfection of 16% the Wall Thickness

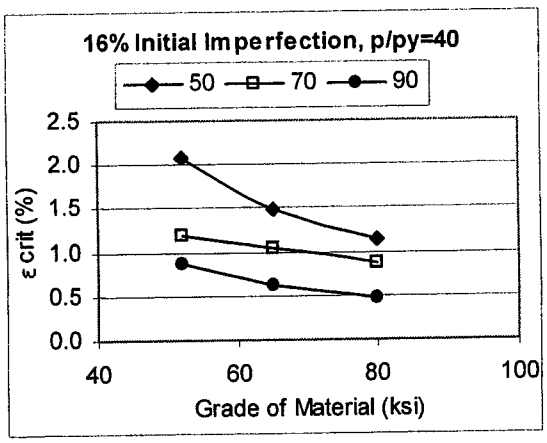

Figure 6.13 – Effect of F_y/E Ratio on Critical Strain for Specimens with an Internal Pressure of 40% and a Blister-type Initial Imperfection of 16% the Wall Thickness

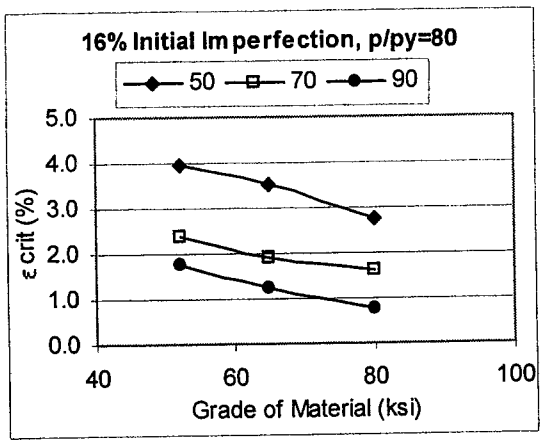

Figure 6.14 – Effect of F_y/E Ratio on Critical Strain for Specimens with an Internal Pressure of 80% and a Blister-type Initial Imperfection of 16% the Wall Thickness

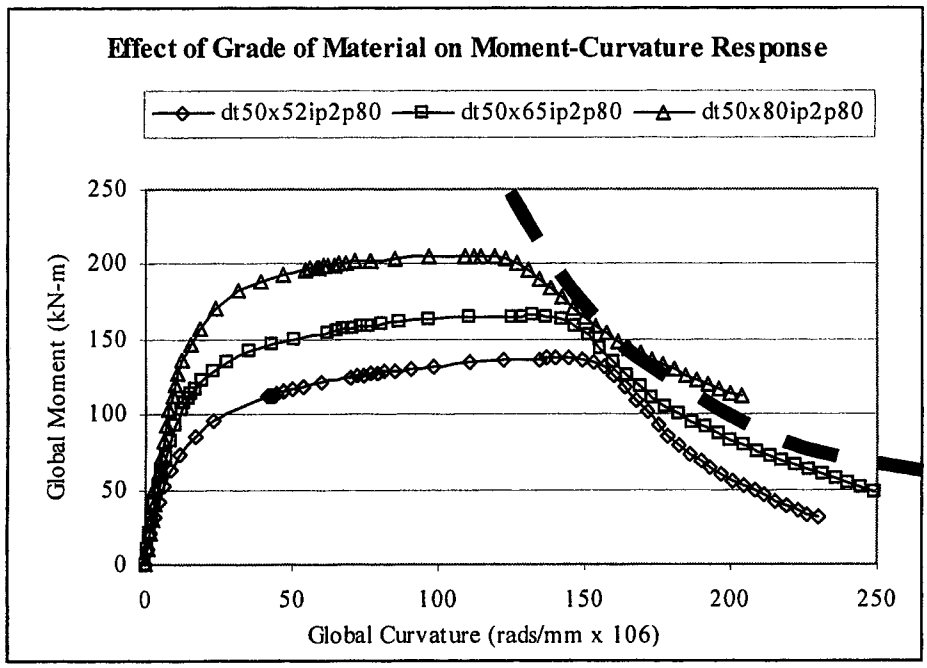

Figure 6.15 – Effect of Grade of Material on the Moment-Curvature for Load Case dt50ip2p80

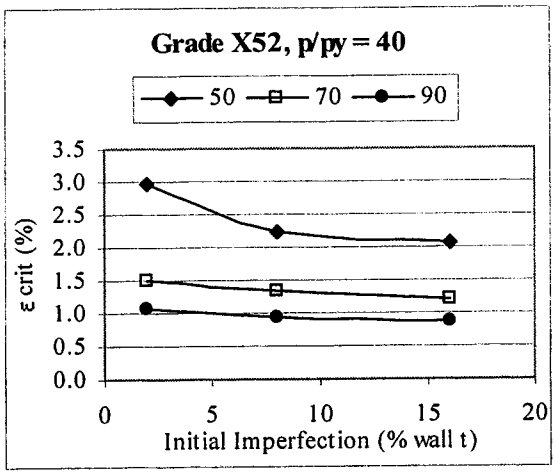

Figure 6.16 – Effect of Amplitude of the Initial Imperfection on Critical Strain for Specimens with an Internal Pressure of 40% and a Grade of Material of X52

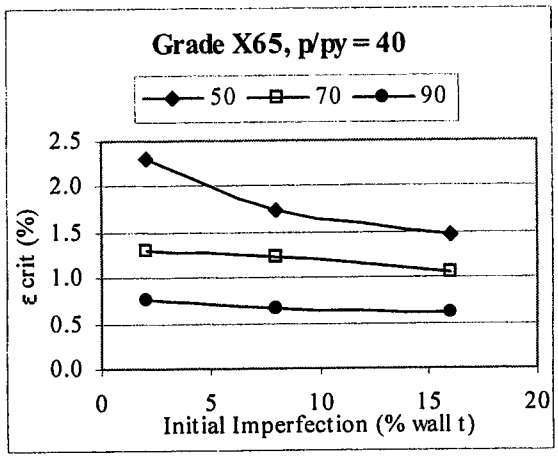

Figure 6.17 – Effect of Amplitude of the Initial Imperfection on Critical Strain for Specimens with an Internal Pressure of 40% and a Grade of Material of X65

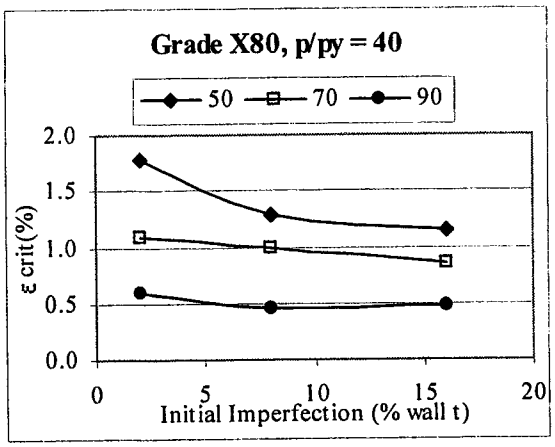

Figure 6.18 – Effect of Amplitude of the Initial Imperfection on Critical Strain for Specimens with an Internal Pressure of 40% and a Grade of Material of X80

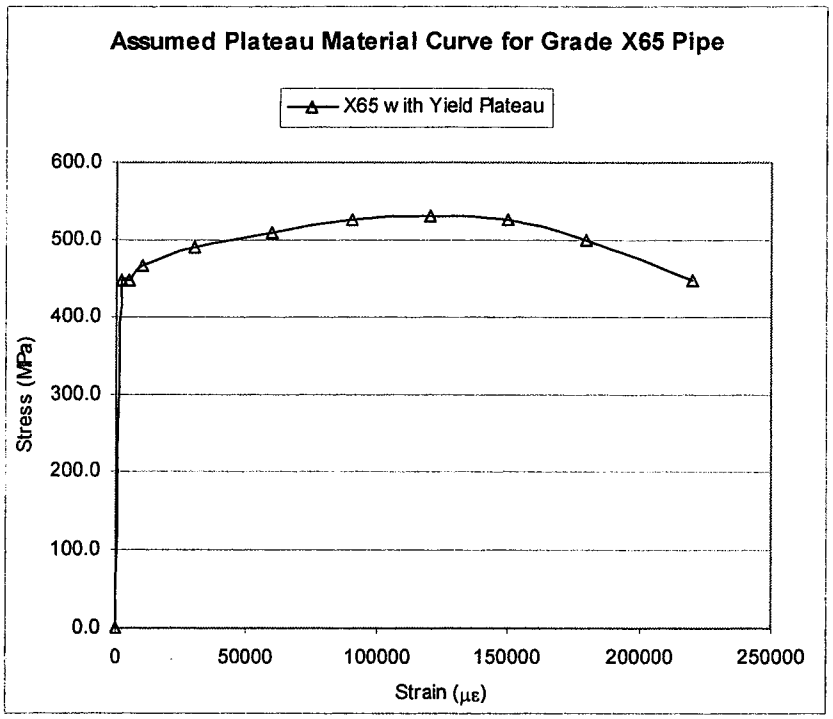

Figure 6.19 – Assumed Plateau Material Curve for Grade X65 Pipe

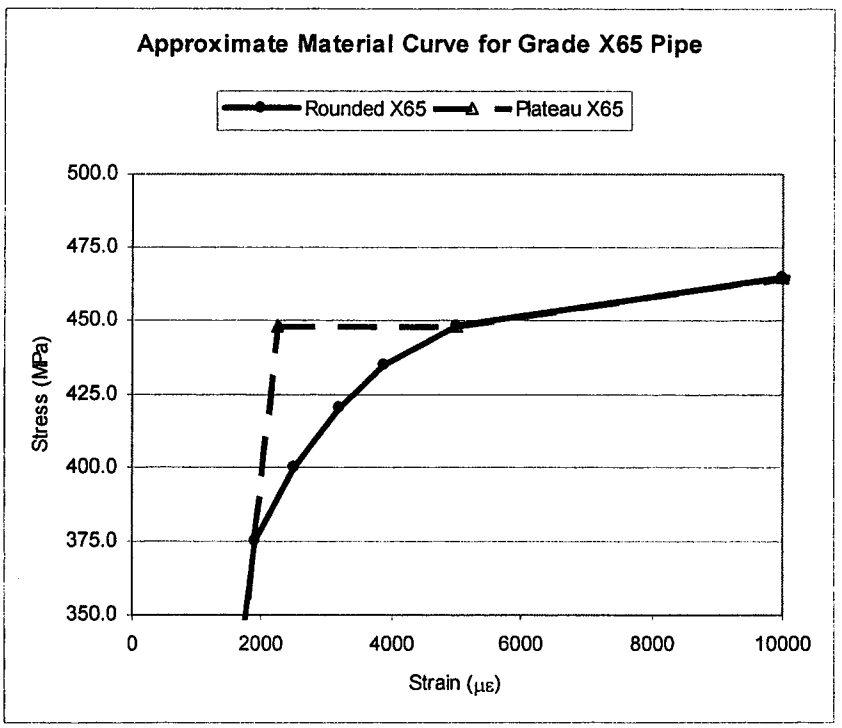

Figure 6.20 – Differences Between the Rounded X65 and the Plateau X65 Material Property Curves in the Region of the Yield Plateau

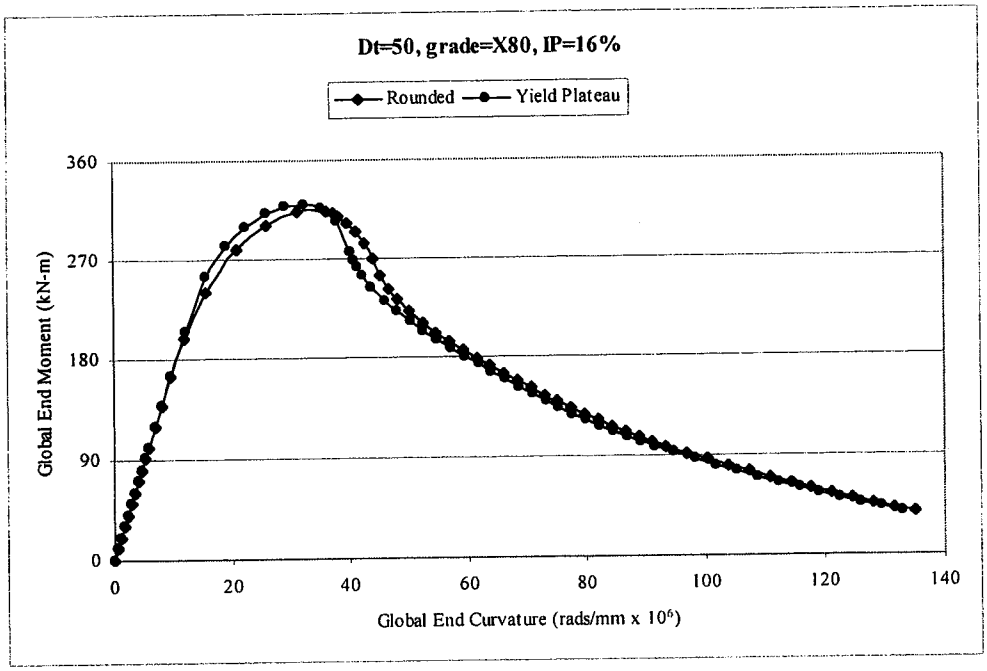

Figure 6.21 – Comparison of Moment-Curvature Plots for Rounded versus Plateau Material Property Curves using Load Case dt50x80ip16p00

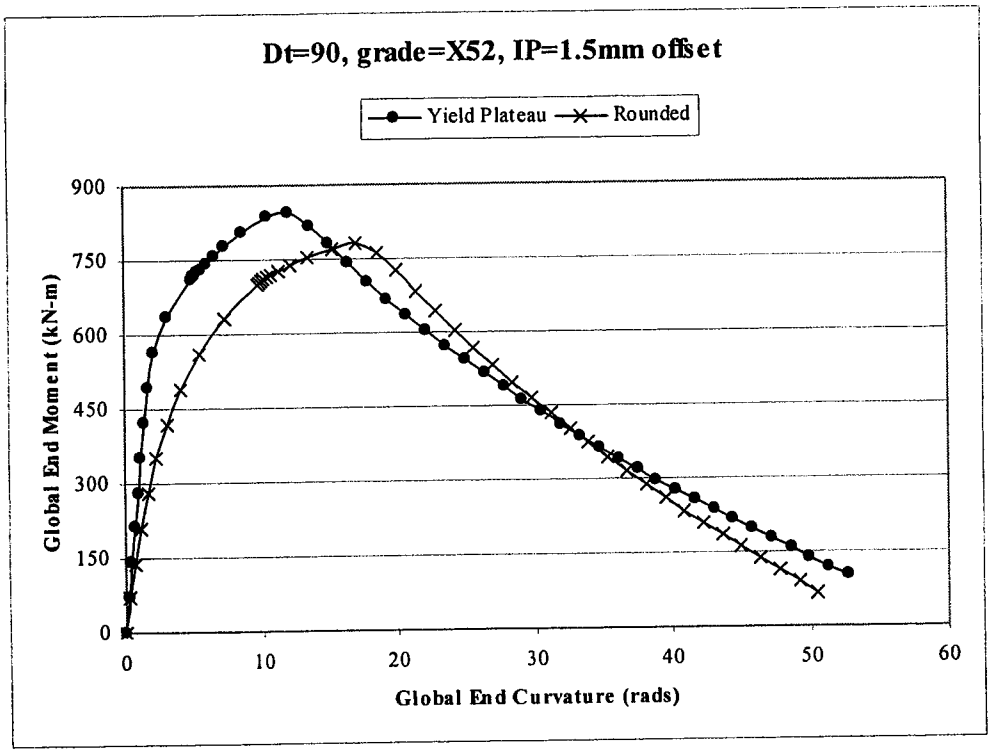

Figure 6.22 – Comparison of Moment-Curvature Plots for Rounded versus Plateau Material Property Curves using Load Case dt90x52ip15wp40

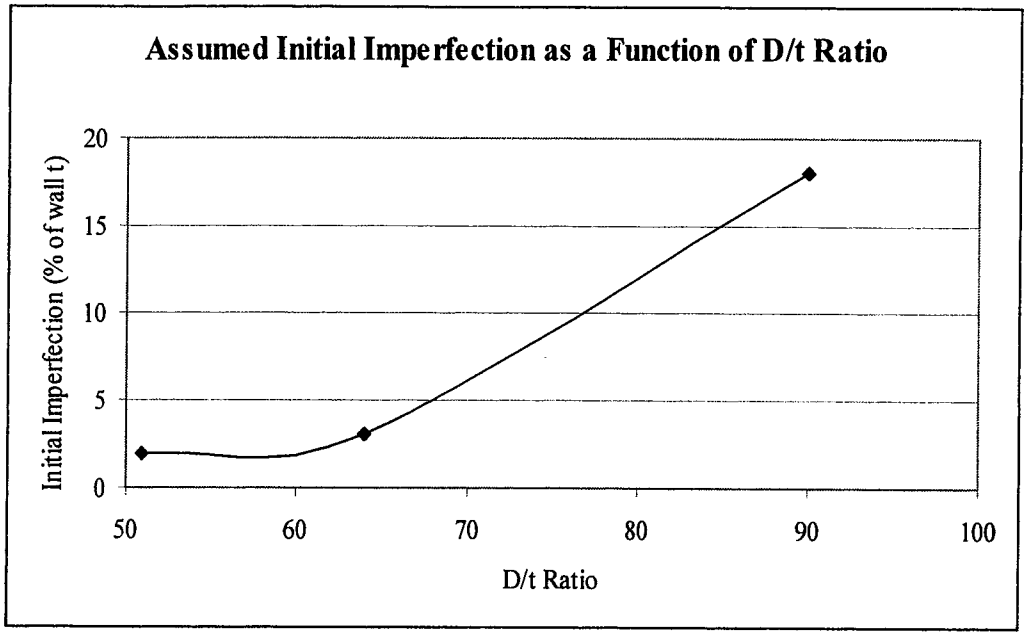

Figure 6.23 – Assumed Initial Imperfection as a Function of D/t Ratio

7.0 SUMMARY, CONCLUSIONS AND RECOMMENDATIONS

7.1 Summary

This research was developed and implemented with the intent of expanding the current understanding of behaviour of segments of line pipe subjected to combined load cases that are representative of 'typical' load cases that may be experienced in the field under normal operating conditions. Specifically, the project was designed to expand the current experimental database by examining segments of line pipe with large D/t ratios and to develop a more accurate FEA model that can be used for predicting this behaviour. An additional objective was to determine limiting strain criteria for design and assessment of energy pipelines.

A total of 15 full-scale experimental tests were conducted on NPS30 line pipe with a D/t ratio of approximately 92, which generated 11 meaningful test results. The test specimens were subjected to load cases that were a combination of axial load, internal pressure and monotonically increasing curvature. The load cases included net axial loads that were compressive as well as load cases in which the net axial load was tensile. The compressive axial loads corresponded to a load that would be created by a temperature differential of 45 °C applied to the test specimen. The tensile axial loads were such that a longitudinal stress equal to 20% SMYS was developed in the wall of the specimen. The test specimens were subjected to a series of different levels of internal pressure ranging from no internal pressure to a level of internal pressure that produced a stress equal to 80% SMYS in the circumferential direction. Intermediate values of internal pressure that caused 20% and 40% SMYS to develop in the circumferential direction were also investigated. Finally, the specimens were loaded in increments of monotonically increasing curvature until a wrinkle had initiated, developed into a large amplitude buckle, and for which adequate data had been collected in the post-buckling region. Specimens were tested with and without a circumferential girth weld at the half height of

the test specimen. Experimental data was recorded to define the load characteristics and corresponding deformation response.

In addition to the different load parameters, experimental data was recorded such that a map of the initial imperfection pattern across the entire length and circumference of each individual test specimen could be developed. Finally, longitudinal material coupons were cut from the same bent of pipe as the test specimens to determine the material properties of each individual test specimen. These results were added to the current U of A database, resulting in an accumulation of over 30 full-scale test results.

Once the experimental phase of this project was completed, an FEA model was developed to incorporate all of the features of the experimental test specimens, most notably the initial imperfection pattern. Inclusion of an experimental initial imperfection pattern was a new feature to this type of modeling at the University of Alberta. With the inclusion of the initial imperfection pattern, the predictive ability of the model proved to be exceptional. The mean test-to-predicted ratio for the peak moment capacity of the specimens tested in this project was 1.035 with a coefficient of variation of 0.047 and a range from 0.970 to 1.060, excluding one out-lying result. The mean test-to-predicted ratio for the critical buckling strain of the specimens tested in this project was 0.967 with a coefficient of variation of 0.066 and a range from 0.910 to 1.028. The computed global moment-curvature plots, global curvature versus local strain plots, and local buckling deformed geometry generated by the FEA model were found to be identical with the experimental results.

The FEA model was validated using the available results from experimental specimens with D/t ratios of 51 and 64. The mean peak moment test-to-predicted ratio was found to be 1.011 with a coefficient of variation of 0.024 and a range from 0.97 to 1.05. The mean critical buckling strain test-to-predicted ratio was found to be 1.034 with a coefficient of variation of 0.051 and a range from 0.96 to 1.10. Again, the computed global moment-curvature plots, global curvature versus local strain plots, and local buckling deformed

geometry generated by the FEA model was found to be identical with the experimental results.

These results show that the FEA model developed in this project is capable of predicting the response of a variety of D/t ratio specimens subjected to a variety of load cases. Consequently, a numerical parametric study was developed to examine the effects of the five key parameters identified during the testing and analysis of the experimental load cases, namely, the D/t ratio, the p/p_y ratio, the grade of the material, the initial imperfection pattern, and the presence or absence of a circumferential girth weld. A total of 162 load cases were examined in the parametric study. A non-linear regression analysis was conducted on the results and a new predictive critical buckling strain equation was developed, based on the parametric study results. The proposed design equations were then evaluated using experimental data from the U of A as well as data from sources external to the U of A. Based on this evaluation, the proposed equations were modified accordingly.

Review of the scope and objectives of this project outlined in Section 1.4 shows that all objectives were achieved.

7.2 Conclusions

A number of conclusions can be drawn from the experimental and analytical results obtained in this project.

1. Current critical buckling strain design equations provided poor correlation with the U of A experimental database. This is partially influenced by the inconsistency between the different methods used to define 'critical buckling strain'. A uniform method for quantifying this important design parameter is required. The bi-linear regression technique presented in Appendix D provides a

numerically based determination of the critical buckling strain in segments of line pipe.

2. The results of the experimental phase of this project show that there are two dominant buckling modes for segments of line pipe subjected to combined loads. These two modes are dependent on the level of internal pressure in the test specimen. For the unpressurized specimens, the wrinkle develops into a 'diamond-shape' buckle. For the specimens with an internal pressure equal to or greater than that required to produce a circumferential stress of 20% SMYS, the wrinkle develops into a 'bulge' buckle. Although additional load cases were included in this research to determine the level of internal pressure where this transition occurs, the results were inconclusive. There is evidence that the transition occurs very close to the 20% SMYS level, however, further investigation is required.

3. The moment-curvature response of a family of specimens, in which the only variable was the level of internal pressure, showed that the higher the internal pressure, the less the magnitude of the softening that occurs in the unloading portion of the response curve. It is believed that this is due to the stabilizing effect on the wall of the specimen provided by the internal pressure.

   The results from the family of specimens with varying levels of pressurization also showed that there is a significant reduction in the limit point moment with increasing pressure and that there is a significant increase in global curvature and critical buckling strain at the limit point with increasing pressure. These phenomena are not unexpected and are consistent with predictions using the von Mises yield criterion.

4. The local and global response of a test specimen is highly dependent on the grade of the material. For specimen groups in which the only variable was the material

strength, an increase in material strength resulted in an increase in peak moment capacity and a reduction in the critical buckling strain.

The phenomenon of increasing peak moment capacity with increasing strength of material is self-explanatory. The phenomenon of decreasing critical buckling strain with increasing strength appears to be a function of a global buckling limit state.

5. The specimens with the large D/t ratio tested in this program did not achieve the fully plastic moment capacity predicted by the Mohareb-Murray plastic moment equation. However, this equation does not account for stability issues in its predictions. Because the D/t = 92 specimens investigated in this project are susceptible to failure due to stability limit states prior to strength limit states, the Mohareb-Murray plastic moment capacity equations provides an upper bound solution for the strength capacity.

6. Initial imperfections are an extremely important feature in the buckling response of segments of line pipe. Inclusion of an appropriate initial imperfection pattern in an FEA model is crucial in predicting experimental behaviour. Detailed recommendations for assumed initial imperfection patterns that produce excellent agreement with the results from measured imperfection patterns are given in Section 5.1.

7. The global and local behaviour of segments of line pipe subjected to combined load cases can be accurately predicted using FEA modeling techniques provided accurate initial imperfection, material property and boundary condition criteria are incorporated into the model. The finite element models used need to be formulated to allow for large displacements, non-linear material properties, and finite membrane strains. The results presented in Chapters 4 and 5 using the model developed in Chapter 3 show that if all of these important facets are given due consideration, excellent correlation with experimental results is obtained.

8. Using an assumed 'blister-type' initial imperfection pattern provides excellent correlation with the experimental data for the plain pipe specimens, as shown in Sections 5.1.1, 5.2.2, and 5.2.3. Using an assumed 'offset-type' initial imperfection pattern provides excellent correlation for the girth-welded specimens, as shown in Sections 5.1.2, 5.2.4, and 5.2.5.

9. For a given D/t ratio, the 'diameter' variable was found to affect the peak moment capacity of the test specimens but not the critical buckling strain, as shown in Section 6.2.1 and Table 6.1.

10. A non-linear regression analysis based on the results of the parametric study showed that the critical buckling strain of segments of line pipe, with typical 'rounded' material property curves subjected to combined load cases could be predicted using the following equations:

For plain pipes (see Table 6.10):

$$\varepsilon_{crit} = \left(\frac{2.94}{D/t}\right)^{1.59} * \left(\frac{1}{1-0.868\left(\frac{p}{p_y}\right)}\right) * \left(\frac{E}{F_y}\right)^{0.854} * \left(1.27-\left(\frac{imp}{100}\right)^{0.150}\right) \qquad (6.14)$$

For girth-welded pipes (see Table 6.14):

$$\varepsilon_{crit} = \left(\frac{8.99}{D/t}\right)^{1.72} * \left(\frac{1}{1-0.892\left(\frac{p}{p_y}\right)}\right) * \left(\frac{E}{F_y}\right)^{0.701} * \left(1.09-\left(\frac{offset}{t}\right)^{0.0863}\right) \qquad (6.17)$$

11. Comparison of the new equations with experimental data collected in this project and from external sources revealed that not only did the numeric values of the

material properties affect the response of the model, but the overall shape of the material property curve had a significant effect as well. For example, the presence of a yield plateau resulted in a substantially smaller value for the critical buckling strain. The predictive equations developed in the parametric study were adjusted to reflect this change. This resulted in equations that will provide a conservative result for all load cases if the material property curve is assumed to have a yield plateau.

The critical buckling strain of segments of line pipe made from steel materials with a distinct yield plateau subjected to combined load cases can be predicted using the following equations:

For plain pipes (see Tables 6.12 and 6.13):

$$\varepsilon_{crit} = 40.4 * \left(\frac{t}{D}\right)^2 * \left(\frac{1}{1 - 0.906\left(\frac{p}{p_y}\right)}\right) * \left(\frac{E}{F_y}\right)^{0.80} * \left(1.12 - \left(\frac{imp}{100}\right)^{0.15}\right) \qquad (6.16)$$

For girth-welded pipes (see Table 6.15):

$$\varepsilon_{crit} = 106 * \left(\frac{t}{D}\right)^2 * \left(\frac{1}{1 - 0.50\left(\frac{p}{p_y}\right)}\right) * \left(\frac{E}{F_y}\right)^{0.70} * \left(1.10 - \left(\frac{offset}{t}\right)^{0.09}\right) \qquad (6.18)$$

7.3 Recommendations

The results of this research provide a number of significant enhancements of the current state-of-the-art for estimating critical buckling strain. Specifically, it has provided an expansion of the current experimental database and has identified the important parameters that influence the critical buckling behaviour of segments of line pipe. In

addition to this, the FEA model developed in this project provides excellent global and local predictive ability for segments of line pipe. However, many areas were identified that require further investigation.

1. The bi-linear regression analysis method adopted from Yoosef-Ghodsi (1994) and refined in this project has proven to be a consistent method with little subjective interpretation required for the experimental data. For the FEA model, limitations on the number of significant figures included in the ABAQUS output files introduces minor levels of subjectivity, the effect of which can be minimized when using the methods described in this project. However, given the level of agreement shown in the test-to-predicted ratios, the recommended method appears to give reliable, reproducible results. Therefore, it is recommended that this method of determining the critical buckling strain developed in this project be adopted in future studies.

2. Additional experimental and FEA model testing is required to identify the level of internal pressure at which the transition between the 'diamond-shape' and the bulge buckle occurs.

3. From the investigation into the effects of the grade of material, it appears that there is a global buckling limit state for segments of line pipe, as shown in Figure 6.15. Further investigation into a global buckling limit state is required.

4. Comparison of the experimental results with the 'classifications' provided in CAN/CSA S16.1-94 shows that the limits proposed in the standard do not reflect the laboratory observations. Additional investigations are required.

5. An assessment of the level of initial imperfections that exist in different segments of line pipe is required. Actual initial imperfection patterns were only measured on the D/t = 92 specimens tested in the project. The initial imperfection patterns used for the other D/t ratio specimens were based on a 'best-fit' between the FEA

model and the experimental data, as discussed in Section 5.2. Using laboratory measurements to quantify the 'typical' level of initial imperfection that can be expected in different segments of line pipe may prove to be very beneficial.

6. From the results of the parametric study and the equation development, it is evident that further investigation into the effects of the material properties is required. Additional assumed material property curves should be developed and input into the FEA model for analysis. The additional material property curves should include a variety of different 'shapes' of the curves, which could be achieved by using the key points specified in this project but with varying proportional limits, as discussed in Section 6.6.2.1.

7. Spiral welded pipe is becoming common in field installations. The effects of the spiral weld geometry on the critical buckling strain should be investigated.

8. A substantial amount of data defining the global moment-curvature response of a family of specimens at varying pressures has been collected. It is recommended that this data be reduced to a single volume that covers all of the different load cases examined. This would provide a designer with a ready-made design chart for different load cases and eliminate the need for sophisticated FEA modeling for each new installation.

9. The effects of the initial imperfection pattern on the moment capacity of the specimen should be investigated with additional D/t ratio specimens. By generating a family of curves representative of this effect, moment capacity reduction could be readily determined for a given combination of D/t ratio and assumed level of initial imperfection.

10. The testing of additional specimens is recommended. For the data available in this project, there is limited data at D/t value of 51 and 64. Furthermore, there is a large gap between the D/t = 64 and the D/t =92 specimens. Additional testing is

required to validate the FEA model and the proposed design equations over this region. In addition, experimental testing outside of the D/t = 51 to D/t = 92 range should be considered. Current field installations are using segments of line pipe with D/t ratios as low as 10 to as high as 120. Experimental validation of the proposed design equations into this region would be very beneficial.

11. Comparison of the proposed critical buckling strain equations developed in this project with the available experimental database indicated that the use of the equations based on the assumed material curve with the 'yield-plateau' provide a conservative prediction. It is therefore recommended that Equation 6.16 be used to predict the critical buckling strain of plain pipes and that Equation 6.18 be used to predict the critical buckling strain of girth welded pipes.

12. Finally, it is recommended that additional critical buckling strains based on more liberal criteria be investigated, namely, critical strain limits for specific amplitudes of the buckles or for specific levels post-buckling unloading moment capacity. The establishment of such limits may allow for less stringent limits on the critical buckling strain without a significant impact on the function of the pipeline.

REFERENCES

American Petroleum Institute, 1995. "Specification for Line Pipes", API Specification 5L, 41st edition, Washington, D.C.

American Society for Testing and Materials, 1994. "Standard Test Methods and Definitions for Mechanical Testing of Steel Products", ASTM Designation A370-94.

Bathe, K-J., 1996. "Finite Element Procedures", Prentice-Hall Inc., Englewood Cliffs, New Jersey.

Beer, F.P., and Johnston, E.R., 1992. "Mechanics of Materials – Second Edition in SI Units", McGraw-Hill Book Company, New York, New York.

Bouwkamp, J., Stephen, R., 1974. "Full Scale Studies on Structural Behaviour of Large Diameter Pipes Under Combined Loading", Report No. UC-SESM 74-1, University of California Berkeley.

Brush, D. O., and Almroth, B. O., 1975. "Buckling of Bars, Plates and Shells", McGraw-Hill Book Company, New York, New York.

Bushnell, D., 1980. "Buckling of Shells – Pitfall for Designers", AIAA/ASME/ASCE/AHS 21st Structures, Structural Dynamics & Materials Conference, Seattle, Washington.

Canadian Standards Association, 1995. "Z245.1-95 Steel Line Pipe, Oil & Gas Industry Systems and Materials", Canadian Standards Association, Etobicoke, Ontario.

Canadian Standards Association, 1996. "Z662-96 Oil and Gas Pipeline Systems", Canadian Standards Association, Etobicoke, Ontario.

Column Research Council, 1966. "Guide to Design Criteria for Metal Compression Members", 2nd Edition. John Wiley and Sons, New York. Edited by B.G. Johnston.

Cook, R. D., and Young, W.C., 1999. "Advanced Mechanics of Materials", 2nd edition, Prentice-Hall Inc., Upper Saddle River, New Jersey.

Del Col, P.R., Grondin, G.Y., Cheng, J.J.R., and Murray, D.W., 1998. "Behaviour of Large Diameter Line Pipe Under Combined Loads", Structural Engineering Report No. 224, Department of Civil Engineering, University of Alberta, Edmonton, Alberta.

Devore, J.L., 1991. "Probability and Statistics for Engineering and the Sciences, 3rd Edition, Brooks/Cole Publishing Company, Pacific Grove, California.

DiBattista, J. D., Cheng, J. J. R., and Murray, D. W., 2000. "Behaviour of Sleeper Supported Line Pipe", Structural Engineering Report No. 230, Department of Civil Engineering, University of Alberta, Edmonton, Alberta.

Dieter, G.E., 1987. "Mechanical Metallurgy", 3rd edition, International edition. McGraw-Hill Book Co., Singapore.

Dinovitzer, A.S., and Smith, R.J., 1998. "Strain-Based Pipeline Design Criteria Review", Proceedings of the International Pipeline Conference – 1998, vol. 2, American Society of Mechanical Engineers, Calgary, Alberta. pp. 763-770.

Dinovitzer, A.S., Lazor, R.B., Walker, R., and Bayley, C., 1999. "A Pipeline Dent Assessment Model", Proceedings of the 18th International Offshore & Arctic Engineering Conference, American Society of Mechanical Engineers, St. John's, Newfoundland. Paper ID: PIPE5041.

DNV-OS-F101, 2000. ""Offshore Standard OS-F101, Submarine Pipeline Systems", Det Norske Veritas, Veritasveien 1, N-13222 Høvik, Norway.

Dorey, A.B., 1998. "Experimental Analysis of Large Diameter, Large D/t ratio Line Pipe Subjected to Combined Loading – Vol. 2 – Experimental Data Files", Department of Civil and Environmental Engineering, University of Alberta, November 1998.

Dorey, A.B., Murray, D.W., and Cheng, J.J.R., 2000. "An Experimental Comparison of Critical Buckling Strain Criteria", Proceedings of the Internal National Pipeline Conference, American Society of Mechanical Engineers, Calgary, Alberta.

Galambos, T. V., 1988. "Guide to Stability Design Criteria for Metal Structures", 5th Edition, John Wiley and Sons, Inc., New York.

Gresnigt, A. M., 1986. "Plastic Design of Buried Steel Pipelines in Settlement Areas", Heron, vol. 31, no.4.

Hibbeler, R.C., 1998. "Engineering Mechanics – Statics", 8th Edition, Prentice-Hall, New Jersey.

Hibbit, Karlsson, & Sorenson, Inc., 1997a. ABAQUS/Standard, Version 5.7-1 (software package). Hibbit, Karlsson, & Sorenson Inc., Pawtucket, Rhode Island.

Hibbit, Karlsson, & Sorenson, Inc., 1997b. ABAQUS/Standard Theory Manual, Version 5.7. Hibbit, Karlsson, & Sorenson Inc., Pawtucket, Rhode Island.

Hibbit, Karlsson, & Sorenson, Inc., 1997c. ABAQUS/Standard User's Manual, Version 5.7-1, vol. I and vol. II. Hibbit, Karlsson, & Sorenson Inc., Pawtucket, Rhode Island.

Hibbit, Karlsson, & Sorenson, Inc., 1997d. ABAQUS/Standard ABAQUS Post Manual, Version 5.7-1. Hibbit, Karlsson, & Sorenson Inc., Pawtucket, Rhode Island.

Horrigmoe, G., and Bergan, P.G., 1976. "Incremental Variational Principles and Finite Element Models for Non-Linear Problems", Computer Methods in Applied Mechanics and Engineering (7), North Holland Publishing Company.

Hu, Shou-Zon, 1991. "An Analytical Investigation of the Compressive Behaviour of Fabricated Steel Tubes", Ph.D. dissertation, Department of Civil Engineering, University of Toronto, Ontario.

Karamanos, S.A., and Tassoulas, J. L., 1996. "Tubular Members. I: Stability Analysis and Preliminary Results", Journal of Engineering Mechanics, January, pp. 64-71.

Khurri, A. I., and Cornell, J. A., 1996. "Response Suirfaces: Designs and Analyses", 2nd Edition, Marcel Dekker Inc., New York, New York.

Kim, H.-S., and Kim, W.-S., 1998. "Analysis of Stresses on Buried Natural Gas Pipeline Subjected to Ground Subsidence", Proceedings of the International Pipeline Conference, vol. 2, ASME (OMAE Division), Calgary, Alberta. pp. 749-756.

Kollar, D.S., and Dulacske, D.S., 1984. "Buckling of Shells for Engineers", John Wiley and Sons, New York. Printed in Budapest, Hungary.

Korol, R. M., 1979. "Critical Buckling Strains of Round Tubes in Flexure", International Journal of Mechanical Science, vol. 21. pp. 719-730.

Kratzig, W.B., Wittek, U., and Basar, Y., 1983. "Buckling of General Shells – Theory and Numerical Analysis", Proceedings of the Symposium on Collapse – the Buckling of Structures in Theory and Practice, International Union of Theoretical and Applied Mechanics at University College, London, Cambridge University Press, Cambridge.

Langhaar, H.L., (1951). "Dimensional Analysis and Theory of Models", John Wiley and Sons, New York, New York.

Lay, M.G., (1982). "Structural Steel Fundamentals – an engineering and metallurgical primer", Australian Research Board, Vermont South, Victoria.

Microsoft Corporation, 1999. Microsoft Excel – ver. 5.0 (software package),

Mohareb, M.E., Elwi, A.E., Kulak, G.L., and Murray, D.W., 1994. "Deformational Behaviour of Line Pipe", Structural Engineering Report No. 202, Department of Civil Engineering, University of Alberta, Edmonton, Alberta.

Mohareb, M.E., and Murray, D.W. "Mobilization of Fully Plastic Moment Capacity for Pressurized Pipes", *Submitted for publication in the* Journal of Offshore Mechanics and Arctic Engineering, ASME.

Myrholm, B., 2001. "Local Buckling and Fracture Behaviour of Line Pipe Under Cyclic Loading", M.Sc. dissertation, Department of Civil Engineering, University of Alberta, Edmonton, Alberta.

Obaia, K.H., Elwi, A.E., and Kulak, G.L., 1991. "Inelastic Transverse Shear Capacity of Large Fabricated Tubes", Structural Engineering Report No. 170, Department of Civil Engineering, University of Alberta, Edmonton, Alberta.

Pugh, E.D.L., Hinton, E., and Zienkiewicz, O.C., 1978. "A Study of Quadrilateral Plate Bending Elements with 'Reduced' Integration", International Journal for Numerical Methods in Engineering, vol. 12.

Ramm, E., 1980. "Strategies for Tracing Nonlinear Response Near Limit Points", Europe- U.S. Workshop on Nonlinear Finite Element Analysis in Structural Mechanics, Bochum, July.

Riks, E., 1979. "An Incremental Approach to the Solution of Snapping and Buckling Problems", International Journal of Solids and Structures, vol. 15, pp. 529-551.

Rockware, Inc., 1988a. MacGRIDZO/Version 2 – Geological Software for Microcomputers (software package), Rockware Inc., Wheat Ridge, Col.

Rockware, Inc., 1988b. "MacGRIDZO/Version 2 User's Manual – Geological Software for Microcomputers", Rockware Inc., Wheat Ridge, Col.

Sherman, D., 1976. "Tests of Circular Steel Tubes in Bending", ASCE Journal of Structural Division, vol. 102, ST11.

Sherman, D., 1983/84. "Bending Capacity of Fabricated Pipes", University of Wisconsin-Milwaukee Report and Supplement, February, 1983 and September, 1984, respectively.

Smith, M.Q., Nicolella, D.P., and Waldhart, C.J., 1998. "Full Scale Wrinkling Tests and Analyses of Large Diameter Corroded Pipes", Proceedings of the International Pipeline Conference – 1998, vol. 1, American Society of Mechanical Engineers, Calgary, Alberta. pp. 543-552.

Sorenson, J., *et al.*, 1970. "Buckling Strength of Offshore Pipelines", Battelle Report to Offshore Pipeline Group, Columbus, Ohio.

Souza, L.T., and Murray, D.W., 1994. "Prediction of Wrinkling Behaviour of Girth-Welded Line Pipe", Structural Engineering Report No. 197, Department of Civil Engineering, University of Alberta, Edmonton, Alberta.

Souza, L.T., and Murray, D.W., 1996. "Analysis for Wrinkling Behaviour of Girth-Welded Line Pipe", International Pipeline Conference, vol. 2, American Society of Mechanical Engineers, Calgary, Alberta. June. pp. 835-844.

SPSS, Inc., 1999. SigmaPlot 5.0 (software package), SPSS Inc., Chicago Illiinois.

Stelco, Inc., 1993. "Steel Pipe – For Commercial, Industrial and Process Use", 5th Edition, Stelpipe Technical Brochure, Stelco, Ontario, Canada.

Stephens, D. R., Olson, R. J., and Rosenfeld, M. J., 1991. "Topical Report on PIPELINE MONITORING – LIMIT STATE CRITERIA", NG-18 Report No. 188, Battelle, Columbus, Ohio.

Sussman, T., and Bathe, K.J., 1986. "Studies of Finite Element Procedures – Stress Band Plots and the Evaluation of Finite Element Meshes", Engineering Computations, Vol. 3.

Taylor, E.S., 1974. "Dimensional Analysis for Engineers", Oxford University Press, London, United Kingdom.

Vitali, L., Bruschi, R., Mork, K.J., Levold, E., and Verley, R, (1999), "Hotpipe Project – Capacity of Pipes Subjected to Internal pressure, Axial Force and Bending Moment", 9th International Offshore and Polar Engineering Conference, ASME. Brest.

Wilhoit, J., Merwin, J. and Jursa, J., 1972. "Critical Plastic Buckling Parameters for Pipe in Pure Bending", ASME Paper 72-Pet-29.

Yoosef-Ghodsi, N., Kulak, G.L., and Murray, D.W., 1994. "Behaviour of Girth-Welded Line Pipe", Structural Engineering Report No. 203, Department of Civil Engineering, University of Alberta, Edmonton, Alberta.

Yoosef-Ghodsi, N., Kulak, G.L., and Murray, D.W., 1995. "Some Test Results for Wrinkling of Girth-Welded Line Pipe", Proceedings of the 14th International Conference on Offshore Mechanics and Arctic Engineering (OMAE 95), vol. V-pipeline Technology, ASME. pp. 379-388.

Zhou, Z., and Murray, D.W., 1993. "Numerical Structural Analysis of Buried Pipelines", Structural Engineering Report No. 181, Department of Civil Engineering, University of Alberta, Edmonton, Alberta.

Zhou, Z.J., Boivin, R.P., Glover, A.G., and Kormann, P.J., 1996. "Pipeline Integrity Design for Differential Settlement in Discontinuous Permafrost Areas", International Pipeline Conference, Calgary, Alberta. pp. 603-612.

Zimmerman, T.J.E., Stephens, M.J., DeGeer, M., and Chen, Q., 1994. "Compressive Strain Limits for Buried Pipelines", Project Report 91024, Centre for Frontier Engineering Research (C-FER), Edmonton, Alberta.

Appendix A

Material Stress-Strain Coupon Plots and True Stress-Strain Curves

Average E-mat properties

Exstens Strain	Eng. Stress
0	0.0
28	6.5
238	50.2
316	67.0
486	102.8
575	120.8
827	173.4
986	206.9
1310	274.8
1623	340.6
1780	373.4
2095	438.3
2404	500.4
2716	549.7
5579	549.7
7717	549.7
11014	549.7
24547	549.8
27700	555.4
35200	566.6
53900	581.2
77425	586.1
103442	587.5
123798	584.0
153584	572.2
164234	566.6
174999	558.2
188744	545.6
202732	531.6
213184	518.4
221256	507.9
234467	486.9
247870	462.5
261322	434.5

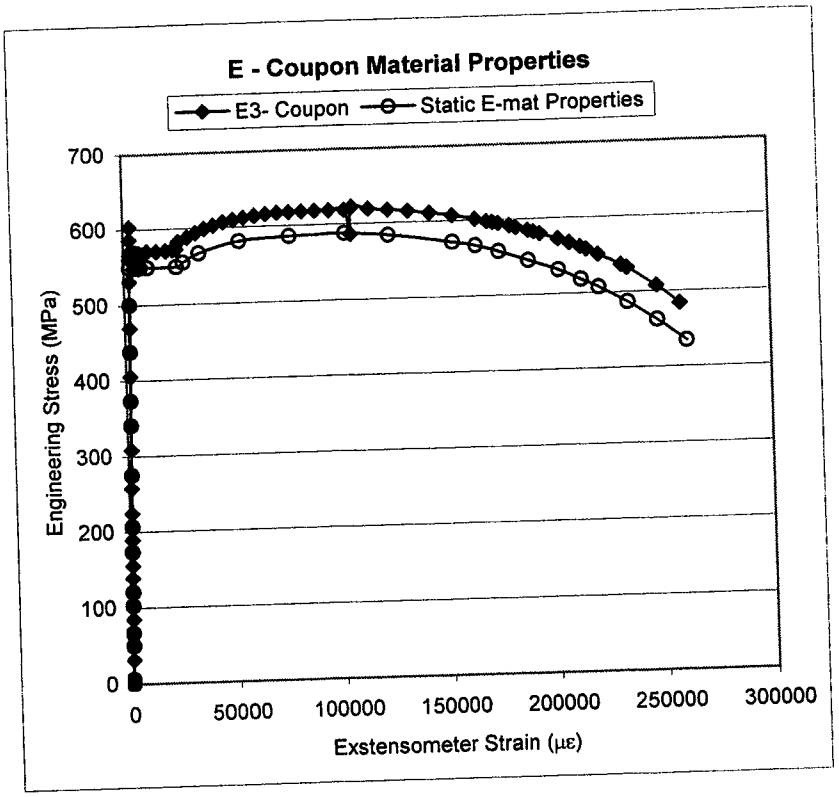

Plastic Component for ABAQUS input

E = 208915

n = 0.27

σ_{true}	ε^{pl}_{ln}
549.7	0.00000
552.8	0.00292
553.9	0.00504
555.8	0.00829
563.3	0.02155
570.8	0.02459
586.5	0.03179
612.5	0.04957
631.5	0.07155
648.3	0.09533
656.3	0.11357
660.1	0.13971
659.7	0.14891
655.9	0.15813
648.6	0.16979
639.4	0.18154
628.9	0.19024
620.3	0.19691
601.1	0.20776
577.1	0.21868
548.0	0.22954

Average N-mat properties

Exstens Strain	Eng. Stress
0	0.0
113	21.9
302	57.3
470	91.4
656	127.0
831	161.3
1002	196.5
1180	230.3
1359	268.6
1605	319.0
1861	368.3
2120	416.6
2367	463.8
2952	535.3
3208	546.6
3799	548.4
4035	523.3
4586	546.6
5835	551.6
6122	532.4
6493	553.8
7389	557.4
10685	566.1
10933	548.3
11315	569.3
12708	571.6
14918	575.5
19413	584.1
19574	563.9
19807	584.4
20715	593.1
31158	605.0
38203	611.8
53120	620.0
74746	623.9
76723	593.5
77078	625.2
104403	622.6
119267	619.1
136436	613.1
154661	603.3
172889	590.1
190730	574.4
208482	553.3
217684	540.5
226681	525.5
235805	508.1
244963	487.0
254381	460.8

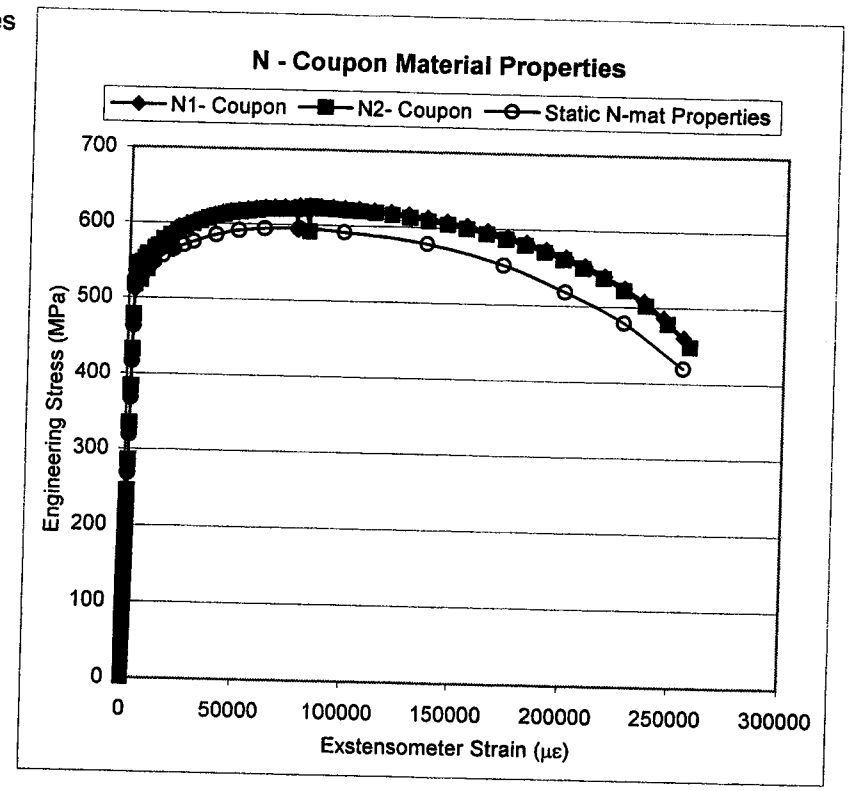

Plastic Component for ABAQUS input

E = 201835
n = 0.265

σ_{true}	ε^{pl}_{ln}
524.2	0.00000
526.4	0.00142
535.7	0.00345
546.1	0.00596
554.4	0.00809
564.6	0.01201
576.3	0.01676
584.1	0.02098
592.1	0.02536
607.8	0.03534
620.8	0.04524
630.8	0.05639
640.9	0.07108
649.2	0.09021
656.9	0.12464
646.6	0.15500
622.1	0.17887
587.8	0.20140
526.8	0.22403

Average P1-mat properties

Exstens Strain	Eng. Stress
0	0.0
107	21.1
272	54.9
449	88.9
621	124.2
708	141.4
881	175.9
1047	208.1
1427	278.4
1704	322.1
2324	392.1
2685	418.8
3512	458.5
4447	484.7
4967	495.1
5275	480.5
5583	504.6
8056	527.6
8324	509.0
8748	532.4
10458	540.0
14915	553.3
15125	533.8
15610	556.6
17813	560.2
22748	568.1
27209	574.3
27436	552.8
27888	577.1
32880	584.8
36329	587.7
39745	590.3
43186	592.5
50690	597.0
62471	600.9
79408	604.3
103333	605.3
105337	576.0
105889	607.7
122392	605.6
142510	602.8
166516	595.8
191883	582.7
208890	570.1
217501	562.4
225941	553.5
243415	531.1
260766	501.2
269623	481.0

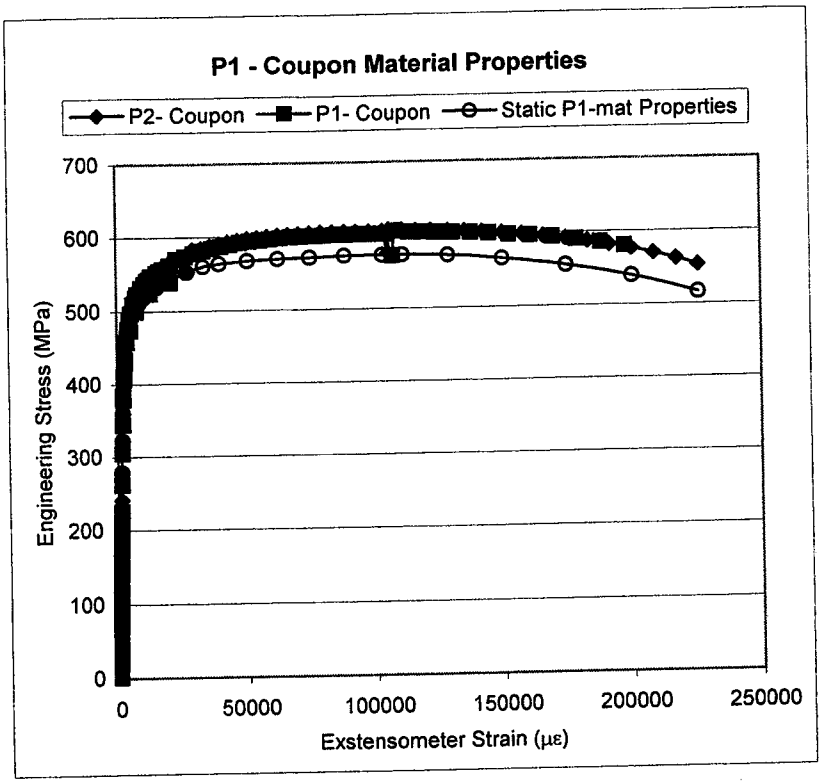

Plastic Component for ABAQUS input

E = 201378

n = 0.28

σ_{true}	ε^{pl}_{ln}
471.7	0.00000
494.3	0.00253
508.0	0.00406
515.9	0.00615
523.1	0.00781
531.3	0.00978
540.6	0.01280
552.3	0.01717
567.6	0.02403
578.8	0.03017
586.2	0.03606
596.1	0.04649
605.0	0.05759
613.6	0.06933
622.9	0.08175
632.1	0.09520
636.5	0.10211
645.2	0.11804
650.8	0.13662
652.6	0.15805
647.4	0.17950
633.0	0.20057

Average P2-mat properties

Exstens Strain	Eng. Stress
0	0.0
147	29.8
398	79.7
662	130.5
927	181.9
1185	230.3
1442	278.0
1725	327.3
2288	403.0
3720	495.1
3961	485.6
4066	502.8
4497	516.6
4964	525.9
5993	538.8
6662	544.6
6842	524.6
7081	548.0
9417	558.9
10645	562.6
13727	569.8
16376	578.6
22638	587.3
25772	591.0
28887	594.2
35485	599.9
42242	603.9
49452	607.0
57141	609.4
61309	610.2
74315	611.7
78924	612.0
94279	611.6
99931	611.2
101782	582.3
103811	613.8
116884	610.9
123795	609.3
146229	603.4
153813	600.6
169502	593.2
184764	584.0
200132	571.7
208232	564.6
216030	556.4
223715	547.4
239103	526.5
246845	513.9
254671	499.0

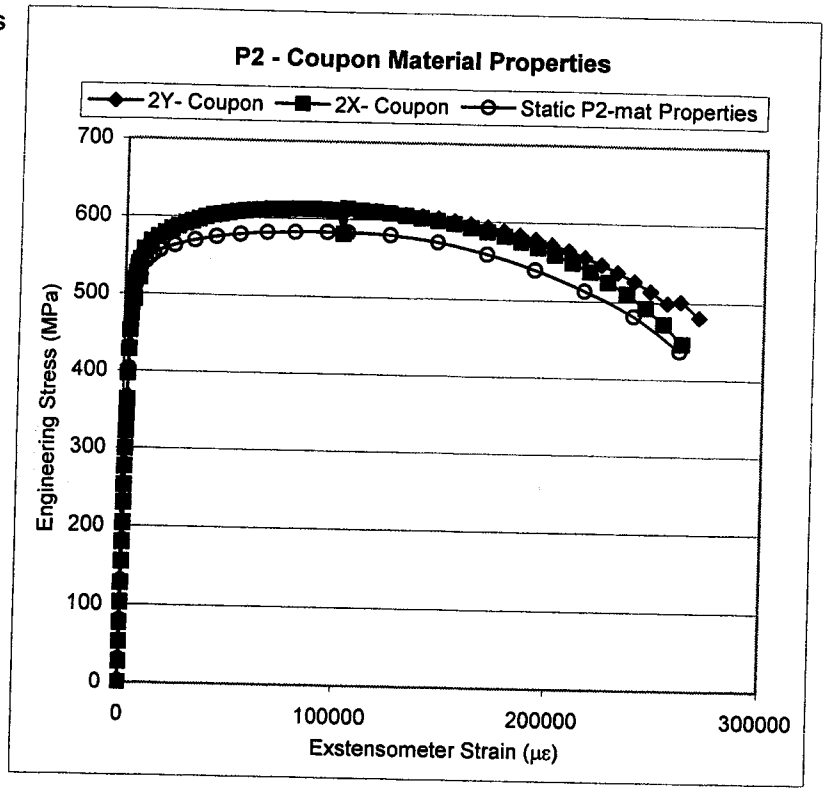

Plastic Component for ABAQUS input

E = 201405
n = 0.28

σ_{true}	ε^{pl}_{ln}
500.7	0.00000
523.3	0.00229
538.0	0.00411
547.5	0.00654
553.8	0.00829
559.3	0.01014
565.5	0.01307
575.9	0.01953
588.2	0.02869
599.3	0.03840
609.5	0.04880
620.0	0.06065
628.4	0.07284
638.2	0.08693
643.5	0.09557
652.6	0.11347
656.3	0.13322
653.2	0.15333
643.0	0.17276
624.2	0.19249
596.6	0.21143
551.0	0.22898

Average W-mat properties

Exstens Strain	Eng. Stress
0	0.0
84	19.1
267	54.5
439	88.2
603	123.2
774	157.6
940	190.9
1112	225.2
1522	307.7
2018	404.6
2506	497.6
3173	574.7
5669	545.6
6663	547.6
7259	530.7
7896	550.3
10619	549.2
11305	531.8
11982	549.7
14578	554.5
20066	559.4
30065	567.6
34358	572.8
40455	576.1
46825	584.0
55265	589.0
59833	591.3
74484	595.3
79935	596.2
91969	596.5
98521	595.9
101093	568.0
101866	600.9
109006	596.7
116860	594.4
124771	591.9
133097	588.1
141332	583.6
157940	572.2
166287	565.4
174650	557.6
182986	548.7
191448	538.6
199923	527.0
208497	513.7
217178	498.6
225948	481.3
234762	460.7
243562	436.1

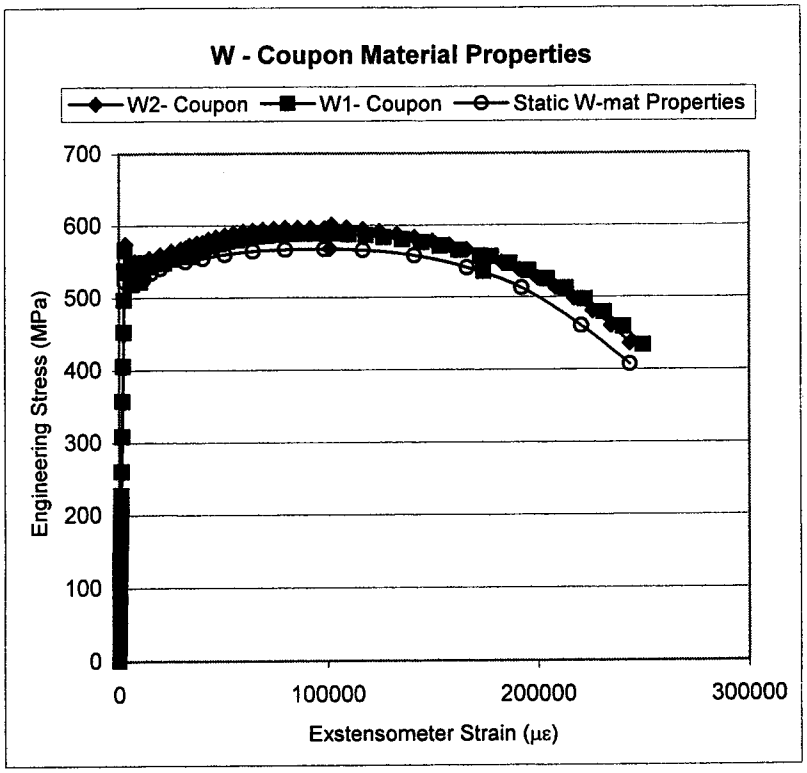

Plastic Component for ABAQUS input

E = 203442

n = 0.265

σ_{true}	ε^{pl}_{ln}
523.0	0.00000
530.8	0.00506
533.3	0.00931
542.6	0.01281
551.3	0.01716
567.7	0.02896
577.1	0.03682
588.2	0.04690
600.6	0.05956
612.0	0.07389
623.0	0.09090
631.7	0.10742
636.7	0.12907
631.0	0.15072
611.7	0.17296
562.3	0.19658
506.5	0.21549

Appendix B

Sample Spreadsheet Used to Determine Global Moment-Curvature Plots

	A	B	C	D	E	F	G	H	I	J	K	L
1		Specimen:	CP80N-2		Spreasheet to determine global moment curvature plot							
2												
3												
4								Cable Trans	Rot. Meters	Rot. Meters	Cable Trans	Rot. Meters
5	Fluke	Cable T.	Cable T.	Cable T.	Cable T.	Cable T.	Cable T.	Rotation	Rotation	Rotation	Rotation	Rotation
6	Scan	NWB	NWT	SWB	SWT	NEB	NET	Bottom	Bottom	Bottom	Top	Top
7	#	mm	mm	mm	mm	mm	mm	deg.	deg.	rad.	deg.	deg.
8	14	0.000	0.000	0.000	0.000	0.000	0.000	0.000	0.000	0.000	0.000	0.000
9	15	-0.012	-0.288	-0.002	-0.371	-0.365	-0.008	0.034	0.030	0.001	-0.007	0.038
10	16	-0.021	-0.567	-0.017	-0.623	-0.535	-0.003	0.048	0.061	0.001	0.005	0.070
11	17	0.023	-0.919	0.042	-1.012	-0.741	0.341	0.073	0.095	0.002	0.046	0.102
12	18	0.122	-1.278	0.207	-1.270	-0.988	0.652	0.108	0.124	0.002	0.073	0.133
13	19	0.123	-1.266	0.208	-1.271	-0.987	0.656	0.108	0.125	0.002	0.072	0.130
14	20	0.296	-1.714	0.329	-1.767	-1.238	1.158	0.145	0.160	0.003	0.124	0.167
15	21	0.454	-2.019	0.436	-2.137	-1.486	1.637	0.181	0.193	0.003	0.162	0.200
16	22	0.498	-2.196	0.474	-2.273	-1.609	1.780	0.196	0.208	0.004	0.176	0.218
17	23	0.572	-2.390	0.565	-2.401	-1.734	2.095	0.216	0.224	0.004	0.205	0.233
18	24	0.693	-2.804	0.765	-2.900	-2.035	2.625	0.259	0.262	0.005	0.250	0.276
19	25	0.740	-3.077	0.828	-3.147	-2.227	2.822	0.282	0.281	0.005	0.271	0.300
20	26	1.030	-3.631	0.990	-3.650	-2.477	3.308	0.327	0.318	0.006	0.324	0.338
21	27	1.302	-3.855	1.412	-3.900	-2.475	3.431	0.359	0.332	0.006	0.324	0.347
22	28	1.447	-3.849	1.564	-3.900	-2.362	3.507	0.363	0.330	0.006	0.327	0.340
23	29	1.360	-3.849	1.517	-3.900	-2.358	3.506	0.356	0.332	0.006	0.334	0.345
24	30	1.164	-3.843	1.322	-3.901	-2.601	3.506	0.360	0.329	0.006	0.329	0.349
25	31	1.158	-4.244	1.315	-4.375	-2.892	3.614	0.387	0.359	0.006	0.350	0.385
26	32	1.294	-5.179	1.429	-5.190	-3.213	4.085	0.429	0.411	0.007	0.440	0.450
27	33	1.383	-5.872	1.590	-5.847	-3.469	4.445	0.465	0.451	0.008	0.503	0.495
28	34	1.556	-6.541	1.721	-6.478	-3.716	4.611	0.502	0.483	0.008	0.544	0.537
29	35	1.666	-7.544	1.940	-7.485	-3.967	4.973	0.541	0.532	0.009	0.633	0.603
30	36	2.173	-9.409	2.320	-9.350	-4.463	5.312	0.629	0.615	0.011	0.751	0.719
31	37	2.429	-11.054	2.531	-10.994	-4.873	5.499	0.689	0.681	0.012	0.862	0.819
32	38	2.941	-13.927	3.074	-14.004	-5.491	5.710	0.797	0.795	0.014	1.044	0.997
33	39	3.560	-17.372	3.693	-19.066	-6.318	6.008	0.932	0.934	0.016	1.259	1.207
34	40	4.059	-20.130	4.175	-21.693	-6.823	6.042	1.026	1.034	0.018	1.427	1.360
35	41	4.590	-23.138	4.717	-24.834	-7.564	6.043	1.146	1.154	0.020	1.589	1.531
36	42	5.127	-25.763	5.157	-27.613	-8.188	6.175	1.250	1.268	0.022	1.742	1.696
37	43	5.627	-28.790	5.733	-30.634	-8.930	6.180	1.370	1.385	0.024	1.906	1.862
38	44	6.271	-32.556	6.375	-34.415	-9.744	6.151	1.506	1.531	0.027	2.119	2.071

	M	N	O	P	Q	R	S	T	U
1					L collar =	150	mm		
2					e =	1.5	m		
3									
4	Rot. Meters		Cable Trans	Rot. Meters	Cable Trans	Rot. Meters		MTS	Global
5	Rotation	Fluke	Total	Total	Total	Total	Jack	Load	Moment
6	Top	Scan	Rotation	Rotation	Curvature	Curvature	Load		at End of Pipe
7	rad.	#	rad	rad	rad/mm x 10^{5}	rad/mm x 10^{5}	kN	kN	kN-m
8	0.000	14	0.000	0.000	0.000	0.000	0.0	3519.8	0.0
9	0.001	15	0.000	0.001	0.191	0.495	104.8	3639.0	157.1
10	0.001	16	0.001	0.002	0.385	0.949	203.7	3718.1	305.6
11	0.002	17	0.002	0.003	0.859	1.434	300.8	3817.9	451.1
12	0.002	18	0.003	0.004	1.316	1.867	399.4	3913.4	599.0
13	0.002	19	0.003	0.004	1.311	1.855	398.9	3917.8	598.2
14	0.003	20	0.005	0.006	1.959	2.371	506.0	4027.1	758.9
15	0.003	21	0.006	0.007	2.493	2.860	603.8	4136.8	905.5
16	0.004	22	0.007	0.007	2.711	3.099	650.1	4179.6	975.0
17	0.004	23	0.007	0.008	3.058	3.328	700.2	4234.2	1050.1
18	0.005	24	0.009	0.009	3.702	3.912	799.0	4322.4	1198.2
19	0.005	25	0.010	0.010	4.023	4.222	843.7	4374.8	1265.3
20	0.006	26	0.011	0.011	4.732	4.771	899.9	4409.6	1349.4
21	0.006	27	0.012	0.012	4.968	4.942	912.5	3629.2	1368.3
22	0.006	28	0.012	0.012	5.016	4.865	900.1	2949.2	1349.7
23	0.006	29	0.012	0.012	5.015	4.919	908.1	3636.5	1361.7
24	0.006	30	0.012	0.012	5.011	4.933	904.2	4417.6	1355.9
25	0.007	31	0.013	0.013	5.358	5.411	951.6	4467.9	1426.9
26	0.008	32	0.015	0.015	6.317	6.259	992.6	4508.0	1488.2
27	0.009	33	0.017	0.017	7.035	6.880	1022.0	4530.6	1532.3
28	0.009	34	0.018	0.018	7.604	7.422	1032.0	4543.8	1547.2
29	0.011	35	0.020	0.020	8.535	8.253	1029.3	4548.1	1543.1
30	0.013	36	0.024	0.023	10.037	9.700	1016.3	4536.5	1523.3
31	0.014	37	0.027	0.026	11.285	10.908	994.9	4526.5	1491.0
32	0.017	38	0.032	0.031	13.387	13.031	936.7	4459.5	1403.6
33	0.021	39	0.038	0.037	15.936	15.567	865.0	4389.6	1295.8
34	0.024	40	0.043	0.042	17.837	17.412	830.2	4345.8	1243.4
35	0.027	41	0.048	0.047	19.885	19.526	794.6	4311.4	1189.9
36	0.030	42	0.052	0.052	21.760	21.554	757.9	4280.5	1134.7
37	0.032	43	0.057	0.057	23.822	23.608	719.8	4245.1	1077.3
38	0.036	44	0.063	0.063	26.361	26.195	698.2	4219.2	1044.7

Appendix C

Sample Spreadsheet Used to Determine Local Moment-Curvature Plots

Specimen: CP80N-2

Spreadsheet to determine local moment at a given increment of load

SCAN #	38	P_{jack} =	936.6	kN	P_{MTS} =	4459.5	kN	θ_{top} =	0.01740	
		e =	1.5	m	d' =	0.262	m	D =	762	mm

	D1	D2	D3	D4	D5	D6	D7	D8	D9
z_t	2.366	2.112	1.858	1.604	1.350	1.096	0.842	0.588	0.334
ε_C	-3977	-4014	-19732	-33583	-3212	-2750	-1944	-2851	-4236
ε_T	2422	2503	2454	2475	2519	2422	2280	2094	1960
ϕ_L	8.362	8.516	28.993	47.121	7.489	6.759	5.520	6.462	8.098
δ_{LVDT}	14.130	18.950	26.976	14.595	24.384	20.718	17.618	14.852	9.085
$\delta_{assumed}$	-	-	20.887	22.135	22.102	-	-	-	-
δ_h	14.130	18.950	20.887	22.135	22.102	20.718	17.618	14.852	9.085
Local Mom	1451.6	1468.9	1476.0	1480.8	1481.0	1476.5	1465.9	1456.5	1436.5

Appendix D

Regression Analysis Used in Determining Critical Buckling Strain

	LOCAL-EXP		
scan	Moment	Curvature	Comp. Strain
1	0.0	0.000	0
8	0.1	-0.009	-375
14	-0.2	0.071	595
19	598.1	2.145	1393
26	1349.6	5.702	3178
32	1488.7	8.045	4730
35	1543.8	12.962	8231
38	1404.9	27.868	19109
41	1191.7	50.762	35473
44	1047.2	68.327	47274

	GLOBAL-EXP	
scan	Moment	Curvature
1	0.0	0.000
8	0.1	0.000
14	-0.2	0.000
19	598.1	1.649
26	1349.6	4.241
32	1488.7	5.564
35	1543.8	7.336
38	1404.9	11.583
41	1191.7	17.356
44	1047.2	23.285

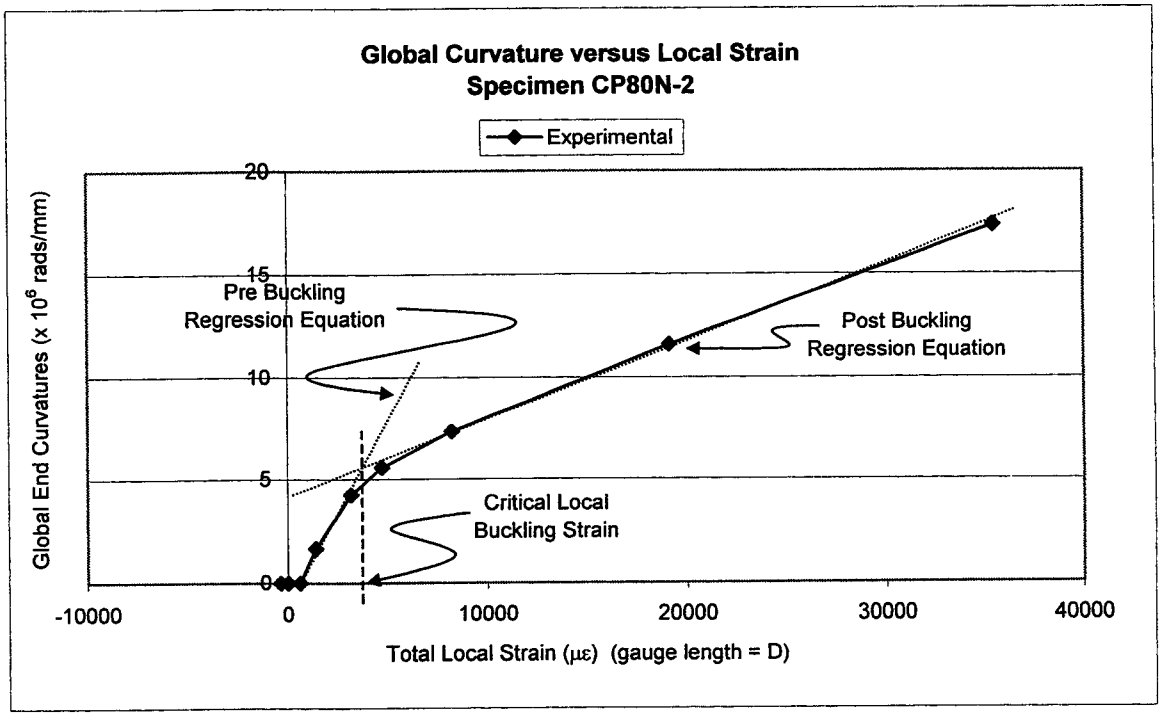

Determination of Experimental Critical Strain:

Pre-buckling Regression Equation

G.C. = -0.001283 * L.S. + -0.06426

Post -buckling Regression Equation

G.C. = -0.00041 * L.S. + 3.43424

Equating:

Local Strain = -4014.541 με = 0.401 %

Appendix E

Parametric Study Load Cases

2% INITIAL IMPERFECTION

ID	D/t	p/p_y	d	F_y	t	r_i	A	p_y[1]	FEA pres.	eq 2.5 Pα	eq 2.7 Pν	eq 2.11 P_p	eq 2.12 FEA P
			mm	MPa	mm	mm	mm^2	MPa	MPa	(kN)	(kN)	(kN)	(kN)
dt50x52ip2p00	50.0	0.0	324	359	6.48	158.8	6332	15.28	0.00	-667	0	0	-667
dt50x52ip2p40	50.0	0.4	324	359	6.48	158.8	6332	15.28	6.11	-667	273	-445	-839
dt50x52ip2p80	50.0	0.8	324	359	6.48	158.8	6332	15.28	12.22	-667	546	-890	-1012
dt50x65ip2p00	50.0	0.0	324	448	6.48	158.8	6332	19.06	0.00	-667	0	0	-667
dt50x65ip2p40	50.0	0.4	324	448	6.48	158.8	6332	19.06	7.63	-667	340	-556	-882
dt50x65ip2p80	50.0	0.8	324	448	6.48	158.8	6332	19.06	15.25	-667	681	-1111	-1097
dt50x80ip2p00	50.0	0.0	324	550	6.48	158.8	6332	23.40	0.00	-667	0	0	-667
dt50x80ip2p40	50.0	0.4	324	550	6.48	158.8	6332	23.40	9.36	-667	418	-682	-931
dt50x80ip2p80	50.0	0.8	324	550	6.48	158.8	6332	23.40	18.72	-667	836	-1364	-1195
dt70x52ip2p00	70.0	0.0	508	359	7.26	250.4	11251	10.72	0.00	-1185	0	0	-1185
dt70x52ip2p40	70.0	0.4	508	359	7.26	250.4	11251	10.72	4.29	-1185	485	-796	-1496
dt70x52ip2p80	70.0	0.8	508	359	7.26	250.4	11251	10.72	8.57	-1185	969	-1592	-1807
dt70x65ip2p00	70.0	0.0	508	448	7.26	250.4	11251	13.37	0.00	-1185	0	0	-1185
dt70x65ip2p40	70.0	0.4	508	448	7.26	250.4	11251	13.37	5.35	-1185	605	-993	-1573
dt70x65ip2p80	70.0	0.8	508	448	7.26	250.4	11251	13.37	10.70	-1185	1210	-1987	-1962
dt70x80ip2p00	70.0	0.0	508	550	7.26	250.4	11251	16.42	0.00	-1185	0	0	-1185
dt70x80ip2p40	70.0	0.4	508	550	7.26	250.4	11251	16.42	6.57	-1185	743	-1219	-1662
dt70x80ip2p80	70.0	0.8	508	550	7.26	250.4	11251	16.42	13.13	-1185	1485	-2439	-2138
dt90x52ip2p00	90.0	0.0	762	359	8.47	376.8	19818	8.25	0.00	-2087	0	0	-2087
dt90x52ip2p40	90.0	0.4	762	359	8.47	376.8	19818	8.25	3.30	-2087	854	-1407	-2640
dt90x52ip2p80	90.0	0.8	762	359	8.47	376.8	19818	8.25	6.60	-2087	1708	-2814	-3193
dt90x65ip2p00	90.0	0.0	762	448	8.47	376.8	19818	10.30	0.00	-2087	0	0	-2087
dt90x65ip2p40	90.0	0.4	762	448	8.47	376.8	19818	10.30	4.12	-2087	1065	-1756	-2777
dt90x65ip2p80	90.0	0.8	762	448	8.47	376.8	19818	10.30	8.24	-2087	2131	-3511	-3467
dt90x80ip2p00	90.0	0.0	762	550	8.47	376.8	19818	12.64	0.00	-2087	0	0	-2087
dt90x80ip2p40	90.0	0.4	762	550	8.47	376.8	19818	12.64	5.06	-2087	1308	-2155	-2934
dt90x80ip2p80	90.0	0.8	762	550	8.47	376.8	19818	12.64	10.11	-2087	2616	-4310	-3781

Notes:

1. $p_y = F_y * t / r_i$

2. FEA pres. = $p_y * p/p_y$

8% INITIAL IMPERFECTION

ID	D/t	p/p_y	d	F_y	t	r_i	A	p_y	FEA pres.	eq 2.5 $P\alpha$	eq 2.7 Pv	eq 2.11 P_p	eq 2.12 FEA P
			mm	MPa	mm	mm	mm^2	MPa	MPa	(kN)	(kN)	(kN)	(kN)
dt50x52ip8p00	50.0	0.0	324	359	6.48	158.8	6332	15.28	0.00	-667	0	0	-667
dt50x52ip8p40	50.0	0.4	324	359	6.48	158.8	6332	15.28	6.11	-667	273	-445	-839
dt50x52ip8p80	50.0	0.8	324	359	6.48	158.8	6332	15.28	12.22	-667	546	-890	-1012
dt50x65ip8p00	50.0	0.0	324	448	6.48	158.8	6332	19.06	0.00	-667	0	0	-667
dt50x65ip8p40	50.0	0.4	324	448	6.48	158.8	6332	19.06	7.63	-667	340	-556	-882
dt50x65ip8p80	50.0	0.8	324	448	6.48	158.8	6332	19.06	15.25	-667	681	-1111	-1097
dt50x80ip8p00	50.0	0.0	324	550	6.48	158.8	6332	23.40	0.00	-667	0	0	-667
dt50x80ip8p40	50.0	0.4	324	550	6.48	158.8	6332	23.40	9.36	-667	418	-682	-931
dt50x80ip8p80	50.0	0.8	324	550	6.48	158.8	6332	23.40	18.72	-667	836	-1364	-1195
dt70x52ip8p00	70.0	0.0	508	359	7.26	250.4	11251	10.72	0.00	-1185	0	0	-1185
dt70x52ip8p40	70.0	0.4	508	359	7.26	250.4	11251	10.72	4.29	-1185	485	-796	-1496
dt70x52ip8p80	70.0	0.8	508	359	7.26	250.4	11251	10.72	8.57	-1185	969	-1592	-1807
dt70x65ip8p00	70.0	0.0	508	448	7.26	250.4	11251	13.37	0.00	-1185	0	0	-1185
dt70x65ip8p40	70.0	0.4	508	448	7.26	250.4	11251	13.37	5.35	-1185	605	-993	-1573
dt70x65ip8p80	70.0	0.8	508	448	7.26	250.4	11251	13.37	10.70	-1185	1210	-1987	-1962
dt70x80ip8p00	70.0	0.0	508	550	7.26	250.4	11251	16.42	0.00	-1185	0	0	-1185
dt70x80ip8p40	70.0	0.4	508	550	7.26	250.4	11251	16.42	6.57	-1185	743	-1219	-1662
dt70x80ip8p80	70.0	0.8	508	550	7.26	250.4	11251	16.42	13.13	-1185	1485	-2439	-2138
dt90x52ip8p00	90.0	0.0	762	359	8.47	376.8	19818	8.25	0.00	-2087	0	0	-2087
dt90x52ip8p40	90.0	0.4	762	359	8.47	376.8	19818	8.25	3.30	-2087	854	-1407	-2640
dt90x52ip8p80	90.0	0.8	762	359	8.47	376.8	19818	8.25	6.60	-2087	1708	-2814	-3193
dt90x65ip8p00	90.0	0.0	762	448	8.47	376.8	19818	10.30	0.00	-2087	0	0	-2087
dt90x65ip8p40	90.0	0.4	762	448	8.47	376.8	19818	10.30	4.12	-2087	1065	-1756	-2777
dt90x65ip8p80	90.0	0.8	762	448	8.47	376.8	19818	10.30	8.24	-2087	2131	-3511	-3467
dt90x80ip8p00	90.0	0.0	762	550	8.47	376.8	19818	12.64	0.00	-2087	0	0	-2087
dt90x80ip8p40	90.0	0.4	762	550	8.47	376.8	19818	12.64	5.06	-2087	1308	-2155	-2934
dt90x80ip8p80	90.0	0.8	762	550	8.47	376.8	19818	12.64	10.11	-2087	2616	-4310	-3781

16% INITIAL IMPERFECTION

ID	D/t	p/p_y	d	F_y	t	r_i	A	p_y	FEA pres.	eq 2.5 $P\alpha$	eq 2.7 Pv	eq 2.11 P_p	eq 2.12 FEA P
			mm	MPa	mm	mm	mm^2	MPa	MPa	(kN)	(kN)	(kN)	(kN)
dt50x52ip16p00	**50.0**	**0.0**	**324**	**359**	6.48	158.8	6332	15.28	0.00	-667	0	0	-667
dt50x52ip16p40	**50.0**	**0.4**	**324**	**359**	6.48	158.8	6332	15.28	6.11	-667	273	-445	-839
dt50x52ip16p80	**50.0**	**0.8**	**324**	**359**	6.48	158.8	6332	15.28	12.22	-667	546	-890	-1012
dt50x65ip16p00	**50.0**	**0.0**	**324**	**448**	6.48	158.8	6332	19.06	0.00	-667	0	0	-667
dt50x65ip16p40	**50.0**	**0.4**	**324**	**448**	6.48	158.8	6332	19.06	7.63	-667	340	-556	-882
dt50x65ip16p80	**50.0**	**0.8**	**324**	**448**	6.48	158.8	6332	19.06	15.25	-667	681	-1111	-1097
dt50x80ip16p00	**50.0**	**0.0**	**324**	**550**	6.48	158.8	6332	23.40	0.00	-667	0	0	-667
dt50x80ip16p40	**50.0**	**0.4**	**324**	**550**	6.48	158.8	6332	23.40	9.36	-667	418	-682	-931
dt50x80ip16p80	**50.0**	**0.8**	**324**	**550**	6.48	158.8	6332	23.40	18.72	-667	836	-1364	-1195
dt70x52ip16p00	**70.0**	**0.0**	**508**	**359**	7.26	250.4	11251	10.72	0.00	-1185	0	0	-1185
dt70x52ip16p40	**70.0**	**0.4**	**508**	**359**	7.26	250.4	11251	10.72	4.29	-1185	485	-796	-1496
dt70x52ip16p80	**70.0**	**0.8**	**508**	**359**	7.26	250.4	11251	10.72	8.57	-1185	969	-1592	-1807
dt70x65ip16p00	**70.0**	**0.0**	**508**	**448**	7.26	250.4	11251	13.37	0.00	-1185	0	0	-1185
dt70x65ip16p40	**70.0**	**0.4**	**508**	**448**	7.26	250.4	11251	13.37	5.35	-1185	605	-993	-1573
dt70x65ip16p80	**70.0**	**0.8**	**508**	**448**	7.26	250.4	11251	13.37	10.70	-1185	1210	-1987	-1962
dt70x80ip16p00	**70.0**	**0.0**	**508**	**550**	7.26	250.4	11251	16.42	0.00	-1185	0	0	-1185
dt70x80ip16p40	**70.0**	**0.4**	**508**	**550**	7.26	250.4	11251	16.42	6.57	-1185	743	-1219	-1662
dt70x80ip16p80	**70.0**	**0.8**	**508**	**550**	7.26	250.4	11251	16.42	13.13	-1185	1485	-2439	-2138
dt90x52ip16p00	**90.0**	**0.0**	**762**	**359**	8.47	376.8	19818	8.25	0.00	-2087	0	0	-2087
dt90x52ip16p40	**90.0**	**0.4**	**762**	**359**	8.47	376.8	19818	8.25	3.30	-2087	854	-1407	-2640
dt90x52ip16p80	**90.0**	**0.8**	**762**	**359**	8.47	376.8	19818	8.25	6.60	-2087	1708	-2814	-3193
dt90x65ip16p00	**90.0**	**0.0**	**762**	**448**	8.47	376.8	19818	10.30	0.00	-2087	0	0	-2087
dt90x65ip16p40	**90.0**	**0.4**	**762**	**448**	8.47	376.8	19818	10.30	4.12	-2087	1065	-1756	-2777
dt90x65ip16p80	**90.0**	**0.8**	**762**	**448**	8.47	376.8	19818	10.30	8.24	-2087	2131	-3511	-3467
dt90x80ip16p00	**90.0**	**0.0**	**762**	**550**	8.47	376.8	19818	12.64	0.00	-2087	0	0	-2087
dt90x80ip16p40	**90.0**	**0.4**	**762**	**550**	8.47	376.8	19818	12.64	5.06	-2087	1308	-2155	-2934
dt90x80ip16p80	**90.0**	**0.8**	**762**	**550**	8.47	376.8	19818	12.64	10.11	-2087	2616	-4310	-3781

30% INITIAL IMPERFECTION

ID	D/t	p/p_y	d	F_y	t	r_i	A	p_y	FEA pres	eq 2.5 $P\alpha$	eq 2.7 Pv	eq 2.11 P_p	eq 2.12 FEA P
			mm	MPa	mm	mm	mm^2	MPa	MPa	(kN)	(kN)	(kN)	(kN)
dt50x52ip30p00	50.0	0.0	324	359	6.48	158.8	6332	15.28	0.00	-667	0	0	-667
dt50x52ip30p40	50.0	0.4	324	359	6.48	158.8	6332	15.28	6.11	-667	273	-445	-839
dt50x52ip30p80	50.0	0.8	324	359	6.48	158.8	6332	15.28	12.22	-667	546	-890	-1012
dt50x65ip30p00	50.0	0.0	324	448	6.48	158.8	6332	19.06	0.00	-667	0	0	-667
dt50x65ip30p40	50.0	0.4	324	448	6.48	158.8	6332	19.06	7.63	-667	340	-556	-882
dt50x65ip30p80	50.0	0.8	324	448	6.48	158.8	6332	19.06	15.25	-667	681	-1111	-1097
dt50x80ip30p00	50.0	0.0	324	550	6.48	158.8	6332	23.40	0.00	-667	0	0	-667
dt50x80ip30p40	50.0	0.4	324	550	6.48	158.8	6332	23.40	9.36	-667	418	-682	-931
dt50x80ip30p80	50.0	0.8	324	550	6.48	158.8	6332	23.40	18.72	-667	836	-1364	-1195
dt70x52ip30p00	70.0	0.0	508	359	7.26	250.4	11251	10.72	0.00	-1185	0	0	-1185
dt70x52ip30p40	70.0	0.4	508	359	7.26	250.4	11251	10.72	4.29	-1185	485	-796	-1496
dt70x52ip30p80	70.0	0.8	508	359	7.26	250.4	11251	10.72	8.57	-1185	969	-1592	-1807
dt70x65ip30p00	70.0	0.0	508	448	7.26	250.4	11251	13.37	0.00	-1185	0	0	-1185
dt70x65ip30p40	70.0	0.4	508	448	7.26	250.4	11251	13.37	5.35	-1185	605	-993	-1573
dt70x65ip30p80	70.0	0.8	508	448	7.26	250.4	11251	13.37	10.70	-1185	1210	-1987	-1962
dt70x80ip30p00	70.0	0.0	508	550	7.26	250.4	11251	16.42	0.00	-1185	0	0	-1185
dt70x80ip30p40	70.0	0.4	508	550	7.26	250.4	11251	16.42	6.57	-1185	743	-1219	-1662
dt70x80ip30p80	70.0	0.8	508	550	7.26	250.4	11251	16.42	13.13	-1185	1485	-2439	-2138
dt90x52ip30p00	90.0	0.0	762	359	8.47	376.8	19818	8.25	0.00	-2087	0	0	-2087
dt90x52ip30p40	90.0	0.4	762	359	8.47	376.8	19818	8.25	3.30	-2087	854	-1407	-2640
dt90x52ip30p80	90.0	0.8	762	359	8.47	376.8	19818	8.25	6.60	-2087	1708	-2814	-3193
dt90x65ip30p00	90.0	0.0	762	448	8.47	376.8	19818	10.30	0.00	-2087	0	0	-2087
dt90x65ip30p40	90.0	0.4	762	448	8.47	376.8	19818	10.30	4.12	-2087	1065	-1756	-2777
dt90x65ip30p80	90.0	0.8	762	448	8.47	376.8	19818	10.30	8.24	-2087	2131	-3511	-3467
dt90x80ip30p00	90.0	0.0	762	550	8.47	376.8	19818	12.64	0.00	-2087	0	0	-2087
dt90x80ip30p40	90.0	0.4	762	550	8.47	376.8	19818	12.64	5.06	-2087	1308	-2155	-2934
dt90x80ip30p80	90.0	0.8	762	550	8.47	376.8	19818	12.64	10.11	-2087	2616	-4310	-3781

1.5 mm WELD OFFSET INITIAL IMPERFECTION

ID	D/t	p/p_y	d	F_y	t	r_i	A	p_y	FEA pres.	eq 2.5 $P\alpha$	eq 2.7 Pv	eq 2.11 P_p	eq 2.12 FEA P
			mm	MPa	mm	mm	mm^2	MPa	MPa	(kN)	(kN)	(kN)	(kN)
dt50x52ip15wp00	50.0	0.0	324	359	6.48	158.8	6332	15.28	0.00	-667	0	0	-667
dt50x52ip15wp40	50.0	0.4	324	359	6.48	158.8	6332	15.28	6.11	-667	273	-445	-839
dt50x52ip15wp80	50.0	0.8	324	359	6.48	158.8	6332	15.28	12.22	-667	546	-890	-1012
dt50x65ip15wp00	50.0	0.0	324	448	6.48	158.8	6332	19.06	0.00	-667	0	0	-667
dt50x65ip15wp40	50.0	0.4	324	448	6.48	158.8	6332	19.06	7.63	-667	340	-556	-882
dt50x65ip15wp80	50.0	0.8	324	448	6.48	158.8	6332	19.06	15.25	-667	681	-1111	-1097
dt50x80ip15wp00	50.0	0.0	324	550	6.48	158.8	6332	23.40	0.00	-667	0	0	-667
dt50x80ip15wp40	50.0	0.4	324	550	6.48	158.8	6332	23.40	9.36	-667	418	-682	-931
dt50x80ip15wp80	50.0	0.8	324	550	6.48	158.8	6332	23.40	18.72	-667	836	-1364	-1195
dt70x52ip15wp00	70.0	0.0	508	359	7.26	250.4	11251	10.72	0.00	-1185	0	0	-1185
dt70x52ip15wp40	70.0	0.4	508	359	7.26	250.4	11251	10.72	4.29	-1185	485	-796	-1496
dt70x52ip15wp80	70.0	0.8	508	359	7.26	250.4	11251	10.72	8.57	-1185	969	-1592	-1807
dt70x65ip15wp00	70.0	0.0	508	448	7.26	250.4	11251	13.37	0.00	-1185	0	0	-1185
dt70x65ip15wp40	70.0	0.4	508	448	7.26	250.4	11251	13.37	5.35	-1185	605	-993	-1573
dt70x65ip15wp80	70.0	0.8	508	448	7.26	250.4	11251	13.37	10.70	-1185	1210	-1987	-1962
dt70x80ip15wp00	70.0	0.0	508	550	7.26	250.4	11251	16.42	0.00	-1185	0	0	-1185
dt70x80ip15wp40	70.0	0.4	508	550	7.26	250.4	11251	16.42	6.57	-1185	743	-1219	-1662
dt70x80ip15wp80	70.0	0.8	508	550	7.26	250.4	11251	16.42	13.13	-1185	1485	-2439	-2138
dt90x52ip15wp00	90.0	0.0	762	359	8.47	376.8	19818	8.25	0.00	-2087	0	0	-2087
dt90x52ip15wp40	90.0	0.4	762	359	8.47	376.8	19818	8.25	3.30	-2087	854	-1407	-2640
dt90x52ip15wp80	90.0	0.8	762	359	8.47	376.8	19818	8.25	6.60	-2087	1708	-2814	-3193
dt90x65ip15wp00	90.0	0.0	762	448	8.47	376.8	19818	10.30	0.00	-2087	0	0	-2087
dt90x65ip15wp40	90.0	0.4	762	448	8.47	376.8	19818	10.30	4.12	-2087	1065	-1756	-2777
dt90x65ip15wp80	90.0	0.8	762	448	8.47	376.8	19818	10.30	8.24	-2087	2131	-3511	-3467
dt90x80ip15wp00	90.0	0.0	762	550	8.47	376.8	19818	12.64	0.00	-2087	0	0	-2087
dt90x80ip15wp40	90.0	0.4	762	550	8.47	376.8	19818	12.64	5.06	-2087	1308	-2155	-2934
dt90x80ip15wp80	90.0	0.8	762	550	8.47	376.8	19818	12.64	10.11	-2087	2616	-4310	-3781

3.0 mm WELD OFFSET INITIAL IMPERFECTION

ID	D/t	p/p_y	d	F_y	t	r_i	A	p_y	FEA pres.	eq 2.5 $P\alpha$	eq 2.7 Pv	eq 2.11 P_p	eq 2.12 FEA P
			mm	MPa	mm	mm	mm^2	MPa	MPa	(kN)	(kN)	(kN)	(kN)
dt50x52ip30wp00	50.0	0.0	324	359	6.48	158.8	6332	15.28	0.00	-667	0	0	-667
dt50x52ip30wp40	50.0	0.4	324	359	6.48	158.8	6332	15.28	6.11	-667	273	-445	-839
dt50x52ip30wp80	50.0	0.8	324	359	6.48	158.8	6332	15.28	12.22	-667	546	-890	-1012
dt50x65ip30wp00	50.0	0.0	324	448	6.48	158.8	6332	19.06	0.00	-667	0	0	-667
dt50x65ip30wp40	50.0	0.4	324	448	6.48	158.8	6332	19.06	7.63	-667	340	-556	-882
dt50x65ip30wp80	50.0	0.8	324	448	6.48	158.8	6332	19.06	15.25	-667	681	-1111	-1097
dt50x80ip30wp00	50.0	0.0	324	550	6.48	158.8	6332	23.40	0.00	-667	0	0	-667
dt50x80ip30wp40	50.0	0.4	324	550	6.48	158.8	6332	23.40	9.36	-667	418	-682	-931
dt50x80ip30wp80	50.0	0.8	324	550	6.48	158.8	6332	23.40	18.72	-667	836	-1364	-1195
dt70x52ip30wp00	70.0	0.0	508	359	7.26	250.4	11251	10.72	0.00	-1185	0	0	-1185
dt70x52ip30wp40	70.0	0.4	508	359	7.26	250.4	11251	10.72	4.29	-1185	485	-796	-1496
dt70x52ip30wp80	70.0	0.8	508	359	7.26	250.4	11251	10.72	8.57	-1185	969	-1592	-1807
dt70x65ip30wp00	70.0	0.0	508	448	7.26	250.4	11251	13.37	0.00	-1185	0	0	-1185
dt70x65ip30wp40	70.0	0.4	508	448	7.26	250.4	11251	13.37	5.35	-1185	605	-993	-1573
dt70x65ip30wp80	70.0	0.8	508	448	7.26	250.4	11251	13.37	10.70	-1185	1210	-1987	-1962
dt70x80ip30wp00	70.0	0.0	508	550	7.26	250.4	11251	16.42	0.00	-1185	0	0	-1185
dt70x80ip30wp40	70.0	0.4	508	550	7.26	250.4	11251	16.42	6.57	-1185	743	-1219	-1662
dt70x80ip30wp80	70.0	0.8	508	550	7.26	250.4	11251	16.42	13.13	-1185	1485	-2439	-2138
dt90x52ip30wp00	90.0	0.0	762	359	8.47	376.8	19818	8.25	0.00	-2087	0	0	-2087
dt90x52ip30wp40	90.0	0.4	762	359	8.47	376.8	19818	8.25	3.30	-2087	854	-1407	-2640
dt90x52ip30wp80	90.0	0.8	762	359	8.47	376.8	19818	8.25	6.60	-2087	1708	-2814	-3193
dt90x65ip30wp00	90.0	0.0	762	448	8.47	376.8	19818	10.30	0.00	-2087	0	0	-2087
dt90x65ip30wp40	90.0	0.4	762	448	8.47	376.8	19818	10.30	4.12	-2087	1065	-1756	-2777
dt90x65ip30wp80	90.0	0.8	762	448	8.47	376.8	19818	10.30	8.24	-2087	2131	-3511	-3467
dt90x80ip30wp00	90.0	0.0	762	550	8.47	376.8	19818	12.64	0.00	-2087	0	0	-2087
dt90x80ip30wp40	90.0	0.4	762	550	8.47	376.8	19818	12.64	5.06	-2087	1308	-2155	-2934
dt90x80ip30wp80	90.0	0.8	762	550	8.47	376.8	19818	12.64	10.11	-2087	2616	-4310	-3781

RECENT STRUCTURAL ENGINEERING REPORTS
Department of Civil and Environmental Engineering
University of Alberta

202. *Deformational Behavior of Line Pipe* by M. Mohareb, A.E. Elwi, G.L. Kulak and D.W. Murray, September 1994.

203. *Behaviour of Girth-Welded Line Pipe* by N. Yoosef-Ghodsi, G.L. Kulak and D.W. Murray, September 1994.

204. *Numerical Investigation of Eccentrically Loaded Tied High Strength Concrete Columns* by Jueren Xie, Alaa E. Elwi and James G. MacGregor, October 1994.

205. *Shear Strengthening of Concrete Girders Using Carbon Fibre Reinforced Plastic Sheets* by Efrosini H. Drimoussis and J.J. Roger Cheng, October 1994.

206. *Shrinkage and Flexural Tests of a Full-Scale Composite Truss* by Michael B. Maurer and D.J.Laurie Kennedy, 1994.

207. *Analytical Investigation of the Compressive Behaviour and Strength of Steel Gusset Plate Connections* by Michael C.H. Yam and J.J. Roger Cheng, December 1994.

208. *The Effect of Tension Flange Movement on the Strength of Point Loaded–Beams* by Dean Mullin and J.J. Roger Cheng, January 1995.

209. *Experimental Study of Transversely Loaded Continuous Steel Plates* by Kurt P. Ratzlaff and D.J. Laurie Kennedy, May 1995.

210. *Fatigue Tests of Riveted Bridge Girders* by Daniel Adamson and Geoffrey L. Kulak, July 1995.

211. *Fatigue of Riveted Tension Members* by Jeffrey DiBattista and Geoffrey L. Kulak, November 1995.

212. *Behaviour of Masonry Cavity Walls Subjected to Vertical Eccentric Loads* by Ru Wang, Alaa E. Elwi, Michael A. Hatzinikolas and Joseph Warwaruk, February 1996.

213. *Thermal Ice Loads on Structures* by Azita Azarnejad and Terry M. Hrudey, November 1996.

214. *Transmission of High Strength Concrete Column Loads Through Concrete Slabs* by Carlos E. Ospina and Scott D.B. Alexander, January 1997.

215. *Seismic Behaviour of Steel Plate Shear Walls* by Robert G. Driver, Geoffrey L. Kulak, D.J.Laurie Kennedy and Alaa E. Elwi, February 1997.

216. *Extended End Plate Moment Connections under Cyclic Loading* by Bryan T. Adey, Gilbert Y. Grondin and J.J. Roger Cheng, June 1997.

217. *Connection of Infill Panels in Steel Plate Shear Walls* by Ann S. Schumacher, Gilbert Y. Grondin and Geoffrey L. Kulak, August 1997.

218. *Shear Rehabilitation of G-Girder Bridges using CFRP Sheets* by John G.S. Alexander and J.J. Roger Cheng, October 1997.

219. *Seismic Evaluation of Steel Buildings with Concentrically Braced Frames* by Manoj S. Medhekar and D.J. Laurie Kennedy, October 1997.

220. *Rational Design of Prestressed and Reinforced Concrete Tanks* by Abdelaziz A. Rashed, David M. Rogowsky and Alaa E. Elwi, December 1997.

221. *Repair of Cracked Steel Elements using Composite Fibre Patching* by Gaylene D. Kennedy and J.J. Roger Cheng, May 1998.

222. *Strength of Joints that Combine Bolts and Welds* by Thomas J. Manuel and Geoffrey L. Kulak, July *1998.*

223. *Strip Model for Capacity of Slab-Column Connections* by Shahab Afhami, Scott D.B. Alexander, and Sidney H. Simmonds, August 1998.

224. *Behaviour of Large Diameter Line Pipe under Combined Loading* by Patrick R. DelCol, Gilbert Y. Grondin, J.J. Roger Cheng and David W. Murray, September 1998.

225. *An Analysis of the Cyclic Behaviour of Steel Gusset Plate Connections* by Scott S. Walbridge, Gilbert Y. Grondin, and J.J. Roger Cheng, September 1998.

226. *Rehabilitation of Unreinforced Masonry Walls with Externally Applied Fiber Reinforced Polymers* by Michael L. Albert, J.J. Roger Cheng, and A.E. Elwi, October, 1998.

227. *Fatigue of Bearing-Type Shear Splices* by Georg Josi, G.Y. Grondin, and G.L. Kulak, April, 1999.

228. *Out-of-Plane Cyclic Behavior of Masonry Walls Reinforced Externally with GFRP* by Marc D. Kuzik, A.E. Elwi, and J.J. Roger Cheng, August 1999.

229. *Cyclic Behavior of Stiffened Gusset Plate–Brace Member Assemblies* by Trina Nast, G.Y. Grondin, and J.J.R. Cheng, November 1999.

230. *Behaviour of Sleeper-supported Line Pipe* by Jeffrey D. DiBattista, J.J.R. Cheng, and D.W. Murray, April 2000.

231. *Field Assessment of Crowchild Trail Bridge* by Kong K. Taing, J.J.R. Cheng, and S. Afhami, January 2000.

232. *Ductile Fracture of Steel* by Heng Aik Khoo, J.J. Roger Cheng, and T.M. Hrudey, August 2000.

233. *Shear Lag in Bolted Cold-Formed Steel Angles and Channels in Tension* by Amy Sin-Man Yip and J.J. Roger Cheng, September 2000.

234. *Behaviour of Reinforced Concrete Beams Strengthened in Shear with FRP Sheets* by Christophe Deniaud and J.J. Roger Cheng, October 2000.

235. *Behaviour of Distortion-Induced Fatigue Cracks in Bridge Girders* by R. Fraser, G.Y. Grondin, and G.L. Kulak, December 2000.

236. *Stiffener Tripping in Stiffened Steel Plates* by I.A. Sheikh, A.E. Elwi and G.Y. Grondin, January 2001.

237. *Critical Buckling Strains for Energy Pipelines by* A.B. Dorey, J.J.R. Cheng and D.W. Murray, April 2001.